



The Design and Optimisation of Poly(Ionic Liquid) Stabilized Metal Nanoparticle Catalysts

Reece Paterson

A thesis submitted in partial fulfilment of the
requirements for the award of

Doctor of Philosophy

School of Natural and Environmental Sciences
Newcastle University

September 2024

Abstract

Metal nanoparticles have been explored extensively as catalysts for a range of reactions, yet the factors that influence their catalytic activity are ill-defined. Although the employment of surface ligands has become commonplace for nanoparticle synthesis, they are, for the most part, removed prior to catalysis. However, there is evidence that surface ligands can have a beneficial effect on the activity of metal nanoparticles through modification of the metal-surface electronic structure, or by working cooperatively with the nanoparticle to stabilise or activate substrates. Thus, this thesis expands on the synthesis and design of ligand functionalised poly(ionic liquids) as supports for generating metal nanoparticle catalysts for several transformations.

Catalysts that facilitate the conversion of carbon dioxide to useful commodities could play a significant role in our energy landscape. Due to their prominence in carbon capture, a series of amines were thus compared as surface ligands for the palladium nanoparticle catalysed hydrogenation of CO₂ to formate. In Chapter 2, an aniline functionalised catalyst was found to be more than twice as active as the corresponding unfunctionalised system, and coordination between the amine and the metal precatalyst was shown using XPS and NMR spectroscopy. However, the poly(ionic liquid) support was found to degrade under the conditions of catalysis. Chapter 3 attempts to address this with the development of new, chemically robust ionic liquid monomers and polymer designs. A highly cross-linked amine decorated poly(ionic liquid) was found to be the most stable, and the mechanism of CO₂ hydrogenation over palladium was explored at the metal-polymer interface using DRIFTS.

Chapter 4, meanwhile, describes how ruthenium nanoparticles immobilized on a phosphine oxide decorated poly(ionic liquid) demonstrate high activity for the selective reduction of nitroarenes to the corresponding N-phenylhydroxylamines. In Chapter 5, the same ruthenium nanoparticles were also found to be active for the hydrolysis of sodium borohydride to hydrogen gas, however, the greatest catalytic activity was achieved in the absence of phosphine oxide and polyethylene glycol groups.

Acknowledgements

Foremost, I must sincerely thank Dr Simon Doherty for his supervision over the course of this project. His keen eye for detail and seemingly infinite supply of useful experiments have significantly contributed to the investigations described in this thesis and have made me a more diligent scientist. I would also like to thank Dr Julian Knight for his co-supervision and wisdom in times of distress.

My thanks are given to our collaborators who have facilitated much of the characterisation that has made this thesis possible; to Dr Thomas Chamberlain and his team in Leeds University for providing TEM images of all the discussed NP materials; to Dr Elisabetta Arca for providing training and guidance on the running and interpretation of X-ray photoelectron spectroscopy; to Dr Christopher Hardacre and Dr Sarayute Chansai at the University of Manchester for their assistance in running the DRIFTS and TPD experiments discussed in Chapter 3; to my colleague Sam Power for completing the DFT calculations seen in Chapter 2; and a special thanks goes to Dr Corinne Wills and Dr Casey Dixon for providing an excellent service in the Newcastle NMR facility that has provided essential characterisation throughout this thesis, including all of the MAS-NMR spectra.

Essential thanks and appreciation is given to the colleagues who have given me friendship and support throughout my studies despite my constant antagonization – to Sam Power, Dominic Shiels, Fran Stals, Magda Pascual-Borràs, Felicity Frank, Hussam Alharbi, Adhwa Alharbi, Amar Mohammed, and Nathan Davison, I have enjoyed my time with all of you immensely.

I am sincerely grateful for the support my family have given me throughout my studies. My parents have been and always will be role models for their unshakeable work ethic and resilience. But above all, I am thankful for the love and support shown to me by my wife, Jordanna – thank you for enduring me at every step.

Lastly, to my daughter Harriet – your patience in these final weeks has not gone unnoticed and will be rewarded appropriately. I hope you surpass me in every way (not least in height).

Table of Contents

Abstract.....	i
Acknowledgements.....	iii
Table of Contents	iv
General Comments	vii
List of Figures	ix
List of Tables.....	xvii
List of Schemes.....	xviii
List of Abbreviations	xxi
List of Publications	xxiii
Chapter 1 – Introduction	1
1.1 After 2000 Years of Chemistry, Nanoparticles are Awarded the Nobel Prize	1
1.2 Metal Nanoparticles – Catalysis and Challenges	2
1.2.1 Nanoparticle Synthesis.....	6
1.2.2 Nanoparticle Stabilization	8
1.2.3 Can Ligands Tune NP Reactivity?	11
1.3 Ionic Liquids.....	14
1.3.1 Ionic Liquids in Catalysis	16
1.3.2 ILs as Stabilizers for Nanoparticle Catalysts.....	17
1.3.3 Solid Supported Ionic Liquid Phases	21
1.3.4 Covalently Immobilized Ionic Liquid Supports.....	23
1.4 Polymer Immobilized Ionic Liquids	26
1.4.1 PIILs as Catalyst Supports.....	27
1.4.2 Doherty PIILs	30
1.5 References.....	34
Chapter 2 – Amine-Modified Pd Catalysts for CO₂ Hydrogenation	42
2.1 Introduction	42
2.2 Synthesis and Characterisation of Monomer, Polymer and Catalyst Materials.....	45
2.2.1 Monomer and Polymer Synthesis	45
2.2.2 Precatalyst Synthesis and Characterisation	49
2.3 Thermal Hydrogenation of CO ₂	51
2.4 Exploring the Pd-N Interaction of Precatalysts 2.8a-e.....	60
2.5 Investigation of Aniline Cross-linking.....	66
2.6 The Fate of the Catalyst	67
2.7 Conclusion.....	74

2.8	Experimental.....	75
2.9	References	81
Chapter 3 – ‘Robust’ Catalysts for CO₂ Hydrogenation		85
3.1	Introduction.....	85
3.2	Synthesis of Robust Ionic Liquid Monomers	86
3.2.1	<i>Preparation of C₀ Ionic Liquid Monomer</i>	<i>86</i>
3.2.2	<i>Preparation of C₂ and C₃ Ionic Liquid Monomers</i>	<i>88</i>
3.3	Synthesis of Robust PIILs and PIIL Supported Precatalysts	93
3.4	Thermal Hydrogenation of CO ₂	96
3.5	Stability of New Polymer Immobilized Ionic Liquid Supports	97
3.6	A Highly Cross-Linked PIIL Support.....	100
3.7	The Iodide Problem	103
3.8	Reaction Mechanism	107
3.8.1	<i>In-situ DRIFTS Experiments</i>	<i>107</i>
3.8.2	<i>CO₂-Temperature Programmed Desorption</i>	<i>112</i>
3.8.4	<i>The Role of Water</i>	<i>115</i>
3.8.5	<i>Influence of Base Concentration</i>	<i>116</i>
3.8.6	<i>Role of the Formate Counterion</i>	<i>119</i>
3.8.7	<i>Proposed Reaction Mechanism</i>	<i>120</i>
3.9	Conclusion	121
3.10	Experimental.....	122
3.11	References	135
Chapter 4 – Ru Catalysed Selective Reduction of Nitroarenes to N-Phenylhydroxylamines		138
4.1	Introduction.....	138
4.2	Synthesis and Characterisation of Monomer, Polymer and Catalyst Materials	141
4.2.1	<i>Synthesis of Monomers</i>	<i>141</i>
4.2.2	<i>Synthesis and Characterisation of RuNP@OPPh₂PEGPIIL</i>	<i>142</i>
4.3	Selective Reduction of Nitrobenzene to N-Phenylhydroxylamine.....	148
4.4	Substrate Screening.....	152
4.5	Poisoning Study	156
4.6	Recycle and Reuse Studies	158
4.7	Conclusion	160
4.8	Experimental.....	161
4.9	References	167

Chapter 5 – Phosphine Oxide Stabilized Ruthenium Nanoparticles for the Hydrolytic Dehydrogenation of NaBH₄	170
5.1 Introduction	170
5.2 Catalyst Synthesis and Characterisation	172
5.3 Catalyst Comparison for NaBH ₄ Hydrolysis.....	175
5.4 Kinetic Studies.....	178
5.5 Reaction Mechanism.....	180
5.6 Catalyst Recycling and Poisoning Studies	183
5.7 Conclusion.....	187
5.8 Experimental.....	188
5.9 References.....	192
Appendix	195

General Comments

All reactions were conducted under an atmosphere of nitrogen, unless otherwise stated, using standard Schlenk techniques. Reagents were sourced from commercial suppliers and were used without further purification. Metal loadings of metal catalysts and precatalysts were determined using inductively coupled plasma optical emission spectroscopy (ICP-OES) on an Agilent 5800 ICP-OES instrument. FT-IR spectroscopy was performed on a Varian 800 FT-IR instrument (Varian Inc.).

NMR Spectroscopy

Solution-state ^1H , $^{13}\text{C}\{^1\text{H}\}$ and $^{31}\text{P}\{^1\text{H}\}$ NMR spectra for typical experiments were recorded on either a Bruker Avance II 400 MHz or Bruker Avance III 300 MHz NMR spectrometer. All chemical shifts are quoted in ppm relative to tetramethylsilane (^1H , ^{13}C) and nitromethane (^{15}N). All spectra were recorded at 298 K unless otherwise stated.

Solid-state ^{13}C MAS NMR, ^{15}N MAS NMR, and ^{31}P MAS NMR spectra were recorded at 125.78, 50.68 and 202.46 MHz, respectively, using a Bruker Avance III HD 500 NMR spectrometer with 4 mm rotors. They were obtained using cross-polarisation (^{13}C and ^{15}N) and sideband suppression (^{13}C) with a 5-10 s relaxation delay, 1.2-2.3 ms (^{13}C), 1.7-2.3 ms (^{15}N) and 3.5 ms (^{31}P) contact time at ambient probe temperature ($\sim 25^\circ\text{C}$) and at a MAS rate of 10 kHz. Spectral referencing was with respect to an external sample of neat tetramethylsilane (carried out by setting the high-frequency signal from adamantane to 37.8 ppm).

Electron Microscopy

SEM images were acquired on a Tescan Vega 3LMU scanning electron microscope with digital image collection. Samples for transmission electron microscopy (TEM) were dispersed in ethanol using an ultrasonic bath and deposited on lacey carbon film coated copper grids. TEM images were acquired on a FEI Tecnai TF20 field emission gun microscope operating at 200 kV. NP size distribution histograms were obtained from measurements of at least 100 different NPs assuming a spherical shape and with random distribution.

X-ray Photoelectron Spectroscopy

XPS analysis was conducted using a Kratos Axis Ultra DLD at Harwell Research Campus (**Chapter 2** and **3**) and using a Thermo Scientific K-alpha X-ray Photoelectron SpectrometerTM at NEXUS, Newcastle University (**Chapter 4** and **5**) with a monochromatic Al K α ($\lambda = 1486.7$ eV) X-ray source operated at 225 W. The analysis chamber base-pressure was better than 1×10^{-8}

mbar. Samples were mounted using double-sided carbon tape for polymers and PdCl₄ precatalysts, and copper tape for PdNP/RuNP samples. Surface charge compensation was performed using a low energy electron flood gun. Initial survey spectra were recorded at a pass energy of 80 eV, using a step size of 0.5 eV, with a scan range between 0 – 1400 eV. High resolution spectra were then collected for individual elements at a pass energy of 20 eV, using a step size of 0.1 eV. The data presented has not been rescaled with respect to any internal or external reference, instead interpretation relied on the comparison of binding energy separations.¹ Data analysis was performed using Igor Pro software with a custom-written program from Schmid et al.² Curves were fitted using a Gaussian/Lorentzian peak shape with a ratio of 70:30 and backgrounds were subtracted using a Shirley algorithm. Metallic Pd 3d signals were fit using an asymmetric Gaussian-Lorentzian line shape, similar to asymmetric pseudo-Voigt profiles previously reported for Pd 3d and Pt 4f.²

References

K. N. Wood and G. Teeter, *ACS Appl. Energy Mater.*, 2018, **1**, 4493–4504.

² M. Schmid, H. P. Steinrück and J. M. Gottfried, *Surf. Interface Anal.*, 2014, **46**, 505–511.

List of Figures

Chapter 1 – Introduction

Figure 1.1 Illustration of the gold nanoparticle growth mechanism.

Figure 1.2 Cartoon showing the speciation of heterogeneous Pd catalysts for cross-coupling reactions.

Figure 1.3 TEM images of silica encapsulated PdNP catalysts for Suzuki-Miyaura cross-couplings after (a) 43% and (b) 100% conversion of substrates. Catalyst isolated after 100% conversion of substrates shows Pd redepositing on the silica shell following the formation of soluble leached species.

Figure 1.4 LC-TEM images over a period of 50 seconds show Cd-CdCl₂ NP ripening through the interaction of crack-defects. White scale bar = 5 nm.

Figure 1.5 Schematic showing the various stages of iron stearate (FeSt₂) thermal decomposition towards iron oxide NPs. FeSt₂ was reported by the same group to exist as the polynuclear complex [Fe₃(μ₃-O)St₆·xH₂O]Cl.

Figure 1.6 Cartoon showing the effect of sodium citrate concentration on Au nanoparticle size.

Figure 1.7 (a) Schematic of PdNP synthesis *via* the thermal degradation of a Pd-TOP complex in the presence of various amounts of oleylamine (b), and (c) the corresponding plots of NP size over time, as determined by *in-situ* SAXS.

Figure 1.8 Illustration of the observed Knight shift in the ¹³C NMR spectra for ¹³C labelled NHC coordinated to PdNP surfaces. The apparent Knight shift increases and the ¹³C peak broadens with increasing particle size.

Figure 1.9 Effect of covalent organic framework functionalisation on the activity and electron density of PdCu₂ bimetallic nanoparticles as catalysts for the partial hydrogenation of phenylacetylene.

Figure 1.10 Major developments in ionic liquid design over time.

Figure 1.11 AC-STEM images of (a) 'dynamic' 0.12wt% PdNP in [BMIM][NTf₂] over time and (b) 2.0 wt% PdNP in [BMIM][NTf₂]. (c) Plot of conversion and selectivity for the diazoethyl acetate mediated cyclopropanation of styrene against the wt% loading of Pd in the IL-dispersed catalyst.

Figure 1.12 Cartoon of solid supported metal nanoparticles (a) dispersed in an IL solvent and (b) coated in a thin ionic liquid layer, commonly referred to as a ‘solid ionic liquid phase’.

Figure 1.13 Immobilization of $[\text{HRh}(\text{CO})(\text{tppti})_3]$ on silica-supported ionic liquid, used as catalyst for the hydroformylation of hexene to heptanal conducted in IL $[\text{BMIM}][\text{BF}_4]$.

Figure 1.14 (a) Structure of *N*-alkyl-substituted poly(vinyl imidazolium bromide) polymers and the corresponding cryo-TEM images when $x = 11$ (b).

Figure 1.15 (a) Preparation of carbene immobilized $\text{Pd}@ \text{PIL}$ materials for use as catalysts in the Heck reaction (b).

Figure 1.16 Cartoons of (a) CuNPs and the coordination modes of pyridine functionalised PIL to (b) CuNPs and (c) Cu^I impregnated PIL at the NP surface.

Figure 1.17 (a) Schematic of $\text{PdNP}@ \text{HAD-PIL}$ catalysed Suzuki-Miyaura coupling reaction and the corresponding comparison of catalytic activity as a function of heteroatom donor (HAD) group (b).

Chapter 2 – Amine-Modified Pd Catalysts for CO_2 Hydrogenation

Figure 2.1 (a) Cyclic voltammograms showing the electrochemical reduction of CO_2 in the presence of various IL electrolytes. (b) Proposed binding modes of IL **Im-2** with a surface bound carboxylate species.

Figure 2.2 Stacked ^1H NMR spectra of polymers **2.7a-d** (400 MHz, Methanol- d_4). For clarity, the solvent peaks at 4.87 and 3.33 ppm have been removed, though unmodified spectra can be found in **Appendix A.2.2**.

Figure 2.3 Stacked FT-IR spectra of polymers **2.7a-d**.

Figure 2.4 Solid state ^{13}C CP-MAS NMR spectra of polymer **2.7b** and precatalyst **2.8b** (500 MHz).

Figure 2.5 SEM images of polymers **2.7a-b** and precatalysts **2.8a-b**; white scale bar is 20 μm .

Figure 2.6 Comparison of initial TOF after 2 hours against various catalysts loaded on PIL support **2.7a**. Reaction conditions: Catalyst (6 $\mu\text{mol}_{\text{metal}}$), H_2/CO_2 (20:20 bar), 100 $^\circ\text{C}$, H_2O (20 mL), NaHCO_3 (0.65 M). $\text{TOF} = \text{mol}_{\text{formate}} \cdot \text{mol}_{\text{Pd}}^{-1} \cdot \text{h}^{-1}$

Figure 2.7 (a) Screening of various bases for the hydrogenation of CO₂, catalysed by **2.8a** (6 μmol Pd), at 100 °C with 40 bar of reactive gas. (b) Screening of reaction temperature for the hydrogenation of CO₂ catalysed by **2.8b.66** (6 μmol Pd), with 40 bar of reactive gas. (c) Screening of stirring speed for the hydrogenation of CO₂ catalysed by **2.8a** (6 μmol Pd), at 100 °C with 40 bar of reactive gas. (d) Screening of total gas pressure (1 : 1 mixture of H₂ : CO₂), catalysed by **2.8a** (6 μmol Pd), at 100 °C.

Figure 2.8 (a) Plot showing TOF against polymer substituent for the thermal hydrogenation of CO₂ to formate using several PdCl₄@PIIL based precatalysts. All polymer supports have an IL:R ratio of 1:1. (b) Plot of TOF against mol% loading of amine for PdCl₄@NH₂PIIL catalysts.

$$^a\text{TOF} = \text{mol}_{\text{formate}} \cdot \text{mol}_{\text{Pd}}^{-1} \cdot \text{h}^{-1}$$

Figure 2.9 Electron density maps of aniline, *N,N*-dimethylaniline, and benzylamine respectively, with charges at the nitrogen atom (blue) given below the structures.

Figure 2.10 Profile of activity against time for PdCl₄@66NH₂PIIL (**2.8b.66**) and PdCl₄@PIIL (**2.8a**) catalysed hydrogenation of CO₂.

Figure 2.11 (a) Particle size distribution of nanoparticles isolated post-catalysis from pre-catalyst **2.8b.66**, where the inset shows a TEM image of the same material (white size bar = 10 nm). (b) Average NP sizes for catalysts generated from pre-catalysts **2.8a-e** after 2 hours of hydrogenation.

Figure 2.12 Recycling study conducted using **2.8b.66** (6 μmol) with reaction times of 16 hours. Catalyst was isolated by centrifugation and washed with deionized water (3 x 10 mL).

Figure 2.13 N 1s core level XPS region (a) polymer **2.7b.66**, (b) precatalyst **2.8b.66** and of precatalysts **2.8a-d**. Spectra also show the residuals corresponding to the line fitting when a N-Pd peak is omitted and included. Black line = overall fitting; Red dotted line = background.

Figure 2.14 N 1s core level XPS region of precatalysts **2.8a-d**. Black line = overall fitting; Red dotted line = background.

Figure 2.15 Relationship between %Pd-NR₂ interaction as determined by N1s XPS and TOF (blue) as well as wt% Pd loading as determined by ICP-OES (orange) for pre-catalysts **2.8b-d**.

Figure 2.16 (a) Pd 3d core level XPS region for precatalysts **2.8a-e** and precursor Na₂PdCl₄. (b) Comparison of residual standard deviation for precatalyst **2.8b** with and without Pd-N peak fitting. Black line = overall fitting; Red dotted line = background.

Figure 2.17 Plot of BE difference between the Pd 3d_{5/2} and the aliphatic C 1s core electrons against the mol% loading of amine on the pre-catalyst support.

Figure 2.18 CP-MAS ¹⁵N NMR spectra of **2.7b.66** and **2.8b.66** (a) as well as **2.7e** and **2.8e** (b). Spectra were referenced to a sample of nitromethane.

Figure 2.19 (a) ¹H-¹⁵N HSQC NMR and (b) ¹H-¹⁵N HMBC NMR spectrum of polystyrylaniline **1e** (700 MHz, DMSO-d₆). (c) Reaction scheme of possible alkene hydroamination during the polymerisation of 4-vinylaniline to afford polymer **2.7e**.

Figure 2.20 Pd 3d core level XPS region for NP materials isolated from the *in-situ* hydrogenation of precatalysts **2.8a-e**. Black line = overall fitting; Red dotted line = background.

Figure 2.21 Plot of BE difference between the Pd 3d_{5/2} and the aliphatic C 1s core electrons against the mol% loading of amine on the support for PdCl₄ pre-catalyst (□) and PdNP (○) samples.

Figure 2.22 CP-MAS ¹⁵N NMR spectra of (a) **2.7b.66** (T₁ = 1.52 s), (b) **2.8b.66** (T₁ = 1.33 s) and (c) NP catalyst generated *in-situ* from **2.8b.66** (T₁ = 0.41 s). ¹⁵N NMR spectra were referenced to nitromethane with a MAS rate of 10 kHz.

Chapter 3 – ‘Robust’ Catalysts for CO₂ Hydrogenation

Figure 3.1 ¹H NMR spectra of polymers **3.19a-d** (400 MHz, DMSO-d₆).

Figure 3.2 SEM images of polymers **3.19a-b** and precatalysts **3.20a-b**; white scale bar is 20 μm.

Figure 3.3 (a) Activity-time profile for the hydrogenation of CO₂ to formate catalysed by materials generated from precatalysts **3.20a-d** and (b) a comparison of TOF and NP size after 2 hours of catalysis. Reaction conditions: PdCl₄-loaded amine polymer (6 μmol), 1:1 H₂/CO₂ (40 bar), 100 °C, K₂CO_{3(aq)} (20 mL, 0.65 M).

Figure 3.4 N1s core levels of polymer, precatalyst and catalyst isolated after 2 hours of hydrogenation for (a) **C1** and (b) **C3** functionalised materials. Black line = overall fitting; Red dotted line = background.

Figure 3.5 SEM images of polymer **3.21** and precatalyst **3.22**; white scale bar is 20 μm.

Figure 3.6 (a) Comparison of initial TOF and catalyst stability (IL remaining as determined by XPS) against mol% cross-linker incorporated into the polymer support for PdCl₄-loaded precatalysts. Initial TOFs were measured after 2 hours of catalysis. (b) Recycling study comparing catalysts generated from PdCl₄@C₁PIIL (**3.20b**) and PdCl₄@CL₁PIIL (**3.22**) as a function of the %initial activity per run of the catalyst. Activity was measured over 14 hours using 17 μmol palladium dispersed in an aqueous solution of K₂CO₃ (20 mL, 0.65 M).

Figure 3.7 Pd 3d core level XPS region for precatalysts **3.20a-d**. Black line = overall fitting; Red dotted line = background.

Figure 3.8 Pd 3d core level XPS region for nanoparticles generated from precatalysts **3.20a-d** following 2 hours of hydrogenation. Black line = overall fitting; Red dotted line = background.

Figure 3.9 Pd 3d core level XPS region of **3.21**-supported PdI₄ (left) and the same precatalyst isolated after 2 hours of catalysis. Black line = overall fitting; Red dotted line = background.

Figure 3.10 *In-situ* DRIFTS spectra of surface species over PdNP@CL₁PIIL. Black spectra show the results from a dry feed of 10 vol% CO₂ diluted with Ar over 10 minutes. After this time 4 vol% H₂O vapour was introduced to the gas feed, and the corresponding spectra are shown in blue. The light blue spectra show CO₂ + H₂O absorption up to 5 minutes.

Figure 3.11 *In-situ* DRIFTS spectra of surface species over (a) PdNP@CL₁PIIL and (b) PdNP@PIIL. Samples were first saturated with a 10 vol% CO₂ + 4 vol% H₂O feed diluted with helium (blue) before introducing 10 vol% H₂ to the gas feed (red) and monitoring the spectra over time.

Figure 3.12 *In-situ* DRIFTS spectra of surface-bound CO (10 vol%) over PdNP@CL₁PIIL (pink) and PdNP@PIIL (grey), generated from the hydrogenation of **3.22** and **2.8a**, respectively.

Figure 3.13 CO₂-TPD graphs of (a) PdNP@CL₁PIIL, (b) PdNP@PIIL, (c) PdCl₄@CL₁PIIL (**3.22**), and (d) PdNP@C₁PIIL. Catalyst materials were first pre-treated with CO₂ at 40 °C for 1 hour, followed by purging with He with ramping temperature. The values in black show the total amount of CO₂ desorbed from the materials when heated up to 160 °C.

Figure 3.14 Investigation of water-derived proton incorporation during the formation of potassium formate. (a) Hydrogenation of CO₂ in a solution of D₂O charged with **3.22** (6 μmol). (b) H/D scrambling experiment conducted in D₂O catalysed by pre-reduced PdCl₄@CL₁

(6 μmol). The percentages represent the relative ratio of the two isotopologues rather than yields.

Figure 3.15 Plot of TOF against potassium carbonate concentration. Reaction conditions: **3.22** (6 μmol Pd), 1:1 H_2/CO_2 (40 bar), 100 $^\circ\text{C}$, 2 hours, H_2O (20 mL).

Figure 3.16 Comparison of aqueous solutions of alkali metal bases as additives in the hydrogenation of CO_2 to formate. Reaction conditions: $\text{PdCl}_4@\text{CL}_1\text{PIIL}$ (6 μmol), 1:1 H_2/CO_2 (40 bar), 100 $^\circ\text{C}$, 2 hours.

Figure 3.17 Comparison of aqueous solutions of alkali metal carbonate bases as additives in the hydrogenation of CO_2 to formate. Reaction conditions: $\text{PdCl}_4@\text{CL}_1\text{PIIL}$ (6 μmol), 1:1 H_2/CO_2 (40 bar), x M base (x = 1.0, 0.09) 100 $^\circ\text{C}$, 2 hours.

Figure 3.18 Proposed reaction mechanism for the PdNP catalysed hydrogenation of CO_2 to formate over aniline decorated supports.

Chapter 4 – Ru Catalysed Selective Reduction of Nitroarenes to *N*-Phenylhydroxylamines

Figure 4.1 Proposed reaction mechanism for the direct reduction of nitrobenzene (**NO2**) to aniline (**NH2**) and the condensation pathway to aniline proceeding via the reaction of nitrosobenzene (**NSB**) with *N*-phenylhydroxylamine (**NHOH**) to form azoxybenzene (**N2O**).

Figure 4.2 (a) ^1H (b) $^{31}\text{P}\{^1\text{H}\}$ (400 MHz, Methanol- d_4) and (c) $^{13}\text{C}\{^1\text{H}\}$ (400 MHz, CDCl_3) NMR spectra of polymer **4.7**.

Figure 4.3 Solid state CP MAS $^{31}\text{P}\{^1\text{H}\}$ NMR spectra (500 MHz) of $\text{RuNP}@\text{OPPh}_2\text{PEGPIIL}$, **4.8**, ran with MAS speeds of 10, 8 and 5 kHz.

Figure 4.4 (a) TEM image of ruthenium nanoparticle catalyst **4.8**, with (b) lattice fringe d-spacing of a ruthenium nanoparticle. (c) Particle size distribution derived from counting >100 particles. (d) HAADF-STEM image and (e-i) corresponding EDX elemental mapping.

Figure 4.5 XPS analysis of the (a) C 1s and (b) Ru 3p $_{3/2}$ regions of catalyst **4.8**. Black line = overall fitting; Red dotted line = background.

Figure 4.6 (a) Composition time profile of **4.8** catalysed nitrobenzene reduction to *N*-phenylhydroxylamine, conducted in batch reactions. (b) Composition time profile of **4.8** catalysed nitrobenzene reduction conducted in ethanol- d_6 within an NMR tube under an inert atmosphere – the sample was maintained at 40 $^\circ\text{C}$, and ^1H NMR spectra were recorded

periodically on a 700 MHz Bruker spectrometer over 4 days until near quantitative conversion to aniline was observed.

Figure 4.7 (a) Composition time profile of **4.8** catalysed nitrobenzene reduction to *N*-phenylhydroxylamine, conducted in air. (b) Decomposition profile of *N*-phenylhydroxylamine dissolved in ethanol stirring in air. Conversion to azoxybenzene was monitored by analysing aliquots by ^1H NMR spectroscopy.

Figure 4.8 Poisoning study conducted by pre-stirring catalyst **4.8** for various amounts of time in the presence of (a) aniline and (b) *N,N*-dimethyl-4-nitrobenzene prior to the addition of hydrazine hydrate and nitrobenzene.

Figure 4.9 (a) Recycling study of catalyst **4.8** conducted at 10x scale of optimum conditions and (b) corresponding TEM analysis of catalyst isolated after 5 recycles. (c) Hot filtration study where the reaction mixture was isolated after 30 minutes of a standard experiment under the optimum conditions and monitored by ^1H NMR spectroscopy at regular intervals. (d) Reuse study of catalyst **4.8**, where the reaction mixture was recharged with additional nitrobenzene (1 mmol) and hydrazine hydrate (3 mmol) after 1 hour of reaction time at 40 °C.

Chapter 5 – Phosphine Oxide Stabilized Ruthenium Nanoparticles for the Hydrolytic Dehydrogenation of NaBH_4

Figure 5.1 XPS spectra showing the Ru $3p_{3/2}$ region for catalysts **5.2a-c** and **4.8**. Black line = overall fitting; Red dotted line = background.

Figure 5.2 (a) RuNP@X-PIIL (0.2 mol%) catalysed hydrolysis of NaBH_4 (0.021 g, 0.56 mmol) in H_2O (2 mL) at 30 °C. (b) The corresponding initial TOFs and conversions, where $\text{TOF} = \text{mol}_{\text{H}_2}\text{mol}_{\text{Ru}}^{-1}\text{min}^{-1}$. Results averaged from at least two runs.

Figure 5.3 (a) Initial TOF's corresponding to the RuNP@PIIL (0.25 mol%) catalysed hydrolysis of NaBH_4 (0.021 g) in $\text{NaOH}_{(\text{aq})}$ solution of various concentrations (2 mL) at 30°C. (b) Expansion of the region at low concentrations of NaOH.

Figure 5.4 Kinetic studies showing: (a) RuNP@PIIL catalysed hydrolysis of NaBH_4 over various temperatures (b) Arrhenius plot of NaBH_4 hydrolysis from 293-313 K (c) RuNP@PIIL catalysed hydrolysis of NaBH_4 over various catalyst loadings (d) Plot showing \ln of reaction rate against \ln of catalyst concentration where slope m is the reaction order in catalyst concentration (e) RuNP@PIIL catalysed hydrolysis of NaBH_4 over various concentrations of

NaBH₄ in alkaline solution (pH 13) (f) Plot showing ln of reaction rate against ln of NaBH₄ concentration where slope m is the reaction order in NaBH₄ concentration.

Figure 5.5 (a) RuNP@PIIL (0.2 mol%) catalysed reaction of NaBH₄ (0.021 g, 0.56 mmol) in H₂O/D₂O (2 mL) at 30 °C. (b) RuNP@PIIL (100 mol%) catalysed reaction of NaBH₄/NaBD₄ (1/1.1 mg, 0.03 mmol) in H₂O (200 mL) at 30 °C.

Figure 5.6 Recycling study showing the RuNP@PIIL (2 mol%) catalysed hydrolysis of NaBH₄ (0.021 g, 0.56 mmol) in H₂O (20 mL) at 30 °C, where the same catalyst was recycled over 6 runs. Before the 6th run, the catalyst was isolated and washed before reuse. Red bars (left) = TOF, black bars (right) = Conversion%

Figure 5.7 ¹¹B{¹H} NMR spectra of aqueous solutions of NaBH₄, NaBO₂, and the filtered product mixture of a **5.2a** catalysed hydrolysis of NaBH₄. The spectrum of NaBH₄ was acquired in an aqueous solution of 0.5 M NaOH to prevent hydrolysis.

Figure 5.8 A plot of pH over time against conversion over time for the RuNP@PIIL (2 mol%) catalysed reaction of NaBH₄ (0.021 g, 0.56 mmol) in H₂O (20 mL) at 30 °C.

Figure 5.9 (a) RuNP@PIIL (0.25 mol%) catalysed reaction of NaBH₄ (0.021 g, 0.56 mmol) in H₂O (2 mL) at 30 °C, after pre-stirring RuNP with NaBO₂·4H₂O (76.5 mg, 0.56 mmol) for x minutes in H₂O. (b) The respective initial TOFs over various poison stirring times.

Figure 5.10 (a) Leaching study where the RuNP@PIIL (0.2 mol%) catalysed hydrolysis of NaBH₄ (0.021 g) in H₂O (2 mL) was stopped and filtered at ca. 60% conversion. Gas evolution from the resulting filtrate was measured – negative readings due to subtraction of background reaction. (b) Leaching study with RuNP@PIIL (7.5 mol%) where the filtrate was charged again with NaBH₄ (0.021 g) and gas evolution measured (red data points).

List of Tables

Chapter 1 – Introduction

Table 1.1 Most commonly studied ionic liquid cations and anions.

Chapter 2 – Amine-Modified Pd Catalysts for CO₂ Hydrogenation

Table 2.1 %Loss of Pd as determined by ICP-OES following 2 hour hydrogenation reactions.

Table 2.2 Loss of imidazolium N as determined by analysis of N 1s XP spectra after 2 hours of catalysis.

Chapter 3 – Allegedly Robust Catalysts for CO₂ Hydrogenation

Table 3.1 Loss of imidazolium N as determined by analysis of N 1s XP spectra after 2 hours of catalysis.

Chapter 4 – Ru Catalysed Selective Reduction of Nitroarenes to *N*-Phenylhydroxylamines

Table 4.1 Optimisation of reaction conditions for the selective reduction of nitrobenzene to *N*-phenylhydroxylamine.

Table 4.2 Partial reduction of aromatic and heteroaromatic nitro compounds to the corresponding hydroxylamine or amine catalysed by **4.8**.

Table 4.3 Partial reduction of electron rich aromatic and heteroaromatic nitro compounds to the corresponding hydroxylamine or amine catalysed by **4.8**.

Chapter 5 – Phosphine Oxide Stabilized Ruthenium Nanoparticles for the Hydrolytic Dehydrogenation of NaBH₄

Table 5.1 Average RuNP diameters derived from TEM micrographs. Micrographs and associated size histograms can be found in **Appendix A.5.4**.

Table 5.2 Absolute RuO₂ binding energies and the corresponding BE separation between the Ru 3p_{3/2} peak and the aliphatic C 1s region.

List of Schemes

Chapter 1 – Introduction

Scheme 1.1 Examples of various “bottom up” and “top down” approaches towards the synthesis of metal nanoparticles.

Scheme 1.2 Imidazolium-derived carbene formation over IrNPs. Hydrogenation of the IrNP precursor using D₂ led to H/D scrambling at the imidazolium protons.

Scheme 1.3 The hydrogenation pathway of furfuralacetone (**1.1**) to 4-(tetrahydrofuranyl)butan-2-ol (**1.4**) catalysed by various SILP-supported RhNP catalysts.

Chapter 2 – Amine-Modified Pd Catalysts for CO₂ Hydrogenation

Scheme 2.1 Generalised schematic of the direct hydrogenation of carbon dioxide to formic acid.

Scheme 2.2 Preparation of imidazolium ionic liquid **2.1** (a) and corresponding cross-linker **2.3** (b) through nucleophilic substitutions of 4-vinylbenzylchloride.

Scheme 2.3 Wittig reaction of 4-(dimethylamino)benzaldehyde to afford alkene **2.4**.

Scheme 2.4 Preparation of 4-vinylbenzylamine **2.6** *via* a Gabriel synthesis from the corresponding haloalkane.

Scheme 2.5 Preparation of amine decorated PIIL supports **2.7a-d**, *via* radical initiated polymerisation. Polymers contained *ca.* 5 mol% cross-linker where $x = 0.91$, $y = 1$, $z = 0.09$.

Scheme 2.6 Preparation of PdCl₄-loaded PIILs **2.8a-d**. Where $x = 0.91$, $y = 1$, $z = 0.09$.

Chapter 3 – Allegedly Robust Catalysts for CO₂ Hydrogenation

Scheme 3.1 Proposed novel ionic liquid monomers stable to hydrogenation.

Scheme 3.2 Attempted N-aryl coupling of 2-methylimidazole to *para*-substituted arylbromides.

Scheme 3.3 Preparation of monomer **3.3** *via* (a) oxidative N-aryl coupling of 2-methylimidazole to 4-formylphenylboronic acid, followed by (b) Wittig-olefination of the imidazole substituted benzaldehyde and then the subsequent (c) amine quarternisation with methyl iodide.

Scheme 3.4 Preparation of **3.4** *via* a Suzuki-Miyaura cross-coupling reaction.

Scheme 3.5 (a) Preparation of alcohols **3.4** and **3.5** *via* a decarboxylative Heck cross-coupling reaction. (b) Mesylation of alcohols **3.4** and **3.5**, and (c) the attempted neat substitution of the resulting mesylated products.

Scheme 3.6 (a) Preparation of **3.8** and **3.9** *via* Suzuki-Miyaura cross-coupling reactions, followed by their subsequent (b) Wittig-olefination, and (c) the attempted neat substitution of the resulting haloalkanes products.

Scheme 3.7 (a) Nucleophilic substitution of halides **3.10** and **3.11** with 2-methylimidazolate, (b) methyl iodide mediated quarternisation of the resulting imidazoles, (c) salt metathesis between **3.16** and **3.17** and NaCl to afford the corresponding imidazolium chloride salts.

Scheme 3.8 Preparation of amine decorated PIIL supports **3.19a-d**, *via* radical initiated polymerisation.

Scheme 3.9 Preparation of PdCl₄-loaded PIILs **3.20a-d**.

Scheme 3.10 Preparation of amine decorated cross-linked PIIL support **3.21**, *via* a radical initiated polymerisation.

Scheme 3.11 Anion exchange of monomer **2.1** to form 2,3-dimethyl-1-(4-vinylbenzyl)-imidazolium iodide.

Chapter 4 – Ru Catalysed Selective Reduction of Nitroarenes to *N*-Phenylhydroxylamines

Scheme 4.1 Tautomeric forms of a secondary phosphine oxide and its potential binding modes to a metal surface.

Scheme 4.2 Preparation of PEG-modified imidazolium bromide monomer, **4.4**.

Scheme 4.3 Preparation of phosphine-decorated styrene monomer, **4.5**, *via* Grignard reaction.

Scheme 4.4 Preparation of phosphine oxide decorated styrene monomer, **4.6**.

Scheme 4.5 Synthesis of OPPh₂PEGPIIL, **4.7**, followed by the wet impregnation of RuCl₃ and subsequent reduction to RuNP@OPPh₂PEGPIIL, **4.8**. Where $x = 1.86$, $y = 1$, $z = 0.14$

Scheme 4.6 Proposed mechanism for 1,4-diaminobenzene formation *via* elimination of hydroxide from 4-aminoarylhydroxylamine to form imine intermediate.

Chapter 5 – Phosphine Oxide Stabilized Ruthenium Nanoparticles for the Hydrolytic Dehydrogenation of NaBH₄

Scheme 5.1 Preparation of RuNP@X-PIIL via wet impregnation of functionalised PIILs with RuCl₃ followed by reduction with NaBH₄. Adjoining table details polymer composition and polymer/catalyst reference codes used in this chapter. Where $x = 1.86$, $y = 1$, $z = 0.14$.

Scheme 5.2 Proposed reaction mechanism of ruthenium catalysed borohydride hydrolysis following the chemisorption of BH₄⁻ to the ruthenium surface.

List of Abbreviations

δ – Chemical shift (ppm)

BDMIM – 1-Butyl-2,3-dimethylimidazolium

BE – Binding energy

BMIM – 1-Butyl-3-methylimidazolium

Bu – Butyl

COD – Cyclooctadiene

COT - Cyclooctatriene

CP – Cross polarisation

cSILP – Covalently supported ionic liquid phase

DFT – Density functional theory

DMF – Dimethylformamide

DMSO – Dimethylsulfoxide

DRIFTS – Diffuse reflectance infrared Fourier transform spectroscopy

EMIM – 1-Ethyl-3-methylimidazolium

EXAFS – Extended X-ray absorption fine structure

FA – Formic acid

FT-IR – Fourier transform infrared

FWHM – Full width at half maximum

ICP-OES – Inductively coupled plasma optical emission spectroscopy

IL – Ionic liquid

*i*Pr - Isopropyl

MAS – Magic angle spinning

NHC – *N*-Heterocyclic carbene

NMR – Nuclear magnetic resonance

NP – Nanoparticle

PEG – Polyethylene glycol

PIL – Poly(ionic liquid)

PIIL – Polymer immobilized ionic liquid

ppm – Parts per million

PVP – Polyvinylpyrrolidone

rpm – Rotations per minute

SAXS – Small-angle X-ray scattering

SEM – Scanning electron microscopy

SILP – Supported ionic liquid phase

TEM – Transmission electron microscopy

THF – Tetrahydrofuran

TOF – Turnover frequency

TON – Turnover number

TOSS – Total suppression of spinning sidebands

TPO – Temperature programmed oxidation

XANES – X-ray absorption near edge structure

XPS – X-ray photoelectron spectroscopy

List of Publications

Chapter 2:

Amine-modified polyionic liquid supports enhance the efficacy of PdNPs for the catalytic hydrogenation of CO₂ to formate

R. Paterson, L. E. Fahy, E. Arca, C. Dixon, C. Y. Wills, H. Yan, A. Griffiths, S. M. Collins, K. Wu, R. A. Bourne, T. W. Chamberlain, J. G. Knight and S. Doherty, *Chem. Commun.*, 2023, **59**, 13470–13473.

Chapter 4:

Highly efficient and selective partial reduction of nitroarenes to N-arylhydroxylamines catalysed by phosphine oxide-decorated polymer immobilized ionic liquid stabilized ruthenium nanoparticles

R. Paterson, A. A. Alharbi, C. Wills, C. Dixon, L. Šiller, T. W. Chamberlain, A. Griffiths, S. M. Collins, K. Wu, M. D. Simmons, R. A. Bourne, K. R. J. Lovelock, J. Seymour, J. G. Knight and S. Doherty, *Mol. Catal.*, 2022, **528**, 112746.

Chapter 5:

Heteroatom modified polymer immobilized ionic liquid stabilized ruthenium nanoparticles: Efficient catalysts for the hydrolytic evolution of hydrogen from sodium borohydride

R. Paterson, H. Y. Alharbi, C. Wills, T. W. Chamberlain, R. A. Bourne, A. Griffiths, S. M. Collins, K. Wu, M. D. Simmons, R. Menzel, A. F. Massey, J. G. Knight and S. Doherty, *J. Catal.*, 2023, **417**, 74–88.

Chapter 1

Introduction

1.1 After 2000 Years of Chemistry, Nanoparticles are Awarded the Nobel Prize

There are some liberties taken in the above title: the Nobel Prize was awarded in 2023 for the discovery and synthesis of quantum dots, semiconductor nanoparticles whose size can influence their optical properties.¹ But the optical properties of metal nanoparticles have been exploited since the 4th century – the Lycurgus Cup is perhaps one of the most famous examples of nanoparticle chemistry, whereby dispersions of colloidal gold and silver nanoparticles throughout the glass cause the Roman cup to change colour in different lights.²

1700 years later and gold nanoparticles remain the textbook example of colloidal chemistry. Metal nanoparticles (NP) with sizes below 100 nm exhibit physical and chemical properties that are not prevalent in the bulk metal,³ and these properties are typically dependent on the size and shape of the NP.⁴ The optical properties of the metal change drastically at the nanoscale⁵ and this effect is well illustrated by gold. When an aqueous solution of chloroauric acid (Au^{III}) is reduced using sodium citrate, one observes the growth of metallic NPs (Au^0) in the order of 2-10 nm (**Figure 1.1**)^{6,7} – the strong surface plasmon band (SPB) of gold nanoparticles results in solutions with a vivid red colour. However, with increasing NP size, a redshift in the SPB results in gold NP solutions appearing purple.⁸ Reducing bulk gold to the nanoscale also influences its reactivity; while gold is classically considered unreactive, its NPs have been extensively explored for their catalytic properties,⁹ most notably as catalysts in CO oxidation and in hydrochlorination reactions.^{10,11} The strong SPB exhibited by Au, Ag and Cu NPs also make them the subject of interest for photocatalytic systems, where irradiation of the catalyst with light has been shown to improve catalytic efficacy.¹²

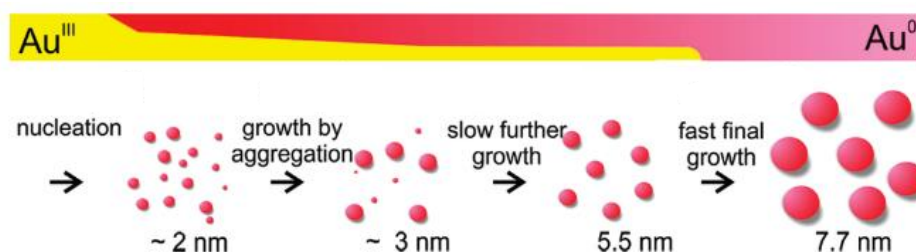


Figure 1.1 Illustration of the gold nanoparticle growth mechanism, reproduced from Ref. 6.

1.2 Metal Nanoparticles – Catalysis and Challenges

In the years following 300 AD, transition metal nanoparticles have found application in a broad range of fields outside of exotic crockery including chemotherapeutics,¹³ solar energy technologies,¹⁴ and electronics.¹⁵ The study of metal nanoparticles has generated a new field of catalysis hoping to bridge the gap between homogenous and heterogeneous catalysis. Suspensions of heterogeneous metal particles (< 5 nm in diameter) have been found to be highly active catalysts for a range of transformations including C-C cross-couplings,¹⁶ carbon monoxide oxidation,¹⁷ and hydrogenation reactions to name a few.¹⁸ Smaller particles provide an increased surface area for catalysis and thus an increase in the number of catalytically active sites when compared to bulk heterogeneous catalysts – this concept has been pushed to the limit with the inception of heterogeneous single atom catalysis, though these materials are currently thought to be less active than the corresponding NP catalysts.¹⁹ While homogenous transition metal catalysts are usually far more active than their heterogeneous counterparts, they suffer from the use of expensive ligands that constitute the dominant contribution to the catalyst's environmental footprint,²⁰ and can be difficult to separate from the reaction product. The development of heterogeneous catalysts that rival the same activity as that of homogenous systems is therefore crucial to tackling catalysis sustainably.

Metal NP size and structure can often have significant influences on catalyst activity.²¹ Analysis of Mg(OH)₂ supported AuNP catalysts using extended X-ray absorption fine structure (EXAFS) spectroscopy found that only AuNPs below 1 nm in size were active for CO oxidation.¹⁷ Tiny clusters (*ca.* < 13 atoms in size), on the other hand, were not found to make significant contributions to the activity, therefore it appears that there may be a lower limit to the NP size-activity relationship in this case. Catalytic activity was also determined to be structure dependent, with icosahedral particles believed to be the most active while larger NPs were more likely to adopt FCC cuboctahedral or decahedral morphologies. The relationship between NP size and activity is believed to be linked to the number of defect sites such as edges and steps.^{22,23} When compared as catalysts for the electrochemical reduction of CO₂, smaller CuNPs, specifically less than 5 nm in diameter, were found to be both more active and more selective for CO and H₂ formation than their larger counterparts.²⁴ Model FCC NPs of various sizes were compared, and smaller NPs were found to contain greater numbers of low-coordinate edge sites, which correlated with increasing activity. The

number of catalytically active edge sites can also be determined experimentally by measuring the adsorption of probe molecules such as CO.²⁵ However, a more recent study challenges the general acceptance of edge-sites promoting catalytic activity, namely for CO oxidation – by analysing the results of *in-situ* DRIFTS and temperature programmed oxidation (TPO) experiments, the conversion of CO to CO₂ over SiO₂ supported PtNPs was proposed to proceed slower at the catalyst edge sites rather than over bulk, well-coordinated Pt.²⁶

To that end, one should note that size is not a universal metric for efficacy, and in some cases, catalyst activity appears to be independent of NP size.²⁷ Such was the case for Al₂O₃-supported PtNP catalysts for CO oxidation²⁸ – although various structures and morphologies were expected for NPs between 1.2 and 20 nm, CO oxidation rates and CO desorption rate constants proved to be independent of NP size. Similarly, there have also been reports of a lack of apparent size-activity relationship for PdNP catalysts, again for CO oxidation.²⁹ Thus, understanding the factors that influence structure-dependent reactivity remains a hotly debated area of research.

NP catalysts are often described to exist at the boundary between homogenous and heterogeneous catalysis due to their high activities that can challenge those of homogenous catalysts. There are several examples of metal NP catalysts that take this boundary quite literally; nanoparticle-derived active homogenous Pd catalysts have been found to leach into solution before redepositing on the Pd NP ‘reservoir’ (**Figure 1.2**).³⁰ Zheng and co-workers encapsulated Pd NPs using Stöber silica to demonstrate that leached Pd was the active species in their Suzuki-Miyaura cross-coupling reactions.¹⁶ The redeposition of Pd was confirmed by recycling the catalyst at different conversion intervals: when the catalyst was recycled

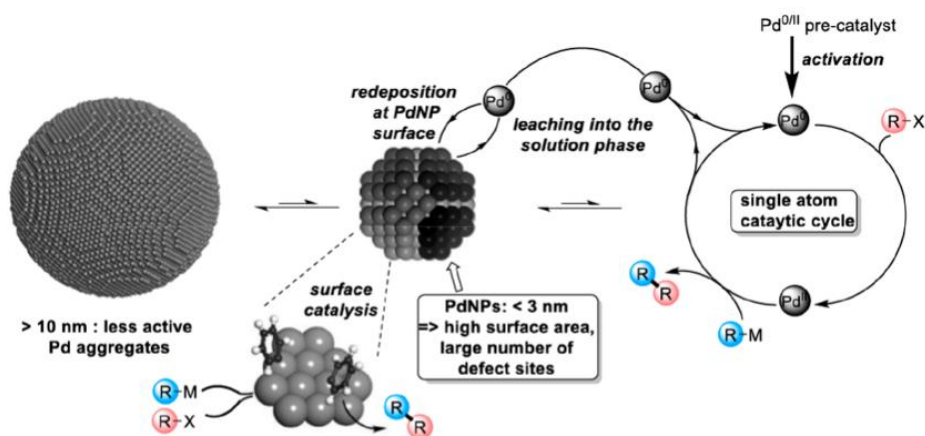


Figure 1.2 Cartoon showing the speciation of heterogeneous Pd catalysts for cross-coupling reactions, reproduced from Ref. 30.

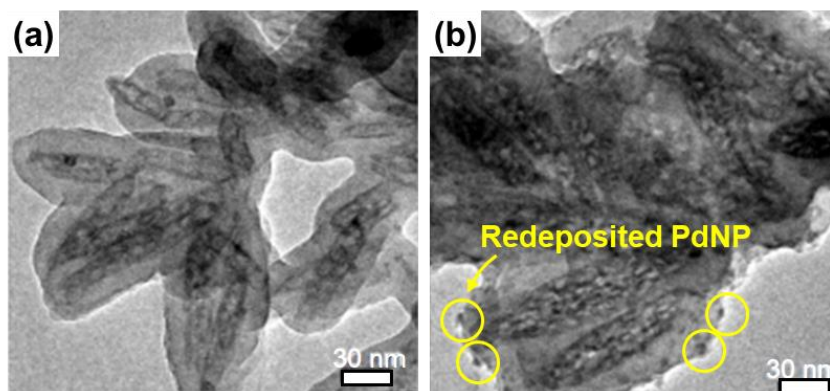


Figure 1.3 TEM images of silica encapsulated PdNP catalysts for Suzuki-Miyaura cross-couplings after (a) 43% and (b) 100% conversion of substrates. Catalyst isolated after 100% conversion of substrates shows Pd redepositing on the silica shell following the formation of soluble leached species. Figures adapted from Ref. 16.

following *ca.* 43% conversion of substrate, a major drop in activity was observed on consecutive runs; on the other hand, recycling the catalyst following full conversion of substrate resulted in a negligible loss in activity. This suggests that in the initial study, leached Pd complexes are being removed from the reaction mixture following work-up due to the formation of soluble Pd^{II} oxidative addition complexes; meanwhile, at complete conversion, there is no substrate remaining to undergo oxidative addition, so the Pd redeposits at the catalyst surface. Indeed, TEM images of the catalyst post-recycling found that the initial study left the catalyst morphologically unchanged, whereas in the second study, Pd NPs of 3-5 nm in diameter were found on the outside of the silica shell, as shown in **Figure 1.3b**.

Despite this, leaching is typically considered a deactivation pathway for NP catalysts due to the depletion of catalytically active material over time, particularly following recycling of the catalyst or during use in flow-bed reactors. Leaching of homogenous Pd species into solution from the NP ‘reservoir’ can also lead to catalytically inactive materials. Hii *et al.* monitored the leaching of Pd *in-situ* from their Heck coupling reaction in flow and found that the degree of Pd leaching was dependent on a multitude of factors including catalyst support, reaction temperature, and solvent.³¹ Reactions in DMF led to the most significant leaching, with the leached Pd species remaining catalytically active; on the other hand, leaching was suppressed in dioxane and toluene, with the scarce leached species appearing catalytically inert. Regardless, as the reactions were conducted in flow, conversion to Heck products decreased over time, even when the leached species was catalytically active, as the leached catalyst was removed in the product stream.

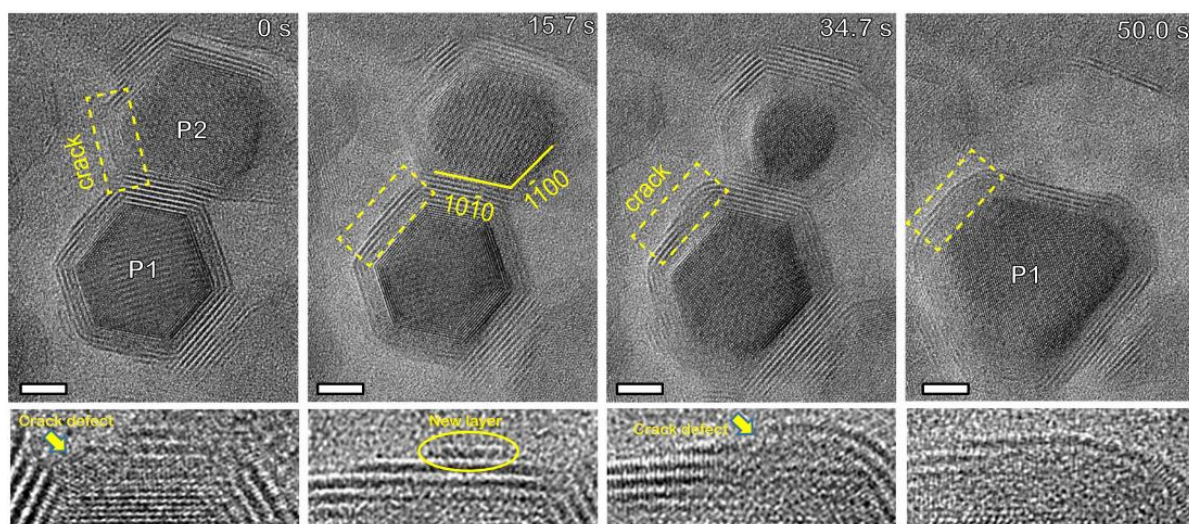


Figure 1.4 LC-TEM images over a period of 50 seconds show Cd-CdCl₂ NP ripening through the interaction of crack-defects. White scale bar = 5 nm. Images reproduced from Ref. 33.

While the depletion of material through NP speciation into soluble clusters or atomic complexes presents a challenge, the opposing scenario of NP aggregation is also a problem. In the absence of a capping agent, metal NPs will continue to aggregate to larger particles, whereby the advantageous properties of the NP size are no longer prevalent. This process is known as Ostwald ripening, and it describes how the agglomeration of smaller particles towards larger particles acts as a thermodynamic sink, minimizing the total free energy of the system.³² Discussions rationalising Ostwald ripening are typically limited to surface energies of particles, though recently, Zheng and co-workers were able to use liquid cell transmission electron microscopy (LC-TEM) to image the defect-mediated ripening of cadmium-cadmium chloride core shell NP structures, as shown in **Figure 1.4**.³³ So-called crack defects were proposed to play a pivotal role in facilitating the mass transfer from one particle to another, leading to NP ripening. The deactivation of catalysts through aggregation is well documented such as in the case of PtNP/GO for the hydrogenation of 4-nitrophenol,³⁴ and for NiO/SiO₂ where a combination of NiO agglomeration and surface coking led to reduced turnovers in methane oxidation reactions.³⁵

The density of metal loading also appears to be highly influential on the catalyst deactivation pathway – at high loadings, Pd/Al₂O₃ catalysts for methane combustion were found to lose 50% of their activity over 17 hours due to sintering; in contrast, at lower metal loadings 50% of the catalytic activity was lost over only 10 minutes due to the leaching of single atom species that appeared catalytically inactive.³⁶ This represents a significant obstacle for the

scale-up of many metal NP catalysed systems, particularly in the pharmaceutical industry where down-stream heavy metal content is monitored strictly due to its toxicity.

While leaching, sintering and aggregation represent the major challenges facing NP catalysis, the problem of catalyst deactivation is multi-faceted. Other notable routes to deactivation include deposition/coking, poisoning, morphological changes as well as passivation of the metal surface through oxidation.³⁷ Design of an appropriate supported catalyst microenvironment through careful choice of ligand, synthetic strategy, and catalyst support is therefore crucial for the successful development of metal NP catalysts resistant to deactivation.

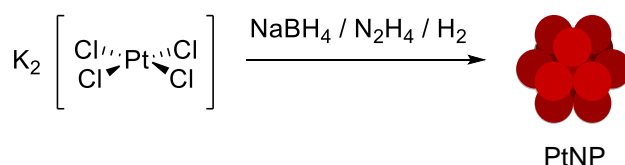
1.2.1 Nanoparticle Synthesis

Metal NPs are synthetically versatile and are prepared using a variety of methods. By far the most widely utilized method of nanoparticle synthesis proceeds *via* the chemical reduction of a metal precursor in the presence of an appropriate ligand stabilizer. Most metal halides undergo facile reduction to metal (zero valent) nanoparticles when mixed with a reducing agent, such as sodium borohydride or hydrazine hydrate, or in the presence of hydrogen gas (**Scheme 1.1**). Hydrogen gas is also employed for the hydrogenation of zero valent metal precursors (*e.g.* $\text{Pd}_2(\text{dba})_3$, $\text{Ni}(\text{COD})_2$, $\text{Ru}(\text{COD})_2$), whereby reducible allyl and diene ligands are hydrogenated to initiate metal nucleation. In a similar approach, microwave radiation has been used due to its ability to facilitate the uniform heating of a sample, purportedly allowing for improved control and therefore improved size homogeneity. Liz-Marzán and co-worker compared the preparation of polyvinylpyrrolidone (PVP) supported AgNPs both under reflux and with the assistance of microwave-radiation where DMF acts as both solvent and reducing agent – under reflux, Ag colloids of 6.61 ± 2.05 nm were generated which are notably larger than the 3.64 ± 2.38 nm particles generated using irradiation.³⁸ Thus, it appears that smaller NPs may be produced using microwave irradiation though they do not appear to be more monodisperse.

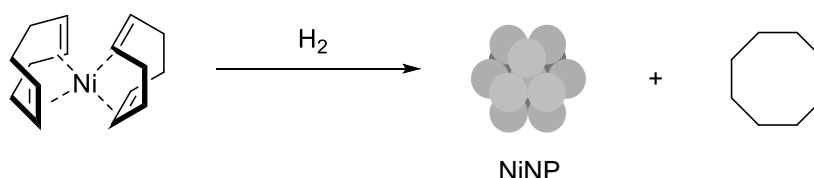
Meanwhile, nanoparticle preparation through thermal decomposition typically involves the degradation of a metal precursor through heating.³⁹ For example, powdered iron stearate precursors formed amorphous droplets on heating, which then began to form crystalline nanostructures above 200 °C (**Figure 1.5**); further heating above 280 °C led to nucleation and the generation of Fe_3O_4 NPs of around 10 nm in size.⁴⁰ The lack of chemical or gaseous

Bottom Up

(i) Chemical reduction of metal salts

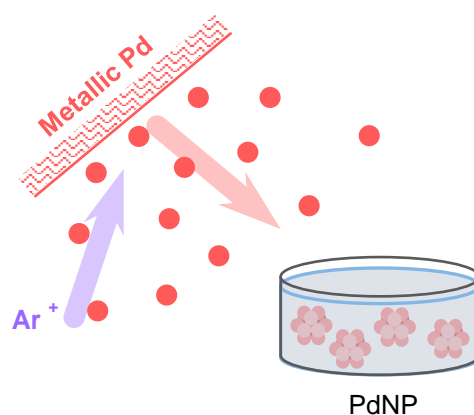


(ii) Hydrogenation of zero valent metal precursor



Top Down

(iii) Magnetron sputtering of a clean metal surface



Scheme 1.1 Examples of various “bottom up” and “top down” approaches towards the synthesis of metal nanoparticles.

reducing agent also makes thermal decomposition an attractive approach to investigate NP growth and nucleation kinetics *in-situ* using X-ray spectroscopy techniques.⁴²

Top-down approaches are also employed for NP preparation and are particularly useful for the fabrication of materials with a high degree of precision of NP size and morphology. One such technique uses magnetron sputtering to eject metal atoms or often clusters from a clean metal surface, the ejected metal particles are then deposited onto a support.⁴³ Higher metal loadings can be achieved simply by allowing longer deposition times of the metal catalyst.⁴⁴ This approach is particularly advantageous as it does not require the use of solvents or stabilizing agents during the NP synthesis, thus allowing for the generation of clean catalyst surfaces.

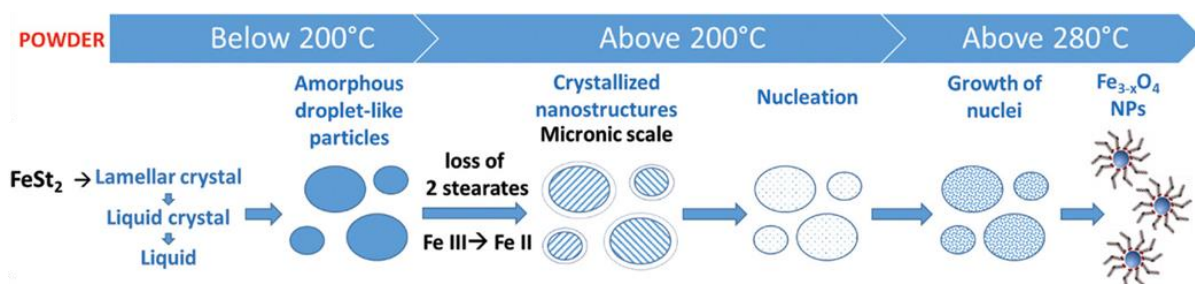


Figure 1.5 Schematic showing the various stages of iron stearate (FeSt_2) thermal decomposition towards iron oxide NPs. FeSt_2 was reported by the same group to exist as the polynuclear complex $[\text{Fe}_3(\mu_3\text{-O})\text{St}_6 \cdot x\text{H}_2\text{O}]\text{Cl}$.⁴¹ Figure reproduced from Ref. 40.

Re-dispersion methods have also been explored for the reactivation of NP catalysts following sintering, though this technique could be used for the precise synthesis of small metal clusters or even single atom sites. Hydrochlorination of surface adsorbed ethylene over Ru NPs (1 nm) led to the redistribution of metal atoms to form low-nuclearity clusters and single atom sites with increasing cycles of the $\text{C}_2\text{H}_2/\text{HCl}$ co-feed.⁴⁵ This approach was also effective for the re-dispersion of Ir and Rh NP catalysts.

1.2.2 Nanoparticle Stabilization

Although it appears that the relationship between nanoparticle size and catalyst activity can be tenuous at times, agglomeration to ‘bulk metal’, infamous palladium black being the most common example,⁴⁶ is considered a universal deactivation pathway. Thus, appropriate stabilization by ligand or support is required to prevent deactivation of the active catalyst.⁴⁷ Nanoparticle stabilization mechanisms are frequently simplified to the consideration of electrostatic and steric stabilization modes. Electrostatic stabilization is best visualised with a DLVO-like double layer of point cations and anions surrounding the metal surface, though this requires the assumption of point charges which is not truly representative of the ions. The example provided in this introduction of citrate stabilized Au NPs is perhaps the classic example of electrostatic NP stabilization,⁶ where citrate anions coordinate to the electropositive gold surface preventing further aggregation; higher concentrations of ligand thus result in smaller Au NPs (**Figure 1.6**). Similar electrostatic interactions were observed when ammonium bromide surfactants were employed in the electrochemical synthesis of Pd and Ni colloids.⁴⁸ However, such stabilizing interactions rarely follow an idealised protocol in multi-component systems. This is well demonstrated by the generation of Pd clusters from the hydrogenation of $\text{Pd}(\text{OAc})_2$ in the presence of 1,10-phenanthroline, followed by treatment with O_2 .⁴⁹ The authors assert that large colloids with an initial stoichiometry of

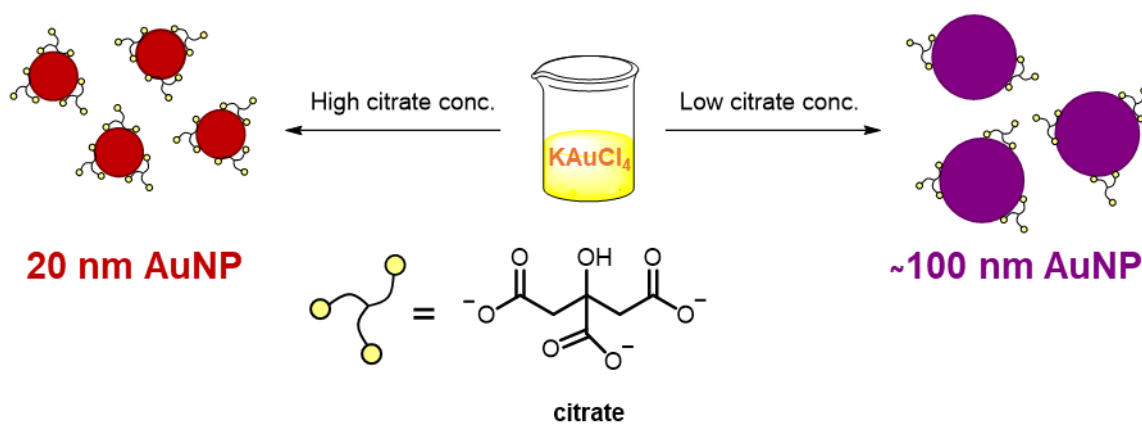


Figure 1.6 Cartoon showing the effect of sodium citrate concentration on Au nanoparticle size.

$[\text{Pd}_9(\text{phen})(\text{O})_3(\text{OAc})_3]_m$ with 570 Pd atoms ($m = 63.5$) form, stabilized in part by the sterically bulky phenanthroline ligands. However, the acetate anions allegedly continue to form part of the wider ensemble, providing electrostatic stabilization from the outer-sphere of the colloid.

What would typically be considered as ‘steric’ stabilizers such as polymers, metal oxides, and metal organic frameworks further complicate the understanding of stabilization as they often contain additional functionalities that may coordinate to the NP surface. For example, Whilton and co-workers describe the use of poly(styrene sulfonate) as a template for wet reduction of various late transition metal salts using a solution of sodium borohydride in 0.1 M NaOH;⁵⁰ however, this system is truly multifaceted, and the authors do not investigate the influence of the sulfonate group, surface hydride species, borate salts, nor the hydroxide buffer on the resulting NP size. Although there are detailed studies considering the factors that influence NP nucleation and stability, most NP catalysts form part of a complex mixture, therefore their stabilization is better considered as a cocktail of competing forces.^{51,52} However, advancements in characterisation techniques are helping to deconvolute these forces. Understanding the factors involved in metal NP stabilization, and how some of these factors may limit reactivity, is paramount for the design of new catalyst materials.

Recently, *in-situ* small-angle X-ray scattering (SAXS) experiments have highlighted the critical influence of ligands on NP nucleation kinetics and therefore size. As a model, Cargnello and co-workers probed the nucleation of phosphine (trioctylphosphine, TOP) stabilized Pd complexes, which were thermally decomposed by heating to 280 °C at a constant ramping rate (**Figure 1.7**).⁵³ Nucleation of particles larger than 1 nm began at 230 °C, and over the next 50 s, rapid nucleation was observed followed by the growth of NPs between 2.8 to 3.7 nm. After 200 s, a small decrease in NP concentration was observed due to Ostwald ripening,

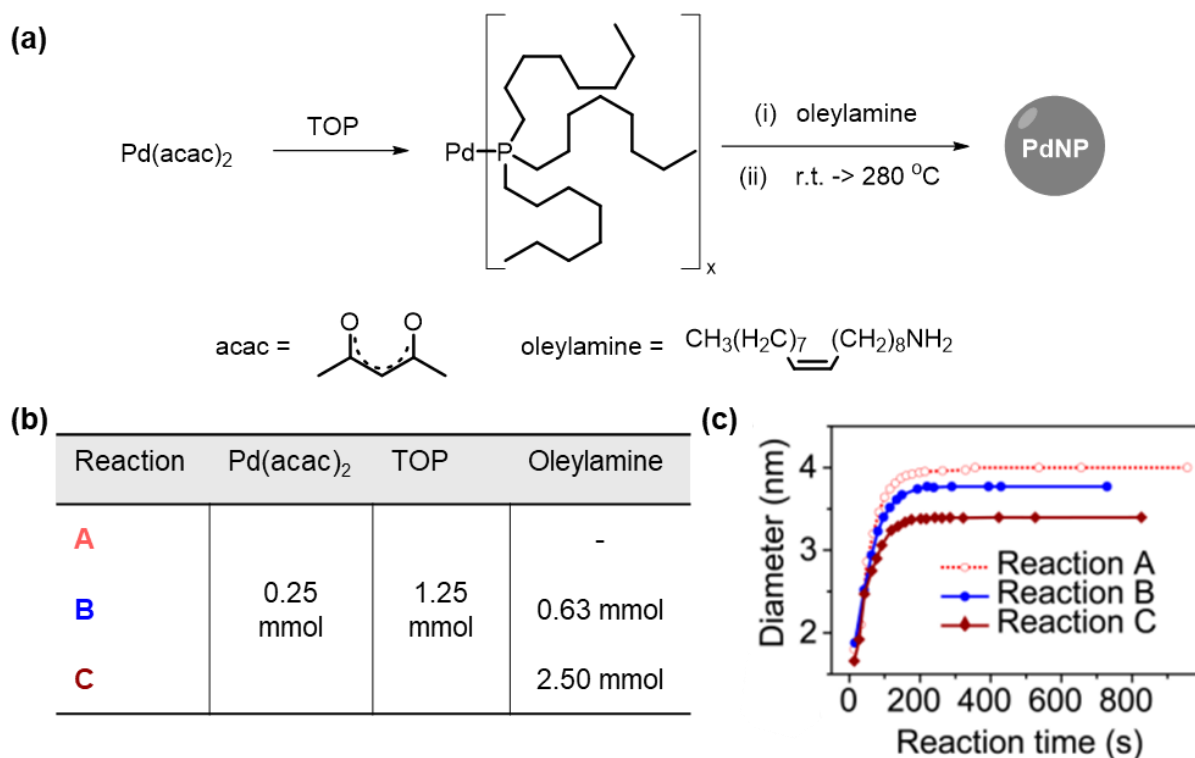


Figure 1.7 (a) Schematic of PdNP synthesis *via* the thermal degradation of a Pd-TOP complex in the presence of various amounts of oleylamine (b), and (c) the corresponding plots of NP size over time, as determined by *in-situ* SAXS. Figures adapted from Ref. 53.

though after 5 minutes (280 °C not reached until after nearly 7 minutes) no further growth was measured and the NPs were near monodisperse with a final size of 4.0 ± 0.4 nm. However, mixing of the initial Pd-TOP complex with oleylamine led to a more rapid nucleation rate and therefore slightly smaller NPs of 3.5 ± 0.3 nm in size. This effect is attributed to the strong binding between the amine and Pd^0 , promoting the formation of more numerous NPs. In stark contrast, increasing the concentration of TOP in the initial mixture led to the formation of much larger NPs (5.5 ± 0.6 nm); TOP is known to form stable complexes with Pd^{II} , resulting in a higher temperature of 255 °C required to initiate a slower nucleation rate, leading to the formation of fewer, larger NPs. An established protocol for controlling NP size is crucial for investigating the influence of NP size on activity, and indeed the same group used this approach to study the effect of particle size on Pd-catalysed methane combustion.²⁷

N-Heterocyclic carbenes (NHC) have also received notable attention in recent years for their ability to coordinate to metal surfaces,⁵⁴ and have been explored as a potential route towards the stabilization of metal NPs.⁵⁵ In a detailed study by Ananikov and co-workers,⁵⁶ *in-situ* ^{13}C MAS NMR spectra of the Pd Mizoroki-Heck reaction help to discern NHC-type carbenes coordinated to tiny (< 1 nm), small (1-1.5 nm), medium (> 1.5 nm) and large (> 3 nm) Pd

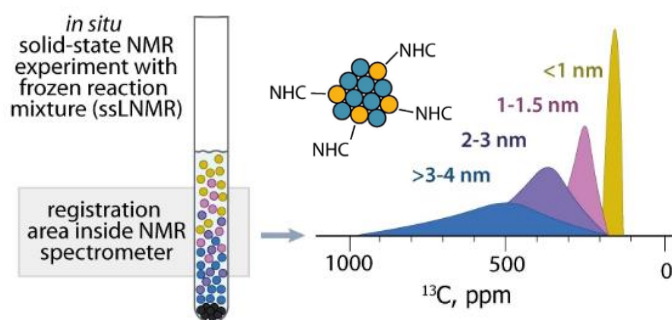


Figure 1.8 Illustration of the observed Knight shift in the ^{13}C NMR spectra for ^{13}C labelled NHC coordinated to PdNP surfaces. The apparent Knight shift increases and the ^{13}C peak broadens with increasing particle size. The illustration is adapted from Ref. 56.

nanoparticle clusters (**Figure 1.8**). Carbene coordination to larger Pd clusters lead to larger Knight shifts in the ^{13}C NMR spectrum, allowing for analysis of Pd NP speciation. By freezing the reaction mixture, the authors were able to analyse the speciation of the catalytically active NPs; however, upon thawing, it was apparent that the carbenes alone were ineffective at preventing agglomeration, as increasingly large Knight shifts were observed in the ^{13}C NMR spectra. Nonetheless, the apparent stabilizing contributions of NHC's will form part of the myriad of stabilization modes incurred in the use of ionic liquids, which is discussed further in **Section 1.3.2**.

Solvent too can act as a weak stabilizer during NP nucleation, thus, careful consideration should be given to the reaction medium. Addition of acetonitrile, during the electrochemical synthesis of Pd NPs in THF led to increasing colloid size with increasing concentration of acetonitrile.⁴⁸ In the absence of additional ligands, the mean particle size of Ru clusters, following hydrogenation of precursor $[\text{Ru}(\text{COD})(\text{COT})]$, was highly contingent on the composition of the THF/MeOH solvent mixture.⁵⁷ THF proved crucial to attaining small NP sizes, as pure MeOH afforded particles 70 nm in diameter (or > 500 nm when using stoichiometric MeOH), whereas in a 9 : 1 THF/MeOH mixture 16 nm particles were obtained. The authors proposed that a hydrogen bonded network between the two solvents formed rings with lipophilic centres that dictated the particle size.

1.2.3 Can Ligands Tune NP Reactivity?

Well, yes, if the ligand can influence NP size, then this may have an effect on the efficacy of the NP catalyst. Though if a surface ligand influences NP size, it can then become difficult to deconvolute whether a change in catalytic activity is due to NP size or a ligand effect.⁵⁸ But can surface ligands modulate activity of a series of NPs with uniform size? The chosen ligand

is often non-innocent, influencing NP catalytic activity through interaction with the metal surface through coordinating heteroatoms such as oxygen, phosphorous, sulphur and nitrogen.⁴⁷ Typically, it is proposed that such heteroatoms with Lewis basic character can donate electron density to the metal surface through a lone-pair, thus improving the metal's ability to back-donate and weaken substrate bonds. Such a metal-ligand interface is difficult to demonstrate, however the employment of surface sensitive techniques such as X-ray photoelectron spectroscopy (XPS), and the use of probe molecules such as CO can elucidate some information surrounding these interactions.

The catalytic activity of AuNPs towards the oxidation of amines to amides was tuned through functionalisation of the silica support with mercaptyl and pyridyl groups.⁵⁹ When compared to the unfunctionalised silica supported NPs, the thiol coordinated AuNPs became 'electron deficient' while the amine coordinated AuNPs were found to be 'electron rich'. Improved catalytic activities of the amine-ligated AuNPs was thus rationalised by a superior ability for electron backdonation promoting C-H scission, as well as O₂ activation towards superoxide.

Selectivity for *N*-phenylhydroxylamine, in the Pt catalysed reduction of nitrobenzene, was enhanced when the Pt nanowires (NW) were modified with ethylenediamine donors.⁶⁰ The Pt NWs were found to become electron rich due to the interaction with interfacial amine ligands, and when these ligands were stripped through acid treatment, the selectivity for *N*-phenylhydroxylamine dropped. XPS analysis of the amine-modified Pt surface found a negligible change in the Pt 4f core electrons when compared to unmodified Pt; however, electrochemical CO stripping experiments found that the amine-modified Pt NW stripping potential was 0.22 V higher than that of Pt black, indicative of more strongly bound CO groups because of stronger Pt back-bonding into CO π^* orbitals. This finding was supported by *in-situ* FTIR of CO adsorbed Pt NW surfaces.

The electrochemical reduction of CO₂ to CO was promoted when AuNPs were decorated with imidazolylidene carbenes.⁵⁵ The carbene-capped AuNPs exhibited higher current densities and lower overpotentials for CO₂ electroreduction when compared to 'naked' AuNPs supported on carbon. The enhanced activity was attributed to the strong σ -donation from the carbene to the Au surface which results in faster electron transfer to surface-bound CO₂. Coordination of carbene to the Au surface was evidenced by a significant shift of the imidazole

aromatic protons in the solid-state ^{13}C NMR spectrum when compared to the free carbene, however, the authors did not analyse the Au surface before and after coordination.

Functionalisation of the donor group can also impact catalytic activity. PdCu₂ nanoparticles were immobilized on a series of pyridyl-based covalent organic frameworks and were used as catalysts for the partial hydrogenation of phenylacetylene.¹⁸ Enhanced conversion of phenylacetylene to styrene was observed when the support pyridyl-unit was modified with a toluene group, and XPS analysis found that the Pd became more electron rich compared to when the pyridyl-unit was substituted with a phenyl ring (**Figure 1.9**). In contrast, when the pyridyl-support was substituted with an electron-withdrawing benzonitrile or trifluoromethylbenzene group, the Pd became electron deficient, and as an apparent consequence, the conversion to styrene was much lower for these catalysts.

On the other hand, Yun and co-workers found that the treatment of a PtNP/Al₂O₃ surface with various amines had a negligible effect on the surface electronic structure of the PtNP.²⁵ However, treatment of Pt with the various amines greatly enhanced its catalytic activity and enantioselectivity for the hydrogenation of methyl pyruvate. FT-IR spectra of CO-adsorbed catalysts found that the amines occupied defect sites such as step, edge and corner sites on the PtNP and the authors report a direct correlation between the occupation of these sites and the %enantiomeric excess of the chiral hydrogenation product.

Surface ligands have also been reported to interact with reaction substrates to tune reactivity. For example, modification of CuNPs with an alkanethiol monolayer was found to reduce susceptibility of the Cu to oxidation, however, the lone pairs of the surface thiols were also

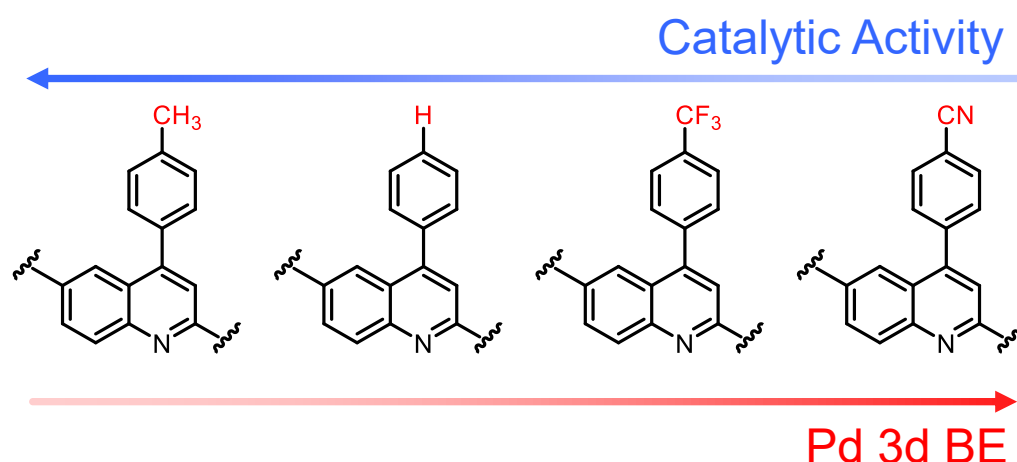


Figure 1.9 Effect of covalent organic framework functionalisation on the activity and electron density of PdCu₂ bimetallic nanoparticles as catalysts for the partial hydrogenation of phenylacetylene.¹⁸

proposed to coordinate to CO, lowering the onset potential for electroreduction.⁶¹ Increased loading of the thiol ligands also led to improved selectivity for the formation of acetate from the electroreduction of CO.

1.3 Ionic Liquids

Ionic liquids (ILs) have been explored extensively as potent stabilizers for metal NP catalysis, with interesting properties that may also influence catalyst reactivity. Ionic liquids have received a meteoric rise in attention since the late 1990's, with nearly 2000 review articles in the last 14 years covering their synthesis and application.⁶² The interest in these materials is derived from their unique properties not exhibited by conventional solvents such as non-volatility, non-flammability, ionic conductivity, tuneable polarity and low toxicity.

Classically, an ionic liquid is a salt with a melting point below 100 °C, however, the popularity of the field and the seemingly infinite designability of these materials has made the title of ionic liquid rather loose. For simplicity, this thesis will use the term ionic liquid to refer to low melting salts that follow the general design principles of what we consider a classic IL. Note that one of the ions (typically the cation) of an IL is often an organic species, thus low melting eutectic mixtures of salts are not considered ionic liquids.⁶³ The most common IL cations and anions are summarised in **Table 1.1**, however, their synthetic versatility has resulted in a seemingly endless amount of cation derivatives and resulting cation and anion pairs to study. Ionic liquids are frequently described as 'green solvents', namely due to their recyclability, though the diversity in possible IL structures makes it difficult to conduct proper life cycle assessments (LCA), and instead most LCA's simply consider [BMIM]-based ILs.⁶⁴

Table 1.1 Most commonly studied ionic liquid cations and anions.

Common IL Cations					
Imidazolium	Pyrrolidinium	Pyridinium	Alkylammonium	Phosphonium	Sulfonium
Common IL Anions					
Halides	Tetrafluoroborate	Bis((trifluoromethyl)sulfonyl)amide	Hexafluorophosphate	Dicyanoamide	Ethylsulfate
					[MCl _x] ⁺

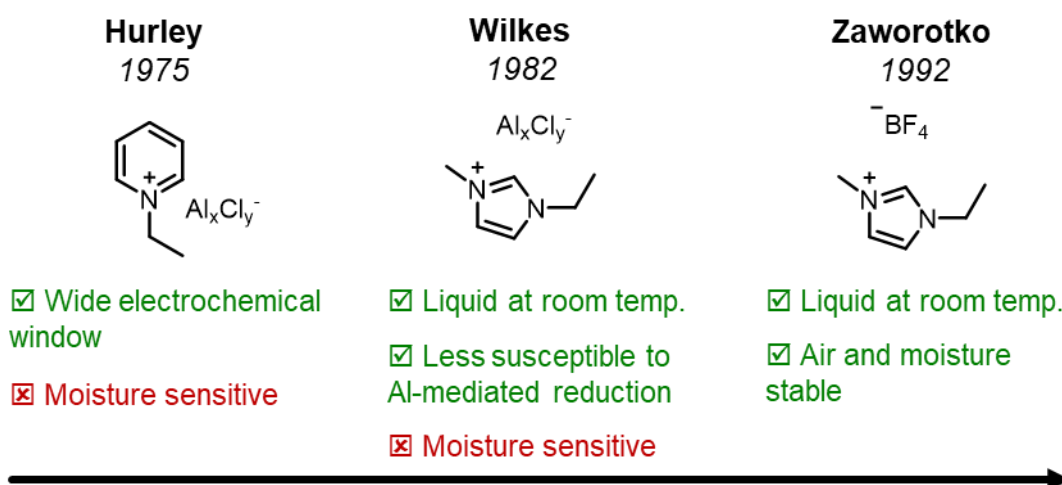


Figure 1.10 Major developments in ionic liquid design over time.

Ionic liquids initially rose to prominence at the end of the 1970's as they began to receive note as promising electrolytes due to their wide electrochemical window. Although early work by Osteryoung based on an *N*-ethylpyridinium chloroaluminate salt received notable attention as a medium to study electrochemistry,⁶⁵ the same pyridinium IL was first reported in 1951 as an aluminium electrodeposition solution.⁶⁶ However, these chloroaluminate-based ILs would react violently with water and were thus difficult to handle. Wilkes improved on this design by preparing an imidazolium chloroaluminate that was both liquid at room temperature and less susceptible to Al-mediated reduction.⁶⁷ Wilkes also comments here on the ability of the IL to solvate metal halides such as CuCl_2 and TiCl_4 , a property that will later facilitate their application in catalysis. Air-stable room temperature ionic liquids were not reported until Zaworotko and Wilkes described the preparation of 1-ethyl-3-methylimidazolium tetrafluoroborate in 1992;⁶⁸ since then numerous reports have shown decreasing melting points when the IL anion has a more diffuse charge.⁶⁹ Although imidazolium halide based ILs that melt at higher temperatures were easy to handle and well established, the finding of air stable room temperature ILs catapulted their application as both a non-volatile reaction medium and as a promising electrolyte for battery applications.^{70,71}

One of the most attractive attributes of ILs is the tunability of the ion pair, as the physical and chemical properties of the material can be manipulated through careful choice of cation and anion. Numerous reports feature cations based on an imidazolium or a pyridinium species, though there are examples of phosphonium and sulfonium based ILs.⁷² The anion on the other hand is for the most part inorganic, from halides to main group borates, phosphates, and aluminates. Manipulation of the anion allows for versatility in the IL design, controlling

physical properties such as solubility and viscosity. For example, when hydrophilic poly(1-vinyl-3-butyl-imidazolium chloride) was stirred with aqueous solutions of NaBF_4 and NaPF_6 , the polymeric IL became insoluble in water but soluble in acetone, and in the case of PF_6^- , tetrahydrofuran and ethyl acetate, allowing for isolation of the exchange products through precipitation.⁷³

1.3.1 Ionic Liquids in Catalysis

In a 1970 perspective on 'multiphase catalysis', a reviewer asks author Peter Rony how he would envision supported liquid-phase catalysis for the Wacker process. In response, Rony describes silica gel particles as 'minicontainers' for molten electrolytes, and highlights the exciting potential of these unexplored electrolytes in catalysis due to their ability to readily dissolve metal complexes.⁷⁴ The first example of these so-called molten electrolytes, or ionic liquids in the modern sense, in homogenous catalysis followed in 1972 when Parshall described the use of tetraethylammonium salts bearing GeCl_3^- and SnCl_3^- anions as solvent for the PtCl_2 catalysed hydrogenation of olefins. These ILs appeared to stabilize PtCl_2 against reduction, as no metal deposition from solution was apparent even at 100 atm pressure of hydrogen and a reaction temperature of 160 °C. Product separation from the catalyst was remarked as facile, as the low volatility and high polarity of the IL solvent allowed for both distillation and organic extraction of the reaction products.⁷⁵

Despite the report of this exciting new reaction medium, ILs were not further exploited in thermal catalysis until the reports of Wilkes in 1986 that mixtures of $[\text{EMIM}][\text{Cl}]$ and AlCl_3 can be used as both solvent and catalyst for Friedel-Crafts acylations.⁷⁶ By using a 2-fold excess of AlCl_3 , the *in-situ* generated $[\text{Al}_2\text{Cl}_7][\text{EMIM}]$ was found to be the catalytically active species. Later in 1990, Carlin and Wilkes reported perhaps the first example of 'heterogenizing' a homogenous catalyst through dissolution in an ionic liquid. *In-situ* generated $[\text{AlCl}_4][\text{EMIM}]$ was used as a medium for Cp_2TiCl_2 catalysed Ziegler-Natta polymerisations.⁷⁷ The authors used the IL as a platform to investigate acidic AlCl_3 coordination to Cp_2TiCl_2 and its effects on catalysis, however, the activity for ethylene polymerisation was lower when reactions were conducted in the IL melts. This was potentially due to poor solubility of the substrate or the coordination of basic alkylimidazole impurities to the metal catalyst, though the exact role of the influence of the IL was not explored.

Despite this, the ability of IL's to dissolve a broad range of metal complexes and organic substrates has led to their extensive use as reaction media in catalysis,⁷⁸ and more recently in biocatalysis.⁷⁹ Moreover, their insolubility in hydrophobic solvents, such as hydrocarbons, facilitates biphasic reaction mixtures, where the metal catalyst is solvated in the IL layer and the product remains in the organic phase. This allows for easy catalyst separation and recovery for recycling. For example, one of the first IL-biphasic systems reported by Chauvin described how $[\text{Rh}(\text{norbornadiene})(\text{PPh}_3)_2]\text{PF}_6$ dispersed in $[\text{BMIM}][\text{SbF}_6]$ effectively catalysed the selective hydrogenation of cyclohexadiene to cyclohexene, as the cyclohexene was 5 times less soluble in the IL.⁸⁰ Upon recycling of the catalyst, a negligible loss of Rh was observed (< 0.02%), highlighting the effective role of the IL in stabilizing the metal complex. However, the high selectivity for cyclohexene in this system is also likely a reflection of the poor solubility of H_2 in ionic liquids, which may explain the relatively low TOF's observed for a homogenous catalyst (333 h^{-1}). In spite of this, ILs continue to be used for hydrogenation reactions with homogenous catalysts, as the designability of the IL can lead to improved activities. Extending the alkyl chain length of both cation and anion of alkylammonium hydroxyvalerate significantly improved the activity of $[\text{Rh}(\text{COD})_2][\text{BF}_4]$ towards the hydrogenation of olefins⁸¹ – likely a result of the increased solubility of hydrogen in non-polar rather than polar solvents.⁸²

Ionic liquids have thus been explored extensively as solvents for catalysis, and their use in heterogenizing typically homogenous catalysts has been summarised in several reviews.⁸³ The designability of the IL medium provides endless scope for the development of bespoke catalyst microenvironments.⁸⁴

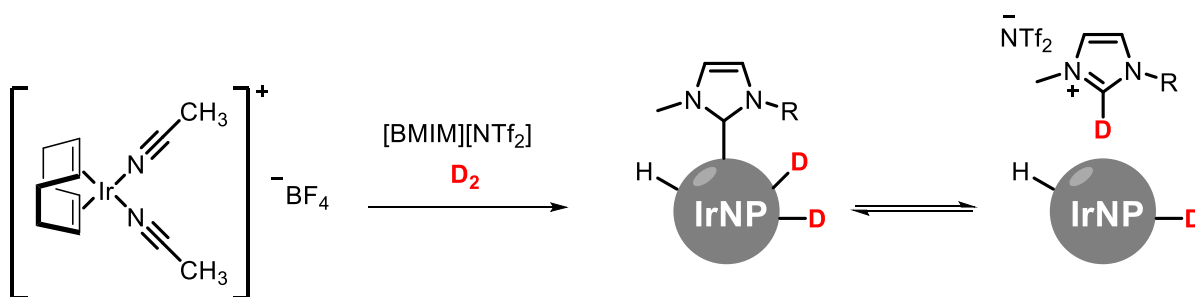
1.3.2 ILs as Stabilizers for Nanoparticle Catalysts

Significant attention has also been paid to the use of ILs to stabilize metal nanoparticles,⁵² and their beneficial effect on catalytic activity.⁸⁵ Although nanoparticle synthesis in ILs is compatible with all of the synthetic strategies described above, by far the most abundant is the simple chemical reduction of a M^{n+} complex or the thermal decomposition of an organometallic precursor, as has been used for Au,⁸⁶ Ag,⁸⁷ Ru,⁸⁸ and Pd⁸⁹ NP systems. In fact, ILs acted as both solvent and reducing agent in the case of $[\text{Ru}(\text{COD})(2\text{-methylallyl})_2]$ which spontaneously decomposed to RuNPs under mild heating (50°C) when dispersed in 1-hexyl-2,3-dimethylimidazolium (HDMIM) bistriflimide.⁹⁰ It was proposed that the allyl-ligand underwent reductive elimination following nucleophilic attack by the IL NTf_2^- anion, followed

by nucleation of the atomic Ru to NPs 2.0 nm in size. This reactivity was anion specific, as when NTf_2^- was substituted for BF_4^- , no NP formation was observed even after several days of stirring. The $[\text{HDMIM}][\text{NTf}_2]$ RuNPs were thus found to be highly active catalysts for the hydrogenation of toluene, attaining 95% conversion over 18 hours; in contrast, RuNPs generated from the *in-situ* hydrogenation of $[\text{Ru}(\text{COD})(2\text{-methylallyl})_2]$ in $[\text{BMIM}][\text{BF}_4]$ were less effective, achieving only 20% conversion over the same time period. A similar strategy was effectively applied to the hydrogen-free reduction of $\text{Ni}(\text{COD})_2$, though ‘sponge-like’ aggregates of NiNPs were observed by TEM.

As well as being an attractive solvent for catalysis, ionic liquids also facilitate the generation of ultrafine NPs and authors usually ascribe this to their ability to provide steric and electrostatic stabilization. Surface adsorption of both anion and cation as stabilizing groups has been investigated extensively using surface sensitive techniques such as XPS.⁹¹ Often IL stabilisation of NPs is considered to occur through an electric double layer, following DLVO theory: Dupont and co-workers used XPS to show that the IL anion coordinated to Ir NPs through Ir-F (for BF_4^- and PF_6^-) and Ir-O (for CF_3SO_3^-) bonds, and proposed that the cations formed a corresponding double layer around the anions.⁹² The thickness of these double layers was determined by using small-angle scattering (SAXS) experiments to estimate the ionic liquid molecular lengths and the size of the particle as a whole. However, the results of several reports suggest a protective double layer is not in fact responsible for NP stabilisation; Dupont himself recognises the limitations of the DLVO-model in the aforementioned report and acknowledges these more recent results in several reviews.^{52,93}

Simulations of a model 2 nm Ru NP solvated in $[\text{BMIM}][\text{NTf}_2]$ found that the charge separation of the IL ion pair was small, resulting in an interfacial layer that was essentially one ion thick.⁹⁴ Plots of radial charge distribution found that the surface IL layer had a 4-5 Å thickness, where the charged species were most likely to be found at the surface. Interestingly, the imidazolium head group preferentially appeared perpendicular to the Ru surface, while interactions between the surface with the imidazolium protons were not prevalent, nor was planar coordination of the ring. The orientation of the cation on the metal surface may be dependent on the metal facet, whereby a 1-ethyl-3-methylimidazolium unit could be found flat, partially upright and upright on various facets of gold ($\{111\}$, $\{100\}$ and $\{110\}$ respectively).⁹⁵ Experimentally, a planar coordination of the imidazolium ring, parallel to the metal surface, was found when Au NPs with mean diameters of 5-20 nm were generated in triethylene glycol



Scheme 1.2 Imidazolium-derived carbene formation over IrNPs. Hydrogenation of the IrNP precursor using D₂ led to H/D scrambling at the imidazolium protons.⁹⁶

functionalised imidazolium methanesulfonate.⁸⁶ Surface-enhanced Raman spectroscopy (SERS) analysis of the AuNP prepared in IL showed a shift to lower wavenumbers for the imidazolium vibrational modes, indicative of coordination to the metal surface; no such shifts were observed for the methanesulfonate anion, suggesting that it was a spectator and was not involved at the metal-ligand interface.

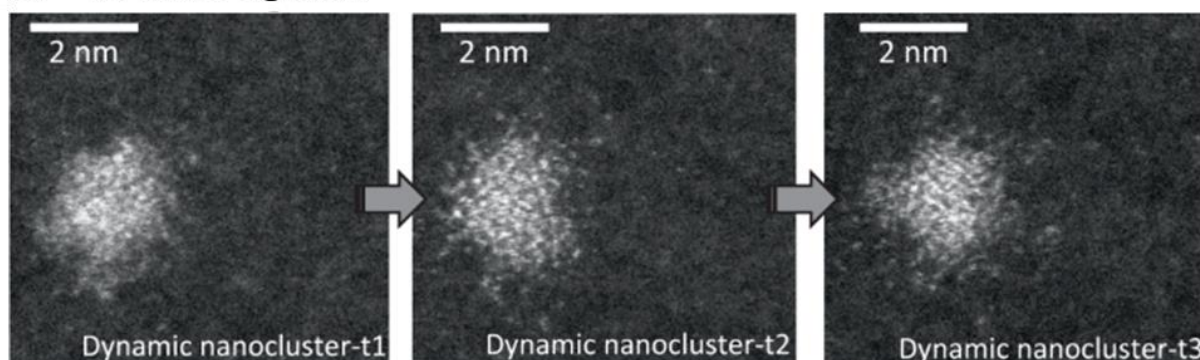
The literature for IL-stabilized NPs is dominated by imidazolium-based systems, and as such it is important to recognise the role of imidazolium-derived carbenes in the stabilization of metal NPs. In a seminal report by Finke and Seddon,⁹⁶ the coordination of [BMIM]-based imidazolium carbenes, and abnormal carbenes,⁹⁷ to Ir NPs was demonstrated using ²H NMR spectroscopy. Hydrogenation of the Ir precursor, [(1,5-COD)Ir(CH₃CN)₂]⁺BF₄⁻, dispersed in [BMIM][NTf₂] using D₂ led to oxidative addition of the acidic imidazolium protons and H/D scrambling (**Scheme 1.2**). Extensive experiments eliminated the influence of chloride contaminants, acetonitrile, and weakly coordinating anions (*i.e.* BF₄⁻, NTf₂⁻) on the stabilisation of the Ir NPs. However, such stabilising forces are not always positive. The same group later reported how [(COD)IrCl]₂ derived IrNP catalysts were significantly less active for the hydrogenation of acetone when generated in the presence of even 0.1 eq of [BMIM][PF₆], rather than the highly active neat Ir catalyst.⁹⁸ Here, D₂ labelling suggested that while imidazolium-carbene species had a stabilizing effect on the NP, they also acted as a catalyst poison. In a more recent study, direct evidence of carbene coordination to Pd NP surfaces was obtained using ¹³C MAS NMR spectroscopy;⁵⁶ however, analysis of Pd NP with a diameter of 1.2-1.5 nm showed that as few as 3 NHC ligands could lead to a 30-40% surface coverage, limiting the number of reactive sites.

As described earlier, the steric stabilisation of NPs can be difficult to deconvolute from the numerous other stabilising forces such as solvent, electrostatic interactions. When Ru(COD)(COT) was hydrogenated in various ionic liquids, denoted [RMIM][NTf₂] (where R =

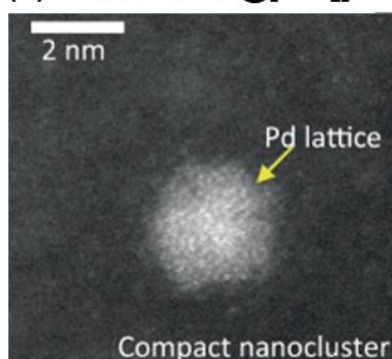
C_nH_{2n+1}), increasing the length of the alkyl-chain R led to a linear increase in the NP size for $n = 4, 6$ and 8 .⁹⁹ Note that the neutral non-polar precursor $Ru(COD)(COT)$ was found to have a greater affinity for the non-polar regions of the IL, therefore RuNPs generated in the presence of cyclooctane had a mean size of 7.5 ± 0.5 nm compared to 2.4 ± 0.3 nm for neat $[BMIM][NTf_2]$. Thus, the increasing alkyl chain length could instead be considered a templating effect rather than steric protection.

At the frontier of homogenous and heterogeneous catalysis, Fernandes and co-workers have used $[BMIM][NTf_2]$ as a medium to generate PdNPs with a diffuse outer-layer of IL stabilized Pd atoms.⁴⁴ At low Pd loadings (0.12 wt%), aberration-corrected scanning transmission electron microscopy (AC-STEM) images show a Pd core of 2.0 ± 1.0 nm, surrounded by a mobile layer of Pd atoms, as shown in **Figure 1.11a**; with increasing Pd loading (e.g. for 2.0 wt%), this dynamic structure is lost and the NP becomes more 'compact', with far fewer apparent atomic Pd sites. EXAFS spectra of the Pd@IL clusters showed a peak at 2.5 \AA attributed to bulk Pd-Pd bonds, in addition to a peak at 1.7 \AA assigned to a Pd-IL bonding

(a) 0.12wt% Pd@[NTf₂]



(b) 2.0wt% Pd@[NTf₂]



(c)

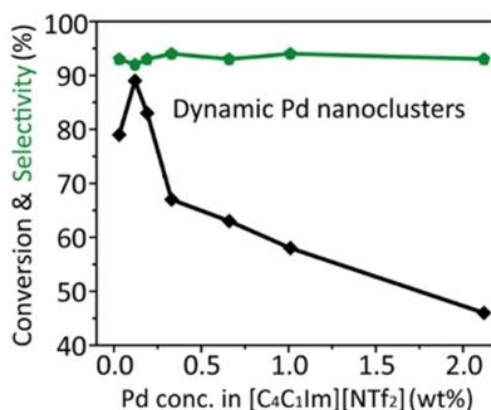


Figure 1.11 AC-STEM images of (a) 'dynamic' 0.12wt% PdNP in $[BMIM][NTf_2]$ over time and (b) 2.0 wt% PdNP in $[BMIM][NTf_2]$. (c) Plot of conversion and selectivity for the diazoethyl acetate mediated cyclopropanation of styrene against the wt% loading of Pd in the IL-dispersed catalyst. Figures adapted from Ref. 44.

interaction. With decreasing Pd loading, the intensity of the Pd-Pd signal dropped drastically, concurrent with the increasing intensity of the Pd-IL peak.

While these Pd clusters were generated in [BMIM][NTf₂], particles dispersed in [BMIM][PF₆] were all found to be compact (even at low Pd loadings), as were those when 1-butyl-2,3-dimethylimidazolium was used as cation, thus the appropriate choice of IL was essential to stabilizing atomic Pd. Supporting DFT calculations show that larger Pd clusters (Pd₁₃) interact strongly with the IL anion, while atomic Pd complexes interact with both the cation and the anion of the IL. The presence of 'dynamic' homogeneous-like Pd sites had a significant influence on the catalytic activity of Pd towards cyclopropanation of alkenes: while conversion increased with decreasing Pd loading, a sharp increase was observed for clusters below 0.25 wt% Pd, which were considered dynamic (**Figure 1.11c**). A mercury poisoning study, which would typically saturate heterogeneous catalyst sites, had little effect on the dynamic Pd catalysts with only a 32% reduction in activity for the 0.12 wt% Pd catalyst, whereas complete inhibition was observed for the higher loading, compact clusters, confirming the homogenous nature of the dynamic clusters.

1.3.3 Solid Supported Ionic Liquid Phases

Although employment of ionic liquid as solvent phase or stabilizer is an effective route to improve the robustness of catalysts, mass-transfer of substrate to the catalyst surface is a frequent limitation that has led to lower activities for some IL-catalyst composites.^{85,100} So-called solid ionic liquid phases (SILP) load small amounts of IL onto a solid-supported catalyst surface through evaporation of a dispersion solvent, creating thin layers of the IL. This approach is not only attractive as an approach to circumvent mass-transfer limitations,¹⁰¹ but SILP supports have the added benefit of minimal IL loading at the catalyst surface mitigating their high cost and facilitating recycling of both the catalyst and the supporting IL.

Modification of Pd/SiO₂ with a surface layer of [BMIM][N(CN)₂] greatly enhanced catalyst selectivity for citronellal in the Pd-catalysed hydrogenation of citral.¹⁰² In the absence of IL, a citronellal selectivity of 37% was obtained, though with a 33 wt% content of [BMIM][N(CN)₂], the catalyst selectivity for citronellal increased to >99% (note that lower conversions were

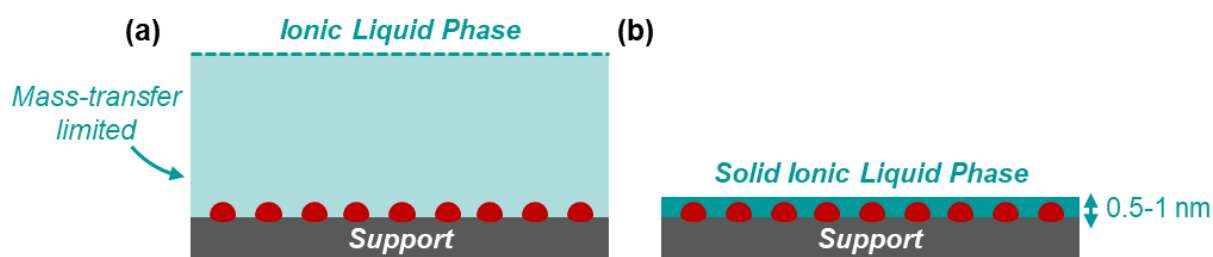


Figure 1.12 Cartoon of solid supported metal nanoparticles (a) dispersed in an IL solvent and (b) coated in a thin ionic liquid layer, commonly referred to as a ‘solid ionic liquid phase’.

obtained when the IL loading was increased to 50 wt%). High selectivities can be attributed to the fact that the hydrogen uptake of Pd/SiO₂ was severely reduced in the presence of the IL layers, which is consistent with the poor solubility of hydrogen in ILs.¹⁰³ Analysis of Pd/SiO₂ surfaces using XPS following treatment of the catalyst with a surface layer of [BMIM][NTf₂] and [BMIM][N(CN)₂] highlighted that metallic Pd, at 335 eV in the unmodified surface, shifted to higher binding energies with additional states between 336-338 eV.¹⁰⁴ The authors attribute these additional features to partially oxidised Pd, however, EXAFS results showed lower Pd-O coordination numbers in the presence of an IL layer. In an analogous report, coating of Pt/SiO₂ with 1-butyl-2,3-dimethyl-imidazolium trifluoromethane sulfonate ([BDMIM][CF₃SO₃]) was found to protect the Pt catalyst against oxidation, and the IL surface coverage had a negligible impact on the catalytic activity of Pt/SiO₂ towards ethylene hydrogenation.¹⁰⁵ The strong sorption of the IL to the catalyst surface was demonstrated using ¹H MAS NMR spectroscopy, whereby a broadening effect of the IL protons upon immobilization on the catalyst was observed indicative of reduced mobility.

More recently, deposition of an IL layer to a solid supported catalyst has even been shown to effectively stabilize single atom catalysts.¹⁰⁶ Pd single atom sites immobilized on hydroxyapatite showed no evidence of sintering in the presence of an ionic liquid coating, even after 90 hours of use on stream for the catalytic hydrogenation of acetylene. The [BMIM][BF₄] coated catalyst was far more selective for ethylene than the IL-free single atom Pd catalysts, though again, this is likely a result of the poor solubility of hydrogen in ILs.¹⁰³

Although IL coatings on porous materials will typically form near-monolayers with a thickness of 0.5-1 nm,¹⁰⁷ filling of the mesopores can lead to sharp increases in the IL coverage and therefore thickness. When a porous Ni catalyst was coated with butylmethylimidazolium octyl-sulfate, a pore filling degree of only 10% lead to a 50% reduction in surface area and thus

a reduction in the catalytic activity towards the hydrogenation of cyclooctadiene.¹⁰⁸ The stability of solid-supported Pt and Ru catalysts for the S-S coupling of thiols was vastly improved by the incorporation of an IL layer, as the IL was proposed to limit catalyst poisoning by weakening the adsorption strength of sulfur to the metal surface;¹⁰⁰ however, the IL-coated catalysts were all slightly less active than their unmodified counterparts. Moreover, the success of ionic liquids and solid supported ionic liquids in biphasic catalysis may also represent a limitation, as systems are restricted from the use of solvents that would dissolve the IL layer.

1.3.4 Covalently Immobilized Ionic Liquid Supports

Covalent attachment of the ionic liquid to a solid support is an attractive solution to the common limitations of IL-phase catalysis, and has thus received considerable attention in the past 20 years to develop effective catalyst supports.^{109,110,111} Covalent attachment of the IL to a solid support has the advantage of forming an IL monolayer that will minimise mass-transfer limitations, provide compatibility with any solvent that would typically dissolve the IL (including water), and mitigate the possibility of leaching of the IL into the organic product phase.

The first example of covalently supported ionic liquids (cSILP) dates from a 2002 report by Mehnert and co-workers, where ionic liquid modified silica was used to support Rh as a hydroformylation catalyst (**Figure 1.13**).¹¹² Despite covalent attachment of an IL monolayer, the Rh catalyst was incorporated with the support as a homogenous suspension in [BMIM][BF₄], analogous to the solid supported ionic liquid catalysts described previously. The authors presumably hypothesised that a covalent ionic liquid monolayer would assist the

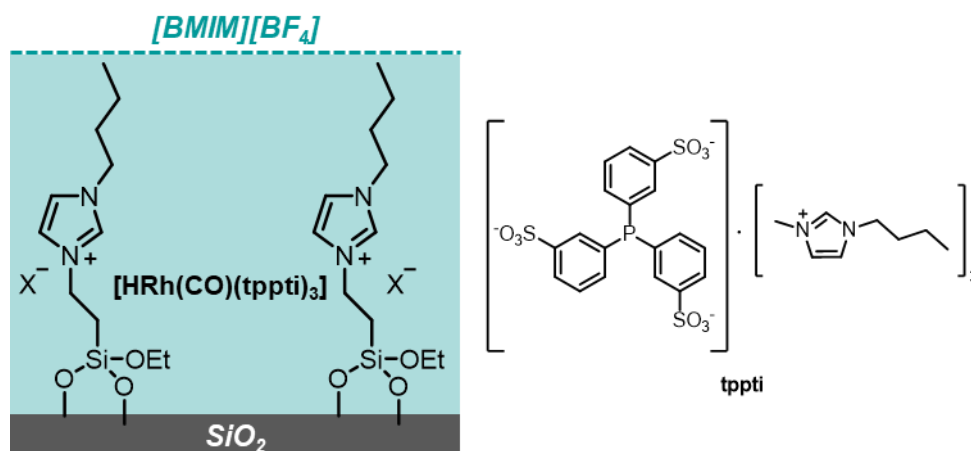
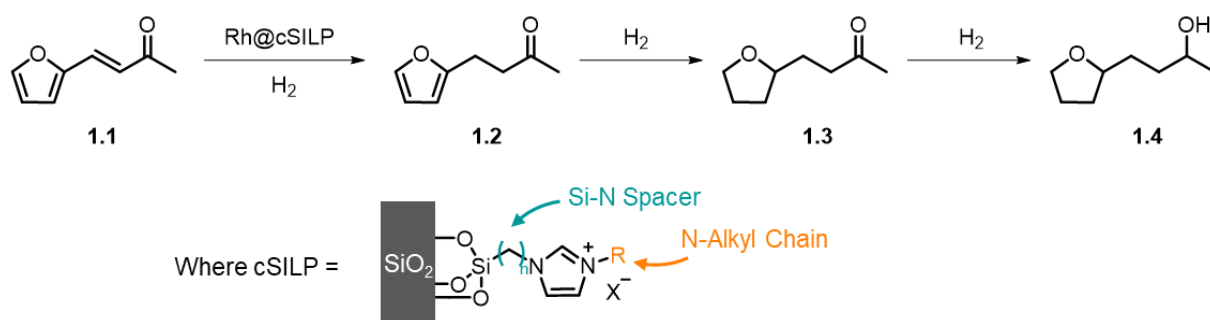


Figure 1.13 Immobilization of [HRh(CO)(tppti)₃] on silica-supported ionic liquid, used as catalyst for the hydroformylation of hexene to heptanal conducted in IL [BMIM][BF₄].¹¹²



Scheme 1.3 The hydrogenation pathway of furfuralacetone (1.1) to 4-(tetrahydrofuran-2-yl)butan-2-ol (1.4) catalysed by various SILP-supported RhNP catalysts.⁵⁸

recovery of the IL-solvated Rh catalyst layer through strong intramolecular interactions, which indeed it did, however, a comparison with IL-Rh treated unmodified silica was not performed. Contemporary reports favour immobilization of the metal catalyst through an exchange of the IL anion for a metal salt, which can then undergo *in-situ* or *ex-situ* reduction to the metal NP; however, there remain reports of homogeneous catalysts dispersed on covalently supported ionic liquids through an additional IL layer, such as in the case of an Fe pincer complex, $[\text{Fe}(\text{PNP-}i\text{Pr})(\text{CO})(\text{H})(\text{Br})]$, used as catalyst for the hydrogenation of aldehydes.¹¹³

Silica immobilized ionic liquids have since been explored in depth as covalent ionic liquid supports for metal NP catalysts, namely due to the ease of synthetic approaches, and the ability to tune pore size of the silica network. Surprisingly, the presence of IL-linkers between Si sites does not appear to compromise the long-range order of mesoporous silica structures.¹¹⁴ Following Mehnert's seminal report,¹¹² the Karimi group were one of the first to demonstrate the beneficial use of silica immobilized ionic liquid supports, in the absence of an additional IL-phase.¹¹⁵ Silica supported imidazolium groups were used as carbene precursors for the coordination of $\text{Pd}(\text{OAc})_2$. The resulting material was an effective catalyst for the Heck coupling reaction of arylbromides/iodides with various acrylates and olefins, with no appreciable loss of activity over 5 cycles. Following reaction, TEM images showed the formation of Pd NPs with a broad size distribution (10-40 nm), though a hot filtration test demonstrated that if any Pd was leaching from the catalyst, the soluble species was not catalytically active.

While the IL-precursors for covalent grafting are generally uninspired, based on triethylsiloxypropylimidazolium salts,¹¹⁶ the Leitner group have made several contributions to this area that incorporate functionalised ionic liquid grafted silica supports.¹¹⁷ In a recent example, the effect of the Si-N alkyl spacer, N-alkyl chain, and anion on the catalytic activity

of Rh NPs for the hydrogenation of furfuralacetone (**1.1**) was investigated (**Scheme 1.2**).⁵⁸ In a finding consistent with the report of Ru NPs generated in neat IL,⁹⁹ increasing the length of the N-alkyl chain had a near linear relationship with increasing NP size from 0.7 to 1.2 nm for methyl, butyl and octyl functionalised ILs. The degree of conversion of furfuralacetone to 4-(tetrahydrofuranyl)butan-2-ol (**1.4**) increased with increasing NP size (and thus increasing chain length) up to 1.2 nm. Note that 1.4 nm RuNPs generated on decyl-substituted ILs led to lower conversions to 4-(tetrahydrofuranyl)butan-2-ol due to a significant degree of partial reduction to 4-(tetrahydrofuranyl)butan-2-one (**1.3**). Remarkably, reducing the length of the Si-N alkyl spacer from C₃ to C₁ also had a significant impact on the NP size with an increase to 2.0 nm, compared to 1.2 nm for C₃. While these larger NPs were not effective for the complete hydrogenation of furfuralacetone, the catalyst was highly selective for partial reduction to 4-(tetrahydrofuranyl)butan-2-one, even over long reaction times. The IL anion also appeared to have a significant influence on Rh NP catalyst activity, whereby catalysts featuring the weakly coordinating NTf₂⁻ anion were significantly more active than those that incorporated strongly coordinating OTf⁻ and Br⁻ anions. Weakly coordinating poly(ionic liquid) catalyst supports featuring NTf₂⁻ anions also showed superior activity for the Pt-catalysed oxidation of hydroxymethylfurfural, where poly(ionic liquids) with more strongly coordinating Cl⁻ and RCOO⁻ anions appeared to hinder catalytic activity.¹¹⁸

In an alternative approach to covalent immobilisation, the Wisser group developed new silica-based SILP materials based on self-healing covalent-like Si-F interactions.¹¹⁹ Functionalised ionic liquids were tagged with fluorine ‘anchors’ that interacted strongly with a commercial silica (SBA-15) support as shown by some elegant MAS NMR spectroscopy studies. The authors posit that these F-anchored materials have the advantage of ‘self-healing’ should the interaction be disrupted during catalysis, something a covalent anchor is not able to do (though this approach is contingent on ligand cleavage occurring at the anchor position and does not account for any additional degradation). The aforementioned SILPs were designed as catalyst supports, though no catalysis has been described, thus, it will be interesting to learn if a reversibly-tethered IL ligand is advantageous for metal NP catalysis.

A range of solid supports have since been used for the covalent immobilization of ionic liquids such as molecular sieves,¹²⁰ minerals,⁸⁸ cellulose,¹²¹ and aluminium oxide.⁴³ Carbonaceous solids such as graphene,¹²² carbon nanotubes (CNT),¹²³ fullerenes,⁸⁹ and reduced graphene oxide¹²⁴ are particularly useful ionic liquid supports as their conductivity also makes them

suitable for electrochemical applications.¹²⁵ In thermal catalysis, Pd NP catalysts immobilized on an IL-grafted CNT support saw no loss in activity for up to 50 cycles of olefin hydrogenation reactions,¹²⁶ highlighting that cSILP's are not only effective at stabilizing metal NP catalysts, but they also preserve catalyst activity over extended periods.

1.4 Polymer Immobilized Ionic Liquids

Polymeric ionic liquids (PILs), or so-called polymer immobilized ionic liquids (PIILs), share many of the same advantages of other solid-supported ionic liquids such as reduced leaching of the ionic liquid and improved chemical stability¹²⁷ and have thus been explored extensively in recent years for the immobilization of enzymes,¹²⁸ as well as for use in drug delivery systems.¹²⁹ Their ionic conductivity, low flammability, negligible volatility and wide electrochemical stability has also made them an attractive replacement for often flammable electrolytes in a range of electrochemical applications such as in supercapacitors¹³⁰ as well as in lithium metal¹³¹ and lithium ion batteries.¹³²

While silica, carbon and MOF supported ILs boast well-defined mesoporous structures, poly(ionic liquids) too are capable of intricate architectures that impart useful properties. Intelligent design of IL monomers can allow for growth of self-arranged polymer morphologies. For example, when alkyl-substituted vinyl imidazolium monomers were polymerised, the hydrophobic alkyl chains facilitated the assembly of ordered lamellar structures (**Figure 1.14b**).¹³³ Interestingly, similar effects can also be obtained through careful choice of anion. For example, the incorporation of a chiral anion can lead to the formation of a chiral PIL; the exchange of hydroxide for enantiopure amino acids introduced chirality to PILs that were then used as asymmetric catalysts in the Baylis-Hilman reaction.¹³⁴ While the achiral

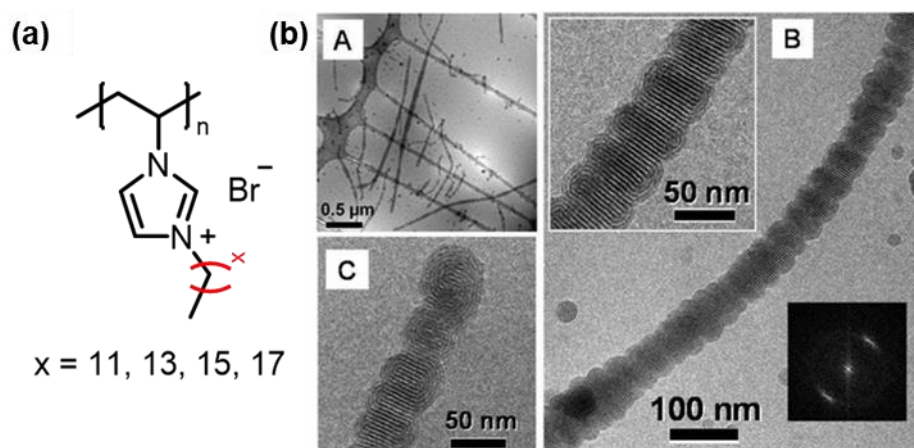


Figure 1.14 (a) Structure of *N*-alkyl-substituted poly(vinyl imidazolium bromide) polymers and the corresponding cryo-TEM images when $x = 11$ (b).

PILs exhibited no notable morphology when examined by SEM and TEM, the introduction of proline and histidine derived anions led to the formation of rod-like double helical structures.

Several researchers have also exploited the malleable nature of PILs to develop multifunctional composite materials through the incorporation of a polymer into existing porous solids. Cooperative effects are observed when metal organic frameworks are filled with PILs; for example, poly(vinyl-imidazolium bromide) impregnated MIL-101 materials were found to be more active for the cycloaddition of CO₂ with epoxide epichlorohydrin than the polymer or the MOF when used independently of each other.¹³⁵ Similar composite materials include multi-walled carbon nanotubes that have been functionalised with highly cross-linked PILs. The Giacalone group have grafted poly(bis-vinylimidazolium) to MWCNT to serve as supports for Pd NP catalysts,¹²³ and more recently as supports for the immobilization of Mg-porphyrin catalysts.¹³⁶

1.4.1 PILs as Catalyst Supports

The designability and potential functionalisation of poly(ionic liquids) therefore presents an exciting platform for the synthesis of interesting and bespoke catalyst materials.^{109,137} Moreover, the accessibility of this approach means that post-modification of commercial polymers can also result in active catalyst supports. Pre-formed Merrifield peptide resins have been used as PIL scaffolds through substitution of pendant chloromethylstyrene groups using 1,2-dimethylimidazole; the afforded resin-immobilized IL units were impregnated with RuCl₃ before successive reduction of the metal with sodium borohydride.¹³⁸ The resulting RuNP@PIL proved to be an effective catalyst for the N-formylation of various amines in the presence of CO₂ and DMAB. Merrifield resin has also been treated 2-methylimidazole to obtain analogous supported IL systems which were deprotonated using potassium *tert*-butoxide to generate the imidazole carbene. Addition of Pd(OAc)₂ led to carbene-complexed Pd^{II} species immobilized on the solid ionic liquid support which were then investigated for the Pd-catalysed Heck reaction (**Figure 1.15**).¹³⁹ The authors found that despite Pd leaching to form highly active soluble catalyst species, aggregation to inactive Pd black was prevented in the presence of the PIL support. Although catalytically active soluble Pd species agglomerated in solution, these aggregates were apparently sequestered by the support, allowing the catalyst to be recycled over 5 runs with no drop in activity (though with slower initial kinetics due to required leaching of Pd from what has become a NP, rather than the supported complex). The Pd release and recapture behaviour of the support could be tuned by varying the PIL anion, for example

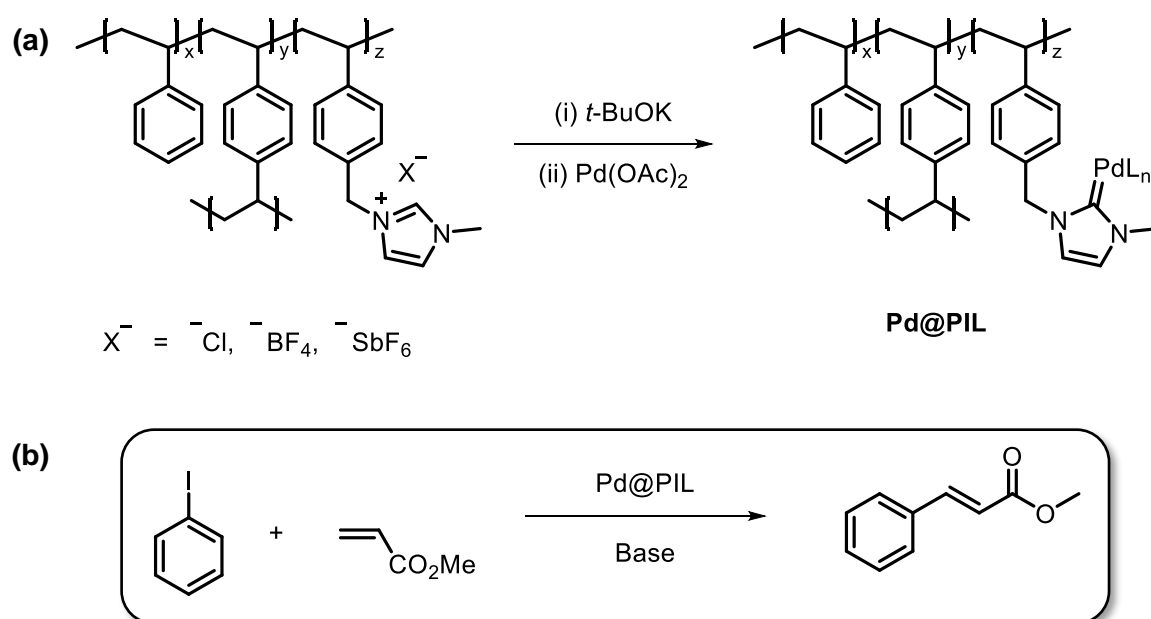


Figure 1.15 (a) Preparation of carbene immobilized Pd@PIL materials for use as catalysts in the Heck reaction (b).

weakly coordinating SbF_6^- and BF_4^- anions led to much larger TOFs, however, increased Pd leaching led to poorer recyclability.

In an alternative approach, rather than exploiting the anion exchange property of ILs to load the support with a metal precursor, authors blended poly(ionic liquids) with an existing polymer supported chiral Ru complex, asserting that the two polymers are physisorbed to one another after mixing.¹⁴⁰ The authors proposed that by incorporating a mixture of Cl^- and NTf_2^- anions in the PIIL support, they were able to prepare catalysts that were highly active for the transfer hydrogenation of aliphatic and aromatic ketones. Higher conversions and selectivities for the corresponding alcohols were obtained for the mixed $\text{Cl}^-/\text{NTf}_2^-$ system, than when the PIIL supported catalyst contained only one of the anions. Moreover, the NTf_2^- decorated PIIL system saw significant leaching of Ru after catalysis, highlighting the importance of anion choice. The improved activity of the catalyst in the presence of the amphiphilic PIIL was rationalised by the ability of the catalyst to form micellar structures which were advantageous for reactions with aliphatic substrates. The group later described the influence of the anion mixture on the phase transition temperatures of analogous PIIL supported Ru/Pd catalysts, whereby the catalyst particle size was heavily influenced by the reaction temperature.¹⁴¹

A similar polymer blend approach led to the formation of mesopores when a cyano-substituted poly(vinylimidazolium) monomer was mixed with poly(acrylic acid) in the presence of ammonia.¹⁴² Deprotonation of poly(acrylic acid) leading to an anion exchange

between the resulting carboxylate and the IL anion was essential for the formation of mesopores as no porous character was observed for the PIIL alone, nor for a physical mix of the PIIL with poly(acrylic acid). The porous acrylate cross-linked PIIL was later complexed with CuCl_2 to afford a heterogenous Cu catalyst that effectively catalysed the aerobic oxidation of benzylic C-H bonds.

Importantly, the introduction of co-monomers to the IL monomer not only allow for the manipulation of the physicochemical properties of the polymer, but they also add functionality and can provide additional stabilisation to NP catalysts. In a 2005 report,¹⁴³ Kou and co-workers developed a copolymer of vinylbutylimidazolium chloride and N-vinylpyrrolidone which was used to stabilize Rh NP catalysts for the hydrogenation of benzene. Despite the forcing conditions (75 °C, 40 bar H_2), the NP size remained unchanged following catalysis and a TON of 20,000 was obtained over 5 recycles of the catalyst. When the same reaction was conducted with polyvinylpyrrolidone as the catalyst stabilizer, negligible activity was observed, potentially due to the rapid formation of black Rh aggregates; however, the hydrogenations were conducted in [BMIM][BF₄] as solvent, and as PVP is typically insoluble in ILs, this is not a valid comparison of the influence of the individual co-monomers. In this vein, while the PIL support in the absence of pyrrolidone was not explored as catalyst stabilizer, a comparison with Rh NPs dispersed in the IL solvent (*i.e.* no polymer) also afforded negligible conversion of substrate. A later report by the same group attempted a comparison with Rh NPs stabilised by the IL homopolymer, however, they report that the reduction of RhCl_3 did not occur in the absence of the pyrrolidone co-monomer, albeit without details regarding characterisation of the resulting material.¹⁴⁴ In addition to this, NPs stabilized by the same ionic liquid – PVP copolymer were reported to be as active as PVP stabilized Pt NPs for the hydrogenation of nitroaromatics.¹⁴⁵ Thus, while the PVP-functionalised poly(ionic liquids) were undoubtedly effective catalyst supports, the role of the ionic liquid moiety is not clear.

Pyridine-functionalised poly(vinyl imidazolium) polymers have been employed as a route to incorporate Cu(I) sites on CuNP catalysts for the electroreduction of CO_2 to multiple-carbon products (**Figure 1.16**).¹⁴⁶ Pyridine-functionalised poly(vinyl imidazolium) polymers were prepared in the presence of preformed CuNPs (25 nm), followed by treatment with a solution of CuCl in methanol to afford $\text{Cu}^0\text{@PIL@Cu}^{\text{I}}$. While the current densities of $\text{Cu}^0\text{@PIL}$ and $\text{Cu}^0\text{@PIL@Cu}^{\text{I}}$ were comparative (381 mA cm^{-2} and 400 mA cm^{-2} respectively), the Cu^{I} decorated catalyst displayed a 66.6% Faradaic efficiency for C_{2+} product formation which was

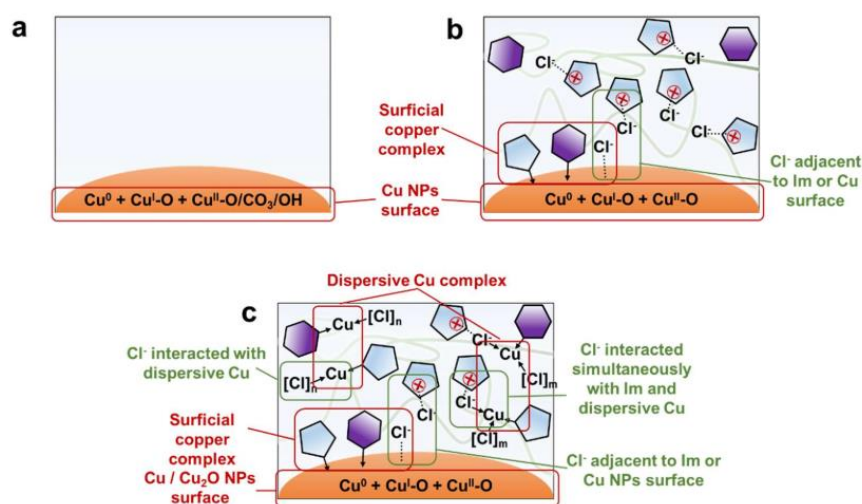


Figure 1.16 Cartoons of (a) CuNPs and the coordination modes of pyridine functionalised PIL to (b) CuNPs and (c) Cu^{I} impregnated PIL at the NP surface. Figures reproduced from Ref. 146.

notably higher than 47.6% for $\text{C}_0@\text{PIL}$. The improved selectivity for C_{2+} formation was attributed to the poor diffusion of CO through the PIL which allowed the Cu^{I} species to catalyse the C-C coupling reaction. However, PIL supported Cu^{I} alone ($\text{Cu}^{\text{I}}@\text{PIL}$) predominantly saw the formation of H_2 and CH_4 during the electrocatalytic reduction of CO_2 ; indeed, when CO was used as the feed gas $\text{Cu}^{\text{I}}@\text{PIL}$ afforded C_{2+} products with a Faradaic efficiency of 93%. Thus, the PIL was able to create a highly active and selective catalyst microenvironment through the introduction of pyridine and imidazole-carbene complexed Cu^{I} to the CuNP interface.

The design scope for intricate catalyst environments through polymer immobilized ionic liquid supports is evidently limitless.¹²⁹ While bespoke polymeric microenvironments have been developed employing a range of stabilising forces for metal NP catalysis, the influence of each component in the support ensemble is often ambiguous, and there is reasonable speculation as to whether some components provide any benefit at all.

1.4.2 Doherty PIILs

The Doherty group have made several contributions to the field of PIIL supported catalysis. By utilizing PIIL supports as catalyst scaffolds, the group have attempted to explore the catalyst-support relationship through the functionalisation of IL monomer units, and through the incorporation of several co-monomers featuring heteroatom donors. Both approaches have led to the development of highly active catalysts for a range of transformations *via* modulation of the catalyst microenvironment.

Modification of a typical styryl-imidazolium unit with a hygroscopic polyethyleneglycol (PEG) side-chain significantly improved the activity of PdNP-catalysed hydrogenation of cinnamaldehyde.¹⁴⁷ Higher conversions of cinnamaldehyde to hydrocinnamaldehyde were consistently observed irrespective of solvent and base additive for PdNP@PPh₂-PEGPIIL catalyst when compared to its PEG-ylated counterpart PdNP@PPh₂-PIIL. The PEG-modified catalysts were also more selective for hydrocinnamaldehyde over the competing formation of cinnamyl alcohol, and the full reduction to 3-phenylpropanol. Importantly, the PEG-functionalised PIL was highly active in water, a solvent that is seldom reported for the hydrogenation of cinnamaldehyde, though hydrogenations in less polar solvents such as toluene, hexane and ethyl acetate were notably less efficient. While the positive influence of the PEG unit appeared clear, removal of the ionic liquid unit also seemed to have a negative effect on the conversion substrate. Similarly, a reduction in activity was observed upon removing the ionic liquid or the PEG units from PdNP@PPh₂-PEGPIIL catalysts in the Pd-catalysed hydrogenation of nitroarenes.¹⁴⁸ As removal of these functionalities did not influence NP size, the differences in activity were attributed to the improved dispersion of the catalysts in water in the presence of both IL and PEG. To this end, dynamic light scattering experiments demonstrated that the dispersion of PEGPIIL-NP composite particles was found to be highly dependent on the solvent mixture. The optimum activity of the PdNP@PPh₂-PEGPIIL as a catalyst for Suzuki-Miyaura cross-couplings was found to be with a 1:1 mixture of H₂O/EtOH as solvent; in water or ethanol independently, composite aggregates between 0.5 – 10 µm were observed, whereas in a 1:1 mixture of the two solvents, aggregates of only 0.1 µm were found.¹⁴⁹

In most instances, ILs alone are considered sufficient for NP stabilisation under a range of conditions, however this may not always be the case.¹⁵⁰ At temperatures exceeding 120 °C, [EMIM][OTf] was insufficient at stabilising Au NPs against aggregation.¹⁵¹ Molecular dynamics simulations of Pd NPs also suggest that leached PdX⁻ and PdPh⁺ species are stabilized by the IL phase during the oxidative addition of arylhalides, while the leaching of monometallic Pd⁰ species was considered less feasible.¹⁵² In an effort to improve NP stability, the Doherty group sought to incorporate various heteroatom donor moieties into their PIL frameworks which could coordinate to metal NP surfaces and enhance catalyst longevity. In a systematic comparison of the influence of various ligands on the catalytic activity of PdNPs for cross-coupling reactions (**Figure 1.17**), diphenylphosphine-functionalised PILs were found to be

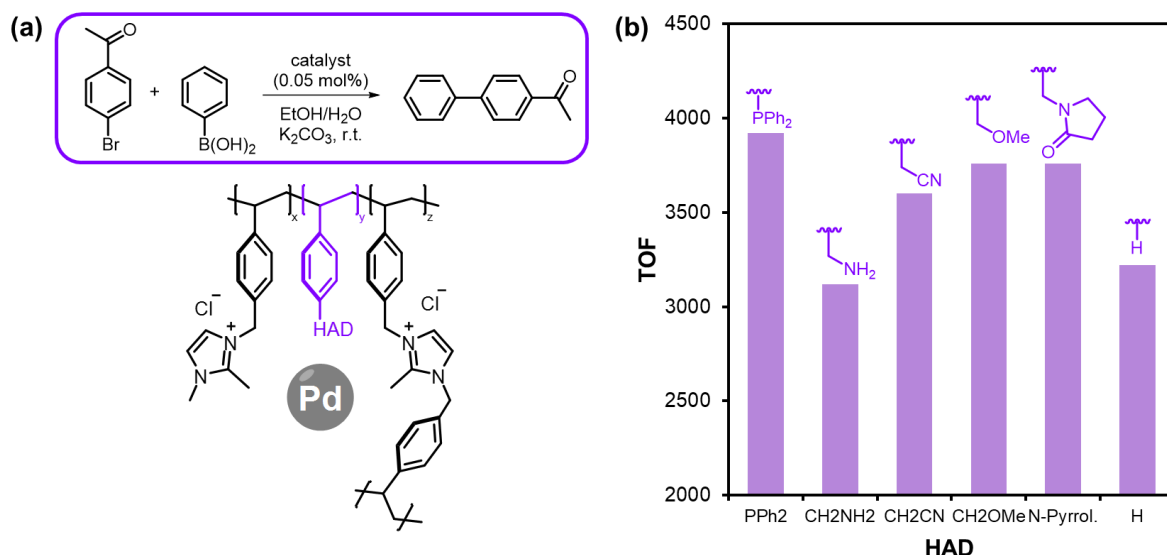


Figure 1.17 (a) Schematic of PdNP@HAD-PIIL catalysed Suzuki-Miyaura coupling reaction and the corresponding comparison of catalytic activity as a function of heteroatom donor (HAD) group (b).

notably more active than its unmodified counterpart,¹⁴⁹ an initial TOF of 3920 h⁻¹ was given compared to 3220 h⁻¹ when the heteroatom donor was substituted for a styrene group (HAD = H). Further optimisation of the PPh₂-decorated polymer by functionalising the ionic liquid with a PEG group led to a slight increase in initial activity with a TOF of 4,000 h⁻¹. While there was no trend between activity and NP size, strongly coordinating benzylamine and methoxy donors generated the smallest NPs with mean diameters of 1.80 nm and 1.75 nm respectively, while weakly coordinating nitrile donors generated the largest NPs at 3.20 nm in diameter, which were even larger than the undecorated NPs (3.01 nm).

As described in **Section 1.2.3**, the employment of heteroatom donors or surface ligands has the added benefit of tuning the surface electronic structure of the NP catalyst. Coordination of the ligand to the metal surface can lead to changes in the metal electron density which then may influence reactivity. Phosphine stabilized PdNP catalysts were analysed by fluorescence-detected X-ray absorption spectroscopy which found an increase in the Pd LIII edge energy of both PdCl₄ precatalysts, and reduced PdNP compared to Na₂PdCl₄ and Pd/C reference samples; this finding is indicative of an electron deficiency of the metal catalyst in the presence of phosphine ligands.¹⁴⁸ However, in a subsequent report of PIIL-supported gold catalysts, modification of the support with triphenylphosphine did not appear to change the Au 4f binding energies when analysed by XPS.¹⁵³ Despite this, a significant improvement in catalytic activity for the partial reduction of nitrobenzene was observed in the presence of the phosphine, with reactions reaching 100% conversion in 40 minutes, compared to 55% when catalysed by the unmodified AuNP. To complicate matters further, the surface of RuNPs was

found to become more electron rich in the presence of a phosphine oxide functionalised PIIL support, again leading to an improved efficacy as a hydrogenation catalyst.¹⁵⁴

Thus, while incorporation of surface ligands into PIIL frameworks appears to exert an advantageous effect on the catalytic activity of transition metal NPs, the influence of these heteroatom donors remains rather ill defined. In some cases, coordination of the ligand to the NP appears to influence the metal surface electronic structure, but, as described here, this has had a positive, negative and no effect on the NP electron density across various metals and ligands in the literature. However, irrespective of electronic donor effects, the incorporation of a surface ligand has in most cases resulted in an increased catalytic activity of the NP. Therefore, further studies clearly need to be undertaken to understand if this is a ligand-electronic effect on the metal, or if the ligand is instead cooperative whereby the ligand may activate substrates or stabilize transition states. This thesis therefore expands on the work carried out on the functionalisation of PIIL supports for development of active metal NP catalysts. The advantages of the poly(ionic liquid) approach will be exploited as a scaffold to continue the investigation of how various heteroatom donors can influence catalyst activity.

1.5 References

-
- ¹ K. Sanderson and D. Castelvechi, *Nature*, 2023, **622**, 227–228.
- ² I. Freestone, N. Meeks, M. Sax and C. Higgitt, *Gold Bull.*, 2007, **40**, 270–277.
- ³ M. Haruta, *Chem. Rec.*, 2003, **3**, 75–87.
- ⁴ C. Burda, X. Chen, R. Narayanan and M. A. El-Sayed, *Chem. Rev.*, 2005, **105**, 1025–1102.
- ⁵ K. Lance Kelly, E. Coronado, L. Lin Zhao and G. C. Schatz, *J. Phys. Chem. B*, 2003, **107**, 668–677.
- ⁶ M. Faraday, *Phil. Trans. R. Soc.*, 1857, **147**, 145–181.
- ⁷ J. Polte, T. T. Ahner, F. Delissen, S. Sokolov, F. Emmerling, A. F. Thünemann and R. Kraehnert, *J. Am. Chem. Soc.*, 2010, **132**, 1296–1301.
- ⁸ A. Liebsch, *Phys. Rev. B*, 1993, **48**, 11317–11328.
- ⁹ M. Sankar, Q. He, R. V. Engel, M. A. Sainna, A. J. Logsdail, A. Roldan, D. J. Willock, N. Agarwal, C. J. Kiely and G. J. Hutchings, *Chem. Rev.*, 2020, **120**, 3890–3938.
- ¹⁰ M. Haruta, T. Kobayashi, H. Sano and N. Yamada, *Chem. Lett.*, 1987, **16**, 405–408.
- ¹¹ P. Johnston, N. Carthey and G. J. Hutchings, *J. Am. Chem. Soc.*, 2015, **137**, 14548–14557.
- ¹² A. Moores and F. Goettmann, *New J. Chem.*, 2006, **30**, 1121–1132.
- ¹³ Y. Liu, X. Zhang, L. Luo, L. Li, Y. He, J. An and D. Gao, *ACS Biomater. Sci. Eng.*, 2018, **4**, 2911–2921.
- ¹⁴ L. Yi, S. Ci, S. Luo, P. Shao, Y. Hou and Z. Wen, *Nano Energy*, 2017, **41**, 600–608.
- ¹⁵ V. Abhinav K, V. K. Rao R, P. S. Karthik and S. P. Singh, *RSC Adv.*, 2015, **5**, 63985–64030.
- ¹⁶ B. Sun, L. Ning and H. C. Zeng, *J. Am. Chem. Soc.*, 2020, **142**, 13823–13832.
- ¹⁷ D. A. H. Cunningham, W. Vogel, H. Kageyama, S. Tsubota and M. Haruta, *J. Catal.*, 1998, **177**, 1–10.
- ¹⁸ M. Guo, Q. Meng, W. Chen, Z. Meng, M. L. Gao, Q. Li, X. Duan and H. L. Jiang, *Angew. Chemie - Int. Ed.*, 2023, **62**, e202305212.
- ¹⁹ E. D. Goodman, A. C. Johnston-Peck, E. M. Dietze, C. J. Wrasman, A. S. Hoffman, F. Abild-Pedersen, S. R. Bare, P. N. Plessow and M. Cargnello, *Nat. Catal.*, 2019, **2**, 748–755.

-
- ²⁰ X. Hai, Y. Zheng, Q. Yu, N. Guo, S. Xi, X. Zhao, S. Mitchell, X. Luo, V. Tulus, M. Wang, X. Sheng, L. Ren, X. Long, J. Li, P. He, H. Lin, Y. Cui, X. Peng, J. Shi, J. Wu, C. Zhang, R. Zou, G. Guillén-Gosálbez, J. Pérez-Ramírez, M. J. Koh, Y. Zhu, J. Li and J. Lu, *Nature*, 2023, **622**, 754–760.
- ²¹ T. Ishida, T. Murayama, A. Taketoshi and M. Haruta, *Chem. Rev.*, 2020, **120**, 464–525.
- ²² C. Vogt and B. M. Weckhuysen, *Nat. Rev. Chem.*, 2022, **6**, 89–111.
- ²³ S. Neumann, T. Gutmann, G. Buntkowsky, S. Paul, G. Thiele, H. Sievers, M. Bäumer and S. Kunz, *J. Catal.*, 2019, **377**, 662–672.
- ²⁴ R. Reske, H. Mistry, F. Behafarid, B. Roldan Cuenya and P. Strasser, *J. Am. Chem. Soc.*, 2014, **136**, 6978–6986.
- ²⁵ B. Song, D. Lee, H. Jeong, M. Yun and Y. Yun, *ACS Catal.*, 2024, **14**, 2620–2630.
- ²⁶ T. S. Kim, C. R. O'Connor and C. Reece, *Nat. Commun.*, 2024, **15**, 1–12.
- ²⁷ J. J. Willis, A. Gallo, D. Sokaras, H. Aljama, S. H. Nowak, E. D. Goodman, L. Wu, C. J. Tassone, T. F. Jaramillo, F. Abild-Pedersen and M. Cargnello, *ACS Catal.*, 2017, **7**, 7810–7821.
- ²⁸ A. D. Allian, K. Takanabe, K. L. Fajdala, X. Hao, T. J. Truex, J. Cai, C. Buda, M. Neurock and E. Iglesia, *J. Am. Chem. Soc.*, 2011, **133**, 4498–4517.
- ²⁹ S. Ladas, H. Poppa and M. Boudart, *Surf. Sci.*, 1981, **102**, 151–171.
- ³⁰ N. Jeddi, N. W. J. Scott and I. J. S. Fairlamb, *ACS Catal.*, 2022, **12**, 11615–11638.
- ³¹ O. J. Newton, M. J. Takle, J. Richardson, K. Hellgardt and K. K. M. Hii, *ACS Catal.*, 2024, 9678–9686.
- ³² P. W. Voorhees, *J. Stat. Phys.*, 1985, **38**, 231–252.
- ³³ Q. Zhang, X. Peng, Y. Nie, Q. Zheng, J. Shangguan, C. Zhu, K. C. Bustillo, P. Ercius, L. Wang, D. T. Limmer and H. Zheng, *Nat. Commun.*, 2022, **13**, 1–10.
- ³⁴ L. Shang, T. Bian, B. Zhang, D. Zhang, L. Z. Wu, C. H. Tung, Y. Yin and T. Zhang, *Angew. Chemie - Int. Ed.*, 2014, **53**, 250–254.
- ³⁵ R. S. Drago, K. Jurczyk, N. Kob, A. Bhattacharyya and J. Masin, *Catal. Letters*, 1998, **51**, 177–181.
- ³⁶ E. D. Goodman, A. C. Johnston-Peck, E. M. Dietze, C. J. Wrasman, A. S. Hoffman, F. Abild-pedersen, S. R. Bare, P. N. Plessow and M. Cargnello, *Nat. Catal.*, 2019, **2**, 748–755.
- ³⁷ A. J. Martín, S. Mitchell, C. Mondelli, S. Jaydev and J. Pérez-Ramírez, *Nat. Catal.*, 2022, **5**, 854–866.
- ³⁸ I. Pastoriza-Santos and L. M. Liz-Marzán, *Langmuir*, 2002, **18**, 2888–2894.
- ³⁹ M. Salavati-Niasari, F. Davar and M. Mazaheri, *Polyhedron*, 2008, **27**, 3467–3471.

-
- ⁴⁰ G. Cotin, B. Heinrich, F. Pertont, C. Kiefer, G. Francius, D. Mertz, B. Freis, B. Pichon, J.-M. Strub, S. Cianféroni, N. O. Peña, D. Ihiwakrim, D. Portehault, O. Ersen, A. Khammari, M. Picher, F. Banhart, C. Sanchez and S. Begin-Colin, *Small*, 2022, **18**, 2200414.
- ⁴¹ F. Pertont, G. Cotin, C. Kiefer, J. M. Strub, S. Cianferani, J. M. Greneche, N. Parizel, B. Heinrich, B. Pichon, D. Mertz and S. Begin-Colin, *Inorg. Chem.*, 2021, **60**, 12445–12456.
- ⁴² S. Wu, M. Li and Y. Sun, *Angew. Chemie - Int. Ed.*, 2019, **58**, 8987–8995.
- ⁴³ L. Luza, A. Gual, D. Eberhardt, S. R. Teixeira, S. S. X. Chiaro and J. Dupont, *ChemCatChem*, 2013, **5**, 2471–2478.
- ⁴⁴ I. Cano, A. Weilhard, C. Martin, J. Pinto, R. W. Lodge, A. R. Santos, G. A. Rance, E. H. Åhlgren, E. Jónsson, J. Yuan, Z. Y. Li, P. Licence, A. N. Khlobystov and J. Alves Fernandes, *Nat. Commun.*, 2021, **12**, 2–7.
- ⁴⁵ V. Giulimondi, S. K. Kaiser, M. Agrachev, F. Krumeich, A. H. Clark, S. Mitchell, G. Jeschke and J. Pérez-Ramírez, *J. Mater. Chem. A*, 2021, **10**, 5953–5961.
- ⁴⁶ M. Tromp, J. R. A. Sietsma, J. A. Van Bokhoven, G. P. F. Van Strijdonck, R. J. Van Haaren, A. M. J. Van der Eerden, P. W. N. M. Van Leeuwen and D. C. Koningsberger, *Chem. Commun.*, 2003, 128–129.
- ⁴⁷ L. Lu, S. Zou and B. Fang, *ACS Catal.*, 2021, **11**, 6020–6058.
- ⁴⁸ M. T. Reetz, M. Winter, R. Breinbauer, T. Thurn-Albrecht and W. Vogel, *Chem. - A Eur. J.*, 2001, **7**, 1084–1094.
- ⁴⁹ M. N. Vargaftik, V. P. Zagorodnikov, I. P. Stolyarov, I. I. Moiseev, V. A. Likholobov, D. I. Kochubey, A. L. Chuvilin, V. I. Zaikovsky, K. I. Zamaraev and G. I. Timofeeva, *J. Chem. Soc. Chem. Commun.*, 1985, 937–939.
- ⁵⁰ N. T. Whilton, B. Berton, L. Bronstein, H. P. Hentze and M. Antonietti, *Adv. Mater.*, 1999, **11**, 1014–1018.
- ⁵¹ L. S. Ott and R. G. Finke, *Coord. Chem. Rev.*, 2007, **251**, 1075–1100.
- ⁵² J. Dupont and M. R. Meneghetti, *Curr. Opin. Colloid Interface Sci.*, 2013, **18**, 54–60.
- ⁵³ L. Wu, H. Lian, J. J. Willis, E. D. Goodman, I. S. McKay, J. Qin, C. J. Tassone and M. Cargnello, *Chem. Mater.*, 2018, **30**, 1127–1135.
- ⁵⁴ C. M. Crudden, J. H. Horton, I. I. Ebralidze, O. V. Zenkina, A. B. McLean, B. Drevniok, Z. She, H. B. Kraatz, N. J. Mosey, T. Seki, E. C. Keske, J. D. Leake, A. Rousina-Webb and G. Wu, *Nat. Chem.*, 2014, **6**, 409–414.
- ⁵⁵ Z. Cao, D. Kim, D. Hong, Y. Yu, J. Xu, S. Lin, X. Wen, E. M. Nichols, K. Jeong, J. A. Reimer, P. Yang and C. J. Chang, *J. Am. Chem. Soc.*, 2016, **138**, 8120–8125.

-
- ⁵⁶ D. O. Prima, N. S. Kulikovskaya, R. A. Novikov, A. Y. Kostyukovich, J. V. Burykina, V. M. Chernyshev and V. P. Ananikov, *Angew. Chemie - Int. Ed.*, 2024, **63**, e202317468.
- ⁵⁷ O. Vidoni, K. Philippot, C. Amiens, B. Chaudret, O. Balmes, J. O. Malm, J. O. Bovin, F. Senocq and M. J. Casanove, *Angew. Chemie - Int. Ed.*, 1999, **38**, 3736–3738.
- ⁵⁸ A. Bordet, G. Moos, C. Welsh, P. Licence, K. L. Luska and W. Leitner, *ACS Catal.*, 2020, **10**, 13904–13912.
- ⁵⁹ P. Chatterjee, H. Wang, J. S. Manzano, U. Kanbur, A. D. Sadow and I. I. Slowing, *Catal. Sci. Technol.*, 2022, **12**, 1922–1933.
- ⁶⁰ G. Chen, C. Xu, X. Huang, J. Ye, L. Gu, G. Li, Z. Tang, B. Wu, H. Yang, Z. Zhao, Z. Zhou, G. Fu and N. Zheng, *Nat. Mater.*, 2016, **15**, 564–569.
- ⁶¹ E. Shirzadi, Q. Jin, A. S. Zeraati, R. Dorakhan, T. J. Goncalves, J. Abed, B. H. Lee, A. S. Rasouli, J. Wicks, J. Zhang, P. Ou, V. Boureau, S. Park, W. Ni, G. Lee, C. Tian, D. M. Meira, D. Sinton, S. Siahrostami and E. H. Sargent, *Nat. Commun.*, 2024, **15**, 2995.
- ⁶² S. K. Singh and A. W. Savoy, *J. Mol. Liq.*, 2020, **297**, 112038.
- ⁶³ Y. Ohtsuka and Y. Tamai, *J. Catal.*, 1981, **67**, 316–323.
- ⁶⁴ V. G. Maciel, D. J. Wales, M. Seferin, C. M. L. Ugaya and V. Sans, *J. Clean. Prod.*, 2019, **217**, 844–858.
- ⁶⁵ E. M. Arnett and J. F. Wolf, *J. Am. Chem. Soc.*, 1975, **97**, 3264–3265.
- ⁶⁶ F. H. Hurley and T. P. Wier, *J. Electrochem. Soc.*, 1951, **98**, 207–212.
- ⁶⁷ J. S. Wilkes, J. A. Levisky, R. A. Wilson and C. L. Hussey, *Inorg. Chem.*, 1982, **21**, 1263–1264.
- ⁶⁸ J. S. Wilkes and M. J. Zaworotko, *J. Chem. Soc. Chem. Commun.*, 1992, 965–967.
- ⁶⁹ P. Wasserscheid and W. Keim, *Angew. Chem. Int. Ed.*, 2000, **39**, 3772–3789.
- ⁷⁰ Y. Wang, C. J. Zanelotti, X. Wang, R. Kerr, L. Jin, W. H. Kan, T. J. Dingemans, M. Forsyth and L. A. Madsen, *Nat. Mater.*, 2021, **20**, 1255–1263.
- ⁷¹ J. Kataria, P. Devi and P. Rani, *J. Mol. Liq.*, 2021, **339**, 116736.
- ⁷² B. Yao, M. Paluch and Z. Wojnarowska, *Sci. Rep.*, 2023, **13**, 1–10.
- ⁷³ R. Marcilla, J. A. Blazquez, J. Rodriguez, J. A. Pomposo and D. Mecerreyes, *J. Polym. Sci. Part A Polym. Chem.*, 2004, **42**, 208–212.
- ⁷⁴ P. R. Rony, *Ann. N. Y. Acad. Sci.*, 1970, **172**, 238–243.
- ⁷⁵ G. W. Parshall, *J. Am. Chem. Soc.*, 1972, **94**, 8716–8719.
- ⁷⁶ J. A. Boon, J. A. Levisky, J. L. Pflug and J. S. Wilkes, *J. Org. Chem.*, 1986, **51**, 480–483.
- ⁷⁷ R. T. Carlin and J. S. Wilkes, *J. Mol. Catal.*, 1990, **63**, 125–129.
- ⁷⁸ R. Sheldon, *Chem. Commun.*, 2001, **1**, 2399–2407.

-
- ⁷⁹ P. Migowski, P. Lozano and J. Dupont, *Green Chem.*, 2023, **25**, 1237–1260.
- ⁸⁰ Y. Chauvin, L. Mussman and H. Olivier, *Angew. Chem. Int. Ed. Engl.*, 1995, **34**, 2698–2700.
- ⁸¹ A. Strádi, M. Molnár, M. Óvári, G. Dibó, F. U. Richter and L. T. Mika, *Green Chem.*, 2013, **15**, 1857–1862.
- ⁸² E. Brunner, *J. Chem. Eng. Data*, 1985, **30**, 3, 269–273.
- ⁸³ H. P. Steinrück and P. Wasserscheid, *Catal. Letters*, 2015, **145**, 380–397.
- ⁸⁴ K. L. Luska and A. Moores, *ChemCatChem*, 2012, **4**, 1534–1546.
- ⁸⁵ J. D. Scholten, B. C. Leal and J. Dupont, *ACS Catal.*, 2012, **2**, 184–200.
- ⁸⁶ H. S. Schrekker, M. A. Gelesky, M. P. Stracke, C. M. L. Schrekker, G. Machado, S. R. Teixeira, J. C. Rubim and J. Dupont, *J. Colloid Interface Sci.*, 2007, **316**, 189–195.
- ⁸⁷ V. Patil, S. Mahajan, M. Kulkarni, K. Patil, C. Rode, A. Coronas and G. R. Yi, *Chemosphere*, 2020, **243**, 1–10.
- ⁸⁸ S. Miao, Z. Liu, B. Han, J. Huang, Z. Sun, J. Zhang and T. Jiang, *Angew. Chemie - Int. Ed.*, 2005, **45**, 266–269.
- ⁸⁹ F. Giacalone, V. Campisciano, C. Calabrese, V. La Parola, L. F. Liotta, C. Aprile and M. Gruttadauria, *J. Mater. Chem. A*, 2016, **4**, 17193–17206.
- ⁹⁰ M. H. G. Precht, P. S. Campbell, J. D. Scholten, G. B. Fraser, G. MacHado, C. C. Santini, J. Dupont and Y. Chauvin, *Nanoscale*, 2010, **2**, 2601–2606.
- ⁹¹ K. R. J. Lovelock, I. J. Villar-Garcia, F. Maier, H. P. Steinrück and P. Licence, *Chem. Rev.*, 2010, **110**, 5158–5190.
- ⁹² G. S. Fonseca, G. Machado, S. R. Teixeira, G. H. Fecher, J. Morais, M. C. M. Alves and J. Dupont, *J. Colloid Interface Sci.*, 2006, **301**, 193–204.
- ⁹³ J. Dupont and J. D. Scholten, *Chem. Soc. Rev.*, 2010, **39**, 1780–1804.
- ⁹⁴ A. S. Pensado and A. A. H. Pádua, *Angew. Chemie - Int. Ed.*, 2011, **50**, 8683–8687.
- ⁹⁵ K. C. Jha, H. Liu, M. R. Bockstaller and H. Heinz, *J. Phys. Chem. C*, 2013, **117**, 25969–25981.
- ⁹⁶ L. S. Ott, M. L. Cline, M. Deetlefs, K. R. Seddon and R. G. Finke, *J. Am. Chem. Soc.*, 2005, **127**, 5758–5759.
- ⁹⁷ S. C. Sau, P. K. Hota, S. K. Mandal, M. Soleilhavoup and G. Bertrand, *Chem. Soc. Rev.*, 2020, **49**, 1233–1252.
- ⁹⁸ L. S. Ott, S. Campbell, K. R. Seddon and R. G. Finte, *Inorg. Chem.*, 2007, **46**, 10335–10344.
- ⁹⁹ T. Gutel, C. C. Santini, K. Philippot, A. Padua, K. Pelzer, B. Chaudret, Y. Chauvin and J. M. Basset, *J. Mater. Chem.*, 2009, **19**, 3624–3631.

-
- ¹⁰⁰ O. D. Pavel, I. Podolean, V. I. Parvulescu, S. F. R. Taylor, H. G. Manyar, K. Ralphs, P. Goodrich and C. Hardacre, *Faraday Discuss.*, 2018, **206**, 535–547.
- ¹⁰¹ G. R. Zhang and B. J. M. Etzold, *Adv. Funct. Mater.*, 2021, **31**, 2010977.
- ¹⁰² J. Arras, M. Steffan, Y. Shayeghi and P. Claus, *Chem. Commun.*, 2008, 4058–4060.
- ¹⁰³ P. J. Dyson, G. Laurenczy, C. A. Ohlin, J. Vallance and T. Welton, *Chem. Commun.*, 2003, **3**, 2418–2419.
- ¹⁰⁴ J. Arras, E. Paki, C. Roth, J. Radnik, M. Lucas and P. Claus, *J. Phys. Chem. C*, 2010, **114**, 10520–10526.
- ¹⁰⁵ R. Knapp, A. Jentys and J. A. Lercher, *Green Chem.*, 2009, **11**, 656–66.
- ¹⁰⁶ S. Ding, Y. Guo, M. J. Hülsey, B. Zhang, H. Asakura, L. Liu, Y. Han, M. Gao, J. ya Hasegawa, B. Qiao, T. Zhang and N. Yan, *Chem*, 2019, **5**, 3207–3219.
- ¹⁰⁷ R. Atkin and G. G. Warr, *J. Phys. Chem. C*, 2007, **111**, 5162–5168.
- ¹⁰⁸ U. Kernchen, B. Etzold, W. Korth and A. Jess, *Chem. Eng. Technol.*, 2007, **30**, 985–994.
- ¹⁰⁹ F. Giacalone and M. Gruttadauria, *ChemCatChem*, 2016, **8**, 664–684.
- ¹¹⁰ R. Fehrmann, A. Riisager and M. Haumann, *Supported Ionic Liquids: Fundamentals and Applications*, Wiley-VCH, Weinheim, 2014.
- ¹¹¹ P. Kaur and H. K. Chopra, *ChemistrySelect*, 2020, **5**, 12057–12086.
- ¹¹² C. P. Mehnert, R. A. Cook, N. C. Dispenziere and M. Afeworki, *J. Am. Chem. Soc.*, 2002, **124**, 12932–12933.
- ¹¹³ J. Brünig, Z. Csendes, S. Weber, N. Gorgas, R. W. Bittner, A. Limbeck, K. Bica, H. Hoffmann and K. Kirchner, *ACS Catal.*, 2018, **8**, 1048–1051.
- ¹¹⁴ T. P. Nguyen, P. Hesemann and J. J. E. Moreau, *Microporous Mesoporous Mater.*, 2011, **142**, 292–300.
- ¹¹⁵ B. Karimi and D. Enders, *Org. Lett.*, 2006, **8**, 1237–1240.
- ¹¹⁶ Y. Kume, K. Qiao, D. Tomida and C. Yokoyama, *Catal. Commun.*, 2008, **9**, 369–375.
- ¹¹⁷ A. Bordet and W. Leitner, *Acc. Chem. Res.*, 2021, **54**, 2144–2157.
- ¹¹⁸ S. Siankevich, S. Mozzettini, F. Bobbink, S. Ding, Z. Fei, N. Yan and P. J. Dyson, *Chempluschem*, 2018, **83**, 19–23.
- ¹¹⁹ C.-L. Tavera-Méndez, A. Bergen, S. Trzeciak, F. W. Heinemann, R. Graf, D. Zahn, K. Meyer, M. Hartmann and D. Wisser, *Chem. - A Eur. J.*, 2024, **30**, e202303673.
- ¹²⁰ J. Huang, T. Jiang, H. Gao, B. Han, Z. Liu, W. Wu, Y. Chang and G. Zhao, *Angew. Chemie - Int. Ed.*, 2004, **43**, 1397–1399.
- ¹²¹ A. Pourjavadi and Z. Habibi, *Appl. Organomet. Chem.*, 2017, **31**, 1–8.

-
- ¹²² J. S. Lee, T. Lee, H. K. Song, J. Cho and B. S. Kim, *Energy Environ. Sci.*, 2011, **4**, 4148–4154.
- ¹²³ V. Campisciano, C. Calabrese, L. F. Liotta, V. La Parola, A. Spinella, C. Aprile, M. Gruttadauria and F. Giacalone, *Appl. Organomet. Chem.*, 2019, **33**, 1–12.
- ¹²⁴ X. Shi and C. Cai, *New J. Chem.*, 2018, **42**, 2364–2367.
- ¹²⁵ T. Li and W. Hu, *Green Energy Environ.*, 2024, **9**, 604–622.
- ¹²⁶ Y. S. Chun, J. Y. Shin, C. E. Song and S. Lee, *Chem. Commun.*, 2008, 942–944.
- ¹²⁷ Y. Ye and Y. A. Elabd, *Macromolecules*, 2011, **44**, 8494–8503.
- ¹²⁸ R. Porcar, I. Lavandera, P. Lozano, B. Altava, S. V. Luis, V. Gotor-Fernández and E. García-Verdugo, *Green Chem.*, 2021, **23**, 5609–5617.
- ¹²⁹ M. Zhu and Y. Yang, *Green Chem.*, 2024, **26**, 5022–5102.
- ¹³⁰ M. Jin, Y. Zhang, C. Yan, Y. Fu, Y. Guo and X. Ma, *ACS Appl. Mater. Interfaces*, 2018, **10**, 39570–39580.
- ¹³¹ K. Yin, Z. Zhang, X. Li, L. Yang, K. Tachibana and S. I. Hirano, *J. Mater. Chem. A*, 2015, **3**, 170–178.
- ¹³² L. Porcarelli, A. S. Shaplov, M. Salsamendi, J. R. Nair, Y. S. Vygodskii, D. Mecerreyes and C. Gerbaldi, *ACS Appl. Mater. Interfaces*, 2016, **8**, 10350–10359.
- ¹³³ J. Yuan, S. Soll, M. Drechsler, A. H. E. Müller and M. Antonietti, *J. Am. Chem. Soc.*, 2011, **133**, 17556–17559.
- ¹³⁴ N. Pothanagandhi, A. Sivaramakrishna and K. Vijayakrishna, *Polym. Chem.*, 2017, **8**, 918–925.
- ¹³⁵ M. Ding and H. L. Jiang, *ACS Catal.*, 2018, **8**, 3194–3201.
- ¹³⁶ L. Valentino, V. Campisciano, C. Célis, V. Lemaury, R. Lazzaroni, M. Gruttadauria, C. Aprile and F. Giacalone, *J. Catal.*, 2023, **428**, 115143.
- ¹³⁷ A. M. P. Salvo, F. Giacalone and M. Gruttadauria, *Molecules*, 2016, **21**, 1288.
- ¹³⁸ V. B. Saptal, T. Sasaki and B. M. Bhanage, *ChemCatChem*, 2018, **10**, 2593–2600.
- ¹³⁹ M. I. Burguete, E. García-Verdugo, I. García-Villar, F. Gelat, P. Licence, S. V. Luis and V. Sans, *J. Catal.*, 2010, **269**, 150–160.
- ¹⁴⁰ X. Li, Y. Sun, S. Wang and X. Jia, *ACS Appl. Polym. Mater.*, 2020, **2**, 1268–1275.
- ¹⁴¹ X. Li, Y. Sun, S. Wang and X. Jia, *ACS Appl. Mater. Interfaces*, 2020, **12**, 44094–44102.
- ¹⁴² Q. Zhao, P. Zhang, M. Antonietti and J. Yuan, *J. Am. Chem. Soc.*, 2012, **134**, 11852–11855.
- ¹⁴³ X. D. Mu, J. Q. Meng, Z. C. Li and Y. Kou, *J. Am. Chem. Soc.*, 2005, **127**, 9694–9695.
- ¹⁴⁴ C. Zhao, H. zhi Wang, N. Yan, C. xian Xiao, X. dong Mu, P. J. Dyson and Y. Kou, *J. Catal.*, 2007, **250**, 33–40.

-
- ¹⁴⁵ X. Yuan, N. Yan, C. Xiao, C. Li, Z. Fei, Z. Cai, Y. Kou and P. J. Dyson, *Green Chem.*, 2010, **12**, 228–233.
- ¹⁴⁶ G. Y. Duan, X. Q. Li, G. R. Ding, L. J. Han, B. H. Xu and S. J. Zhang, *Angew. Chemie - Int. Ed.*, 2022, **61**, e202110657.
- ¹⁴⁷ S. Doherty, J. G. Knight, T. Backhouse, E. Abood, H. Alshaikh, I. J. S. Fairlamb, R. A. Bourne, T. W. Chamberlain and R. Stones, *Green Chem.*, 2017, **19**, 1635–1641.
- ¹⁴⁸ S. Doherty, J. G. Knight, T. Backhouse, A. Bradford, F. Saunders, R. A. Bourne, T. W. Chamberlain, R. Stones, A. Clayton and K. Lovelock, *Catal. Sci. Technol.*, 2018, **8**, 1454–1467.
- ¹⁴⁹ S. Doherty, J. G. Knight, T. Backhouse, E. Abood, H. Al-shaikh, A. R. Clemmet, J. R. Ellison, R. A. Bourne, T. W. Chamberlain, R. Stones, N. J. Warren, I. J. S. Fairlamb and K. R. J. Lovelock, *Adv. Synth. Catal.*, 2018, **360**, 3716–3731.
- ¹⁵⁰ M. J. Beier, J. M. Andanson and A. Baiker, *ACS Catal.*, 2012, **2**, 2587–2595.
- ¹⁵¹ V. Khare, Z. Li, A. Manton, A. A. Ayi, S. Sonkaria, A. Voelkl, A. F. Thünemann and A. Taubert, *J. Mater. Chem.*, 2010, **20**, 1332–1339.
- ¹⁵² E. E. Zvereva, S. A. Katsyuba, P. J. Dyson and A. V. Aleksandrov, *J. Phys. Chem. Lett.*, 2017, **8**, 3452–3456.
- ¹⁵³ S. Doherty, J. G. Knight, T. Backhouse, R. J. Summers, E. Abood, W. Simpson, W. Paget, R. A. Bourne, T. W. Chamberlain, R. Stones, K. R. J. Lovelock, J. M. Seymour, M. A. Isaacs, C. Hardacre, H. Daly and N. H. Rees, *ACS Catal.*, 2019, **9**, 4777–4791.
- ¹⁵⁴ S. Doherty, J. G. Knight, T. Backhouse, T. S. T. Tran, R. Paterson, F. Stahl, H. Y. Alharbi, T. W. Chamberlain, R. A. Bourne, R. Stones, A. Griffiths, J. P. White, Z. Aslam, C. Hardare, H. Daly, J. Hart, R. H. Temperton, J. N. O’Shea and N. H. Rees, *Catal. Sci. Technol.*, 2022, **12**, 3549–3567.

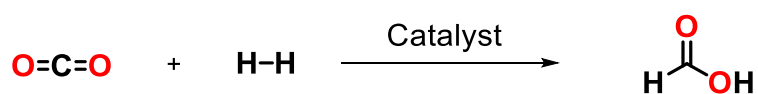
Chapter 2

Amine-Modified Pd Catalysts for CO₂ Hydrogenation

2.1 Introduction

To mitigate the adverse effects of climate change, rising global temperatures must be capped at 1.5 °C above pre-industrial levels.¹ The international energy agency (IEA), and other governing bodies on climate change, have highlighted that, in addition to the mass-adoption of renewable energy sources, CO₂ capture and storage will be a contributing factor to the energy transition and essential for achieving negative CO₂ emissions.² So-called carbon capture and storage technologies are employed to capture CO₂ from flue-gas chimneys immediately after combustion of natural gas or petroleum-based fuels. Alternatively, CO₂ can be captured directly from the air, though this technology is underdeveloped.³ Currently, captured CO₂ is mostly stored in natural geological sites (*e.g.* salt caverns in the North Sea) or is used to recover oil from depleted reserves.

The global demand for a circular economy has led to the exploration of CO₂ utilisation to produce value added chemicals such as fuels and feedstocks.⁴ Amongst these CO₂-derived commodities, formic acid has been highlighted as a future energy carrier, either acting as a hydrogen storage medium⁵ or *via* direct use in formic acid fuel cells.⁶ However, formic acid production currently depends on the hydrolysis of methyl formate, itself obtained from the carbonylation of methanol; while this process is costly and energy intensive, direct hydrogenation of CO₂ to formic acid is attractive as it is single step, and can be achieved under mild conditions with the appropriate catalyst.



Scheme 2.1 Generalised schematic of the direct hydrogenation of carbon dioxide to formic acid.

While Au^{7,8} and Ru^{9,10,11} metal nanoparticles (NP) are reported to catalyse the hydrogenation of CO₂ to formic acid/formate, studies have been dominated by catalysts based on monometallic^{12,13,14,15,16} and bimetallic^{17,18,19} Pd nanoparticles. A range of supports have been shown to stabilise PdNPs for the hydrogenation of CO₂, including mesoporous carbon,^{18,20} reduced graphene oxide,¹⁹ metal oxides,^{15,21,22} mesoporous silica,^{16,23} mesoporous hollow carbon spheres,¹⁷ micelles,¹⁴ and porous organic polymers,¹³ and most examples have shown

that surface functionalisation of the support with a weakly basic amine leads to an enhancement of catalytic activity. For instance, an improvement in the performance of PdNPs and PdAgNPs supported on amine-grafted mesoporous carbon or SBA-15, compared with their unmodified counterparts, has been attributed to several factors including; (i) the growth of small well-dispersed NPs, (ii) the formation of electron-rich palladium species resulting from charge transfer from silver, (iii) a cooperative role in facilitating the elementary steps of the catalytic cycle by stabilising reaction intermediates and (iv) increasing the CO₂ adsorption capacity/adsorption rate and concentrating the CO₂ around the active site.²³ Other examples of supports that appear to promote the hydrogenation of CO₂ by interaction of a surface nitrogen donor include AuNP@SiO₂-Schiff base and PdNP@C₃N₄.^{7,24} An amide and pyridine functionalised porous organic polymer was found to promote PdNPs towards CO₂ hydrogenation,¹³ as did coordination of a Ru catalyst to a diaminopyridine-based polymer.²⁵

As well as the use of amine donors, the incorporation of ionic liquids (ILs) is an obvious choice in the design of catalysts for CO₂ hydrogenation.²⁶ ILs are not only effective at stabilizing metal nanoparticles but they also sequester CO₂ and are being explored for applications in carbon capture and storage.^{27,28} In addition to their use as solvent,^{10,12,29} the role of ILs as sorbents appears critical in attaining high turnovers during CO₂ hydrogenation. A comparison of amino acid based ionic liquids found greater CO₂ capture for tetrabutylammonium arginate, and this translated into superior rates of hydrogenation to formate when in the presence of a Ru nanoparticle catalyst.³⁰ Silica supported RuNPs generated in IL solutions were found to retain the IL after washing, and CO₂-TPD profiles found weakly basic sites that were not present in the IL-free Ru/SiO₂ materials.⁹ The IL-mediated sorption of CO₂ can also 'activate' CO₂ towards hydrogenation, without the use of additional base additives.³¹ Imidazolium-based ILs are well-known to generate *N*-heterocyclic carbenes at the C2-position, and such carbenes are sufficiently basic to coordinate to CO₂, and this has been demonstrated with ¹H NMR spectroscopy.¹² DFT calculations have shown a strong intermolecular interaction between the imidazolium C2 carbene and CO₂ with an energy of -0.36 eV (for comparison, the interaction between water and CO₂ had an energy of -0.11 eV);³² this IL-CO₂ adduct resulted in the structural reorganization of linear CO₂ to bent CO₂, which apparently promoted the acceptance of photogenerated electrons from a AuNP catalyst. Despite this, herein, a C2-methylated imidazolium IL will be incorporated into our catalysts; this chapter aims to compare the effect of various amines on the catalytic activity of Pd NPs, therefore it seemed

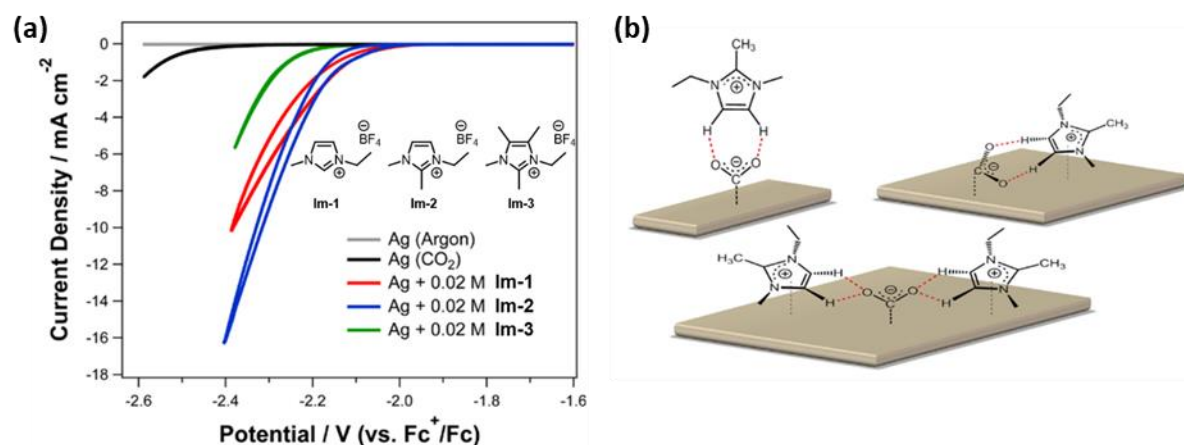


Figure 2.1 (a) Cyclic voltammograms showing the electrochemical reduction of CO₂ in the presence of various IL electrolytes. (b) Proposed binding modes of IL **Im-2** with a surface bound carboxylate species. Figures adapted from Ref ³³.

prudent to avoid the formation of an imidazolium based carbene. Coordination of the imidazolium C2 to either the metal centre or to CO₂ could obfuscate investigations into the effect of the various amine donors. However, methylation of the C2 position may not hinder the ability of the IL to promote CO₂ reduction: when a series of imidazolium ILs were employed as co-catalyst for the electrochemical reduction of CO₂ (**Figure 2.1**), higher current densities were obtained for C2-methyl imidazolium **Im-2** than for the corresponding C2-H imidazolium, **Im-1**.³³ Instead, a notable drop in current density was observed when the C4 and C5 positions were methylated (**Im-3**), indicative of the crucial role that the C4- and C5-protons may play in stabilizing anionic CO₂ surface species.

To this end, while polymer immobilized ionic liquids (PIILs) have attractive credentials as supports for metal nanoparticle catalysts, they also exhibit excellent CO₂ sorption capacity and their CO₂ sorption/desorption kinetics exceed their IL counterparts.^{34,35} PIILs have therefore seen exhaustive use as catalysts for the reaction of epoxides with CO₂ to produce cyclic carbonates, and this work has been summarized in detail in several reviews.^{36,37} However, there are seldom any reports of the use of poly(ionic liquids) in the direct hydrogenation of CO₂ to valuable commodities. Song and co-workers employed a bis(bromomethyl)biphenyl imidazolium based PIIL to support Pd NPs as catalysts for the sodium borohydride³⁸ and gaseous hydrogen³⁵ mediated hydrogenation of CO₂ to formate. Although the Pd/PIIL catalyst was reported to be 8-fold more active than commercial Pd/C, the influence of the IL was not explored in depth. In another report, a series of imidazolium bromide PIILs were prepared *via* radical polymerisation with polyhedral oligomeric

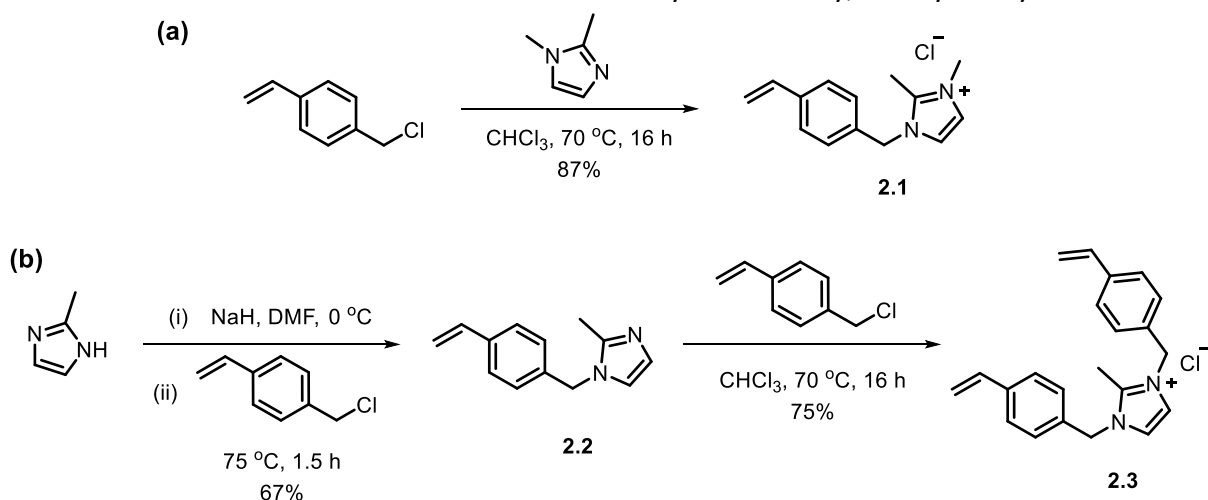
silsesquioxanes, wherein immobilized $\text{Ru}_3(\text{CO})_{12}$ catalysed the hydrogenation of CO_2 to methane.³⁹ However, to our knowledge, there have been no additional contributions to this area, therefore there is a significant knowledge gap in the potential for PIILs as supports for CO_2 utilisation, despite the precedent of their activity for CO_2 capture and conversion.³⁷

This chapter describes the first example of amine-decorated polymer immobilised ionic liquid stabilised PdNPs as catalysts for the hydrogenation of CO_2 to formate. Preliminary studies to explore the efficacy of the catalyst as a function of the composition of the support revealed that the performance depends on the type of amine and its loading on the support (*i.e.* the ionic liquid to amine ratio), and the highest TOF of 500 h^{-1} , obtained with PdNPs stabilised by aniline decorated PIIL, is among the highest to be reported. In addition, XPS studies on the precatalysts confirmed the existence of a Pd-N interaction which may play a role in the growth and dispersion of the PdNPs. Palladium in both the precatalysts, and the corresponding NPs, became electron-deficient when coordinated to the amine donors, an observation that was supported by ^{15}N MAS NMR spectroscopy.

2.2 Synthesis and Characterisation of Monomer, Polymer and Catalyst Materials

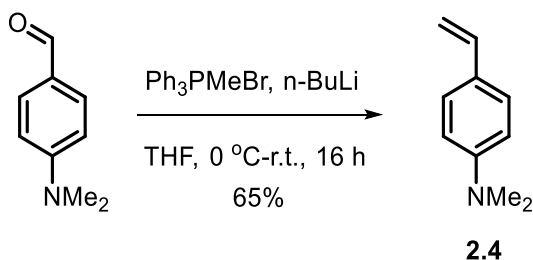
2.2.1 Monomer and Polymer Synthesis

Ionic liquid imidazolium monomer 1,2-dimethyl(4-vinylbenzyl)imidazolium chloride (**2.1**) and the cross-linker 2-methyl-1,3-bis(4-vinylbenzyl)imidazolium chloride (**2.3**) have been prepared previously and have served as benchmark ILs for the investigation of functionalised PIILs within the Doherty group.⁴⁰ Monomer **2.1** was first reported for its ‘metal scavenging ability’ and was found to sequester CuI , $\text{Pd}(\text{OAc})_2$, IrCl_3 , and Pd^0 effectively, making it well-suited for our desire to stabilize metal NPs catalysts.⁴¹ Briefly, 4-vinylbenzylchloride was



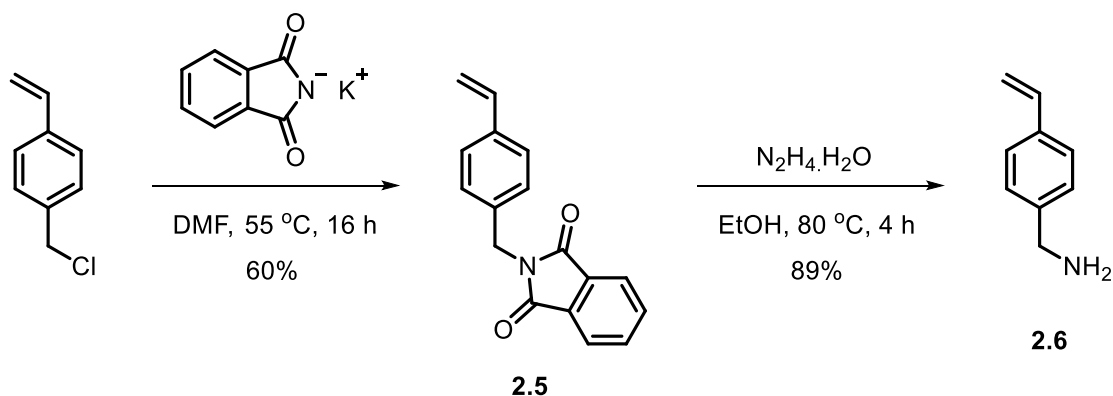
Scheme 2.2 Preparation of imidazolium ionic liquid **2.1** (a) and corresponding cross-linker **2.3** (b) through nucleophilic substitutions of 4-vinylbenzylchloride.

substituted with 1,2-dimethylimidazole in chloroform, affording a white fluffy powder in good yield following precipitation into diethyl ether, as described in **Scheme 2.2a**. The corresponding cross-linker was prepared in a similar fashion – first 2-methylimidazole was deprotonated with NaH before addition of 4-chloromethylstyrene to the resulting imidazolate. 4-(Vinylbenzyl)-2-methylimidazole was obtained following an acid-base work-up before stirring the pure product with further 4-vinylbenzylchloride. The quarternised product was obtained again by precipitation in diethyl ether.



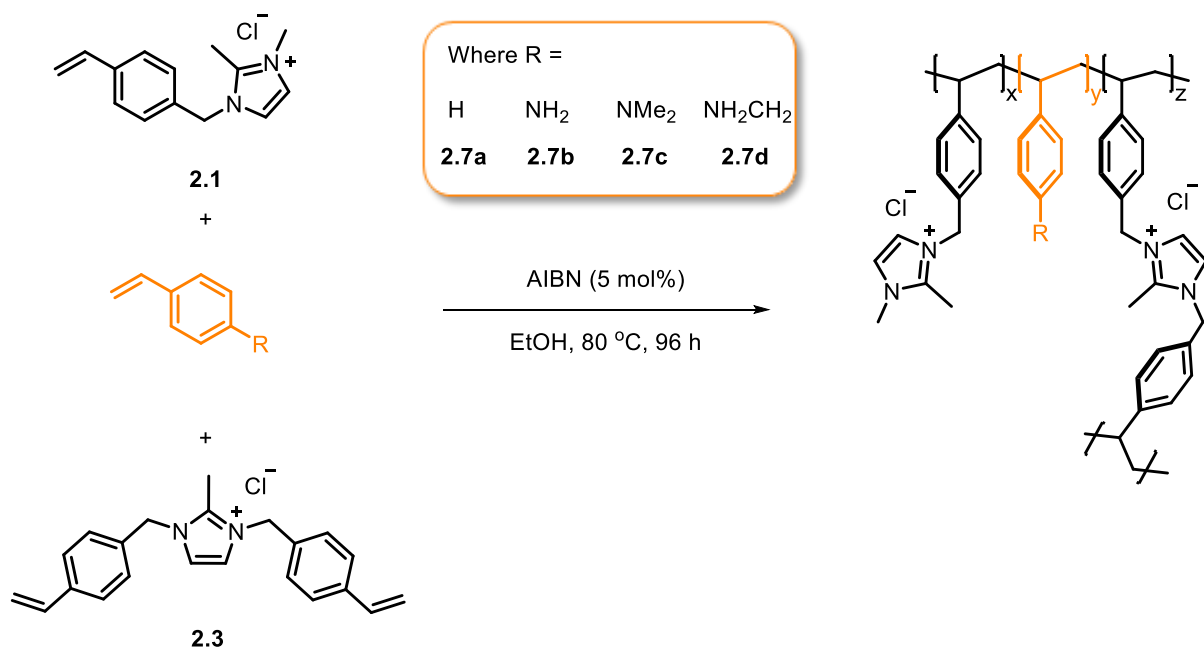
Scheme 2.3 Wittig reaction of 4-(dimethylamino)benzaldehyde to afford alkene **2.4**.

A series of three amine donors were compared against an unfunctionalised polymer whereby the amine donor was substituted with a styrene unit. Styrene and 4-aminostyrene were obtained from commercial suppliers, while tertiary amine and benzylic amine monomers were prepared from straightforward syntheses. Tertiary amine, 4-(dimethylamino)styrene, was prepared *via* a Wittig olefination of 4-(dimethylamino)benzaldehyde with methyltriphenylphosphonium bromide (**Scheme 2.3**); phosphine oxide impurities were removed by passing the crude product through a silica plug pre-treated with NEt_3 to afford amine **2.4** in 65% yield.⁴²



Scheme 2.4 Preparation of 4-vinylbenzylamine **2.6** *via* a Gabriel synthesis from the corresponding haloalkane.

4-Vinylbenzylamine was prepared according to previous literature reports.⁴³ Reaction of 4-vinylbenzylchloride with potassium phthalimide afforded Gabriel product **2.5**, following recrystallisation from hot methanol (**Scheme 2.4**). The purified product was then subjected



Scheme 2.5 Preparation of amine decorated PIIL supports **2.7a-d**, via radical initiated polymerisation. Polymers contained *ca.* 5 mol% cross-linker where $x = 0.91$, $y = 1$, $z = 0.09$.

to hydrazinolysis at reflux, and after aqueous work-up, the desired monomer **2.6** was isolated as a clear yellow oil in 89% yield.

Amine modified PIILs **2.7a-d** were prepared through an AIBN radical-initiated polymerisation of either the amine monomers or styrene with ionic liquid monomers 1,2-dimethyl(4-vinylbenzyl)imidazolium chloride (**2.1**) and 2-methyl-1,3-bis(4-vinylbenzyl)imidazolium chloride (**2.3**) in degassed ethanol (**Scheme 2.5**). The monomer composition was comprised of 4.5 mol% cross-linker so that the resulting polymer would have comparative mechanical properties to those of previous Doherty PIIL supports.⁴⁰ Polymerisations were monitored by ¹H NMR spectroscopy and were typically complete after 4 days of stirring at 80 °C; completion was indicated by the disappearance of the vinylic protons (**Figure 2.2**). Polymers were obtained by precipitation into diethyl ether and isolated as fine off-white/yellow powders in good yields of >85%. The presence of residual monomers was detected in the solution-state ¹H NMR spectra of some of the isolated solids, thus the polymers were purified by dialysis (0.5-1 kDa). While the monomer composition was intended to give an IL:amine (or styrene) ratio of 1 : 1 in the resulting polymers, the ¹H NMR spectra of the isolated polymers showed some disparity in these monomer ratios. Despite the broad signals of the polymer ¹H NMR spectra, comparing the integrals of the total aromatic protons (δ 7.69-6.1 ppm) to those of the imidazolium CH₃ peak (δ 3.84 ppm) allow us to estimate the relative monomer incorporation. Accordingly, polymers **2.7a** and **2.7b** showed IL : donor ratios of 1.03 : 1 and

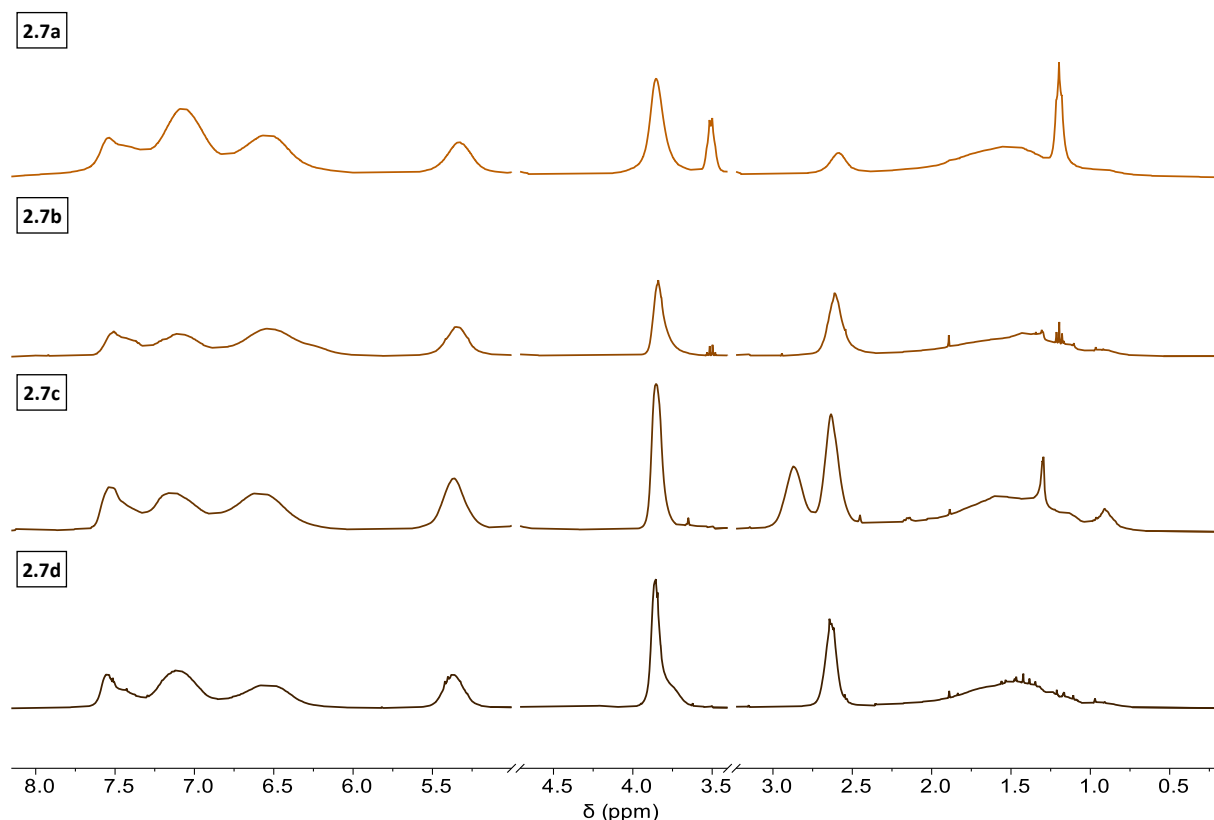


Figure 2.2 Stacked ^1H NMR spectra of polymers **2.7a-d** (400 MHz, Methanol- d_4). The residual methanol solvent peaks at 4.87 and 3.33 ppm have been removed for clarity, though unmodified spectra can be found in **Appendix A.2.2**.

1.04 : 1 consistent with expected results, yet ratios of 1.28 : 1 and 0.68 : 1 were obtained for polymers **2.7c** and **2.7d** respectively. This is likely a consequence of variable rates of polymerisation for the different monomers. However, these values are again only estimates due to the broad nature of the ^1H NMR signals, thus the integrals of these peaks will be accompanied by notable errors.

FT-IR spectra of polymers **2.7a-d** all showed a broad band at 3300 cm^{-1} due to physisorbed water (this is evident with broad features in the above ^1H NMR spectra at δ 1.5 ppm also). Characteristic C-H stretches were evident at 2920 cm^{-1} and aniline functionalised polymer **2.7b** showed a strong signal due to N-H bending at 1513 cm^{-1} that was not as prominent in the spectrum of benzylamine-modified **2.7d**.

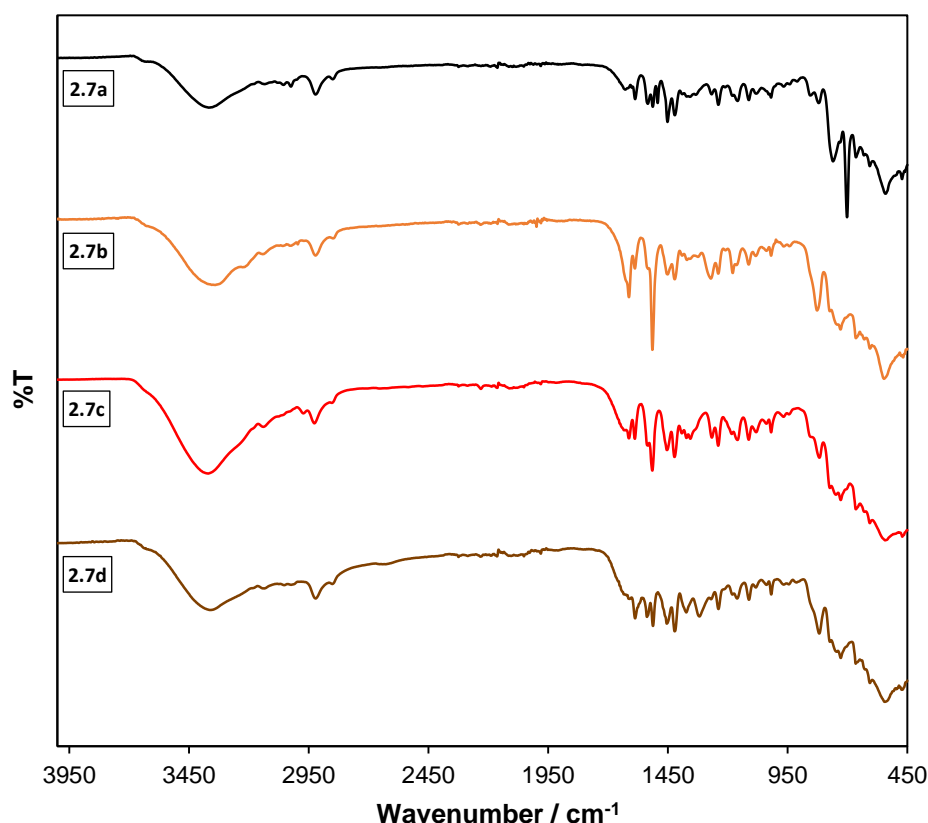
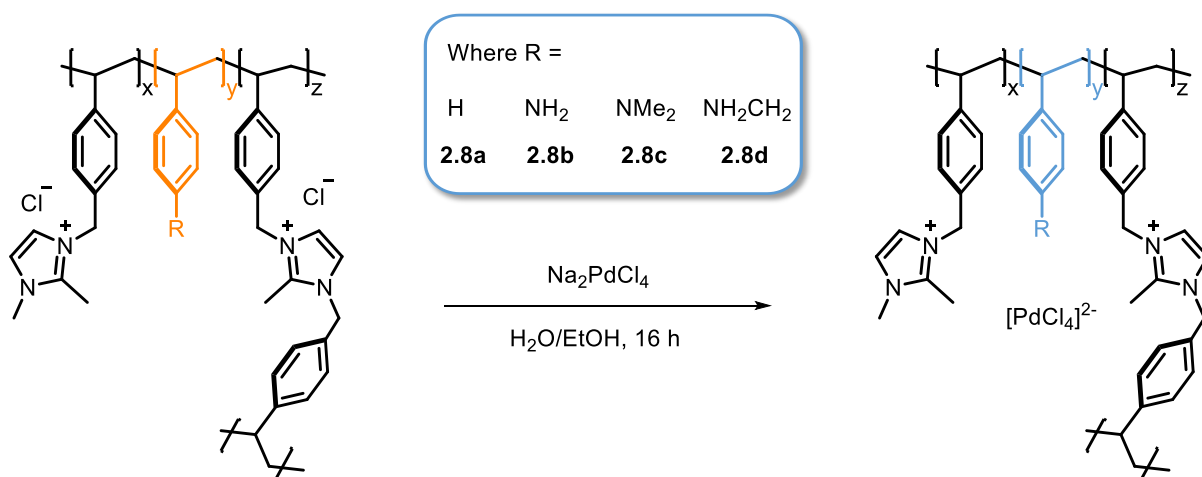


Figure 2.3 Stacked FT-IR spectra of polymers **2.7a-d**.

2.2.2 Precatalyst Synthesis and Characterisation

Ionic liquid polymers **2.7a-d** were then impregnated with sodium tetrachloropalladate by ion exchange in ethanol; polymers were dispersed in ethanol with stirring and were charged with hot aqueous solutions of Na_2PdCl_4 , resulting in the immediate precipitation of orange solids. The mixtures were stirred overnight to afford precatalysts **2.8a-d**, which were isolated as orange/yellow solids by filtration. To ensure full substitution of the sodium counterions, 2 mole equivalents of polymer were used to load 1 mole equivalent of $[\text{PdCl}_4]^{2-}$, resulting in an amine to Pd ratio of 2 : 1.



Scheme 2.6 Preparation of PdCl_4 -loaded PIILs **2.8a-d**. Where $x = 0.91$, $y = 1$, $z = 0.09$.

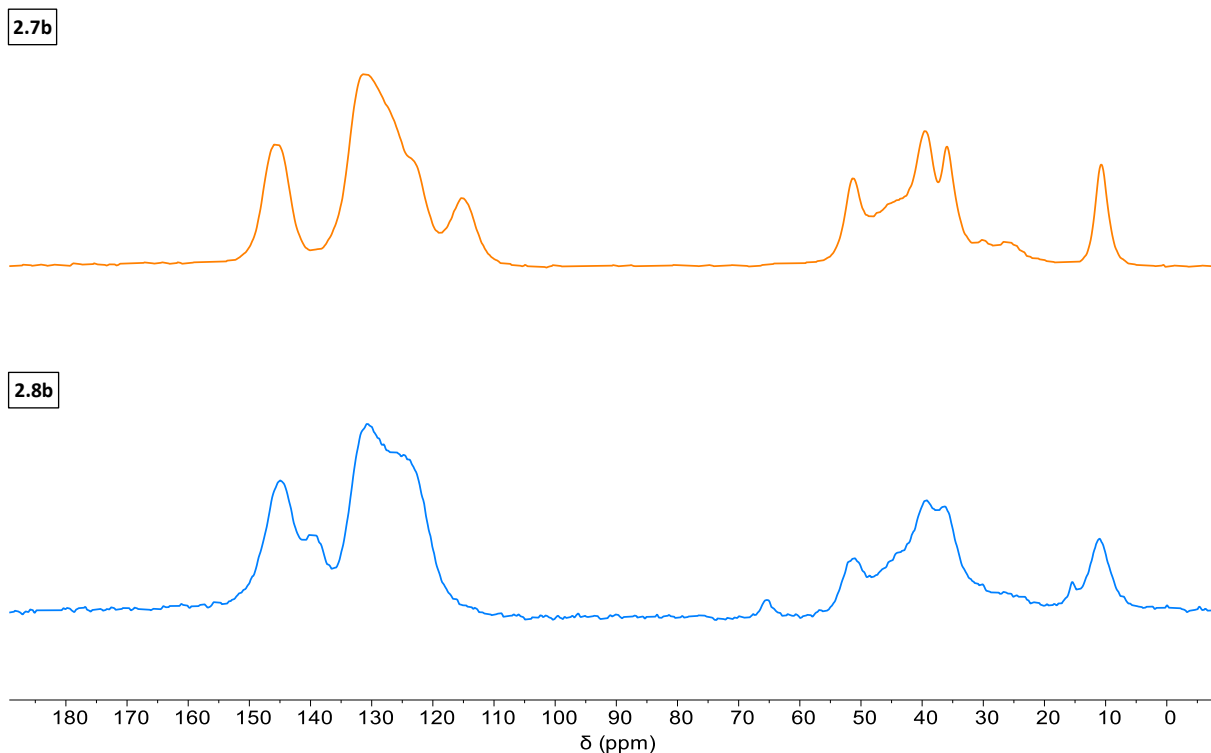


Figure 2.4 Solid state ^{13}C CP-MAS NMR spectra of polymer **2.7b** and precatalyst **2.8b** (500 MHz).

Solid-state ^{13}C CP-MAS NMR spectra showed no change in the polymer support following impregnation with $[\text{PdCl}_4]^{2-}$ and aromatic features present at 151-139 ppm and 136-118 ppm were attributed to the imidazolium and phenyl carbons, while benzylic and aliphatic carbons were assigned at 55-48 ppm and 47-31 ppm respectively (**Figure 2.4**). An exception to this was $\text{PdCl}_4@\text{NH}_2\text{PIIL}$, **2.8b**, where resonances assigned to the *ipso* C-NH₂ carbon appeared to shift 30 ppm downfield from δ 115 ppm in **2.7b** to δ 139 ppm in **2.8b**. The palladium content of the precatalysts was determined to be between 8.5-11.7 wt% using ICP-OES.

An unsurprisingly irregular morphology of the polymers was determined by SEM; images of the materials show them to be granular, with little to no crystallinity or porous character, though one would not expect any form of regular morphology from lightly cross-linked random polymer assemblies. Loading of the polymers with Na_2PdCl_4 also appeared to have

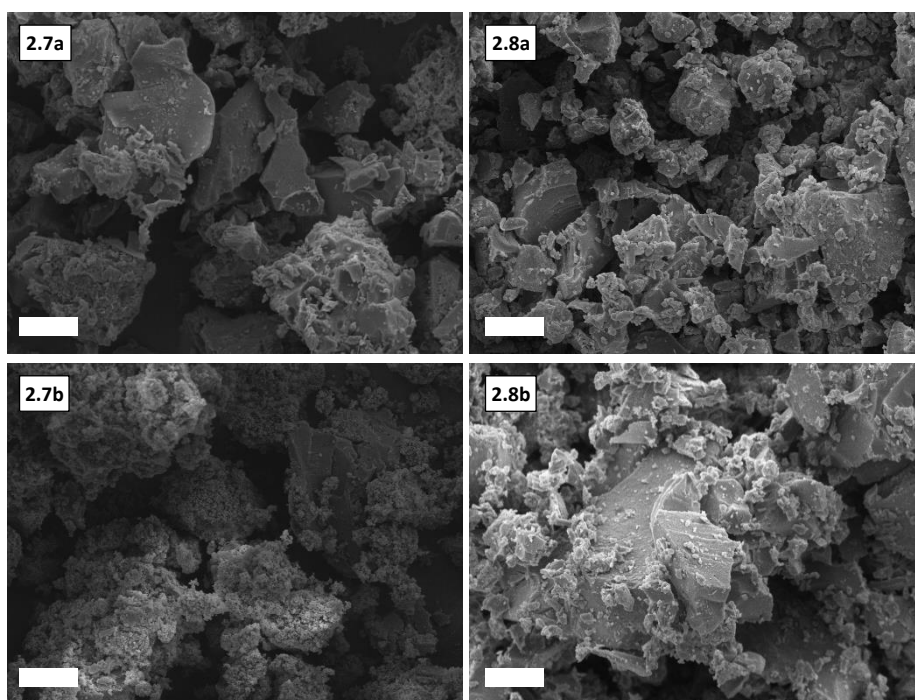


Figure 2.5 SEM images of polymers **2.7a-b** and precatalysts **2.8a-b**; white scale bar is 20 μm .

no effect on the microscopic structure of the materials, as evidenced by SEM images in **Figure 2.5** (the remaining SEM images polymers **2.7a-d** and precatalysts **2.8a-d** can be found in **Appendix A.2.7**).

2.3 Thermal Hydrogenation of CO_2

A typical hydrogenation was conducted in a HEL DigiCAT high pressure reactor, charged with aqueous base (20 mL, 0.65 M), 6 μmol Pd in the form of supported PdCl_4 precatalyst and a total pressure of 4 MPa ($\text{H}_2 : \text{CO}_2 = 1 : 1$) at 373 K for 2 h. Formate formation was quantified by ^1H NMR spectroscopy, using DMSO as an internal standard.⁴⁴ The rates of formate formation were based on the total amount of metal as determined by ICP-OES, rather than estimating surface sites, and were expressed as turnover frequencies (TOF) with units of $\text{mol}_{\text{formate}} \cdot \text{mol}_{\text{Pd}}^{-1} \cdot \text{h}^{-1}$ (abbreviated to h^{-1}). Initially, a preliminary screening of metal catalysts immobilized on unfunctionalised polymer **2.7a** was conducted, comparing the activity of Ru, Au and Pd impregnated catalysts – while there are reports of active Ir-based catalysts for the hydrogenation of CO_2 , they are predominantly comprised of immobilized molecular catalysts,⁴⁵ thus their activity has not been explored here. While RuNP generated from the *ex-situ* reduction of $\text{RuCl}_3 @ \text{PIIL}$ using sodium borohydride were slightly more active than the corresponding AuNP catalyst, both were surpassed, 2-fold and 4-fold respectively, by PdNP@PIIL (**Figure 2.6**). Moreover, when the nanoparticles were formed *in-situ* during the hydrogenation of CO_2 from the $[\text{PdCl}_4]^{2-}$ loaded precatalyst (**2.8a**) there was a significant

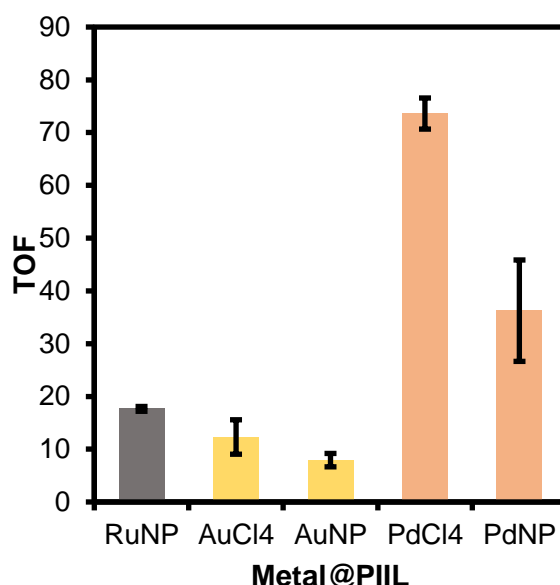


Figure 2.6 Comparison of initial TOF after 2 hours against various catalysts loaded on PIIL support **2.7a**. Reaction conditions: Catalyst (6 $\mu\text{mol}_{\text{metal}}$), H_2/CO_2 (20:20 bar), 100 °C, H_2O (20 mL), NaHCO_3 (0.65 M). $\text{TOF} = \text{mol}_{\text{formate}} \cdot \text{mol}_{\text{Pd}}^{-1} \cdot \text{h}^{-1}$

enhancement in activity with a TOF of 74 h^{-1} , measured over 2 hours, compared to a TOF of 36 h^{-1} for the NPs generated *ex-situ* from reduction with NaBH_4 . This same enhancement was also observed for the $[\text{AuCl}_4]^-$ loaded precatalyst, however, the resulting catalyst was still inferior to the RuNP and both Pd catalysed systems. The reason behind the superior activity of the *in-situ* generated NPs is unclear; TEM data of the two Pd samples revealed that the NaBH_4 generated NPs had an average size of $2.13 \pm 0.53 \text{ nm}$, which is slightly smaller than those isolated after *in-situ* hydrogenation ($2.98 \pm 0.63 \text{ nm}$). It is also possible that the *ex-situ* Pd species was deactivated through fouling of spent borohydride salts, however, elemental mapping images were not collected to confirm this.

The direct hydrogenation of CO_2 to formic acid is a thermodynamically unfavourable process, with a Gibbs free energy ($\Delta G_{298\text{K}}^\circ$) of $32.9 \text{ kJ} \cdot \text{mol}^{-1}$,⁴⁶ this is unsurprising as it is entropically disfavoured to convert two gases to a liquid, despite the reaction's exothermic nature. The energetics improve when the reaction is conducted in water, where $\Delta G_{298\text{K}}^\circ = -4 \text{ kJ} \cdot \text{mol}^{-1}$, and the reaction is further favoured when conducted in the presence of a base additive – for example, a negative Gibbs energy of $-9.5 \text{ kJ} \cdot \text{mol}^{-1}$ was determined when CO_2 was hydrogenated in the presence of aqueous ammonia to afford ammonium formate. There are several reports of formic acid derived from additive-free catalytic systems; the use and recycling of ionic liquids as both solvent and base has led to TON of $>360\,000 \text{ h}^{-1}$ when CO_2 hydrogenation is facilitated with a homogeneous catalyst.⁴⁷ However, TONs for base-free heterogeneous systems are consistently low (including when a base is immobilized on the

support) and thus don't correspond to a meaningful route for the industrial scale generation of formic acid.⁵² For comparison, a hydrogenation catalysed by **2.8a** in the absence of base was conducted though no formic acid was observed after 2 hours at 100 °C (nor was any formic acid obtained when catalysed by the optimal amine-functionalised catalyst identified later in this chapter). To this end, several bases have been explored as additives towards the hydrogenation of CO₂ in the literature, with no clear consensus on an optimum base. Here, in a survey of bases, precatalyst **2.8a** showed varying catalytic performance when different alkaline additives were used (**Figure 2.7a**). Reactions conducted in the presence of K₂CO₃ gave higher TOFs than those with KHCO₃, NaOH, NEt₃ or KOH, and as such further optimisation of reaction parameters was performed in aqueous K₂CO₃. Potassium carbonate is also the optimum additive reported for the polymeric phosphine supported Ru(II) catalysed reduction of CO₂.⁴⁸ It is worth noting that the use of a carbonate (CO₃²⁻) as additive is uncommon, with many systems observing higher activities with bicarbonate (HCO₃⁻) and amine additives such as NEt₃.^{7,49,50} Elucidating a rationale behind the disparate catalytic performance across the various bases is difficult – each base has its own complex equilibrium that will be influenced by reaction temperature, pressure, and solvent, thus making a direct comparison is not trivial.

A study of the influence of temperature on catalyst performance revealed that TOFs increased with increasing reaction temperature and reached 500 h⁻¹ at 100 °C – further increasing the reaction temperature to 120 °C led to a significant drop in the initial TOF from 500 h⁻¹ to 306 h⁻¹. Similar volcano plots describing the temperature-activity relationship were reported for Pd-PPh₃/TiO₂²¹ and Ru²⁵ catalysed systems though the activity maxima sat at lower and higher temperatures, respectively (60 and 120 °C). Optimum reaction temperatures will undoubtedly vary across catalysts due to the complexity of the systems, considering factors such as base additive, solvent volume, pressure, NP size, metal catalyst, and support; however, for all systems reaction rates appear to decrease beyond a certain temperature. The hydrogenation of CO₂ is both reversible and exothermic, thus, higher temperatures drive the decomposition of formic acid/formate back to the gaseous starting materials. The initial rates further decreased when the stirring speed was reduced below 750 rpm, with a notable drop in TOF to 104 h⁻¹ at 100 rpm suggesting that the reaction is diffusion limited. The TOF's also decreased when the pressure of the 1 : 1 CO₂ : H₂ mixture was increased above 40 bar; it

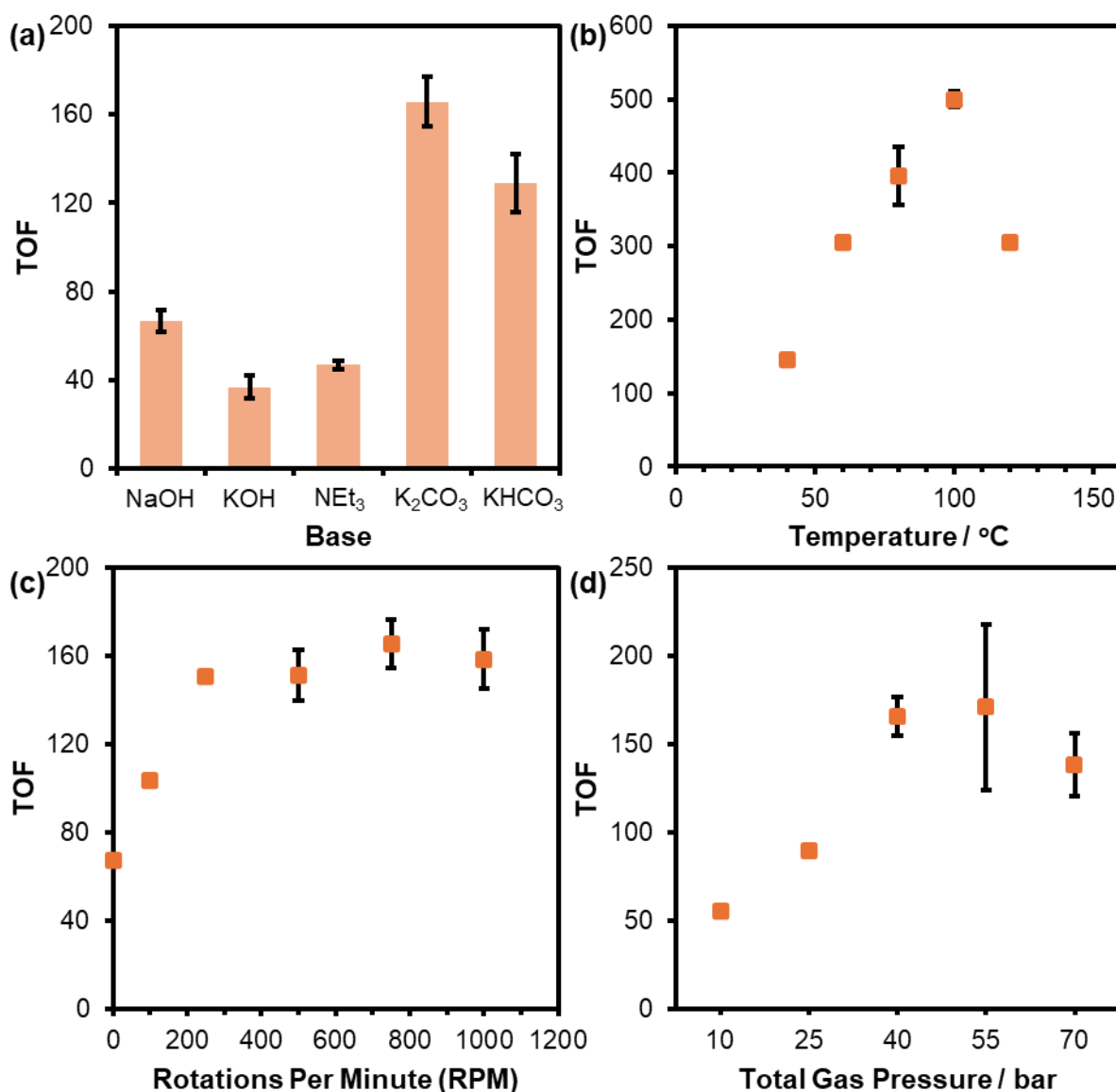


Figure 2.7 (a) Screening of various bases for the hydrogenation of CO_2 , catalysed by **2.8a** (6 μmol Pd), at 100 °C with 40 bar of reactive gas. (b) Screening of reaction temperature for the hydrogenation of CO_2 catalysed by **2.8b.66** (6 μmol Pd), with 40 bar of reactive gas. (c) Screening of stirring speed for the hydrogenation of CO_2 catalysed by **2.8a** (6 μmol Pd), at 100 °C with 40 bar of reactive gas. (d) Screening of total gas pressure (1 : 1 mixture of H_2 : CO_2), catalysed by **2.8a** (6 μmol Pd), at 100 °C.

is likely that the reaction solution is at its saturation limit, as hydrogen gas is already poorly soluble in water, thus an increase in pressure leads to little change in activity. As such, these optimum parameters were used for all further studies.

Using these reaction conditions, a comparison of catalyst performance as a function of the amine-modified support against unmodified catalyst revealed that weakly basic aniline (**2.8b**) gave a dramatic enhancement in efficacy to afford a TOF of 340 h^{-1} , compared with 146 h^{-1} for unmodified catalyst **2.8a** (Figure 2.8). While benzylamine (**2.8b**) also showed a positive

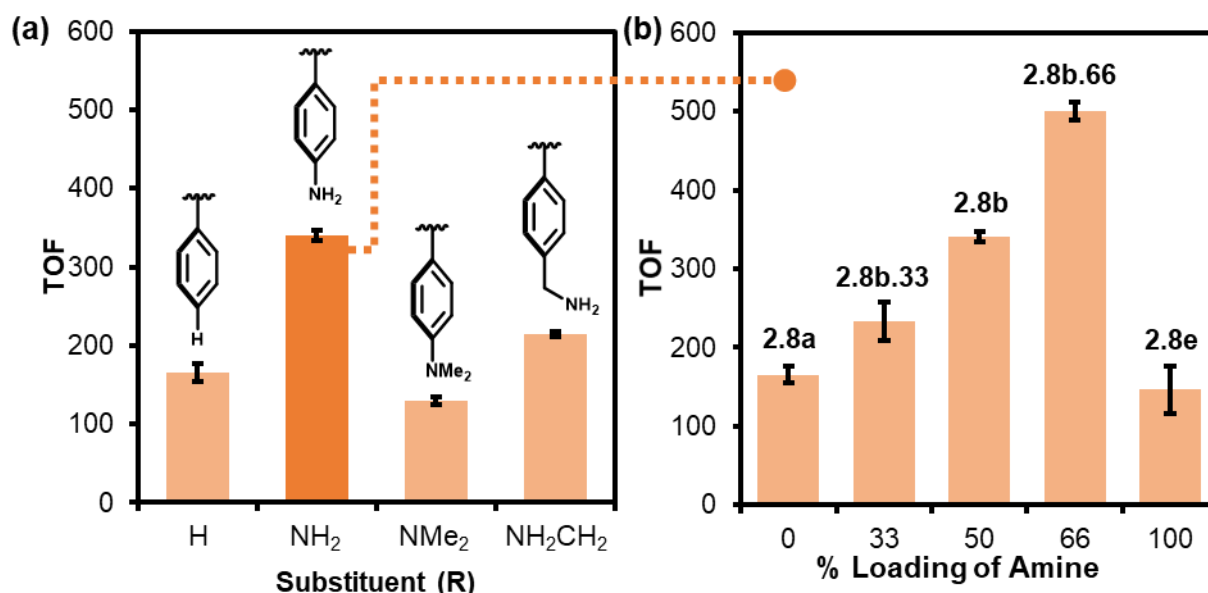


Figure 2.8 (a) Plot showing TOF against polymer substituent for the thermal hydrogenation of CO_2 to formate using several $\text{PdCl}_4@ \text{PIIL}$ based precatalysts. All polymer supports have an IL:R ratio of 1:1. (b) Plot of TOF against mol% loading of amine for $\text{PdCl}_4@ \text{NH}_2\text{PIIL}$ catalysts. $^a\text{TOF} = \text{mol}_{\text{formate}} \cdot \text{mol}_{\text{Pd}}^{-1} \cdot \text{h}^{-1}$

effect on catalyst performance, with a TOF of 214 h^{-1} , *N,N*-dimethylaniline modified catalyst **2.8c** gave a TOF of 130 h^{-1} , slightly lower than the 146 h^{-1} obtained with its unmodified counterpart, $\text{PdCl}_4@ \text{PIIL}$ (**2.8a**). Thus, while primary amines enhance catalyst performance a weakly basic amine is most effective, and a tertiary amine has a negligible impact on the efficacy. Yamashita and co-workers have also reported a similar effect as PdAgNPs supported by *N,N*-dimethyl-1-propylamine modified SBA-15 were slightly less active than unmodified catalyst, for the same reaction, whereas aniline modified SBA-15 showed a large positive effect.²³ A systematic study of primary, secondary and tertiary amine-modified SBA-15 as supports for the PdNP catalysed dehydrogenation of FA reported a decrease in catalyst activity with increasing substitution of the amine; the poor activity of the tertiary amine decorated catalyst was attributed to the large size of the NPs and hydrophobicity of the heteroatom.⁵¹ Whilst Ren and co-workers also reported a slight negative effect of a tertiary amine versus a primary amine, they instead found an enhancement in activity when a secondary amine was grafted to activated carbon, liberating free formic acid without the use of an additive base.⁵²

Using density functional theory computations, the structures of aniline, *N,N*-dimethylaniline and benzylamine were optimized and their electron densities were mapped to assess the basicity of the amine donors. Notably, the tertiary amine had a negligible electron density at nitrogen with a value of -0.035 , thus it is unlikely to strongly coordinate with CO_2 or the Pd

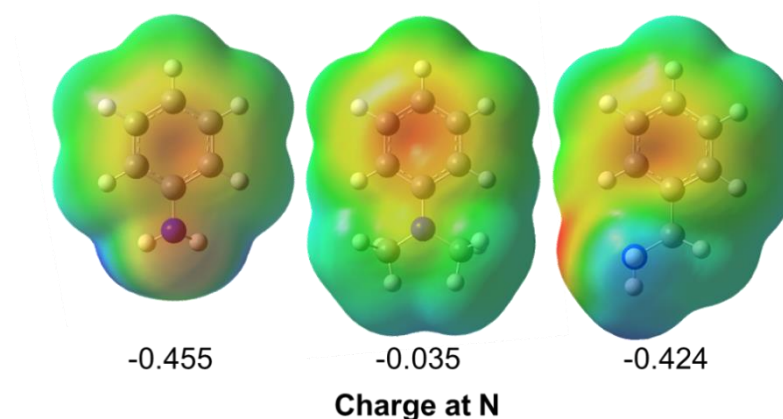


Figure 2.9 Electron density maps of aniline, *N,N*-dimethylaniline, and benzylamine respectively, with charges at the nitrogen atom (blue) given below the structures.

precatalyst. Indeed, Yang and co-workers reported a positive free energy for the chemisorption of CO₂ to trimethylamine, indicative of the process being unfavourable.⁷ In comparison, aniline and benzylamine appeared relatively basic with charges at the nitrogen atom of -0.455 and -0.424, respectively, consistent with their higher activity against the tertiary amine modified catalyst.

A study of the influence of increasing the amount of aniline on the support on catalyst efficacy was undertaken by preparing precatalysts stabilised by polymers with 4-aminostyrene and imidazolium monomer ratios of 1:2 and 2:1. An additional homopolymer was prepared from 4-aminostyrene alone, referred to as poly-4-aminostyrene (**2.7e**). These polymers were impregnated with Na₂PdCl₄ using the same procedure described for **2.8a-d** (1 : 1 ratio of Na₂PdCl₄ : **2.7e** for poly-4-aminostyrene supported precatalyst) to form a series of precatalysts PdCl₄@xNH₂PIIL, where x corresponds to the theoretical % loading of amine on the polymer (x = 0 (**2.8a**), 33 (**2.8b.33**), 50 (**2.8b**), 66 (**2.8b.66**) and 100 (**2.8e**)). Again, solid-state ¹³C CP-MAS NMR spectra of precatalysts showed an apparent shift in the *ipso* C-NH₂ carbon from δ 115 ppm in **2.8b.33** and **2.8b.66** to δ 137 ppm in the corresponding precatalysts. This shift was less pronounced for **2.8e**, likely due to an excess of uncoordinated C-NH₂ sites. SEM images of the additional polymers and precatalysts showed similar granular morphologies to those of **2.7a-d** and **2.8a-d**.

Interestingly, an almost linear increase in activity was observed as the aniline content increased, reaching a maximum of 500 h⁻¹ for the Pd catalyst generated from **2.8b.66**, which is among the highest to be reported for a PdNP-based system. A TOF of 147 h⁻¹ was obtained for catalyst supported by homopolymer poly-4-aminostyrene (**2.8e**), similar to 146 h⁻¹

obtained with unfunctionalised precatalyst **2.8a**. This is indicative of a positive influence of the ionic liquid on catalyst efficacy as amine alone is not sufficient to achieve high activity. Loaded as such, one would expect an amine : Pd ratio of 1:1 for **2.8e**, as would be the case for **2.8b.33**; despite this, the use of precatalyst **2.8b.33** led to an initial TOF of 233 h^{-1} , again demonstrating the cooperative relationship between IL and amine. It's worth noting that Kou and co-workers found that increasing the ratio of N-vinylpyrrolidone monomer in an IL:PVP copolymer led to increased activity of their supported Rh catalyst, though this was attributed to a decreased IL-derived Cl^- content.⁵³ To investigate the influence of potential chloride poisoning at the NP surface, one could conduct an anion exchange of xNH_2PIIL polymers with weakly coordinating NTf_2^- or BF_4^- anions prior to metal impregnation; further to this, residual Cl^- from the reduction of PdCl_4 could be mitigated through the use of $\text{Pd}_2(\text{dba})_3$ as catalyst precursor; although worthwhile, such experiments were not completed here.

Modification of the support by covalent attachment of the aniline was crucial to achieving high activity as a hydrogenation conducted with catalyst generated from unmodified **2.8a** but with the equivalent amount of aniline corresponding to that present on the support of **2.8b.66** added to the reaction resulted in a slight decrease in the TOF to $116\text{ mol}\cdot\text{mol}_{\text{Pd}}^{-1}\cdot\text{h}^{-1}$, compared with $146\text{ mol}\cdot\text{mol}_{\text{Pd}}^{-1}\cdot\text{h}^{-1}$ obtained with **2.8a**; moreover, the TOF decreased to $92\text{ mol}\cdot\text{mol}_{\text{Pd}}^{-1}\cdot\text{h}^{-1}$ when the amount of aniline additive was further increased by 10-fold. In this system, a strongly coordinated carbamate salt formed from the reaction between aniline and CO_2 solution appears to be less efficient at converting to formate, as was the case for the reactions charged with NEt_3 described earlier in the base screening study.

In-situ generation of PdNP catalysts could result in an initiation period for the catalyst, thus the quoted TOFs may not be representative of the true initial rates of reaction. If Pd^0 NPs are the active species during catalysis then one would expect a slower initial rate of reaction as Pd^{2+} is first reduced to Pd^0 . However, a plot of TON against time for the optimum precatalyst **2.8b.66** shows no evidence of an initiation period. Even after 15 minutes of reaction time a high TON of 277 was measured, corresponding to a TOF of 1109 h^{-1} , much higher than the 500 h^{-1} reported for the same catalyst after 2 hours. A comparison against the less active, unfunctionalised precatalyst **2.8a** also showed no evidence of catalyst initiation. Therefore, if there is an initiation period for these systems, it is rapid and has no effect on the resulting catalyst TOF. Alternatively, there may be no apparent initiation period if Pd^{2+} also facilitates catalysis. After 6 hours of catalysis, the reaction rate sharply decreases with the formate TON

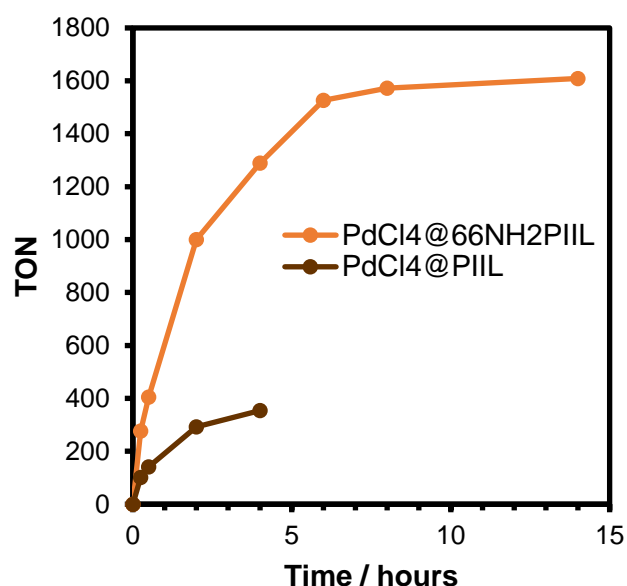


Figure 2.10 Profile of activity against time for PdCl₄@66NH₂PIIL (**2.8b.66**) and PdCl₄@PIIL (**2.8a**) catalysed hydrogenation of CO₂.

approaching a plateau after 8 hours. This plateau in activity is not unique and similar profiles have been reported for PPh₃-capped PdNPs²¹ and for porous organic polymer supported PdNPs.¹³ The plateau is most likely indicative of the reaction reaching an equilibrium between formate formation and decomposition. This equilibrium was briefly discussed by Leitner, as when their SILP supported Ru catalyst was stirred in a 2 : 1 ratio of HCOOH and NEt₃ additive, the formic acid rapidly decomposed; however, in the presence of a 1 : 1 mixture, the formic acid was stable under a positive CO₂/H₂ pressure.¹¹

Reassuringly, all catalysts described here were more active than commercial Pd/C (10 wt%, Sigma Aldrich), which gave an initial TOF of only 74 h⁻¹ under the conditions identified above. In addition, pre-treatment of 6 μmol of Pd/C with a homogeneous solution of aniline-decorated polymer **2.7b.66** (12 μmol) for 16 h prior to performing a hydrogenation did not have a significant effect on the activity as the TOF of 89 h⁻¹ was only marginally greater than that of 74 h⁻¹ obtained with the same loading of Pd/C, in the absence of **2.7b.66**. To this end, a reaction conducted with the same Pd loading but with Na₂PdCl₄ as catalyst led to a much lower TOF of 42 h⁻¹. For further reference, a hydrogenation conducted at 100 °C in aqueous K₂CO₃ under 40 bar CO₂/H₂ in the presence of 6 μmol of **2.7b.66** as additive, but in the absence of palladium, showed no activity confirming that palladium is essential for the formation of formate under these conditions.

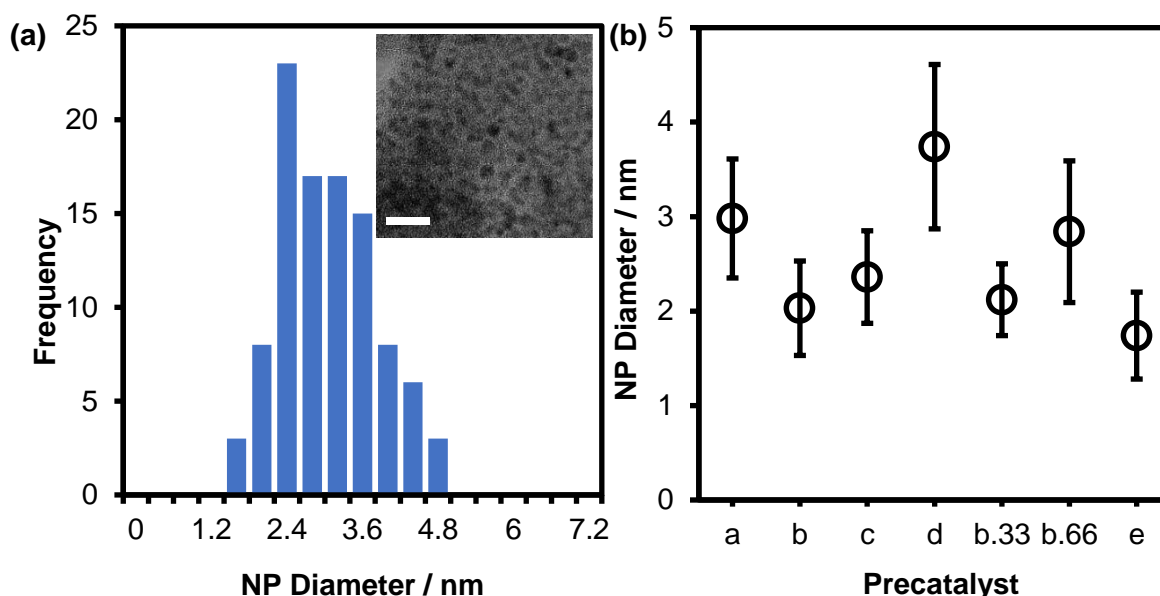


Figure 2.11 (a) Particle size distribution of nanoparticles isolated post-catalysis from pre-catalyst **2.8b.66**, where the inset shows a TEM image of the same material (white size bar = 10 nm). (b) Average NP sizes for catalysts generated from pre-catalysts **2.8a-e** after 2 hours of hydrogenation.

Following catalysis, a heterogeneous black solid was recovered from the reaction mixture of the various catalysts by centrifugation. After washing with water and ethanol the solids were analysed by TEM. Nanoparticle sizes ranged from 1.74-3.74 nm across samples, however, there was no correlation between NP size and activity. The smallest NPs of 1.74 nm were obtained from the hydrogenation of precatalyst **2.8e**; the large excess of amine sites in poly-(4-amino)-styrene could play an important role in controlling NP nucleation, as was the case for polyaniline supported Pd NPs which had an average particle size of 0.91 nm.⁵⁴ However, a much lower loading of palladium was obtained for poly-(4-aminostyrene) supported **2.8e** (3.8 wt% compared to an average of 10.9 wt% for the remaining PIIL systems); this highlights the advantageous role ILs play in the loading of metal salts through anion exchange. The reduced loading of Pd on precatalyst **2.8e** could lead to more dispersed, smaller NPs which may have implications on the catalytic activity. To assess this, aniline-decorated PIIL, **2.7b**, was loaded with one third of the amount of palladium used to prepare precatalyst **2.8b** (11.7 wt% Pd), whereby the resulting material was found to have a Pd loading of 3.9 wt% as determined by ICP-OES. When the subsequent material was evaluated for the hydrogenation of CO₂, charging with the same amount of Pd used previously (6 μ mol), a negligible drop in activity was measured from a TOF of 340 h⁻¹ for **2.8b** to 314 h⁻¹ for the **2.7b**-supported precatalyst with a reduced Pd loading. This is still much higher than the TOF of 147 h⁻¹ obtained for **2.8e** loaded with 3.8 wt% Pd highlighting that a lower wt% Pd loading on the precatalyst does not lead to a significant decrease in catalytic activity.

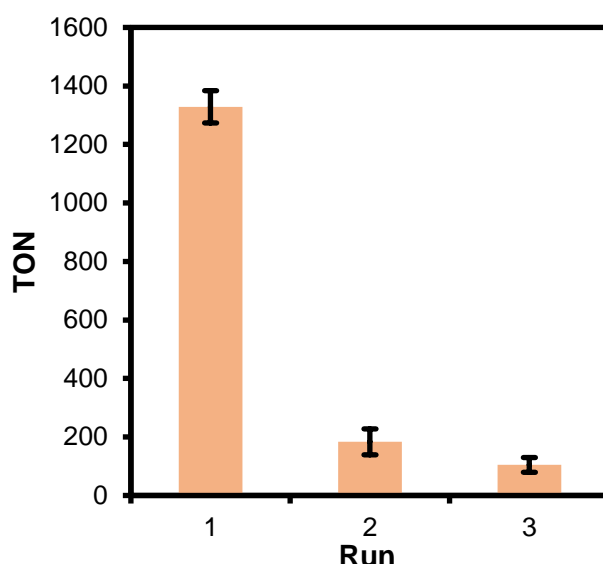


Figure 2.12 Recycling study conducted using **2.8b.66** (6 μ mol) with reaction times of 16 hours. Catalyst was isolated by centrifugation and washed with deionized water (3 x 10 mL).

Despite the respectable initial activity of the catalyst generated from **2.8b.66**, its recyclability was disappointing. While a TON of 1329 was obtained after 14 hours, the following use of the catalyst attained a TON of 183, though, an additional use led to a much smaller drop in activity. This drastic reduction in activity suggests that a significant change had occurred following the first use of the catalyst, resulting in notable passivation. TEM images of the catalyst isolated after 3 uses suggested that there was little difference in the NP diameters when compared to images taken after a single use (2.40 ± 0.64 nm and 2.84 ± 0.75 nm respectively).

2.4 Exploring the Pd-N Interaction of Precatalysts 2.8a-e

In order to explore the coordination of amine to palladium in precatalysts **2.8b-d**, the core-electron excitations of N and Pd were analysed using XPS. Note that charge neutralisation was used for all samples and no rescaling has been applied to quoted binding energies (BEs). Due to the limitations of using adventitious carbon as a reference,⁵⁵ peak assignment was based on the characteristic BE separation between the elements. First, the local N environment of aniline-decorated polymer **2.7b.66** revealed two peaks at 397.4 and 395.0 eV which were assigned to the imidazolium and the amine nitrogen atoms, respectively (**Figure 2.13a**). This assignment was based on the N 1s spectrum of unmodified **2.7a** which showed only a single nitrogen environment at 397.4 eV (**Figure 2.13c**), which can only be attributed to imidazolium N. While XPS characterisation of PdNP materials is commonplace in the literature, it is difficult to derive detailed information concerning any metal-surface interactions; frequently, PdNP

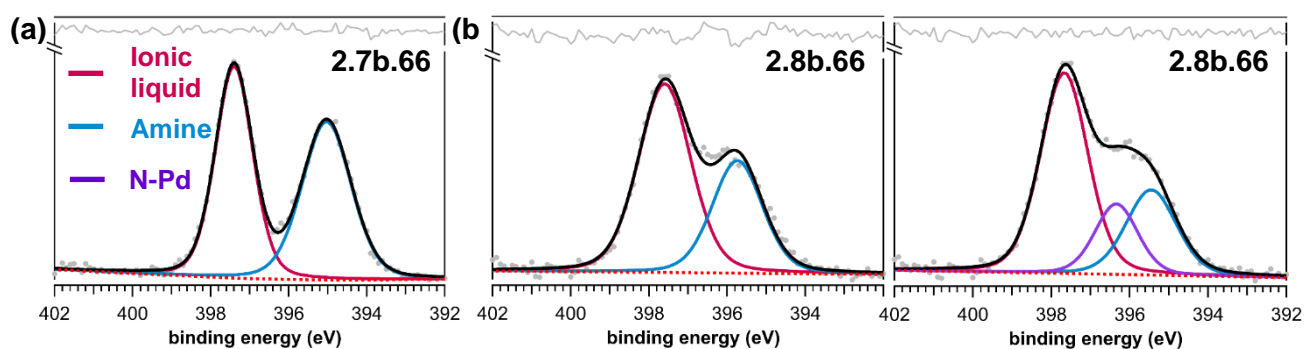


Figure 2.13 N 1s core level XPS region (a) polymer **2.7b.66**, (b) precatalyst **2.8b.66** and of precatalysts **2.8a-d**. Spectra also show the residuals corresponding to the line fitting when a N-Pd peak is omitted and included. Black line = overall fitting; Red dotted line = background.

catalysts are a mixture of Pd^{2+} and Pd^0 species and the small BE separation between these species often lead to broad spectra, where the identification of interesting features can be challenging. In addition to this, NP sizing effects can lead to shifts in BE which may obfuscate the interpretation of any metal-surface relationship.⁵⁶ For these reasons, the $[\text{PdCl}_4]^{2-}$ precatalysts **2.8a-e** were first analysed to probe the nature of the interaction between Pd and the amine decorated supports.

Following impregnation with $[\text{PdCl}_4]^{2-}$, the imidazolium N 1s peak did not appear to shift significantly for all samples reported in this study (397.5 ± 0.1 eV). The separation in the BE scale of this peak in comparison to the aliphatic C 1s also showed close to no deviation across samples (116.9 ± 0.1 eV). This means that the chemical environment of the imidazolium-N is unchanged following metal impregnation, thus, it can be concluded that there was no

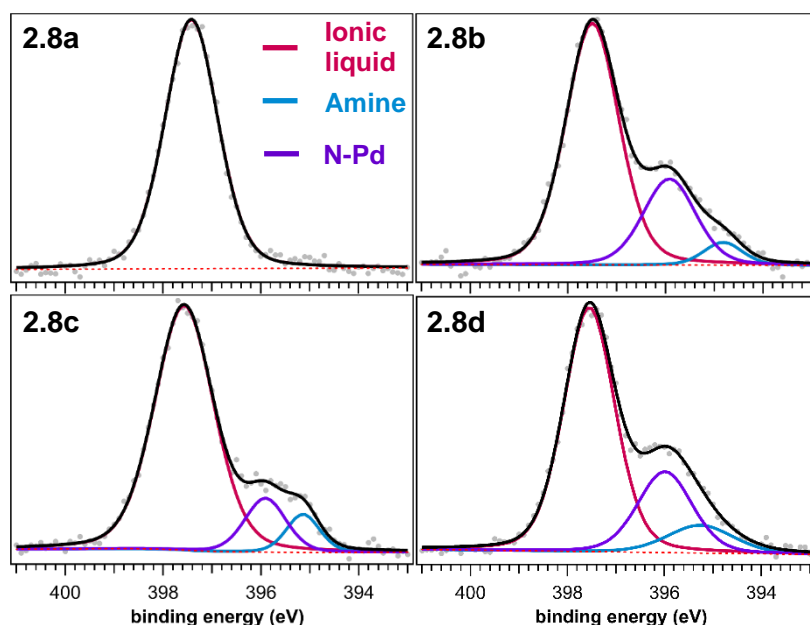


Figure 2.14 N 1s core level XPS region of precatalysts **2.8a-d**. Black line = overall fitting; Red dotted line = background.

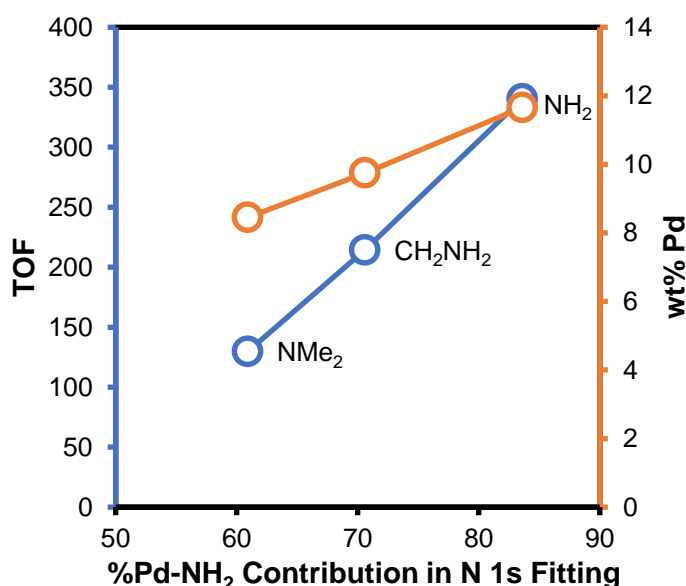


Figure 2.15 Relationship between %Pd-NR₂ interaction as determined by N1s XPS and TOF (blue) as well as wt% Pd loading as determined by ICP-OES (orange) for pre-catalysts **2.8b-d**.

interaction between the Pd and the nitrogen atoms of the imidazolium ring. However, after loading of the polymer supports with [PdCl₄]²⁻, an additional component became apparent between 396.4 - 395.9 eV, which is consistent with a Pd-N interaction (**Figure 2.13b**). Several authors have acknowledged the contribution of a M-N interaction in the deconvolution of N 1s spectra for amine supported metal catalysts: a pyridinic Pd-N interaction was observed for Pd deposited on nitrogen-doped carbon nanotubes,⁵⁷ as was the case for Fe, Co and Ni supported on nitrogen-doped carbon for use as oxygen reduction catalysts.⁵⁸ Similarly, Ru catalysts immobilized on a bipyridine-based triazine framework also showed Ru coordinated to a nitrogen atom of a bipyridine unit with a N 1s peak at 399.2 eV;⁵⁹ reassuringly, the 1.0 eV BE separation between this peak and that of uncoordinated bipyridine at 398.2 eV is consistent with the 1.0 ± 0.2 eV BE separation observed for the precatalyst series described herein. Quantitative analysis of the N 1s components was used to determine the amount of amine coordinated to surface Pd species in the various precatalysts. The proportion of coordinated amine decreased in the order 84 at.% (NH₂) > 71 at.% (NH₂CH₂) > 61 at.% (NMe₂). The trend in %amine-coordination to Pd is consistent with the trend in activity across the different amine modified precatalysts, whereby precatalyst **2.8b** with the greatest %amine-coordination achieved the greatest TOF of the three materials; however, this relationship is likely spurious and is more likely to correlate with the increasing loading of Pd across the samples, thereby increasing surface sites for coordination (**Figure 2.15**).

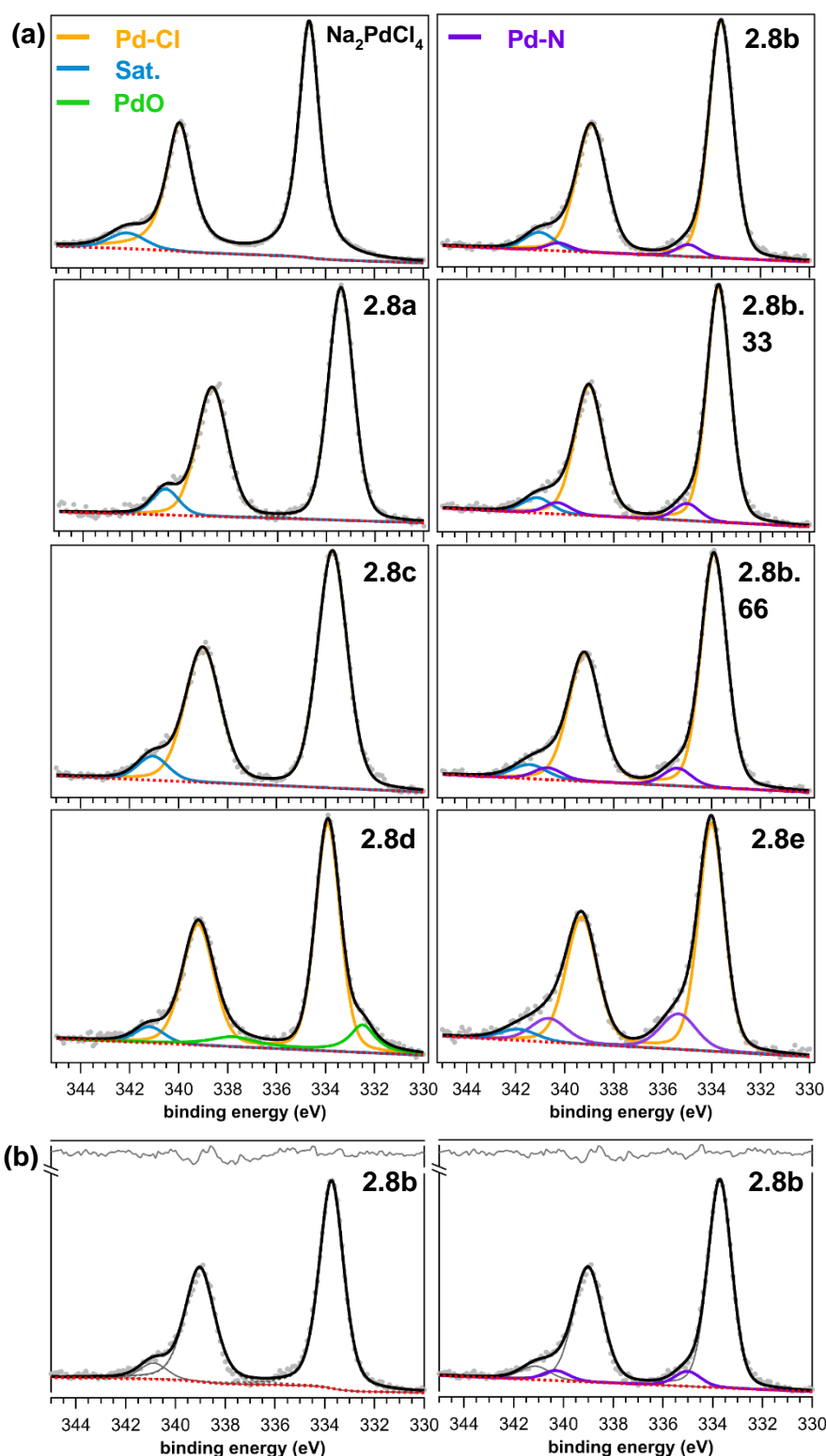


Figure 2.16 (a) Pd 3d core level XPS region for precatalysts **2.8a-e** and precursor Na₂PdCl₄. **(b)** Comparison of residual standard deviation for precatalyst **2.8b** with and without Pd-N peak fitting. Black line = overall fitting; Red dotted line = background.

Analysis of the Pd 3d core level for **2.8b.66** revealed a doublet attributed to divalent Pd coordinated to Cl with 3d_{5/2} and 3d_{3/2} peaks at 333.9 eV and 339.2 eV, respectively, as well as a shake-up satellite line at 341.4 eV (**Figure 2.16a**).⁶⁰ Interestingly, the doublet showed

asymmetric broadening with the full width at half maximum (FWHM) value of the $3d_{3/2}$ peak being 1.2 times that of the $3d_{5/2}$ peak. The phenomenon of asymmetric doublet broadening is uncommon, and one can find no acknowledgement of such broadening in the literature for Pd^{2+} samples. It is unlikely that a $3d_{3/2}$ plasmon is contributing to this broadening as this would require Pd particles larger than 10 nm in order to generate the plasmon, whereas these samples consist of singly complexed Pd sites. This phenomenon could be attributed to a Coster-Kronig transition, which are more typical for the first-row transition metals. For example, for Ti(IV) in TiO_2 and $SrTiO_3$ the Ti $2p_{1/2}$ peak has almost twice the FWHM of the $2p_{3/2}$.⁶¹

For aniline-modified precatalysts **2.8b**, **2.8b.33**, **2.8b.66**, **2.8e**, an additional doublet was apparent at a higher BE with a $3d_{5/2}$ peak of 335.4 ± 0.2 eV, most likely due to coordination of Pd to the aniline NH_2 . No such peak was evident for unfunctionalised precatalyst **2.8a**, nor for tertiary amine nor benzylamine modified precatalysts, **2.8c** and **2.8d**. Assignment of such a peak could be contentious for **2.8b**, though addition of the third peak leads to an improvement in the residual standard deviation (difference between the fitting and the raw data), as shown in **Figure 2.16b**. Fitting the Pd 3d core level of **2.8e** showed a much more definitive peak in this region, further evidencing the assignment to a Pd-N interaction. A doublet at lower binding energy that was unique to benzylic amine modified precatalyst **2.8d** was tentatively assigned to PdO; a BE separation of 1.0 eV between this peak and the Pd-Cl peak is consistent with previous reports of Pd^{2+} coordinated with Cl^- in the presence of PdO (0.9 eV).⁶² It is unlikely that this peak can be assigned to reduced Pd^0 as a result of beam damage, as the BE separation between Pd^{2+} -Cl and Pd^0 is larger, in the region of 2.1-2.6 eV.^{62,63} However, the presence of PdO in only one sample is also difficult to justify, as they were handled under the same conditions with similar polymer supports. While one may attribute the presence of PdO in precatalyst **2.8d** to the diminished activity of the resulting catalyst when compared to aniline-modified **2.8b**, Han reported that vanadium supported PdO outcompeted its pre-reduced Pd^0 counterpart for the hydrogenation of CO_2 to formic acid.⁶⁴

As for the N 1s spectra, the Pd BEs were compared for the various amine supported precatalysts. A shift to higher BEs was observed when the amine modified precatalysts **2.8b-e** were compared to unfunctionalized **2.8a**; by comparing the separation between the Pd $3d_{5/2}$ and aliphatic C 1s BEs, it was determined that the Pd BE for the various supported precatalysts

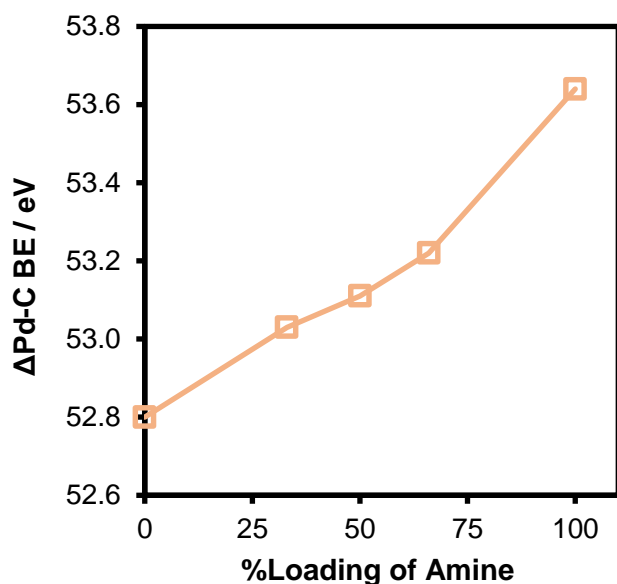


Figure 2.17 Plot of BE difference between the Pd 3d_{5/2} and the aliphatic C 1s core electrons against the mol% loading of amine on the pre-catalyst support.

shift to higher BE in the following order: PIIL < NMe₂PIIL < NH₂PIIL < NH₂CH₂PIIL. To verify this, the shift to higher BE followed the same trend when the BE separation of the Pd 3d peak was compared to the imidazolium N 1s peak. A shift to higher BE after coordination to an amine indicates that the Pd atoms are more electron deficient due to charge transfer from the Pd 3d orbitals to the amine. Moreover, the Pd 3d BEs appeared to increase with increasing loading of amine on the polymer as shown by a comparison of the $\Delta BE_{(Pd-C)}$ for **2.8a**, **2.8b.33**, **2.8b**, **2.8b.66** and **2.8e** (**Figure 2.17**). This trend instead is indicative of a changing coordination environment for palladium: chloride is both a strong σ donor and strong π donor, thus increasing substitution of chloride for more weakly donating amine ligands will result in decreased electron density at the metal centre.

The coordination of amine to Pd was also confirmed by solid-state CP-MAS ¹⁵N NMR spectroscopy (**Figure 2.18**). Analysis of the CP-MAS ¹⁵N NMR spectrum of polymer **2.7b.66** revealed two signals attributed to imidazolium at δ -198 ppm and δ -209 ppm,⁶⁵ while an additional signal at δ -319 ppm was assigned to amine. This assignment was supported by the analysis of 4-aminopolystyrene (**2.7e**) which revealed a major peak at δ -323 ppm. Following impregnation with [PdCl₄]²⁻, the amine signal of **2.8b.66** shifted upfield at δ -372 ppm, while the spectrum of **2.8** also contained an additional up field shifted peak at δ -373 ppm. The high field shift of these signals indicates that the amine has become more electron-rich, consistent with the XPS analysis of **2.8e** and **2.8b.66**, which suggests that the Pd donates electron density to the coordinated amine. Similarly, when PdCl₂ was coordinated to a bipyridyl-based porous

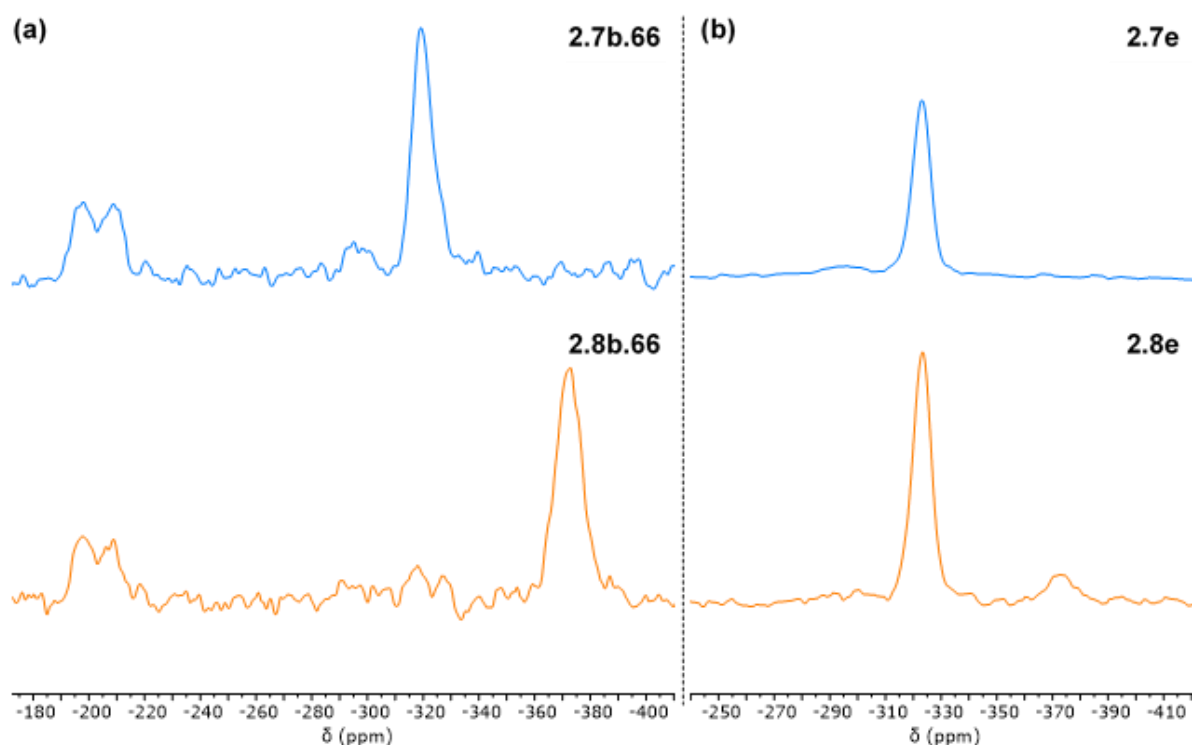


Figure 2.18 CP-MAS ^{15}N NMR spectra of **2.7b.66** and **2.8b.66** (a) as well as **2.7e** and **2.8e** (b). Spectra were referenced to a sample of nitromethane.

organic polymer, a δ 61 ppm shift upfield was observed when the solid-state ^{15}N NMR spectrum was compared to the uncoordinated polymer.⁶⁶

2.5 Investigation of Aniline Cross-linking

An additional weak, broad feature is apparent in the CP-MAS ^{15}N NMR spectrum of **2.7e** at δ -296 ppm, though one would only expect a single nitrogen environment for 4-aminopolystyrene. If one is optimistic, you could argue that a similar feature is apparent in the spectrum of **2.7b.66** at -300 ppm, however, the poorer signal to noise ratio makes this more contentious. Aniline is well known to polymerise under oxidative conditions to form polyaniline, thus, this additional weak signal may be associated with a small amount of cross linking in the sample. To explore this, solution-state 2D NMR spectroscopy experiments were used to probe the coupling of any nitrogen species in polymer **2.7e**. First, a ^1H - ^{15}N HSQC experiment showed two ^{15}N signals at -321.84 ppm and -317.62 ppm which coupled to N-H ^1H NMR signals at 5.24 ppm and a 4.67 ppm respectively. The intensity of the signal at 4.67 ppm dwarfed the signal at 5.24 ppm, nonetheless, coupling between the resonance at 5.24 ppm and that at -317.62 ppm in the ^{15}N spectrum appears strong and therefore genuine. A ^1H - ^{15}N HMBC NMR experiment (**Figure 2.19b**) also suggested that there were two nitrogen environments present albeit at -330.20 ppm and -302.60 ppm, which coupled to ^1H

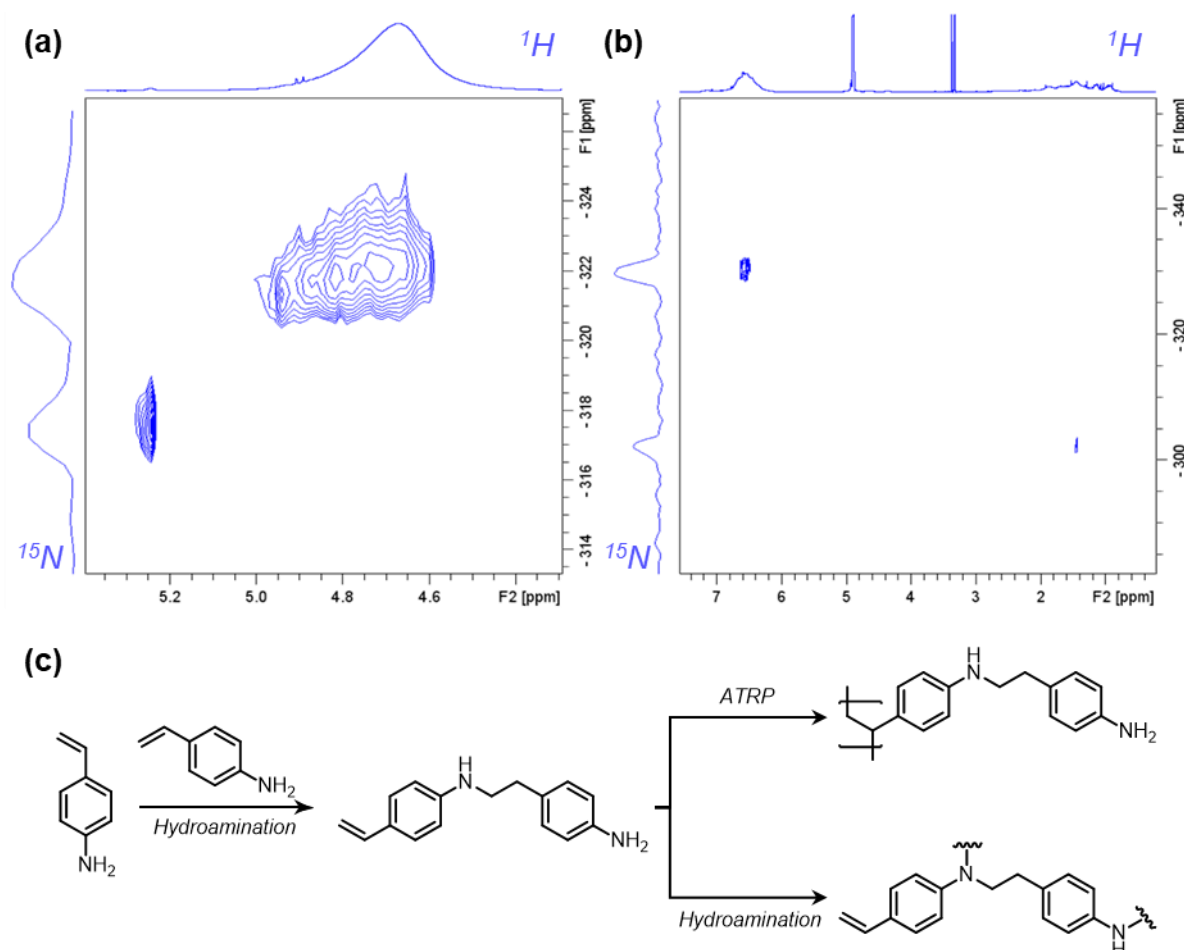


Figure 2.19 (a) ^1H - ^{15}N HSQC NMR and (b) ^1H - ^{15}N HMBC NMR spectrum of polystyrylaniline **1e** (700 MHz, DMSO-d_6). (c) Reaction scheme of possible alkene hydroamination during the polymerisation of 4-vinylaniline to afford polymer **2.7e**.

environments at 6.58 ppm and 1.44 ppm respectively. Multiple bond coupling between amine and the aliphatic protons could be indicative of alkene hydroamination as shown in **Figure 2.19c**. The hydroamination of alkenes typically proceeds in the presence of a transition metal catalyst, however, catalyst-free anti-Markovnikov hydroaminations have been reported to proceed *via* a radical initiator,⁶⁷ or in the case of some vinylheteroarenes with no additive at all.⁶⁸ While more experiments will be required to validate the existence of such a bonding mechanism in the aniline-decorated PIILs, the possibility of aliphatic cross-linking through the amine nitrogen is exciting as it may confer an additional degree of stability to the catalyst support.

2.6 The Fate of the Catalyst

The X-ray photoelectron spectra of the nanoparticles recovered after conducting the hydrogenation of CO_2 with **2.8b-e**, typically contained two pairs of $3d_{5/2}$ and $3d_{3/2}$ doublets; the pair with $3d_{5/2}$ BEs of 331.8-330.9 eV correspond to Pd^0 ,⁶³ while those with $3d_{5/2}$ BEs of

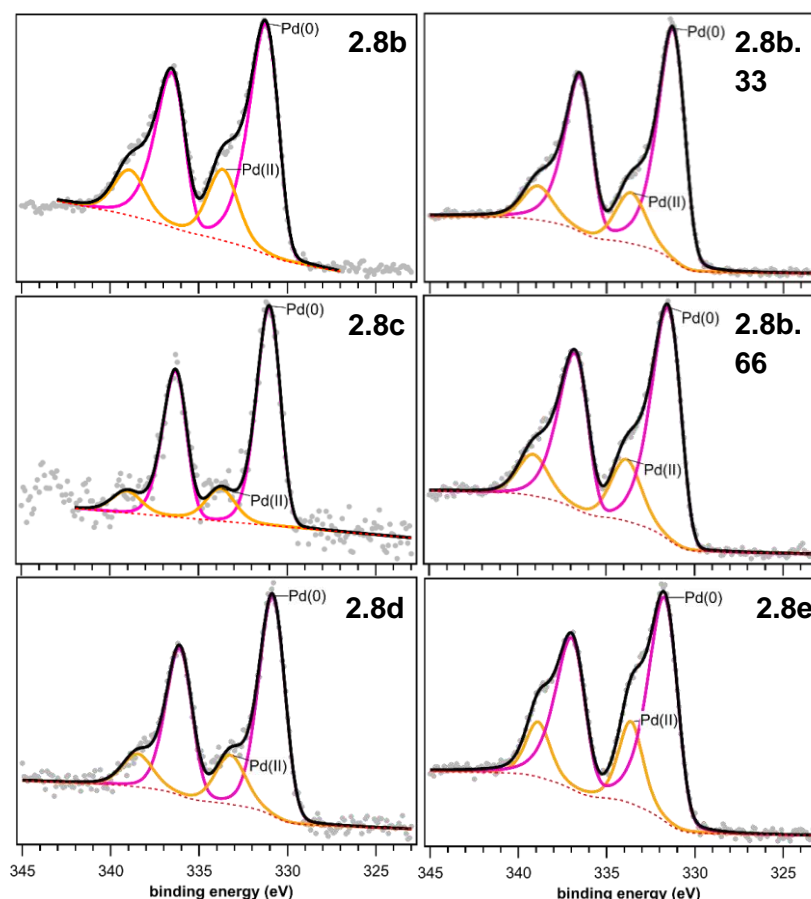


Figure 2.20 Pd 3d core level XPS region for NP materials isolated from the *in-situ* hydrogenation of precatalysts **2.8a-e**. Black line = overall fitting; Red dotted line = background.

333.9-333.2 eV are due to divalent Pd coordinated to chloride. There was no evidence of PdO formation after catalysis, as this would have a PdCl-PdO separation of 1.0 eV, appearing at a slightly higher BE than Pd⁰.^{63,69} Arrigo and co-workers report a Pd⁰-PdO separation of 1.35 eV,⁷⁰ meanwhile Zemlyanov studied the oxidation of a Pd single crystal *in-situ* and found two PdO components with Pd⁰-PdO separations of 0.62 and 1.36 eV.⁷¹ The degree of reduction to Pd⁰ following 2 hours of hydrogenation was fairly reproducible for all catalysts with *ca.* 20-24 at.% of unreduced Pd²⁺ remaining after this time. Precatalyst **2.8c** was an exception with 84 at.% reduction to Pd⁰ after 2 hours. The presence of unreduced Pd²⁺ could be indicative of Pd species strongly coordinated to Lewis basic sites as this would limit their reducibility.⁵⁷ Surprisingly, precatalyst **2.8a** showed no evidence of Pd at the surface of the material following catalysis, a finding that was consistent across four spots on two unique samples analysed by XPS; this is indicative of Pd leaching into solution, however, EDX mapping of TEM images of the isolated catalyst material showed significant amounts of Pd dispersed through the bulk of the sample (**Appendix A.2.9**).

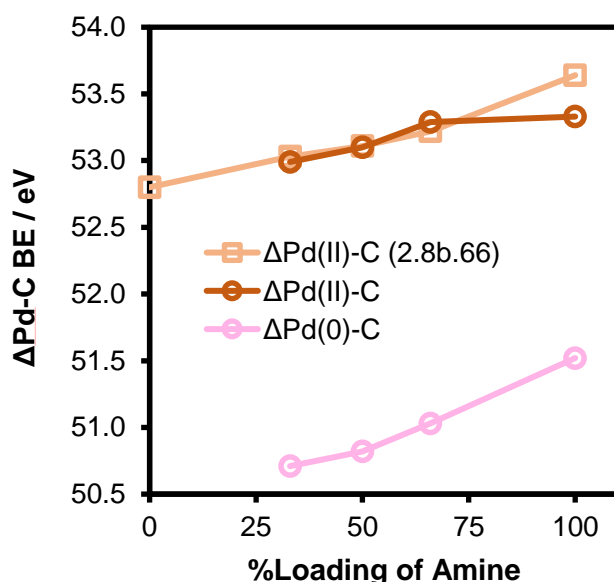


Figure 2.21 Plot of BE difference between the Pd 3d_{5/2} and the aliphatic C 1s core electrons against the mol% loading of amine on the support for PdCl₄ pre-catalyst (□) and PdNP (O) samples.

Following reduction of the PdCl₄@PIIL precatalysts under the conditions of catalysis, we continued to see an apparent charge transfer effect between the ligand and the metal when the BE separations of the Pd 3d_{5/2} and the C 1s (aliphatic) peaks were compared (**Figure 2.21**). This BE separation appeared to increase for zero valent Pd as the loading of amine on the catalyst support increased; assuming that the aliphatic C 1s peak is unchanged by the formation of Pd⁰, this indicates that the Pd⁰ peaks are shifting to a higher BE with increasing number of amine sites. This trend is consistent with Pd(II) peaks in the precatalyst shifting to higher BE with increasing amine, as did residual Pd(II) sites in the reduced catalyst material. The most significant shift was observed for catalyst generated from **2.8e** with a $\Delta\text{BE}_{\text{Pd(0)-C}}$ of 51.5 eV and a $\Delta\text{BE}_{\text{Pd(II)-Pd(0)}}$ 1.8 eV (average $\Delta\text{BE}_{\text{Pd(II)-Pd(0)}}$ of 2.3 eV), likely due to strong charge transfer from the Pd to the support, as reported for PdNP supported on nitrogen-doped carbon nanotubes.⁷⁰ Note that it is difficult to discuss the effect of the various amine donors on the electronic structure of Pd(0)NPs without analysis of surface Pd on unfunctionalised PIIL support **2.7a** as a benchmark; however, catalyst decorated with aniline ligands (**2.8b**) showed the highest BE shift for zero valent Pd when compared to the other ligands. Catalyst generated from **2.8c** had the smallest $\Delta\text{BE}_{\text{Pd(0)-C}}$ separation of 50.2 eV, compared to 50.8 eV for **2.8b**, which suggests a weaker interaction between Pd and the support.

While coordination of a heteroatom to a metal typically results in an increase in the electron density at the metal, there have been reports in which a metal has become more electron deficient upon coordination of a heteroatom donor. For example, PdNPs on N-doped carbon

nanotubes become more electron deficient by virtue of donating electrons to pyridinic nitrogen, and the palladium was shown to become more electron poor with increased loading of nitrogen,⁷² in strong agreement with the results described herein. Similarly, bimetallic PtRu NPs were found to transfer charge to a nitrogen doped carbon support when compared to commercial Ru/C.⁷³ Introduction of biphenyl to a PIIL support caused Pd⁰ to shift to higher BEs when compared to its phenyl counterpart, attributed to interactions of Pd with the larger π -system.³⁴ X-ray absorption near edge structure (XANES) spectroscopy studies of PdNP immobilized on graphitic carbon nitride showed a strong interaction between the Pd and the support attributed to orbital hybridization.²⁴

Due to the mixture of oxidation states following catalysis, it is unclear whether Pd²⁺ or Pd⁰ is the active species for the hydrogenation of CO₂ to formate. Typically, Pd⁰ is considered to be the active catalyst for this transformation, though Han and co-authors claim that Pd²⁺ based PdO catalyst doped with vanadium shows superior activity to its pre-reduced Pd⁰ counterpart, for the thermal hydrogenation of CO₂ to formate;⁶⁴ it is worth noting, however, that the authors did not conduct post-mortem analysis of the catalyst materials, thus the oxidation state of Pd after hydrogenation under the conditions of catalysis is ambiguous. In this vein, Arrigo *et al.* demonstrated that N-coordinated Pd²⁺ species were inactive for the hydrogenation of alkynes.⁶⁹

Qualitatively, Pd 3d spectra of NP generated from **2.8c** and **2.8d** showed a significant reduction in the concentration of Pd in the samples post-catalysis, and as mentioned, the material isolated from **2.8a** showed no surface Pd at all. Hii et al. report that the base K₂CO₃ had a significant effect on the leaching of Pd from Al₂O₃ supported catalyst;⁷⁴ the mechanism of detachment of Pd from the support appeared to be due to a combination of attack of the support by carbonate, and the adsorption of K⁺ to the NP surface; interference of the electrostatic interaction between the PdNP and the support (partially through induced reduction of PdO) by the adsorbed species ultimately led to Pd depletion from the catalyst.

To investigate the degree of Pd leaching following 2 hour reactions under standard conditions, reaction mixtures were passed through syringe filters (0.45 μ m) and analysed by ICP-OES. Indeed, reactions charged with precatalysts **2.8a**, **2.8c** and **2.8d** showed significant leaching of Pd into solution (**Table 2.1**). In contrast, aniline-decorated precatalysts **2.8b**, **2.8b.33**, **2.8b.66** and **2.8e** lost significantly less Pd, with precatalyst **2.8b.33** losing only 0.2% of its

initial loading of Pd. The %loss of Pd appeared to increase with decreasing loading of ionic liquid, whereby the amount of Pd lost followed **2.8b.33** < **2.8b** < **2.8b.66** < **2.8e** for aniline decorated precatalysts. While important, the ionic liquid did not act alone in the stabilization of Pd, as precatalyst **2.8e** lost only 3.9% of its initial Pd, highlighting the pivotal role of the amine. Despite having the same IL : amine ratio as **2.8b**, tertiary and benzylic amines proved markedly less effective at retaining the palladium with **2.8c** and **2.8d** losing 13.5% and 33.0% of their initial Pd, respectively. This could be because of superior coordination of aniline to residual Pd(II) sites, or potentially due to the apparent cross-linking network of amines in aniline decorated catalysts, as described in **Section 2.2.6**.

Alarmed by the loss of Pd following catalysis, the N 1s core electrons were examined after hydrogenation by XPS to investigate the stability of the catalyst supports. Indeed, analysis of the N 1s spectra of all samples post-catalysis revealed a loss of imidazolium nitrogen with precatalyst **2.8a** appearing to lose all surface imidazolium species. The loss was substantial for all catalysts, though precatalyst **2.8b.66** appeared to lose the least amount of imidazolium species, with 21% remaining after catalysis. This could in part rationalise the superior activity of **2.8b.66**, as the poor efficacy of **2.8e** demonstrated that the presence of the imidazolium has a beneficial effect on catalyst activity. Interestingly, the amount of imidazolium retained after catalysis appears to increase with increasing loading of amine. Tentatively, one might consider whether additional stability is obtained through the amine crosslinking of polystyrylaniline in a similar fashion to that observed in the oxidative polymerisation of polyaniline.⁷⁵

Retrospectively, the finding that the polymer supports undergo degradation under the conditions of catalysis is perhaps not surprising; benzyl groups are widely used for the

Table 2.2 Loss of imidazolium N as determined by analysis of N 1s XP spectra after 2 hours of catalysis.

Precatalyst	at.% Imidazolium N		% Imidazolium N Remaining ^a
	<i>Precatalyst</i>	<i>After 2 Hours</i>	
2.8a	100	0	0
2.8b	70	23	12
2.8c	81	5	1
2.8d	67	12	7
2.8b.33	80	22	7
2.8b.66	57	22	21

^aAmount of remaining imidazolium normalized under the assumption that no amine is lost after catalysis.

protection of alcohols and amines in organic synthesis and are removed using Pd-catalysed hydrogenation.⁷⁶ This deprotection is then accentuated by a nearby electronegative atom such as an oxygen (benzyl ether), or in this case nitrogen. The cleavage of *N*-benzylimidazole groups in the presence of Pd/C has also been demonstrated using triethylsilane as a H source.⁷⁷ To further confirm this observation, the autoclave was charged with benzylic IL monomer 1,2-dimethyl-3-(4-vinylbenzyl)-imidazolium chloride (100 mg, 0.4 mmol), K₂CO₃ (1.80 g, 13.0 mmol), Pd/C (5 mol%, 10 wt% of Pd on carbon) and deionized water (20 mL); the contents of the vessel were then hydrogenated under the conditions of catalysis for 2 hours. Water was removed from the reaction products under reduced pressure, and a ¹H NMR spectrum of the residue revealed complete hydrogenation of the benzyl group to afford 1,2-dimethylimidazole. The clear loss of IL from the supports during catalysis may rationalise the leaching of Pd catalyst into the reaction solution; for **2.8a**, **2.8c** and **2.8d** the loss of imidazolium was more significant, with no imidazolium at all detected at the surface of **2.8a** post-catalysis. The benzylic amine group of **2.8d** is also likely to be susceptible to cleavage, although relative to the imidazolium peak, any loss appears diminutive by comparison. This finding is of relevance to other work as similar benzylic groups have been incorporated into other catalyst supports used for CO₂ hydrogenations under comparative conditions, such as in biphenyl substituted imidazolium PIILs.³⁴ Post-mortem analysis of the aforementioned catalysts does not identify degradation of the catalyst support; in-fact, the authors assert that the polymer support remains intact as evidenced by a comparison of the fresh and spent catalyst using FT-IR (despite clear differences in the two spectra). Thus, XPS presents itself as an essential tool to probe the degradation of these catalyst supports posthumously.

Although a N-Pd peak has been fitted in the N 1s XPS for aniline-decorated NP materials (**Appendix A.2.11**), such a peak was only weakly present – no such peak was apparent for tertiary amine and benzylamine decorated NP materials generated from **2.8c** and **2.8d**. The catalyst material isolated following the *in-situ* reduction of **2.8b.66** was therefore analysed by CP-MAS ¹⁵N NMR spectroscopy. As discussed earlier, it was evident that the aniline NH₂ signal at δ -319 ppm shifted on impregnation with the metal salt to δ -372 ppm, consistent with coordination of the amine to Pd. However, the subsequent *in-situ* hydrogenation of **2.8b.66** led to an additional shift to δ -321 ppm which is close to the original position of the amine peak for **2.7b.66**. The δ 2 ppm separation between this peak and that of the amine signal in **2.7b.66** could be indicative of charge transfer from Pd to the support, though the signals are

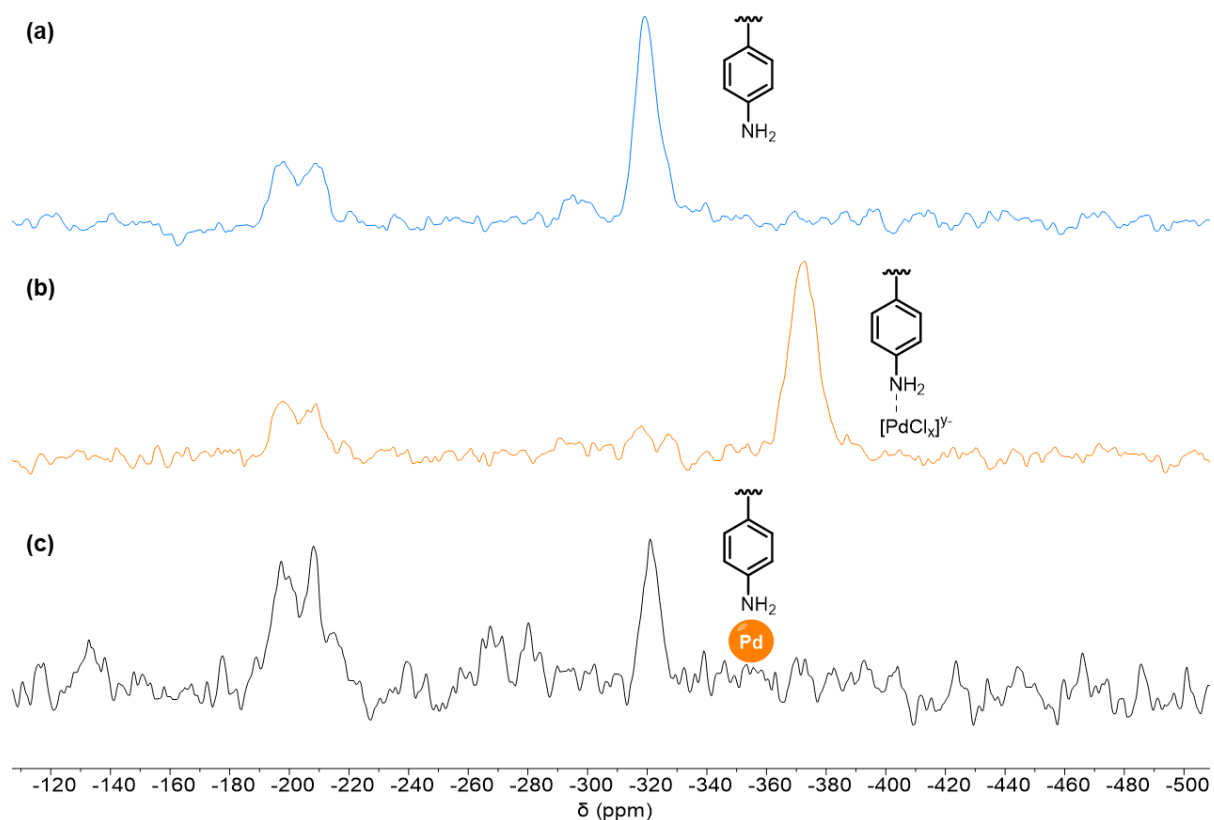


Figure 2.22 CP-MAS ^{15}N NMR spectra of (a) **2.7b.66** ($T_1 = 1.52$ s), (b) **2.8b.66** ($T_1 = 1.33$ s) and (c) NP catalyst generated *in-situ* from **2.8b.66** ($T_1 = 0.41$ s). ^{15}N NMR spectra were referenced to nitromethane with a MAS rate of 10 kHz.

more likely to be equivalent within a margin of error. Unexpectedly, there are further signals evident at -268 and -281 ppm, however their low intensities make any attempt to assign them contentious – the natural abundance of ^{15}N is very low, thus, it is not difficult to rationalise that these peaks are a product of a poor signal to noise ratio. In order to improve the resolution of these signals, one could analyse the sample using a smaller sample rotor, enabling faster spinning speeds and therefore higher resolution spectra.

Note that although the imidazolium N signals in **Figure 2.22c** appear more intense relative to the amine signal than they do in the corresponding precatalyst and polymer spectra, this does not reflect an increased abundance of the imidazolium environments in the sample; rather, the imidazolium signals were less intense following hydrogenation. Consequently, the contact time (T_1) used to acquire the spectrum in **Figure 2.22c** was markedly lower than that used in the acquisition of spectra for **2.7b.66** and **2.8b.66** ($T_1 = 0.41$ s vs 1.52 s and 1.53 s respectively). As contact time does not apply uniform magnetization across a molecule, some groups may appear more intense in the resulting spectrum.

2.7 Conclusion

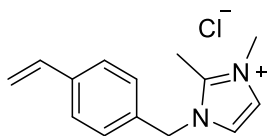
This chapter has demonstrated that PdNPs stabilized by weakly basic primary amine donors are much more active catalysts for the hydrogenation of CO₂ to formate than their unfunctionalised and tertiary amine counterparts. This result was exploited, and it was found that the catalyst activity increased with increasing loading of amine on the polymer, whereby catalyst generated from **2.8b.66** was over three times more active than unmodified catalyst generated from **2.8a** with an optimum TOF of 500 h⁻¹. However, the incorporation of IL was essential to achieving high activities as Pd supported by amine alone (**2.8e**) had a much lower TOF of 147 h⁻¹.

XPS proved to be an invaluable technique in the characterisation of the PdCl₄-loaded precatalysts, as it revealed that the amine donors coordinate to the palladium, a result that was supported by CP-MAS ¹⁵N NMR spectroscopy. Electron transfer between the metal catalyst and the support was demonstrated using these approaches, thus, it may be possible to tune the surface electronic properties of metal NP catalysts and thereby their reactivity through a judicious choice of heteroatom donor and its loading. However, more work is required to understand the nature of this interaction, as XPS analysis alone is insufficient to describe the electronic effect of ligand binding to metal.⁷⁸ In particular, *in-situ* DRIFTS would complement this study as it would allow us to probe the electronic state of Pd by measuring the binding strength of carbon monoxide.

While the amine-PIIL motif is an effective design principle for developing active catalysts for CO₂ hydrogenation, more work will be required to improve their stability as the PIIL support undergoes significant degradation under the conditions of catalysis, which appears to have a detrimental effect on the recyclability of the catalyst, both due to the loss of IL and the subsequent leaching of Pd. The design of robust systems that are stable under the conditions of catalysis described herein is therefore paramount to develop highly active hydrogenation catalysts that are amenable for scale-up. The following chapter aims to build on this study by investigating new approaches towards the development of robust PIIL supports for hydrogenation catalysts.

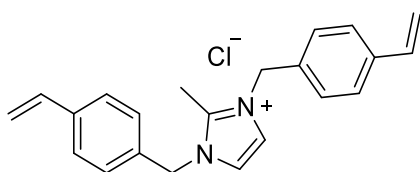
2.8 Experimental

2.8.1 Synthesis of 1,2-dimethyl-3-(4-vinylbenzyl)imidazolium chloride (2.1)



A Schlenk flask was charged with 1,2-dimethylimidazole (5.77 g, 60.0 mmol) and 4-chloromethylstyrene (11.72 g, 76.8 mmol) which were dissolved in chloroform (50 mL). The mixture was heated to 70 °C and stirred overnight. After cooling to room temperature, the mixture was concentrated *in vacuo* and precipitated by dropwise addition to a large volume of diethyl ether with rapid stirring. The resulting white solid was isolated by filtration and dried under high vacuum (13.00 g, 87%). **¹H NMR (400 MHz, CDCl₃)** δ 7.66 (d, *J* = 2.1 Hz, 1H), 7.61 (d, *J* = 2.1 Hz, 1H), 7.40 (m, 2H), 7.29 (m, 2H), 6.67 (dd, *J* = 17.6, 10.9 Hz, 1H), 5.76 (d, *J* = 17.6 Hz, 1H), 5.53 (s, 2H), 5.30 (d, *J* = 10.9 Hz, 1H), 3.97 (s, 3H), 2.79 (s, 3H). **¹³C NMR (101 MHz, CDCl₃)** δ 144.53, 138.64, 135.87, 132.25, 128.63, 127.27, 122.92, 121.92, 115.53, 52.37, 35.99, 11.11.

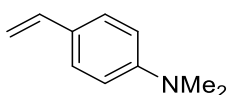
2.8.2 Synthesis of 2-methyl-1,3-bis(4-vinylbenzyl)imidazolium chloride (2.3)



In an oven dried Schlenk flask, NaH in mineral oil (2.19 g, 91.2 mmol) was dispersed in anhydrous DMF (30 mL) and cooled to 0 °C with stirring in an ice bath. Once cool, 2-methylimidazole (5.99 g, 73.0 mmol) was added in portions resulting in an exotherm and notable effervescence. After the exotherm had subsided, 4-chloromethylstyrene (9.28 g, 60.8 mmol) was added gradually, also resulting in an exotherm. The reaction mixture was then heated to 75 °C and stirred for 1.5 hours. After cooling to room temperature, the mixture was quenched with the careful addition of deionized water (50 mL), before extracting the product using ethyl acetate (4 x 50 mL). The organic fractions were washed with deionized water (10 mL), and then acidified with 2 M HCl (2 x 25 mL). The acidic aqueous phase was then washed with diethyl ether (2 x 50 mL), before treating with 2M KOH until alkaline. The product was then extracted from the aqueous phase using diethyl ether (4 x 25 mL), dried over MgSO₄, filtered, and the volatiles were removed *in vacuo* to afford 2-methyl-(4-vinylbenzyl)imidazole as a yellow oil (8.02 g, 67%).

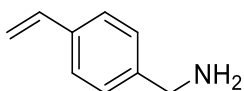
The isolated 2-methyl-(4-vinylbenzyl)imidazole (8.02 g, 40.4 mmol) was added to a Schlenk flask together with 4-chloromethylstyrene (7.40 g, 48.5 mmol) which were dissolved in chloroform (70 mL) with stirring. The mixture was then heated to 70 °C and stirred vigorously overnight. After cooling, the product was then concentrated *in vacuo* and precipitated by dropwise addition to stirring diethyl ether. The resulting white solid was isolated by filtration and dried under high vacuum (10.64 g, 75%). **¹H NMR (400 MHz, CDCl₃)** δ 7.61 (s, 2H), 7.27 (m, 4H), 7.18 (m, 4H), 6.56 (dd, *J* = 17.6, 10.9 Hz, 2H), 5.64 (d, *J* = 17.6 Hz, 2H), 5.45 (s, 4H), 5.19 (d, *J* = 10.9 Hz, 2H), 2.67 (s, 3H). **¹³C NMR (101 MHz, CDCl₃)** δ 144.30, 138.42, 135.86, 132.35, 128.58, 127.15, 122.13, 115.35, 52.13, 11.33.

2.8.3 Synthesis of *N,N*-Dimethyl-4-aminostyrene (2.4)



In an oven-dried Schlenk flask, *n*-butyl lithium (2.5 M in hexane, 13.4 mL, 33.5 mmol) was added dropwise to a stirred solution of methyltriphenylphosphonium bromide (12.0 g, 33.5 mmol) in anhydrous tetrahydrofuran (100 mL). The reaction mixture was allowed to stir for 15 minutes at room temperature, affording an orange solution. After this time, 4-(dimethylamino)benzaldehyde (5.0 g, 33.5 mmol) was added dropwise before stirring the solution at room temperature forming a pale yellow. After 2 hours, the mixture was quenched with saturated aqueous ammonium chloride solution and the product extracted with dichloromethane (4 x 30 mL). The organic fractions were collected, dried over MgSO₄, and filtered before removing the volatiles *in vacuo*. The product was then purified by silica-gel column chromatography (ethyl acetate/petroleum ether, 1:9, 1% NEt₃) to afford a yellow oil (2.27 g, 46%). **¹H NMR (400 MHz, CDCl₃)** δ 7.32 (m, 2H), 6.66 (m, 3H), 5.55 (d, *J* = 17.6 Hz, 1H), 5.03 (d, *J* = 10.8 Hz, 1H), 2.97 (s, 6H). **¹³C NMR (101 MHz, CDCl₃)** δ 150.40, 136.74, 127.28, 126.36, 112.47, 109.48, 40.65.

2.8.4 Synthesis of 4-Vinylbenzylamine (2.6)



In a Schlenk flask, potassium phthalimide (10.68 g, 57.7 mmol) was dissolved in anhydrous DMF (60 mL) with heating and stirring. To this, was added 4-vinylbenzylchloride (8.00 g, 52.4 mmol) before heating the mixture to 55 °C and stirring overnight. After cooling, the mixture was taken up in DCM (50 mL) and washed with deionized water (6 x 100 mL). The organic

phase was then washed with 0.2 M NaOH (2 x 15 mL) followed by further deionized water (3 x 50 mL). The volatiles were then removed *in vacuo* before purifying the resulting off-white solid by recrystallisation from hot methanol (some solid remained insoluble and was removed by hot filtration). 2-(4-Vinylbenzyl)isoindoline-1,3-dione was isolated as a white crystalline solid following filtration, washing with ice-cold methanol, and drying under high vacuum (7.01 g, 51%).

In a Schlenk flask, 2-(4-vinylbenzyl)isoindoline-1,3-dione (6.85 g, 26.0 mmol) was dissolved in hot ethanol (70 mL), to which hydrazine monohydrate (1.96 g, 39.1 mmol) was added dropwise with stirring. The mixture was heated to 75 °C and stirred for 4 hours. On heating, the clear solution turned yellow, and after only 10 minutes solid white precipitate began to form. After cooling to room temperature, the volatiles were removed *in vacuo* and the mixture was taken in chloroform (100 mL) before washing with 20 wt% aqueous NaOH solution (50 mL), followed by water (50 mL). The organic phase was dried over MgSO₄, filtered, and concentrated *in vacuo* to afford a clear yellow oil (3.09 g, 89%). **¹H NMR (300 MHz, CDCl₃)** δ 7.38 (d, *J* = 8.2 Hz, 1H), 7.27 (d, *J* = 8.2 Hz, 1H), 6.71 (dd, *J* = 17.6, 10.9 Hz, 1H), 5.73 (dd, *J* = 17.6, 1.0 Hz, 1H), 5.22 (dd, *J* = 10.9, 1.0 Hz, 1H), 3.86 (s, 1H). **¹³C NMR (101 MHz, CDCl₃)** δ 143.14, 136.68, 136.36, 127.39, 126.54, 113.60, 46.40.

2.8.5 General Procedure for Synthesis of Functionalised Polymer Immobilized Ionic Liquid Supports 2.7a-d.

A screw-top Schlenk flask was charged with 1,2-dimethyl-3-(4-vinylbenzyl)-imidazolium chloride (**2.1**), styrene or amine-modified styrene monomer, 2-methyl-1,3- bis(4-vinylbenzyl)-imidazolium chloride (**2.3**), corresponding to an ionic liquid : amine : crosslinker ratio of 0.91 : 1 : 0.09. The monomers were dissolved in degassed ethanol so that the total concentration of monomer in solution corresponded to 0.2 M. Upon complete dissolution, the mixture was charged with azobis(2-methylpropionitrile) (5 mol%), before immediately degassing the solution via the freeze-thaw technique (6 cycles). The mixture was then stirred and heated at 80 °C. After 96 hours, the flask was charged with an additional portion of azobis(2-methylpropionitrile) (5 mol%), before degassing and stirring for a further 24 hours at 80 °C. After this time, the flask was allowed to cool to room temperature before precipitating the polymer by dropwise addition to stirring diethyl ether. The resulting precipitate was isolated by filtration, washed with diethyl ether, and dried *in vacuo* to afford an off-white/yellow powder. The same procedure was repeated for the preparation of polymers **2.7b.33** and

2.7b.66, though with an ionic liquid : amine : crosslinker ratio of 1.86:1:0.14 and 0.86:2:0.14 respectively.

For the preparation of polymer **2.7a**, it was first necessary to remove any stabiliser from the commercial styrene prior to use. Styrene was thus passed through a short column of aluminium oxide, packed at the top with a thin layer of potassium carbonate, before use in polymerisation.

Polymers were purified by dialysis. Typically, a solution of polymer in methanol was added to dialysis tubing (0.5-1 kDa) which was then sealed and added to a beaker of deionized water. The water was stirred gently for 2 days before removing the solution from the tubing and removing the solvent *in-vacuo*. The resulting residue was then redissolved in the minimum amount of methanol and re-precipitated by dropwise addition to stirring diethyl ether. Again, the resulting powder was isolated by filtration and dried *in vacuo*.

2.8.6 Synthesis of Poly-(4-amino)-styrene (2.7e).

A screw-top Schlenk flask was charged with 4-vinylaniline (11.0 mmol) and ethanol (20 mL) and after complete dissolution azobis(2-methylpropionitrile) (5 mol%) was added. The contents of the flask were degassed via the freeze-thaw technique (6 cycles). The mixture was then stirred and heated at 80 °C. After 72 hours, the flask was cooled to room temperature before precipitating the polymer by dropwise addition to stirring diethyl ether. The resulting precipitate was isolated by filtration, washed with diethyl ether, and dried under *vacuo* to afford a pale-yellow powder.

2.8.7 General Procedure for Synthesis of PdCl₄-Loaded Functionalised Polymer Immobilized Ionic Liquid Precatalysts.

For **2.7a-d**, **2.7b.66**, a round-bottomed flask charged with palladium dichloride (4.2 mmol), NaCl (92.4 mmol) and water (20 mL) was heated to 80 °C for *ca.* 15 min to afford a clear red solution. A solution of the corresponding polymer **2.7a-d** or **2.7b.66** (8.4 mmol) in ethanol (20 mL) was subsequently added in one portion (Pd : polymer ratio of 1 : 2), and the resulting mixture allowed to stir overnight at room temperature, during which time a brick-red precipitate formed. A pale orange/yellow solid was isolated from the suspension *via* centrifugation and was washed with deionized water (4 x 40 mL), ethanol (4 x 40 mL) and diethyl ether (2 x 20 mL) and dried under *vacuo* to afford a fine orange powder. The same

procedure was repeated for the preparation of precatalyst **2.8b.33**, albeit using 4.2 mmol of polymer **2.7b.33** (Pd : polymer ratio of 1 : 1).

Precatalyst	Yield / %	wt% Palladium	Palladium Loading / mmol·g ⁻¹
2.8a	76	10.44	0.98
2.8b	84	11.66	1.10
2.8c	53	8.45	0.79
2.8d	63	9.75	0.92
2.8b.33	88	13.15	1.24
2.8b.66	82	8.14	0.76

2.8.8 Synthesis of PdCl₄-Loaded Poly-(4-amino)-styrene (2.8e).

A round-bottom flask charged with NaCl (92.4 mmol) deionized water (20 mL) and PdCl₂ (4.2 mmol) and the mixture stirred at 80 °C. Upon the formation of a clear red solution, poly-(4-amino)-styrene (4.2 mmol) dissolved in ethanol (10 mL) was added in one portion, and the resulting mixture allowed to stir overnight at room temperature, during which time a brick-red precipitate formed. A pale orange solid was isolated from the suspension via centrifugation, washed with deionized water (4 x 40 mL), ethanol (4 x 40 mL) and diethyl ether (2 x 20 mL) and dried under vacuo to afford **2.8e** as a fine orange powder in 56% yield. ICP-OES: 3.83 wt%_{Pd}, 0.36 mmol·g⁻¹.

2.8.9 General Procedure for the Thermal Hydrogenation of CO₂

A stainless-steel autoclave was charged with precatalyst **2.8a-e** (6 μmol Pd) and an aqueous solution of base (20 mL, 0.65 M). The autoclave was sealed and purged with a 1:1 mixture of H₂ : CO₂ gas (5 cycles), before pressurising to 40 bar at room temperature. The vessel was then heated to 100 °C and stirred mechanically for 2 hours. After this time, the autoclave was allowed to cool to room temperature before venting the gas. ¹H NMR spectra of CO₂ hydrogenation products were recorded on a Bruker Avance III 300 NMR spectrometer, operating at 300.13 MHz, with an 80 s relaxation delay; 50 μL of D₂O was added to samples for locking and non-deuterated dimethylsulfoxide was used as an internal standard.

2.8.10 Density Functional Theory Derived Electron Density Maps of Amines

Calculations were performed using Newcastle University's high performance computing service. The computations were performed in Gaussian 09 using the B3LYP method and 6-

311++G(2d,p) basis set. The structures were optimized, and the presence of minima were confirmed by the absence of negative vibrational frequencies.

2.9 References

-
- ¹ K. Anderson, J. F. Broderick and I. Stoddard, *Clim. Policy*, 2020, **0**, 1–15.
- ² 2023 Net Zero Roadmap, *Int. Energy Agency*, 2023, 1–226.
- ³ M. Zanatta, *ACS Mater. Au*, 2023, **3**, 576–583.
- ⁴ C. Hepburn, E. Adlen, J. Beddington, E. A. Carter, S. Fuss, N. Mac Dowell, J. C. Minx, P. Smith and C. K. Williams, *Nature*, 2019, **575**, 87–97.
- ⁵ I. Dutta, S. Chatterjee, H. Cheng, R. K. Parsapur, Z. Liu, Z. Li, E. Ye, H. Kawanami, J. S. C. Low, Z. Lai, X. J. Loh and K.-W. Huang, *Adv. Energy Mater.*, 2022, **12**, 2103799.
- ⁶ H. Cheng, J. Zhou, H. Xie, S. Zhang, J. Zhang, S. Sun, P. Luo, M. Lin, S. Wang, Z. Pan, J. Wang, X. J. Loh and Z. Liu, *Adv. Energy Mater.*, 2023, **13**, 2203893.
- ⁷ Q. Liu, X. Yang, L. Li, S. Miao, Y. Li, Y. Li, X. Wang, Y. Huang and T. Zhang, *Nat. Commun.*, 2017, **8**, 1–8.
- ⁸ G. A. Filonenko, W. L. Vrijburg, E. J. M. Hensen and E. A. Pidko, *J. Catal.*, 2016, **343**, 97–105.
- ⁹ X. Guo, Z. Peng, A. Traitangwong, G. Wang, H. Xu, V. Meeyoo, C. Li and S. Zhang, *Green Chem.*, 2018, **20**, 4932–4945.
- ¹⁰ P. Gautam, P. R. Upadhyay and V. Srivastava, *Catal. Letters*, 2019, **149**, 1464–1475.
- ¹¹ S. J. Louis Anandaraj, L. Kang, S. DeBeer, A. Bordet and W. Leitner, *Small*, 2023, **19**, 2206806.
- ¹² Y. Wu, Y. Zhao, H. Wang, B. Yu, X. Yu, H. Zhang and Z. Liu, *Ind. Eng. Chem. Res.*, 2019, **58**, 6333–6339.
- ¹³ X. Shao, X. Miao, X. Yu, W. Wang and X. Ji, *RSC Adv.*, 2020, **10**, 9414–9419.
- ¹⁴ L. C. Lee, X. Xing and Y. Zhao, *ACS Appl. Mater. Interfaces*, 2017, **9**, 38436–38444.
- ¹⁵ Z. Zhang, L. Zhang, S. Yao, X. Song, W. Huang, M. J. Hülsey and N. Yan, *J. Catal.*, 2019, **376**, 57–67.
- ¹⁶ K. J. Betsy, A. Lazar, A. Pavithran and C. P. Vinod, *ACS Sustain. Chem. Eng.*, 2020, **8**, 14765–14774.
- ¹⁷ G. Yang, Y. Kuwahara, K. Mori, C. Louis and H. Yamashita, *J. Phys. Chem. C*, 2021, **125**, 3961–3971.
- ¹⁸ S. Masuda, K. Mori, Y. Futamura and H. Yamashita, *ACS Catal.*, 2018, **8**, 2277–2285.

-
- ¹⁹ H. Zhong, M. Iguchi, M. Chatterjee, T. Ishizaka, M. Kitta, Q. Xu and H. Kawanami, *ACS Catal.*, 2018, **8**, 5355–5362.
- ²⁰ Wang, J. Xu, X. Shao, X. Su, Y. Huang and T. Zhang, *ChemSusChem*, 2016, **9**, 246–251.
- ²¹ M. D. Fernández-Martínez and C. Godard, *ChemCatChem*, 2023, **15**, e202201408.
- ²² K. Mori, T. Sano, H. Kobayashi and H. Yamashita, *J. Am. Chem. Soc.*, 2018, **140**, 8902–8909.
- ²³ K. Mori, S. Masuda, H. Tanaka, K. Yoshizawa, M. Che and H. Yamashita, *Chem. Commun.*, 2017, **53**, 4677–4680.
- ²⁴ J. H. Lee, J. Ryu, J. Y. Kim, S. W. Nam, J. H. Han, T. H. Lim, S. Gautam, K. H. Chae and C. W. Yoon, *J. Mater. Chem. A*, 2014, **2**, 9490–9495.
- ²⁵ B. Chen, M. Dong, S. Liu, Z. Xie, J. Yang, S. Li, Y. Wang, J. Du, H. Liu and B. Han, *ACS Catal.*, 2020, **10**, 8557–8566.
- ²⁶ T. Sasaki, *Curr. Opin. Green Sustain. Chem.*, 2022, **36**, 100633.
- ²⁷ S. Zeng, X. Zhang, L. Bai, X. Zhang, H. Wang, J. Wang, D. Bao, M. Li, X. Liu and S. Zhang, *Chem. Rev.*, 2017, **117**, 9625–9673.
- ²⁸ S. Zeng, X. Zhang, L. Bai, X. Zhang, H. Wang, J. Wang, D. Bao, M. Li, X. Liu and S. Zhang, *Chem. Rev.*, 2017, **117**, 9625–9673.
- ²⁹ Z. Zhang, S. Hu, J. Song, W. Li, G. Yang and B. Han, *ChemSusChem*, 2009, **2**, 234–238.
- ³⁰ A. Moazzezbarabadi, D. Wei, H. Junge and M. Beller, *ChemSusChem*, 2022, **15**, e202201502.
- ³¹ Z. Zhang, Y. Xie, W. Li, S. Hu, J. Song, T. Jiang and B. Han, *Angew. Chemie - Int. Ed.*, 2008, **47**, 1127–1129.
- ³² S. Yu and P. K. Jain, *Nat. Commun.*, 2019, **10**, 1–7.
- ³³ G. P. S. Lau, M. Schreier, D. Vasilyev, R. Scopelliti, M. Grätzel and P. J. Dyson, *J. Am. Chem. Soc.*, 2016, **138**, 7820–7823.
- ³⁴ S. Zulfiqar, M. I. Sarwar and D. Mecerreyes, *Polym. Chem.*, 2015, **6**, 6435–6451.
- ³⁵ B. Feng, Z. Zhang, J. Wang, D. Yang, Q. Li, Y. Liu, H. Gai, T. Huang and H. Song, *Fuel*, 2022, **325**, 124853.
- ³⁶ R. Luo, X. Liu, M. Chen, B. Liu and Y. Fang, *ChemSusChem*, 2020, **13**, 3945–3966.
- ³⁷ G. Li, S. Dong, P. Fu, Q. Yue, Y. Zhou and J. Wang, *Green Chem.*, 2022, 3433–3460.
- ³⁸ Q. Li, T. Huang, Z. Zhang, M. Xiao, H. Gai, Y. Zhou and H. Song, *Mol. Catal.*, 2021, **509**, 111644.
- ³⁹ R. Wang, Y. R. Du, G. R. Ding, R. Zhang, P. X. Guan and B. H. Xu, *ACS Sustain. Chem. Eng.*, 2022, **10**, 5363–5373.
- ⁴⁰ S. Doherty, J. G. Knight, T. Backhouse, E. Abood, H. Alshaikh, I. J. S. Fairlamb, R. A. Bourne, T. W. Chamberlain, R. Stones, *Green Chem.*, 2017, **19**, 1635–1641.

-
- ⁴¹ W. Chen, Y. Zhang, L. Zhu, J. Lan, R. Xie and J. You, *J. Am. Chem. Soc.*, 2007, **129**, 13879–13886.
- ⁴² C. A. Faler and M. M. Joullié, *Org. Lett.*, 2007, **9**, 1987–1990.
- ⁴³ V. Bertini, S. Alfei, M. Pocci, F. Lucchesini, N. Picci and F. Iemma, *Tetrahedron*, 2004, **60**, 11407–11414.
- ⁴⁴ T. Chatterjee, E. Boutin and M. Robert, *Dalt. Trans.*, 2020, **49**, 4257–4265.
- ⁴⁵ (a) H.-K. Lo, I. Thiel and C. Copéret, *Chem. – A Eur. J.*, 2019, **25**, 9443–9446. (b) R. Webber, M. I. Qadir, E. Sola, M. Martín, E. Suárez and J. Dupont, *Catal. Commun.*, 2020, **146**, 106125.
- ⁴⁶ P. Jessop, T. Ikariya and R. Noyori, *Chem. Rev.*, 1995, **95**, 259–272.
- ⁴⁷ W. Ma, J. Hu, L. Zhou, Y. Wu, J. Geng and X. Hu, *Green Chem.*, 2022, **24**, 6727–6732.
- ⁴⁸ A. Kann, H. Hartmann, A. Besmehn, P. J. C. Hausoul and R. Palkovits, *ChemSusChem*, 2018, **11**, 1857–1865.
- ⁴⁹ Q. Liu, X. Yang, L. Li, S. Miao, Y. Li, Y. Li, X. Wang, Y. Huang and T. Zhang, *Nat. Commun.*, 2017, **8**, 1–8.
- ⁵⁰ L. C. Lee, X. Xing and Y. Zhao, *ACS Appl. Mater. Interfaces*, 2017, **9**, 38436–38444.
- ⁵¹ K. Koh, M. Jeon, C. W. Yoon and T. Asefa, *J. Mater. Chem. A*, 2017, **5**, 16150–16161.
- ⁵² S. Jiang, X. Liu, S. Zhai, X. Ci, T. Yu, L. Sun, D. Zhai, W. Deng and G. Ren, *Green Chem.*, 2023, **25**, 6025–6031.
- ⁵³ X. D. Mu, J. Q. Meng, Z. C. Li and Y. Kou, *J. Am. Chem. Soc.*, 2005, **127**, 9694–9695.
- ⁵⁴ D. Guo, K. Jiang, H. Gan, Y. Ren, J. Long, Y. Li and B. Yin, *Angew. Chemie - Int. Ed.*, 2023, e202304662.
- ⁵⁵ G. Greczynski and L. Hultman, *Prog. Mater. Sci.*, 2020, 107, 100591.
- ⁵⁶ M. G. Mason, *Phys. Rev. B*, 1983, **27**, 748–762.
- ⁵⁷ D. A. Bulushev, M. Zacharska, E. V Shlyakhova, A. L. Chuvilin, Y. Guo, S. Beloshapkin, A. V Okotrub and L. G. Bulusheva, *ACS Catal.*, 2016, **6**, 681–691.
- ⁵⁸ Z. Li, H. Yu, Y. Zhang, D. Wu, Y. Bai, S. Liu and H. Zhao, *Chem. Commun.*, 2023, **59**, 4535–4538.
- ⁵⁹ G. H. Gunasekar, J. Shin, K. D. Jung, K. Park and S. Yoon, *ACS Catal.*, 2018, **8**, 4346–4353.
- ⁶⁰ M. C. Militello and S. J. Simko, *Surf. Sci. Spectra*, 1994, **3**, 402–409.
- ⁶¹ P. S. Bagus, C. J. Nelin, C. R. Brundle and S. A. Chambers, *J. Phys. Chem. C*, 2019, **123**, 7705–7716.
- ⁶² Y. Zhang, Y. Cai, Y. Guo, H. Wang, L. Wang, Y. Lou, Y. Guo, G. Lu and Y. Wang, *Catal. Sci. Technol.*, 2014, **4**, 3973–3980.

-
- ⁶³ Q. Zhang, S. Zheng, J. Zhang, W. Li and Y. Fu, *Catal. Letters*, 2021, **151**, 2537–2546.
- ⁶⁴ Y. Wang, M. Dong, S. Li, B. Chen, H. Liu and B. Han, *Chem. Sci.*, 2024, **15**, 5525–5530.
- ⁶⁵ (a) T. Takamuku, T. Tokuda, T. Uchida, K. Sonoda, B. A. Marekha, A. Idrissi, O. Takahashi, Y. Horikawa, J. Matsumura, T. Tokushima, H. Sakurai, M. Kawano, K. Sadakane and H. Iwase, *Phys. Chem. Chem. Phys.*, 2018, **20**, 12858–12869. (b) A. Lyčka, R. Doleček, P. Šimůnek and V. Macháček, *Magn. Reson. Chem.*, 2006, **44**, 521–523.
- ⁶⁶ M. Bhadra, H. S. Sasmal, A. Basu, S. P. Midya, S. Kandambeth, P. Pachfule, E. Balaraman and R. Banerjee, *ACS Appl. Mater. Interfaces*, 2017, **9**, 13785–13792.
- ⁶⁷ S. W. Lardy and V. A. Schmidt, *J. Am. Chem. Soc.*, 2018, **140**, 12318–12322.
- ⁶⁸ A. Yadav, M. D. Ambule and A. K. Srivastava, *Org. Biomol. Chem.*, 2024, **22**, 1721–1726.
- ⁶⁹ R. Arrigo, M. E. Schuster, Z. Xie, Y. Yi, G. Wowsnick, L. L. Sun, K. E. Hermann, M. Friedrich, P. Kast, M. Hävecker, A. Knop-Gericke and R. Schlögl, *ACS Catal.*, 2015, **5**, 2740–2753.
- ⁷⁰ R. Arrigo, M. E. Schuster, S. Abate, S. Wrabetz, K. Amakawa, D. Teschner, M. Freni, G. Centi, S. Perathoner, M. Havecker and R. Schlögl, *ChemSusChem*, 2014, **7**, 179–194.
- ⁷¹ D. Zemlyanov, B. Aszalos-Kiss, E. Kleimenov, D. Teschner, S. Zafeiratos, M. Hävecker, A. Knop-Gericke, R. Schlögl, H. Gabasch, W. Unterberger, K. Hayek and B. Klötzer, *Surf. Sci.*, 2006, **600**, 983–994.
- ⁷² Z. He, B. Dong, W. Wang, G. Yang, Y. Cao, H. Wang, Y. Yang, Q. Wang, F. Peng and H. Yu, *ACS Catal.*, 2019, **9**, 2893–2901.
- ⁷³ W. Ni, J. L. Meibom, N. U. Hassan, M. Chang, Y.-C. Chu, A. Krammer, S. Sun, Y. Zheng, L. Bai, W. Ma, S. Lee, S. Jin, J. S. Luterbacher, A. Schüler, H. M. Chen, W. E. Mustain and X. Hu, *Nat. Catal.*, 2023, **6**, 773–783.
- ⁷⁴ M. A. Newton, D. Ferri, C. J. Mulligan, I. Alxneit, H. Emerich, P. B. J. Thompson and K. K. Hii, *Catal. Sci. Technol.*, 2020, **10**, 466–474.
- ⁷⁵ G. Neshar, G. Marom and D. Avnir, *Chem. Mater.*, 2008, **20**, 4425–4432.
- ⁷⁶ H.-J. Cristau, A. Hervé, F. Loiseau, D. Virieux, *Synth.*, 2003, **14**, 2216–2220.
- ⁷⁷ T. H. Graham, *Tetrahedron Lett.*, 2015, **56**, 2688–2690.
- ⁷⁸ G. Chen, C. Xu, X. Huang, J. Ye, L. Gu, G. Li, Z. Tang, B. Wu, H. Yang, Z. Zhao, Z. Zhou, G. Fu and N. Zheng, *Nat. Mater.*, 2016, **15**, 564–569.

Chapter 3

'Robust' Catalysts for CO₂ Hydrogenation

3.1 Introduction

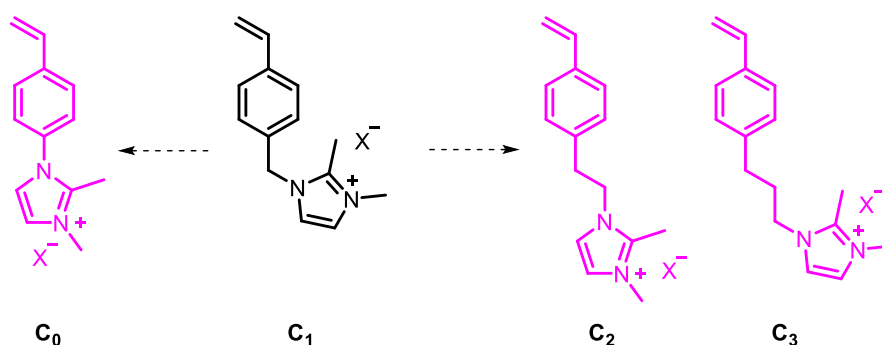
Due to the high temperatures and pressures required for direct CO₂ hydrogenation, it is imperative that robust supports are identified for heterogeneous catalysts. While metal oxide catalyst supports such as CeO₂¹ and TiO₂² are often stable at temperatures in excess of 500 °C, organic supports such as polymers or ligand-modified silica will degrade at temperatures in excess of 250-300 °C. Such organic-based supports are also often vulnerable to chemical transformations that may also lead to degradation. While ample examples report the recyclability of polymer-supported catalysts, post-mortem analysis of the catalyst support is often not included or insufficient and the discussion instead focusses on *in-operando* changes made to the metal catalyst. Following the cleavage of the benzylic group in the PIIL supports discussed in **Chapter 2**, we have identified several systems in the literature that may suffer from similar degradation pathways: a popular motif for polymer supports in CO₂ catalysis is based on so-called Schiff-base/triazine networks that are prepared through the condensation of an amine with an arylaldehyde, melamine polymers being a prominent example of this.³ Similarly, there is no comment on the support stability post-catalysis for resorcinol-formaldehyde polymer supported PdAgNPs, despite the presence of reductively vulnerable benzylic groups; however, the report acknowledges the poor recyclability of the catalyst, losing 30% activity after its first recycle, which could be indicative of catalyst degradation.⁴

Kawanami and co-authors postulate that another phenylenediamine (PDA) modified rGO undergoes deactivation under a H₂ and CO₂ atmosphere *via* conversion of the amine to an amide or urea,⁵ though in a later communication, they propose that the support instead undergoes degradation due to loss of the amine groups, as determined by FT-IR analysis of the spent catalyst.⁶ The use of ionic liquids in hydrogenation catalysis,⁷ and the prevalence of such imine/imide linkers in covalent organic framework supports, thus makes it pertinent to understand the stability of these materials under a highly reducing environment.

To address the finding that the PIIL supports used in **Chapter 2** were susceptible to degradation under the conditions of catalysis, alternative IL motifs, thought to be more chemically robust, were prepared for the synthesis of CO₂ hydrogenation catalysts with improved longevity.

3.2 Synthesis of Robust Ionic Liquid Monomers

A series of ionic liquid monomers were targeted to improve on the stability of the styrylbenzylimidazolium monomer used in **Chapter 2**. As described in **Chapter 2**, the benzylic methylene bridge underwent cleavage *via* hydrogenation in the presence of a Pd catalyst to liberate 1,2-dimethylimidazole. **Scheme 3.1** shows the two strategies considered in the design of new robust monomers: the first approach involved the removal of the benzylic group through direct arylation of 2-methylimidazole (**C₀**); the second approach involved increasing the length of the alkyl separating unit (**C₂** and **C₃**), whereby the N-ethyl/propyl unit should be less susceptible to hydrogenation due to increased separation from the inductively withdrawing styrene.

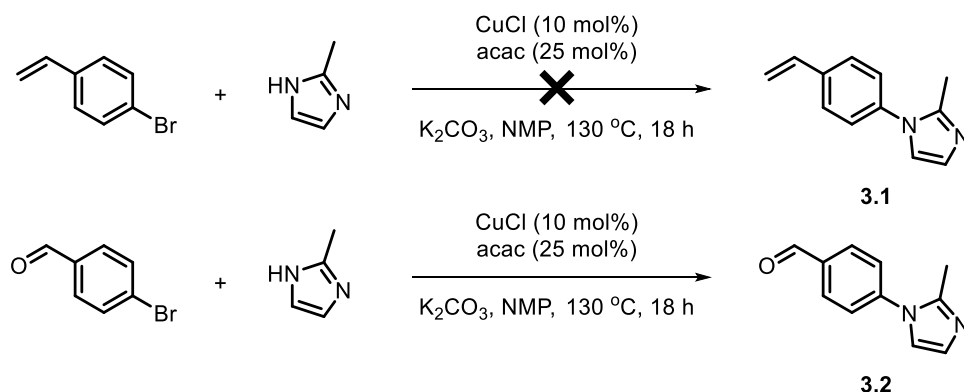


Scheme 3.1 Proposed novel ionic liquid monomers stable to hydrogenation.

3.2.1 Preparation of **C₀** Ionic Liquid Monomer

The *N*-arylation of 2-methylimidazole was first attempted using an Ullman-type cross-coupling with 4-bromostyrene catalysed by CuCl (**Scheme 3.2**).⁸ After 18 hours, a gum-like solid had precipitated from solution which proved to be insoluble in organic solvents and water. While the literature report showed a broad substrate scope for this arylation of imidazoles, the substrate scope did not include bromostyrenes. It is worth noting that Cu(I) catalysts have also been reported to catalyse atom transfer radical polymerisation (ATRP) reactions,⁹ thus, the formation of a solid precipitate is perhaps unsurprising, as the vinyl group is susceptible to polymerisation. By substituting the vinyl group with an aldehyde, we instead aim to introduce the alkene later following a Wittig olefination. In a preliminary experiment, imidazole was *N*-arylated with 4-bromobenzaldehyde to afford 4-(imidazolyl)benzaldehyde in 49% yield. However, the same cross-coupling with 2-methylimidazole proved more difficult, affording **3.2** though contaminated with NMP, despite several attempts to remove it. In the report of Vries and coworkers,⁸ aryl bromides with para-substituted electron withdrawing groups such as in 4-bromobenzonitrile afforded low yields in arylation reactions with

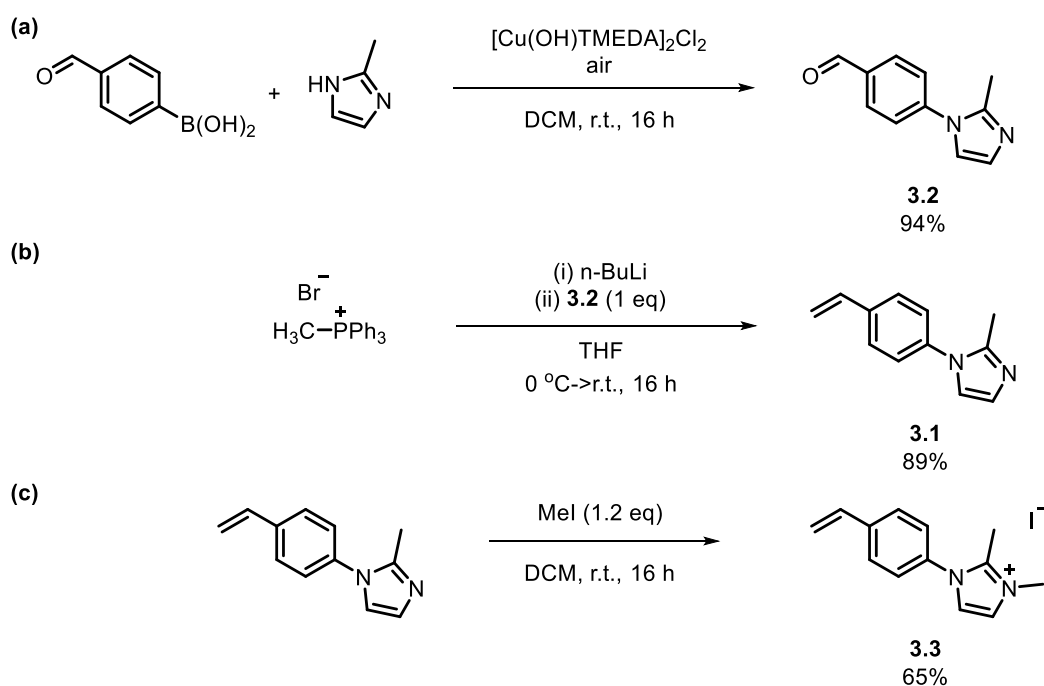
benzylamine when compared to the unsubstituted bromobenzene. While the authors reported high yields for the coupling between bromobenzene and imidazole, yields were lower for more sterically demanding amines such as piperidine, morpholine and *N*-methylpiperazine.



Scheme 3.2 Attempted N-aryl coupling of 2-methylimidazole to *para*-substituted arylbromides.

In an effort to avoid the use of NMP and the high temperatures applied in the aforementioned Ullman-style coupling, an oxidative coupling catalysed by $[\text{Cu}(\text{OH})\text{TMEDA}]_2\text{Cl}_2$, as reported by Collman,¹⁰ was explored. In air, 2-methylimidazole and 4-formylphenylboronic acid were mixed with $[\text{Cu}(\text{OH})\text{TMEDA}]_2\text{Cl}_2$ in DCM overnight to afford **3.2** in 94% yield following purification of the crude mixture by column chromatography. The associated coupling with 4-vinylphenylboronic acid showed little to no conversion even after 96 hours of stirring; however, there was some signal broadening apparent in the ^1H NMR spectra which could be indicative of polymerisation of the vinyl group, either from prolonged stirring in air or *via* a Cu(I) induced ATRP reaction. While the catalyst initially exists as Cu(II), the authors proposed that the mechanism involves Cu(I) intermediate which could catalyse a radical ATRP process.

Subsequently, the vinyl group was introduced through a Wittig olefination under mild conditions, whereby the aldehyde reacts with an *in-situ* generated phosphonium ylide to form the alkene and phosphine oxide. Thus, methyltriphenylphosphonium bromide was first reacted with *n*-BuLi to generate the ylide; treatment of this mixture with benzaldehyde **3.2** generated 2-methyl-(4-vinylphenyl)-imidazole (**3.1**), which was isolated in 89% yield following an aqueous work-up. Small amounts of phosphine oxide impurities were easily removed by passing the product through a silica plug, eluting with ethyl acetate. Methylation of **3.1** with iodomethane in DCM led to the formation of 4-vinylphenylimidazolium iodide which was obtained as a spectroscopically pure powder by dropwise addition to stirring diethyl ether.

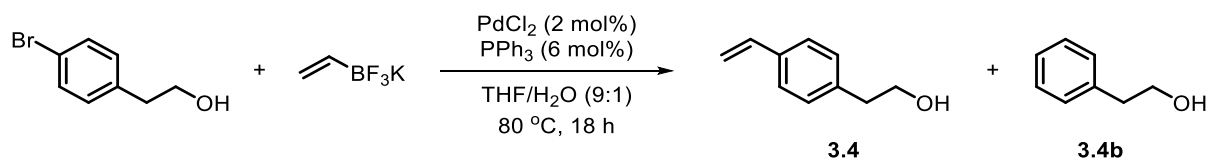


Scheme 3.3 Preparation of monomer **3.3** via (a) oxidative N-aryl coupling of 2-methylimidazole to 4-formylphenylboronic acid, followed by (b) Wittig-olefination of the imidazole substituted benzaldehyde and then the subsequent (c) amine quaternisation with methyl iodide.

3.2.2 Preparation of **C₂** and **C₃** Ionic Liquid Monomers

Due to their structural and thus chemical similarities, the same synthetic approaches were considered for the preparation of both the **C₂** and the **C₃**-based ILs. The principal strategy involved the substitution of a leaving group on the alkyl chain of the monomer with an imidazole amine. Obvious precursors such as 1-(2-chloro/bromoethyl)-4-vinylbenzene and 2-(4-vinylphenyl)ethan-1-ol were either unavailable commercially or very expensive. 2-(4-Vinylphenyl)ethan-1-ol has been substituted with imidazoles, following mesylation of the alcohol, and has previously been prepared through a Grignard reaction between 4-chlorostyrene and ethylene oxide,¹¹ however, ethylene oxide is both toxic and gaseous making it difficult to work with. Instead, a Suzuki-Miyaura coupling was initially explored using 2-(4-bromophenyl)ethan-1-ol and potassium vinyltrifluoroborate as coupling partners (**Scheme 3.4**).¹² After stirring overnight, alcohol **3.4** was isolated as a clear yellow oil in 66% yield, following purification by flash chromatography; however, an impurity constituting 15% of the isolated product was determined by GC-MS to be 2-phenylethanol, which presumably forms *via* Pd-catalysed hydrodehalogenation of the starting arylbromide.¹³ The similar polarity of 2-phenylethanol to **3.4** makes them incredibly difficult to separate by column chromatography. While the resulting imidazolium species would not be incorporated into the

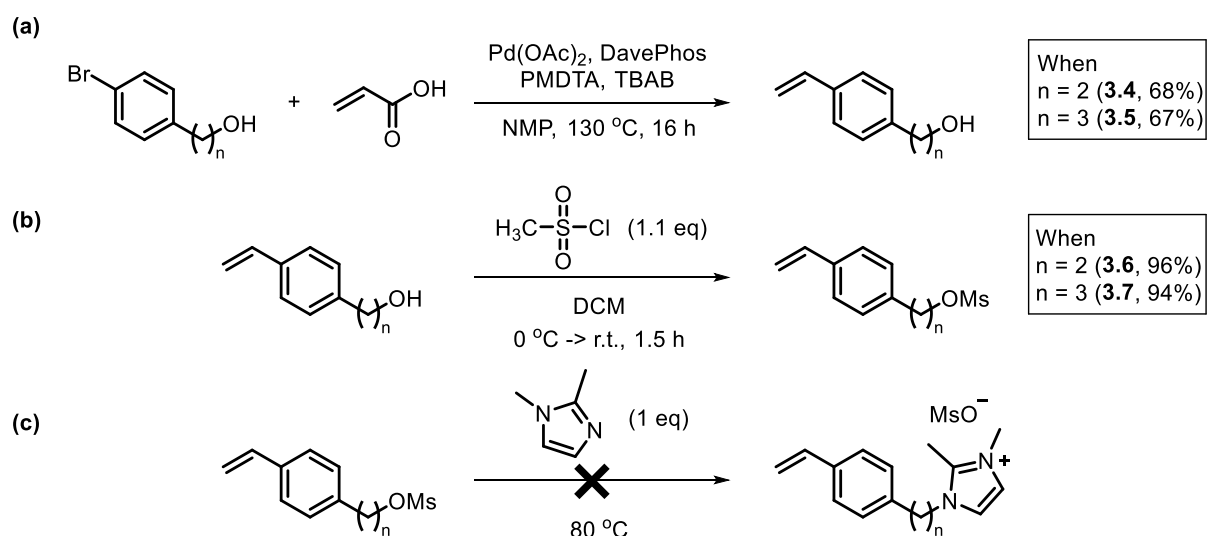
polymer backbone due to a lack of radical polymerisable groups, alternate approaches were considered to avoid incorporation of this impurity into the extended polymer network through chemisorption or physisorption.



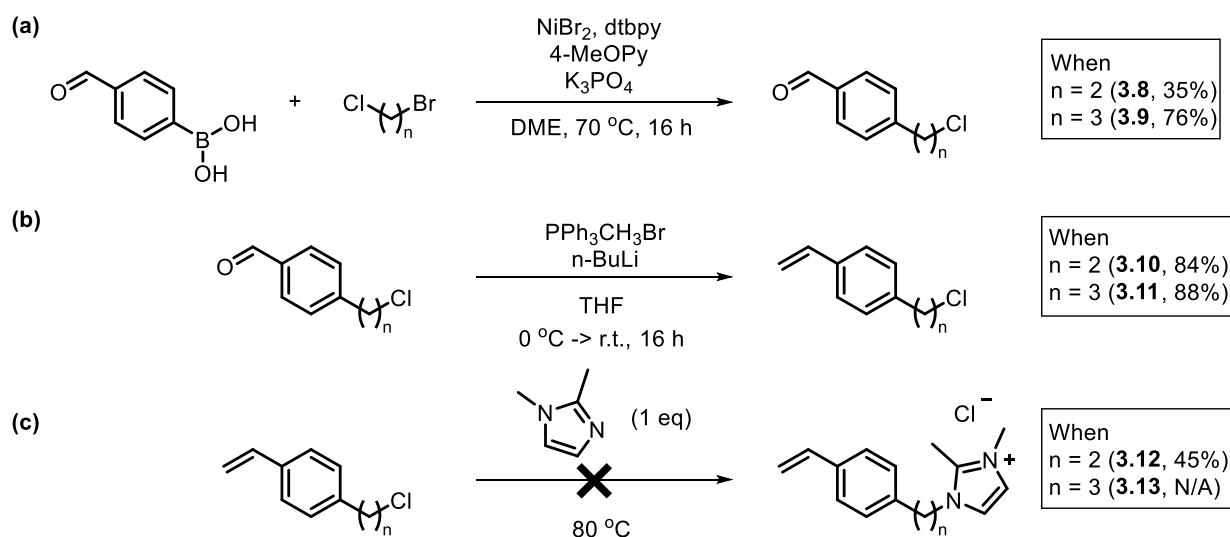
Scheme 3.4 Preparation of **3.4** *via* a Suzuki-Miyaura cross-coupling reaction.

The vinylation of 2-(4-bromophenyl)ethan-1-ol has been reported to proceed *via* a decarboxylative Heck reaction with acrylic acid.¹⁴ When the reaction was catalysed by DavePhos complexed Pd(OAc)₂, alcohol **3.4** was afforded cleanly in 68% yield after washing the organic fractions with 0.2 M NaOH_(aq) to remove any acrylic acid substituted aromatic products (**Scheme 3.5**). The same approach was applied to obtain 3-(4-vinylphenyl)propan-1-ol, **3.5**, cleanly in 67% yield. While both reactions proceeded overnight at 150 mg scale, when the reactions were scaled up to gram-scale, longer reaction times of 48 hours were required to achieve full decarboxylation of the Heck products.

Mesylation of the two arylalcohols with methanesulfonyl chloride led to near instant precipitation of the products; after stirring for an hour, complete conversion was confirmed by ¹H NMR spectroscopy, and products **3.6** and **3.7** were obtained in 96% and 94% yield, respectively. Encouraged by the report from Dyson that arylethylimidazolium ILs can be



Scheme 3.5 (a) Preparation of alcohols **3.4** and **3.5** *via* a decarboxylative Heck cross-coupling reaction. (b) Mesylation of alcohols **3.4** and **3.5**, and (c) the attempted neat substitution of the resulting mesylated products.



Scheme 3.6 (a) Preparation of **3.8** and **3.9** via Suzuki-Miyaura cross-coupling reactions, followed by their subsequent (b) Wittig-olefination, and (c) the attempted neat substitution of the resulting haloalkanes products.

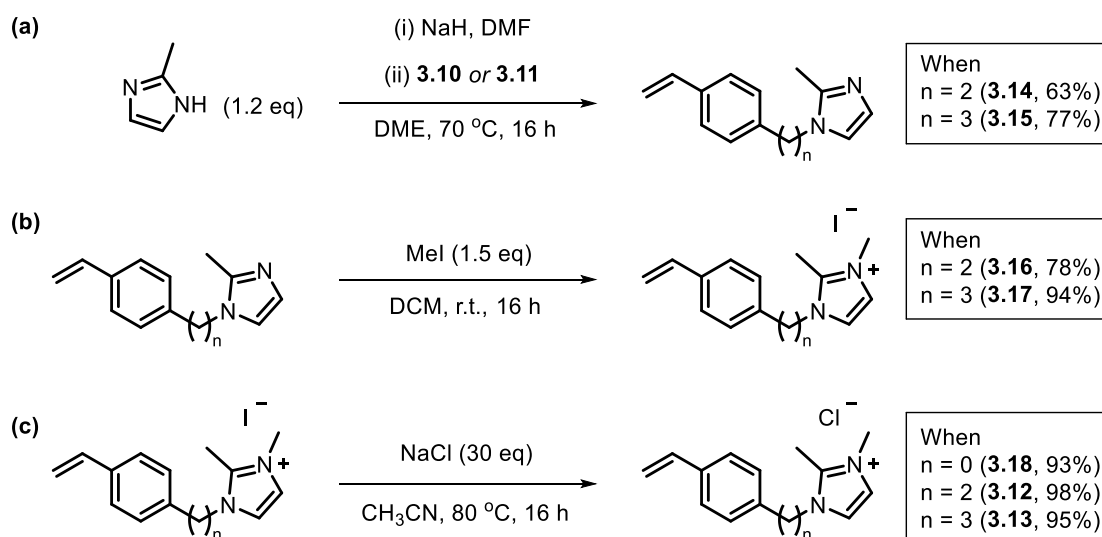
prepared from the neat reaction of 1,2-dimethylimidazolium and chloroethylbenzene,¹⁵ our mesylated alcohols were mixed with 1 equivalent of 1,2-dimethylimidazolium at 80 °C. In contrast to the result of the Dyson group, both substitution reactions were unsuccessful, instead preferring an elimination pathway whereby the amine eliminates mesylate to afford 1,2-dimethylimidazolium mesylate and either 1,4-divinylbenzene ($n = 2$) or 4-allylstyrene ($n = 3$). Moreover, most of the alkene species appeared to polymerise after heating as a neat mixture overnight, as evidenced by the formation of a sticky insoluble gum.

In an approach that hoped to emulate the aforementioned Dyson report, 1-(2-chloroethyl)-4-vinylbenzene and 1-(3-chloropropyl)-4-vinylbenzene were next targeted for reaction with 1,2-dimethylimidazole to afford the target IL monomers (**Scheme 3.6**). Aiming to avoid β -hydride elimination pathways, a nickel catalyst was selected to facilitate a Suzuki-Miyaura coupling between the appropriate haloalkane and 4-(formylphenyl)boronic acid, as described previously.¹⁶ Performing the reaction with a benzaldehyde coupling partner, with the intention of introducing the alkene later, was a precautionary step as Ni is reported to catalyse ATRP reactions as was the case for the Cu catalyst in the **C₀** monomer preparation described above.¹⁷ Despite these efforts, the coupling of 4-(formylphenyl)boronic acid with 1-chloro-2-bromoethane was challenging with low yields of 20-35%. Although β -hydride elimination to afford 4-vinylbenzaldehyde proved unavoidable, this side-product was removed easily by column chromatography. However, while conversion to product **3.8** was initially promising, after purification by column chromatography many fractions were contaminated with an

apparent decarbonylation product (2-chloroethylbenzene), which was difficult to separate from the desired product. Nonetheless, the corresponding coupling between 1-chloro-3-bromopropane and 4-(formylphenyl)boronic acid afforded 1-(3-chloropropyl)-4-vinylbenzene, **3.9**, as a pale-yellow oil in 76% yield, a stark improvement on the preparation of **3.8**.

Following the successful Wittig olefination of the **C₀** aldehyde above, the same approach was used to introduce the vinyl group to the **C₂** and **C₃** precursors. Reaction of the methyltriphenylphosphonium bromide derived ylide with aldehydes **3.8** and **3.9**, led to the formation of alkenes **3.10** and **3.11** in good yields, following purification by elution through silica plugs. However, the subsequent substitutions in neat 1,2-dimethylimidazole were less successful – the attempted substitution of **3.11** showed no sign of product formation even after stirring for several days at 80 °C, meanwhile reaction with **3.10** gave **3.12** in 48% yield. However, once more this product was contaminated with protonated imidazolium chloride salt (5%), presumably derived from the elimination reaction to form divinylbenzene. Although no unreacted imidazole was detected by ¹H NMR spectroscopy after 48 hours, significant amounts of the monomer, and most definitely 1,4-divinylbenzene, appeared to have polymerised after heating for such an extended period.

As the neat substitution of halide and mesylate leaving groups with 1,2-dimethylimidazole proved to be ineffective in the preparation of the target IL monomers, the substitution was instead attempted with the 2-methylimidazolate anion (**Scheme 3.7**), analogous to the preparation of cross-linker **2.3** in **Chapter 2**. First, 2-methylimidazolate was generated by deprotonation of 2-methylimidazole with NaH in DMF before adding **3.10** to the suspension. The resulting mixture was stirred at 70 °C for 1.5 hours, after which time analysis of an aliquot by ¹H NMR spectroscopy confirmed that all the starting material had been consumed. The target, 2-methyl-1-(4-vinylphenethyl)-imidazole (**3.14**) was isolated cleanly from the reaction mixture following an acid-base work-up to remove any unreacted haloalkane. Reassuringly, the same approach also gave 2-methyl-1-(4-vinylphenpropyl)-imidazole (**3.15**) in 77% yield from the reaction of 2-methylimidazolate with **3.11**. The successive amine quarternisations were achieved at room temperature by treating the *N*-substituted imidazoles with methyl iodide in a solution of DCM overnight and ethyl- and propyl-styryl substituted imidazolium iodide monomers **3.16** and **3.17** were isolated in 78% and 94% yield after filtering the resulting precipitates from diethyl ether.



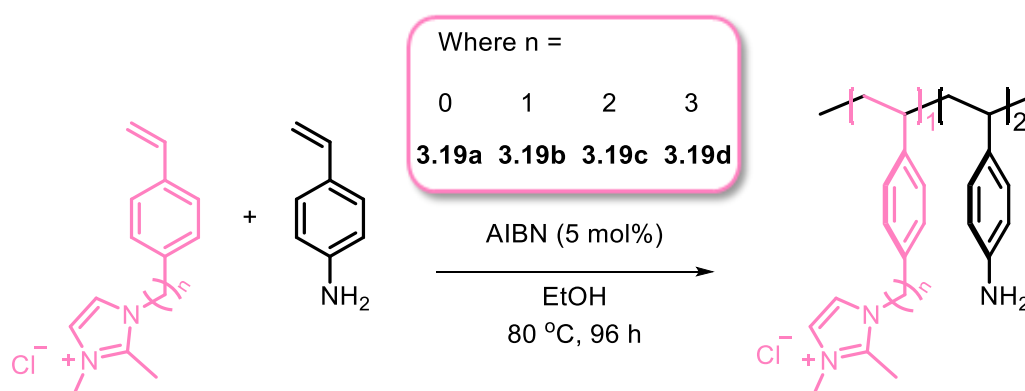
Scheme 3.7 (a) Nucleophilic substitution of halides **3.10** and **3.11** with 2-methylimidazole, (b) methyl iodide mediated quarternisation of the resulting imidazoles, (c) salt metathesis between **3.16** and **3.17** and NaCl to afford the corresponding imidazolium chloride salts.

When comparing ionic liquid polymers as supports for nanoparticle catalysts, the influence of the anions associated to the IL supports is currently unexplored within the group. However, the influence of the IL anion on catalyst activity is well reported in the literature;¹⁸ Dupont and co-authors reported that in the presence of chloride and imidazolate ILs, no conversion of CO₂ to formate was observed for their system, however, high TONs were obtained when an acetate-based IL was implemented.¹⁹ In order to form a meaningful comparison of the IL monomers prepared in this chapter to 4-vinylbenzylimidazolium chloride (**2.1**), a salt metathesis of monomers **3.3**, **3.16** and **3.17** with NaCl was conducted in acetonitrile to afford the corresponding chloride IL monomers (**Scheme 3.7c**).²⁰ After stirring the monomers at 80 °C in the presence of 30 equivalents of NaCl, ¹H NMR spectra of the products typically showed a downfield shift of the imidazolium protons, indicative of product formation; for example, for **3.16** substitution of iodide for a chloride counterion led to a shift from δ 7.36 and 7.31 ppm to δ 7.49 and 7.47 ppm. The reaction mixture was filtered and recharged with fresh NaCl before allowing to stir overnight. By monitoring the shift of the imidazolium protons, we observed full exchange of the ionic liquid anion for all 3 monomers overnight. Monomers **3.18**, **3.12** and **3.13** were isolated by filtering the reaction mixtures and removing the volatiles *in vacuo*. However, the by-product NaI possesses very high solubility in a range of solvents, including acetonitrile, therefore the monomers were purified by taking the dried residues in dichloromethane, and removing any precipitate by filtration. The monomers were once again

dried *in vacuo* and the process was repeated until no precipitation was observed on addition of dichloromethane.

While **C₂** and **C₃** monomers **3.12** and **3.13** were successfully prepared from the corresponding chloroalkyl-4-vinylbenzene precursors, the preparation of precursor **3.12** was low yielding, and both required purification by flash chromatography. Although the reaction was not explored here, the substitution of alkylmesylates by 2-methylimidazolate is certainly feasible; therefore, moving forward, the decarboxylative Heck coupling to form the styrylalcohols described above may be a more practical route to these monomers, as the reactions were high yielding and had straightforward purification steps.

3.3 Synthesis of Robust PIILs and PIIL Supported Precatalysts



Scheme 3.8 Preparation of amine decorated PIIL supports **3.19a-d**, *via* radical initiated polymerisation.

Following the procedure described in **Chapter 2**, monomers **3.18**, **2.1**, **3.12** and **3.13** were polymerised with 4-vinylaniline *via* an AIBN radical initiated polymerisation (**Scheme 3.8**). The ratio of IL monomer to amine was maintained at 1 : 2 in line with the most active catalyst system identified from the studies described in **Chapter 2**, namely PdCl₄@66NH₂PIIL (**2.8b.66**). However, in contrast to the previous work, the following polymer series was prepared in the absence of cross-linker – this should facilitate a direct comparison on the effect of the alkyl chain length on the stability of the monomers under the conditions of catalysis. Although polymers **3.19a-d** were isolated after 96 hours of heating at 80 °C to ensure near-full conversion of monomers, in most cases notable amounts of polymerisation had occurred in the first 24 hours. For example, polymer **3.19a** was less soluble in ethanol

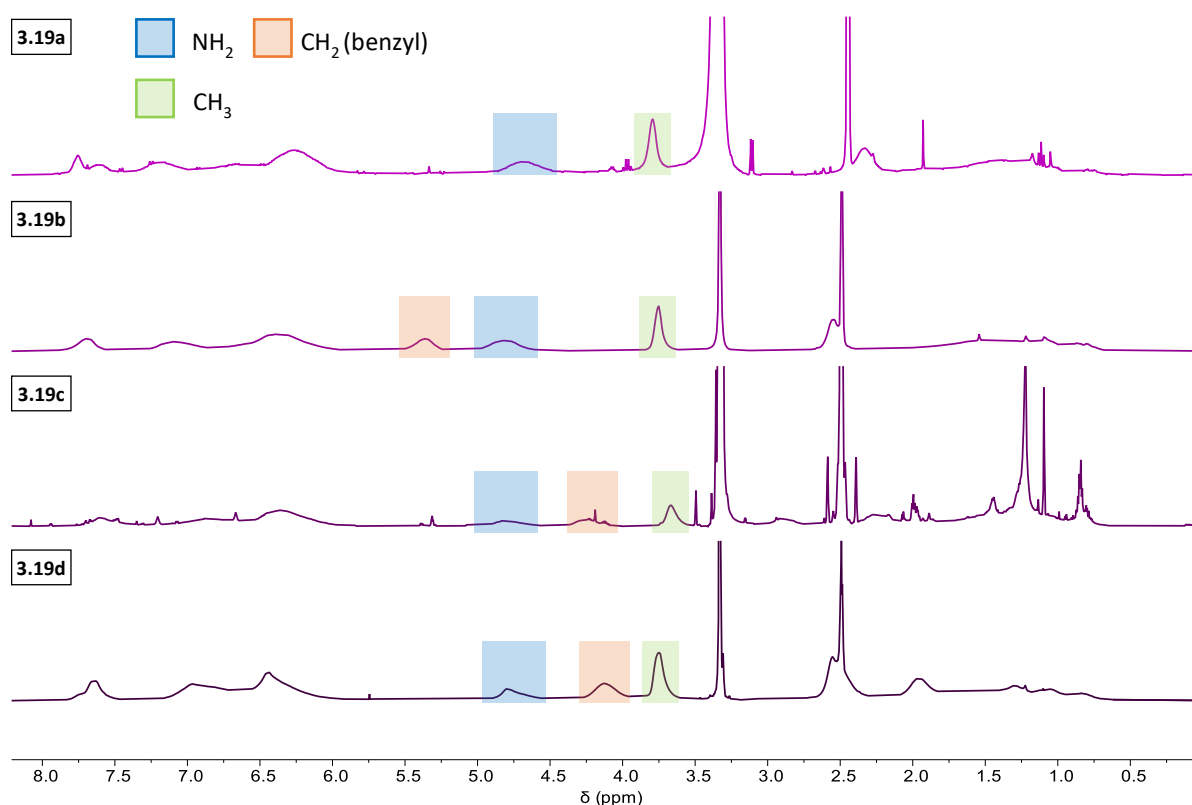
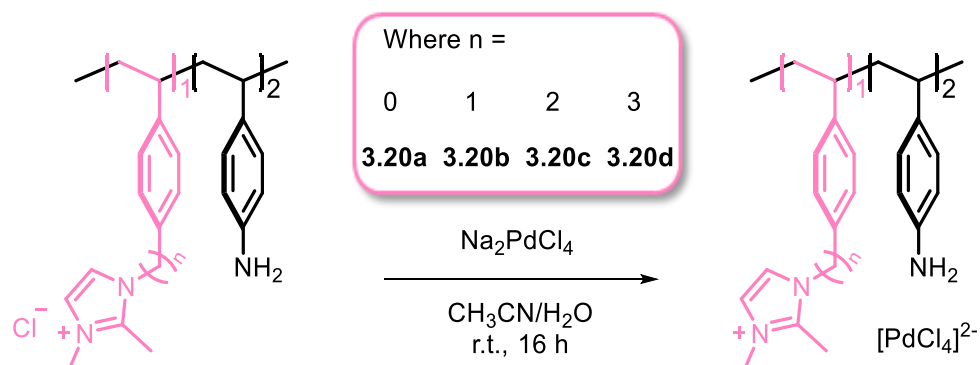


Figure 3.1 ^1H NMR spectra of polymers **3.19a-d** (400 MHz, DMSO-d_6).

than its counterparts and precipitation was evident after 1 hour. On the other hand, the formation of polymer **3.19d** was much slower, where even after stirring for 6 days residual amounts of monomer persisted in solution, as such, purification using dialysis tubing was required. ^1H NMR spectra of the isolated polymers show typical broad signals, though with a notable shift upfield of the benzylic protons from δ 5.38 ppm in **3.19b** to δ 4.26 and 4.13 ppm for **3.19c** and **3.19d**, respectively. As the described spectra were collected in solutions of DMSO-d_6 , clear signals for the aniline NH_2 protons can be seen at δ 4.82-4.74 ppm, consistent with a strong N-H bend at $1515\text{-}1507\text{ cm}^{-1}$ in the corresponding FT-IR spectra (**Appendix A.3.5**). By comparing the integrals of the total aromatic region and those of the imidazolium CH_3 we can estimate the IL/amine monomer incorporation to be 1 : 2.1, 1 : 1.7, 1 : 2.8, and 1 : 1.4 for **3.19a-d** respectively. These values show notable disparity from the intended 1 : 2 monomer ratio, particularly for polymers **3.19c** and **3.19d**.

The preparation of $[\text{PdCl}_4]^{2-}$ loaded catalyst precursors was conducted as previously described, whereby an aqueous solution of Na_2PdCl_4 , prepared from heating PdCl_2 with an excess of NaCl , was added dropwise to a stirring solution of polymer. While the Doherty-type PIILs typically dissolve readily in ethanol, polymers **3.19a**, **3.19c**, and **3.19d** all showed poor solubility in alcohols; after screening a range of solvents, acetonitrile/water mixtures (20 vol%



Scheme 3.9 Preparation of PdCl₄-loaded PIILs **3.20a-d**.

water) were found to dissolve the polymers well. Note that acetonitrile readily coordinates to [PdCl₄]²⁻ to form PdCl₂(CH₃CN)₂ which may influence the reactivity/reducibility of pre-catalysts **3.20a**, **3.20c**, and **3.20d**.

Morphologically, both the polymers and the precatalysts were reminiscent of those described in **Chapter 2** when analysed by SEM. Both polymer and precatalyst appeared irregular in structure across the series, though the materials did become more granular following metal impregnation. There was some disparity in particle sizes across the series, whereby polymer **3.19b** was comprised of small clusters of particles < 1 μm in size, whereas **3.19a**, in particular, consisted predominantly of very large particles 50-100 μm in size (**Figure 3.2**). Although SEM images do not reflect polymer morphology nor dynamics in the solution-state, precatalyst **3.20a** appears to maintain many of these larger particles, which may suggest that Pd is not

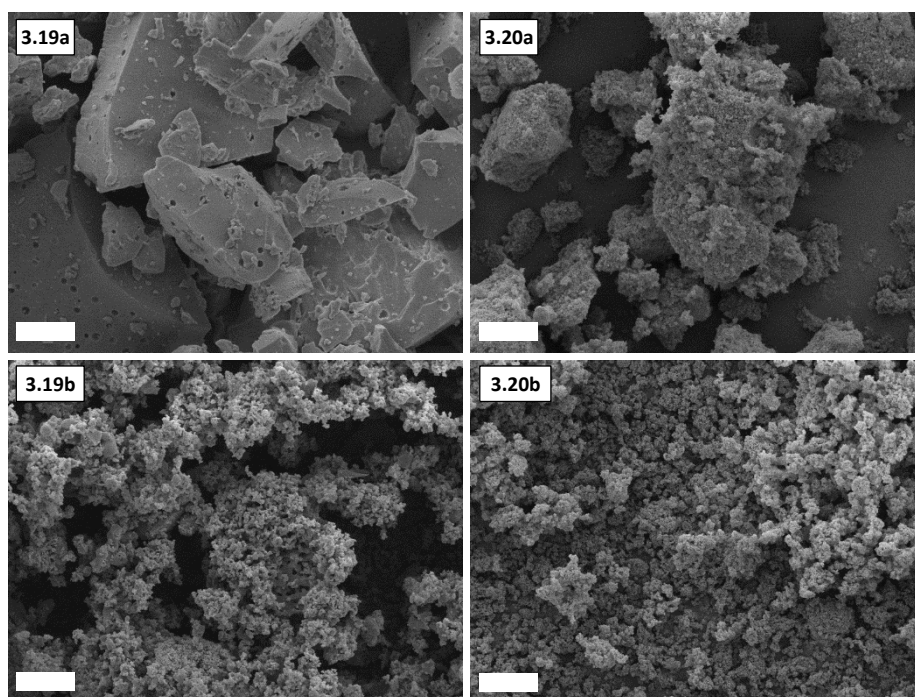


Figure 3.2 SEM images of polymers **3.19a-b** and precatalysts **3.20a-b**; white scale bar is 20 μm.

well dispersed through the material following impregnation. SEM images of the remaining polymers and precatalysts can be found in **Appendix A.3.7**.

3.4 Thermal Hydrogenation of CO₂

As described in Chapter 2, to maintain consistency, initial TOFs are again expressed as $\text{mol}_{\text{formate}} \cdot \text{mol}_{\text{Pd}}^{-1} \cdot \text{h}^{-1}$ but abbreviated to h^{-1} . Using the preliminary reaction conditions identified in **Chapter 2** as an initial guide, the activity and stability of PdCl₄@C_nPIIL pre-catalysts were assessed for the thermal hydrogenation of CO₂. Interestingly, an activity-time profile for formate formation shows that the **3.19a**, **3.19c** and **3.19d** supported catalysts were far less active than their **3.19b** supported counterpart over a period of 14 hours. The catalyst generated from PdCl₄@C₁PIIL (**3.20b**) was by far the most active, with an initial TOF of 346 h^{-1} measured after 2 hours. For reference, the same catalyst generated in the presence of 5 mol% cross-linker (**2.8b.66**) was notably more active, achieving a TOF of 500 h^{-1} over the same time. In comparison, C₀PIIL, C₂PIIL and C₃PIIL supported pre-catalysts initially showed very similar activities to each other with TOFs of 132 h^{-1} , 138 h^{-1} , and 125 h^{-1} respectively. In fact, the initial activities of these three catalysts were nearly identical for the first 4 hours; however, after 8 hours there was more disparity between the catalysts with the overall activity following the order **3.20b** >> **3.20a** > **3.20c** > **3.20d**. Despite the difference in activity between catalyst generated from PdCl₄@C₁PIIL and those generated from **3.20a** and **3.20c-d**, there does not appear to be an induction period for the latter, instead the activity begins to

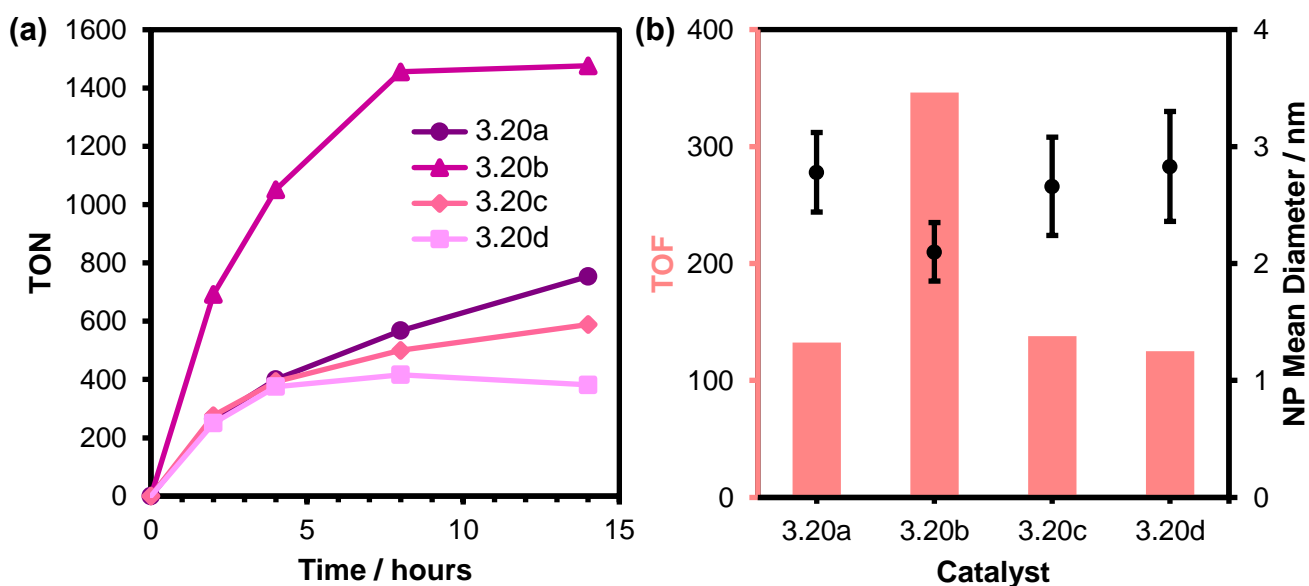


Figure 3.3 (a) Activity-time profile for the hydrogenation of CO₂ to formate catalysed by materials generated from precatalysts **3.20a-d** and (b) a comparison of TOF and NP size after 2 hours of catalysis. Reaction conditions: PdCl₄-loaded amine polymer (6 μmol), 1:1 H₂/CO₂ (40 bar), 100 °C, K₂CO_{3(aq)} (20 mL, 0.65 M).

plateau earlier than for **3.20b**, though more severely for PdCl₄@C₃PIIL. The efficacy of the most active catalyst, derived from **3.20b**, also plateaus, albeit after 8 hours, with a maximum TON of 1456; the activity profile of the C₁ supported catalyst closely resembles that of its lightly cross-linked counterpart, PdCl₄@66NH₂PIIL (**2.8b.66**), however, the cross-linked catalyst showed greater conversion to potassium formate over the same time period, beginning to plateau after 8 hours with a TON of 1573.

Following 2 hours of catalysis, solid black powders were isolated by centrifugation and analysed by TEM. Nanoparticles generated from precatalysts **3.20a**, **3.20c** and **3.20d** were found to have similar average diameters from 2.66-2.83 nm, and were generally monodisperse. Nanoparticles generated from precatalyst **3.20b**, on the other hand, were slightly smaller with an average diameter of 2.10 nm (**Figure 3.3b**). Although the smaller NP size coincides with the high activity of precatalyst **3.20b**, it is difficult to draw a correlation between NP size and activity when the remaining catalysts were all so similar in both NP size and activity.

3.5 Stability of New Polymer Immobilized Ionic Liquid Supports

As described in **Chapter 2**, post-mortem analysis of the catalysts by XPS showed that the benzylic imidazolium groups of the support were cleaved during catalysis, as evidence by a reduction in the imidazolium N 1s peak. Thus, once more, the N 1s region of the polymers, pre-catalysts and recovered metal NPs were compared for the C_n functionalised materials (**Figure 3.4**). For polymers **3.19a-d**, two distinct peaks were observed at 397.0 ± 0.1 eV and 394.6 ± 0.1 eV attributed to the imidazolium and aniline groups, respectively. These binding energies are in good agreement with those of the amine-modified PIIL series described in **Chapter 2**. The distance from the styrene ring (*i.e.* length of the *N*-alkyl spacer) appeared to have a negligible influence on the N 1s imidazolium binding energies ($\Delta BE_{N-C} = 117.0 \pm 0.1$ eV). As previously described, there was little to no influence on the imidazolium BEs following impregnation with [PdCl₄]²⁻ ($\Delta BE_{N-C} = 117.0 \pm 0.0$ eV); however, signal broadening between the two peaks was indicative of a third N signal at 395.6 ± 0.1 eV that was once again attributed to a Pd-N interaction. One will notice that there is some disparity between the relative intensities of imidazolium and aniline nitrogen regions (**Table 3.1**); while one would expect a 1 : 1 ratio of imidazolium : amine nitrogen atoms based on the theoretical monomer loading shown in **Scheme 3.8**, this is not always observed for the polymers and precatalysts analysed. This can be explained by the nature of the random polymerisation of monomers in the

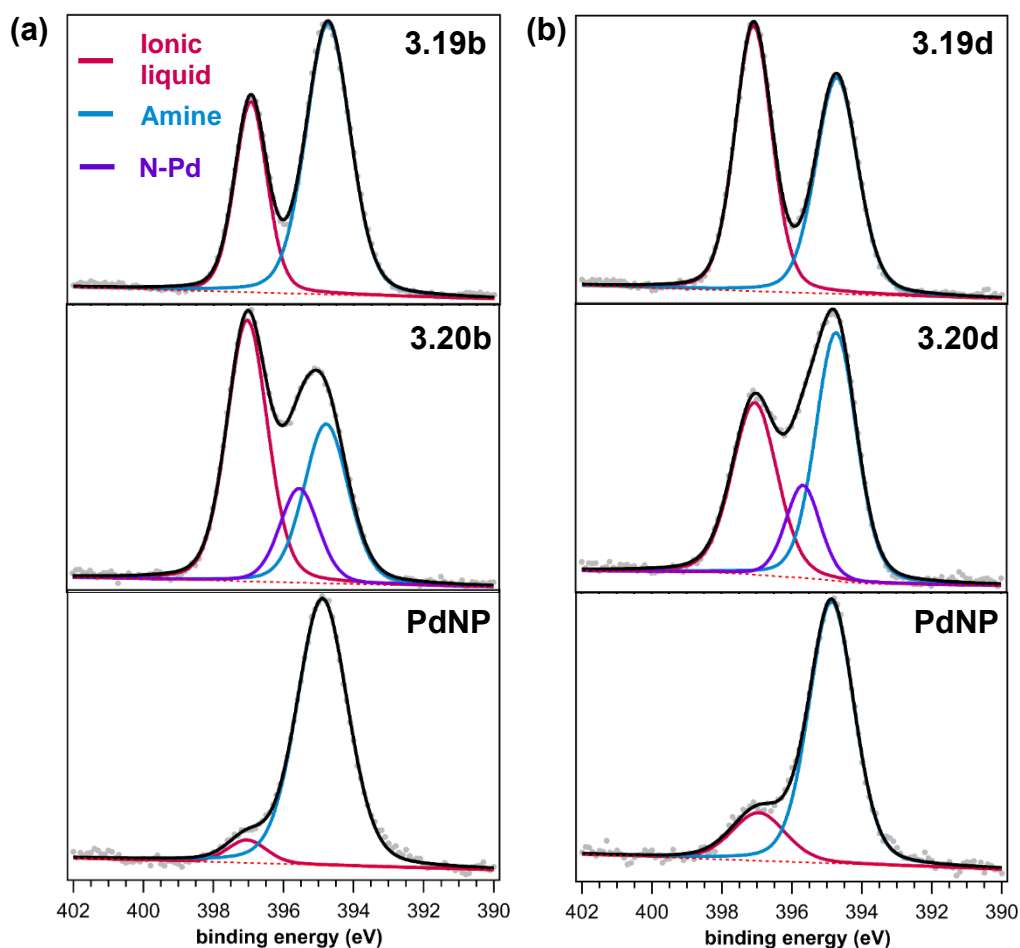


Figure 3.4 N1s core levels of polymer, precatalyst and catalyst isolated after 2 hours of hydrogenation for (a) **C₁** and (b) **C₃** functionalised materials. Black line = overall fitting; Red dotted line = background.

preparation of these materials. Clearly, there are areas of discrete functionality where we do not observe clean 1 : 2 ratios of IL/amine monomers (1 : 1 in at.% N, as there are two IL nitrogens for every one amine nitrogen). However, across the bulk we know from the ^1H NMR spectra of the as-prepared polymers that the ratio of IL/amine monomers is approximately 1 : 2 (± 0.5) in each material.

As expected, following hydrogenation the relative amount of imidazolium nitrogen to amine nitrogen dropped significantly for **C₁PIIL**-supported precatalyst, whereby 94% of ionic liquid units were lost after 2 hours of catalysis – the relative amounts of N atoms as determined by XPS are provided in **Table 3.1**. Fortuitously, both of the strategies for improving IL retention (removal of the benzylic position and extension of the alkyl chain) appeared to be effective in reducing the loss of the imidazolium fragment. Of the four supported precatalysts, $\text{PdCl}_4@\text{C}_1\text{PIIL}$ lost the most IL, followed by **3.20a** with a loss of 78% of imidazolium species, then **3.20c** with 70%, while **C₃PIIL** appeared to be the most stable support as only 63% of the IL units appeared to be cleaved during hydrogenation. Care should be taken in this analysis –

Table 3.1 Loss of imidazolium N as determined by analysis of N 1s XP spectra after 2 hours of catalysis.

Sample	Relative Amount of Nitrogen Species / at. %			% Imidazolium N Remaining ^a
	<i>IL</i>	<i>Aniline</i>	<i>N-Pd</i>	
C ₀ PIIL	50	50	-	
PdCl ₄ @C ₀ PIIL	53	36	12	
PdNP@C ₀ PIIL	20	80	-	22
C ₁ PIIL	34	66	-	
PdCl ₄ @C ₁ PIIL	50	33	17	
PdNP@C ₁ PIIL	6	94	-	6
C ₂ PIIL	37	63	-	
PdCl ₄ @C ₂ PIIL	47	36	17	
PdNP@C ₂ PIIL	21	79	-	30
C ₃ PIIL	52	48	-	
PdCl ₄ @C ₃ PIIL	37	48	15	
PdNP@C ₃ PIIL	18	82	-	37

^aAmount of remaining imidazolium normalized under the assumption that no amine is lost after catalysis.

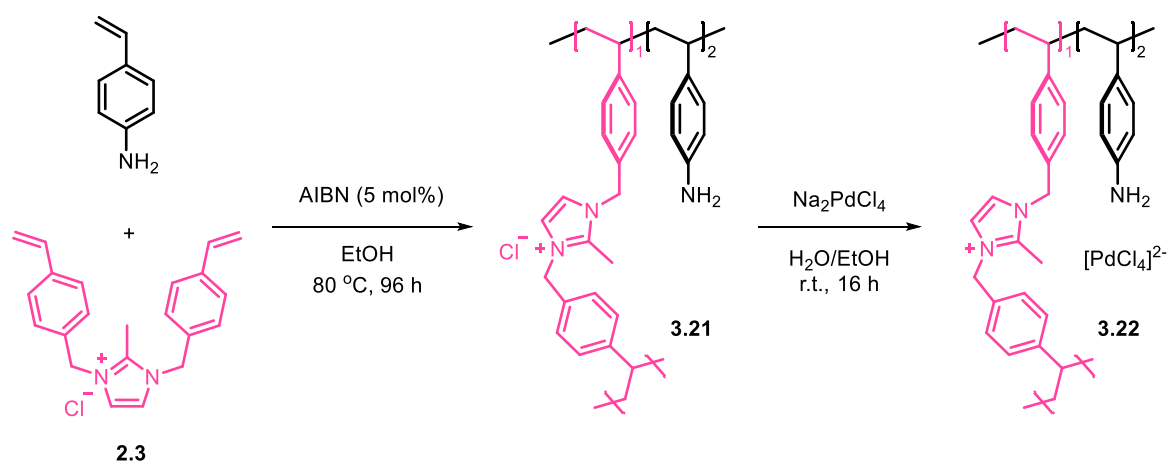
as mentioned earlier, the proportion of IL : amine monomers is not uniform across the samples. In this assessment, the loss of IL is measured against the PdCl₄-loaded polymers as a reference; however, for PdCl₄@C₃PIIL the IL loading is notably lower than that of the parent polymer (37 at.% vs. 52 at.%). If the same assessment is made using the polymer as reference, then the IL loss increases from 63% to 80%. Nonetheless, this is still lower than the 93% loss of imidazolium observed for C₁PIIL, therefore, this approach improves polymer stability under the conditions of catalysis.

However, it was surprising to observe the loss in intensity of the imidazolium N 1s peak for the new polymer supports – the lack of benzylic position in C₀PIIL and the distance between the imidazolium nitrogen and the phenyl ring in C₂PIIL and C₃PIIL should make the cleavage very difficult. While the apparent drop in intensity of the imidazolium peak is undeniable, this could instead be a consequence of the amine N 1s peak increasing relative to the imidazolium core electrons. The hydrogenation of imidazoles and imidazoliums to the corresponding imidazolidines was previously considered to be difficult, and indeed requires the use of a precious metal catalyst;²¹ however, there are several recent reports of the hydrogenation of cationic and anionic imidazole derivatives under mild conditions. For example, *N,N'*-

diphenylimidazolium was hydrogenated at 10 bar in the presence of trimethylamine and a homogeneous Fe catalyst to afford the corresponding imidazolidine at room temperature.²² Similarly, an imidazole-based carbene (imidazolylidene) ligand, that formed part of a larger pincer ligated Ir complex, was found to hydrogenate at a hydrogen pressure of 2 bar after prolonged reaction time in the presence of base.²³ On the other hand, nitrile functionalised ionic liquids were used as solvent for RuNP catalysed CO₂ hydrogenation and no hydrogenation products of the imidazolium ring were detected,²⁴ nor was any change detected following 5 hydrogenations of IL 1-(*N,N*-dimethylaminoethyl)-2,3-dimethylimidazolium trifluoromethanesulfonate under 30 bar of H₂ (though one should note that the authors were not investigating the hydrogenation of the ILs).²⁵ To this end, the use of imidazolium-based ILs to support precious metal catalysts for hydrogenation reactions is extensively reported in the literature, though there is seldom any mention of unexpected hydrogenation of the imidazolium ring.

3.6 A Highly Cross-Linked PIIL Support

While the apparent stability of the C₁PIIL support was shown to be inferior to its C₀, C₂ and C₃ counterparts, catalyst formed from PdCl₄@C₁PIIL was by far the most active in the series. Therefore, in the interest of achieving high catalyst activity without sacrificing stability, an alternative approach was investigated utilizing the benzylic C₁PIIL motif. Although PdCl₄@C₁PIIL appeared to retain only 6 at.% of its initial imidazolium groups after catalysis, over the same time period, PdCl₄@66NH₂PIIL (**2.8b.66**) appeared to retain 21% of its imidazolium group, suggesting that the 5 mol% cross-linker in PdCl₄@66NH₂PIIL has a significant beneficial effect on catalyst stability.



Scheme 3.10 Preparation of amine decorated cross-linked PIIL support **3.21**, via a radical initiated polymerisation.

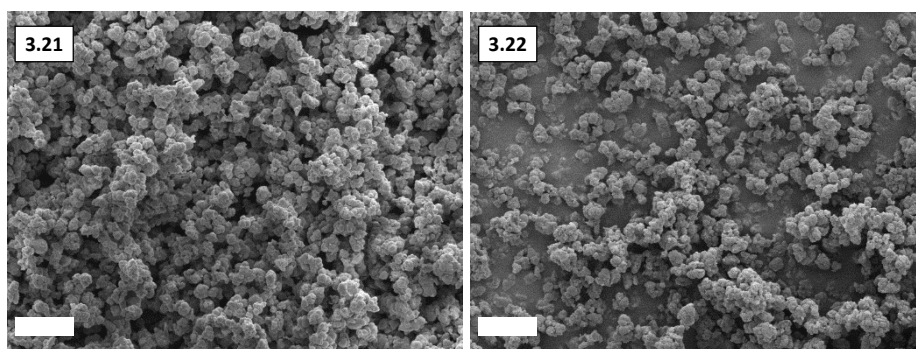


Figure 3.5 SEM images of polymer **3.21** and precatalyst **3.22**; white scale bar is 20 μm .

Encouraged by this, a highly cross-linked aniline functionalised PIIL was targeted whereby the only IL unit incorporated was the benzylic cross-linker, **2.3**. Continuing with an amine : IL ratio of 2 : 1, cross-linked polymer denoted CL₁PIIL was obtained as an off-white solid (**3.21**) in 85% yield following a typical AIBN radical-initiated procedure as described previously (**Scheme 3.10**). Likely due to the high degree of cross-linking, polymer **3.21** proved to be insoluble, however, the CP-MAS ¹³C NMR spectrum of the polymer was typical of the series, with the characteristic imidazolium peak at 145 ppm, the benzyl peak at 52 ppm and the imidazolium methyl at 39 ppm. FT-IR confirmed incorporation of the amine with an N-H stretch at 1515 cm⁻¹, consistent with the aniline decorated polymers described above. Morphologically, polymer **3.21** appeared quite different to the remaining polymers described in this thesis. Typically, SEM images of our polymers and precatalysts reveal them to be irregular and granular, where larger particles appear to form plate-like structures. In contrast, polymer **3.21** appears to form regular spheres ranging from approximately 3.5-2.5 μm in diameter, almost reminiscent of the structure of polystyrene. This regular ordered morphology is no doubt a result of the high degree of cross-linking. The subsequent impregnation of polymer **3.21** with aqueous Na₂PdCl₄ led to the formation of an orange precipitate which was isolated by filtration and washed with further portions of water and ethanol to afford precatalyst PdCl₄@CL₁PIIL (**3.22**) as a yellow solid. The regular morphology of **3.21** was for the most part maintained following impregnation with Na₂PdCl₄.

Fortuitously, a typical hydrogenation of CO₂ in the presence of K₂CO₃ led to an initial TOF of 518 h⁻¹ when the mixture was charged with precatalyst PdCl₄@CL₁PIIL (6 μmol Pd). This is slightly higher than the TOF of 500 h⁻¹ obtained for PdCl₄@66NH₂PIIL (**2.8b.66**) over the same time period and notably higher than the TOF of 346 h⁻¹ obtained for the catalyst generated from uncross-linked PdCl₄@C₁PIIL (**Figure 3.6a**). Nanoparticles analysed by TEM after catalysis were found to be 2.92 \pm 0.54 nm in diameter, which is larger than the average size of 2.10 \pm

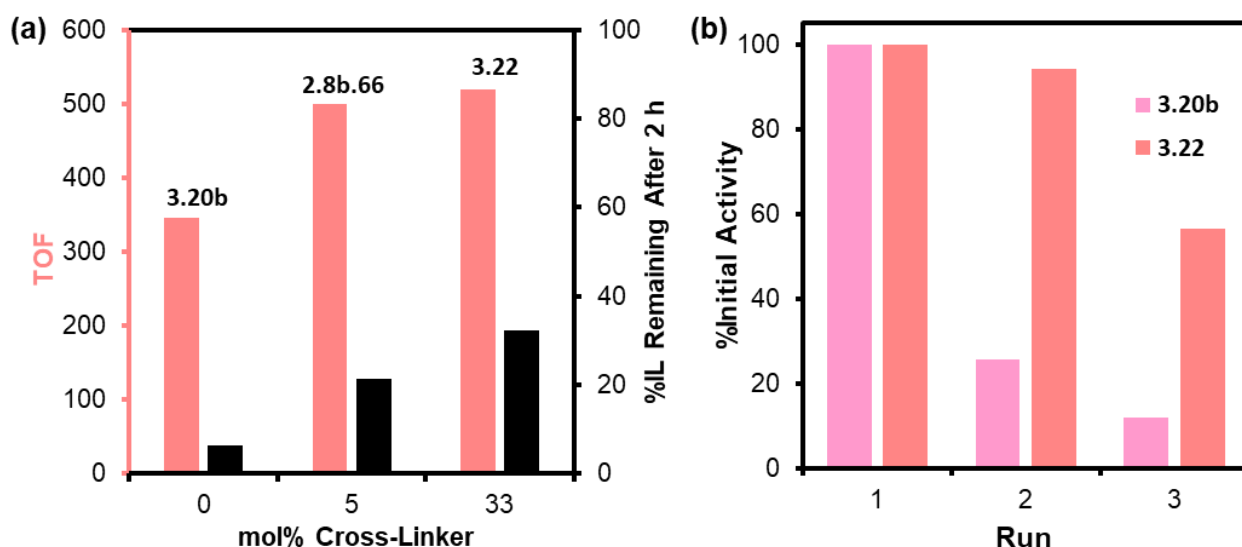


Figure 3.6 (a) Comparison of initial TOF and catalyst stability (IL remaining as determined by XPS) against mol% cross-linker incorporated into the polymer support for PdCl₄-loaded precatalysts. Initial TOFs were measured after 2 hours of catalysis. (b) Recycling study comparing catalysts generated from PdCl₄@C₁PIIL (**3.20b**) and PdCl₄@CL₁PIIL (**3.22**) as a function of the %initial activity per run of the catalyst. Activity was measured over 14 hours using 17 μ mol palladium dispersed in an aqueous solution of K₂CO₃ (20 mL, 0.65 M).

0.25 nm measured for the corresponding uncross-linked catalyst generated from **3.20b**, though it is comparative to NP generated from **2.8b.66** sized at 2.84 ± 0.75 nm.

Analysis of the catalyst surface by XPS following hydrogenation also revealed an enhancement in stability; while PdCl₄-supported on linear polymer **3.19b** was found to lose 94% of its IL groups after only 2 hours of catalysis, the catalyst generated from **3.22** was found to lose only 68% of its IL units over the same time. This is a significant enhancement of stability when one considers that precatalyst **3.22** still contains the vulnerable benzylic bridges. For comparison, C₂-supported precatalyst **3.20c** saw a 70% reduction of the imidazolium N after catalysis, though catalyst generated from C₃-supported **3.20d** was apparently more stable than even the cross-linked catalyst as it only showed a 63% reduction in the imidazolium nitrogen.

A comparison of the performance of catalysts generated from **3.20b** and **3.22** as a function of the recycle number was undertaken to assess the relative stability and activity (**Figure 3.6b**). Recycle experiments were conducted with 17 μ mol of palladium rather than 6 μ mol to limit catalyst lost during isolation and washing. The catalyst generated from PdCl₄@C₁PIIL (**3.20b**) after 14 hours showed poor activity following its initial use, similar to that of lightly cross-linked **2.8b.66**, whereby the resulting catalyst lost 74% of its activity after the initial run, and 88 % in the third run. In contrast, catalyst generated from PdCl₄@CL₁PIIL (**3.22**) maintained 94% of its activity in the first recycle although this dropped to 56% of the initial activity in the

third run, demonstrating that the high degree of cross-linking led to a significant improvement in the recyclability of the catalyst. TEM images of the catalysts isolated after three 14 hour reactions revealed a stark difference; nanoparticles generated from **3.20b** were found to have an average diameter of 2.32 ± 0.41 nm after 3 uses, similar to the diameter of 2.10 ± 0.25 nm measured after 2 hours of catalysis, whereas nanoparticles generated from **3.22** had a diameter of 4.04 ± 0.62 nm, compared with 2.92 ± 0.54 nm after a 2h reaction, which suggests that the NPs had undergone aggregation or sintering. However, the disparate performance of catalysts generated from **3.20b** and **3.22** indicates that NP aggregation and NP size do not rationalise their differences in activity towards CO₂ hydrogenation; NP aggregation may play a role in catalyst deactivation, though it is clearly not the leading cause of catalyst passivation for these systems.

3.7 The Iodide Problem

In spite of the salt metathesis reactions described in section **3.2.2** to substitute IL monomer (**3.3**, **3.16**, **3.17**) counterions from iodide to chloride, XPS spectra of the corresponding polymers **3.19a**, **3.19c**, and **3.19d** suggested that there was no chloride present in the resulting polymers and instead only iodide was present as the PIIL anion. Moreover, even following impregnation with Na₂PdCl₄, significant amounts of iodide remained in the sample. For the PdCl₄-loaded polymers, iodide comprised 42, 33 and 67 at.% of the halide composition for **3.20a**, **3.20c**, and **3.20d**, respectively, the remaining halide being chloride. Analysis of the Pd 3d core electrons indicated that some of the iodide may have complexed with palladium to

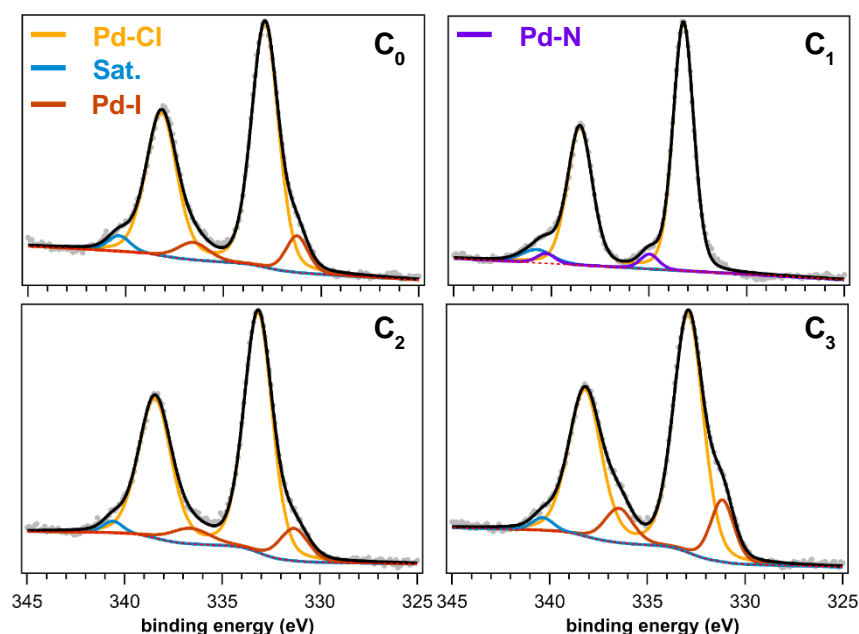


Figure 3.7 Pd 3d core level XPS region for precatalysts **3.20a-d**. Black line = overall fitting; Red dotted line = background.

presumably make a mixed halide salt of the form $[\text{PdCl}_x\text{I}_y]^{2-}$ (**Figure 3.7**), rather than undergoing an anion substitution as expected. A doublet attributed to Pd-Cl can be observed with a $3d_{5/2}$ peak at 333.2-332.9 eV ($\Delta\text{BE}_{\text{Pd-Cl}}$ of 53.0 ± 0.1 eV, consistent with 53.1 ± 0.2 eV in **Chapter 2**), with an apparent Pd-N doublet at 340.3 and 335.0 eV for **3.20b**; interestingly, such a Pd-N environment was only apparent for the C_1PIIL -supported precatalyst. This suggests that coordination of aniline to the palladium salt could be contingent on the arrangement in space of the imidazolium-tetrachloropalladate couple. Moreover, an additional doublet, assigned to Pd-I, with a $3d_{5/2}$ signal at 331.3-331.2 eV appears in the spectra of C_0 , C_2 and C_3PIIL supported Pd salts. A BE separation of 1.7 eV between this peak and that of the Pd-Cl core electrons is consistent with the 1.8 eV separation between K_2PdCl_4 and PdI_2 as reported by Jones *et al.*²⁶ To the best of our knowledge, there are no examples of the XPS analysis of any $[\text{PdI}_4]^{2-}$ salt reported in the literature. The presence of iodide coordinated palladium in these samples is not an unreasonable proposition – following hard-soft acid-base theory, one would expect Pd to coordinate strongly to a soft ligand such as iodide, rather than chloride which is comparatively ‘harder’.²⁷ In a similar fashion, impregnation of PEG-functionalised PIIL with K_2PtCl_4 did not lead to full exchange of the PIIL bromide anion with $[\text{PtCl}_4]^{2-}$; instead, notable amounts of bromide were found in the precatalyst and the reduced NP materials, with some of the bromide found to be coordinated with Pt in the precatalyst.²⁸

XPS spectra of nanoparticle materials isolated after 2 hours of catalysis were fitted with two Pd 3d components, with $3d_{5/2}$ peaks at 330.7 ± 0.3 eV and 333.1 ± 0.3 eV, as shown in **Figure 3.8**. The first peak corresponds to reduced Pd, while the latter has been ambiguously assigned to Pd^{2+} due to the difficulty in distinguishing between unreduced Pd-Cl and Pd-I species in these spectra. A significant difference in the $\text{Pd}^0 : \text{Pd}^{2+}$ ratios was observed; for iodide containing materials $\text{PdCl}_4@\text{C}_0\text{PIIL}$, $\text{PdCl}_4@\text{C}_2\text{PIIL}$ and $\text{PdCl}_4@\text{C}_3\text{PIIL}$, the mixture was predominantly comprised of Pd^0 with a small amount of Pd^{2+} remaining. The Pd^{2+} species is assigned to halide complexed Pd, rather than palladium oxide as the BE separation between this peak and metallic Pd is too large (see **Section 2.4** for a detailed discussion of assignments). This was most prominent for $\text{PdCl}_4@\text{C}_3\text{PIIL}$ where 95 at.% of Pd^{2+} species were reduced to Pd^0 . On the other hand, the material isolated following the *in-situ* reduction of $\text{PdCl}_4@\text{C}_1\text{PIIL}$

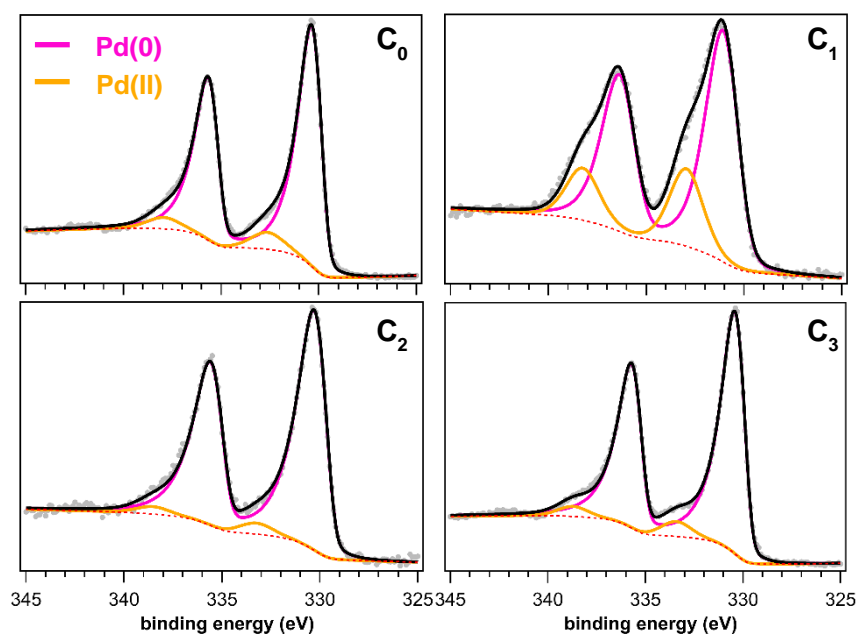


Figure 3.8 Pd 3d core level XPS region for nanoparticles generated from precatalysts **3.20a-d** following 2 hours of hydrogenation. Black line = overall fitting; Red dotted line = background.

showed a significant portion of Pd^{2+} remaining after catalysis, with a $\text{Pd}^0 : \text{Pd}^{2+}$ ratio of 3 : 1. Reports of mixing Na_2PdCl_4 with NaI have shown that the resulting palladium species undergo a much more facile reduction to nanoparticles when compared to the corresponding palladium chloride salts;²⁹ one should note that this observation in the aforementioned report is based on qualitative analysis of TEM images and therefore not a true assessment of the degree of reduction. This raises the question of what the active species is during the catalytic transformation of CO_2 to formate, as catalyst generated from $\text{PdCl}_4@\text{C}_1\text{PIIL}$ was far more active than its counterparts. Typically, reports describe the hydrogenation of CO_2 to be catalysed over a PdNP surface;³⁰ here the catalyst containing the least amount of Pd^0 is the most active, and that is without determining TOF based on the surface accessible palladium. Following this trend, $\text{PdCl}_4@\text{CL}_1\text{PIIL}$, which is more efficient than $\text{PdCl}_4@\text{C}_1\text{PIIL}$, contained 41 at.% unreduced Pd^{2+} post-catalysis supporting the hypothesis that Pd^{2+} may play an active role during catalysis.

To further investigate the effect of iodide, or more specifically palladium iodide, cross-linked polymer **3.21** was impregnated with Na_2PdI_4 which was prepared from the reaction of PdI_2 and NaI.³¹ A CO_2 hydrogenation reaction conducted with 6 μmol of $\text{PdI}_4@\text{CL}_1\text{PIIL}$ conducted under the optimum conditions described above gave poor conversion to formate, with a TOF of 74 h^{-1} obtained after 2 hours; this is markedly lower than the TOF of 518 h^{-1} obtained with the corresponding PdCl_4 -loaded precatalyst. Analysis of the $[\text{PdI}_4]^{2-}$ -loaded precatalyst by XPS

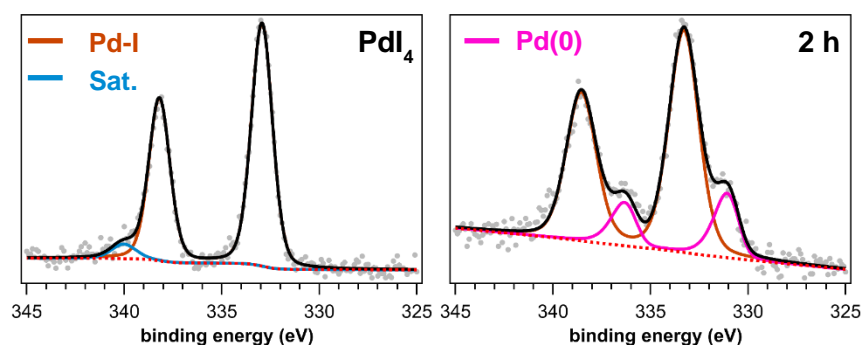
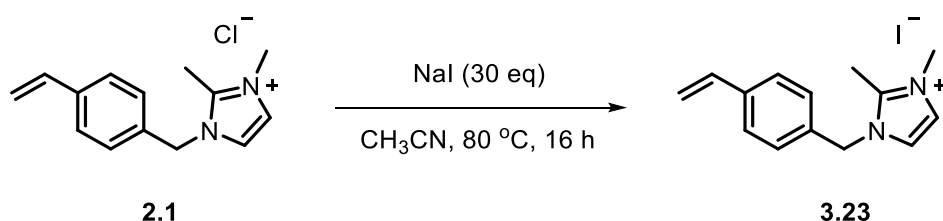


Figure 3.9 Pd 3d core level XPS region of **3.21**-supported PdI_4 (left) and the same precatalyst isolated after 2 hours of catalysis. Black line = overall fitting; Red dotted line = background.

revealed a single Pd region at 332.9 eV ($3d_{5/2}$), shifted towards higher BE when compared to precatalysts **3.20a**, **3.20c** and **3.20d**, indicative that the latter are comprised of mixed halide species. However, following catalysis, very little Pd^0 was observed (**Figure 3.9**) in stark contrast to materials generated from the hydrogenation of iodide containing **3.20a**, **3.20c** and **3.20d**. Here, only 20 at.% Pd was reduced to Pd^0 as opposed to 59 at.% for the corresponding PdCl_4 -loaded precatalyst **3.22** and an average of 93 at.% for the iodide contaminated C_0 , C_2 and C_3 -based precatalysts. This suggests that $[\text{PdI}_4]^{2-}$ is notably less reducible than $[\text{PdCl}_4]^{2-}$, albeit the catalyst generated from $[\text{PdI}_4]^{2-}$ is also notably less active. Thus, the high amount of Pd^0 following the hydrogenation of **3.20a**, **3.20c** and **3.20d** is left unexplained. During the initial Na_2PdCl_4 impregnation, polymers **3.19a**, **3.19c**, and **3.20d** were dissolved with the aid of acetonitrile which was not the case for polymer **3.19b**; although acetonitrile ligands readily bind to divalent Pd, Song and co-workers found that the NaBH_4 -mediated reduction of $\text{PdCl}_4@\text{PIIL}$ conducted in acetonitrile lead to an even distribution of Pd^{2+} and Pd^0 species.³⁰ Clearly, more experiments on the reduction of $[\text{PdX}_4]^{2-}$ loaded PIILs will need to be conducted to develop a full understanding of the reduction mechanism of Pd under our conditions of catalysis.

Knowing that the presence of iodide has a negative influence on the catalytic activity of Pd salts reduced *in-situ*, the comparison between precatalysts **3.20a-d** becomes less meaningful as precatalyst **3.20b** was generated in the absence of any iodide, while **3.20a**, **3.20c** and **3.20d** all contained iodide. The anion of monomer **2.1** was thus exchanged using an excess of sodium iodide, with the intention of generating a PdCl_4 -loaded polymer that would more closely correspond to precatalysts **3.20a**, **3.20c** and **3.20d** and thus enable a more meaningful comparison of the catalyst performance. In this case, the conversion of chloride to iodide should be more favourable than the inverse as sodium chloride has poor solubility in

acetonitrile (0.3 mg / 100 g solvent);³² the precipitation of NaCl from solution should therefore drive the reaction. After stirring overnight, ¹H NMR spectroscopy showed that the imidazolium protons shifted from δ 7.66 and 7.61 ppm to δ 7.39 and 7.26 ppm while the benzylic protons shifted 0.12 ppm upfield to δ 5.41 ppm, indicative of complete anion exchange. The solution was then filtered, the volatiles removed under vacuum, and the residue taken up in dichloromethane resulting in precipitation of a white solid which was removed by filtration through a syringe filter. ESI-MS of the isolated product (**3.23**) confirmed full exchange of chloride to iodide. Unfortunately, preparation of the corresponding polymer and precatalyst was not successfully completed in time for the submission of this thesis; however, this experiment will be essential for understanding the influence of the alkyl chain length on the Pd catalysed hydrogenation of CO₂ to formate.



Scheme 3.11 Anion exchange of monomer **2.1** to form 2,3-dimethyl-1-(4-vinylbenzyl)-imidazolium iodide.

3.8 Reaction Mechanism

3.8.1 *In-situ* DRIFTS Experiments

In an effort to investigate the CO₂ hydrogenation reaction mechanism at the Pd-polymer interface a sample of PdNP@CL₁PIIL was generated by reduction of PdCl₄@CL₁PIIL (**3.22**) and its surface chemistry in the presence of CO₂, H₂ and H₂O was probed using *in-situ* DRIFTS. Assignment of the generated surface species in these studies is challenging as their vibrations overlap considerably; despite exhaustive literature reports of CO₂ binding to various materials, the chemical environments of these materials vary drastically. For example, there are ample examples of DRIFTS studies for metal oxide supported precious metal catalysts, however, the oxide support is often basic and promotes the formation of bicarbonate species that can exist solely on the metal oxide support, or in a bridging formation across the support and the metal NP.³³ Alternatively, studies interested in the CO₂ capture potential of amine decorated silica are useful as silica is relatively inert, thus, interaction of CO₂ and CO₂-derived species with the silica support is weak (these studies often do not acknowledge the existence of carbonates or even refute their existence);³⁴ however, these studies typically do not include the incorporation of metal NPs, and therefore can be limited in their use as

coordination to the NP surface has a significant impact on the absorption peak. Chemically, the available literature is therefore quite different to the polymer supported metal NP systems investigated here. Although there has been an attempt to deconvolute the species in the following spectra, the assignments should be treated with caution, as the interpretation may be ambiguous.

First, precatalyst $\text{PdCl}_4@\text{CL}_1\text{PIIL}$ (**3.22**) was reduced by stirring an aqueous solution at 100 °C under 20 bar of H_2 for 2 hours to mimic the catalyst material that is generated *in-situ* under standard conditions. This material was isolated by centrifugation and dried in a vacuum oven overnight. Before exposure to the reactive gas feed, samples were heated to 100 °C and purged with argon gas to remove any surface Pd-H species formed during the hydrogenation of the PdCl_4 salt. DRIFTS experiments using the resulting $\text{PdNP}@\text{CL}_1\text{PIIL}$ were all conducted at 100 °C and the gas mix was diluted with helium unless otherwise stated.

Initial experiments in the absence of H_2 demonstrated that water plays a key role in CO_2 binding at the catalyst surface. CO_2 is well known to bind poorly to the platinum group metals,³⁵ and in the absence of water there was little evidence of CO_2 binding even to surface amine groups (**Figure 3.10**). On introduction of H_2O to the gas feed there was immediate binding of several species at the catalyst surface, and these species continued to grow over 30 minutes, after which time the surface appeared to be close to saturation. The major band between 1650-1630 cm^{-1} corresponds to the bending mode of water.³⁶ Within the first minute

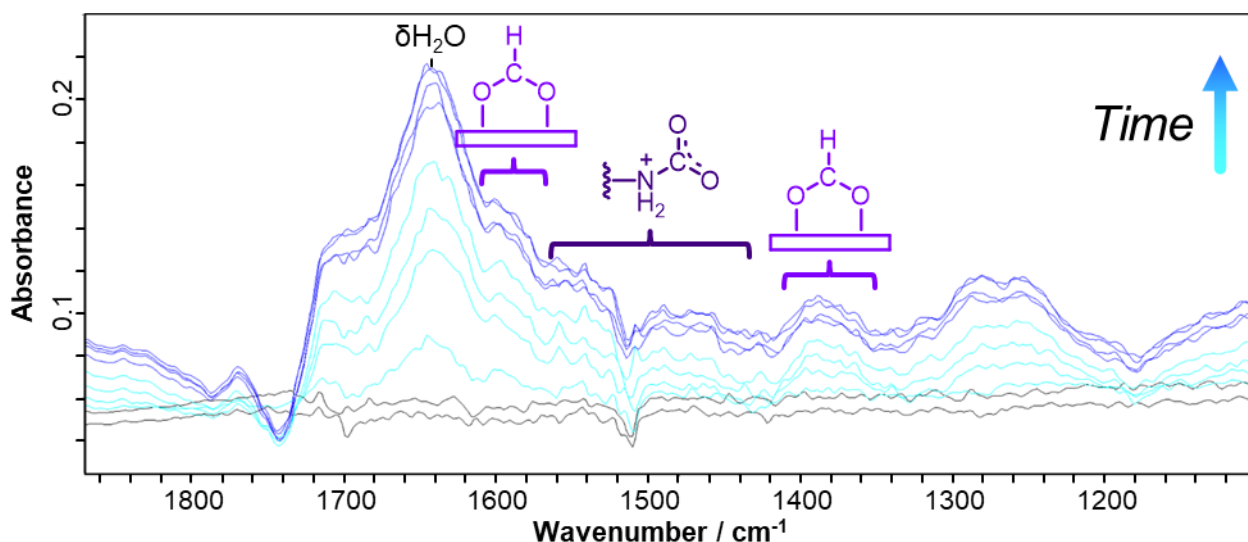


Figure 3.10 *In-situ* DRIFTS spectra of surface species over $\text{PdNP}@\text{CL}_1\text{PIIL}$. Black spectra show the results from a dry feed of 10 vol% CO_2 diluted with Ar over 10 minutes. After this time 4 vol% H_2O vapour was introduced to the gas feed, and the corresponding spectra are shown in blue. The light blue spectra show $\text{CO}_2 + \text{H}_2\text{O}$ absorption up to 5 minutes.

of water exposure vibrations in the region of 1580-1430 cm^{-1} appear, which are indicative of $\nu_{\text{sym}}\text{COO}^-$, $\nu_{\text{asym}}\text{COO}^-$ and $\nu\text{-NH}_3^+$ stretches associated with carbamate.^{34,37} One can also see the growth of peaks in the regions of 1600-1590 cm^{-1} and 1410-1350 cm^{-1} which are frequently assigned to the $\nu_{\text{sym}}\text{HCOO}^-$ and $\nu_{\text{asym}}\text{HCOO}^-$ vibrations of formate, respectively.^{33,38,39} This is rather surprising, as the experiments were conducted in the absence of hydrogen, however, the assignment is supported by weak signals at 2815 cm^{-1} , indicative of C-H stretching (**Appendix A.3.14**);³³ a corresponding experiment, conducted in the autoclave batch reactor, in the absence of H_2 , did not afford any detectable formate or formic acid when PdNP@CL₁PIIL (6 μmol) was stirred under a 20 bar pressure of CO_2 . Although efforts were made to purge surface hydride species from the catalyst surface prior to the DRIFTS studies, Pd has a strong affinity for hydrogen and, thus, it is possible that not all of the Pd-H species had been removed prior to the DRIFTS study. It is also not unreasonable to imagine how oxidative addition of water to the catalyst surface could form a reactive surface-adsorbed H species that could generate a small but spectroscopically observable quantity of formate (see **Section 3.8.4**). The assignment of formate in the absence of hydrogen has also been reported when DRIFTS studies of TiO_2 -supported Cu catalysts were conducted under a similar atmosphere of $\text{CO}_2 + \text{H}_2\text{O}$;² the authors rationalised this observation by attributing formate formation to the reaction of CO_2 with surface hydroxyl groups.

While no assignments have been made here to bicarbonate or carbonate species, we cannot exclude them from contributing to the cocktail of species seen in **Figure 3.10**. The carbonyl region, from 1720-1650 cm^{-1} , for example, is potentially comprised of 4 unique species that will undoubtedly include surface-bound bicarbonate; peaks in this region at 1650 and 1690 cm^{-1} have previously been assigned to bicarbonate,³³ while peaks from 1680-1660 cm^{-1} have been attributed to bidentate carbonate.¹ Note that both of the aforementioned references are based on metal oxide supported NP catalysts, therefore, while informative, they do not allow us to make direct comparisons to surface species on our polymer supported catalyst, as the bicarbonate/carbonate species is quite often found on the metal oxide support. When similar DRIFTS studies were conducted over AuNP supported on Schiff base modified silica, Liu and co-workers asserted that no bicarbonate species were detected; instead, assignments in this region were limited to surface-bound carbamate at 1690 cm^{-1} , as well as a contentious assignment of Schiff base coordinated CO_2 at 1712 cm^{-1} .⁴⁰

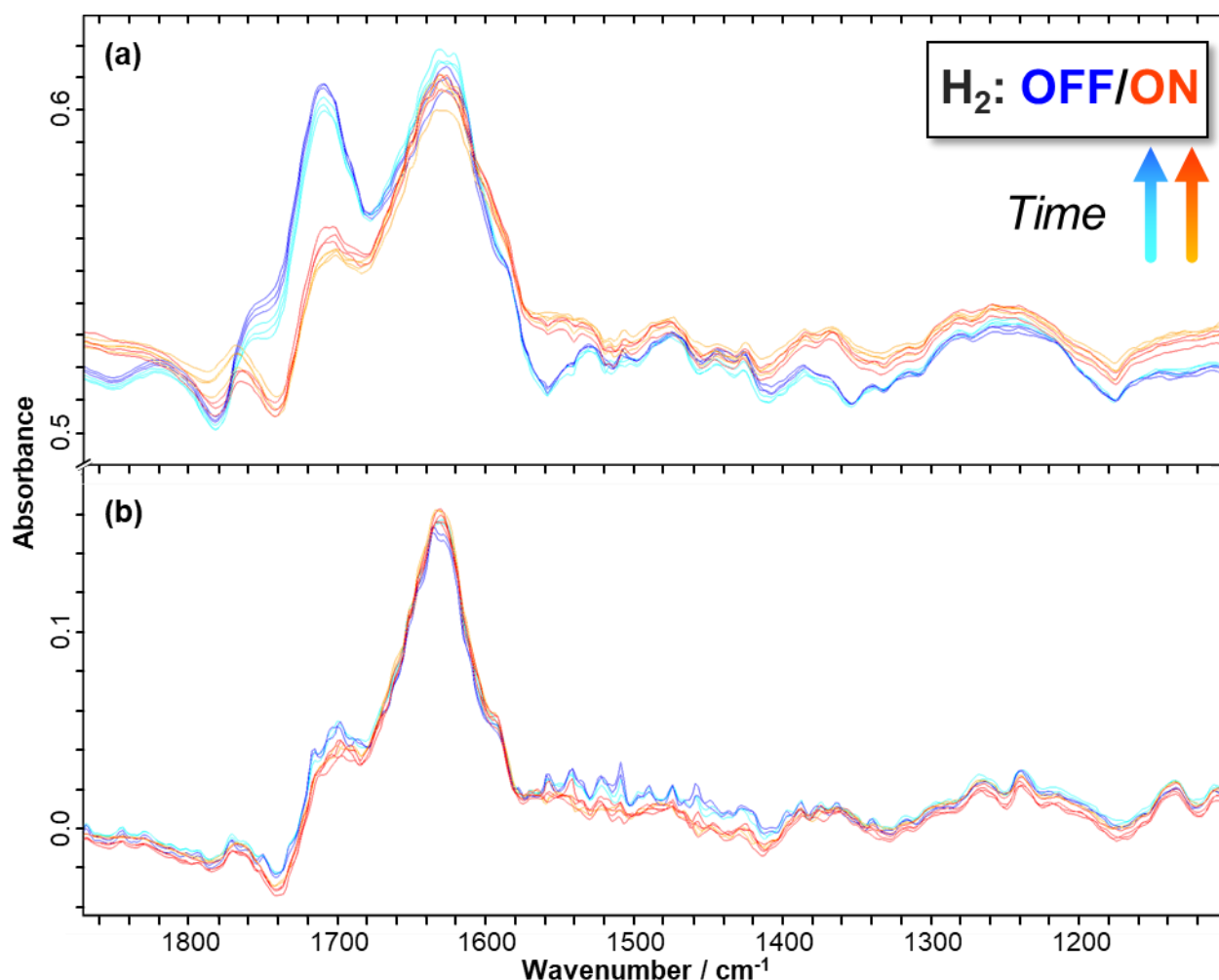


Figure 3.11 *In-situ* DRIFTS spectra of surface species over (a) PdNP@CL₁PIIL and (b) PdNP@PIIL. Samples were first saturated with a 10 vol% CO₂ + 4 vol% H₂O feed diluted with helium (blue) before introducing 10 vol% H₂ to the gas feed (red) and monitoring the spectra over time.

In a separate experiment, PdNP@CL₁PIIL was first saturated with a feed of CO₂ + H₂O over 25 minutes, before introducing H₂ gas (**Figure 3.11a**). In this instance, the carbonyl region appeared very intense when compared to that shown in **Figure 3.10** over the same material, and this region, with an additional broad feature at 1740 cm⁻¹, appeared to increase in intensity with time. The carbonyl region showed a significant response following introduction of H₂, whereby the intensity of the broad bands at 1757 and 1710 cm⁻¹ decreased considerably, coupled with an apparent increase in intensity of the formate bands at 1595 cm⁻¹ and from 1415-1350 cm⁻¹. A complimentary experiment was conducted in the absence of amine, whereby CO₂ hydrogenation was studied over the surface of PdNP@PIIL, derived from the hydrogenation of precatalyst **2.8a**. In contrast, here there was a much more subtle response following the introduction of H₂ to the gas feed, and surprisingly there was no apparent change in the intensity of the formate regions at all (**Figure 3.11b**).

In order to investigate the hydrogenation of carbamate over PdNP@CL₁PIIL, a sample of catalyst was 'doped' with an aqueous solution of ammonium carbamate and allowed to dry. Using untreated PdNP@CL₁PIIL as a background, the doped ammonium carbamate was treated with hydrogen (10 vol%) for 60 minutes; however, during this time, there was no discernible change in the acquired DRIFTS spectra (**Appendix A.3.15**). Note that the spectrum of doped carbamate did not exhibit major bands in the region of 1750-1650 cm⁻¹, and instead intense peaks at 1621 and 1514 cm⁻¹ were indicative of free ionic carbamate.^{34,37} We can therefore assign the intense carbonyl bands in **Figure 3.8a** to surface bound carbamate species, although monodentate bicarbonate and formate species will also contribute to this region, as evidenced by the band at 1701 cm⁻¹ for PdNP@PIIL. However, the unmodified catalyst does not show peaks of the same intensity as the amine modified catalyst at 1755 and 1710 cm⁻¹, which supports their assignment to a carbamate species. These results are consistent with the finding from **Chapter 2 (Section 2.3)** that aniline as an additive to a reaction catalysed by PdNP@PIIL is not sufficient to obtain high turnovers to formate. Thus, the appearance of bands associated with formate coupled with the decrease in the intensity of bands attributed to carbamate, as well as the absence of formation of formate from the hydrogenation of carbamate 'doped' catalyst, suggests that the PdNP and the amine must be held in close proximity for the rapid conversion of CO₂.

There is limited evidence from the above spectra that competitive CO formation from the reverse water gas shift occurs to a significant degree over PdNP@X-PIIL catalysts. In every *in-situ* experiment conducted, there was little evidence of CO binding at the Pd surface which suggests that the reverse water-gas shift reaction is not a dominant pathway. A weak broad signal at 1823 cm⁻¹ identified over PdNP@CL₁PIIL (**Figure 3.11a**) could be attributed to CO binding to 3-fold Pd hollow sites, though such a signal is more typical from 1900-1850 cm⁻¹.⁴¹ When gaseous CO was passed over the catalyst surface, in the absence of CO₂ and H₂, several peaks were observed at higher wavenumbers: a major intense band at 1908 cm⁻¹ is indicative of bridged CO over Pd, while a much smaller peak at 2008 cm⁻¹ can be assigned to linear Pd-CO species (**Figure 3.12**).^{33,42,43} A shoulder to the right of the major peak at 1908 cm⁻¹ suggests the presence of some multi-bonded CO, however, the signals are too broad to assign a definitive wavenumber. However, the broad peak at 1823 cm⁻¹ in **Figure 3.11a** is coincident with this shoulder, which implies that some CO is generated under the conditions of catalysis. On the other hand, when CO was passed over the surface of PdNP@PIIL a single less intense

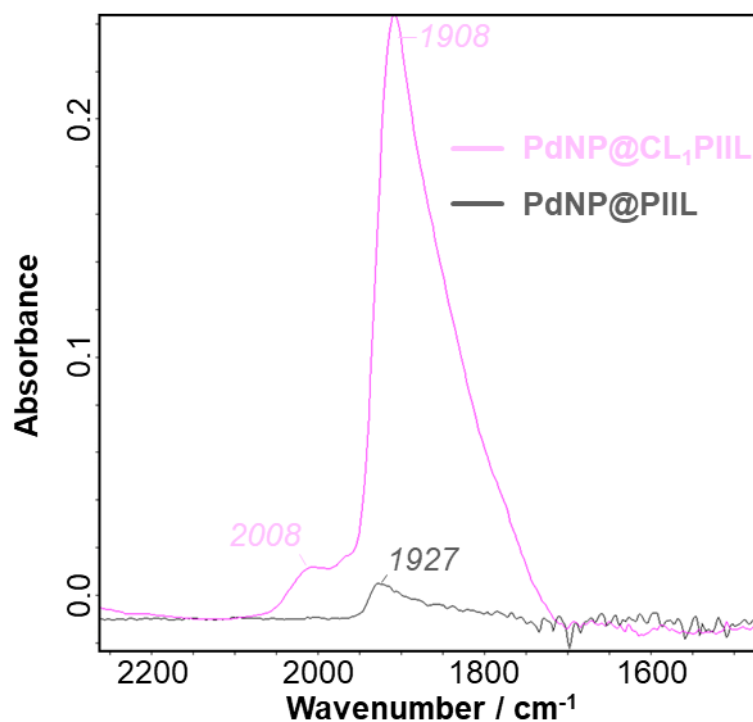


Figure 3.12 *In-situ* DRIFTS spectra of surface-bound CO (10 vol%) over PdNP@CL₁PIIL (pink) and PdNP@PIIL (grey), generated from the hydrogenation of **3.22** and **2.8a**, respectively.

band at 1927 cm⁻¹ appeared. A similar shoulder to that of PdNP@CL₁PIIL was observed at lower wavenumbers which again suggests the presence of bridged CO species. Interestingly, a redshift was observed when the bridged CO peak for amine-modified PdNP@CL₁PIIL was compared to that of the unmodified catalyst, indicative of stronger backbonding to CO for the amine-functionalised catalyst; this contradicts the XPS results in **Chapter 2** that describe PdNP to be electron deficient following coordination of surface amine groups. The lack of linear CO at the surface of PdNP@PIIL is unlikely to be a NP size effect as NP's generated from the hydrogenation of **2.8a** and **3.22** have comparative average diameters of 2.98 and 2.92 nm, respectively. A comparison of the relative intensities of the bridged CO bands suggests that there is limited access to active sites at the surface of PdNP@PIIL, presumably due to surface coverage by the polymer support.

3.8.2 CO₂-Temperature Programmed Desorption

As shown in the dry DRIFTS experiments above, CO₂ does not bind strongly to the PdNP surface; indeed, when Pd loading was increased on basic Al₂O₃, Szanyi and Kwak observed a drastic reduction in CO₂ adsorption capacity of the catalyst.⁴⁴ While the dry feed of CO₂ over PdNP@CL₁PIIL showed no, or very little, surface adsorbed CO₂ species, that does not mean that CO₂ is not sequestered – DRIFTS is a surface sensitive technique, therefore adsorbed

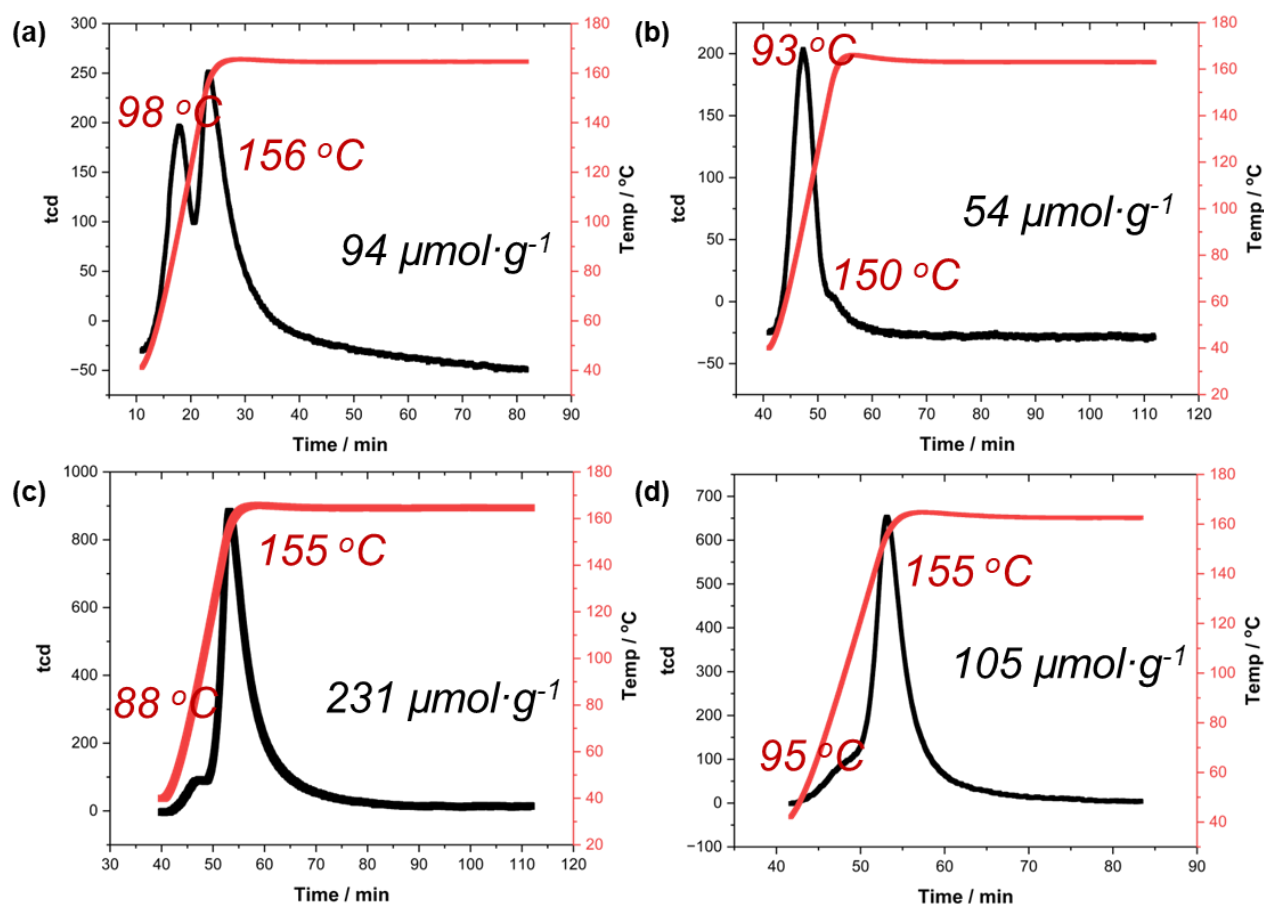


Figure 3.13 CO₂-TPD graphs of (a) PdNP@CL₁PIIL, (b) PdNP@PIIL, (c) PdCl₄@CL₁PIIL (**3.22**), and (d) PdNP@C₁PIIL. Catalyst materials were first pre-treated with CO₂ at 40 °C for 1 hour, followed by purging with He with ramping temperature. The values in black show the total amount of CO₂ desorbed from the materials when heated up to 160 °C.

gasses in the bulk of the material may not be prominent in the spectra. Thus, the as prepared PdNP@CL₁PIIL were analysed by CO₂ temperature programmed desorption (TPD) experiments.

To avoid decomposition of the polymer support, heating was limited to 160 °C, well below the thermal minima for the degradation of similar PIIL-based materials (see **Chapter 4** for an example). First, PdNP catalysts were heated to 100 °C and held for an hour under a flow of He to remove any surface adsorbed species. Next, the catalyst was treated for 1 hour with a flow of CO₂ at 40 °C. Purging with He with ramping temperature revealed two adsorption sites (**Figure 3.13a**); an initial desorption was observed at 98 °C which has tentatively been attributed to CO₂ weakly bound to the PdNP surface; this was followed by a slightly more intense desorption at 156 °C which corresponds to amine-bound CO₂, consistent with the presence of carbamate as shown in the DRIFTS experiments above. The assignment of CO₂ weakly bound to the PdNP surface is contentious, because as mentioned earlier, CO₂ is known

to bind poorly to the platinum group metals.³⁵ Reference TPD experiments are currently underway to investigate whether or not this peak can be attributed to an interaction between CO₂ and the free polymer (**3.21**), though these experiments were not completed in time for this submission.

To verify the assignment of an amine-bound CO₂ molecule desorbing at 156 °C, a comparison was made with an unmodified PIIL catalyst. Indeed, CO₂-TPD of unmodified catalyst generated from **2.8a** showed only a single major desorption at 93 °C, consistent with PdNP-bound CO₂; a minor shoulder at *ca.* 150 °C could correspond to adsorption at 1,2-dimethylimidazole, which is liberated following the hydrogenation of the benzylic bridge in the PIIL support. An imide-based polymer-silica composite was also found to sequester CO₂ when used as a support for PdAgNP catalysed CO₂ hydrogenation – CO₂-TPD of the polymer found a single desorption band observed at 75 °C, presumably due to CO₂ binding to the imide site; however, the corresponding CO₂-TPD experiments of the PdAgNP loaded polymer was not conducted.⁴⁵

A complimentary experiment conducted using unreduced PdCl₄@CL₁PIIL (**Figure 3.13c**), again revealed a major desorption associated with amine-bound CO₂ at 155 °C. By integrating the region under the individual adsorption sites, a comparison can be made between the adsorption capacity of the amines on the individual materials. Interestingly, the measured CO₂ adsorption capacity of amine in **3.22** was much higher than that for the corresponding NP material isolated after 2 hours of hydrogenation (217 vs 60 μmol·g⁻¹). Such a drop in CO₂ adsorption could be indicative of amine loss following hydrogenation, though the XPS results do not support this; alternatively, the PdNPs may well limit access to the amines by blocking micropores of the polymer. A much smaller desorption peak was found for **3.22** after heating to 88 °C; this is slightly lower than the 93-98 °C observed for PdNP-bound CO₂ and could instead be associated with CO₂ coordinated to monometallic divalent Pd species. Alternatively, this peak could be rationalised by CO₂ binding to an imidazolium-derived abnormal carbene, though this is unlikely as similar desorptions were not observed for PdNP@CL₁PIIL and PdNP@PIIL above.

A comparison was also made between PdNP@CL₁PIIL and catalyst isolated after the hydrogenation of PdCl₄@C₁PIIL (**Figure 3.13d**), supported by the corresponding linear C₁PIIL. Here, 92 μmol of CO₂ per gramme of material were sequestered by amine sites in **3.20b** in

contrast to the 60 $\mu\text{mol}\cdot\text{g}^{-1}$ bound by hydrogenated **3.22**; despite this, there was less than a third of the total amount of CO_2 desorbed from the surface of **3.20b**-derived NPs than for its cross-linked counterpart. This is indicative of fewer reactive sites at the surface of $\text{PdNP}@C_1\text{PIIL}$, which will likely contribute to its poor catalytic efficacy compared to $\text{PdNP}@CL_1\text{PIIL}$.

While slightly lower, the total values of CO_2 desorption from these materials are comparative to the values obtained for bis-imidazolium-based PIIL supported PdNP catalysts. Song and co-workers found that PdNP immobilized on phenyl and biphenyl linked bis-imidazolium PIILs had CO_2 uptakes of 200 and 110 $\mu\text{mol}\cdot\text{g}^{-1}$, respectively, both of which are higher than the 94 $\mu\text{mol}\cdot\text{g}^{-1}$ sequestered by $\text{PdNP}@CL_1\text{PIIL}$ but lower than the 231 $\mu\text{mol}\cdot\text{g}^{-1}$ obtained for the precatalyst (**3.22**) prior to hydrogenation.⁴⁶

3.8.4 The Role of Water

The DRIFTS experiments above demonstrate that water is not only non-innocent in this transformation, but it may also be incorporated into the final product. A complimentary experiment was conducted where a $\text{Pd}@CL_1$ catalysed CO_2 hydrogenation was conducted in D_2O rather than H_2O . The remaining parameters were kept constant, including the use of K_2CO_3 (1 M) as base. Following completion of the reaction, two aliquots were taken and charged with dimethyl sulfoxide and dimethyl sulfoxide- d_6 separately in order to quantify any deuterium incorporation. Analysis of the resulting ^2H NMR spectrum indeed found incorporation of deuterium at the formyl C-H position of formate; note that not all of the

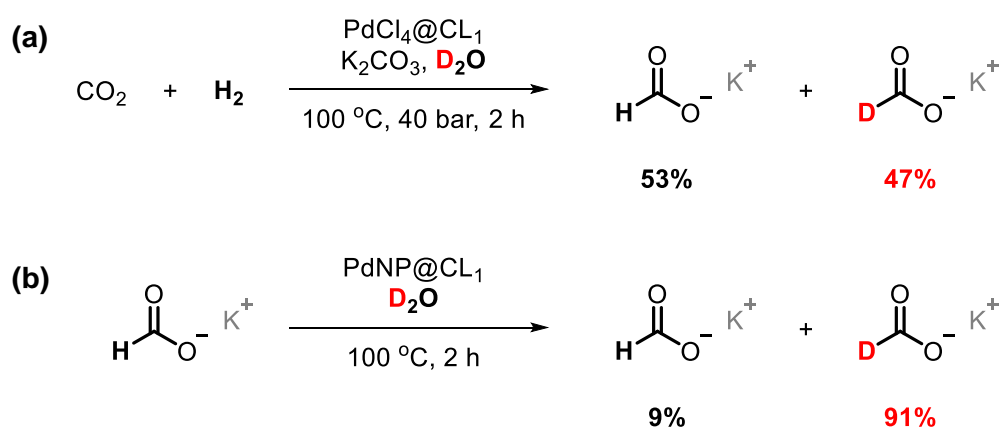


Figure 3.14 Investigation of water-derived proton incorporation during the formation of potassium formate. (a) Hydrogenation of CO_2 in a solution of D_2O charged with **3.22** (6 μmol). (b) H/D scrambling experiment conducted in D_2O catalysed by pre-reduced $\text{PdCl}_4@CL_1$ (6 μmol). The percentages represent the relative ratio of the two isotopologues rather than yields.

formate protons were derived from water as the ^1H NMR spectrum also showed the presence of non-deuterated formate. In fact, the ratio of non-deuterated to deuterated formate was almost 1 : 1, though there was a slight excess of the ^1H isotopologue (1.14 : 1.00).

However, it is impossible to tell from this experiment whether CO_2 is in part hydrogenated by water-derived protons (deuterons), or if formate is afforded from the direct hydrogenation of CO_2 followed by ^1H - ^2H scrambling at the NP surface. Leitner and co-workers have reported that formate H/D exchange occurs over RuNP catalysts modified with sulfonic acid groups; under a positive pressure of hydrogen, 45% deuterium incorporation was reported when ammonium formate was stirred for 20 hours in D_2O .⁴⁷ The sulfonic acid moiety played an active role in this exchange, as in its absence only 20% deuterium was incorporated at the formyl C-H. Interestingly, the authors observed no H/D scrambling when the same reaction was conducted under a positive pressure of D_2 in non-deuterated water, suggesting that exchange with gaseous hydrogen is slow.

Thus, pre-reduced **3.22** (PdNP@CL_1 , 6 μmol) was stirred for 2 hours at 100 $^\circ\text{C}$ with potassium formate in D_2O (**Figure 3.14b**). On completion of the reaction, almost all of the formate had been hydrolysed to liberate gaseous hydrogen, with *ca.* 0.1 μmol of formate detected by NMR spectroscopy, after initially charging the reaction with 1.25 mmol of potassium formate. Despite this, significant H/D scrambling appeared to have occurred at the NP surface with the deuterated isotopologue constituting 91% of the product mixture. A reference experiment conducted with D_2O dissolved potassium formate in the absence of catalyst did not appear to result in exchange of the formyl C-H. Although these results demonstrate that H/D scrambling is facile at the NP surface, they do not allow us to exclude the possibility that the formyl C-H is in part derived from water.

3.8.5 Influence of Base Concentration

Despite DRIFTS providing invaluable insight surrounding the CO_2 hydrogenation mechanism, the data gathered is at the solid-gas interface, making it difficult to investigate the influence of the base additive. Thus, several experiments were conducted to probe the effect of the base on the catalytic hydrogenation of CO_2 . A negative relationship between base concentration and activity must be considered as several authors have reported such an effect. When catalysed by micellar supported palladium NPs, the conversion of CO_2 to formate was reduced at NEt_3 additive concentrations above 0.7 M.⁴⁸ Similarly, when heterogeneous

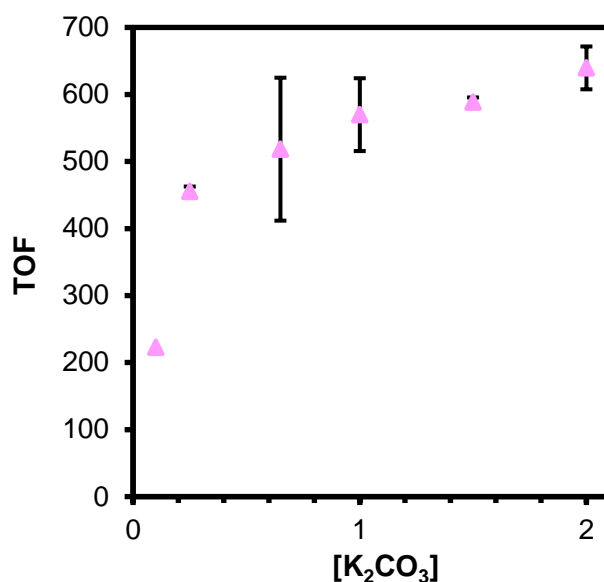


Figure 3.15 Plot of TOF against potassium carbonate concentration. Reaction conditions: **3.22** (6 μ mol Pd), 1:1 H₂/CO₂ (40 bar), 100 °C, 2 hours, H₂O (20 mL).

Ru catalysts were studied in a fixed bed flow system a drop in CO₂ conversion was observed at NEt₃ concentrations of above 3 M, though this was attributed to the immiscibility of NEt₃ in water.⁴⁹ Reduced yields of potassium formate were obtained for the hydrogenation of KHCO₃ catalysed by graphene oxide supported PdAu bimetallic NPs (in the absence of CO₂) when the concentration of bicarbonate was increased to 2 M.⁵⁰

A survey of the influence of the concentration of base on catalyst activity showed an initial sharp increase in efficacy when the concentration was increased from 0.1 M to 0.25 M. Further increases in base concentration, however, led to a much more gradual increase in TOF. However, despite increasing the concentration of potassium carbonate up to 2 M, no drop in activity was observed. A sharp initial increase in activity followed by a plateau could be indicative of Pd surface coverage with potassium – small amounts of potassium doping has been reported to significantly enhance CO₂ binding to platinum group metals due, in part, to manipulation of the metal surface electronic structure.^{35b}

Yamashita has reported that when PdAg bimetallic NPs were supported on amine-modified resorcinol-formaldehyde polymers, the effect of bicarbonate concentration on catalyst TON was highly dependent on the amine content of the catalyst such that the reaction order in base decreased with increasing amine content (0.52 for 1.7 wt% N vs. 0.32 for 3.5 wt% N).⁴ Interestingly, Yan and co-workers also found that the reaction rate in base was heavily dependent on the support, measuring a reaction order in bicarbonate of around 1.4 when Pd was supported on ZnO, whereas an order of 0.6 was measured when supported on CeO.¹

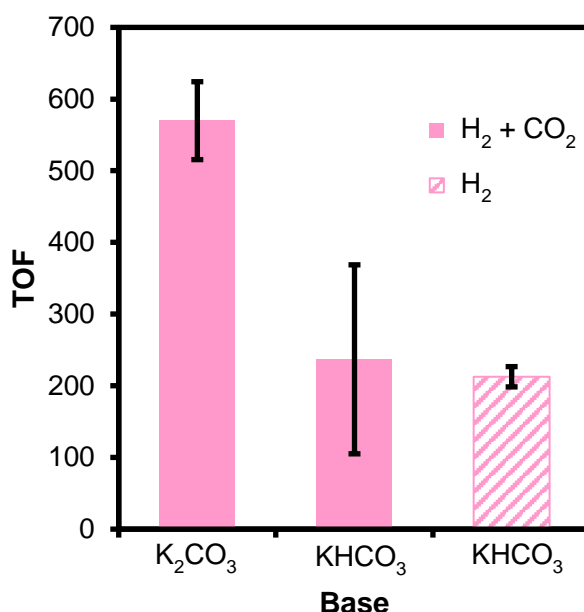


Figure 3.16 Comparison of aqueous solutions of alkali metal bases as additives in the hydrogenation of CO₂ to formate. Reaction conditions: PdCl₄@CL₁PIIL (6 μmol), 1:1 H₂/CO₂ (40 bar), 100 °C, 2 hours.

It is important to note that the formate generated is derived from CO₂ rather than the additive, K₂CO₃; a reference reaction using PdCl₄@CL₁PIIL as catalyst in the absence of CO₂ (H₂ partial pressure of 20 bar) found no conversion to potassium formate after stirring for 2 hours at 100 °C – this shows unequivocally that the formate is derived from CO₂ under these conditions. However, several catalysts have shown efficacy for the hydrogenation of bicarbonate to formate in addition to the hydrogenation of CO₂.^{48,51} Indeed, when the reactor was charged with 1 M KHCO₃ as additive, 2.74 mmol of formate was generated in the absence of CO₂ from the gas mix, although this was significantly lower than 6.60 mmol of formate obtained in the presence of K₂CO₃ (TOF = 237 h⁻¹ and 570 h⁻¹ respectively). Interestingly when KHCO₃ was hydrogenated in the presence of CO₂, as per the typical reaction conditions, the TOF dropped slightly to 213 h⁻¹. Liu and co-workers also report the diminished activity of AuNP catalysed KHCO₃ hydrogenation, when compared to the hydrogenation of CO₂ in the presence of NEt₃ additive.⁴⁰ These results suggest that the hydrogenation of CO₂ over PdNP@CL₁PIIL is unlikely to proceed *via* a pathway involving bicarbonate as a key intermediate; while we have demonstrated that KHCO₃ can be hydrogenated to potassium formate, if this was a dominant pathway when K₂CO₃ is used as additive, it would be reasonable to expect comparative TON's for the two additives. While the DRIFTS results suggest that KHCO₃ forms at the catalyst surface, it would appear that hydrogenation of surface bound carbamate species is the dominant pathway.

3.8.6 Role of the Formate Counterion

The comparison of base additives in **Chapter 2** found that K_2CO_3 outcompeted several other bases such as NaOH , NEt_3 , and potassium bicarbonate. While one could test the efficacy of every known base as additive for the hydrogenation of CO_2 , we instead sought to expand on this study by investigating the effect of the carbonate cation on the formation of formate. Previous studies on the influence of the alkali metal bicarbonate salts as additives in formate formation saw a decrease in formate yield with decreasing cation size in the order $\text{KHCO}_3 > \text{NaHCO}_3 > \text{LiHCO}_3$.^{51,52} Another study identified CsHCO_3 as a promising candidate for hydrogen storage and release when hydrolysed in the presence of a homogenous Ru(II) catalyst.⁵³ However, there have been no attempts to understand the role of the alkali metal in direct formate synthesis, nor a comparison of catalytic activity in the presence of the various metal carbonate salts.

The challenges associated with comparing the alkali carbonate salts was immediately apparent due to their disparate solubility in water. While K_2CO_3 is highly soluble in water (110 g/100 mL at 20 °C), the other salts studied were less soluble, Li_2CO_3 being the least soluble (1.29 g/100 mL at 25 °C). When 1 M solutions of Li_2CO_3 , Na_2CO_3 , K_2CO_3 , and Cs_2CO_3 were studied under the conditions of catalysis (**Figure 3.17**), there was little difference in the activities of the systems and there was no obvious relationship between formate formation and additive cation. However, at this concentration, the amount of Li_2CO_3 and Cs_2CO_3 used

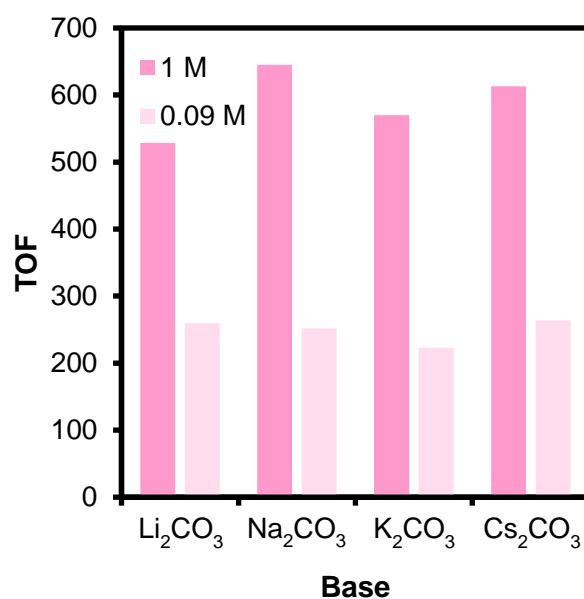


Figure 3.17 Comparison of aqueous solutions of alkali metal carbonate bases as additives in the hydrogenation of CO_2 to formate. Reaction conditions: $\text{PdCl}_4@\text{CL}_1\text{PIIL}$ (6 μmol), 1:1 H_2/CO_2 (40 bar), x M base (x = 1.0, 0.09) 100 °C, 2 hours.

was above the solubility limit of the bases, thus, the study does not provide a meaningful comparison. Instead, the bases were compared at a concentration of 0.09 M to ensure the full solvation of the lithium salt. At this concentration, there was again little difference in reactions conducted in Li_2CO_3 , Na_2CO_3 and Cs_2CO_3 with an average TOF of $259 \pm 5 \text{ h}^{-1}$, albeit reactions with K_2CO_3 exhibited a slightly lower TOF of 223 h^{-1} . Likewise, at 1 M concentration of base, the use of K_2CO_3 led to the formation of less formate than both Cs_2CO_3 and Na_2CO_3 with TOFs of 613 h^{-1} and 645 h^{-1} , respectively.

3.8.7 Proposed Reaction Mechanism

Together, the described mechanistic studies provide some insight of a potential reaction pathway for the hydrogenation of CO_2 at the surface of $\text{PdNP@CL}_1\text{PIIL}$. First, with the aid of water, CO_2 is directed to the catalyst surface to form a mixture of carbamate and bicarbonate species. If sufficiently close to the NP surface, carbamate species can coordinate to become surface bound carbamates. Hydrogen gas appears to react rapidly with surface bound carbamates. Hydrogen gas appears to react rapidly with surface bound carbamate species to liberate formate which can then exchange the formyl hydrogen

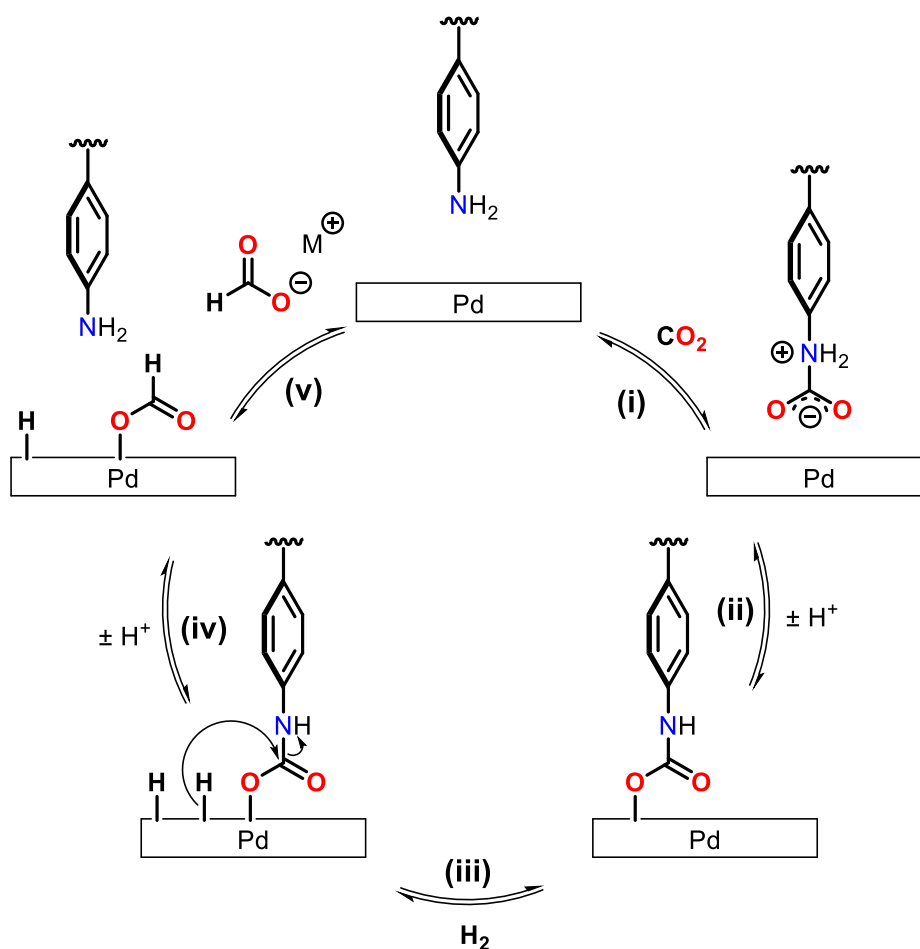


Figure 3.18 Proposed reaction mechanism for the PdNP catalysed hydrogenation of CO_2 to formate over aniline decorated supports.

presumably *via* reversible beta hydride elimination reinsertion with a water derived H^{*}. The role of the base additive, K₂CO₃, remains ambiguous – increases of carbonate at low concentrations led to rapid increases in formate turnover, which suggests that it could displace formate from the catalyst surface, though at higher concentrations, this effect is less profound due to a potential saturation of active sites. The carbonate cation appears to have a negligible effect on the activity of the system, though small increases in activity were observed when Na₂CO₃ was used as additive rather than K₂CO₃.

3.9 Conclusion

This chapter has described the synthesis of three novel ionic liquid monomers and their application in the preparation of amine-modified polymer supports for Pd catalysed CO₂ hydrogenation. All three novel ionic liquids demonstrated improved stability following hydrogenation when compared to their benzyl-based predecessor, however, significant loss of the IL was still observed following catalysis. We speculate that the IL-imidazolium could be hydrogenated to the corresponding imidazolidine, rather than cleaved into solution, though further experiments will be required to test this hypothesis.

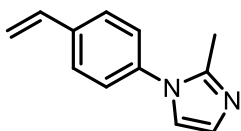
Despite poor retention of the IL, the linear benzyl-imidazolium benchmark, **3.20b**, was found to be significantly more active than all of the new PIIL supported catalysts. The poor apparent stability of **3.20b** was improved by introducing extensive cross-linking (**3.22**) which also improved the activity of the corresponding catalyst and its recyclability. The work in this chapter also highlighted the significant influence of the IL anion on the resulting catalyst, whereby the reactivity and the oxidation state of the formed Pd catalyst appears to depend on the presence of iodide. While the role of IL anions has already been highlighted as a convenient way to tune catalyst properties,¹⁸ this area has not been explored in this thesis due to time constraints.

Preliminary *in-situ* DRIFTS experiments over the surface of NPs generated from **3.22** were used to probe the reaction mechanism of CO₂ hydrogenation. Rather than proceeding *via* a bicarbonate species, it appears that surface-bound carbamate reacts rapidly in the presence of hydrogen to liberate formate, highlighting the pivotal role of the amine which may be two-fold; firstly, activating the CO₂ through the formation of a carbamate intermediate, and secondly assisting adsorption and concentration of the CO₂ at the active sites of the NPs.

However, additional surface studies will be required to deconvolute the cocktail of species apparent at the catalyst surface.

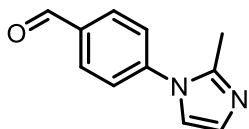
3.10 Experimental

3.10.1 Attempted Synthesis of 2-methyl-1-(4-vinylphenyl)-imidazole (3.1) via Ullman Coupling⁸



In a Schlenk flask, 2-Methylimidazole (0.87 g, 10.65 mmol) was dissolved in NMP (1.64 mL) with gentle heating. The solution was then charged with K_2CO_3 (2.27 g, 16.39 mmol), CuCl (0.08 g, 0.82 mmol), and acetylacetone (0.20 g, 2.05 mmol). On addition of CuCl the suspension turned brown, though this sharply turned turquoise on addition of acetylacetone. After heating the mixture to 130 °C, 4-bromostyrene (1.50 g, 8.19 mmol) was added dropwise with stirring, which returned the colour of the mixture to brown. The mixture was allowed to stir overnight at 130 °C, after which time a gum-like solid had formed that appeared to be insoluble in water and every common organic solvent.

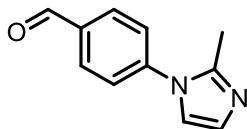
3.10.2 Attempted Synthesis of 2-methyl-1-(4-formylphenyl)-imidazole (3.2) via Ullman Coupling⁸



In a Schlenk flask, 2-Methylimidazole (3.46 g, 42.2 mmol) was dissolved in NMP (10 mL) with gentle heating. The solution was then charged with K_2CO_3 (8.96 g, 64.8 mmol), CuCl (0.32 g, 3.2 mmol), and acetylacetone (0.81 g, 8.1 mmol). On addition of CuCl the suspension turned brown, though this sharply turned turquoise on addition of acetylacetone. After heating the mixture to 130 °C, 4-bromostyrene (6.00 g, 32.4 mmol) was added dropwise with stirring, which returned the colour of the mixture to brown. The mixture was allowed to stir overnight at 130 °C. After this period, an aliquot of the mixture was analysed by 1H NMR spectroscopy and was indicative of the full conversion of the 4-bromobenzaldehyde. The solid carbonate salt was filtered and washed with DCM, before combining the organic fractions and washing with copious amounts of saturated aqueous $NaHCO_3$ solution. This resulted in a persistent emulsion, from which the product was difficult to extract. The organic fractions were then

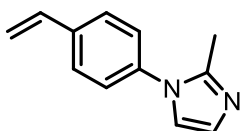
dried over magnesium sulphate and filtered, before removing the volatiles under vacuum. NMP continued to be evident in the ^1H NMR spectra, despite further washing with deionized water.

3.10.3 Synthesis of 2-methyl-1-(4-formylphenyl)-imidazole (3.2) via Oxidative Coupling¹⁰



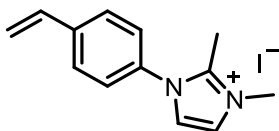
In a round bottom flask, under an atmosphere of air, 4-formylphenylboronic acid (3.00 g, 20 mmol), 2-methylimidazole (0.82 g, 10 mmol) and $[\text{Cu}(\text{OH})\text{TMEDA}]_2\text{Cl}_2$ (0.47 g, 1 mmol) were dispersed in anhydrous DCM (40 mL). The mixture was stirred overnight at room temperature. The mixture was then filtered and concentrated under vacuum, before purification by column chromatography (chloroform/hexane, 3:1, 1% NEt_3) to afford a yellow oil (1.73 g, 94%). R_f = 0.25 (chloroform/hexane, 3:1, 1% NEt_3). ^1H NMR (400 MHz, CDCl_3) δ 10.08 (s, 1H), 8.02 (m, 2H), 7.49 (m, 2H), 7.07 (dd, J = 5.0, 1.5 Hz, 2H), 2.43 (s, 3H). ^{13}C NMR (101 MHz, CDCl_3) δ 190.89, 144.63, 143.04, 135.63, 131.11, 128.69, 125.82, 120.36, 14.28.

3.10.4 Synthesis of 2-methyl-1-(4-vinylphenyl)-imidazole (3.1)



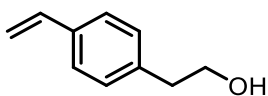
In an oven-dried Schlenk flask, methyltriphenylphosphonium bromide (2.03 g, 5.69 mmol) was dispersed in anhydrous THF (20 mL). To this, 2.5 M $n\text{-BuLi}$ (2.28 mL, 5.69 mmol) in hexane was added dropwise, affording a clear orange solution with stirring. The mixture was allowed to stir at room temperature for 30 minutes before the dropwise addition of 4-(2-methylimidazolyl)benzaldehyde (1.06 g, 5.69 mmol) dissolved in anhydrous THF (20 mL), resulting in instantaneous precipitation. After stirring overnight at room temperature, the mixture was quenched with saturated aqueous ammonium chloride solution (20 mL). The product was then extracted with dichloromethane before drying over MgSO_4 , filtering and removing the volatiles under reduced pressure. Alkene **3.1** was obtained as an off-white solid and used without further purification. The ^1H NMR spectrum showed no evidence of aldehyde environments. ^1H NMR (400 MHz, CDCl_3) δ 7.72 – 7.63 (m, 5H), 7.57 – 7.42 (m, 10H), 7.25 (d, J = 8.1 Hz, 2H), 7.01 (d, J = 11.4 Hz, 2H), 6.76 (dd, J = 17.5, 10.8 Hz, 1H), 5.81 (d, J = 17.6 Hz, 1H), 5.35 (d, J = 10.8 Hz, 1H), 2.37 (s, 3H).

3.10.5 Synthesis of 2,3-dimethyl-1-(4-vinylphenyl)-imidazolium iodide (**3.3**)



In an oven-dried Schlenk flask, dissolved vinylphenylimidazole, **3.1** (0.20 g, 1.09 mmol) in anhydrous DCM (5 mL) to which methyl iodide (0.10 mL, 1.63 mmol) was added dropwise. The mixture was stirred overnight at room temperature. The reaction mixture was quenched with the addition of methanolic ammonia (0.23 mL, 7 M), and then the volatiles were removed under vacuum. The product was then precipitated from dropwise addition of the resulting oil into stirring diethyl ether (100 mL). The solid was isolated by filtration, drying under vacuum to afford **3.3** as an off-white solid (0.23 g, 65%). **¹H NMR (400 MHz, MeOD)** δ 7.72 (m, 2H), 7.67 (dd, J = 10.0, 2.2 Hz, 2H), 7.51 (m, 2H), 6.86 (dd, J = 17.8, 11.0 Hz, 1H), 5.97 (d, J = 17.6 Hz, 1H), 5.44 (d, J = 10.8 Hz, 1H), 3.93 (s, 3H), 3.31 (s, 3H). **¹³C NMR (101 MHz, CDCl₃)** δ 145.52, 140.63, 135.09, 132.05, 128.00, 126.66, 123.27, 122.08, 117.46, 37.24, 12.82.

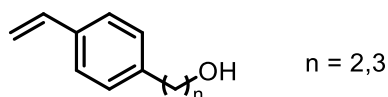
3.10.6 Synthesis of 2-(4-vinylphenyl)ethan-1-ol (**3.4**) via Suzuki-Miyaura Coupling¹²



To a Schlenk flask, added potassium vinyltrifluoroborate (1.00 g, 7.46 mmol), PdCl₂ (0.02 g, 0.12 mmol), PPh₃ (0.10 g, 0.37 mmol) and CsCO₃ (6.08 g, 18.66 mmol) which were dispersed in 9:1 THF/H₂O (12.5 mL) with stirring. Following the addition of 2-(4-bromophenyl)ethanol (1.24 g, 6.22 mmol), the suspension turned from a dark green to black. The mixture was then heated to 80 °C and stirred overnight. After cooling to room temperature, the mixture was taken in DCM (20 mL), filtered over Celite, and washed with deionized water. The organic phase was then dried over MgSO₄, filtered, and concentrated *in vacuo* before purifying by silica-gel column chromatography (hexane/EtOAc, 4:1). Alcohol **3.4** was afforded as a clear yellow oil (0.61 g, 66%) though contained several major impurities. R_f = 0.44 (hexane/EtOAc, 4:1). **¹H NMR (400 MHz, CDCl₃)** δ 7.37 (m, 2H), 7.20 (m, 2H), 6.70 (dd, J = 17.6, 10.9 Hz, 1H), 5.72 (d, J = 17.5 Hz, 1H), 5.22 (d, J = 10.8 Hz, 1H), 3.86 (q, J = 6.4 Hz, 2H), 2.87 (t, J = 6.5 Hz, 2H), 1.37 (t, J = 5.8 Hz, 1H).

Peaks potentially corresponding to 2-phenylethanol evident at δ 7.44 (m), 7.11 (m), 3.85 (q), 2.82 (t), 1.33 (t). Additional unassigned impurity at δ 7.31, 7.23.

3.10.7 Synthesis of 2-(4-vinylphenyl)ethan-1-ol (**3.4**) and 3-(4-vinylphenyl)propan-1-ol (**3.5**) via Heck coupling¹⁴

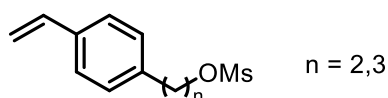


To a Schlenk flask, added Pd(OAc)₂ (0.02 g, 0.10 mmol), DavePhos (0.08 g, 0.20 mmol), *tert*-butylammonium bromide (0.32 g, 1.00 mmol), TMEDA (0.35 g, 3.00 mmol) and 2-(4-bromophenyl)-ethan-1-ol (0.20 g, 1.00 mmol), or 3-(4-bromophenyl)propan-1-ol (0.22 g, 1 mmol), which were dispersed in NMP (4 mL) with stirring. The dropwise addition of acrylic acid (0.11 g, 1.50 mmol) led to the evolution of gas. The mixture was then heated to 130 °C and stirred overnight, after which time a silver mirror had formed on the walls of the flask. After cooling to room temperature, the mixture was poured over saturated aqueous NH₄Cl solution (10 mL) and extracted with diethyl ether (3 x 20 mL), and the organic phase was washed with 1 M HCl (30 mL). The combined organic fractions were then treated with 2 M NaOH (5 mL), before washing with deionized water (2 x 20 mL). The organic phase was then concentrated and passed through a short silica-gel column, eluting with ethyl acetate, to remove residual phosphorous species. The purified alcohol was then dried over MgSO₄, filtered, and the volatiles were removed *in vacuo* to afford yellow oils (**3.4**: 0.10 g, 68%, **3.5**: 0.11 g, 67%). The ¹H NMR spectra show residual aliphatic and aromatic peaks associated with the DavePhos ligand, though the products were used without further purification.

3.4: ¹H NMR (400 MHz, DMSO-d₆) δ 7.37 (m, 2H), 7.19 (m, 2H), 6.69 (dd, *J* = 17.6, 10.8 Hz, 1H), 5.76 (d, *J* = 17.6 Hz, 1H), 5.19 (d, *J* = 11.0 Hz, 1H), 4.62 (t, *J* = 5.2 Hz, 1H), 3.58 (m, 2H), 2.70 (t, *J* = 7.0 Hz, 2H). ¹³C NMR (101 MHz, DMSO-d₆) δ 139.42, 136.54, 134.83, 129.11, 125.94, 113.30, 62.07, 38.75.

3.5: ¹H NMR (400 MHz, DMSO-d₆) δ 7.37 (m, 2H), 7.17 (m, 2H), 6.69 (dd, *J* = 17.8, 10.8 Hz, 1H), 5.76 (d, *J* = 17.6 Hz, 1H), 5.19 (d, *J* = 11.0 Hz, 1H), 4.45 (t, *J* = 5.1 Hz, 1H), 3.40 (m, 2H), 2.59 (t, *J* = 7.6 Hz, 2H), 1.69 (m, 2H).

3.10.8 Synthesis of 2-(4-vinylphenyl)ethyl methanesulfonate (**3.6**) and 3-(4-vinylphenyl)propyl methanesulfonate (**3.7**)



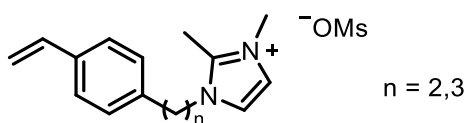
In an oven-dried Schlenk flask, 2-(4-vinylphenyl)ethan-1-ol **3.4** (0.10 g, 0.67 mmol), or 3-(4-vinylphenyl)propan-1-ol **3.5** (0.11 g, 0.67 mmol), was dissolved in anhydrous DCM (2 mL) and

was cooled to 0 °C using an ice bath. While stirring, added anhydrous NEt₃ (113 µL, 0.81 mmol) followed by the dropwise addition of methanesulfonyl chloride (58 µL, 0.75 mmol) which caused the yellow solution to turn orange with the formation of precipitate. The mixture was stirred for 15 minutes, before warming to room temperature and stirring for an hour. The mixture was then taken in DCM (10 mL) and washed with 2 M HCl (50 mL). The aqueous fraction was extracted with further DCM (2 x 10 mL), then the organic fractions were combined, dried over MgSO₄, filtered, and the volatiles were removed in vacuo to afford yellow oils (**3.6**: 0.14 g, 96%, **3.7**: 0.15 g, 94%). The ¹H NMR spectra show residual aliphatic and aromatic peaks associated with the DavePhos ligand, though the products were used without further purification.

3.6: ¹H NMR (300 MHz, DMSO) δ 7.42 (m, 2H), 7.27 (m, 2H), 6.71 (dd, *J* = 17.7, 10.9 Hz, 1H), 5.80 (dd, *J* = 17.7, 1.1 Hz, 1H), 5.23 (dd, *J* = 10.9, 1.1 Hz, 1H), 4.40 (t, *J* = 6.7 Hz, 2H), 3.10 (s, 3H), 2.99 (t, *J* = 6.7 Hz, 2H). **¹³C NMR (75 MHz, DMSO)** δ 136.72, 136.36, 135.57, 129.22, 126.20, 113.89, 70.47, 36.57, 34.38.

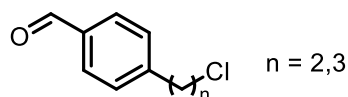
3.7: ¹H NMR (400 MHz, DMSO) δ 7.40 (m, 2H), 7.21 (m, 2H), 6.70 (dd, *J* = 17.6, 11.0 Hz, 1H), 5.78 (d, *J* = 19.0 Hz, 1H), 5.21 (d, *J* = 11.0 Hz, 1H), 4.19 (t, *J* = 6.4 Hz, 2H), 3.17 (s, 3H), 2.66 (t, *J* = 7.1 Hz, 2H), 1.96 (m, 2H). **¹³C NMR (101 MHz, DMSO)** δ 140.58, 136.45, 128.60, 126.23, 113.53, 69.67, 36.60, 31.53, 30.63, 30.10.

3.10.9 Attempted synthesis of 1,2-dimethyl-(2-(4-vinylphenyl)ethyl)-imidazolium mesylate and 1,2-dimethyl-(3-(4-vinylphenyl)propyl)-imidazolium mesylate



In an oven-dried Schlenk flask, added 2-(4-vinylphenyl)ethyl methanesulfonate **3.6** (0.11 g, 0.50 mmol), or 3-(4-vinylphenyl)propyl methanesulfonate **3.7** (0.12 g, 0.50 mmol), and 1,2-dimethylimidazole (0.05 g, 0.50 mmol). The mixture was stirred neat at 80 °C overnight. A ¹H NMR spectrum of the resulting solid (at room temperature) taken in DMSO-d₆ revealed formation of the desired products, in addition to 1,2-dimethylimidazolium mesylate, as well as the corresponding elimination products. Washing of the solid with ethyl acetate removed much of the undesired alkene by-products, but the imidazolium salt persisted.

3.10.10 Synthesis of 4-(2-chloroethyl)benzaldehyde (3.8) and 4-(3-chloropropyl)benzaldehyde (3.9)

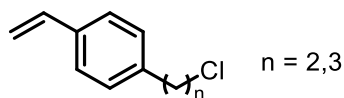


To a Schlenk flask, added NiBr_2 (0.44 g, 2.0 mmol), 4,4'-di-tert-butyl-2,2'-dipyridyl (0.54 g, 2.0 mmol) and 4-methoxypyridine (0.65 g, 6.0 mmol) which were dispersed in dimethoxyethane (20 mL). With stirring, added a solution of 1-chloro-2-bromoethane (2.87 g, 20.0 mmol), or 1-chloro-3-bromopropane (3.15 g, 20.0 mmol), and 4-formylphenylboronic acid (4.50 g, 30.0 mmol) dissolved in dimethoxyethane (40 mL). Finally, K_3PO_4 (12.74 g, 60.0 mmol) was added in portions before heating the mixture to 70 °C and stirring overnight. After cooling to room temperature, the mixture was poured over saturated aqueous NH_4Cl solution (40 mL) and the organics were extracted with diethyl ether (4 x 20 mL). The combined organic fractions were dried over MgSO_4 , filtered, and concentrated *in vacuo*. The resulting dark red oil was purified by silica-gel column chromatography (petroleum ether/ethyl acetate, 9:1) to afford colourless oils (**3.8**: 1.18 g, 35%, **3.9**: 2.78 g, 76%).

3.8: R_f = 0.38 (petroleum ether/ethyl acetate, 9:1). ^1H NMR (400 MHz, CDCl_3) δ 9.98 (s, 1H), 7.83 (d, J = 7.8 Hz, 2H), 7.39 (d, J = 7.7 Hz, 2H), 3.75 (t, J = 7.1 Hz, 2H), 3.14 (t, J = 7.1 Hz, 2H).

3.9: R_f = 0.59 (petroleum ether/ethyl acetate, 9:1). ^1H NMR (400 MHz, CDCl_3) δ 9.98 (s, 1H), 7.82 (m, 2H), 7.37 (m, 2H), 3.53 (t, J = 6.4 Hz, 2H), 2.88 (m, J = 7.38 Hz, 2H), 2.12 (m, 2H). ^{13}C NMR (101 MHz, CDCl_3) δ 191.91, 148.16, 134.82, 130.08, 129.27, 43.98, 33.53, 32.97.

3.10.11 Synthesis of 4-(2-chloroethyl)styrene (3.10) and 4-(3-chloropropyl)styrene (3.11)



In an oven-dried Schlenk flask, methyltriphenylphosphonium bromide (1.78 g, 5.0 mmol) was dispersed in anhydrous THF (20 mL), to which n-butyllithium in hexane (2.00 mL, 5.0 mmol) was added dropwise with stirring. Complete addition of n-butyllithium, afforded a clear orange solution. The solution was stirred for 15 minutes at room temperature before the dropwise addition of aldehyde **X** (0.84 g, 5.0 mmol), or aldehyde **X** (0.91 g, 5.0 mmol). The reaction mixture was stirred overnight at room temperature and then quenched with saturated aqueous NH_4Cl solution (10 mL). The product was extracted with DCM (3 x 20 mL), concentrated *in vacuo*, and passed through a short silica-gel column, eluting with ethyl acetate, to remove residual phosphorous species. The purified styrene was then dried over

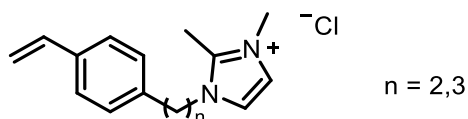
MgSO₄, filtered, and the volatiles were removed *in vacuo* to afford a colourless oil (**3.10**: 0.70 g, 84%, **3.11**: 0.79 g, 88%). Used without further purification.

3.10: ¹H NMR (400 MHz, CDCl₃) δ 7.38 (m, 2H), 7.19 (m, 2H), 6.72 (dd, *J* = 17.6, 10.9 Hz, 1H), 5.74 (d, *J* = 17.5 Hz, 1H), 5.25 (d, *J* = 11.0 Hz, 1H), 3.72 (t, *J* = 7.4 Hz, 2H), 3.07 (t, *J* = 7.4 Hz, 2H).

¹³C NMR (101 MHz, CDCl₃) δ 137.82, 136.58, 136.45, 129.14, 126.56, 113.82, 45.02, 39.01.

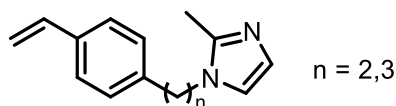
3.11: ¹H NMR (400 MHz, CDCl₃) δ 7.35 (m, 2H), 7.17 (m, 2H), 6.70 (dd, *J* = 17.6, 10.9 Hz, 1H), 5.72 (d, *J* = 17.6 Hz, 1H), 5.22 (d, *J* = 10.8 Hz, 1H), 3.53 (t, *J* = 6.5 Hz, 2H), 2.78 (t, *J* = 7.5 Hz, 2H), 2.08 (m, 2H). ¹³C NMR (101 MHz, CDCl₃) δ 140.53, 136.69, 135.74, 128.87, 126.49, 113.39, 44.32, 34.08, 32.61.

3.10.12 Attempted synthesis of 1,2-dimethyl-(2-(4-vinylphenyl)ethyl)-imidazolium chloride (3.12) and 1,2-dimethyl-(3-(4-vinylphenyl)propyl)-imidazolium chloride (3.13)



In an oven-dried Schlenk flask, added 4-(2-chloroethyl)styrene **3.10** (0.24 g, 1.44 mmol), or 4-(3-chloropropyl)styrene **3.11** (0.26 g, 1.44 mmol), and 1,2-dimethylimidazole (0.10 g, 1.08 mmol). The mixture was stirred neat at 80 °C overnight. A ¹H NMR spectrum of the resulting solid (at room temperature) taken in DMSO-d₆ revealed the formation of the desired product, in addition to 1,2-dimethylimidazolium chloride and the corresponding elimination product. However, in the case of 4-(3-chloropropyl)styrene **3.13**, no substitution at all was observed even after 72 hours of stirring. Washing of the solid with ethyl acetate removed much of the undesired alkene by-products, but the imidazolium salt persisted.

3.10.13 Synthesis of 2-methyl-(3-(4-vinylphenyl)ethyl)-imidazole (3.14) and 2-methyl-(3-(4-vinylphenyl)propyl)-imidazole (3.15)



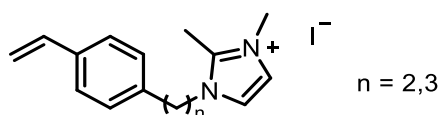
In an oven-dried Schlenk flask, NaH dispersed in mineral oil (0.04 g, 1.66 mmol) was added to anhydrous DMF (20 mL), and the suspension was cooled to 0 °C in an ice bath with stirring. Once cooled, 2-methylimidazole (0.11 g, 1.38 mmol) was added in portions resulting in effervescence and mild heat generation. After the exotherm had subsided, 4-(2-chloroethyl)styrene **3.10** (0.28 g, 1.66 mmol), or 4-(3-chloropropyl)styrene **3.11** (0.30 g, 1.66 mmol), dissolved in anhydrous DMF (5 mL) was added dropwise. The mixture was then heated

to 80 °C and stirred overnight. After cooling to room temperature, the mixture was quenched with the gradual addition of deionized water (50 mL), and the organics were extracted with ethyl acetate (4 x 20 mL). The imidazole product was protonated and extracted with 2 M HCl (2 x 25 mL) and the combined aqueous fractions were then washed with diethyl ether (2 x 20 mL). The aqueous phase was then treated with 2 M KOH until alkaline, and from this the product was extracted with diethyl ether (4 x 20 mL). The organic phase was then dried over MgSO₄, filtered, and the volatiles were removed *in vacuo* to afford a yellow oil (**3.14**: 0.22 g, 63%, **3.15**: 0.24 g, 77%).

3.14: ¹H NMR (400 MHz, DMSO) δ 7.37 (m, 2H), 7.10 (m, 2H), 7.00 (d, *J* = 1.3 Hz, 1H), 6.74 – 6.64 (m, 2H), 5.79 (d, *J* = 17.6 Hz, 1H), 5.21 (d, *J* = 11.0 Hz, 1H), 4.07 (t, *J* = 7.2 Hz, 2H), 2.94 (t, *J* = 7.2 Hz, 2H), 2.05 (s, 3H). **¹³C NMR (75 MHz, DMSO)** δ 143.65, 138.03, 136.38, 135.37, 129.06, 126.11, 119.28, 113.74, 46.41, 36.24, 12.40.

3.15: ¹H NMR (400 MHz, CDCl₃) δ 7.35 (m, 2H), 7.11 (m, 2H), 6.92 (d, *J* = 1.3 Hz, 1H), 6.81 (d, *J* = 1.3 Hz, 1H), 6.69 (dd, *J* = 17.6, 10.9 Hz, 1H), 5.72 (dd, *J* = 17.6, 0.9 Hz, 1H), 5.22 (dd, *J* = 10.9, 0.9 Hz, 1H), 3.82 (t, *J* = 7.2 Hz, 2H), 2.62 (t, *J* = 7.6 Hz, 2H), 2.32 (s, 3H), 2.06 (m, 2H). **¹³C NMR (101 MHz, CDCl₃)** δ 144.55, 140.18, 136.56, 135.90, 128.59, 127.38, 126.57, 119.04, 113.55, 45.35, 32.41, 31.97, 13.21.

3.10.14 Synthesis of 1,2-dimethyl-(3-(4-vinylphenyl)ethyl)-imidazolium iodide (3.16) and 1,2-dimethyl-(3-(4-vinylphenyl)propyl)-imidazolium iodide (3.17)



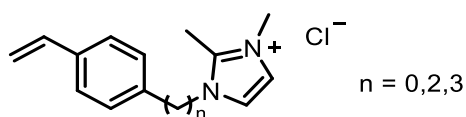
In an oven-dried Schlenk flask, 2-methyl-(3-(4-vinylphenyl)ethyl)-imidazole **3.14** (0.23 g, 1.04 mmol), or 2-methyl-(3-(4-vinylphenyl)propyl)-imidazole **3.15** (0.22 g, 1.04 mmol), was dissolved in anhydrous DCM (5 mL) to which methyl iodide (0.22 g, 1.56 mmol) was added dropwise with stirring. The mixture was stirred overnight at room temperature, after which time, 7 M methanolic ammonia (5 mL) was added and stirred for 15 minutes. The mixture was then concentrated *in vacuo* and the remaining residue was triturated with diethyl ether (3 x 20 mL) to afford a pale orange solid after drying (**3.16**: 0.29 g, 78%, **3.17**: 0.36 g, 94%).

Ethyl imidazolium iodide, 3.16: ¹H NMR (400 MHz, CDCl₃) δ 7.37 – 7.29 (m, 4H), 7.06 (m, 2H), 6.67 (dd, *J* = 17.6, 10.9 Hz, 1H), 5.74 (d, *J* = 17.6 Hz, 1H), 5.27 (d, *J* = 10.8 Hz, 1H), 4.45 (t, *J* = 6.6 Hz, 2H), 3.86 (s, 3H), 3.16 (t, *J* = 6.7 Hz, 2H), 2.45 (s, 3H). **¹³C NMR (101 MHz, CDCl₃)** δ

144.36, 137.09, 136.15, 135.66, 129.29, 126.97, 122.91, 121.48, 114.56, 50.69, 36.61, 36.10, 11.45.

Propyl imidazolium iodide, 3.17: ^1H NMR (400 MHz, CDCl_3) δ 7.39 – 7.32 (m, 4H), 7.16 (m, 2H), 6.68 (dd, J = 17.6, 10.9 Hz, 1H), 5.72 (d, J = 16.7 Hz, 1H), 5.23 (d, J = 10.8 Hz, 1H), 4.15 (t, J = 7.4 Hz, 2H), 3.91 (s, 3H), 2.76 (t, J = 7.3 Hz, 2H), 2.71 (s, 3H), 2.23 (m, 2H). ^{13}C NMR (176 MHz, CDCl_3) δ 144.15, 139.19, 136.42, 136.20, 128.73, 126.70, 122.96, 121.20, 113.89, 48.46, 36.74, 32.09, 30.88, 11.94.

3.10.15 Chloride Metathesis of Imidazolium Iodide Salts



A round bottom flask was charged with the appropriate imidazolium iodide salt which was dissolved in acetonitrile (0.02 M in imidazolium iodide). The flask was charged with NaCl (30 equivalents) before heating to 80 °C and stirring vigorously overnight. After cooling to room temperature, the solution was filtered and concentrated *in vacuo*. The product was then dissolved DCM, filtered to remove excess NaCl/NaI, and concentrated. This process was repeated until no solid was present on addition of DCM. The resulting chloride salts were afforded as off-white solids in quantitative yield.

3.10.16 General Procedure for Synthesis of ‘Robust’ Polymer Immobilized Ionic Liquid Supports 3.19a-d.

A screw-top Schlenk flask was charged with IL monomer (following chloride salt metathesis) and 4-aminostyrene, corresponding to an ionic liquid : amine ratio of 1 : 2. The monomers were dissolved in degassed ethanol so that the total concentration of monomer in solution corresponded to 0.2 M. Upon complete dissolution, the mixture was charged with azobis(2-methylpropionitrile) (5 mol%), before immediately degassing the solution via the freeze-thaw technique (6 cycles). The mixture was then stirred and heated at 80 °C. After 96 hours, the flask was charged with an additional portion of azobis(2-methylpropionitrile) (5 mol%), before degassing and stirring for a further 24 hours at 80 °C. After this time, the flask was allowed to cool to room temperature before precipitating the polymer by dropwise addition to stirring diethyl ether. The resulting precipitate was isolated by filtration, washed with diethyl ether, and dried *in vacuo* to afford orange powders.

3.10.17 General Procedure for Synthesis of PdCl₄-Loaded Functionalised Polymer Immobilized Ionic Liquid Precatalysts 3.20a-d.

A round-bottomed flask charged with palladium dichloride (2 mmol), NaCl (44 mmol) and water (10 mL) was heated to 80 °C for *ca.* 15 min to afford a clear red solution. A solution of the corresponding polymer (4 mmol) in 4:1 acetonitrile/water (10 mL) was subsequently added in one portion (Pd : polymer ratio of 1 : 2), and the resulting mixture allowed to stir overnight at room temperature, during which time a dark orange/brown precipitate formed. An orange solid was isolated from the suspension *via* centrifugation and was washed with deionized water (4 x 40 mL), ethanol (4 x 40 mL) and diethyl ether (2 x 20 mL) and dried under *vacuo* to afford fine orange powders.

Precatalyst	Yield / %	wt% Palladium	Palladium Loading / mmol·g ⁻¹
3.20a	30	2.14	0.20
3.20b	79	10.03	0.94
3.20c	47	3.70	0.35
3.20d	32	2.12	0.20

3.10.18 Synthesis of Highly Cross-Linked Polymer 3.21

A screw-top Schlenk flask was charged with IL cross-linker (**2.3**) and 4-aminostyrene, corresponding to an ionic liquid : amine ratio of 1 : 2. The monomers were dissolved in degassed ethanol so that the total concentration of monomer in solution corresponded to 0.2 M. Upon complete dissolution, the mixture was charged with azobis(2-methylpropionitrile) (5 mol%), before immediately degassing the solution via the freeze-thaw technique (6 cycles). The mixture was then stirred and heated at 80 °C. After 96 hours, the flask was charged with an additional portion of azobis(2- methylpropionitrile) (5 mol%), before degassing and stirring for a further 24 hours at 80 °C. After this time, the flask was allowed to cool to room temperature before precipitating the polymer by dropwise addition to stirring diethyl ether. The resulting precipitate was isolated by filtration, washed with diethyl ether, and dried *in vacuo* to afford an off-white powder.

3.10.19 Synthesis of PdCl₄-Loaded Precatalyst 3.22

A round-bottomed flask charged with palladium dichloride (5 mmol), NaCl (110 mmol) and water (20 mL) was heated to 80 °C for *ca.* 15 min to afford a clear red solution. A solution of

polymer **3.21** (10 mmol) in ethanol (20 mL) was subsequently added in one portion (Pd : polymer ratio of 1 : 2), and the resulting mixture allowed to stir overnight at room temperature, during which time an orange precipitate formed. An orange solid was isolated from the suspension *via* centrifugation and was washed with deionized water (4 x 40 mL), ethanol (4 x 40 mL) and diethyl ether (2 x 20 mL) and dried under vacuo to afford a fine yellow powder (84%). ICP-OES: 7.85 wt%_{Pd}, 0.74 mmol·g⁻¹.

3.10.20 Synthesis of PdI₄-Loaded Precatalyst

A round-bottomed flask charged with palladium diiodide (0.8 mmol), NaI (1.7 mmol) and water (20 mL) was heated to 80 °C and stirred. After *ca.* 1 hour a deep red solution had formed, though a notable amount of black solid persisted in the flask. The mixture was therefore charged with an additional portion of NaI (17 mmol) and stirred overnight at 80 °C. After this time, the mixture appeared more homogeneous, though some solid remained. The solution was thus passed through a syringe filter before dropwise addition of a solution of polymer **3.21** (10 mmol) in ethanol (20 mL) with stirring (Pd : polymer ratio of 1 : 2). The resulting mixture was allowed to stir overnight at room temperature, during which time the solution darkened, and a very fine precipitate formed. A dark red solid was isolated from the suspension *via* centrifugation and was washed with deionized water (4 x 40 mL), ethanol (4 x 40 mL) and diethyl ether (2 x 20 mL) and dried under vacuo to afford a fine maroon powder (56%). ICP-OES: 5.11 wt%_{Pd}, 0.48 mmol·g⁻¹.

3.10.21 DRIFTS Experiments

PdNP catalyst materials analysed by *in-situ* DRIFTS were generated under the conditions of catalysis, albeit in the absence of CO₂. The autoclave was charged with the appropriate PdCl₄-precatalyst (200 mg) which was dispersed in deionized water (20 mL). The autoclave was then sealed, purged with H₂ (5 bar) five times, before pressurizing to 20 bar with H₂, and heating to 100 °C. The mixture was then stirred for 2 hours, before cooling to room temperature and venting the reactive gas. Black solids were isolated by centrifugation of the reaction mixture, washing with water (2 x 10 mL) and ethanol (2 x 10 mL) before drying *in vacuo* to obtain fine black powders.

In-situ DRIFTS experiments were conducted using a Bruker Vertex 70 FTIR spectrometer. A ceramic crucible in the DRIFTS cell was packed with PdNP sample (*ca.* 25 mg) and pre-treated under a flow of Ar for 1 hour at 100 °C. An FTIR spectrum of the PdNP sample was taken under

Ar at 100 °C and was used as a background. Various gas feeds comprised of H₂/CO₂/H₂O mixtures were then introduced into the cell and were diluted with Ar to avoid signal saturation in the FTIR spectra. Gas switching was facilitated with a 4-way 2-port valve, and water was introduced using a saturator with Ar as a carrier gas. The recorded spectra were analysed using the OPUS software.

3.10.22 CO₂ TPD Experiments

Approximately 50 mg of sample was first pre-treated under a flow of He, with a flow rate of 50 cm³·min⁻¹, for 1 hour at 100 °C. The sample was then cooled to 40 °C and exposed to CO₂ (10 vol%, diluted with He) under the same flow rate for 1 hour. After this time, CO₂ was removed from the gas mixture, and the sample was heated to 160 °C with a temperature ramp rate of 10 °C·min⁻¹ and a He gas flow. The amount of CO₂ desorbed was quantified using a BELCAT II Catalyst Analyser with a thermal conductivity detector.

3.10.23 Deuterium Labelling Experiment

A stainless-steel autoclave was charged with precatalyst **3.22** (6 µmol Pd) and a solution of base (20 mL, 1 M) dissolved in D₂O. The autoclave was sealed and purged with a 1:1 mixture of H₂ : CO₂ gas (5 cycles), before pressurising to 40 bar at room temperature. The vessel was then heated to 100 °C and stirred mechanically for 2 hours. After this time, the autoclave was allowed to cool to room temperature before venting the gas. Two lots of reaction mixture were isolated (5 mL), to which one was charged with dimethylsulfoxide (0.1 M), while the other was charged with deuterated dimethylsulfoxide (0.1 M). The degree of ²H incorporation into the resulting formate was determined by comparing the ¹H and ²H NMR spectra of the DMSO and DMSO-d₆ charged solutions respectively, using the DMSO/DMSO-d₆ as internal standards to quantify formate/deuterated formate formation.

3.10.24 H/D Exchange of Potassium Formate in D₂O

A stainless-steel autoclave was charged with pre-reduced precatalyst **3.22** (6 µmol Pd, isolated after 2 hours of hydrogenation under 20 bar H₂), potassium formate (0.105 g, 1.25 mmol) and D₂O (20 mL). The autoclave was sealed and heated to 100 °C before stirring mechanically for 2 hours. After this time, the autoclave was allowed to cool to room temperature before venting any gas build-up. Two lots of reaction mixture were isolated (5 mL), to which one was charged with dimethylsulfoxide (0.1 M), while the other was charged with deuterated dimethylsulfoxide (0.1 M). The degree of ²H incorporation into the resulting

formate was determined by comparing the ^1H and ^2H NMR spectra of the DMSO and DMSO- d_6 charged solutions respectively, using the DMSO/DMSO- d_6 as internal standards to quantify formate/deuterated formate formation.

3.11 References

-
- ¹ Z. Zhang, L. Zhang, S. Yao, X. Song, W. Huang, M. J. Hülsey and N. Yan, *J. Catal.*, 2019, **376**, 57–67.
- ² R. Belgamwar, R. Verma, T. Das, S. Chakraborty, P. Sarawade and V. Polshettiwar, *J. Am. Chem. Soc.*, 2023, **145**, 8634–8646.
- ³ A. Jaleel, S. H. Kim, P. Natarajan, G. H. Gunasekar, K. Park, S. Yoon and K. D. Jung, *J. CO2 Util.*, 2020, **35**, 245–255.
- ⁴ S. Masuda, K. Mori, Y. Kuwahara and H. Yamashita, *J. Mater. Chem. A*, 2019, **7**, 16356–16363.
- ⁵ H. Zhong, M. Iguchi, F. Z. Song, M. Chatterjee, T. Ishizaka, I. Nagao, Q. Xu and H. Kawanami, *Sustain. Energy Fuels*, 2017, **1**, 1049–1055.
- ⁶ H. Zhong, M. Iguchi, M. Chatterjee, T. Ishizaka, M. Kitta, Q. Xu and H. Kawanami, *ACS Catal.*, 2018, **8**, 5355–5362.
- ⁷ T. Sasaki, *Curr. Opin. Green Sustain. Chem.*, 2022, **36**, 100633.
- ⁸ B. De Lange, M. H. Lambers-Verstappen, L. Schmieder-Van De Vondervoort, N. Sereinig, R. De Rijk, A. H. M. De Vries and J. G. De Vries, *Synlett*, 2006, **18**, 3105–3109.
- ⁹ C. Boyer, N. A. Corrigan, K. Jung, D. Nguyen, T. K. Nguyen, N. N. M. Adnan, S. Oliver, S. Shanmugam and J. Yeow, *Chem. Rev.*, 2016, **116**, 1803–1949.
- ¹⁰ J. P. Collman and M. Zhong, *Org. Lett.*, 2000, **2**, 1233–1236.
- ¹¹ S. Tanimoto, R. Oda, *Kogyo Kagaku Zasshi*, 1961, **69**, 932–935
- ¹² (a) B. Yang, X. H. Xu and F. L. Qing, *Org. Lett.*, 2015, **17**, 1906–1909. (b) B. N. Bhawal, J. C. Reisenbauer, C. Ehinger and B. Morandi, *J. Am. Chem. Soc.*, 2020, **142**, 10914–10920.
- ¹³ A. Burhenn, R. Bavaro and V. H. Gessner, *Catal. Sci. Technol.*, 2023, **13**, 3545–3550.
- ¹⁴ Y. Gao, Y. Ou and L. J. Gooßen, *Chem. Eur. J.*, 2019, **25**, 8709–8712.
- ¹⁵ S. Siankevich, Z. Fei, R. Scopelliti, P. G. Jessop, J. Zhang, N. Yan and P. J. Dyson, *ChemSusChem*, 2016, **9**, 2089–2096.
- ¹⁶ Y. Yang, J. Cai, G. Luo, X. Tong, Y. Su, Y. Jiang, Y. Liu, Y. Zheng, J. Zeng and C. Li, *Tetrahedron Lett.*, 2019, **60**, 1130–1134.
- ¹⁷ E. Duquesne, J. Habimana, P. Degée and P. Dubois, *Macromolecules*, 2005, **38**, 9999–10006.

-
- ¹⁸ (a) A. Bordet, G. Moos, C. Welsh, P. Licence, K. L. Luska and W. Leitner, *ACS Catal.*, 2020, **10**, 13904–13912. (b) S. Siankevich, S. Mozzettini, F. Bobbink, S. Ding, Z. Fei, N. Yan and P. J. Dyson, *Chempluschem*, 2018, **83**, 19–23.
- ¹⁹ A. Weilhard, M. I. Qadir, V. Sans and J. Dupont, *ACS Catal.*, 2018, **8**, 1628–1634.
- ²⁰ M. I. Burguete, E. García-Verdugo, I. Garcia-Villar, F. Gelat, P. Licence, S. V. Luis and V. Sans, *J. Catal.*, 2010, **269**, 150–160.
- ²¹ H. Bauer, *J. Org. Chem.*, 1961, **26**, 1649.
- ²² L. C. Song, Z. Q. Zhang, B. B. Liu, Y. P. Wang and S. Chen, *Chem. Commun.*, 2022, **58**, 12168–12171.
- ²³ M. Hernández-Juárez, J. López-Serrano, P. González-Herrero, N. Rendón, E. Álvarez, M. Paneque and A. Suárez, *Chem. Commun.*, 2018, **54**, 3843–3846.
- ²⁴ M. H. G. Precht, J. D. Scholten and J. Dupont, *J. Mol. Catal. A Chem.*, 2009, **313**, 74–78.
- ²⁵ Z. Zhang, Y. Xie, W. Li, S. Hu, J. Song, T. Jiang and B. Han, *Angew. Chemie - Int. Ed.*, 2008, **47**, 1127–1129.
- ²⁶ G. Kumar, J. R. Blackburn, R. G. Albridge, W. E. Moddeman and M. M. Jones, *Inorg. Chem.*, 1972, **11**, 296–300.
- ²⁷ A. D. Pournara, J. H. Tang, L. Yang, J. T. Liu, X. Y. Huang, M. L. Feng and M. G. Kanatzidis, *Chem. Mater.*, 2024, **36**, 3013–3021.
- ²⁸ A. A. Alharbi, C. Wills, C. Dixon, E. Arca, T. W. Chamberlain, A. Griffiths, S. M. Collins, K. Wu, H. Yan, R. A. Bourne, J. G. Knight and S. Doherty, *Catal. Letters*, 2024, DOI:10.1007/s10562-024-04725-8.
- ²⁹ M. E. King and M. L. Personick, *J. Mater. Chem. A*, 2018, **6**, 22179–22188.
- ³⁰ Q. Li, T. Huang, Z. Zhang, M. Xiao, H. Gai, Y. Zhou and H. Song, *Mol. Catal.*, 2021, **509**, 111644.
- ³¹ I. Ziccarelli, R. Mancuso, F. Giacalone, C. Calabrese, V. La Parola, A. De Salvo, N. Della Ca', M. Gruttadauria and B. Gabriele, *J. Catal.*, 2022, **413**, 1098–1110.
- ³² J. Burgess, *Metal Ions in Solution*, Ellis Horwood Ltd., Chichester, 1978.
- ³³ K. Zhao, L. Wang, M. Calizzi, E. Moioli and A. Züttel, *J. Phys. Chem. C*, 2018, **122**, 20888–20893.
- ³⁴ A. Danon, P. C. Stair and E. Weitz, *J. Phys. Chem. C*, 2011, **115**, 11540–11549.
- ³⁵ (a) F. Solymosi, *J. Mol. Catal.*, 1991, **65**, 337–358. (b) F. Solymosi and A. Berkó, *J. Catal.*, 1986, **101**, 458–472.
- ³⁶ T. Seki, K. Y. Chiang, C. C. Yu, X. Yu, M. Okuno, J. Hunger, Y. Nagata and M. Bonn, *J. Phys. Chem. Lett.*, 2020, **11**, 8459–8469.

-
- ³⁷ G. S. Foo, J. J. Lee, C. H. Chen, S. E. Hayes, C. Sievers and C. W. Jones, *ChemSusChem*, 2017, **10**, 266–276.
- ³⁸ X. Wang, H. Shi, J. H. Kwak and J. Szanyi, *ACS Catal.*, 2015, **5**, 6337–6349.
- ³⁹ A. Haghofer, D. Ferri, K. Föttinger and G. Rupprechter, *ACS Catal.*, 2012, **2**, 2305–2315.
- ⁴⁰ Q. Liu, X. Yang, L. Li, S. Miao, Y. Li, Y. Li, X. Wang, Y. Huang and T. Zhang, *Nat. Commun.*, 2017, **8**, 1–8.
- ⁴¹ B. L. Mojet, S. D. Ebbesen and L. Lefferts, *Chem. Soc. Rev.*, 2010, **39**, 4643–4655.
- ⁴² Y. Zhang, Y. Cai, Y. Guo, H. Wang, L. Wang, Y. Lou, Y. Guo, G. Lu and Y. Wang, *Catal. Sci. Technol.*, 2014, **4**, 3973–3980.
- ⁴³ F. C. Meunier, *J. Phys. Chem. C*, 2021, **125**, 21810–21823.
- ⁴⁴ J. Szanyi and J. H. Kwak, *Phys. Chem. Chem. Phys.*, 2014, **16**, 15126–15138.
- ⁴⁵ S. Masuda, K. Mori, Y. Kuwahara, C. Louis and H. Yamashita, *ACS Appl. Energy Mater.*, 2020, **3**, 5847–5855.
- ⁴⁶ B. Feng, Z. Zhang, J. Wang, D. Yang, Q. Li, Y. Liu, H. Gai, T. Huang and H. Song, *Fuel*, 2022, **325**, 124853.
- ⁴⁷ S. J. Louis Anandaraj, L. Kang, S. DeBeer, A. Bordet and W. Leitner, *Small*, 2023, **19**, 2206806.
- ⁴⁸ L. C. Lee, X. Xing and Y. Zhao, *ACS Appl. Mater. Interfaces*, 2017, **9**, 38436–38444.
- ⁴⁹ K. Park, G. H. Gunasekar, S. H. Kim, H. Park, S. Kim, K. Park, K. D. Jung and S. Yoon, *Green Chem.*, 2020, **22**, 1639–1649.
- ⁵⁰ H. Zhong, M. Iguchi, M. Chatterjee, T. Ishizaka, M. Kitta, Q. Xu and H. Kawanami, *ACS Catal.*, 2018, **8**, 5355–5362.
- ⁵¹ X. Shao, J. Xu, Y. Huang, X. Su, H. Duan, X. Wang and T. Zhang, *AIChE J.*, 2016, **62**, 2410–2418.
- ⁵² A. Cherevotan, B. Ray, A. Yadav, D. Bagchi, A. K. Singh, M. Riyaz, S. R. Churipard, V. Naral, K. Kaur, U. K. Gautam, C. P. Vinod and S. C. Peter, *J. Mater. Chem. A*, 2022, **10**, 18354–18362.
- ⁵³ K. Sordakis, A. F. Dalebrook and G. Laurenczy, *ChemCatChem*, 2015, **7**, 2332–2339.

Chapter 4

Ru Catalysed Selective Reduction of Nitroarenes to *N*-Phenylhydroxylamines

4.1 Introduction

Both the hydrogenation and transfer hydrogenation of nitrobenzene are used as benchmark reactions to test the efficacy of nanoparticle catalysts.¹ The reduction of nitrobenzene has a complex multi-step mechanism (**Figure 4.1**) and the complete reduction to aniline can proceed *via* two competing pathways: the direct route proceeds from nitrosobenzene to *N*-phenylhydroxylamine which is then reduced to aniline; alternatively, nitrosobenzene and *N*-phenylhydroxylamine can condense through the loss of water to form azoxybenzene, which is further reduced to azobenzene, then hydrazobenzene and finally aniline. While complete reduction of nitroarenes to anilines is widely reported,² examples of the selective formation of intermediates derived from the partial reduction of nitroarenes are less common. *N*-Arylhydroxylamines are important motifs in the synthesis of bioactive chemicals and natural products,^{3,4,5} as well as being reagents towards the synthesis of various fine chemicals.^{6,7} Hydroxylamines are also well-known to undergo 1,3-cycloaddition reactions to form isoxazolidines, which are scaffolds for further natural product synthesis.⁸ Under acidic

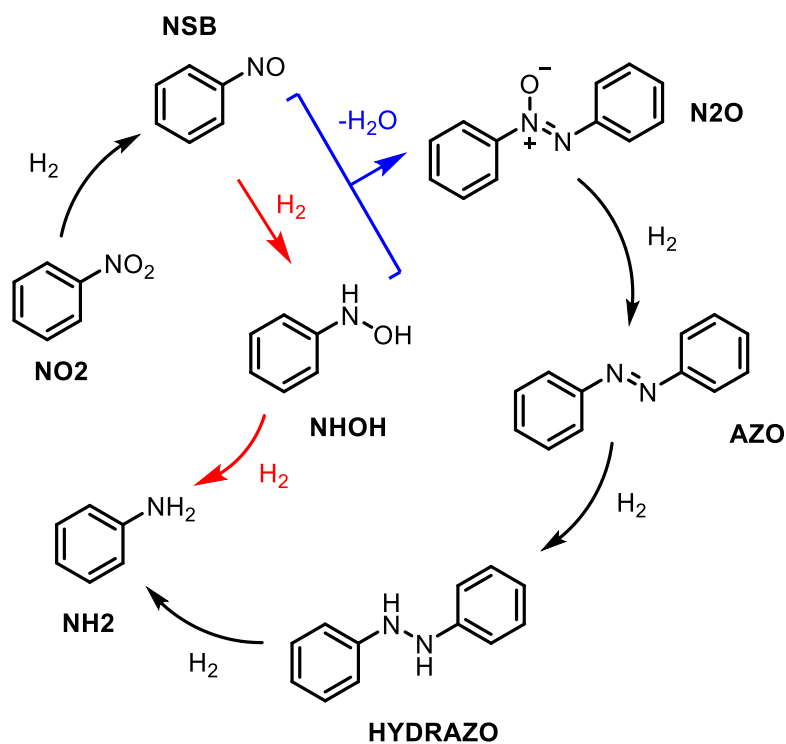


Figure 4.1 Proposed reaction mechanism for the direct reduction of nitrobenzene (NO₂) to aniline (NH₂) and the condensation pathway to aniline proceeding *via* the reaction of nitrosobenzene (NSB) with *N*-phenylhydroxylamine (NHOH) to form azoxybenzene (N₂O).

conditions, *N*-phenylhydroxylamine can also undergo a Bamberger rearrangement to form 4-aminophenol,⁹ which can then be acetylated to make paracetamol.

Current protocols for the synthesis of arylhydroxylamines include the reduction of nitrobenzene in the presence of stoichiometric amounts of Zn or Sb catalyst,^{5,10,11} as well as Pd catalysed coupling reactions.¹² More recently, supported metal nanoparticle catalysts have been employed to efficiently prepare arylhydroxylamines without the unsustainable use of stoichiometric metal reagents or stepwise processes that incur large volumes of solvent. For example, iridium¹³ nanoparticles immobilized on polystyrene catalyse the hydrazine mediated reduction of nitrobenzene in environmentally benign PEG-400 with high selectivity for *N*-phenylhydroxylamine. Unsupported platinum nanowires showed selectivity for *N*-phenylhydroxylamine after modification with ethylenediamine,¹⁴ while platinum nanoparticles have been supported on Amberlite resin,¹⁵ carbon,¹⁶ and silica,^{17,18} to afford arylhydroxylamines *via* both hydrogenations and transfer hydrogenations. Similar activity was also observed for palladium nanoclusters obtained from the reduction of Pd(OAc)₂ with NaBH₄.¹⁹ Over reduction to aniline in a continuous-flow packed bed system was avoided by passivating a Raney nickel catalyst with NH₃/DMSO to afford *N*-phenylhydroxylamine in high yield.³ While the above procedures provide routes to form arylhydroxylamine derivatives selectively, they all require either high temperature, high catalyst loading or a toxic solvent.

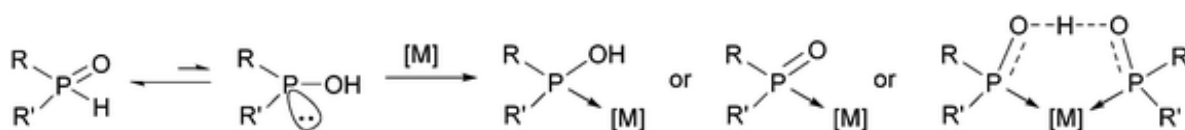
Endeavours by the Doherty group have afforded supported metal catalysts that are highly efficient and chemoselective for the transfer hydrogenation of nitrobenzene.²⁰ Initially, a styrene-based polymer support was used to immobilize imidazolium-type ionic liquids functionalised with a hydrophilic polyethyleneglycol (PEG) chain. Surface-bound PEG groups have been shown to effectively stabilize metal NPs against aggregation and can also improve the dispersion of the catalyst in polar solvents.²¹ However, the PEG-modified IL groups alone are not always sufficient to prevent aggregation,²² thus, the incorporation of an additional stabilizer such as a heteroatom donor is desirable.

To this end the Doherty group have functionalised the PIIL backbone with a diphenylphosphine group as they are well known as NP stabilizing agents,^{23,24} and can potentially modify the surface electronic structure of the metal.²⁵ The phosphine-functionalised ionic polymer, denoted PPh₂PEGPIIL, was used to stabilize palladium nanoparticles which catalysed the hydrogenation and transfer hydrogenation of nitroaromatics and *N*-heteroaromatics to the corresponding anilines under mild conditions

and low catalyst loading.²⁰ Following this, gold nanoparticles were also impregnated within PPh₂PEGPIIL using potassium tetrachloroaurate as precursor – the resulting catalyst, AuNP@PPh₂PEGPIIL showed a remarkable ability to selectively reduce nitrobenzene to aniline, *N*-phenylhydroxylamine and azoxybenzene simply by changing the solvent system or temperature.²⁶ However, following impregnation with KAuCl₄, we now believe that the phosphine undergoes oxidation, with concomitant reduction of Au^{III} to Au^I, an oversight that has potentially been made several times in the literature.^{27,28} A detailed follow-up investigation found that similar activities were obtained with AuNP generated from [AuCl₄][–] loaded PPh₂PEGPIIL (generating ‘AuCl’@OPPh₂PEGPIIL) as well as [AuCl₄][–] loaded onto pre-oxidised OPPh₂PEGPIIL.²⁹ In contrast, when the phosphine was preserved through impregnation using a Au^I precursor, AuCl(THT), the catalytic activity for nitrobenzene reduction vastly diminished, highlighting the essential role of the phosphine oxide in achieving high activity for this transformation.

Phosphine oxides are underexplored as ligands in NP catalysis, however, van Leeuwen and co-workers have demonstrated that secondary phosphine oxide decorated Au NPs are active catalysts for the hydrogenation of aldehydes.³⁰ The authors proposed that a surface bound phosphine oxide can assist the heterolytic cleavage of hydrogen, generating a surface bound hydride and a phosphine oxide stabilized proton, a mechanism that was later supported using DFT.³¹ A more recent report by the same group using MAS-NMR spectroscopy demonstrated three possible binding modes of secondary phosphine oxides at the surface of IrNPs: as a deprotonated phosphinito ligand (O=PR₂), as a neutral acid (R₂POH) and as a monoanionic bidentate H-bonded dimer (R₂P-O-H-O=PR₂), as shown in **Scheme 4.1**.³²

More recently, the Doherty group have employed phosphine oxide as a hemi-labile ligand to stabilize ruthenium nanoparticles in RuNP@OPPh₂PEGPIIL for the selective aqueous phase hydrogenation of arylketones, furfural and levulinic acid demonstrating high efficiency under mild conditions.³³ Following on from this report, this chapter expands the use of OPPh₂PEGPIIL as a catalyst support to investigate whether (a) our supported ruthenium nanoparticles could



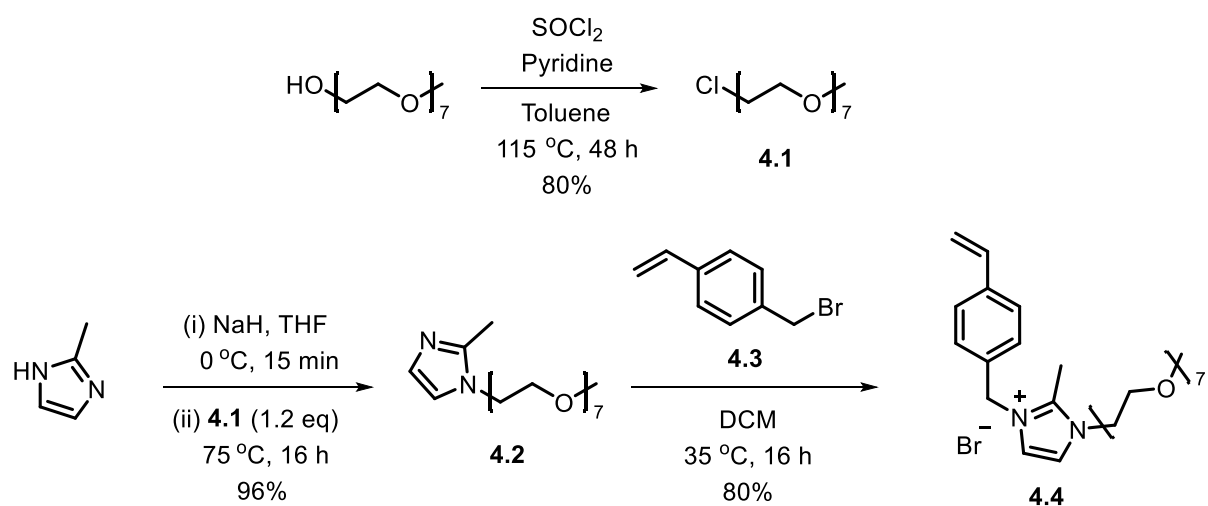
Scheme 4.1 Tautomeric forms of a secondary phosphine oxide and its potential binding modes to a metal surface, reproduced from Ref 32.

selectively form arylhydroxylamines from the transfer hydrogenation of nitroaromatics and (b) a similar solvent effect was apparent for ruthenium nanoparticles as was the case for their gold supported counterpart.²⁶

4.2 Synthesis and Characterisation of Monomer, Polymer and Catalyst Materials

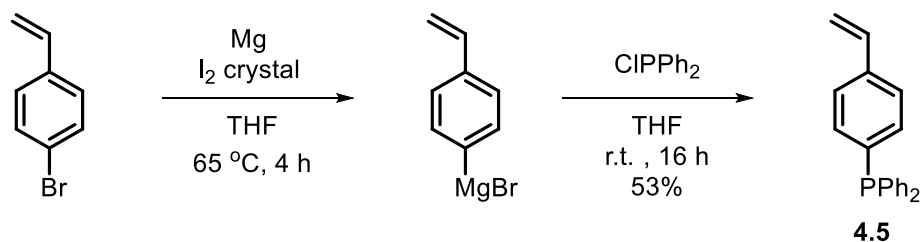
4.2.1 Synthesis of Monomers

PEG-functionalised imidazolium monomer, **4.4**, was prepared *via* a multi-step synthesis as described in **Scheme 4.2**. The reaction of methoxypolyethylene glycol (average molecular weight 350 g·mol⁻¹) with thionyl chloride, in the presence of base, afforded chloro-substituted PEG, **4.1**, after refluxing for 2 days. Precursor **4.1** then reacted readily with NaH-derived 2-methylimidazolate to afford **4.2** cleanly once the crude residue had been washed extensively with diethyl ether. Prepared *via* a Finkelstein reaction of 4-chloromethylstyrene with NaBr, 4-bromomethylstyrene **4.3** was substituted using PEG-imidazole **4.2** and the desired monomer **4.4** was isolated after washing the crude residue with diethyl ether.



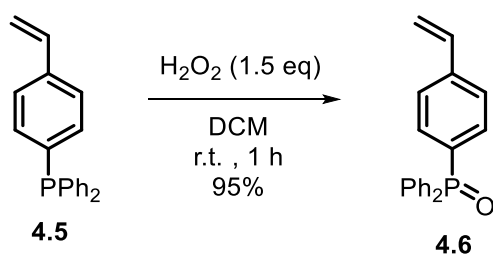
Scheme 4.2 Preparation of PEG-modified imidazolium bromide monomer, **4.4**.

Phosphine-oxide decorated styrene monomer **4.6** was prepared *via* the hydrogen peroxide-mediated oxidation of the corresponding phosphine. First, phosphine **4.5** was prepared through the reaction between 4-vinylphenylmagnesium bromide and chlorodiphenylphosphine as described in **Scheme 4.3**. 4-Bromostyrene was heated with Mg and a crystal of I₂ over 4 hours, before introducing chlorodiphenylphosphine at room temperature, allowing to stir overnight. The aqueous work-up was then conducted under an inert atmosphere to isolate phosphine **4.5** as a white powder in 53% yield.



Scheme 4.3 Preparation of phosphine-decorated styrene monomer, **4.5**, via Grignard reaction.

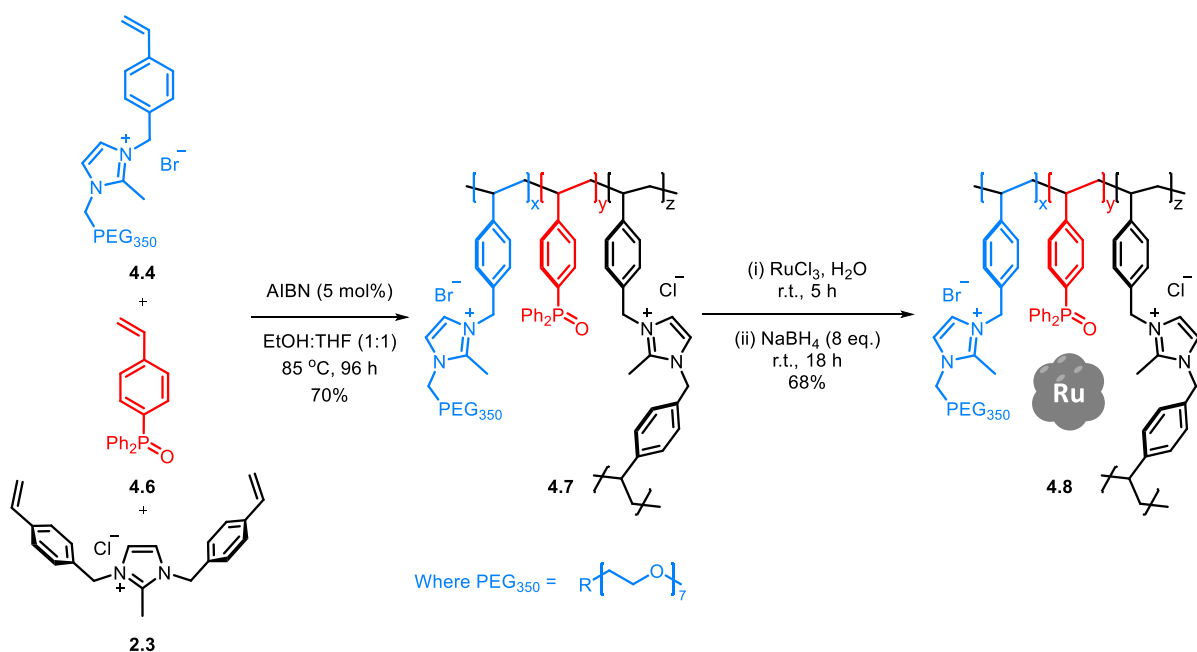
Subsequent treatment of **4.5** with hydrogen peroxide at room temperature afforded phosphine oxide monomer **4.6** in 95% yield after stirring for 1 hour. A comparison of the $^{31}\text{P}\{^1\text{H}\}$ NMR spectra following treatment with the oxidant revealed a complete shift of the phosphine peak at δ -5.87 ppm to δ 29.13 ppm, confirming full conversion to the oxide.



Scheme 4.4 Preparation of phosphine oxide decorated styrene monomer, **4.6**.

4.2.2 Synthesis and Characterisation of RuNP@OPPh₂PEGPIIL

Phosphine oxide decorated polyethylene glycol functionalised ionic liquid support (OPPh₂PEGPIIL), **4.7**, was prepared *via* an AIBN initiated radical polymerisation of the



Scheme 4.5 Synthesis of OPPh₂PEGPIIL, **4.7**, followed by the wet impregnation of RuCl₃ and subsequent reduction to RuNP@OPPh₂PEGPIIL, **4.8**. Where $x=1.86$, $y=1$, $z=0.14$

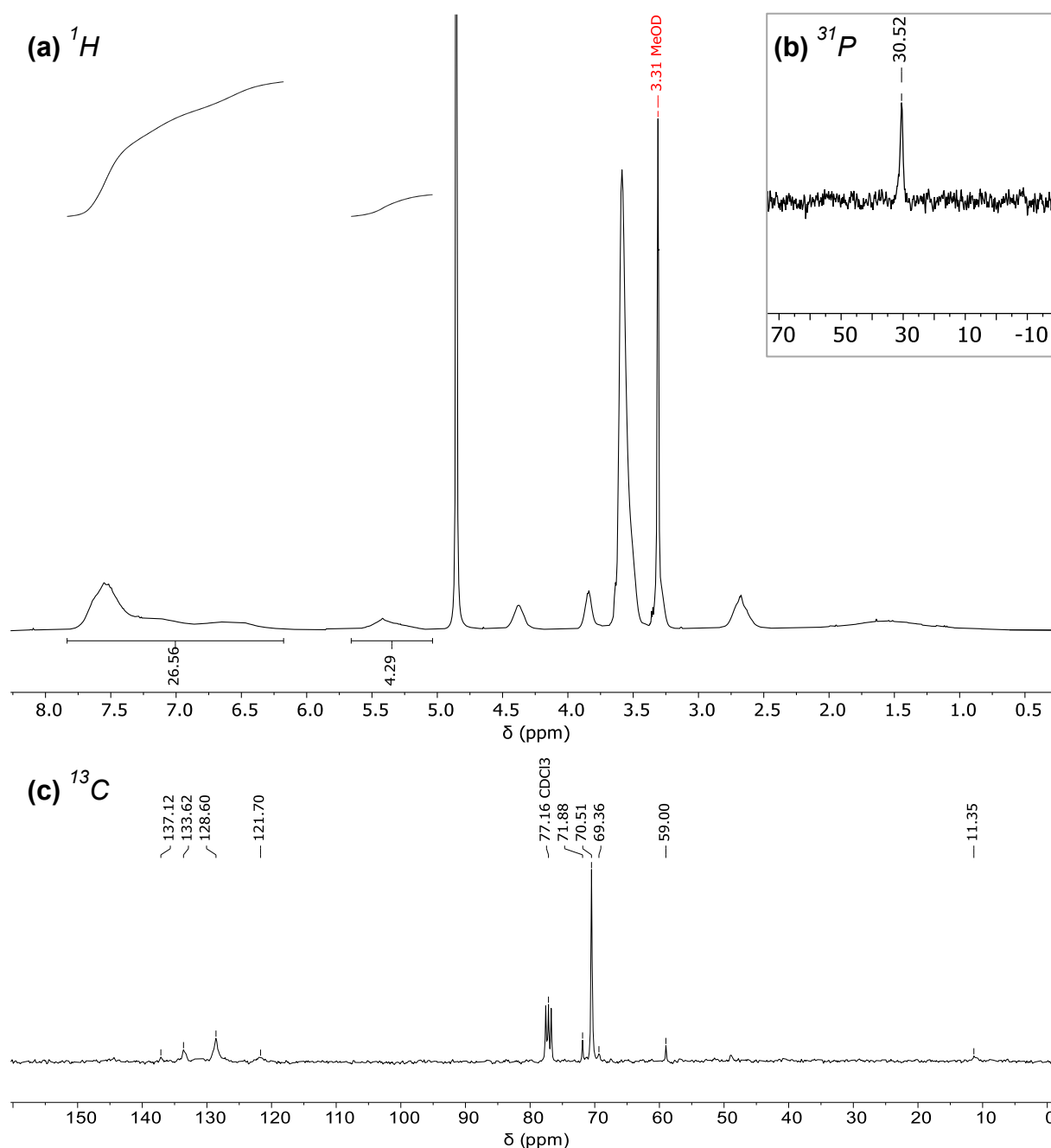


Figure 4.2 (a) ^1H (b) $^{31}\text{P}\{^1\text{H}\}$ (400 MHz, Methanol- d_4) and (c) $^{13}\text{C}\{^1\text{H}\}$ (400 MHz, CDCl_3) NMR spectra of polymer **4.7**.

associated monomers as described previously.³³ In a slight adaptation from the previous protocol,³³ phosphine **4.5** was oxidised prior to polymerisation, whereas in the prior report it was oxidised after polymerisation. After 4 days of stirring, the solution of polymer **4.7** was concentrated and the product isolated by precipitating the reaction mixture into diethyl ether, to afford a white powder after filtration. The absence of vinylic protons (*ca.* δ 6-5 ppm) in the ^1H NMR spectrum of **4.7** confirmed that full polymerisation of the monomers had taken place, and an intense signal at δ 3.59 ppm evidenced the incorporation of the PEG group. The relative incorporation of the IL units to the phosphine oxide monomer was confirmed to be *ca.* 2 : 1, as the integrals of the aromatic and benzylic protons were consistent with the theoretical

values (**Figure 4.2a**). The $^{31}\text{P}\{^1\text{H}\}$ NMR spectrum of **4.7** showed a single peak at 30.52 ppm (**Figure 4.2b**); this peak shifted upfield slightly to 26 ppm in the corresponding CP-MAS $^{31}\text{P}\{^1\text{H}\}$ NMR spectrum (**Appendix A.4.3**), though this is likely due to a combination of solvent effects and the lack of anisotropic tumbling. A solution state ^{13}C NMR spectrum showed broad aromatic signals, indicative of restricted motion of the polymer backbone; however, sharp signals at 71.88, 70.51 and 59.00 ppm corresponding to the PEG group are indicative of a degree of motion. This could suggest that the PEG groups cause the polymer to have a dendritic character with a hydrophobic polystyrene core while hydrophilic PEG groups point away from the polymer centre. Thermogravimetric analysis (TGA) was used to probe the thermal stability of polymer **4.7** – gratifyingly, decomposition was not observed until >250 °C, which is far in excess of temperatures required for liquid-phase catalysis (**Appendix A.4.4**). No notable drop in weight was measured from 0-200 °C suggesting that despite the hygroscopic PEG group, the material was largely solvent free; the 40% drop in weight from 250-350 °C is likely due to the loss of the aforementioned PEG groups. The smaller drop of *ca.* 25% from 400-500 °C can be attributed to the loss of imidazolium, as similar decomposition profiles are reported for benzylic-imidazolium polystyrene polymers prepared *via* RAFT polymerisation.³⁴ The final slow drop in weight from 550 °C is likely due to the decomposition of the polystyrene backbone.

In contrast to the palladium catalysts prepared in **Chapters 2 and 3**, and the PIIL supported Au catalysts reported by the Doherty group in 2019,²⁶ herein, ruthenium was not impregnated into the PIIL support *via* anion exchange. Salts containing a ruthenium-based anion are uncommon, and those that are available are difficult to handle; for instance, potassium ruthenate (K_2RuO_4) is a strong oxidant and unstable outside of basic media.³⁵ Ruthenium trichloride (RuCl_3), on the other hand, is easy to handle and relatively affordable when compared to other ruthenium precursors, and as such has been used extensively for RuNP synthesis. RuNP catalyst **4.8** was thus prepared *via* wet impregnation of **4.7** with an aqueous solution of ruthenium trichloride hydrate, as described in **Scheme 4.5**; after allowing sufficient time for the ruthenium to disperse through the polymer solution, the Ru(III) precursor was reduced to Ru(0) metal nanoparticles at room temperature overnight by stirring with 8 equivalents of sodium borohydride. The resulting black nanoparticles were isolated by centrifugation and washed extensively with water and ethanol to remove excess borohydride salt and residual polymer. In order to determine the loading of ruthenium, a portion of catalyst

4.8 was digested with an oxidative fusion of KNO_3/KOH to facilitate ICP-OES analysis, and the 1.83 wt% ruthenium determined corresponds to a metal loading of $0.18 \text{ mmol}\cdot\text{g}^{-1}$. Solid state CP-MAS $^{13}\text{C}\{^1\text{H}\}$ (**Appendix A.4.2**) and $^{31}\text{P}\{^1\text{H}\}$ NMR spectroscopy confirm incorporation of the phosphine oxide decorated polymer support; $^{13}\text{C}\{^1\text{H}\}$ NMR signals at 145 and 131 ppm correspond to the imidazolium and styrene rings, respectively, while the intense signal at 70 ppm can be assigned to the PEG-chain. Incorporation of the phosphine-oxide group was evidenced by a peak at 27 ppm in the solid state $^{31}\text{P}\{^1\text{H}\}$ NMR spectrum. Here, the CP-MAS $^{31}\text{P}\{^1\text{H}\}$ NMR spectrum showed asymmetry in the intensity of the satellite peaks, an observation also made for polymer **4.7**. While the peak separation is consistent with the MAS speed, the $^{31}\text{P}\{^1\text{H}\}$ NMR spectrum was also collected at 8 kHz and 5 kHz to confirm that there are no additional peaks present (**Figure 4.3**). Indeed, the oxide peak at 27 ppm does not appear to move, while the separation between the apparent spinning sidebands remains consistent with the changing MAS speed, without providing evidence of any additional peaks. TEM micrographs of freshly prepared **4.8** displayed ultrafine monodisperse nanoparticles (**Figure 4.4a**) and an average diameter of $2.3 \pm 0.5 \text{ nm}$ was estimated by measuring over 100 particles. From these images, the distance between two successive perpendicular planes of

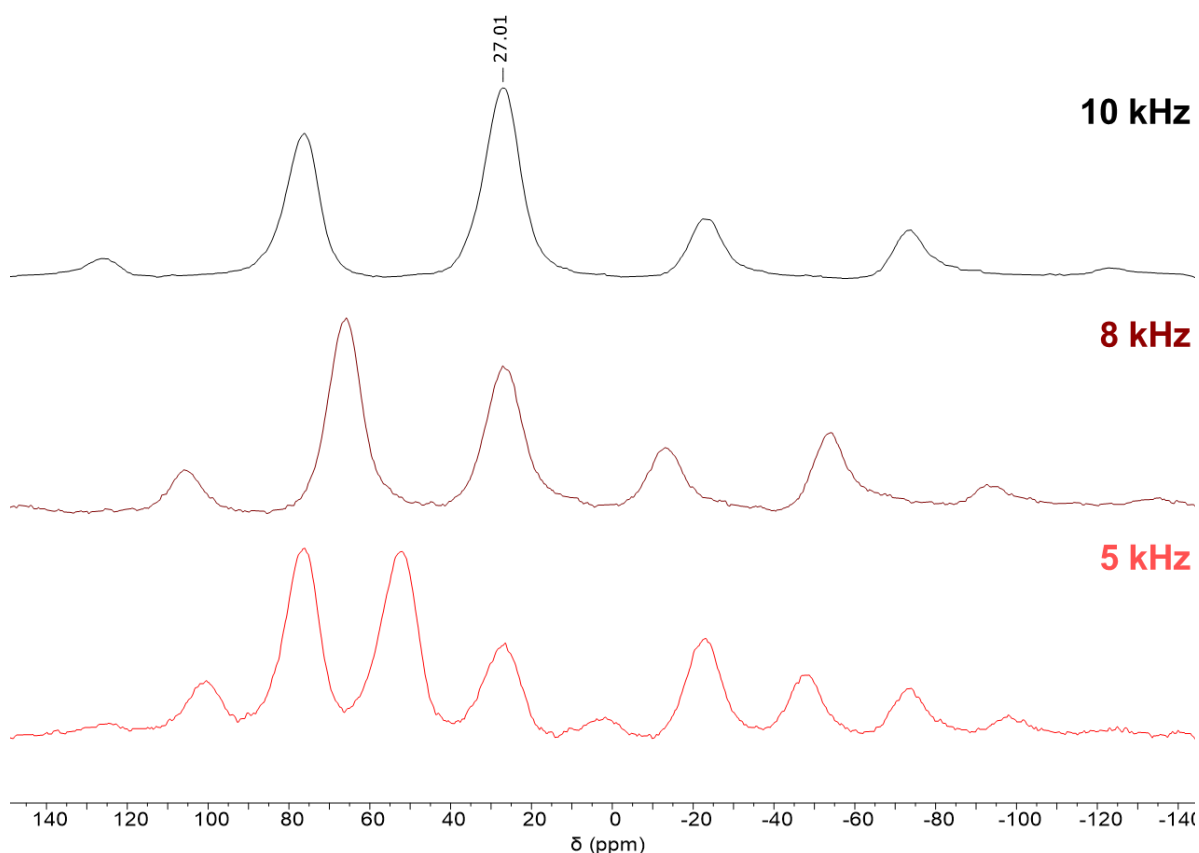


Figure 4.3 Solid state CP MAS $^{31}\text{P}\{^1\text{H}\}$ NMR spectra (500 MHz) of RuNP@OPPh₂PEGPIIL, **4.8**, ran with MAS speeds of 10, 8 and 5 kHz.

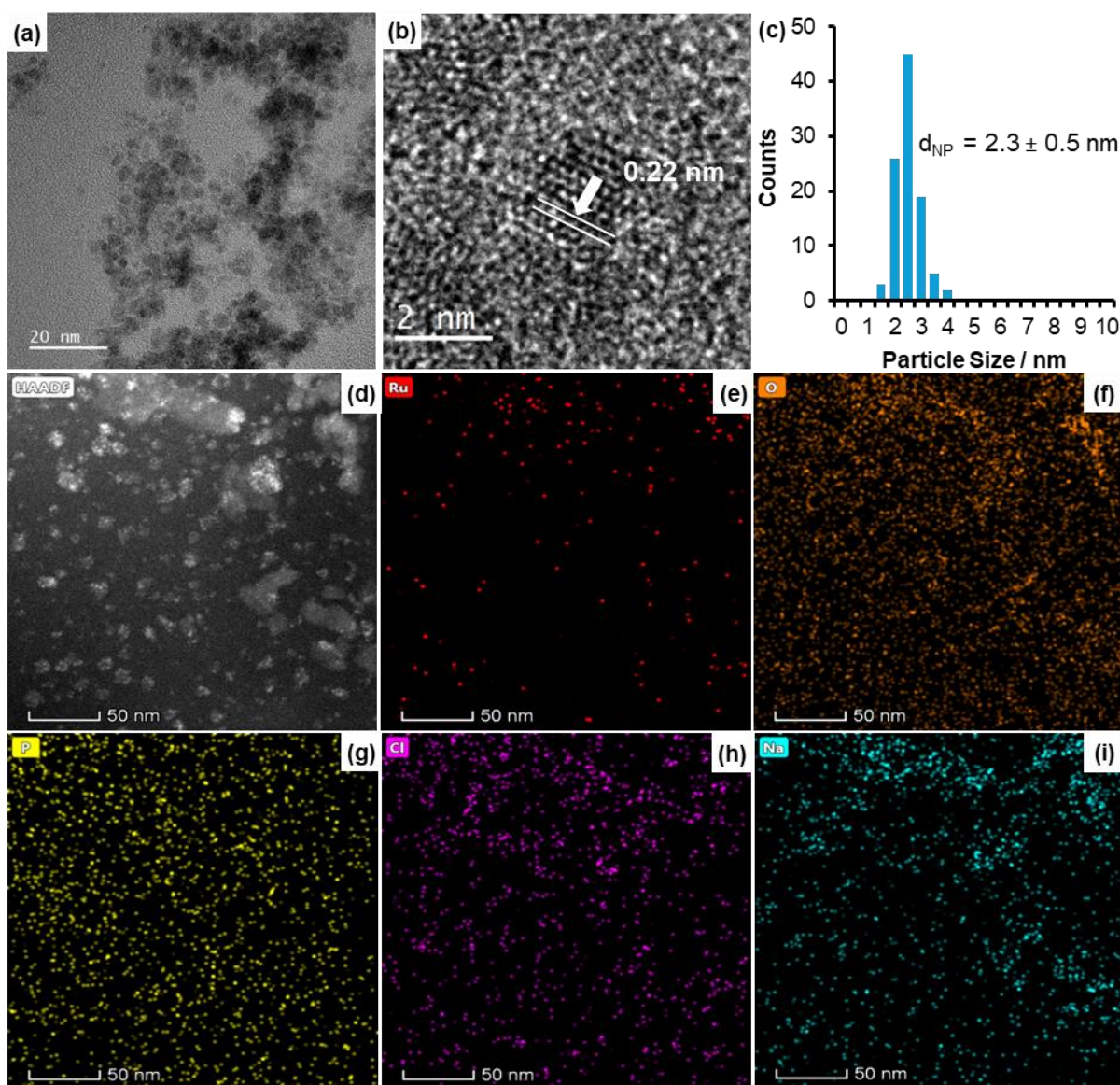


Figure 4.4 (a) TEM image of ruthenium nanoparticle catalyst **4.8**, with (b) lattice fringe *d*-spacing of a ruthenium nanoparticle. (c) Particle size distribution derived from counting >100 particles. (d) HAADF-STEM image and (e-i) corresponding EDX elemental mapping.

atoms (*d*-spacing) was measured and a *d*-spacing of 0.22 nm was found for **4.8**, characteristic of ruthenium oxide. A *d*-spacing of 0.2257 nm was assigned to RuO₂ (200) planes for RuNP@RuO₂ core-shell nanorods,³⁶ while *d*-spacings of 0.2060 nm and 0.2055 nm were assigned to metallic Ru (101) planes, as were spacings of 0.21 nm for RuNP/C-silica.³⁷ Energy-dispersive X-ray (EDX) maps for TEM images of **4.8**, such as those shown in **Figure 4.4e-i**, revealed that there is significant fouling of sodium, particularly in saturated areas of ruthenium, presumably deposited following reduction of RuCl₃ with NaBH₄, persisting despite extensive washing of the nanoparticles with water and ethanol following reduction. This also

implies the presence of spent borate salts that could also passivate the catalyst surface or obscure active sites.

The surface composition and electronic state of ruthenium in catalyst **4.8** was examined using X-ray photoelectron spectroscopy (XPS). Consistent with the low metal loading as determined by ICP-OES, there appeared to be a low concentration of surface ruthenium species, a finding that is supported by the apparent high dispersion of Ru in the EDX images shown in **Figure 4.4e**. The ruthenium 3d valence electrons appeared almost indistinguishable from the background of the XPS spectra, and moreover, there is considerable overlap between the Ru 3d electrons and those of carbon 1s (**Figure 4.5a**). For this reason, the Ru 3p electrons were analysed in order to establish the chemical state of the RuNP catalyst. Two peaks were identified at 461.6 and 464.1 eV, and both were fit with asymmetric line shapes, which are typical for the Ru 3p electrons.³⁸ When compared to the aliphatic C 1s peak, a BE separation ($\Delta E_{\text{Ru-C}}$) of 178.2 eV was found for the peak at 461.6 eV, which was consequently assigned to RuO_2 while the peak at 464.1 eV was therefore assigned to the RuO_2 satellite peak.^{38,39} Morgan has reported a comprehensive analysis of the XPS fitting for a range of ruthenium compounds; a $\Delta E_{\text{Ru-C}}$ of 177.9 eV was reported for the RuO_2 3p_{3/2} peak, while a $\Delta E_{\text{Ru-C}}$ of 180.8 eV was reported for the corresponding satellite, consistent with the 180.7 eV separation measured for catalyst **4.8**; the spectrum of **4.8** is unlikely to contain any unreduced RuCl_3 as Morgan reports a peak with a $\Delta E_{\text{Ru-C}}$ of 179.3 eV, while a peak assigned to metallic Ru appeared at lower binding energies with a $\Delta E_{\text{Ru-C}}$ of 176.4 eV.⁴⁰ Further analysis must be conducted to determine whether the RuO_2 identified at the surface is in fact a layer surrounding a metallic RuNP; depth profiling prior to XPS analysis may facilitate such an investigation, though the

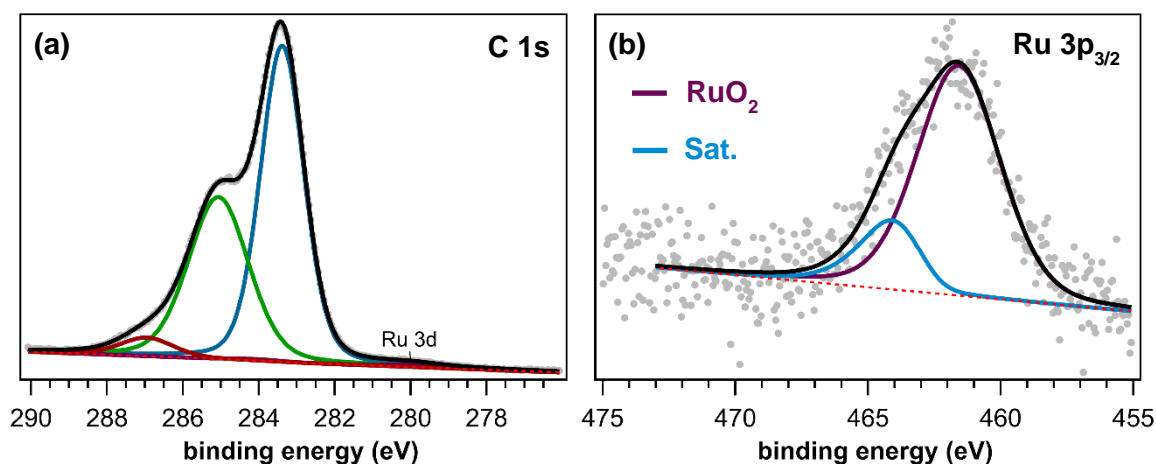


Figure 4.5 XPS analysis of the (a) C 1s and (b) Ru 3p_{3/2} regions of catalyst **4.8**. Black line = overall fitting; Red dotted line = background.

corresponding data should be treated with caution, as argon sputtering, and other methods, are known to result in reduction of the material during analysis.

4.3 Selective Reduction of Nitrobenzene to *N*-Phenylhydroxylamine

A preliminary experiment in water where nitrobenzene was reduced by 3 mole equivalents of hydrazine hydrate in the presence of a 0.1 mol% loading of **4.8** at 40 °C (**Table 4.1**, Entry 1) achieved 44% conversion of nitrobenzene after 1 hour, with 54% selectivity for *N*-phenylhydroxylamine. Even under mild conditions (**Table 4.1**, Entry 2), selectivity for *N*-phenylhydroxylamine was low at 66% conversion, therefore a solvent screen was undertaken. Fortunately, catalyst **4.8** was highly active for the hydrazine hydrate mediated reduction of nitrobenzene in organic solvents ethanol, methanol, tetrahydrofuran (**Table 4.1**, Entries 3-5) as well as highly selective for *N*-phenylhydroxylamine; the improved conversions compared to water is most probably a reflection of the poor solubility of nitrobenzene in water. Conversion of nitrobenzene was also high in toluene, though the selectivity for *N*-phenylhydroxylamine was much lower, favouring full conversion to aniline (**Table 4.1**, Entry 6). In this solvent screen, unrivalled selectivity for *N*-phenylhydroxylamine (98%) was obtained in ethanol with only trace quantities of azoxybenzene observed and no formation of aniline; this is in contrast to the result obtained by the corresponding AuNP catalyst, AuNP@OPPh₂PEGPIIL, which catalysed the NaBH₄ mediated reduction of nitrobenzene with 100% selectivity for azoxybenzene in ethanol, highlighting the significant influence of the metal on product selectivity during catalysis.^{26,29} Alcohols were also found to be the solvent of choice for arylhydroxylamine formation in the Pt/SiO₂ catalysed hydrogenation of nitroaromatics.¹⁷

There are a number of reports of heterogenous, and homogenous ruthenium catalysts that reduce nitroarenes to the corresponding anilines;^{16,41} however, examples of ruthenium based catalysts that facilitate the partial reduction of nitroarenes to arylhydroxylamines are sparse. Michaelis *et al.* report that ruthenium nanoparticles immobilized on polystyrene catalyse the hydrazine mediated transfer hydrogenation of nitrobenzene to *N*-phenylhydroxylamine.⁴² Interestingly, Doris and co-workers have reported that ruthenium nanoparticles supported on functionalized carbon nanotubes show analogous solvent dependent selectivity to AuNP@OPPh₂PEGPIIL as catalysts for the reduction of nitrobenzene;²⁶ however, in contrast to the AuNP catalyst which was completely selective for *N*-phenylhydroxylamine in water,²⁶ RuNP@CNT facilitated the complete hydrogenation to aniline in water, while the reaction in THF was highly selective for the partial reduction to hydroxylamine.⁴³

Table 4.1 Optimisation of reaction conditions for the selective reduction of nitrobenzene to *N*-phenylhydroxylamine.

Entry	Catalyst (mol%)	Reducing Agent	Solvent	Time / min	Temp. / °C	Conversion %	Selectivity %
1	4.8 (0.1)	N ₂ H ₄ .H ₂ O	H ₂ O	60	40	54	44
2	4.8 (0.1)	N ₂ H ₄ .H ₂ O	H ₂ O	120	25	66	76
3	4.8 (0.1)	N ₂ H ₄ .H ₂ O	EtOH	60	40	100	98
4	4.8 (0.1)	N ₂ H ₄ .H ₂ O	MeOH	60	40	89	94
5	4.8 (0.1)	N ₂ H ₄ .H ₂ O	THF	60	40	100	90
6	4.8 (0.1)	N ₂ H ₄ .H ₂ O	Toluene	60	40	97	56
7	4.8 (0.1)	N ₂ H ₄ .H ₂ O	EtOH	45	40	>99	99
8	4.8 (0.1)	NaBH ₄	EtOH	30	40	>99	85
9	4.8 (0.1)	Me ₂ NHBH ₃	EtOH	60	40	6	57
10	4.8 (0.1)	HCOOH	EtOH	60	40	0	N/A
11	4.8 (0.05)	N ₂ H ₄ .H ₂ O	EtOH	60	40	74	98
12	4.8 (0.2)	N ₂ H ₄ .H ₂ O	EtOH	60	40	100	94
13	4.8 (0.1)	N ₂ H ₄ .H ₂ O	EtOH	120	25	>99	99
14	AuNP@OPPh ₂ PEGPIIL (0.1)	N ₂ H ₄ .H ₂ O	EtOH	120	25	0	N/A
15	AuNP@OPPh ₂ PEGPIIL (0.1)	N ₂ H ₄ .H ₂ O	H ₂ O	120	25	1	44
16	PtNP@PPh ₂ PEGPIIL (0.1)	N ₂ H ₄ .H ₂ O	EtOH	120	25	56	91
17	PtNP@PPh ₂ PEGPIIL (0.1)	N ₂ H ₄ .H ₂ O	H ₂ O	120	25	75	89
18	Ru/C (0.1)	N ₂ H ₄ .H ₂ O	EtOH	120	25	20	77

Proceeding with ethanol as reaction medium, hydrazine hydrate was compared with other reducing agents for the transfer hydrogenation of nitrobenzene. Sodium borohydride was the closest competitor to hydrazine with 85% selectivity at >99% conversion (**Table 4.1**, Entries 7-8), though selectivity suffered due to over reduction to aniline. Dimethylamineborane and formic acid were also screened as reducing agents (**Table 4.1**, Entries 9-10), though dimethylamineborane showed low activity and a preference for complete reduction to aniline (63% sel.) while formic acid showed no activity at all. Hydrazine hydrate has also been shown to partially reduce nitroarenes to the corresponding arylhydroxylamine when catalysed by polystyrene supported iridium and ruthenium nanoparticles,^{13,42} Amberlite supported platinum nanoparticles,¹⁵ and ruthenium nanoparticles supported on carbon nanotubes,⁴³ however, full conversion to the corresponding arylamine was observed when the hydrazine

mediated reduction of nitrobenzene was catalysed by a homogenous dipyridinylanthridine ligated diruthenium complex.^{41c} Although hydrazine is known for its toxicity, the transfer hydrogenation by-product of dinitrogen is environmentally benign, and its activity and selectivity for *N*-phenylhydroxylamine formation was unmatched in this study, therefore, further reactions were conducted using hydrazine monohydrate as the reducing agent.

Reducing the catalyst loading to 0.05 mol% did not improve selectivity and instead reduced conversion, on the contrary, an increase in catalyst loading to 0.2 mol% reduced selectivity due to over reduction to aniline (**Table 4.1**, Entries 11-12). Reassuringly, selectivity improved upon reducing the reaction temperature, as >99% conversion was obtained with a 99% selectivity for *N*-phenylhydroxylamine after 120 minutes at 25 °C (**Table 4.1**, Entry 13). We have thus demonstrated that *N*-phenylhydroxylamine can be obtained in near quantitative yield under mild conditions, using ethanol as a sustainable solvent with low catalyst loading, and all further studies were conducted under these conditions.

As a result of its high selectivity for azoxybenzene in ethanol, AuNP@OPPh₂PEGPIIL was also screened for the hydrazine-mediated reduction of nitrobenzene, as the preliminary study investigated the reduction as a function of the hydrogen donor. Interestingly, despite its efficacy in the presence of NaBH₄, AuNP@OPPh₂PEGPIIL showed negligible activity in water and was completely inactive in ethanol for the hydrazine-mediated partial reduction of nitrobenzene, achieving only 1% conversion after 2 hours (**Table 4.1**, Entries 14-15). Similarly, the activity of PtNP@PPh₂PEGPIIL was compared against **4.8** under the optimum conditions described above, however, the PtNP system displayed poor selectivity, due to competitive reduction to aniline, in both ethanol and water at the same catalyst loading. A comparison between **4.8** and a commercial sample of Ru/C (Alfa Aesar, Ruthenium, 5% on activated carbon powder 11748) at 0.1 mol% catalyst loading was also undertaken, though the commercial sample achieved only 22% conversion of nitrobenzene in 2 hours, and 77% selectivity for *N*-phenylhydroxylamine. Competitive reduction to aniline was responsible for further reducing hydroxylamine selectivity to 67% at 50% conversion after 7 hours. The initial TOF of 163 mol_{Product}·mol_{Ru}⁻¹·h⁻¹ for Ru/C is significantly lower than the 982 mol_{Product}·mol_{Ru}⁻¹·h⁻¹ obtained with **4.8** at 40 °C.

A reaction time profile for the reduction of nitrobenzene (**Figure 4.6a**) under the optimum conditions described above, was conducted by quantifying the reaction products of a series of individual experiments conducted over different time intervals. *N*-phenylhydroxylamine

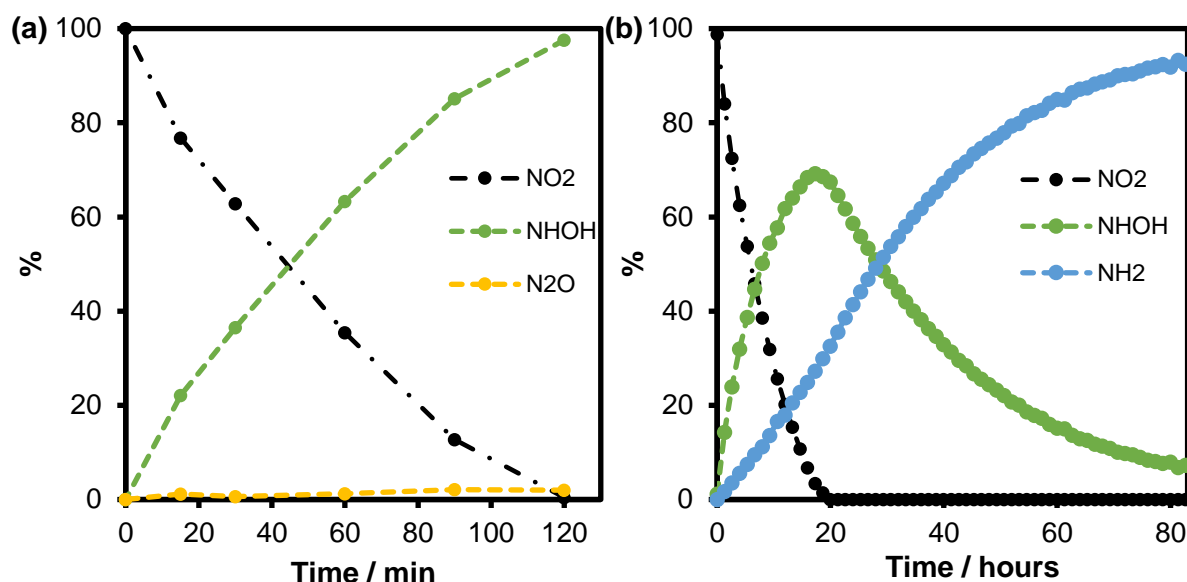


Figure 4.6 (a) Composition time profile of **4.8** catalysed nitrobenzene reduction to *N*-phenylhydroxylamine, conducted in batch reactions. (b) Composition time profile of **4.8** catalysed nitrobenzene reduction conducted in ethanol- d_6 within an NMR tube under an inert atmosphere – the sample was maintained at 40 °C, and ^1H NMR spectra were recorded periodically on a 700 MHz Bruker spectrometer over 4 days until near quantitative conversion to aniline was observed.

was shown to form quantitatively after 120 minutes with a residual amount of azoxybenzene (1%) as the only other observed product. The small amount of azoxybenzene formation most likely originated from the oxidation of the reaction mixture when in contact with air during work-up.

To confirm that the presence of azoxybenzene in the product mixture was derived from contact with air, rather than the condensation pathway to aniline, an *operando* ^1H NMR experiment was conducted to plot the formation of *N*-phenylhydroxylamine over time without exposing the sample to air (**Figure 4.6b**); indeed, no azoxybenzene was observed during *N*-phenylhydroxylamine formation nor in the subsequent aniline formation, demonstrating that aniline forms *via* direct reduction of *N*-phenylhydroxylamine rather than through a condensation pathway involving azoxybenzene as an intermediate. A large catalyst loading (2 mol%) was used for this experiment due to the difficulty of accurately measuring milligrams of catalyst for NMR scale reactions, thus, as a consequence of this we see rapid aniline formation in contrast to the results of the benchtop batch experiments which were conducted at a much lower catalyst loading.

In an initial failed attempt to acquire the data in **Figure 4.6b**, serendipitous hydrogen release caused the experiment to be exposed to air during acquisition within the NMR spectrometer.

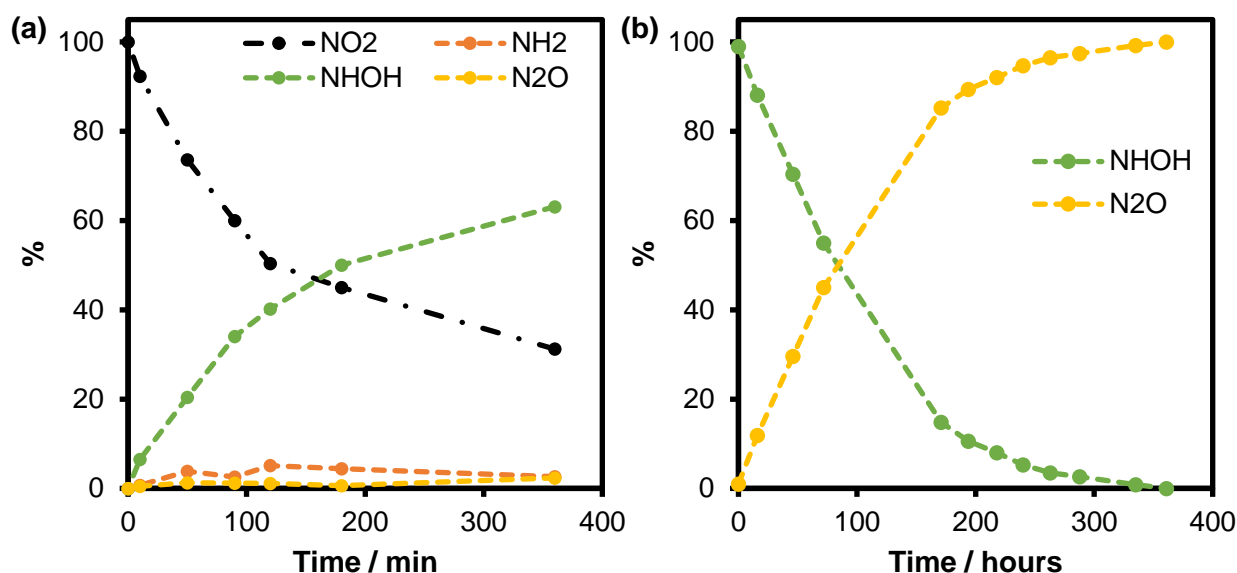


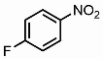
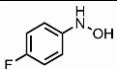
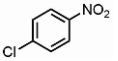
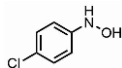
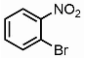
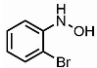
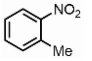
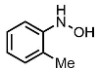
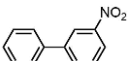
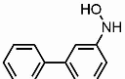
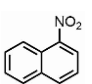
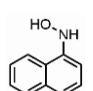
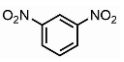
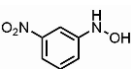
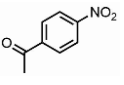
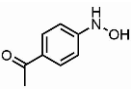
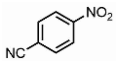
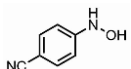
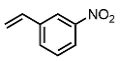
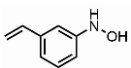
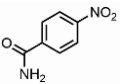
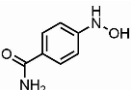
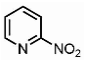
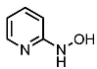
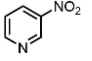
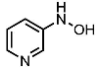
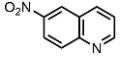
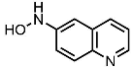
Figure 4.7 (a) Composition time profile of **4.8** catalysed nitrobenzene reduction to *N*-phenylhydroxylamine, conducted in air. (b) Decomposition profile of *N*-phenylhydroxylamine dissolved in ethanol stirring in air. Conversion to azoxybenzene was monitored by analysing aliquots by ¹H NMR spectroscopy.

Upon exposure to air, the formation of condensation intermediates, notably azobenzene and hydrazobenzene, was observed. To investigate this further, a series of batch experiments were conducted in air to understand its effect on the RuNP catalysed reaction pathway (**Figure 4.7a**). In contrast to the aforementioned results, azoxybenzene formation remained suppressed when the transfer hydrogenation of nitrobenzene was conducted in air, whereby *N*-phenylhydroxylamine prevailed as the dominant product with 92% selectivity at 79% conversion; however, it is worth noting that in air, the conversion of nitrobenzene was markedly slower – under an inert atmosphere, full conversion was obtained after 120 minutes, whereas in air, only 50% conversion of nitrobenzene was observed after the same time. We postulated that the negligible formation of azoxybenzene in air could be mass-transfer limited, and indeed, a decomposition profile of freshly prepared *N*-phenylhydroxylamine dissolved in ethanol revealed that full conversion to azoxybenzene was only observed after stirring in air at 25 °C for 360 hours (**Figure 4.7b**).

4.4 Substrate Screening

Applying the above optimum protocol, catalyst **4.8** was screened against a catalogue of nitroaromatic substrates (**Table 4.2**). All of the nitroaromatics were reduced over 2 hours to make a direct comparison of their reactivity against nitrobenzene; where necessary, reaction times were extended to obtain high conversion and selectivity for the *N*-arylhydroxylamine.

Table 4.2 Partial reduction of aromatic and heteroaromatic nitro compounds to the corresponding hydroxylamine or amine catalysed by **4.8**.

Entry	Product Ref.	Substrate	Product	Time (hours)	Conv. (%) ^b	Selectivity (%) ^c
1	4a			2 / 3	90 / 95	87 / 88
2	4b			2 / 3	73 / 98	95 / 94
3	4c			2 / 3	76 / 95	100 / 100
4	4d			2 / 2.5	79 / 95	92 / 95
5	4e			2 / 3	71 / 100	100 / 88
6	4f			2 / 18	31 / 100	100 / 93
7	4g			2	97	>99
8	4h			2 / 2.5	83 / 100	90 / 76
9	4i			2 / 1.5	100 / 99	84 / 91
10	4j			2 / 8	46 / 100	100 / 100
11	4k			2 / 3.5	82 / 96	94 / 93
12	4l			2 / 4	69 / 95	95 / 94
13	4m			2 / 3	66 / 100	89 / 86
14	4n			2 / 4	69 / 100	100 / 100

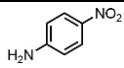
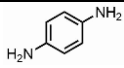
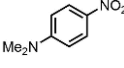
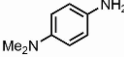
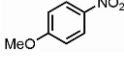
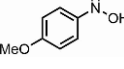
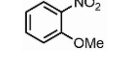
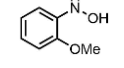
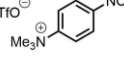
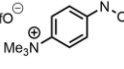
^a Reaction conditions: Conducted under nitrogen, 1 mmol substrate, 0.1 mol% **4.8**, 2 mL ethanol, 3 mmol hydrazine hydrate, 25 °C. ^b % Conversion determined by ¹H NMR spectroscopy using dioxane as the internal standard. Average of three runs. ^c Selectivity for the hydroxylamine = [% hydroxylamine / (% hydroxylamine + % azoxyarene + % azoarene + % aniline)] x 100%. ^d Selectivity for the corresponding arylamine.

Gratifyingly, catalyst **4.8** was shown to be versatile as it was highly chemoselective for the reduction of nitroarenes bearing potentially reactive functional groups, generating the corresponding hydroxylamines with high selectivity. Halogenated aromatics were well

tolerated with no hydrodehalogenation observed (**Table 4.2**, Entries 1-3); F-, Cl- and Br-arylhydroxylamines were all obtained in high yield, with the sterically demanding *ortho*-Br substituent failing to inhibit reaction, and instead obtained hydroxylamine **4c** with 100% selectivity and 95% conversion after 3 hours. Likewise, for the *ortho*-methyl substituted 2-nitrotoluene only a slight increase in reaction time was observed, compared to the benchmark nitrobenzene reaction, to obtain **4d** in 89% yield after 2.5 hours (**Table 4.2**, Entry 4). However, substrates with more steric bulk presented a greater challenge; 3-nitrobiphenyl reacted to form **4e** selectively but with 71% conversion after 2 hours, fortunately this increased to 100% after 3 hours to afford **4e** with 88% selectivity (**Table 4.2**, Entry 5). More notably, nitronaphthalene achieved only 31% conversion after 2 hours, though full conversion was achieved after 18 hours and **4f** was obtained in high yield (**Table 4.2**, Entry 6). A remarkable amount of functional group tolerance was achieved for nitro, acetyl, cyano, imido and vinyl groups as *N*-arylhydroxylamines **4g-j** were obtained in high yields (85-96%) whilst their reductively vulnerable functional groups remained unchanged (**Table 4.2**, Entries 7-10). The reduction of 4-nitrobenzamide to **4k** stands as an exception due to a small degree (4%) of amide hydrolysis to form the resulting carboxylic acid (**Table 4.2**, Entry 11), however, there was no evidence of hydrazone formation or ketone reduction in the isolated hydroxylamine **4h**, nor was there any evidence of alkene or nitrile hydrogenation in **4j** and **4i**, respectively. In contrast, Pt/Al₂O₃ is reported to show very little chemoselectivity in the hydrogenation of 3-nitrostyrene, though styrene hydrogenation was suppressed with decreasing NP size (hydrogenation of the nitro group on the other hand was insensitive to particle size).⁴⁴ Similarly, 1,3-dinitrobenzene was reduced to **4g** in 99% yield, with no hydrogenation of the second nitro group, demonstrating regioselectivity. Several nitro-substituted heteroaromatics, prominent motifs in pharmaceuticals and agrochemicals, were also screened and were found to afford the corresponding hydroxylamines **4l-n** in high yield although slightly longer reaction times were required to reach near quantitative conversion of substrate (**Table 4.2**, Entries 12-14).

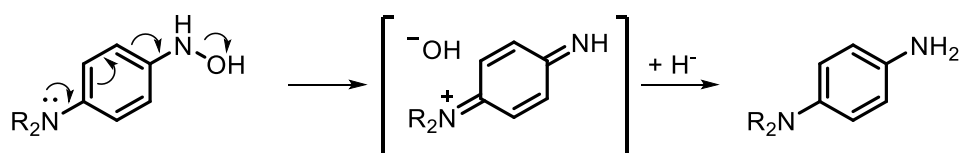
Interestingly, the reduction of electron rich substrates 4-nitroaniline and *N,N*-dimethyl-4-nitroaniline failed to afford the corresponding hydroxylamines – instead complete reduction to amines **4o** and **4p** was observed with no trace of the hydroxylamine partial reduction products either in the ¹H NMR spectra or by LC-MS analysis (**Table 4.3**, Entries 1-2). Michaelis *et al.* also reported a stark drop in selectivity when reducing electron rich substrates⁴² –

Table 4.3 Partial reduction of electron rich aromatic and heteroaromatic nitro compounds to the corresponding hydroxylamine or amine catalysed by **4.8**.

Entry	Product Ref.	Substrate	Product	Time (hours)	Conv. (%) ^b	Selectivity (%) ^c
1	4o			2 / 72	6 / 15	100 ^d / 100 ^d
2	4p			2 / 72	7 / 24	100 ^d / 100 ^d
3	4q			2 / 6	58 / 95	90 / 88
4	4r			2 / 5.5	50 / 97	98 / 94
5	4s			2 / 72	23 / 100	69 / 56

^a Reaction conditions: Conducted under nitrogen, 1 mmol substrate, 0.1 mol% **4.8**, 2 mL ethanol, 3 mmol hydrazine hydrate, 25 °C. ^b % Conversion determined by ¹H NMR spectroscopy using dioxane as the internal standard. Average of three runs. ^c Selectivity for the hydroxylamine = [% hydroxylamine / (% hydroxylamine + % azoxyarene + % azoarene + % aniline)] x 100%. ^d Selectivity for the arylamine.

although polystyrene supported ruthenium nanoparticles catalysed the hydrazine-mediated reduction of nitroarenes to selectively form arylhydroxlamines, they too reported a preference for complete reduction to amines for electron rich substrates such as anilines and anisoles. Likewise, Ma¹⁹ reported that reduction of 2-nitroanisole to the corresponding hydroxylamine was difficult when catalysed by *in-situ* generated PdNP, though this was attributed to the ‘bulky methoxy group at the ortho position’. Reassuringly we are able to selectively form hydroxylamine substituted anisoles in high yield, though 4-nitroanisole suffered from some over reduction to the corresponding aniline (13%) – 4-nitroanisole and 2-nitroanisole were reduced to hydroxylamines **4q** and **4r** with 88% and 94% selectivity after 6 hours and 5.5 hours, respectively (**Table 4.3**, Entries 3-4). The amine lone pair, which is a much more prominent electron donor than that of an –OR group, could explain the change in selectivity for amine functionalized nitroaromatics; it is feasible that following the formation of the para-aminoarylhydroxylamine, the amine lone pair eliminates OH⁻ to form a reactive 1,4-quinonediimine derived iminium ion, which is then readily reduced to 1,4-diaminobenzene, as described by **Scheme 4.6**.



Scheme 4.6 Proposed mechanism for 1,4-diaminobenzene formation via elimination of hydroxide from 4-aminoarylhydroxylamine to form imine intermediate.

To probe this hypothesis, we aimed to occupy the amine lone pair and eliminate its involvement *via* methylation of *N,N*-dimethyl-4-nitroaniline with methyl triflate to produce *N,N,N*-trimethyl-4-nitroanilinium triflate. The quarternized ammonium triflate ion was then reduced using the optimum protocol resulting in 69% selectivity for the corresponding hydroxylamine, **4s**, at 23% conversion after 2 hours (**Table 4.3**, Entry 5). This selectivity is maintained even with long reaction times – after 72 hours, 100% conversion was achieved with 56% selectivity for hydroxylamine.

4.5 Poisoning Study

All of the electron rich substrates screened above suffered from poor reactivity when compared to benchmark nitrobenzene, all requiring extended reaction times to reach near quantitative conversion (**4o-4r**). In fact, the amine substituted nitroaromatics failed to surpass 24% conversion even after 72 hours of reaction time. A passivation of reaction rate for nitroaromatics with para-substituted electron donating groups was also reported for gold nanoparticles supported on titania nanotubes,⁴⁵ as was the case for a homogenous molybdenum nitride catalyst,⁴⁶ whereas electron withdrawing groups were found to have enhanced hydrogenation rates for both catalysts. Zheng and colleagues investigated how interfacial electronic effects influenced the reactivity of ethylenediamine modified platinum wires for the reduction of nitrobenzene and superior reactivity was observed for electron deficient reagents over electron rich substrates.¹⁴ Zheng proposed that the near-fully occupied *d* orbitals of Pt favour coordination of electron deficient substrates through *d*- π^* interactions, whereas the coordination of an electron rich substrate forces electron density into antibonding orbitals.

In a similar vein, it is well known that electron rich heteroatoms coordinate strongly to metal nanoparticle surfaces and are frequently employed to provide stabilization and to modify the electrosteric properties of the material.⁴⁷ For this reason, we sought to investigate whether electron rich amines, such as those described above, are capable of saturating active sites and deactivating the catalyst towards substrate binding. First, catalyst **4.8** (0.1 mol%) was pre-

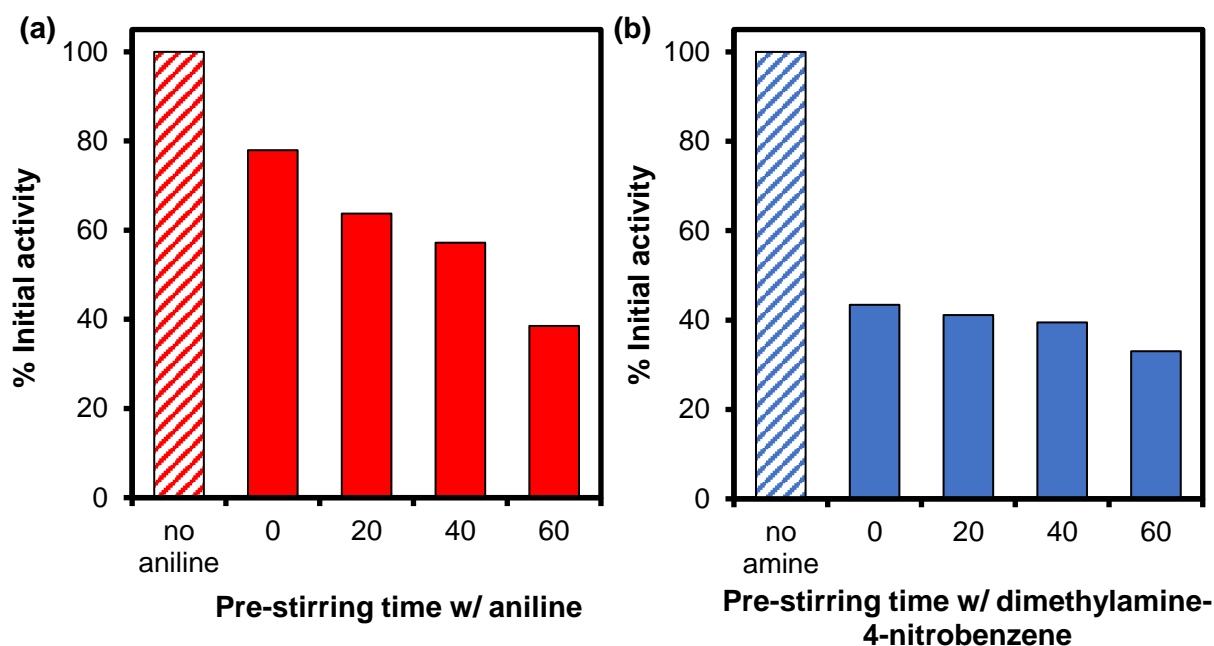


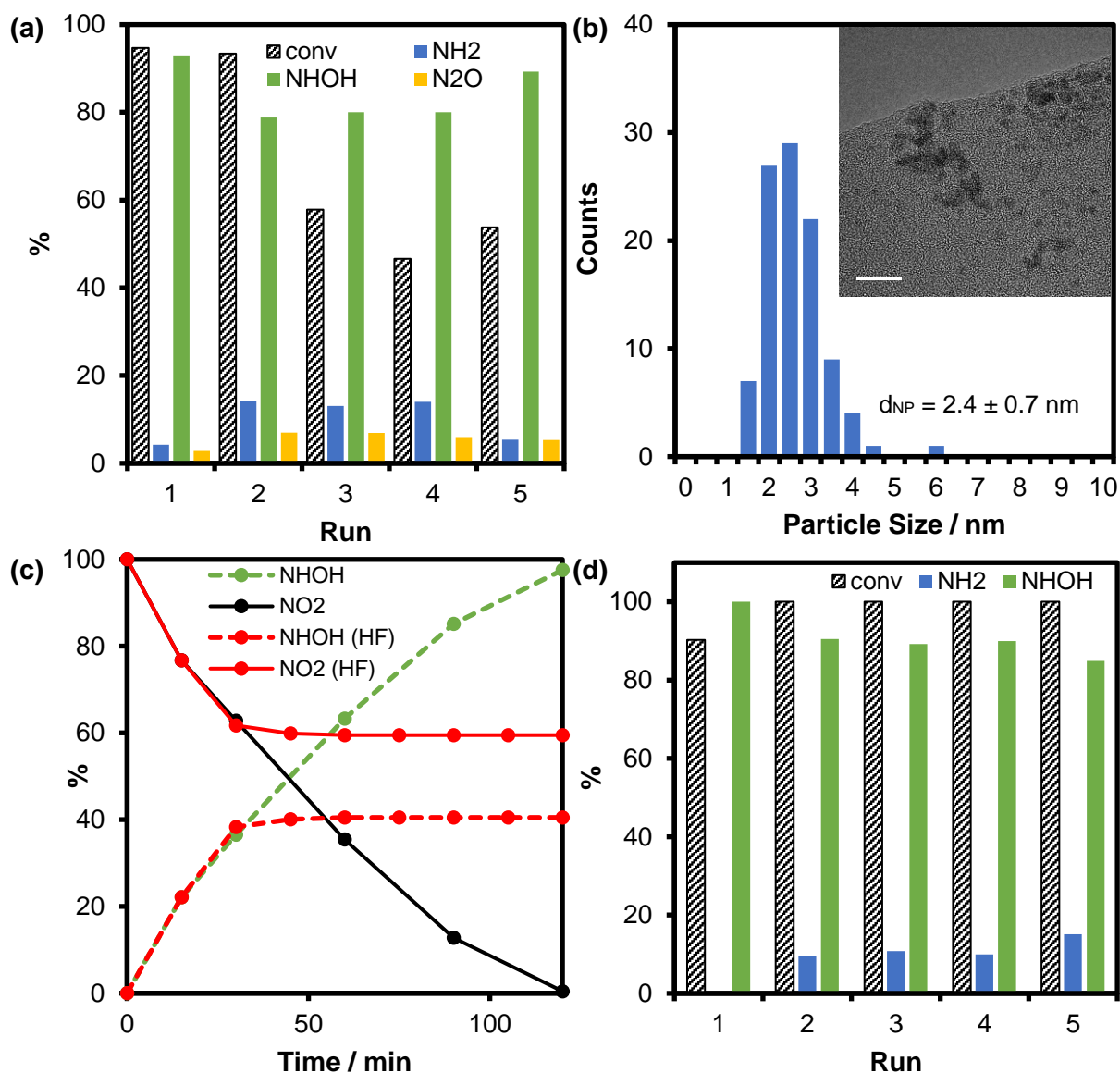
Figure 4.8 Poisoning study conducted by pre-stirring catalyst **4.8** for various amounts of time in the presence of (a) aniline and (b) *N,N*-dimethyl-4-nitrobenzene prior to the addition of hydrazine hydrate and nitrobenzene.

stirred in ethanol (2 mL) with aniline (1 mmol) for various stirring times (0, 20, 40 and 60 minutes). After pre-stirring with aniline, the reaction flask was charged with hydrazine hydrate (3 mmol) and nitrobenzene (1 mmol) as above and the contents were stirred for 120 minutes. It is apparent from **Figure 4.8a** that there is a clear decrease in the conversion of nitrobenzene with increasing pre-stirring time with aniline, indicative of a fouling effect between aniline and the RuNP catalyst. After 0 minutes of pre-stirring time (where hydrazine hydrate and nitrobenzene are added immediately after addition of aniline) there is a 10% drop in the activity of the catalyst when compared to the unpoisoned reaction (no aniline), and a further 62% drop in activity was observed after 60 minutes of pre-stirring with aniline.

To expand this study, catalyst **4.8** was also pre-stirred with *N,N*-dimethylamine-4-nitrobenzene due to its poor performance in the substrate screen. To our surprise, an instantaneous drop in activity was observed after 0 minutes of pre-stirring time (Figure 7b), and only a slight decrease in subsequent activities was observed with stirring times up to 60 minutes. Due to the poor solubility of the substrate, this effect could easily be attributed to a mass transfer limitation – attempts to dissolve the substrate with heating and sonication prior to addition of catalyst were unsuccessful, supporting this explanation.

4.6 Recycle and Reuse Studies

For a catalyst to be amenable for industrial application it must be suitable for use in continuous flow processes in addition to batch reactions. It is also of significance that catalysts are sustainable and can be reused many times, especially when they contain expensive, precious metals such as ruthenium. There are limitations and challenges to recovering and washing such small amounts of catalyst as used in the general procedure herein (typically 5.5 mg), so to reduce the error in this experiment the scale of the reaction was increased tenfold to minimise the effect of losses between runs. Thusly, catalyst **4.8** (55 mg, 0.1 mol%) was dispersed in ethanol (20 mL) and stirred with hydrazine monohydrate (1.46 mL, 30 mmol) for 2 minutes before adding nitrobenzene (1.03 mL, 10 mmol) under an inert atmosphere and stirring vigorously for 120 minutes at 25 °C. After extracting the reaction product with ethyl acetate, catalyst **4.8** was isolated by centrifugation and washed with water (20 mL) and ethanol (2 x 20 mL) to remove residual hydrazine and other organics. The catalyst was then returned to the reaction flask, and the above procedure repeated 4 more times, analysing each reaction mixture by ^1H NMR spectroscopy. Encouragingly, the initial scale-up experiment performed almost as well as under standard conditions, achieving 95% conversion of nitrobenzene and high selectivity for *N*-phenylhydroxylamine with only 4% reduction to aniline (**Figure 4.9a**). This is a promising result, demonstrating that similar results to those under the optimum conditions can be achieved at gram scale which is important for the process to be viable for scale-up. The second use of catalyst **4.8** when isolated in this fashion was also promising, maintaining a high conversion of 93% albeit with a drop in *N*-phenylhydroxylamine selectivity to 79%. However, subsequent runs returned poorer conversions, dropping to 58%, then 47% and increasing slightly to 54% on the fifth run. Selectivity for *N*-phenylhydroxylamine remained high reaching 80% on the third and fourth run and again increasing slightly to 89% on the fifth run.



reaction mixture was stirred at 25 °C for 90 minutes, and the composition analysed every 15 minutes by ^1H NMR spectroscopy. Post-filtration, conversion of nitrobenzene was terminated completely demonstrating that the catalyst is most likely heterogenous though a catalytically inactive leached species is possible (**Figure 4.9c**). As described above (**Figure 4.8**), fouling of the catalyst by electron rich aromatics can lead to catalyst deactivation, and though aniline is not a major product in this experiment, accumulation at the catalyst surface could lead to passivation over multiple uses. A similar rational could be applied to accumulation of *N*-phenylhydroxylamine at the catalyst surface across several uses as it is a comparatively strong donor, though similar poisoning studies as in **Figure 4.8** were not conducted.

Loss of catalyst between isolation and washings is a major source of error in a recycling experiment such as the one described above – even small losses of catalyst under the scale-up conditions used could have a large impact on the results of catalysis. To develop an idea of the ‘true’ nature of the catalyst during recycling, we conducted a reuse study, wherein the catalyst was not isolated between runs and instead was charged with a further 3 equivalents of hydrazine hydrate and a further 1 equivalent of nitrobenzene (1 mmol) after each run. As the product mixtures were not extracted, the reaction was conducted in the presence of 1,4-dioxane (1 mmol) as an internal standard, and aliquots were taken after every run to analyse the reaction mixture by ^1H NMR spectroscopy (**Figure 4.9d**). Following an initial increase in conversion between runs 1 and 2, conversion of nitrobenzene remained at 100% after each reuse, though one would expect that accumulation of hydrazine hydrate could contribute to a heightened conversion. Accumulation of hydrazine hydrate across runs would also explain the increasing formation of aniline, though despite this, selectivity for *N*-phenylhydroxylamine remained high across runs, dropping to 90% after run 2 but remaining at this level until run 5 where a slight drop to 85% was quantified – all together, a vast improvement from the results of the initial catalyst recycling experiment shown in **Figure 4.9a**.

4.7 Conclusion

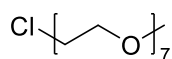
In conclusion, RuNP@OPPh₂PEGPIIL (**4.8**) was highly active and selective as a catalyst for *N*-phenylhydroxylamine in the hydrazine-mediated reduction of nitrobenzene, achieving a TOF of 492 h⁻¹ at 25 °C, which increased to 983 h⁻¹ when the reaction was conducted at 40 °C. Catalyst **4.8** was significantly more active than commercial Ru/C which achieved a TOF of only 78 h⁻¹ at 25 °C over the same time. Interestingly, despite the high activity reported for the AuNP@OPPh₂PEGPIIL catalysed NaBH₄-mediated reduction of nitroarenes,^{26,29} when the

same reactions were conducted using hydrazine hydrate as the reducing agent the catalyst appeared inactive. Similarly, PtNP@PPh₂PEGPIIL was also less active than **4.8**, as evidenced by the initial TOF of 252 h⁻¹ obtained over 2 hours. A high substrate tolerance was observed for reactions catalysed by **4.8**, and the catalyst remained selective for the *N*-arylhydroxylamine for a range of nitro-substituted heteroaromatics. Electron rich substrates proved to be more challenging, whereby 4-nitroaniline was reduced selectively to the *para*-phenylenediamine *via* a proposed quinone-like diimine intermediate.

It is unclear from this study whether or not the phosphine oxide influences the reactivity of the RuNP catalyst. A recent study by the Doherty group found that there was a slight improvement in both conversion and selectivity in the hydrogenation of acetophenone when the RuNP catalyst was modified with phosphine oxide and PEG functional groups.³³ The CP-MAS ³¹P{¹H} NMR spectra described herein did not show a significant difference between the free polymer (**4.7**) and the RuNP loaded composite (**4.8**), therefore computational modelling or perhaps *operando* surface studies would be useful to establish whether the phosphine oxide plays a cooperative role in activating or stabilizing the nitroaromatics and their intermediates.

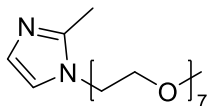
4.8 Experimental

4.8.1 Synthesis of 1-chloro-3,6,9,12,15,18,21-heptaodocose (4.1)



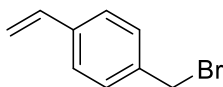
In an oven-dried Schlenk flask, PEG₃₅₀-monomethyl ether (14.0 g, 40 mmol) and pyridine (6.3 g, 80 mmol) were dissolved in anhydrous toluene (80 mL) with stirring. The mixture was heated to 80 °C and thionyl chloride (9.5 g, 80 mmol) was added dropwise, resulting in the evolution of HCl vapour. Gradually a pale-yellow solution formed which turned dark orange over time. The temperature was increased to 115 °C and the mixture was refluxed for 2 days. After cooling to room temperature, excess thionyl chloride was quenched with the addition of deionized water (10 mL). The organic phase was then extracted with toluene (4 x 50 mL) and washed with brine (50 mL). The combined organic fractions were dried over MgSO₄, filtered and the volatiles were removed *in vacuo*, to afford **4.1** as an amber oil (11.8 g, 80%). ¹H NMR (300 MHz, CDCl₃) δ 3.75 (t, *J* = 5.8 Hz, 2H), 3.70 – 3.60 (m, 25H), 3.58 – 3.52 (m, 2H), 3.38 (s, 3H). ¹³C NMR (75 MHz, CDCl₃) δ 72.09, 71.51, 70.74, 59.18, 42.85.

4.8.2 Synthesis of 1-(3,6,9,12,15,18,21-heptaodocosanyl)-2-methylimidazole (4.2)



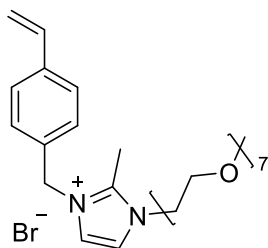
In an oven-dried Schlenk flask, NaH dispersed in mineral oil (1.0 g, 42 mmol) was washed with hexane (2 x 15 mL), before dispersing in anhydrous THF (70 mL) and cooling to 0 °C with stirring. 2-Methylimidazole (2.3 g, 28 mmol) was then added in portions, which resulted in an exothermic evolution of gas. Once the exotherm had subsided, **4.1** (11.8 g, 34 mmol) was added gradually with stirring, before heating to 75 °C and stirring overnight. After cooling to room temperature, the mixture was quenched with the addition of deionized water (2 mL). The solution was then concentrated *in vacuo* before washing the resulting residue with diethyl ether (5 x 50 mL). The ether washings were decanted, then the residue taken in DCM (40 mL), dried over MgSO₄, filtered, and the volatiles removed *in vacuo* to afford a brown oil (12.1 g, 96%). ¹H NMR (300 MHz, CDCl₃) δ 6.89 (s, 2H), 4.01 (t, *J* = 5.5 Hz, 2H), 3.71 (t, *J* = 5.5 Hz, 2H), 3.67 – 3.49 (m, 33H), 3.37 (s, 3H), 2.39 (s, 3H). ¹³C NMR (75 MHz, CDCl₃) δ 127.11, 119.69, 72.07, 70.71, 59.16, 46.17.

4.8.3 Synthesis of 4-bromomethylstyrene (4.3)



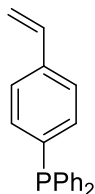
A round-bottom flask was charged with 4-chloromethylstyrene (11.5 g, 75 mmol) and NaBr (30.8 g, 300 mmol) which were dispersed in acetonitrile (80 mL), with stirring. The mixture was then heated to 80 °C and stirred overnight. After cooling to room temperature, the mixture was filtered, and the volatiles removed *in vacuo* to afford a yellow oil (13.68 g, 93%). A ¹H NMR spectrum of the product showed that the product comprised of 12% starting material (measured against singlet at 4.58 ppm). ¹H NMR (300 MHz, CDCl₃) δ 7.45 – 7.30 (m, 7H), 6.71 (dd, *J* = 17.6, 10.9 Hz, 2H), 5.77 (d, *J* = 17.6 Hz, 2H), 5.28 (d, *J* = 10.8 Hz, 2H), 4.50 (s, 3H).

4.8.4 Synthesis of 1-(3,6,9,12,15,18,21-heptaodocosanyl)-2-methyl-3-(4-vinylphenyl)-imidazolium bromide (4.4)



In a round-bottom flask, **4.2** (12.6 g, 28 mmol) was dissolved in DCM (100 mL), to which 4-bromomethylstyrene, **4.3** (6.6 g, 34 mmol) was added with stirring. The mixture was heated to 35 °C and stirred overnight, after which time the solvent was removed *in vacuo*. The resulting residue was washed with diethyl ether (4 x 100 mL). After decanting the ether, the product was redissolved in DCM (100 mL), dried over MgSO₄, filtered, and the volatiles were removed *in vacuo* to afford a dark amber oil (13.6 g, 80%). ¹H NMR (300 MHz, CDCl₃) δ 7.88 (s, 1H), 7.42 (d, *J* = 8.2 Hz, 3H), 7.26 (d, *J* = 8.0 Hz, 4H), 6.69 (dd, *J* = 17.6, 10.9 Hz, 1H), 5.76 (d, *J* = 17.6 Hz, 1H), 5.47 (s, 2H), 5.30 (d, *J* = 10.9 Hz, 1H), 4.53 (t, *J* = 4.7 Hz, 2H), 3.91 (t, *J* = 4.8 Hz, 2H), 3.69 – 3.46 (m, 25H), 3.40 – 3.29 (m, 3H), 2.80 (s, 3H). ¹³C NMR (75 MHz, CDCl₃) δ 145.08, 138.61, 135.89, 132.31, 128.46, 127.27, 122.58, 121.65, 115.50, 72.03, 70.66, 69.37, 59.14, 49.17.

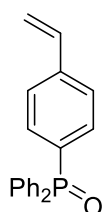
4.8.5 Synthesis of diphenyl(4-vinylphenyl)phosphine (4.5)



Special care should be taken to maintain an inert atmosphere over the course of this experiment. In a two-necked round-bottom flask, Mg turnings (2.4 g, 99 mmol) were suspended in anhydrous THF (30 mL) and stirred with a crystal of iodine for 15 minutes at room temperature. Separately, 4-bromostyrene (10.0 g, 55 mmol) was dissolved in anhydrous THF (25 mL) and then transferred dropwise to the stirring magnesium *via* cannula. With gentle heating, the reaction turned from orange to clear to dark green, at which point the reaction became exothermic. Once the reaction self-initiated, a reflux condenser was attached, and the reaction was stirred at 65 °C for 4 hours. After this time, the reaction mixture was cooled to 0 °C with an ice bath. Once cooled, the Grignard solution was added dropwise to a stirring solution of chlorodiphenylphosphine (9.0 g, 41 mmol) dissolved in anhydrous THF (25 mL) *via*

cannula. The solution was then allowed to stir at room temperature overnight, after which time the mixture was quenched by the addition of deionized water (150 mL), and the organic phase extracted with diethyl ether (5 x 100 mL). The combined organic fractions were dried over MgSO_4 , filtered, and the volatiles removed *in vacuo* to afford a white solid (6.3 g, 53%). A residual peak at 29 ppm in the $^{31}\text{P}\{^1\text{H}\}$ NMR spectrum confirmed the presence of *ca.* 1% oxide (proton decoupled experiments typically do not utilize the nuclear Overhauser effect (NOE) and thus cannot truly be used quantitatively; instead the estimation given here should be taken as an approximation of the level of purity). **^1H NMR (300 MHz, CDCl_3)** δ 7.33 – 7.27 (m, 3H), 7.25 – 7.16 (m, 6H), 6.63 (dd, J = 17.6, 10.9 Hz, 1H), 5.69 (d, J = 17.6 Hz, 1H), 5.20 (d, J = 9.9 Hz, 1H). **$^{31}\text{P}\{^1\text{H}\}$ NMR (121 MHz, CDCl_3)** δ -5.87.

4.8.6 Synthesis of diphenyl(4-vinylphenyl)phosphine oxide (4.6)



In a Schlenk flask, phosphine **4.5** (2.7 g, 9.3 mmol) was dissolved in DCM (30 mL), to which a solution of 30% aqueous hydrogen peroxide (0.5 g, 14 mmol) was added dropwise with stirring. The mixture was allowed to stir at room temperature for 1 hour, after which time the mixture was quenched with the addition of sodium sulphite (1.8 g, 14 mmol). The reaction mixture was washed with deionized water, before the organic phase was dried over MgSO_4 , filtered, and the volatiles were removed *in vacuo* to afford **4.6** as a white solid (2.7 g, 95%). **^1H NMR (300 MHz, CDCl_3)** δ 7.74 – 7.39 (m, 14H), 6.73 (dd, J = 17.6, 10.9 Hz, 1H), 5.85 (d, J = 17.6 Hz, 1H), 5.37 (d, J = 10.9 Hz, 1H). **$^{31}\text{P}\{^1\text{H}\}$ NMR (121 MHz, CDCl_3)** δ 29.13.

4.8.7 Synthesis of Polymer OPPh₂PEGPIIL (4.7)

A screw-top Schlenk flask was charged with PEG-IL monomer **4.4** (17.4 mmol), phosphine oxide **4.6** (9.4 mmol), 2-methyl-1,3- bis(4-vinylbenzyl)-imidazolium chloride **2.3** (1.3 mmol) corresponding to an ionic liquid : phosphine oxide : crosslinker ratio of 1.86 : 1 : 0.14). Upon complete dissolution of the monomers in 2:1 THF/ethanol (with a total monomer concentration of 0.2 M), the mixture was charged with azobis(2-methylpropionitrile) (5 mol%), before immediately degassing the solution via the freeze-thaw technique (6 cycles). The mixture was then stirred and heated at 80 °C. After 96 hours, the flask was charged with an additional portion of azobis(2- methylpropionitrile) (5 mol%), before degassing and stirring for

a further 24 hours at 80 °C. After this time, the flask was allowed to cool to room temperature before precipitating the polymer by dropwise addition to stirring diethyl ether. The resulting precipitate was isolated by filtration, washed with diethyl ether, and dried *in vacuo* to afford a pale-yellow powder (9.6 g, 70%). Note that the polymer was highly hygroscopic and even short exposure to air resulted in the powder becoming sticky and difficult to handle.

4.8.8 Synthesis of RuNP@O=PPh₂-PEGPIILS (4.8)

A round bottom flask was charged with **4.7** (4.0 g, 2.7 mmol) and ethanol (55 mL). To this, a solution of RuCl₃·3H₂O (0.6 g, 2.7 mmol) in deionized water (20 mL) was added in a single portion and the resulting mixture stirred vigorously for 5 h at room temperature. After this time, an aqueous solution of NaBH₄ (0.8 g, 21.4 mmol in 10 mL of water) was added dropwise and the suspension stirred for an additional 18 hours at room temperature before concentrating to near dryness *in vacuo*. The crude black solid was triturated with cold acetone (2 x 100 mL), washed with water (100 mL) and ethanol (2 x 40 mL) and the resulting black solid was recovered from the washings via centrifugation followed by filtration through a frit. The final product was washed with ether until a granular black solid was obtained. The solid was then dried *in vacuo* to afford a fine black powder (3.3 g, 79%). ICP-OES data: 1.83 wt% ruthenium and a ruthenium loading of 0.18 mmol·g⁻¹.

4.8.9 General Procedure for Reduction of Nitroarenes to Arylhydroxylamines

Under an inert atmosphere, an oven-dried Schlenk flask was charged with **4.8** (5.6 mg, 0.1 mol%), hydrazine monohydrate (0.15 mL, 3 mmol) and anhydrous ethanol (2 mL). After allowing the resulting suspension to stir for 5 minutes, nitroarene (1 mmol) was added and the mixture stirred at 25 °C for the appropriate time. The reaction mixture was then diluted by addition of deionized water (5 mL), and the product extracted with ethyl acetate (3 x 5 mL). The organic fractions were collected, and the solvent was removed under reduced pressure to obtain the product. The residue was analysed by ¹H NMR spectroscopy using 1,4-dioxane as internal standard to quantify the composition of starting material and products and determine the selectivity.

4.8.10 General Procedure for Reduction of Nitroarenes to Arylamines

Under an inert atmosphere, an oven-dried Schlenk flask was charged with **4.8** (5.6 mg, 0.1 mol%), hydrazine monohydrate (0.15 mL, 3 mmol) and anhydrous ethanol (2 mL). After allowing the resulting suspension to stir for 5 minutes, nitroarene (1 mmol) was added and the mixture stirred at 60 °C for the appropriate time. The reaction mixture was then diluted

with deionized water (5 mL), and the product extracted with ethyl acetate (3 x 5 mL). The organic fractions were collected, and the solvent removed under reduced pressure to yield the product. The residue was analysed by ^1H NMR spectroscopy using 1,4-dioxane as internal standard to quantify the composition of starting material and products and determine the selectivity.

4.8.11 Procedure for the Hot Filtration Study

Nitrobenzene (0.103 mL, 1.0 mmol) was reduced to *N*-phenylhydroxylamine at 25 °C following the general procedure described above. After 30 minutes the reaction mixture was filtered through a 0.45-micron syringe filter into a clean Schlenk flask under an inert atmosphere. The filtered reaction mixture was then stirred at 25 °C for a further 90 minutes and the progress of the reaction monitored as a function of time by removing aliquots every 15 min for analysis by NMR spectroscopy.

4.8.12 Procedure for the Catalyst Recycle Study

Nitrobenzene (0.103 mL, 1.0 mmol) was reduced to *N*-phenylhydroxylamine at 25 °C following the general protocol above, monitoring the progress of the reaction by ^1H NMR spectroscopy. Upon complete consumption of nitrobenzene, the catalyst was isolated by centrifugation and washes with ethanol (2 x 10 mL) and water (10 mL) prior to reuse. Following the 5th run using the same catalyst material, the catalyst was isolated, washed with water (2 x 10 mL) and ethyl acetate (2 x 10 mL) and analysed by TEM.

4.8.13 Procedure for the Catalyst Reuse Study

Nitrobenzene (0.103 mL, 1.0 mmol) was reduced to *N*-phenylhydroxylamine at 25 °C following the general protocol above, monitoring the progress of the reaction by ^1H NMR spectroscopy. Upon complete consumption of nitrobenzene, the reaction flask was recharged with a further portion of nitrobenzene and a further three equivalents of hydrazine hydrate (0.150 mL, 3.0 mmol) and the procedure was repeated 4 times.

4.9 References

-
- ¹ T. Aditya, A. Pal and T. Pal, *Chem. Commun.*, 2015, **51**, 9410–9431.
- ² G. Liu, C. Chen and J. Chen, *J. Phys. Chem. C*, 2023, **127**, 4375–4386.
- ³ F. Xu, J. L. Chen, Z. J. Jiang, P. F. Cheng, Z. Q. Yu and W. K. Su, *RSC Adv.*, 2020, **10**, 28585–28594.
- ⁴ T. Shudo, Koichi; Okamoto, *Tetrahedron Lett.*, 1973, **21**, 1839–1842.
- ⁵ A. D. McGill, W. Zhang, J. Wittbrodt, J. Wang, H. B. Schlegel and P. G. Wang, *Bioorganic Med. Chem.*, 2000, **8**, 405–412.
- ⁶ Y. Liu, S. Bai, Y. Du, X. Qi and H. Gao, *Angew. Chemie Int. Ed.*, 2022, **61**, e202115611.
- ⁷ J. S. Yadav, B. V. S. Reddy and P. Sreedhar, *Adv. Synth. Catal.*, 2003, **345**, 564–567.
- ⁸ M. Berthet, T. Cheviet, G. Dujardin, I. Parrot and J. Martinez, *Chem. Rev.*, 2016, **116**, 15235–15283.
- ⁹ J. C. Fishbein and R. A. McClelland, *Can. J. Chem.*, 1996, **74**, 1321–1328.
- ¹⁰ β -PHENYLHYDROXYLAMINE. *Org. Synth.* 1925, **4**, 57.
- ¹¹ P. Ren, T. Dong and S. Wu, *Synth. Commun.*, 1997, **27**, 1547–1552.
- ¹² D. Beaudoin and J. D. Wuest, *Tetrahedron Lett.*, 2011, **52**, 2221–2223.
- ¹³ D. Bhattacharjee, Shaifali, A. Kumar, G. V. Zyryanov and P. Das, *Mol. Catal.*, 2021, **514**, 111836.
- ¹⁴ G. Chen, C. Xu, X. Huang, J. Ye, L. Gu, G. Li, Z. Tang, B. Wu, H. Yang, Z. Zhao, Z. Zhou, G. Fu and N. Zheng, *Nat. Mater.*, 2016, **15**, 564–569.
- ¹⁵ A. K. Shil and P. Das, *Green Chem.*, 2013, **15**, 3421–3428.
- ¹⁶ E. H. Boymans, P. T. Witte and D. Vogt, *Catal. Sci. Technol.*, 2015, **5**, 176–183.
- ¹⁷ Y. Takenaka, T. Kiyosu, J. C. Choi, T. Sakakura and H. Yasuda, *Green Chem.*, 2009, **11**, 1385–1390.
- ¹⁸ K. V. R. Chary and C. S. Srikanth, *Catal. Letters*, 2009, **128**, 164–170.
- ¹⁹ Z. Yan, X. Xie, Q. Song, F. Ma, X. Sui, Z. Huo and M. Ma, *Green Chem.*, 2020, **22**, 1301–1307.
- ²⁰ S. Doherty, J. G. Knight, T. Backhouse, A. Bradford, F. Saunders, R. A. Bourne, T. W. Chamberlain, R. Stones, A. Clayton and K. Lovelock, *Catal. Sci. Technol.*, 2018, **8**, 1454–1467.

-
- ²¹ Z. Hou, N. Theyssen and W. Leitner, *Green Chem.*, 2007, **9**, 127–13.
- ²² M. Liu and Y. Wang, *Appl. Catal. O Open*, 2024, **193**, 206968.
- ²³ K. L. Luska and A. Moores, *Adv. Synth. Catal.*, 2011, **353**, 3167–3177.
- ²⁴ L. Lu, S. Zou and B. Fang, *ACS Catal.*, 2021, **11**, 6020–6058.
- ²⁵ M. Guo, H. Li, Y. Ren, X. Ren, Q. Yang and C. Li, *ACS Catal.*, 2018, **8**, 6476–6485.
- ²⁶ S. Doherty, J. G. Knight, T. Backhouse, R. J. Summers, E. Abood, W. Simpson, W. Paget, R. A. Bourne, T. W. Chamberlain, R. Stones, K. R. J. Lovelock, J. M. Seymour, M. A. Isaacs, C. Hardacre, H. Daly and N. H. Rees, *ACS Catal.*, 2019, **9**, 4777–4791.
- ²⁷ X. Cai, J. Nie, G. Yang, F. Wang, C. Ma, C. Lu and Z. Chen, *Mater. Lett.*, 2019, **240**, 80–83.
- ²⁸ X. Ren, M. Guo, H. Li, C. Li, L. Yu, J. Liu and Q. Yang, *Angew. Chemie - Int. Ed.*, 2019, **58**, 14483–14488.
- ²⁹ S. Doherty, J. G. Knight, H. Y. Alharbi, R. Paterson, C. Y. Wills, T. W. Chamberlain, H. Daly, and C. Hardacre, *ChemCatChem*, 2024, paper in review.
- ³⁰ I. Cano, M. A. Huertos, A. M. Chapman, G. Buntkowsky, T. Gutmann, P. B. Groszewicz and P. W. N. M. Van Leeuwen, *J. Am. Chem. Soc.*, 2015, **137**, 7718–7727.
- ³¹ N. Almora-Barrios, I. Cano, P. W. N. M. Van Leeuwen and N. López, *ACS Catal.*, 2017, **7**, 3949–3954.
- ³² I. Cano, L. M. Martínez-Prieto, P. F. Fazzini, Y. Coppel, B. Chaudret and P. W. N. M. Van Leeuwen, *Phys. Chem. Chem. Phys.*, 2017, **19**, 21655–21662.
- ³³ S. Doherty, J. G. Knight, T. Backhouse, T. S. T. Tran, R. Paterson, F. Stahl, H. Y. Alharbi, T. W. Chamberlain, R. A. Bourne, R. Stones, A. Griffiths, J. P. White, Z. Aslam, C. Hardare, H. Daly, J. Hart, R. H. Temperton, J. N. O’Shea and N. H. Rees, *Catal. Sci. Technol.*, 2022, 3549–3567.
- ³⁴ S. Montolio, C. Vicent, V. Aseyev, I. Alfonso, M. I. Burguete, H. Tenhu, E. García-Verdugo and S. V. Luis, *ACS Catal.*, 2016, **6**, 7230–7237.
- ³⁵ N. N. Greenwood and A. Earnshaw, *Chemistry of the Elements*, Pergamon Press Ltd., Oxford, 1984, ch. 25, pp. 1257.
- ³⁶ R. Jiang, D. T. Tran, J. Li and D. Chu, *Energy Environ. Mater.*, 2019, **2**, 201–208.
- ³⁷ F. Su, L. Lv, Y. L. Fang, T. Liu, A. I. Cooper and S. Z. Xiu, *J. Am. Chem. Soc.*, 2007, **129**, 14213–14223.
- ³⁸ M. A. Ernst and W. G. Sloof, *Surf. Interface Anal.*, 2008, **40**, 334–337.
- ³⁹ R. Bavand, A. Yelon and E. Sacher, *Appl. Surf. Sci.*, 2015, **355**, 279–289.
- ⁴⁰ D. J. Morgan, *Surf. Interface Anal.*, 2015, **47**, 1072–1079.

-
- ⁴¹ (a) B. Paul, K. Chakrabarti, S. Shee, M. Maji, A. Mishra and S. Kundu, *RSC Adv.*, 2016, **6**, 100532–100545. (b) N. M. Patil, T. Sasaki and B. M. Bhanage, *RSC Adv.*, 2016, **6**, 52347–52352. (c) S. C. A. Lin, Y. H. Liu, S. M. Peng and S. T. Liu, *Mol. Catal.*, 2019, **466**, 46–51. (d) R. V. Jagadeesh, G. Wienhöfer, F. A. Westerhaus, A. E. Surkus, H. Junge, K. Junge and M. Beller, *Chem. - A Eur. J.*, 2011, **17**, 14375–14379. (e) K. Nomura, *J. Mol. Catal. A. Chem.*, 1995, **95**, 203–210.
- ⁴² J. H. Tyler, S. H. Nazari, R. H. Patterson, V. Udumula, S. J. Smith and D. J. Michaelis, *Tetrahedron Lett.*, 2017, **58**, 82–86.
- ⁴³ D. V. Jawale, E. Gravel, C. Boudet, N. Shah, V. Geertsen, H. Li, I. N. N. Namboothiri and E. Doris, *Chem. Commun.*, 2015, **51**, 1739–1742.
- ⁴⁴ A. Corma, P. Serna, P. Concepción and J. J. Calvino, *ACS Catal.*, 2008, **130**, 8748–8753.
- ⁴⁵ C. C. Torres, V. A. Jiménez, C. H. Campos, J. B. Alderete, R. Dinamarca, T. M. Bustamente and B. Pawelec, *Mol. Catal.*, 2018, **447**, 21–27.
- ⁴⁶ F. Cárdenas-Lizana, D. Lamey, S. Gómez-Quero, N. Perret, L. Kiwi-Minsker and M. A. Keane, *Catal. Today*, 2011, **173**, 53–61.
- ⁴⁷ (a) M. Sankar, Q. He, R. V. Engel, M. A. Sainna, A. J. Logsdail, A. Roldan, D. J. Willock, N. Agarwal, C. J. Kiely and G. J. Hutchings, *Chem. Rev.*, 2020, **120**, 3890–3938. (b) K. L. Luska and A. Moores, *Adv. Synth. Catal.*, 2011, **353**, 3167–3177.

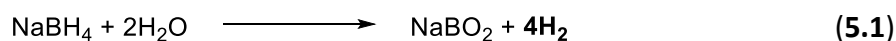
Chapter 5

Phosphine Oxide Stabilized Ruthenium Nanoparticles for the Hydrolytic Dehydrogenation of NaBH₄

5.1 Introduction

There is increasing global demand to identify an alternative energy source to fossil fuels to meet the imminent need to supply sustainable, clean energy. Hydrogen is an attractive candidate for green energy production as it has a high energy density (142 MJ·kg⁻¹ vs 54 MJ·kg⁻¹ for natural gas) as well as the potential to be produced from water splitting where the only by-product is oxygen.^{1,2} Hydrogen is a flammable gas and forms potentially explosive environments, therefore there are significant safety concerns over its storage and transport. While formic acid is attractive as a liquid hydrogen carrier, as discussed in **Chapters 2 and 3**, it is particularly toxic and corrosive which may make its transport problematic. Several chemical hydrogen carriers such as formic acid and ammonia may also face problems with the purity of the gas liberated by dehydrogenation – hydrogen fuel cells require high purity hydrogen to function efficiently,³ therefore the separation of CO, CO₂, H₂O and other impurities from the resulting gas mixtures complicates their use as hydrogen storage media. Thus, there is interest in solid hydrogen storage materials that would be safer to handle, allowing for the generation of high purity hydrogen on site.

In the course of using sodium borohydride (NaBH₄) as a hydride-transfer reagent, we have observed that its aqueous solutions rapidly liberate hydrogen when mixed with our PIIL-stabilized NP catalysts; colleague Hussam Alharbi observed gas evolution when mixing an aqueous NaBH₄ solution with PtNP@PIIL catalysts prior to addition of quinoline substrates;⁴ similarly, we observed significant gas evolution when aqueous NaBH₄ solutions were mixed with OPPh₂PEGPIIL-supported RuNP catalyst **4.8** described in **Chapter 4**. To this end, sodium borohydride is currently being investigated as a hydrogen storage material due to its stability, non-toxicity, and high hydrogen content (10.8 wt%).⁵ NaBH₄ also has the capacity to produce several moles of hydrogen per mole of substrate (**Equation 5.1**). Numerous analogous investigations have been conducted on the hydrolysis of ammonia borane,⁶ though this again faces the problem of gas purity as ammonia and nitrogen can be liberated in addition to hydrogen.

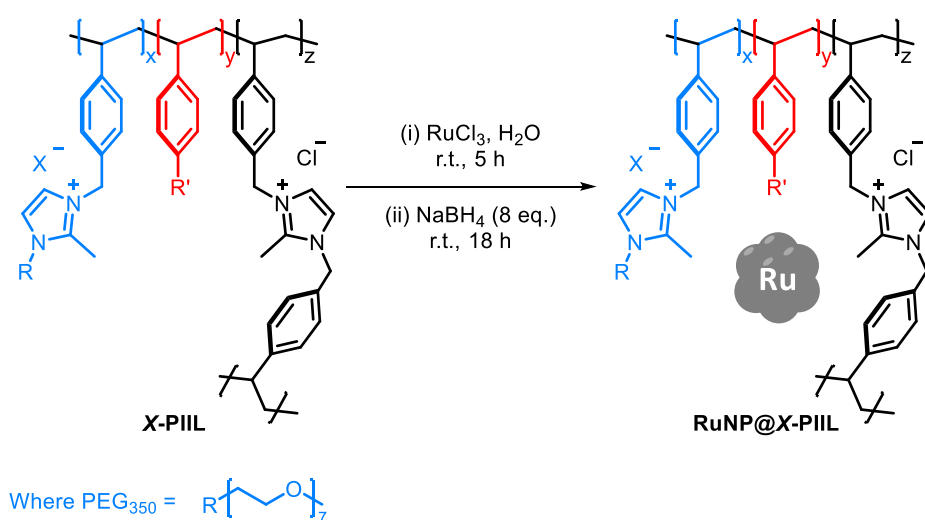


NaBH₄ is hydrolysed very slowly in water, so to be industrially viable it will be necessary to identify cost effective catalysts that facilitate rapid and controllable release of hydrogen on demand. Several metal NP systems have been reported to catalyse NaBH₄ hydrolysis such as Ni,⁷ Au,⁸ Co,⁹ and Pd,¹⁰ however, the most active catalysts reported for this reaction are typically based on ruthenium, platinum and rhodium NPs.^{11,12} At present, the best known supported NP catalyst for the hydrolysis of sodium borohydride are Ru NPs immobilized on the so-called Zeolite-Y with an initial TOF of 550 mol_{H₂}mol_{Ru}⁻¹min⁻¹,¹³ though such comparisons should be treated with caution as the conditions of catalysis in each report can be wildly different.

Recently, bimetallic PdAu bimetallic NPs were reported to be efficient catalysts for ammonia-borane hydrolysis when supported on an imidazolium-based organic polymer;¹⁴ however, to our knowledge, there are seldom any reports of polymer immobilized ionic liquids as metal NP supports for the hydrolytic evolution of hydrogen from NaBH₄. Poly(vinyl pyridinium) composites have previously been used to immobilize CoNP catalysts for the hydrolysis of NaBH₄;¹⁵ however, additional prior reports do not immobilize the IL unit, and the IL is instead non-covalently intercalated within polymer/nanofiber materials, which inevitably leads to loss of the IL-immobilized catalyst following recycling.¹⁶ To this end, we have reported that PtNP stabilized by a phosphine and PEG decorated PIIL support, PPh₂PEGPIIL, was a highly active catalyst for the hydrolysis of NaBH₄, achieving an optimal TOF of 169 mol_{H₂}mol_{Ru}⁻¹min⁻¹ with 0.08 mol% catalyst loading.⁴ Substitution of the imidazolium modified PEG chain for a hydrophobic N-decyl chain led to a significant drop in the initial TOF to 78 mol_{H₂}mol_{Ru}⁻¹min⁻¹. Here, this study has been expanded to investigate the activity of phosphine oxide decorated RuNP@OPPh₂PEGPIIL (**4.8**) for the hydrolysis of NaBH₄, as both Ru and Pt have competitive activity for this transformation.¹¹ A series of PIIL supported RuNP catalysts were prepared in an effort to understand the influence of the various functional groups of the OPPh₂PEGPIIL support. Moreover, in a complimentary study that was published alongside the work described in this chapter, colleague Adhwa Alharbi investigated the influence of a benzylamine functionalised PEGPIIL support on the efficacy of our RuNP catalysts.¹⁷ While these additional results will not be described in depth here, benzylamine-modified RuNP@NH₂PEGPIIL was in fact the most active catalyst of the series, with an initial TOF of 135 mol_{H₂}mol_{Ru}⁻¹min⁻¹, which was slightly higher than the 121 mol_{H₂}mol_{Ru}⁻¹min⁻¹ obtained for the optimum catalyst described in this chapter.

5.2 Catalyst Synthesis and Characterisation

As described in the previous chapters, functionalised X-PIIL supports were prepared *via* the AIBN-initiated radical polymerisation of a functionalised imidazolium-based ionic liquid monomer, an imidazolium-based ionic liquid cross-linker and a styrene spacer or phosphine oxide heteroatom-donor unit (**Scheme 5.1**). To investigate the influence of the various functional groups, PIIL polymers were systematically prepared with no functional group (**5.1a**), a phosphine oxide heteroatom donor (**5.1b**), a PEG-functionalised IL (**5.1c**), and both phosphine oxide and PEG groups as prepared in **Chapter 4** (**4.7**). ^1H NMR spectra of the polymers after 4 days of stirring at 80 °C confirmed near total consumption of the styrene-based monomers, and the resulting polymers were purified *via* dialysis. CP-MAS $^{31}\text{P}\{^1\text{H}\}$ NMR spectroscopy confirmed the incorporation of the phosphine oxide in polymer **5.1c** with a peak at 26.72 ppm, consistent with the peak at 26.05 ppm observed for $\text{OPPh}_2\text{PEGPIIL}$ (**4.7**); polymer **5.1b** also showed the same asymmetric satellite peaks.



RuNP@X-PIIL	R	R'	X	Polymer	Catalyst
RuNP@PIIL	Me	H	Cl	5.1a	5.2a
RuNP@OPPh ₂ PIIL	Me	O=PPh ₂	Cl	5.1b	5.2b
RuNP@PEGPIIL	PEG ₃₅₀	H	Br	5.1c	5.2c
RuNP@OPPh ₂ PEGPIIL	PEG ₃₅₀	O=PPh ₂	Br	4.7	4.8

Scheme 5.1 Preparation of RuNP@X-PIIL *via* wet impregnation of functionalised PIILs with RuCl_3 followed by reduction with NaBH_4 . Adjoining table details polymer composition and polymer/catalyst reference codes used in this chapter. Where $x = 1.86$, $y = 1$, $z = 0.14$.

Table 5.1 Average RuNP diameters derived from TEM micrographs. Micrographs and associated size histograms can be found in **Appendix A.5.4**.

#	Catalyst	Average Size / nm
5.2a	RuNP@PIIL	1.9 ± 0.5
5.2b	RuNP@OPPh ₂ PIIL	2.0 ± 0.6
5.2c	RuNP@PEGPIIL	1.7 ± 0.3
4.8	RuNP@OPPh ₂ PEGPIIL	2.3 ± 0.6

Ruthenium NPs were then generated by the wet impregnation of the polymer support with commercial RuCl₃·xH₂O, followed by *in-situ* reduction of Ru(III) to Ru(0) using an aqueous solution of NaBH₄; the corresponding RuNP **5.2a-c** and were obtained as fine black powders in high yield, as described for **4.8** in **Chapter 4**. Again, CP-MAS ¹³C{¹H} and ³¹P{¹H} NMR spectroscopy confirmed the incorporation of the PIIL supports into the catalysts, though there was no major shift in the ³¹P{¹H} NMR spectra upon metal impregnation. A downfield shift from 26.72 ppm to 27.57 ppm was observed on Ru loading to form **5.2b**, similar to the slightly smaller downfield shift from 26.05 ppm to 26.34 ppm on formation of Ru-loaded PEG-modified **4.8**, however, the broadness of the ³¹P signals means that these shifts are too small to be attributed to a Ru-P(O)Ph₂ interaction. A Ru-P interaction is unlikely for phosphine oxide, however, one may expect a shift in the ³¹P NMR signal following coordination of the oxide oxygen to a NP surface. The CP-MAS ¹⁵N NMR spectra discussed in **Chapter 2** also do not support the direct coordination of a heteroatom to a metal NP surface as detected by CP-MAS NMR, but that does not mean to say that such an interaction is not present.

Following digestion of the catalysts by a KNO₃/KOH melt, the Ru loadings were determined to be 0.18-0.75 mmol·g⁻¹ by ICP-OES. Analysis of the RuNP's by TEM revealed that they were all ultrafine and near-monodisperse with average diameters ranging from 1.7 to 2.3 nm (**Table 5.1**). The smallest NP's sized 1.7 ± 0.3 nm and 1.9 ± 0.5 nm were obtained for catalysts **5.2c** and **5.1a** respectively. Note that attributing an increase in NP size with the incorporation of the phosphine oxide group would be tenuous as the NP series are extremely similar in size when the errors associated with the NP sizes are considered.

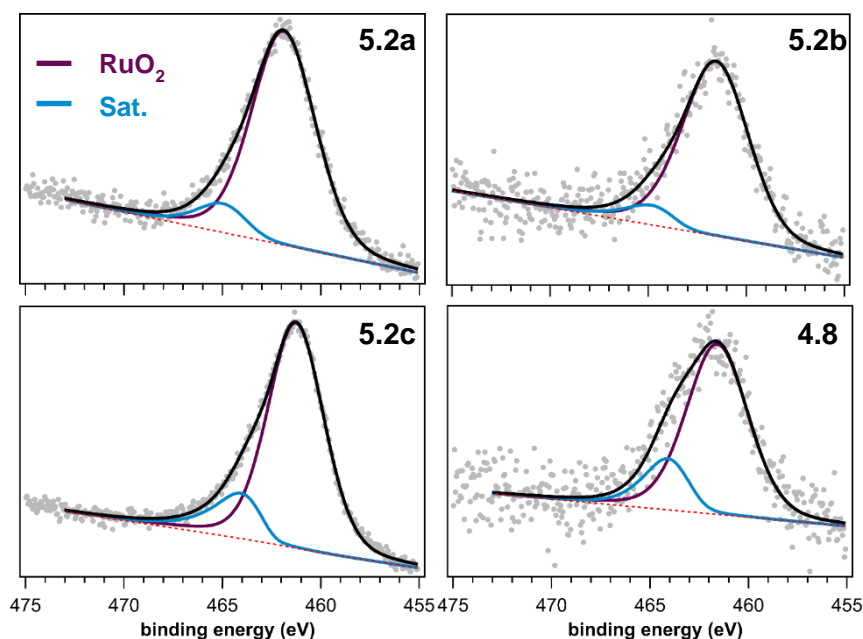


Figure 5.1 XPS spectra showing the Ru 3p_{3/2} region for catalysts **5.2a-c** and **4.8**. Black line = overall fitting; Red dotted line = background.

For the reasons described in **Chapter 4 (Section 4.2.2)**, a surface investigation of **5.2a-c** was conducted through the analysis of the Ru 3p electrons. The spectra of **5.2a-c** were consistent with that of **4.8** with a peak at 461.6 ± 0.3 eV attributed to RuO₂, and a corresponding satellite at 464.6 ± 0.4 eV (**Figure 5.1**).¹⁸ Interestingly, the Ru 3p_{3/2} peak shifted to lower BE for all of the catalysts when compared to unfunctionalised **5.2a**; the most significant shift was observed for PEG-modified **5.2c** with a Ru 3p_{3/2} to aliphatic C 1s separation of 178.0 eV, which is 0.6 eV lower than that measured for **5.2a**. Overall, the RuO₂ Ru 3p_{3/2} BE decreased following **5.2a** >> **4.8** > **5.2b** > **5.2c**. A shift to lower binding energies could be indicative of charge transfer from the support to the metal catalyst, specifically from coordination of the phosphine oxide and/or PEG groups. In **Chapter 2**, it appeared that coordination of an amine to PdNPs led to an increase in BE, in contrast to the results described here, though the nature of such interactions

Table 5.2 Absolute RuO₂ binding energies and the corresponding BE separation between the Ru 3p_{3/2} peak and the aliphatic C 1s region.

#	Catalyst	Ru 3p _{3/2} / eV	$\Delta\text{BE}_{\text{Ru-C1s}}$ / eV	FWHM / eV
5.2a	RuNP@PIIL	491.9	178.6	3.8
5.2b	RuNP@OPPh ₂ PIIL	461.5	178.1	4.1
5.2c	RuNP@PEGPIIL	461.3	178.0	3.4
4.8	RuNP@OPPh ₂ PEGPIIL	461.6	178.2	3.7

may be specific to both metal and ligand. Note that while **Chapter 2** described how coordination of an amine donor to immobilized-[PdCl₄]²⁻ salts led to an increase in the Pd 3d BE, a comparative study of the corresponding PdNP catalysts could not be completed as no surface Pd species were observed following the reduction of unmodified PdNP@PIIL (**2.8a**). However, the Pd 3d BE was found to increase with increasing loading of amine on the NP support. This result still may not be meaningful without a comparison with the unmodified catalyst, particularly as DRIFTS spectra showed that bridged CO species over NP generated from amine modified **3.22** (PdNP@CL₁PIIL) were found to be blue-shifted when compared to bridged CO species over PdNP@PIIL. This would suggest that amine donors do in fact lead to more electron rich PdNP surfaces, consistent with the results for PIIL stabilized RuNP catalysts above.

In addition to the binding energy positions, there also appeared to be some disparity in the full width at half maximum (FWHM) of the Ru 3p_{3/2} peaks. Sloof and co-workers have reported that the Ru 3p_{3/2} FWHM increased with increasing thickness of the RuO₂ layer on a metallic Ru single crystal;¹⁹ Here, the FWHM varied between 3.4-4.1 eV, increasing in the order of **5.2b** < **5.2c** < **5.2d** < **4.8**. This is within the range described by Sloof, whereby the thinnest oxide layers (*ca.* 0.1 nm) had an average FWHM of 2.5 eV, while RuO₂ layers of 2.0-4.0 nm had a FWHM of around 4.5 eV. For comparison, Morgan has reported a FWHM of 3.42 eV for hydrated RuO₂ and 3.22 eV for the anhydrous oxide.²⁰

5.3 Catalyst Comparison for NaBH₄ Hydrolysis

The X-PIIL supported RuNP catalysts prepared above were tested and compared for the hydrolysis of NaBH₄ at 30 °C with a catalyst loading of 0.2 mol%. Hydrogen generation commenced immediately on addition of NaBH₄ with no obvious induction period, indicating the absence of unreduced RuCl₃ (or that the generation of the active catalyst is rapid). The volume of hydrogen generated was measured by the displacement of water in a gas burette and plotted as a function of time. Initial rates of hydrogen liberation, given as turnover frequencies (TOF), have been expressed with units of mol_{H₂}mol_{Ru}⁻¹min⁻¹, abbreviated to min⁻¹. TOF's were determined by measuring the slope of the linear portion of the activity/time profiles. In a comparison of the prepared catalyst series (**Figure 5.2**), unfunctionalised catalyst **5.2a** was found to be the most active with an initial TOF of 121 min⁻¹. In contrast, PEG-functionalised **5.2c** was the least active with a TOF of 70 min⁻¹, while phosphine oxide modified catalyst, **5.2b**, was slightly more active with a TOF of 89 min⁻¹. The combination of the two

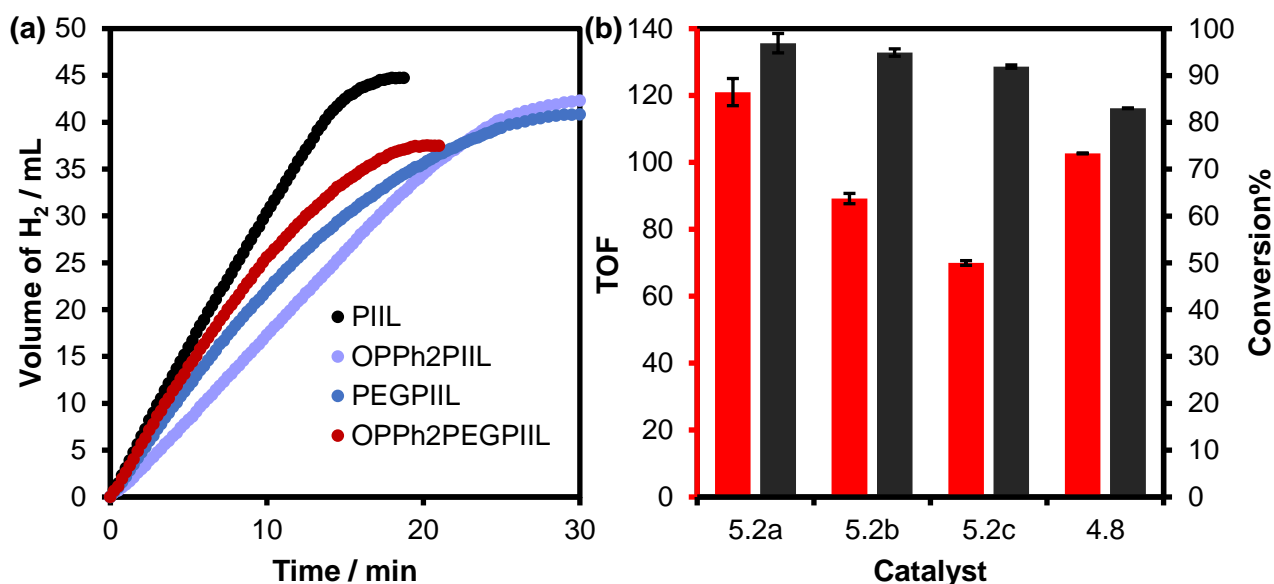


Figure 5.2 (a) RuNP@X-PIIL (0.2 mol%) catalysed hydrolysis of NaBH₄ (0.021 g, 0.56 mmol) in H₂O (2 mL) at 30 °C. (b) The corresponding initial TOFs and conversions, where TOF = mol_{LH₂}mol_{Ru}⁻¹min⁻¹. Results averaged from at least two runs.

functional groups appeared to result in a greater activity than that of the pair individually, as catalyst **4.8** afforded a TOF of 103 min⁻¹, though this was still less active than the unfunctionalised RuNP@PIIL catalyst. Despite this, NaBH₄ hydrolysis catalysed by **4.8** led to the lowest conversion of NaBH₄ at 83%, compared to 97% for optimal catalyst **5.2a**; catalysts **5.2b** and **5.2c** also afforded relatively high conversions of 95% and 92%, respectively, though both were lower than that of **5.2a**. Decreasing conversion with increasing functionalisation may be a reflection of reduced access to active Ru sites which are then deactivated, through fouling or morphological change, over the course of the reaction.

In spite of this, all of the prepared catalysts were more active than many RuNP catalysts reported in the literature; the optimal TOF of 121 min⁻¹ achieved with **5.2a** is higher than 2 min⁻¹ for Ru immobilized on an ion exchange resin,²¹ 62 min⁻¹ for acetate stabilized RuNPs,²² 25 min⁻¹ for Ru on supported metal-organic framework ZIF-67,²³ 37 min⁻¹ for hydrogel encapsulated RuNPs,²⁴ as well as 80 min⁻¹ and 47 min⁻¹ for Ru and Ru/Au bimetallic NPs, respectively, supported on a micellular dendrimer support.⁸ However, an initial TOF of 121 min⁻¹ is notably less active than the TOF of 550 min⁻¹ obtained for RuNPs immobilized on Zeolite-Y, which, to our knowledge, remains the most active reported catalyst for this transformation.¹³ Though as mentioned earlier, such comparisons should be treated with caution, due to the disparate nature of catalytic conditions across reports.

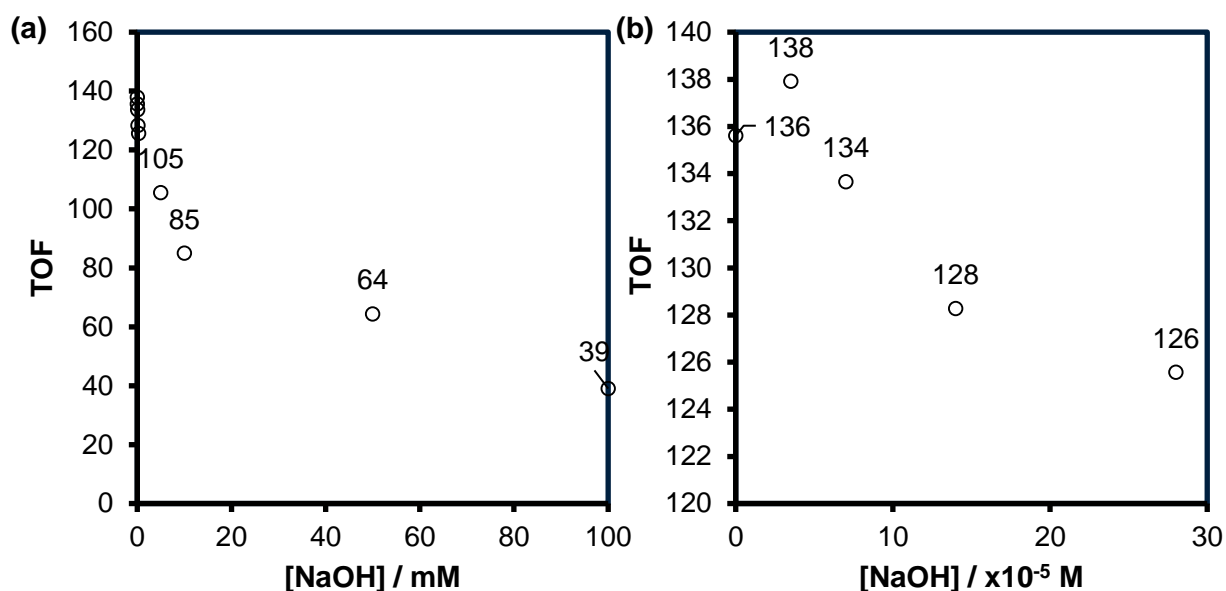


Figure 5.3 (a) Initial TOF's corresponding to the **5.2a** (0.25 mol%) catalysed hydrolysis of NaBH_4 (0.021 g) in $\text{NaOH}_{(\text{aq})}$ solution of various concentrations (2 mL) at 30°C . (b) Expansion of the region at low concentrations of NaOH.

It has been reported that the catalytic hydrolysis of NaBH_4 (and NH_3BH_3) is augmented in the presence of an aqueous solution of NaOH at certain concentrations, in particular for earth abundant metals.^{6,25} For example, Ni-Co bimetallic NPs achieved an optimal TOF only when the hydrolysis was conducted in a 15 wt% aqueous solution of NaOH (*ca.* 3.75 M).⁷ In contrast, here we show a negative relationship between increasing NaOH concentration and TOF (**Figure 5.3**), where activity is reduced even at low concentrations of hydroxide (< 0.5 mM). Basic media is known to stabilize solutions of NaBH_4 so at high NaOH concentrations (0.01-0.1 M) catalytic activity was notably suppressed, with a drop in TOF from 136 min^{-1} in the absence of NaOH to 39 min^{-1} in a 0.1 M NaOH solution. Therefore, in this study, the amounts of NaOH investigated were reduced to the 0.05:1 to 0.37:1 scale ($\text{OH}^-:\text{Ru}$) to minimise the potential saturation of active sites. In **Figure 5.3b**, a clear trend was observed showing decreasing activity with increasing NaOH concentration; an initial increase from 136 to 138 min^{-1} was observed in the presence of $3.5 \times 10^{-5} \text{ M}$ NaOH, though this is a negligible increase and within the expected error. Reassuringly, a similar negative relationship was reported for Ru- RuO_2/C ,²⁶ aminosilane treated Ru@graphite,²⁷ Ru supported on ion exchange resin beads,²¹ as well as Ru/ LiCoO_2 and Pt/ LiCoO_2 .¹¹ Amendola *et al.* proposed that the hydrolysis is deactivated by complexation of water by OH^- ions.²¹ On the observation that NaOH solution promoted the $\text{Ni}_2\text{Pt@ZIF-8}$ catalysed hydrolysis of NH_3BH_3 ,⁶ Astruc *et al.* suggested that OH^- ions coordinate to the NP surface and increase the electron density which facilitates the alleged rate limiting

cleavage of the O-H bond of a water molecule to enhance the reaction rate; however, for the corresponding PtNP catalyst (Pt@ZIF-8) a negative effect was observed with increasing NaOH concentration. If OH⁻ promotes NP activity for non-noble metals due to them being relatively ‘electron poor’, it is credible that a positive effect is not observed for late transition metal NPs (*i.e.* Ru, Rh, Pt) as they are ‘electron rich’, thereby the OH⁻ ions only act to block active sites and inhibit reaction.

5.4 Kinetic Studies

Kinetic studies were undertaken to obtain insight on the factors that influence reaction rate for the hydrolysis of NaBH₄. The temperature dependence for the RuNP catalysed hydrolysis is shown by a clear increase in reaction rate with increasing temperature (293-313K), as seen in **Figure 5.4a**. By plotting $\ln v_0$ against $1/T$ in accordance with the Arrhenius equation (**Equation 5.2**), the slope could be used to determine activation energies (E_a) for all systems, where v_0 is the initial rate of reaction (mol_{H₂}/min), A is the pre-exponential factor, R is the gas constant and T is the temperature; note that while the Arrhenius equation would typically consider the rate constant, k , here this has been substituted for the initial rate of reaction, v_0 , as an estimate. From this, activation energies were obtained in the range of 26-52 kJmol⁻¹. However, there is no obvious correlation between apparent activation energy and catalyst activity, though this appears to be consistent with the previous reports of transition metal catalysed hydrolysis of NaBH₄ referenced above. To this end, optimal catalyst **5.2a** also had the highest apparent activation energy at 51.9 kJ·mol⁻¹, counter intuitive to the general belief that a higher activation energy will lead to a lower reaction rate.

$$\ln v_0 = \ln A - \frac{E_a}{RT} \quad (5.2)$$

The dependence of reaction rate on catalyst concentration was investigated with a constant concentration of NaBH₄, taking the linear slope of the graph as the reaction rate. The method of initial rates allows one to derive the reaction order in catalyst by considering the reaction rate at various catalyst concentrations with **Equation 5.3**, where v_0 is the initial rate of reaction (mol_{H₂}/min), $[M]$ is the concentration of substrate with its rate-order expressed as x , and c represents a constant.

$$\ln v_0 = x \ln [M] + c \quad (5.3)$$

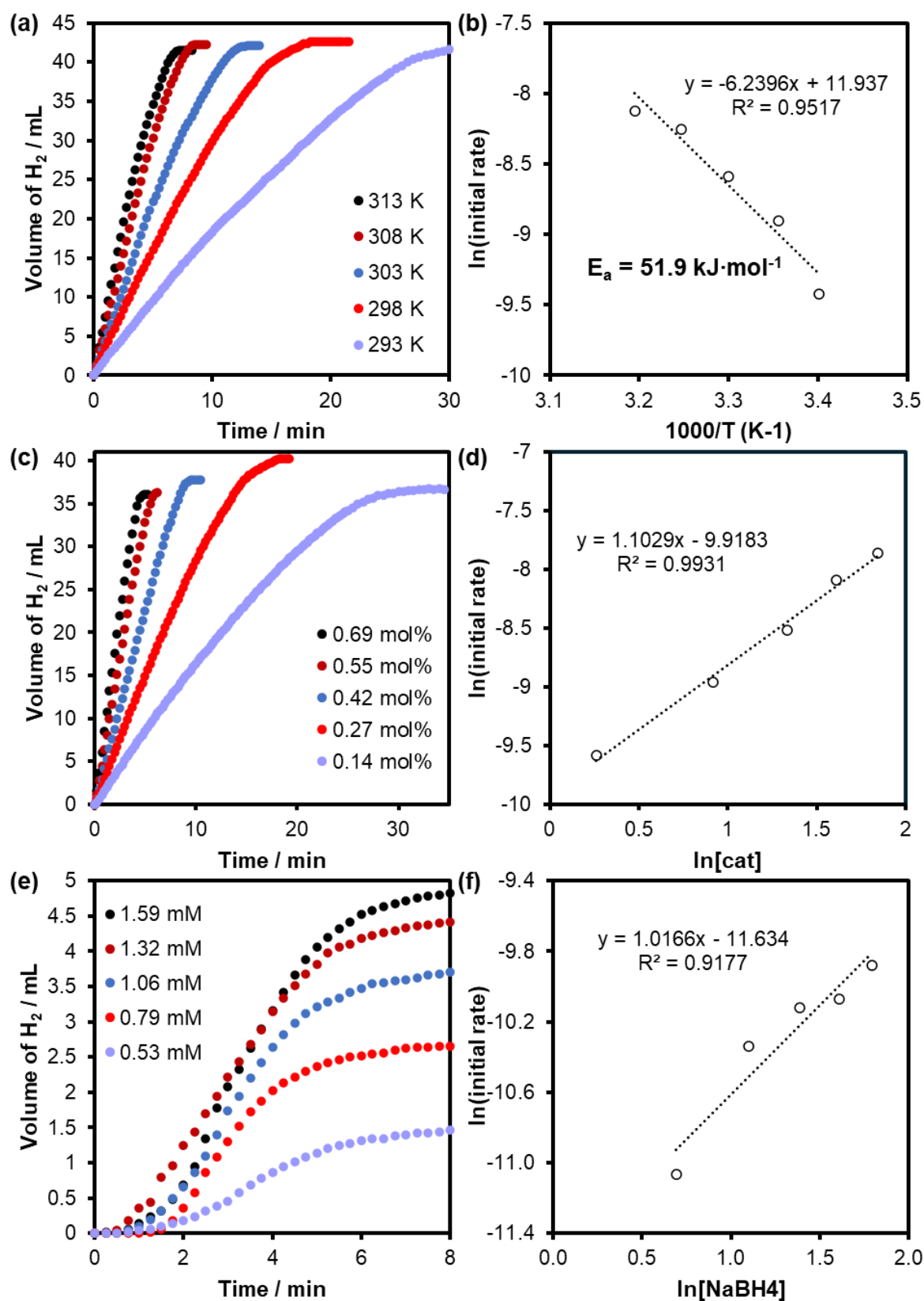


Figure 5.4 Kinetic studies showing: (a) RuNP@PIIL catalysed hydrolysis of NaBH₄ over various temperatures (b) Arrhenius plot of NaBH₄ hydrolysis from 293-313 K (c) RuNP@PIIL catalysed hydrolysis of NaBH₄ over various catalyst loadings (d) Plot showing ln of reaction rate against ln of catalyst concentration where slope m is the reaction order in catalyst concentration (e) RuNP@PIIL catalysed hydrolysis of NaBH₄ over various concentrations of NaBH₄ in alkaline solution (pH 13) (f) Plot showing ln of reaction rate against ln of NaBH₄ concentration where slope m is the reaction order in NaBH₄ concentration.

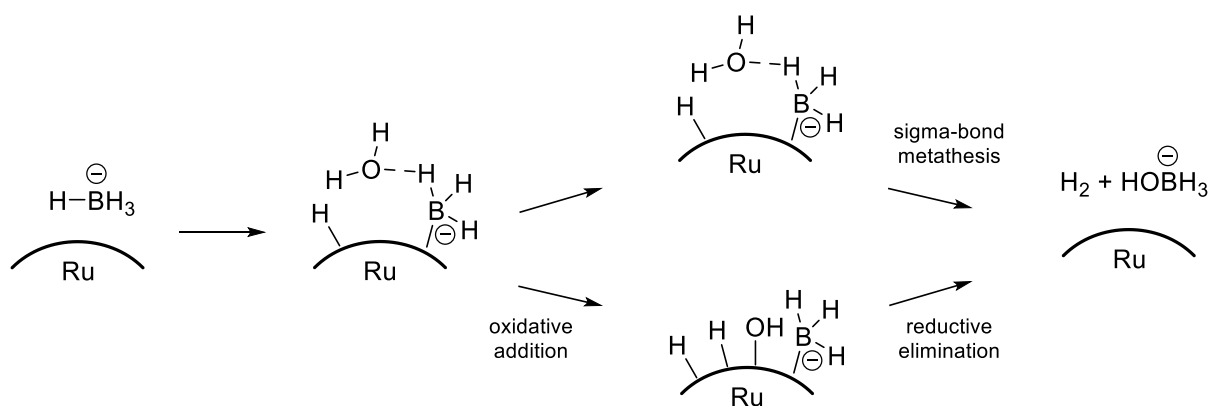
Thus, a logarithmic plot of reaction rate against catalyst concentration gave a slope of 1.10 for catalyst **5.2a**, consistent with first-order reaction kinetics with respect to catalyst concentration (**Figure 5.4d**). Similar plots were generated for catalysts **5.2b**, **5.2c**, and **4.8**

(**Appendix A.5.6**); the reaction order in catalyst was found to be 0.97 for catalyst **5.2b**, though lower orders of 0.69 and 0.84 were found for catalysts **5.2c** and **4.8**, respectively. A smaller reaction order in catalyst could be indicative of reduced access to Ru sites, although similar values have been reported in the literature and have been used to describe first-order kinetics. For example, reaction orders in catalyst concentration have been reported as 1.05 for a Co-P-B composite,²⁸ 1.07 for Ru@acetate,²⁹ 1.26 for MOF-supported Co,³⁰ 0.73 for Ru@Zeolite,¹³ 0.85 for Pt/Co@Dendrimer,³¹ and 0.82 for the adjacent Ni₂Pt@ZIF-8 catalysed hydrolysis of NH₃-BH₃.⁶

Application of **Equation 5.3** in a study of variable NaBH₄ concentration at a constant concentration of catalyst was also used to derive the reaction-order with respect to sodium borohydride. However, the concentration of NaBH₄ used in the studies above (*ca.* 0.28 M) is in a 300-fold excess to the catalyst concentration, therefore catalyst sites are almost definitely saturated; to this end, several studies at high concentrations of NaBH₄ have demonstrated that the substrate appears to be zero-order with respect to NaBH₄.³² In order to generate meaningful data, the ratio of borohydride to catalyst was reduced to a comparative scale of 2:1 to 6:1. To prevent rapid hydrolysis, the concentrations of NaBH₄ were diluted to 0.5-1.6 mM and the experiments were run in a 100 mL aqueous solution of 2.5 mM NaOH, which we have shown to have a stabilising effect on the rate of NaBH₄ hydrolysis. Indeed, the logarithmic plot of initial rate vs NaBH₄ concentration confirmed that the hydrolysis of NaBH₄ was first order in substrate with a slope of 1.02, as shown by **Figure 5.4f**. There is disparity in the literature between authors finding zero or first order kinetics with respect to NaBH₄ concentration though this has been highlighted by Patel *et al.*²⁸ to be an artefact of whether the study was conducted with a high or low concentration of NaBH₄ relative to the catalyst amount.

5.5 Reaction Mechanism

Sensibly, the only products of NaBH₄ hydrolysis are molecular hydrogen and various hydrated borate salts. The generation of hydrogen was confirmed using a tandem reaction where the gas evolved from the hydrolysis of NaBH₄ was used to hydrogenate an alkene. Two Schlenk



Scheme 5.2 Proposed reaction mechanism of ruthenium catalysed borohydride hydrolysis following the chemisorption of BH_4^- to the ruthenium surface.

flasks were sealed and connected to one another by rubber tubing – in one flask, gas was generated from the RuNP@PIIL (**5.2a**) catalysed hydrolysis of sodium borohydride; in the other flask, 1,1-diphenylethylene was magnetically stirred in methanol with Pd/C. After 18 hours of stirring analysis of the reaction mixture by ^1H -NMR spectroscopy confirmed that 1,1-diphenylethylene had been completely converted to 1,1-diphenylethane. It is proposed that the hydrogen gas is formed from the reductive elimination of a water-derived proton and a NaBH_4 -derived hydride from the metal surface. To investigate the contribution of solvent and substrate to the resulting hydrogen evolved, water was substituted for D_2O in the hydrolysis of NaBH_4 towards the tandem reaction with 1,1-diphenylethylene; deuterium labelling of the product was identified by ^2H -NMR spectroscopy, and analysis of the methine region of the $^{13}\text{C}\{^1\text{H}\}$ NMR spectrum revealed a mixture of 8 isotopologues, resulting from H/D scrambling at the surface of the Pd/C catalyst. Gas-phase mass spectrometry of the reaction product revealed that the undeuterated product comprised only 20% of the mixture while the remaining isotopes showed deuterium incorporation at the methine and methyl position to various degrees (**Appendix A.5.7**).

A ubiquitous mechanism for the heterogeneous catalysed hydrolysis of NaBH_4 has not been established, instead it is likely that there is no single kinetic model that is appropriate for every catalyst and conditions.³³ There is precedent for the chemisorption of BH_4^- to the metal surface in the initial step, as described by Raj *et al.* for Pt and PdNPs on functionalised carbon nanotubes,³⁴ Fisher *et al.* for Ru on carbon,³⁵ and Wang *et al.* for Co-B catalyst.³⁶ However, the exact role of water in the reaction mechanism is ill-defined. The kinetic isotope effect (KIE) is a valuable tool for elucidating information about the rate limiting step (RLS) of a reaction, determined by comparing reaction rates after the substitution of a substrate atom with a

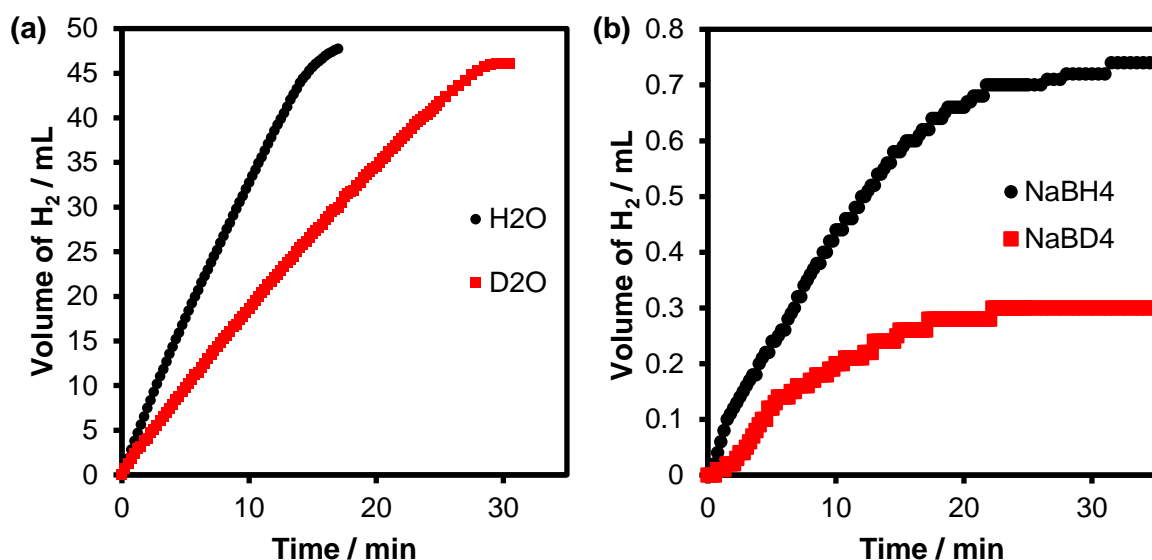


Figure 5.5 (a) RuNP@PIIL (0.2 mol%) catalysed reaction of NaBH₄ (0.021 g, 0.56 mmol) in H₂O/D₂O (2 mL) at 30 °C. (b) RuNP@PIIL (100 mol%) catalysed reaction of NaBH₄/NaBD₄ (1/1.1 mg, 0.03 mmol) in H₂O (200 mL) at 30 °C.

heavier isotope.³⁷ The deuterium KIE (k_H/k_D) has been used by several authors to demonstrate the involvement of H₂O in the RLS of borohydride hydrolysis by substitution with D₂O,^{8,9,32,30} though it is not clear if O-H(D) bond cleavage occurs through oxidative addition to the metal surface or through direct reaction with surface adsorbed M-H and M-BH₃⁻ to liberate H₂. Here, substituting H₂O for D₂O in the hydrolysis of NaBH₄ with **5.2a** as the catalyst led to a reduction in the rate of reaction from 3.24 mL_{H₂}·min⁻¹ to 1.84 mL_{H₂}·min⁻¹, corresponding to a primary KIE of 1.25 (**Figure 5.5a**). This value was slightly lower than the KIE of 1.53 obtained for catalyst **4.8**. While a KIE could reflect the involvement of H(D)-O oxidative addition in the RLS, a value of 1.25 is quite low and is in the range expected for a secondary kinetic isotope effect, meaning that the substituted isotope is not involved in bond breaking or forming during the RLS, but is instead a spectator.^{38,39}

Meanwhile, substitution of NaBH₄ for NaBD₄ in a stoichiometric scale hydrolysis (100 mol% catalyst, analogous to the experimental set-up to determine the reaction order in NaBH₄ above) afforded a much more notable KIE of 2.37 (**Figure 5.5b**). This is suggestive of B-H cleavage playing a pivotal role in the RLS of borohydride hydrolysis – although hydride transfer from metal borohydrides is typically considered to be fast, a high KIE value could indicate that hydride adsorption is slow to reach equilibrium at a surface saturated by water molecules, and water-derived protons.³⁵ In contrast, when the hydrolysis was catalysed by PtNP@PPH₂PEGPIIL a relatively low KIE of 1.3 was found on substitution of NaBH₄ for NaBD₄,

while a KIE of 1.9 was found on substitution of H_2O for D_2O .⁴ Assuming that the PIIL-supported phosphine and phosphine oxide do not participate in the reaction mechanism, this notable difference in KIE's could suggest that the mechanism of NaBH_4 hydrolysis is metal specific. Ruthenium is well known to be oxyphilic, and displacement of water from its surface may therefore have a higher activation barrier than for platinum.

Reductive elimination of two surface bound hydrogen species is unlikely to be the rate determining step, as then one would expect a comparative KIE for both D_2O and NaBD_4 substituted reactions. Instead, the rate limiting step is proposed to involve oxidative addition of a B-H bond, or through hydride transfer to the RuNP surface; the activity of $[\text{BH}_4]^-$ during this step is likely mediated by a hydrogen-bonded network with water, that may stabilize intermediates at the catalyst surface. However, it is not clear from this data whether the water-proton in the resulting H_2 gas is derived from oxidative addition of the water to the catalyst surface or through a metathesis-type pathway of hydrogen-bonded water interacting with the surface bound hydride.

5.6 Catalyst Recycling and Poisoning Studies

For a catalyst to be attractive for industrial application it must be robust and maintain its activity over multiple reuses. The recyclability of the most active catalyst RuNP@PIIL, **5.2a**, was therefore examined. Due to the near homogenous dispersion of NPs in solution, it was

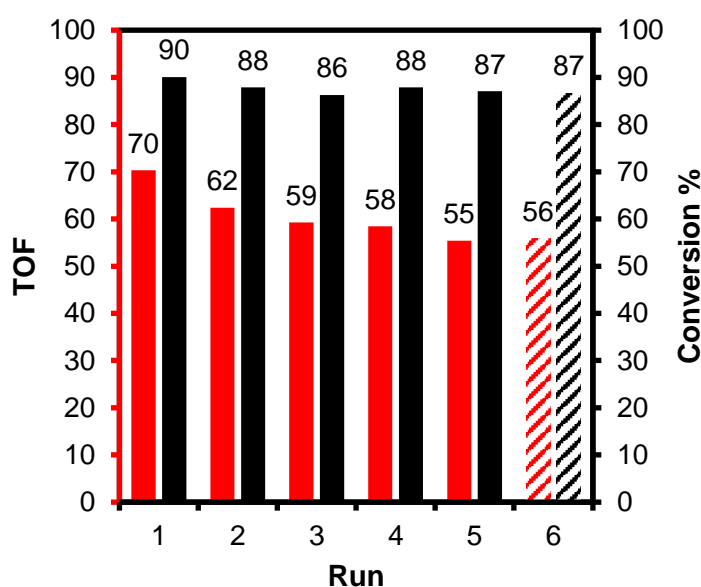


Figure 5.6 Recycling study showing the RuNP@PIIL (2 mol%) catalysed hydrolysis of NaBH_4 (0.021 g, 0.56 mmol) in H_2O (20 mL) at 30 °C, where the same catalyst was recycled over 6 runs. Before the 6th run, the catalyst was isolated and washed before reuse. Red bars (left) = TOF, black bars (right) = Conversion%

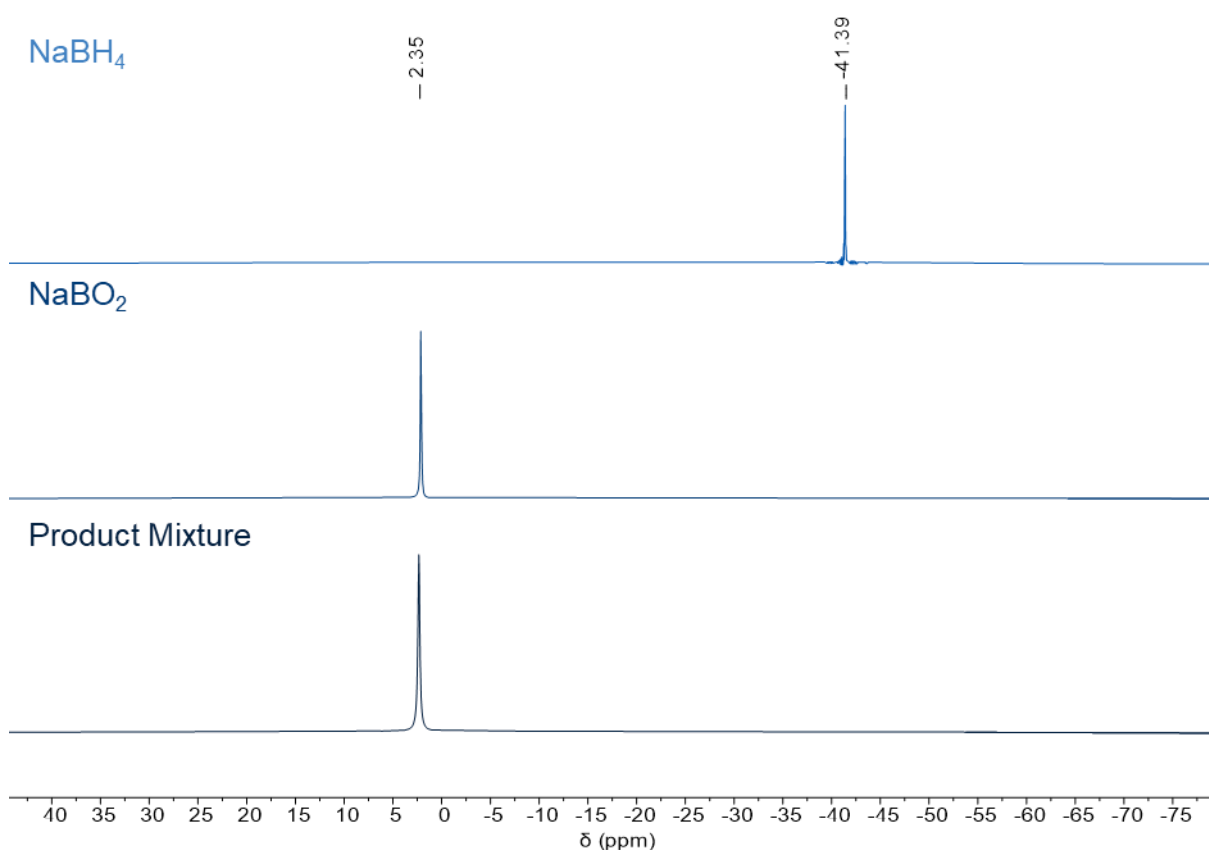


Figure 5.7 $^{11}\text{B}\{^1\text{H}\}$ NMR spectra of aqueous solutions of NaBH_4 , NaBO_2 , and the filtered product mixture of a **5.2a** catalysed hydrolysis of NaBH_4 . The spectrum of NaBH_4 was acquired in an aqueous solution of 0.5 M NaOH to prevent hydrolysis.

not practical to recover and wash the catalyst between cycles without incurring significant loss of catalyst material. Rather, the catalyst solution was recharged and stirred with a further equivalent of NaBH_4 upon complete consumption of substrate, indicated by a plateau in hydrogen evolution. A remarkable retention of activity was observed, whereby the total conversion of NaBH_4 dropped by only 3% after 5 uses of the catalyst, from 90% after run 1 to 87% after run 5. The rate of hydrogen evolution, on the other hand, reduced more notably with an initial TOF of 55 min^{-1} after the fifth run compared to 70 min^{-1} for the first use, a 21% reduction in activity. While impractical, it was not impossible to wash catalyst **5.2a** before reuse – after the 5th run the catalyst was isolated by centrifugation and washed several times with water to remove any surface borate species. Gratifyingly, both TOF and conversion were maintained following a 6th run using the washed catalyst, as shown by **Figure 5.6**. Indeed, a drop in catalyst efficacy over the 6 uses is unlikely to be a consequence of NP aggregation, as TEM micrographs of the catalyst isolated after the 6th run showed NP with an average diameter of $1.9 \pm 0.6 \text{ nm}$, which is practically unchanged from the $1.9 \pm 0.5 \text{ nm}$ determined for **5.2a** prior to use (**Appendix A.5.4**).

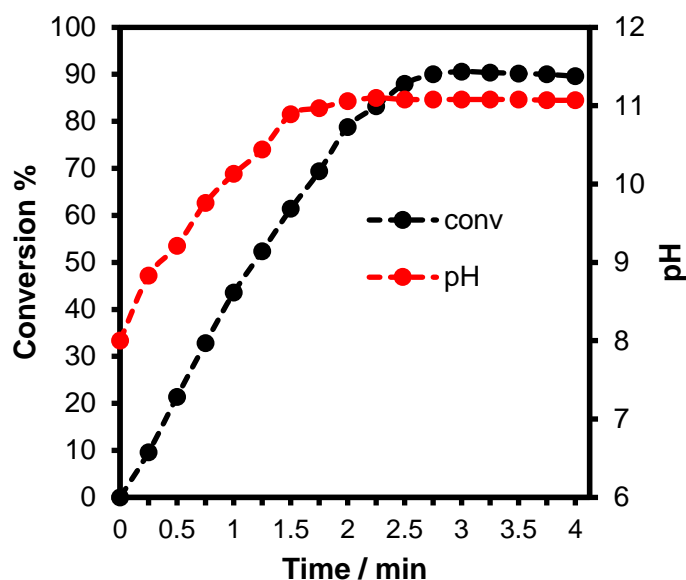


Figure 5.8 A plot of pH over time against conversion over time for the RuNP@PIIL (2 mol%) catalysed reaction of NaBH₄ (0.021 g, 0.56 mmol) in H₂O (20 mL) at 30 °C.

The gradual decrease in activity, which was then ameliorated by washing, is indicative of a poisoning effect at the catalyst surface over several uses. Accumulation of sodium metaborate (NaBO₂) by-product at the catalyst surface may limit access to the active sites, thus it was therefore prudent to investigate the poisoning effect of NaBO₂ for RuNP catalysed NaBH₄ hydrolysis. First, to confirm that NaBO₂·xH₂O was in fact the product of NaBH₄ hydrolysis under the conditions of catalysis, a reaction was run to completion and the resulting mixture filtered and analysed by ¹¹B{¹H} NMR spectroscopy. A single peak at 2.35 ppm was consistent with a commercial sample of NaBO₂·4H₂O, as shown in **Figure 5.7**. Unreacted NaBH₄, on the other hand, appeared upfield with a single peak at -41.39 ppm, consistent with the literature.⁴⁰ The formation of NaBO₂ can also be monitored by measuring the pH of the reaction as it progresses; **Figure 5.8** shows increasing pH with increasing conversion for the RuNP catalysed hydrolysis of NaBH₄ without prior addition of NaBO₂. The pH value of 8 at time = 0 min was recorded immediately after the addition of NaBH₄; for comparison, the initial concentration of NaBH₄ was 28 mM, and a 28 mM solution of NaBO₂·4H₂O in the absence of catalyst or NaBH₄ has a pH of 11.30. The pH of the reaction mixture at 80% conversion was 11.06, suggesting that NaBO₂ was the predominant species in solution and could potentially saturate the active sites on the catalyst surface.

Thus, to investigate this poisoning effect, RuNP@PIIL (**5.2a**) was pre-stirred in aqueous solutions with *ca.* 400 equivalents of NaBO₂·4H₂O (equivalents compared to moles of Ru) over various time periods before addition of NaBH₄. By pre-treating the catalyst with the reaction

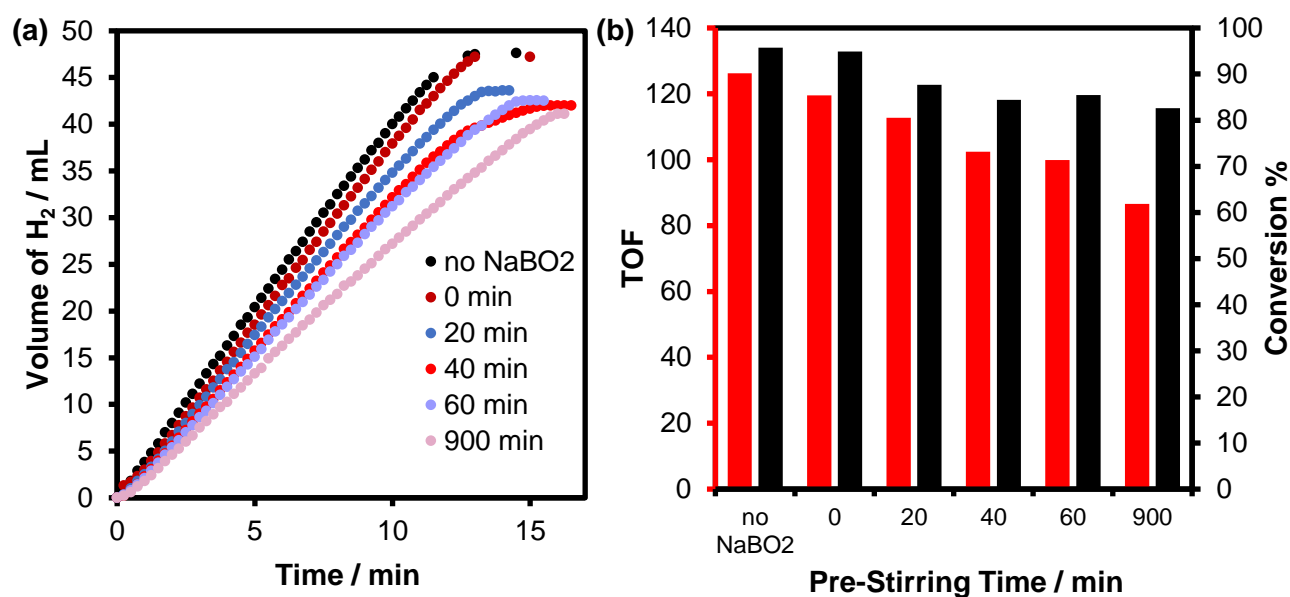


Figure 5.9 (a) RuNP@PIIL (0.25 mol%) catalysed reaction of NaBH₄ (0.021 g, 0.56 mmol) in H₂O (2 mL) at 30 °C, after pre-stirring RuNP with NaBO₂·4H₂O (76.5 mg, 0.56 mmol) for x minutes in H₂O. (b) The respective initial TOFs over various poison stirring times.

product, we can investigate whether NaBO₂ is having a poisoning effect at the catalyst surface, limiting the activity of the catalyst over consecutive uses due to accumulation of the suspected poison. The poisoning effect of NaBO₂ was indeed evident as shown by **Figure 5.9**, though it was not initially significant. On direct addition of NaBO₂ and no pre-stirring (0 min) we saw a slight drop in TOF of 5% compared to the reaction in the absence of NaBO₂, along with a negligible change in conversion. However, as the pre-stirring times with NaBO₂ increased a notable decrease in both TOF and conversion was apparent. A reduction in initial TOF of 21% was observed after 60 minutes of pre-stirring with NaBO₂, and after pre-stirring overnight for 15 hours a further drop to 69% of the initial activity was observed. A reference experiment which pre-stirred catalyst **5.2a** in neat water for 15 hours prior to use led to a negligible change in activity.

While the poisoning experiments above highlights the likely role of sodium metaborate in catalyst deactivation over extended periods, we also investigated potential Ru leaching from the catalyst support. A typical hydrolysis catalysed by **5.2a** (0.2 mol%) was allowed to reach *ca.* 60% conversion, at which point the reaction mixture was passed through a 0.45 µm syringe filter, and the hydrogen evolution from the filtrate was monitored. As shown in **Figure 5.10a**, following filtration, no hydrogen was evolved in the absence of catalyst; this indicates either that the catalyst is completely heterogeneous, or that any leached Ru species is inactive for NaBH₄ hydrolysis. However, the former assumption is most probable as analysis of the filtrate

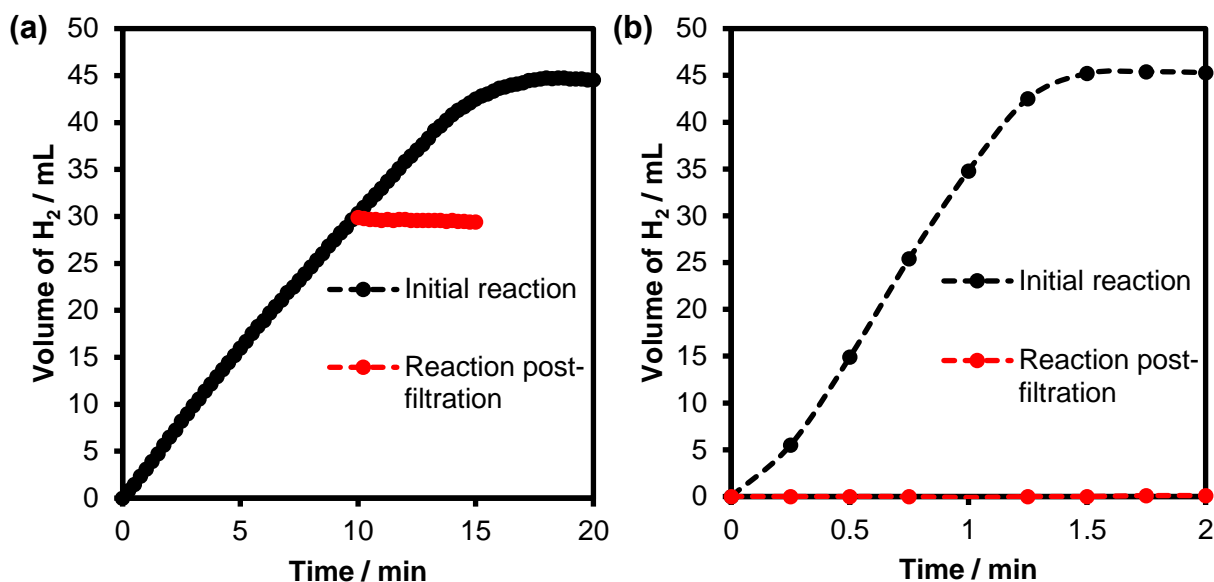


Figure 5.10 (a) Leaching study where the RuNP@PIIL (0.2 mol%) catalysed hydrolysis of NaBH₄ (0.021 g) in H₂O (2 mL) was stopped and filtered at *ca.* 60% conversion. Gas evolution from the resulting filtrate was measured – negative readings due to subtraction of background reaction. **(b)** Leaching study with RuNP@PIIL (7.5 mol%) where the filtrate was charged again with NaBH₄ (0.021 g) and gas evolution measured (red data points).

by ICP-OES determined that any leached Ru species was below the detection limit of the instrument. In a complimentary study, a reaction catalysed by a much higher loading of **5.2a** (7.5 mol%) was allowed to reach completion, before filtering and recharging the filtrate with a fresh portion of NaBH₄; once more, any hydrogen generated corresponded to the background liberation of hydrogen from uncatalysed NaBH₄ hydrolysis. Note that following the reaction with 7.5 mol% catalyst, some leached Ru was detected by ICP-OES, although the amount of soluble Ru species represented <1% of the initial Ru charged into the reaction mixture.

5.7 Conclusion

Polymer immobilized ionic liquids are effective supports for generating highly active RuNP catalysts for the hydrolysis of NaBH₄ and are also highly recyclable, whereby RuNP@PIIL (**5.2a**) maintained 79% of its initial activity over 5 runs, even without isolation and washing of the catalyst. However, additional studies will be required to understand why catalyst modification with phosphine oxide and PEG groups led to a decrease in catalyst efficacy. Initial XPS studies of the catalyst surface found that it was composed of a RuO₂ layer that became more electron-rich following catalyst functionalisation. It is possible that hydride transfer to RuO₂ occurs more readily at an electron-deficient surface, which would rationalise the improved activity of RuNP@PIIL compared to its functionalised counterparts. To this end, mechanistic studies

found that NaBH_4 may be involved in the rate limiting step, therefore, the factors that control its adsorption/desorption from the catalyst surface may be crucial for obtaining high activities. Additional studies will be required to understand how catalyst modification, particularly with large hygroscopic groups such as PEG, affect the mechanical properties of the material – if functionalisation of the catalyst leads to significant changes in porosity and wettability, then this could have ramifications for facilitating access of substrates to the active sites of the catalyst.

5.8 Experimental

5.8.1 General Procedure for Synthesis of Functionalised Polymer Immobilized Ionic Liquid Supports 5.1a-c

A screw-top Schlenk flask was charged with 1,2-dimethyl-3-(4-vinylbenzyl)-imidazolium chloride (**2.1**) or PEG-modified IL monomer **4.4**, styrene or phosphine oxide monomer **4.6**, and 2-methyl-1,3- bis(4-vinylbenzyl)-imidazolium chloride (**2.3**), corresponding to an ionic liquid : phosphine oxide (or styrene) : crosslinker ratio of 1.86 : 1 : 0.14. Upon complete dissolution of the monomers in 2:1 THF/ethanol (with a total monomer concentration of 0.2 M), the mixture was charged with azobis(2-methylpropionitrile) (5 mol%), before immediately degassing the solution via the freeze-thaw technique (6 cycles). The mixture was then stirred and heated at 80 °C. After 96 hours, the flask was charged with an additional portion of azobis(2- methylpropionitrile) (5 mol%), before degassing and stirring for a further 24 hours at 80 °C. After this time, the flask was allowed to cool to room temperature before precipitating the polymer by dropwise addition to stirring diethyl ether. The resulting precipitate was isolated by filtration, washed with diethyl ether, and dried *in vacuo* to afford off-white/pale-yellow powders. Note that **5.1c** was incredibly hygroscopic and even short periods in contact with air made the material difficult to handle.

5.8.2 General Procedure for the Synthesis of PIIL-Supported RuNP Catalysts 5.2a-c

A round bottom flask was charged with X-PIIL (2.5 mmol) and ethanol (50 mL). To this, a solution of $\text{RuCl}_3 \cdot 3\text{H}_2\text{O}$ (0.65 g, 2.5 mmol) in deionized water (20 mL) was added in a single portion and the resulting mixture was stirred vigorously for 5 h at room temperature. After this time, an aqueous solution of NaBH_4 (0.76 g, 20 mmol in 10 mL of water) was added dropwise and the suspension stirred for an additional 18 hours at room temperature before concentrating to near dryness *in vacuo*. The crude black solid was triturated with cold acetone (2 x 100 mL), washed with water (100 mL) and ethanol (2 x 40 mL) and a black solid was

recovered from the washings *via* centrifugation followed by filtration through a frit. The final product was washed with diethyl ether until a granular black solid was obtained which was dried *in vacuo* to afford free flowing black powders.

Catalyst	Yield / %	Wt% Ruthenium	Ruthenium Loading / mmol·g ⁻¹
5.2a	87	5.85	0.61
5.2b	50	7.02	0.70
5.2c	53	7.24	0.72

5.8.3 Ruthenium Nanoparticle Catalyzed Hydrolysis of Sodium Borohydride

Comparative catalytic hydrolysis reactions were conducted in water at the appropriate temperature in a thermostated 50 mL round bottom flask. The flask was charged with a stir bar, an appropriate quantity of catalyst **5.2a-c** or **4.8** (0.2 mol%) and NaBH₄ (0.021 g, 0.57 mmol) and fitted with a gas outlet which was connected to the top of an inverted water-filled burette. The reaction was initiated by adding water (2 mL), immediately sealing the system by replacing the gas outlet, opening the tap of the water filled burette and recording the time zero volume. Gas evolution began immediately, and the progress of the reaction was monitored by measuring the amount of gas generated by recording the volume of water displaced from the burette at regular time intervals (15 sec). Kinetic studies were also conducted as described above using 0.26 mol% **5.2a**, 0.32 mol% **5.2b**, 0.45 mol% **5.2c**, and 0.11 mol% **4.8** across a range of temperatures (21 °C, 25 °C, 30 °C, 35 °C and 40 °C) and the corresponding activation energies (*E_a*) were determined from an Arrhenius plot of the initial rate against 1/*T*.

5.8.4 Determination of the Reaction Order for the RuNP-Catalyzed Hydrolysis of Sodium Borohydride

The rate law was investigated by conducting catalytic hydrolysis reactions at the specified temperature with a constant concentration of NaBH₄ (0.28 M, 0.021 g in water (2 mL)) across a range of catalyst concentrations from 0.14 mol% to 0.69 mol% for **5.2a**, 0.16 mol% to 0.63 mol% for **5.2b**, 0.23 mol% to 1.1 mol% for **5.2c**, and 0.058 mol% to 0.28 mol% for **4.8**. The influence of sodium borohydride concentration on the rate of hydrolysis was determined by conducting reactions at the specified temperature in an aqueous solution of NaOH (100 mL, 2.5 mM) using catalyst **5.2a** (26 μmol) and varying the quantity of sodium borohydride between 6.6 μmol and 185 μmol (*i.e.* [NaBH₄]₀ = 0.053–1.59 mM), which corresponds to a catalyst:NaBH₄ ratio of 1:2 to 1:6.

5.8.5 Study of the Catalytic Efficiency as a Function of the Concentration of NaOH

The influence of the concentration of NaOH on catalyst efficacy was investigated by conducting hydrolysis reactions with catalyst **5.2a** (0.27 mol%) and 2 mL of alkaline 0.28 M NaBH₄ (0.021 g) across a range of sodium hydroxide concentrations (*i.e.* [NaOH] = 0.035, 0.07, 0.14, 0.28, 5.0, 10, 50, 100 mM) and monitoring the gas evolution as a function of time.

5.8.6 Catalyst Recycle Studies for the Hydrolysis of Sodium Borohydride

Recycle studies were conducted at 30 °C as described above using 2 mol% of **5.2a** to catalyze the hydrolysis of sodium borohydride (0.021 g, 0.57 mmol in water (20 mL)). After gas evolution had ceased the flask was recharged with a fresh portion of sodium borohydride (0.021 g, 0.57 mmol) and the gas evolution monitored by recording the volume of water displaced from the burette at regular time intervals; this procedure was repeated five times. After the fifth run, the catalyst was washed with deionized water (3 x 10 mL) prior to use, isolating the catalyst from the washings by centrifugation. The recovered catalyst was then charged once more with sodium borohydride (0.021 g, 0.57 mmol) in water (20 mL), and the evolved gas was monitored over time, as described above.

5.8.7 Filtration Tests

Hot filtration studies were conducted at 30 °C following the protocol described above using 0.2 mol% **5.2a** to catalyze the hydrolysis of sodium borohydride (0.021 g, 0.57 mmol in water (2 mL)). The reaction was monitored by periodically measuring the amount of gas generated and when the reaction had reached about 50% conversion (10 min) the reaction mixture was quickly filtered through a 0.45 µm syringe filter, and the gas generated was monitored for a further 30 min. In an alternative procedure, a catalytic hydrolysis of NaBH₄ (0.021 g, 0.57 mmol) using 0.2 mol% **5.2a** was allowed to reach completion after which the reaction mixture was filtered through a 0.45 µm diameter syringe filter, a further portion of NaBH₄ added (0.021 g, 0.57 mmol) and the amount of gas evolved measured.

5.8.8 Catalyst Poisoning Study

A 50 mL round bottom flask was charged with a stirrer bar, **5.2a** (2 mol%), water (20 mL) and sodium metaborate (0.0765 g, 0.57 mmol) and the mixture stirred at 30 °C for the allocated time (*t* = 0 min, 20 min, 40 min, 60 min) to explore the effect of poisoning time on catalyst efficacy. The reaction was initiated by adding NaBH₄ (0.021 g, 0.57 mmol) and the progress of the reaction monitored by periodically measuring the amount of gas generated, according to the procedure described above.

5.8.9 Tandem Reactions for the Hydrogenation of 1,1-Diphenylethene

Tandem reactions were conducted in a double Schlenk flask system connected by tubing. One flask was charged with a stir bar, NaBH₄ (0.042 g, 1.11 mmol) and 0.2 mol% **5.2a**. The hydrolysis was initiated by adding D₂O (2 mL) or H₂O (2 mL) and the reaction flask was sealed with a stopper and isolated from the second flask. Meanwhile the second flask was charged with a stir bar, 1,1-diphenylethene (0.180 g, 1.00 mmol), 0.5 mol% Pd/C and CH₃OH (2 mL) or d₄-methanol (2 mL). The hydrolysis was left for 30 mins after which time the second flask was evacuated briefly, and the connector opened. The hydrogenation mixture was stirred at 30 °C for 18 h, after which time the solvent was removed under vacuum and the resulting residue analyzed by ¹³C{¹H} NMR spectroscopy and GC-MS to determine the composition and the distribution of isotopologues.

5.9 References

-
- ¹ L. Schlapbach and A. Züttel, *Nature*, 2001, **414**, 353–358.
- ² A. F. Dalebrook, W. Gan, M. Grasmann, S. Moret and G. Laurenczy, *Chem. Commun.*, 2013, **49**, 8735–8751.
- ³ Y. Ligen, H. Vrubel and H. Girault, *Int. J. Hydrogen Energy*, 2020, **45**, 10639–10647.
- ⁴ S. Doherty, J. G. Knight, H. Y. Alharbi, R. Paterson, C. Wills, C. Dixon, L. Šiller, T. W. Chamberlain, A. Griffiths, S. M. Collins, K. Wu, M. D. Simmons, R. A. Bourne, K. R. J. Lovelock and J. Seymour, *ChemCatChem*, 2022, **14**, e202101752.
- ⁵ M. Sankir, L. Semiz, R. B. Serin, N. D. Sankir and D. Baker, *Adv. Catal. Mater.*, 2009, 145–192.
- ⁶ F. Fu, C. Wang, Q. Wang, A. M. Martinez-Villacorta, A. Escobar, H. Chong, X. Wang, S. Moya, L. Salmon, E. Fouquet, J. Ruiz and D. Astruc, *J. Am. Chem. Soc.*, 2018, **140**, 10034–10042.
- ⁷ J. C. Ingersoll, N. Mani, J. C. Thenmozhiyal and A. Muthaiah, *J. Power Sources*, 2007, **173**, 450–457.
- ⁸ N. Kang, Q. Wang, R. Djeda, W. Wang, F. Fu, M. M. Moro, M. D. L. A. Ramirez, S. Moya, E. Coy, L. Salmon, J. L. Pozzo and D. Astruc, *ACS Appl. Mater. Interfaces*, 2020, **12**, 53816–53826.
- ⁹ C. Luo, F. Fu, X. Yang, J. Wei, C. Wang, J. Zhu, D. Huang, D. Astruc and P. Zhao, *ChemCatChem*, 2019, **11**, 1643–1649.
- ¹⁰ C. Yue, P. Yang, J. Wang, X. Zhao, Y. Wang and L. Yang, *Chem. Phys. Lett.*, 2020, **743**, 137170.
- ¹¹ (a) C. Wang, Q. Wang, F. Fu and D. Astruc, *Acc. Chem. Res.*, 2020, **53**, 2483–2493. (b) U. B. Demirci and F. Garin, *J. Alloys Compd.*, 2008, **463**, 107–111.
- ¹² Z. Liu, B. Guo, S. H. Chan, E. H. Tang and L. Hong, *J. Power Sources*, 2008, **176**, 306–311.
- ¹³ M. Zahmakiran and S. Özkar, *Langmuir*, 2009, **25**, 2667–2678.
- ¹⁴ Y. Gong, H. Zhong, W. Liu, B. Zhang, S. Hu and R. Wang, *ACS Appl. Mater. Interfaces*, 2018, **10**, 776–786.
- ¹⁵ N. Sahiner, A. O. Yasar and N. Aktas, *J. Ind. Eng. Chem.*, 2015, **23**, 100–108.
- ¹⁶ (a) A. Chinnappan and H. Kim, *Int. J. Hydrogen Energy*, 2012, **37**, 18851–18859. (b) A. Chinnappan, A. H. Jadhav, J. M. C. Puguán, R. Appiah-Ntiamoah and H. Kim, *Energy*, 2015, **79**, 482–488.

-
- ¹⁷ R. Paterson, A. A. Alharbi, C. Wills, C. Dixon, L. Šiller, T. W. Chamberlain, A. Griffiths, S. M. Collins, K. Wu, M. D. Simmons, R. A. Bourne, K. R. J. Lovelock, J. Seymour, J. G. Knight and S. Doherty, *Mol. Catal.*, 2022, **528**, 1–16.
- ¹⁸ D. J. Morgan, *Surf. Interface Anal.*, 2015, **47**, 1072–1079.
- ¹⁹ M. A. Ernst and W. G. Sloof, *Surf. Interface Anal.*, 2008, **40**, 334–337.
- ²⁰ D. J. Morgan, *Surf. Interface Anal.*, 2015, **47**, 1072–1079.
- ²¹ S. C. Amendola, S. L. Sharp-Goldman, M. S. Janjua, N. C. Spencer, M. T. Kelly, P. J. Petillo and M. Binder, *Int. J. Hydrogen Energy*, 2000, **25**, 969–975.
- ²² M. Zahmakiran and S. Özkar, *J. Mol. Catal. A Chem.*, 2006, **258**, 95–103.
- ²³ D. D. Tuan and K. Y. A. Lin, *Chem. Eng. J.*, 2018, **351**, 48–55.
- ²⁴ N. Sahiner, O. Ozay, E. Inger and N. Aktas, *J. Power Sources*, 2011, **196**, 10105–10111.
- ²⁵ S. U. Jeong, R. K. Kim, E. A. Cho, H. J. Kim, S. W. Nam, I. H. Oh, S. A. Hong and S. H. Kim, *J. Power Sources*, 2005, **144**, 129–134.
- ²⁶ Y. Li, Q. Zhang, N. Zhang, L. Zhu, J. Zheng and B. H. Chen, *Int. J. Hydrogen Energy*, 2013, **38**, 13360–13367.
- ²⁷ Y. Liang, H. Bin Dai, L. P. Ma, P. Wang and H. M. Cheng, *Int. J. Hydrogen Energy*, 2010, **35**, 3023–3028.
- ²⁸ N. Patel, R. Fernandes and A. Miotello, *J. Power Sources*, 2009, **188**, 411–420.
- ²⁹ S. Özkar and M. Zahmakiran, *J. Alloys Compd.*, 2005, **404–406**, 728–731.
- ³⁰ M. Bagheri, M. Y. Masoomi, E. Domínguez and H. García, *Sustain. Energy Fuels*, 2021, **5**, 4587–4596.
- ³¹ N. Kang, R. Djeda, Q. Wang, F. Fu, J. Ruiz, J. Pozzo and D. Astruc, *ChemCatChem*, 2019, **11**, 2341–2349.
- ³² G. Guella, B. Patton, A. Miotello, D. Fisica and V. Uni, 2007, 18744–18750.
- ³³ L. Yu, P. Pellechia and M. A. Matthews, *Int. J. Hydrogen Energy*, 2014, **39**, 442–448.
- ³⁴ R. Peña-Alonso, A. Sicurelli, E. Callone, G. Carturan and R. Raj, *J. Power Sources*, 2007, **165**, 315–323.
- ³⁵ J. S. Zhang, W. N. Delgass, T. S. Fisher and J. P. Gore, *J. Power Sources*, 2007, **164**, 772–781.
- ³⁶ H. Bin Dai, Y. Liang, L. P. Ma and P. Wang, *J. Phys. Chem. C*, 2008, **112**, 15886–15892.
- ³⁷ E. M. Simmons and J. F. Hartwig, *Angew. Chemie - Int. Ed.*, 2012, **51**, 3066–3072.
- ³⁸ M. Gómez-Gallego and M. A. Sierra, *Chem. Rev.*, 2011, **111**, 4857–4963.
- ³⁹ E. C. M. Tse, T. T. H. Hoang, J. A. Varnell and A. A. Gewirth, *ACS Catal.*, 2016, **6**, 5706–5714.

⁴⁰ Z. Łodziana, P. Błoński, Y. Yan, D. Rentsch and A. Remhof, *J. Phys. Chem. C*, 2014, **118**, 6594–6603.

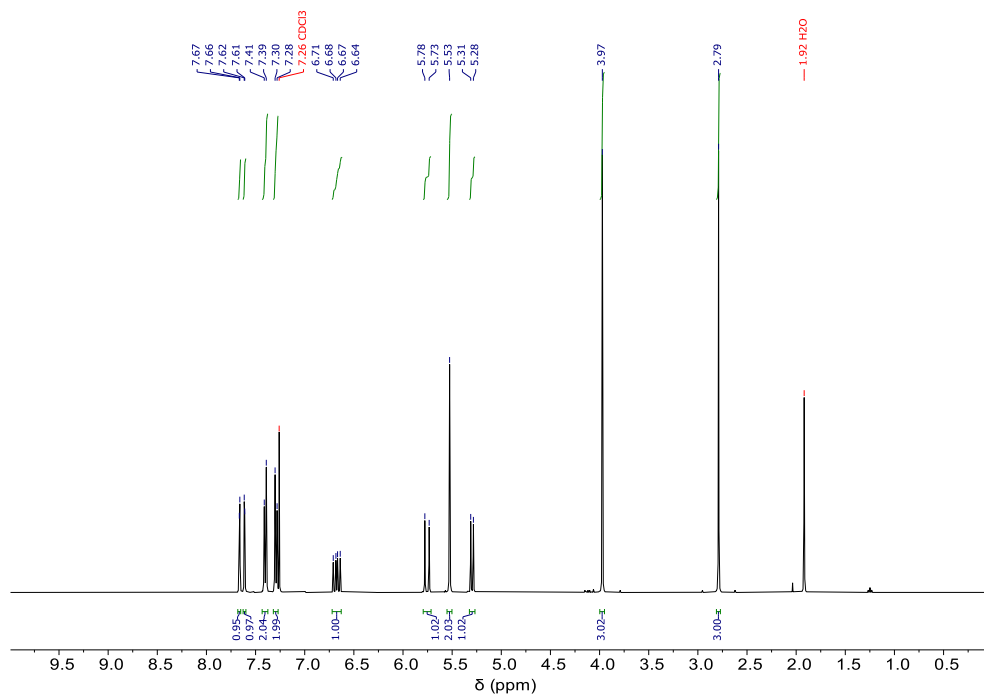
Appendix

A.2 Chapter 2

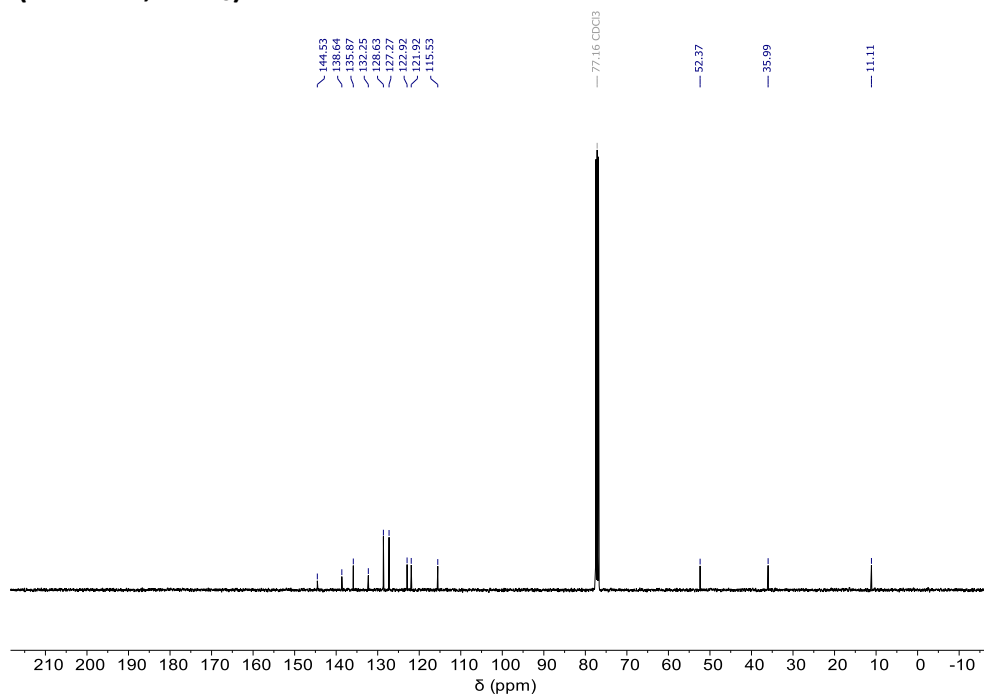
A.2.1 NMR Spectra of Monomers and Monomer Precursors

1,2-Dimethyl-3-(4-vinylbenzyl)imidazolium chloride (**2.1**)

^1H NMR (400 MHz, CDCl_3):

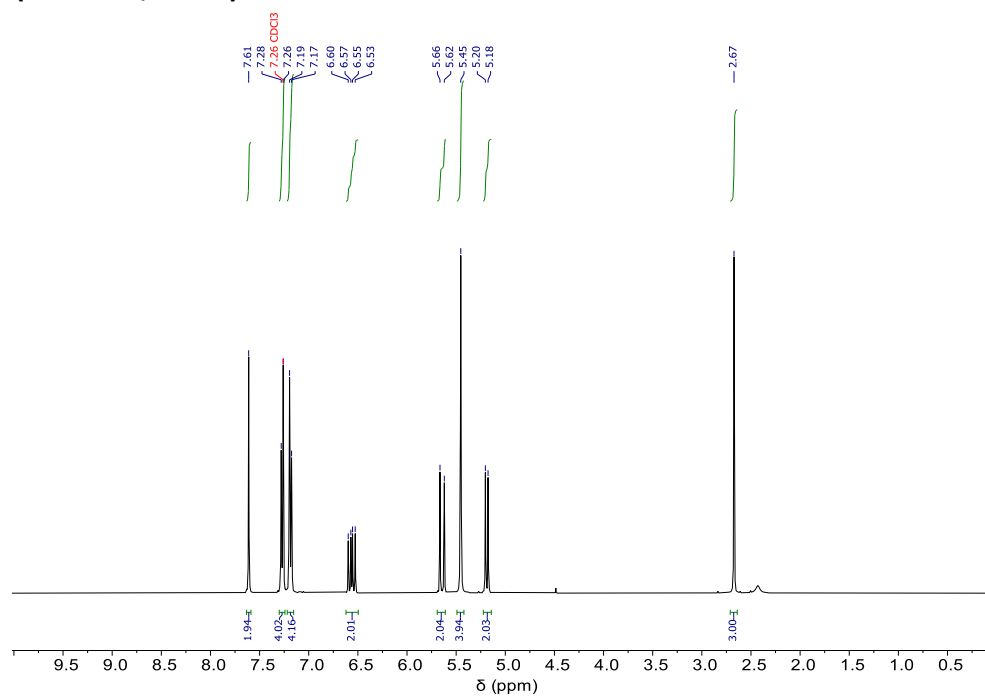


^{13}C NMR (101 MHz, CDCl_3):

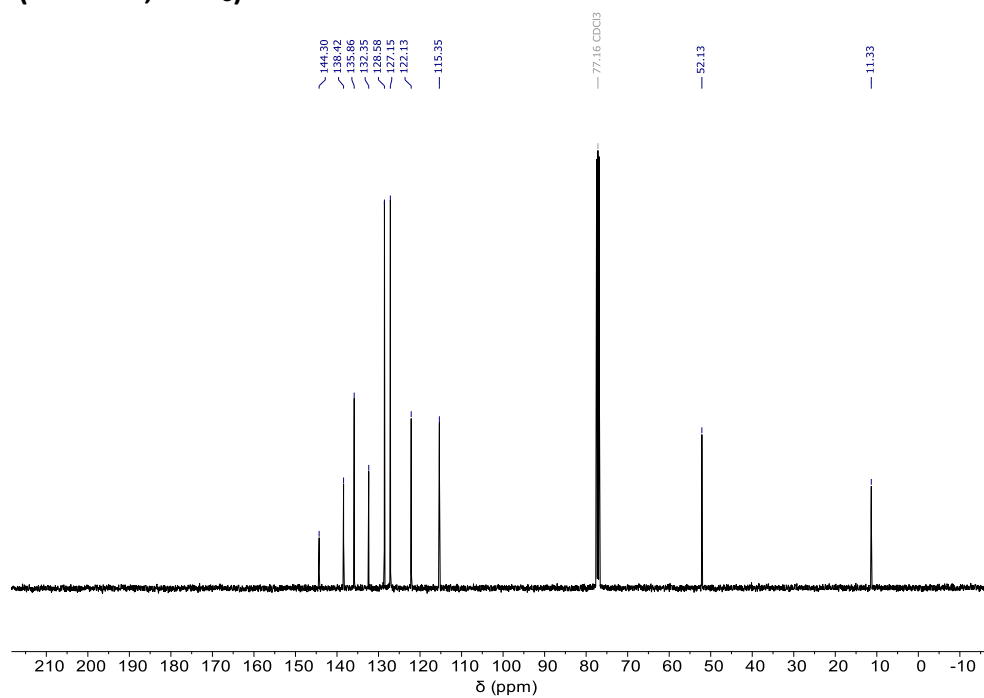


2-Methyl-1,3-bis(4-vinylbenzyl)imidazolium chloride (**2.3**)

^1H NMR (400 MHz, CDCl_3):

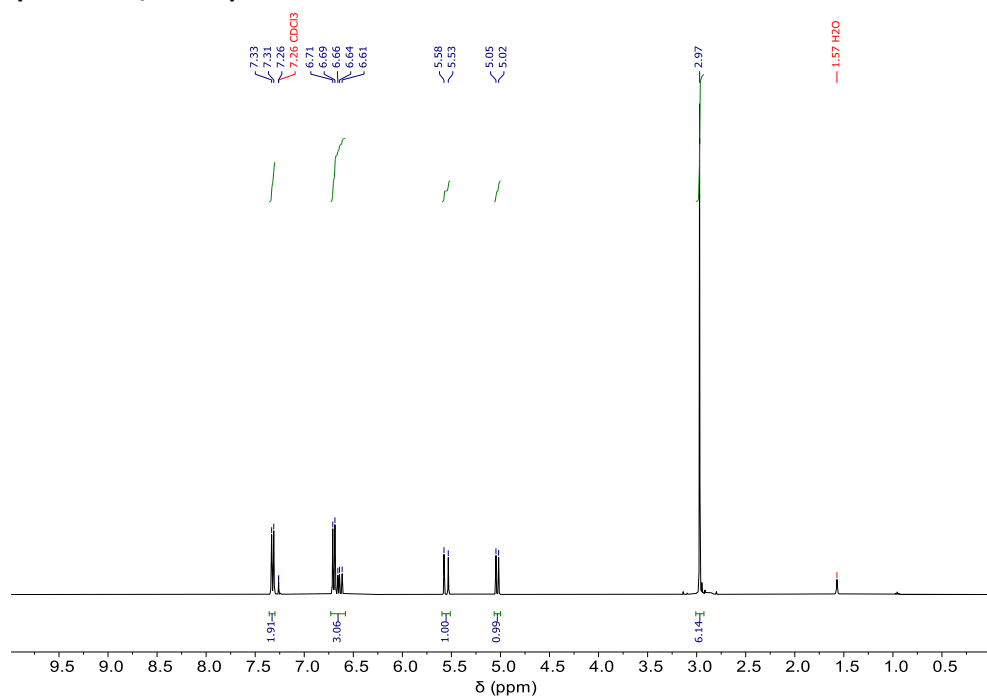


^{13}C NMR (101 MHz, CDCl_3):

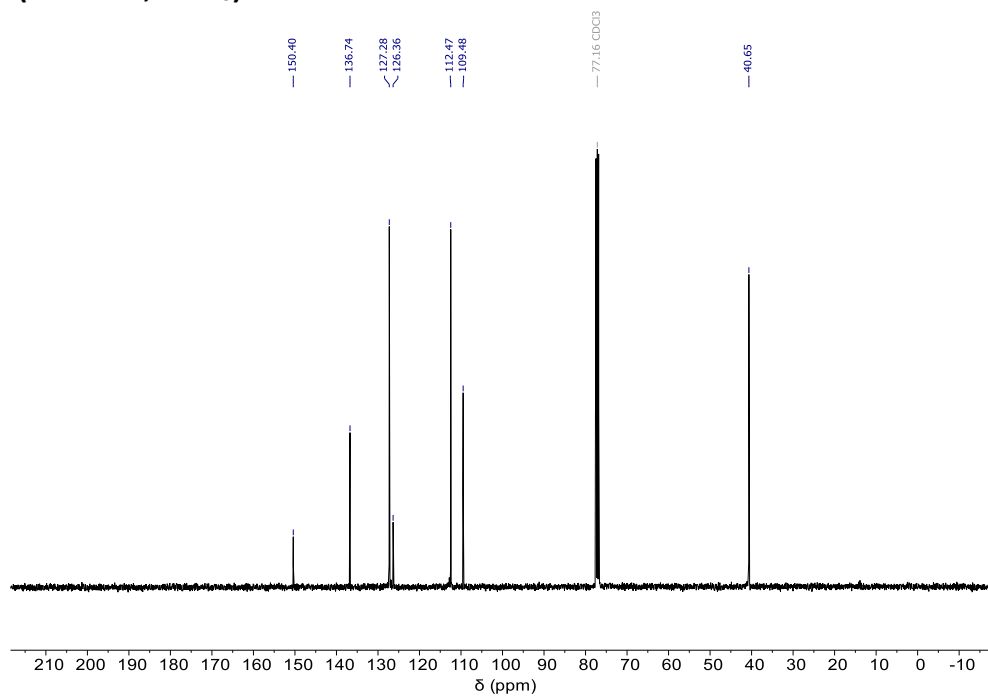


N,N-Dimethyl-4-aminostyrene (**2.4**)

^1H NMR (400 MHz, CDCl_3):

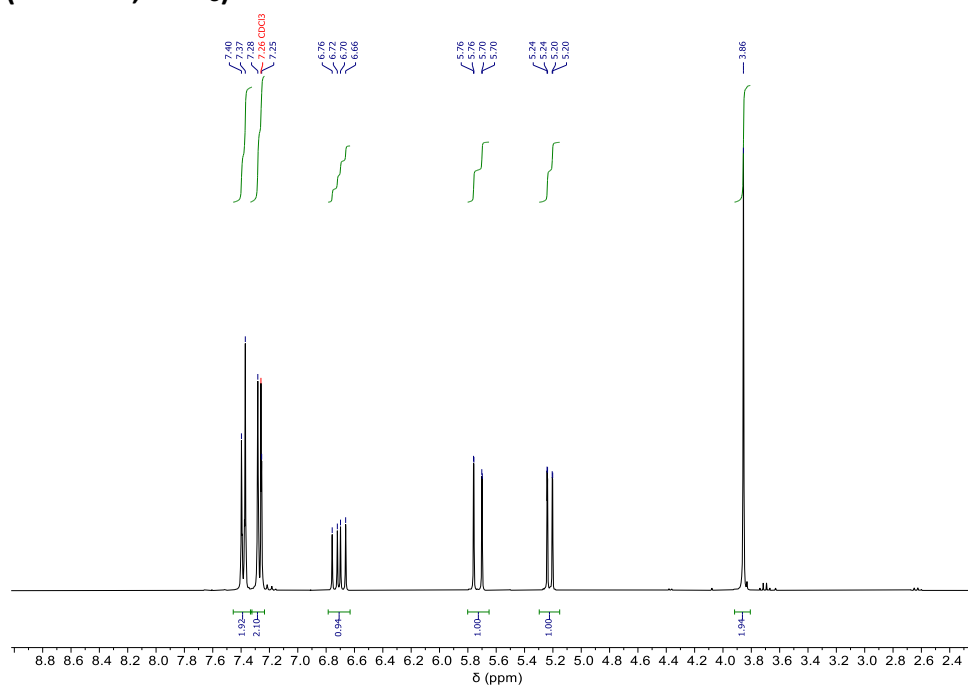


^{13}C NMR (101 MHz, CDCl_3):

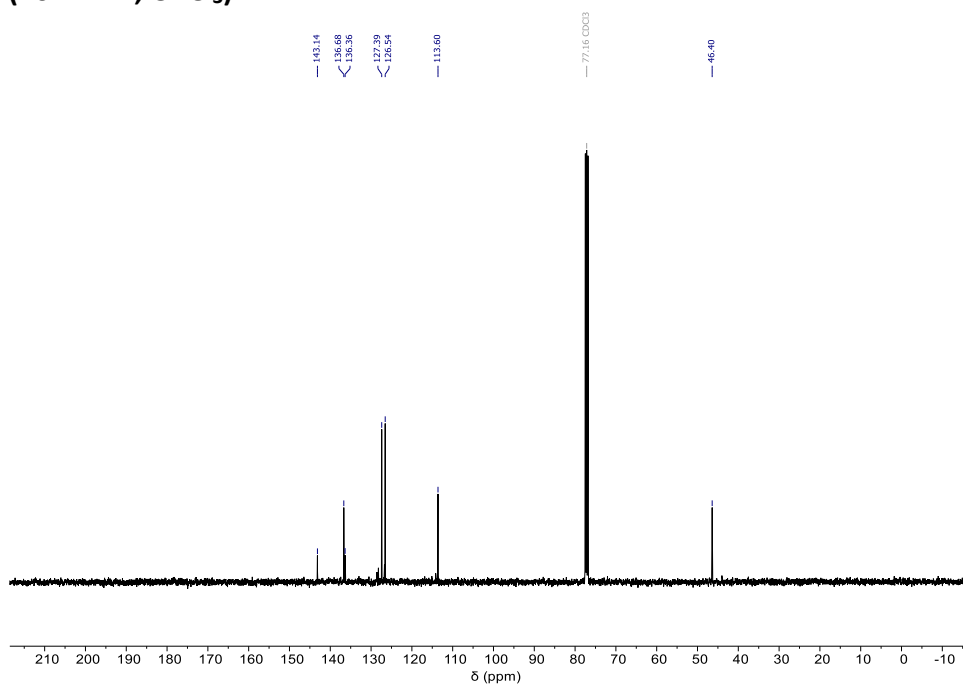


4-Vinylbenzylamine (2.6)

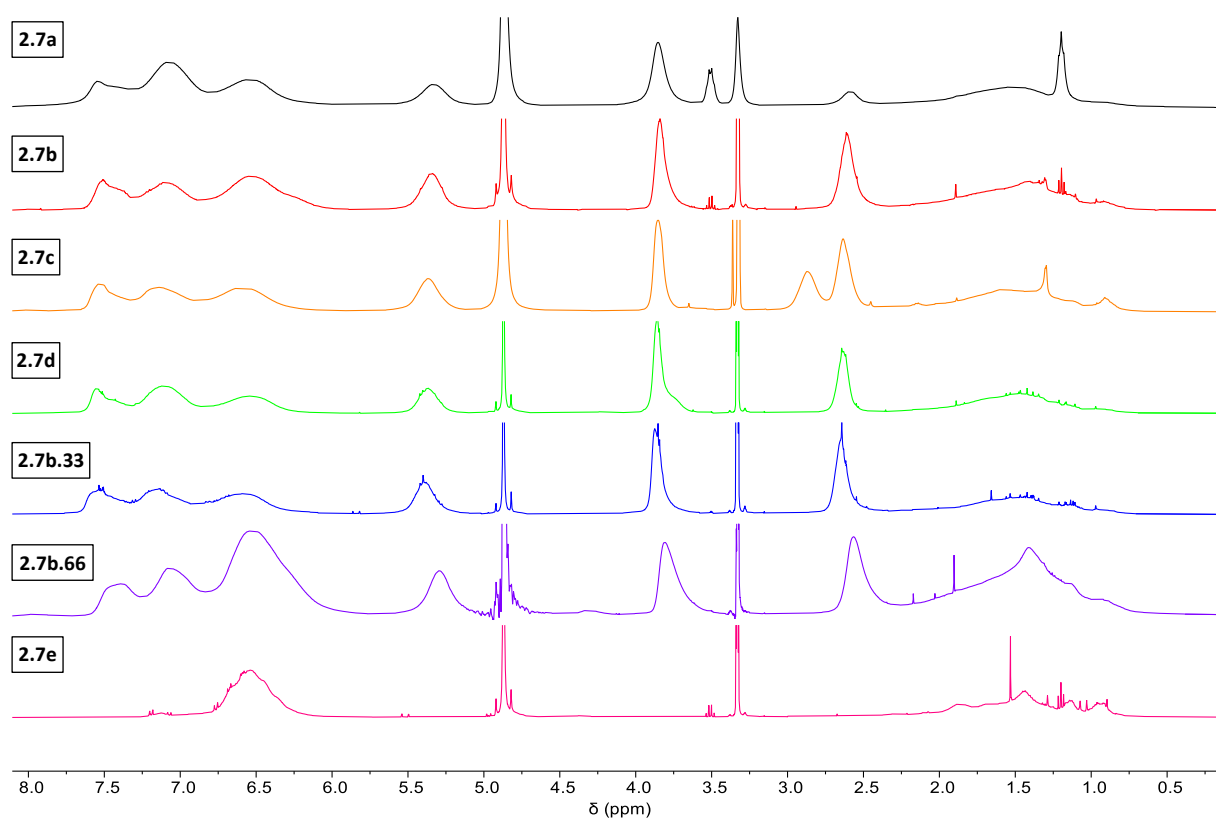
¹H NMR (300 MHz, CDCl₃):



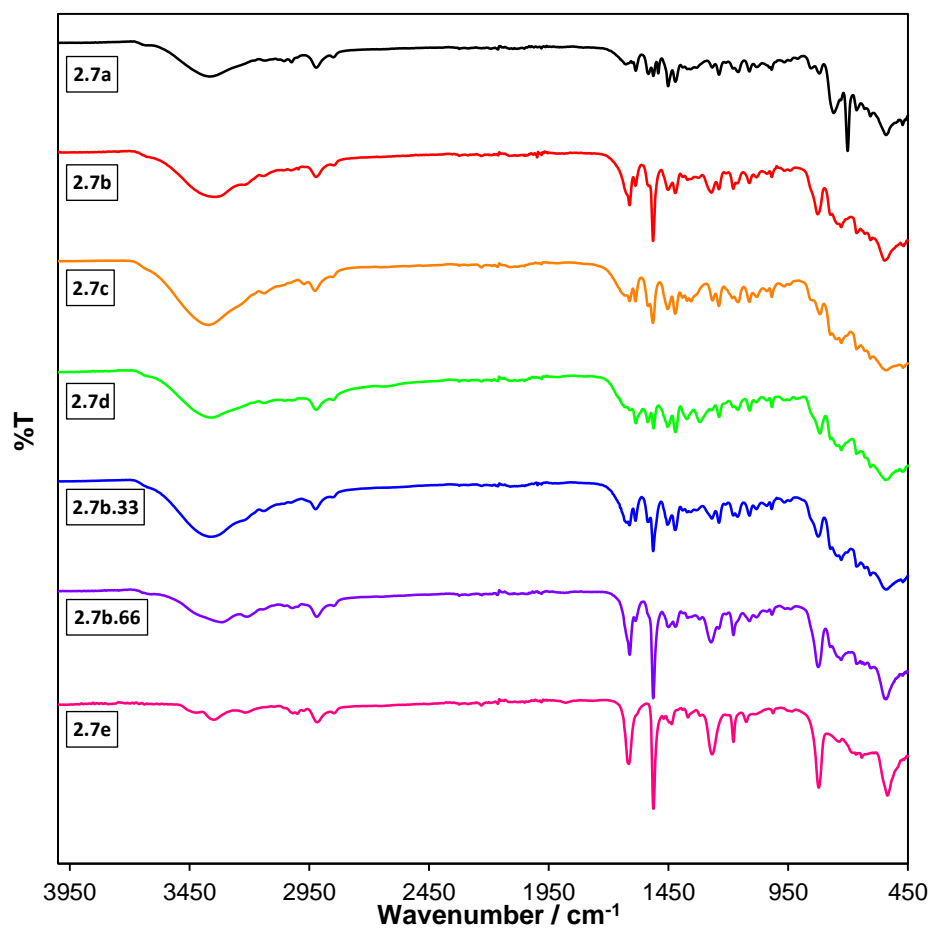
¹³C NMR (101 MHz, CDCl₃):



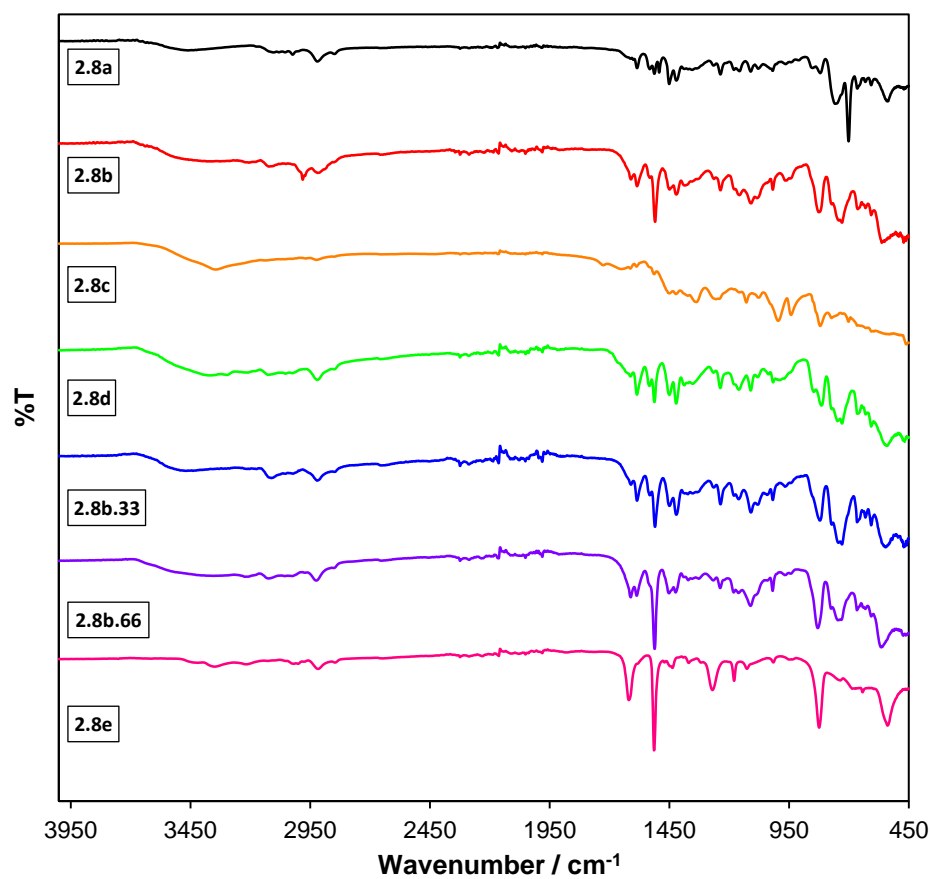
A.2.2 Solution State ^1H NMR Spectra of PIIL Supports 2.7a-e (400 MHz, Methanol- d_4)



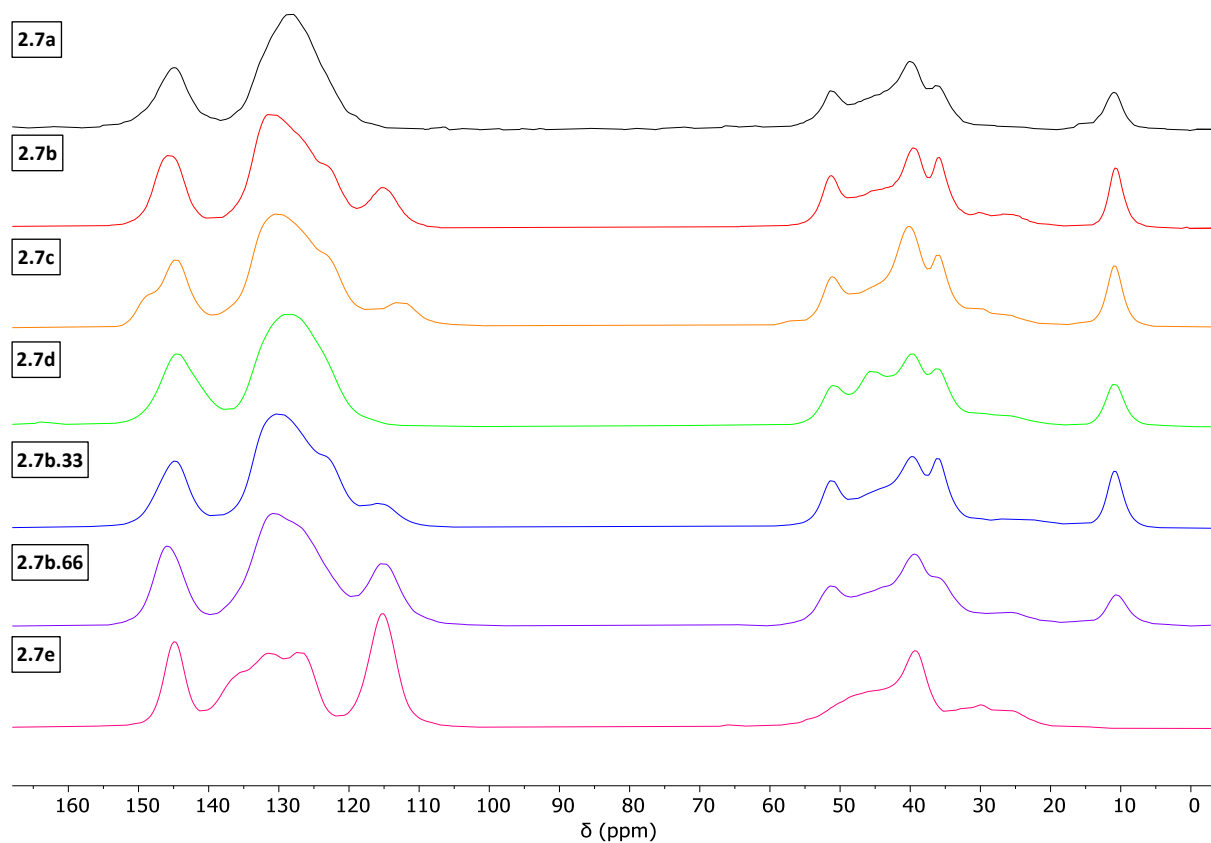
A.2.3 FT-IR Spectra of PIIL Supports 2.7a-e



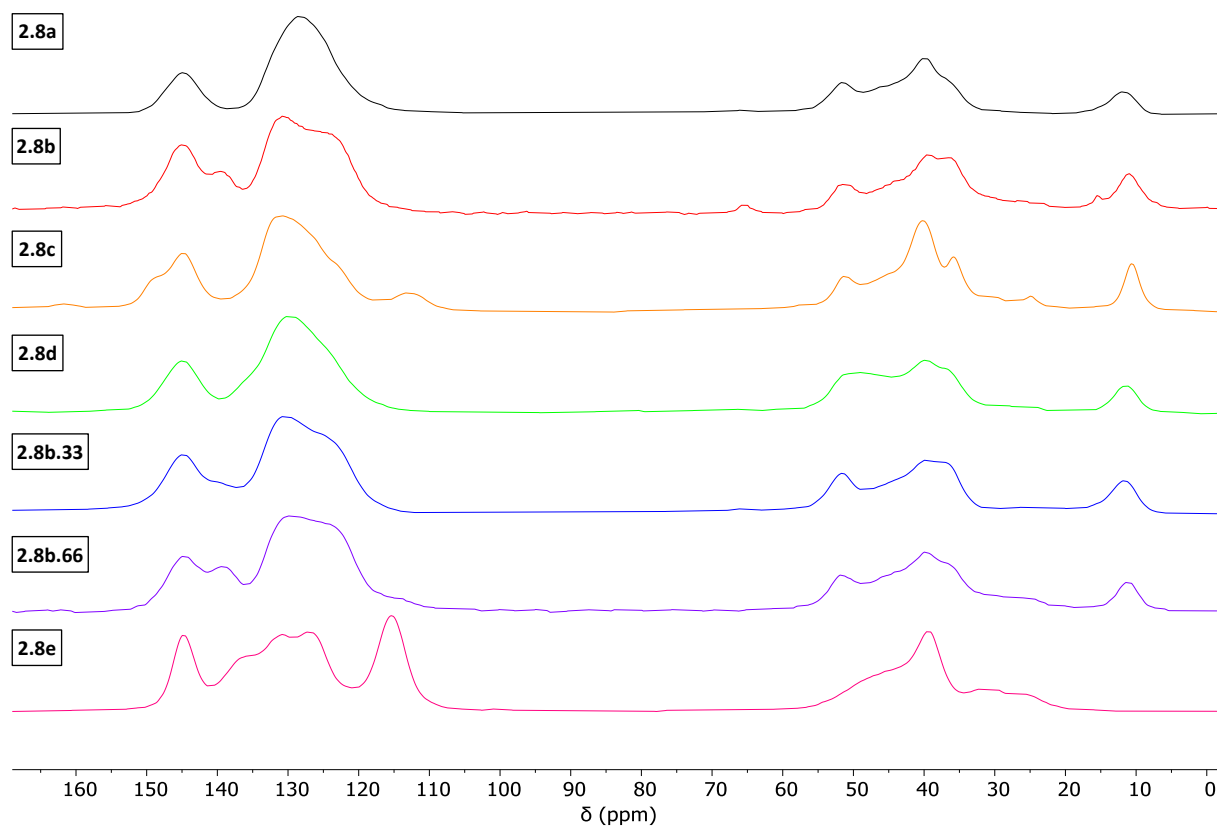
A.2.4 FT-IR Spectra of PdCl₄ Precatalysts 2.8a-e



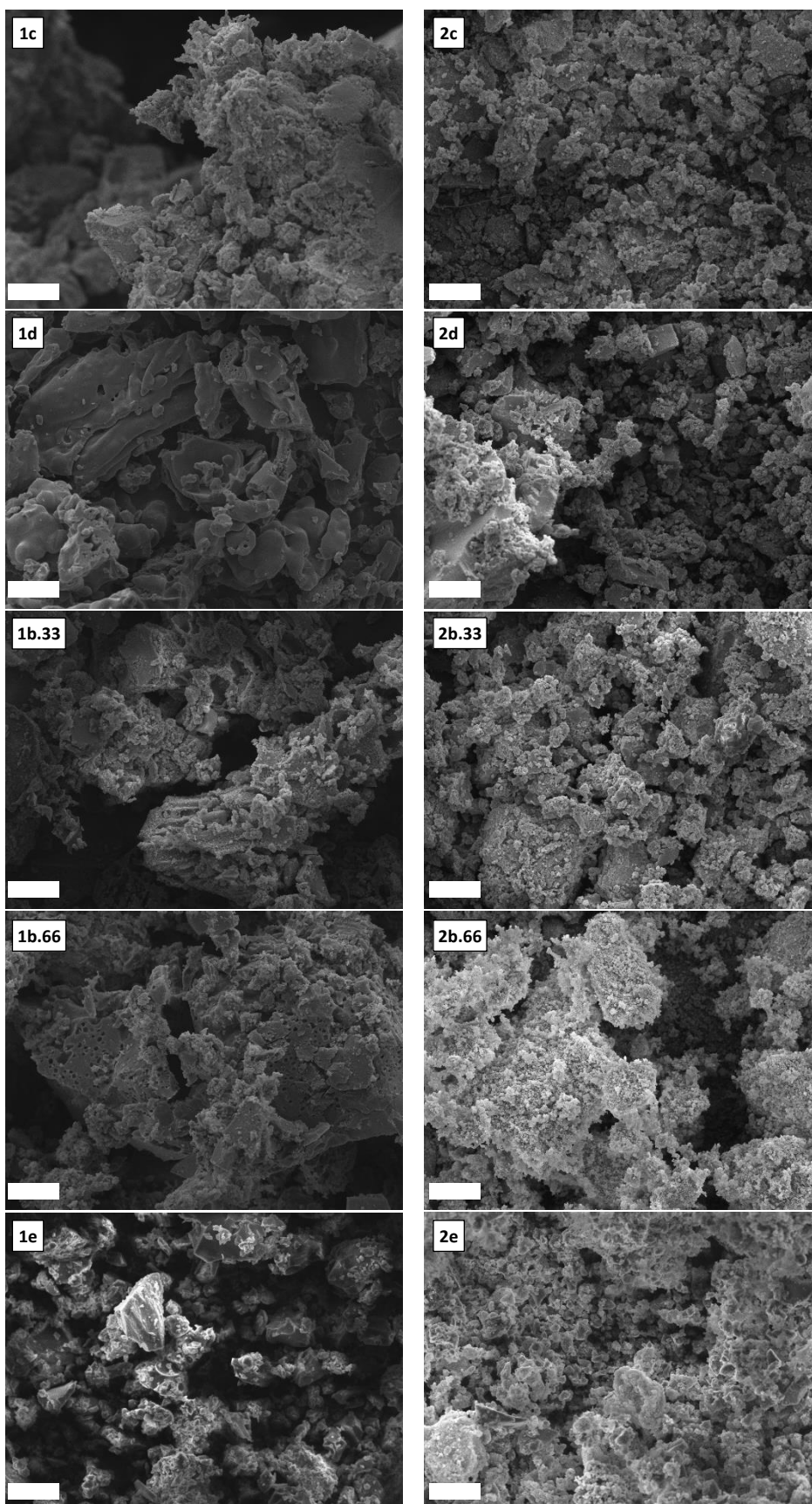
A.2.5 Solid state CP-TOSS MAS ^{13}C NMR spectra of Polymers 2.7a-e.



A.2.6 Solid state CP-TOSS MAS ^{13}C NMR Spectra of Precatalysts 2.8a-e.



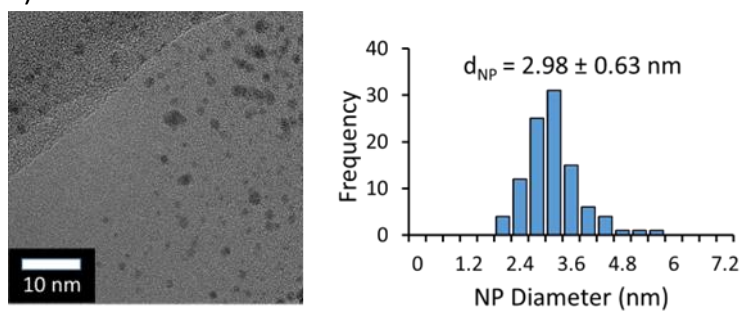
A.2.7 SEM Images of Freshly Prepared Polymers and Precatalysts



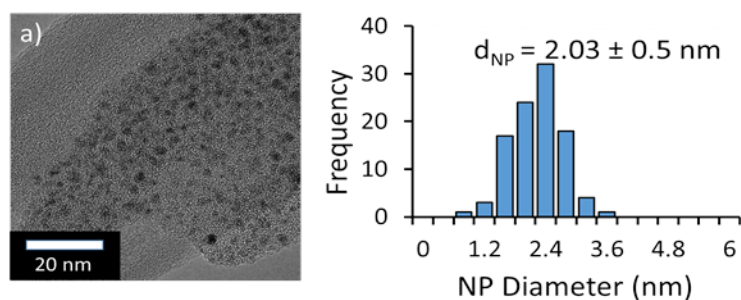
White scale bar = 20 μm .

A.2.8 TEM Images of Nanoparticles Generated from Precatalysts 2.8a-e

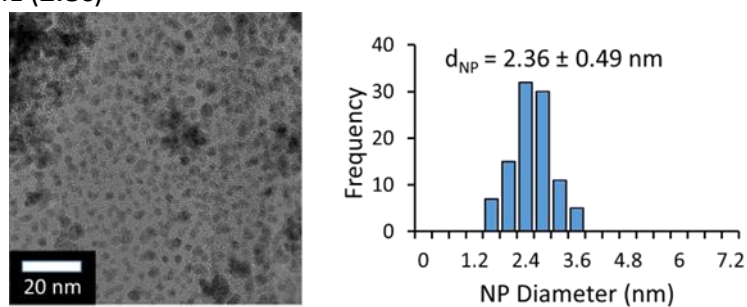
PdNP@PIIL (**2.8a**)



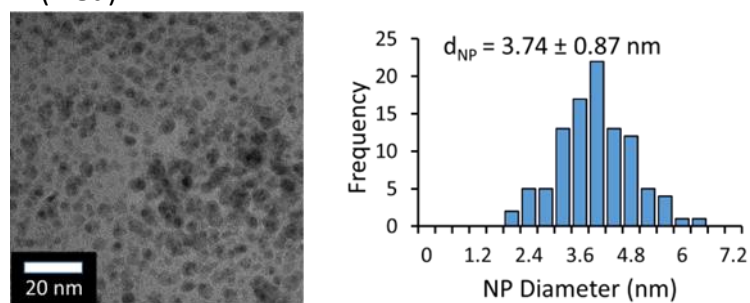
PdNP@NH₂PIIL (**2.8b**)



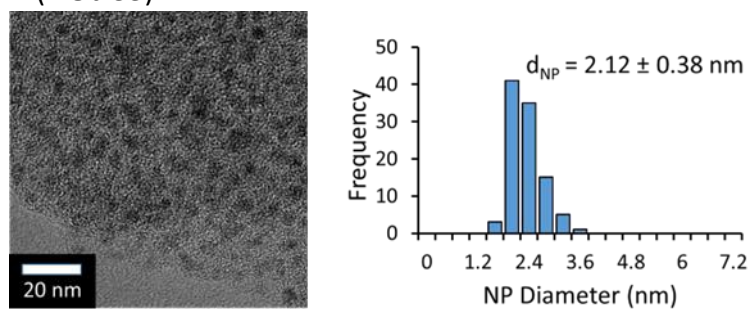
PdNP@NMe₂PIIL (**2.8c**)



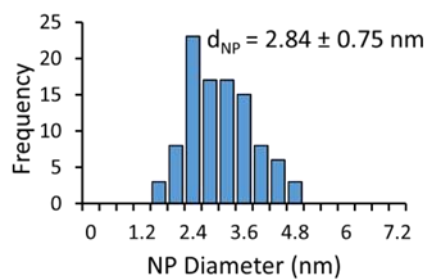
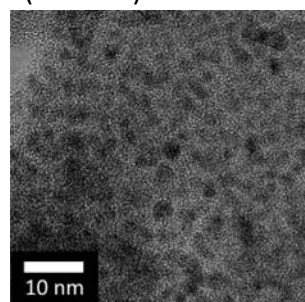
PdNP@NH₂CH₂PIIL (**2.8d**)



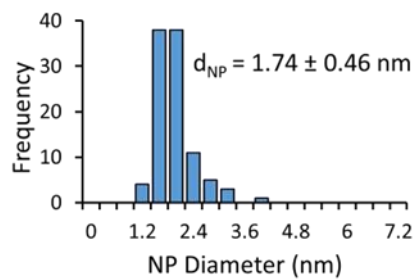
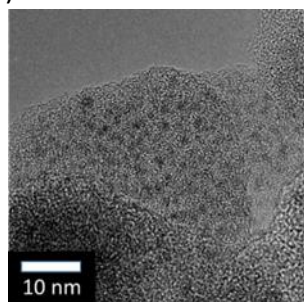
PdNP@33NH₂PIIL (**2.8b.33**)



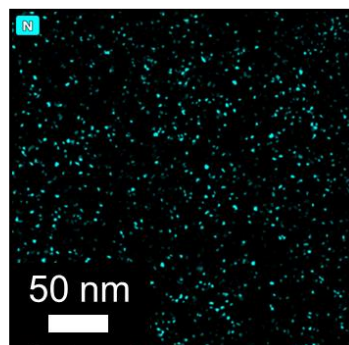
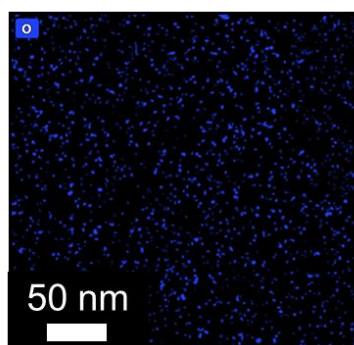
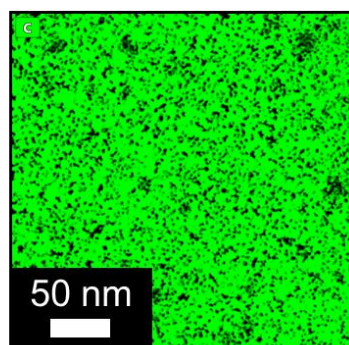
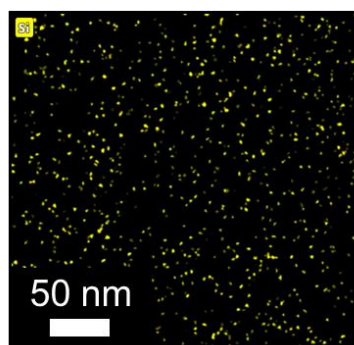
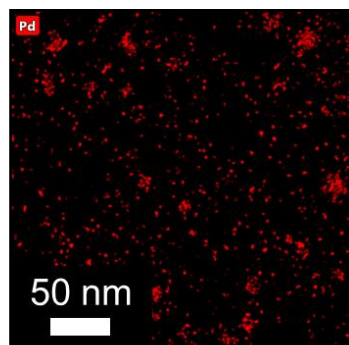
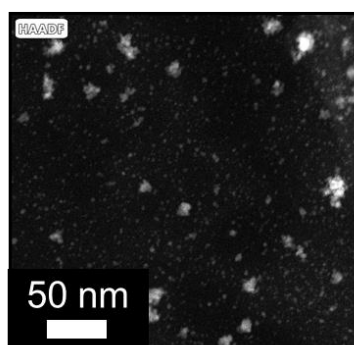
PdNP@66NH₂PIIL (2.8b.66)



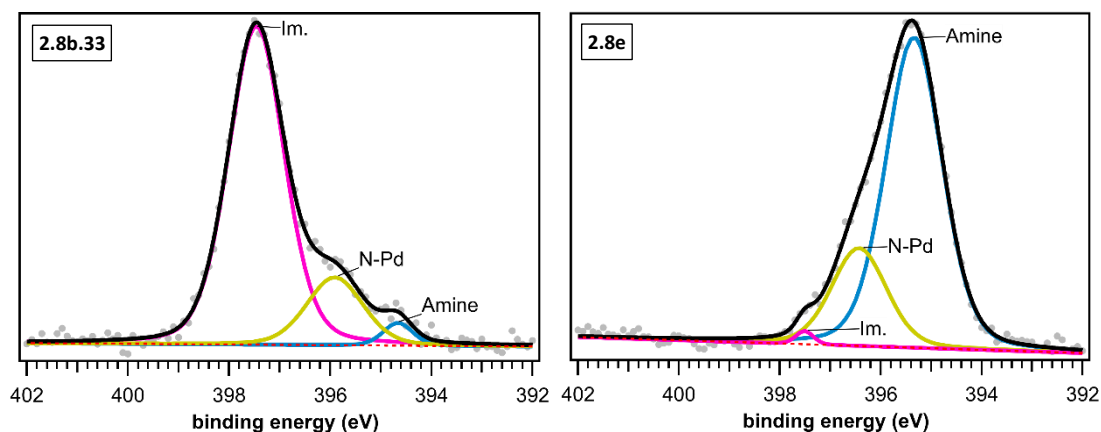
PdNP@NH₂ (2.8e)



A.2.9 HAADF-TEM Image and EDX Maps of Nanoparticles Generated from 2.8a

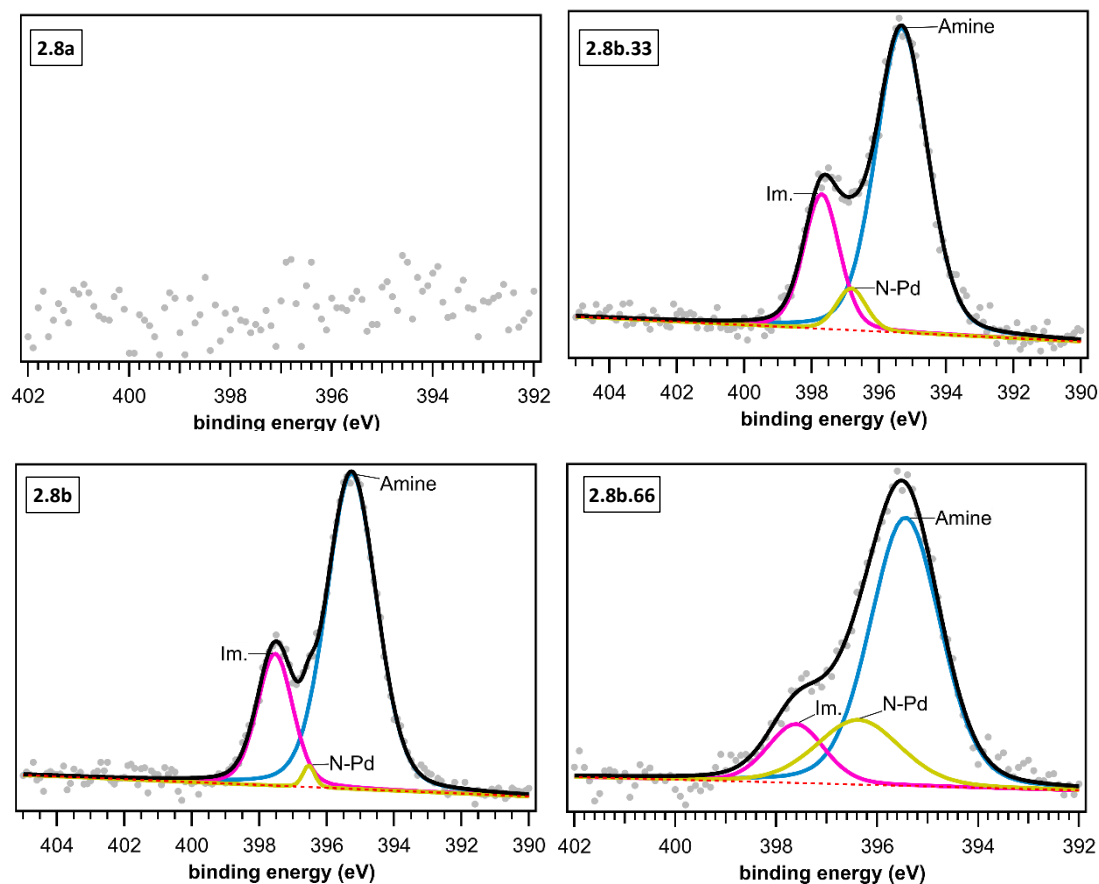


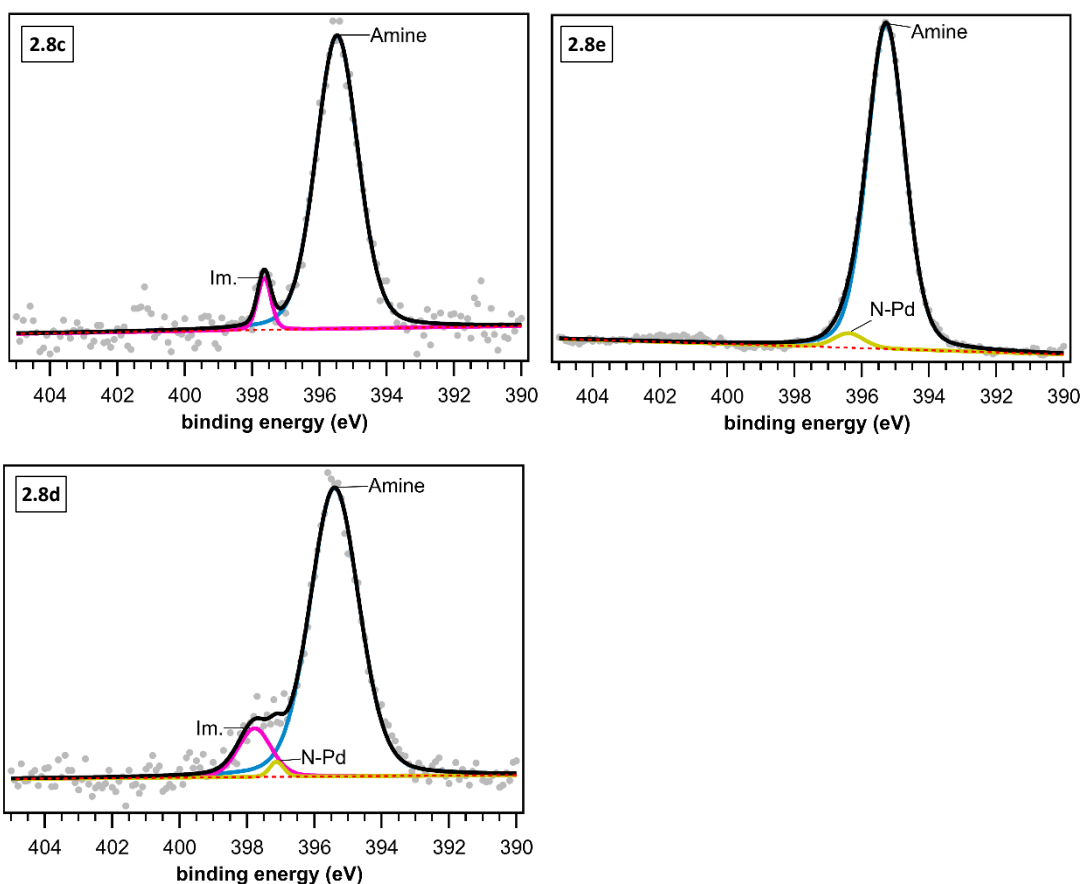
A.2.10 N 1s Core Level XPS Spectra of Precatalysts 2.8b.33 and 2.8e



The N1s spectrum of sample **2.8e** shows a small impurity with a binding energy consistent with that of imidazolium (397.5 eV) – as this impurity was in such low abundance (1%), it has been attributed to cross-contamination across samples during analysis.

A.2.11 N 1s Core Level XPS Spectra of Nanoparticles Generated from Precatalysts 2.8a-e





A.2.12 Table of N 1s Core Level Binding Energies for Precatalysts 2.8a-e and Polymer 2.7b.66

Sample	C1s	Imidazolium	Amine	N-Pd	Imidazolium	Amine	N-Pd
	Aliphatic				at.%	at.%	at.%
2.8a	280.6	397.4			100		
2.8b	280.6	397.5	394.8	395.9	70	5	25
2.8c	280.7	397.6	395.1	395.9	81	8	12
2.8d	280.7	397.6	395.3	396.0	67	10	23
2.8b.33	280.6	397.5	394.7	395.9	80	3	17
2.8b.66	280.7	397.5	395.5	396.3	57	25	18
2.8e	280.4	397.5	395.3	396.4	1	76	23
2.7b.66	280.5	397.4	395.0		51	49	

The aliphatic C1s peak is given as a reference point.

The N1s spectrum of sample **2.8e** shows a small impurity with a binding energy consistent with that of imidazolium (397.5 eV) – as this impurity was in such low abundance (1 at.%), it has been attributed to cross-contamination across samples during analysis.

A.2.13 Table of N 1s Core Level Binding Energies for Nanoparticles Generated from Precatalysts 2.8a-e

Precatalyst	C1s	Imidazolium	Amine	N-Pd	Imidazolium	Amine	N-Pd
	Aliphatic				at.%	at.%	at.%
2.8a	280.7	-	-	-	-	-	-
2.8b	280.5	397.5	395.3	396.5	23	76	1
2.8c	280.6	397.6	395.5		5	95	
2.8d	280.7	397.8	395.4	397.1	10	89	1
2.8b.33	280.6	397.7	395.3	396.8	22	76	3
2.8b.66	280.6	397.6	395.4	396.4	12	68	20
2.8e	280.3	-	395.3	395.4	-	97	3

The aliphatic C1s peak is given as a reference point.

A.2.14 Table of Pd 3d Core Level Binding Energies for Precatalysts 2.8a-e

Sample	C1s	Pd(II)-Cl	Sat.	Pd(II)-N	PdO	Pd(II)-Cl	Sat.	Pd(II)-N	PdO
	Aliphatic	3d _{5/2}		3d _{5/2}	3d _{5/2}	at.%	at.%	at.%	at.%
2.8a	280.6	333.4	340.6	-	-	93	7	-	-
2.8b	280.6	333.7	340.1	335.0	-	89	4	7	-
2.8c	280.7	333.7	341.1	-	-	94	6	-	-
2.8d	280.7	333.9	341.1	-	332.9	82	5	-	13
2.8b.33	280.6	333.6	341.0	335.0	-	91	5	4	-
2.8b.66	280.7	333.9	341.4	335.4	-	88	4	7	-
2.8e	280.4	334.0	341.9	335.4	-	80	3	17	-

The aliphatic C1s peak is given as a reference point.

A.2.15 Table of Pd 3d Core Level Binding Energies for Nanoparticles Generated from Precatalysts 2.8a-e

Precatalyst	C1s	Pd(II)-Cl	Pd(0)	Pd(II)-Cl	Pd(0)
	Aliphatic	3d _{5/2}	3d _{5/2}	at.%	at.%
2.8a	280.7	-	-	-	-
2.8b	280.5	333.6	331.3	22	78
2.8c	280.6	333.8	331.1	16	84
2.8d	280.7	333.2	330.9	21	79
2.8b.33	280.6	333.6	331.4	20	80
2.8b.66	280.6	333.9	331.6	22	78
2.8e	280.3	333.6	331.8	24	76

The aliphatic C1s peak is given as a reference point.

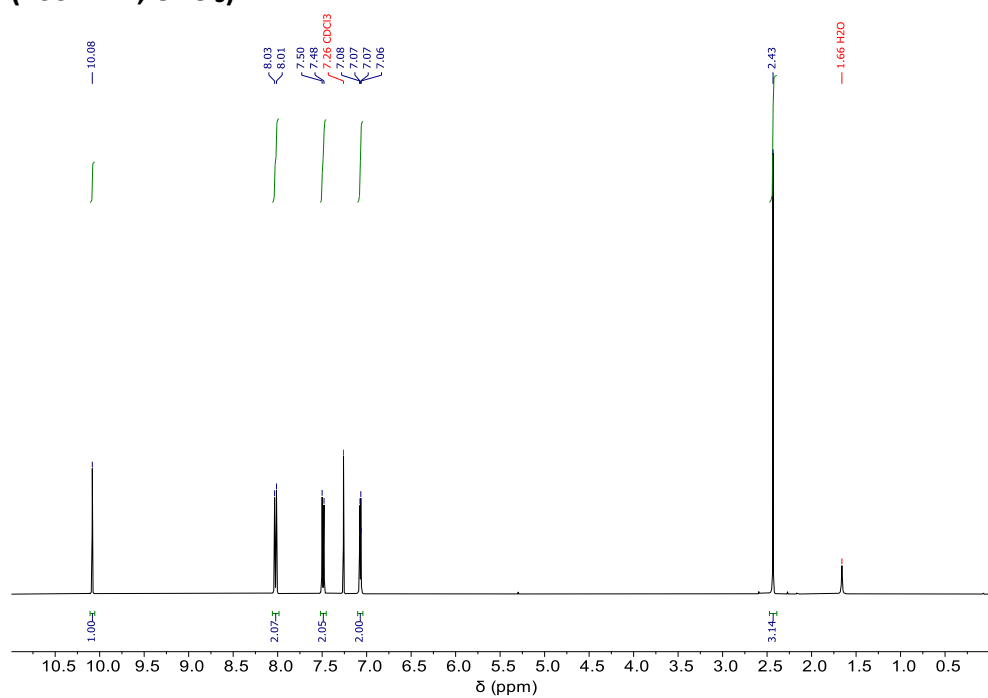
Fitting of NP generated from **2.8c** was restricted to a maximum of 342 eV due to the presence of an apparent calcium contaminant at 343.5 eV.

A.3 Chapter 3

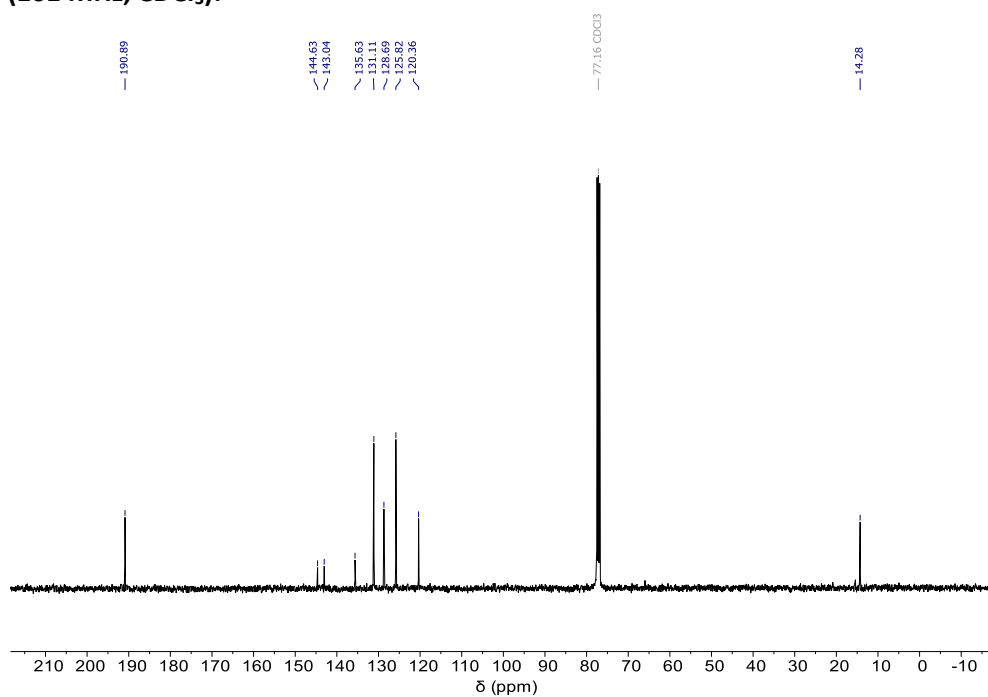
A.3.1 NMR Spectra of Monomers and Monomer Precursors

2-Methyl-1-(4-formylphenyl)-imidazole (**3.2**)

^1H NMR (400 MHz, CDCl_3):

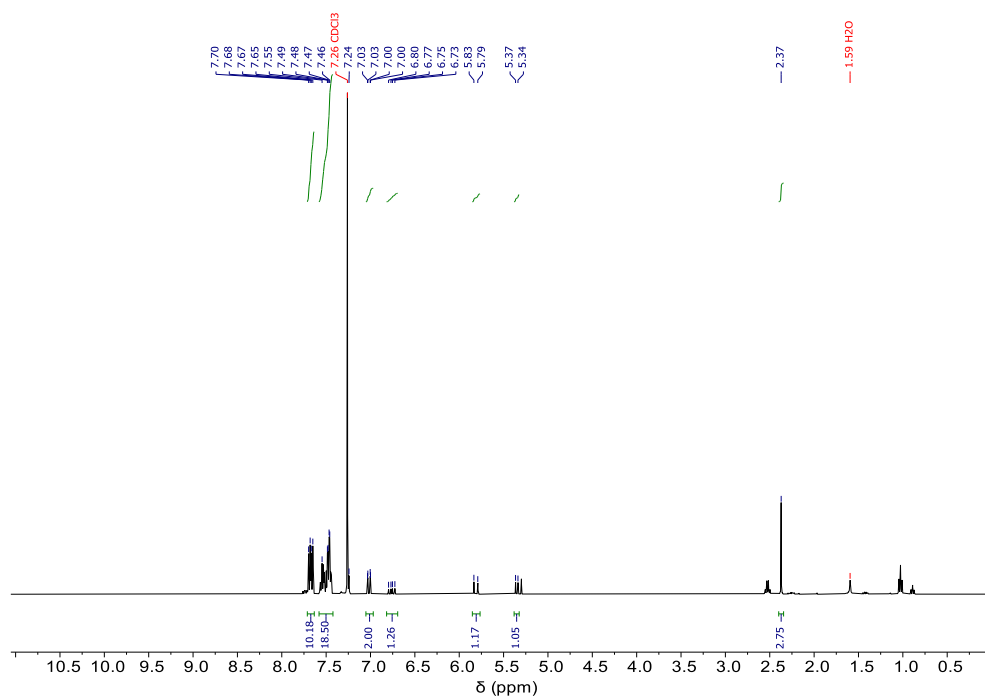


^{13}C NMR (101 MHz, CDCl_3):

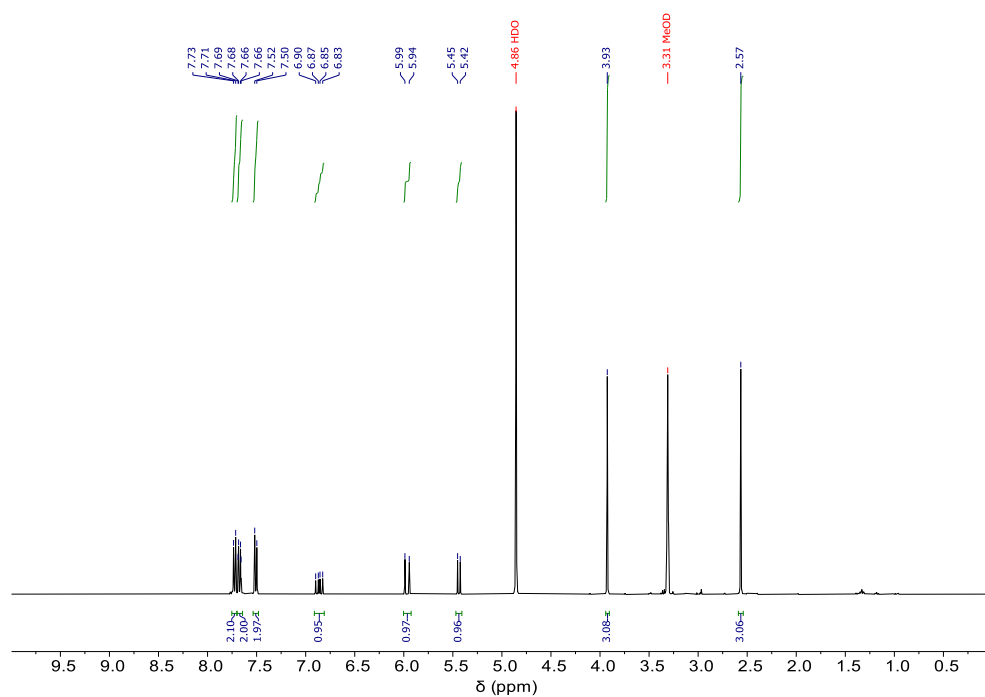


2-Methyl-1-(4-vinylphenyl)-imidazole (**3.1**)

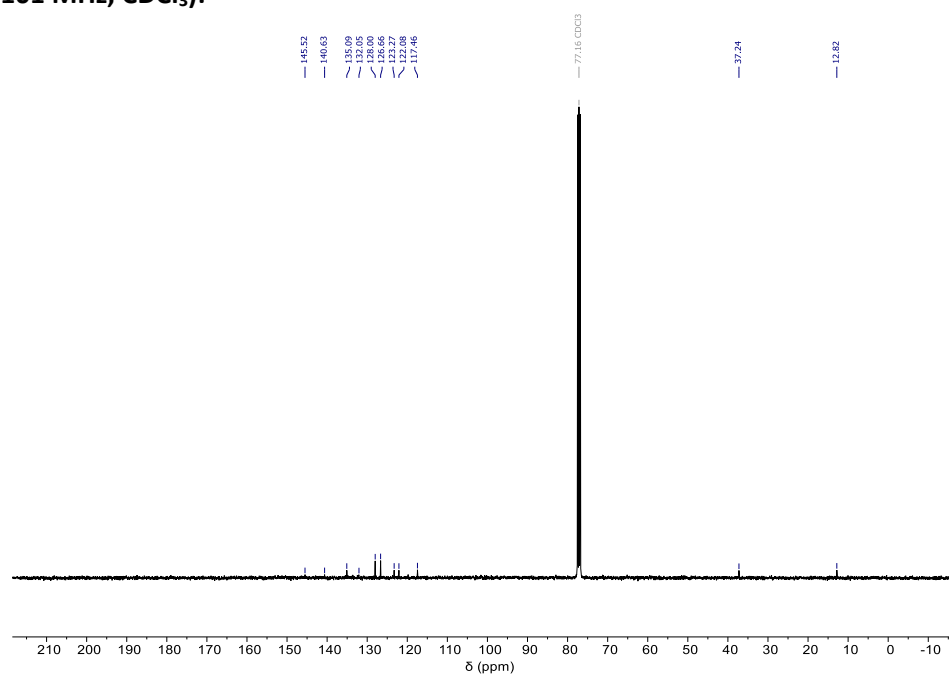
¹H NMR (400 MHz, CDCl₃):

2,3-Dimethyl-1-(4-vinylphenyl)-imidazolium iodide (**3.3**)

¹H NMR (400 MHz, MeOD):

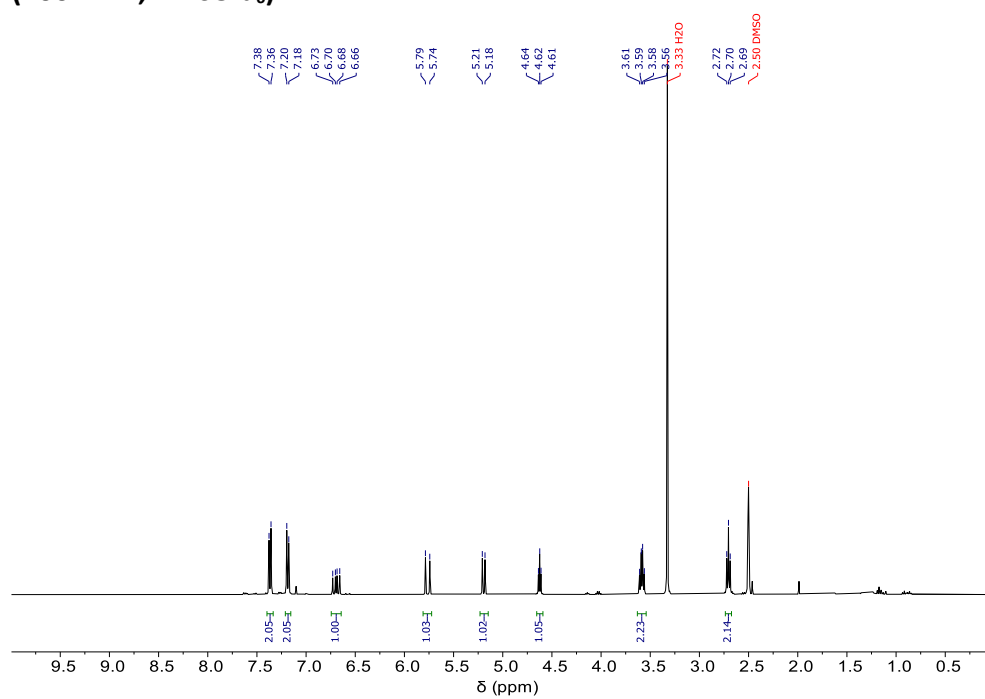


^{13}C NMR (101 MHz, CDCl_3):

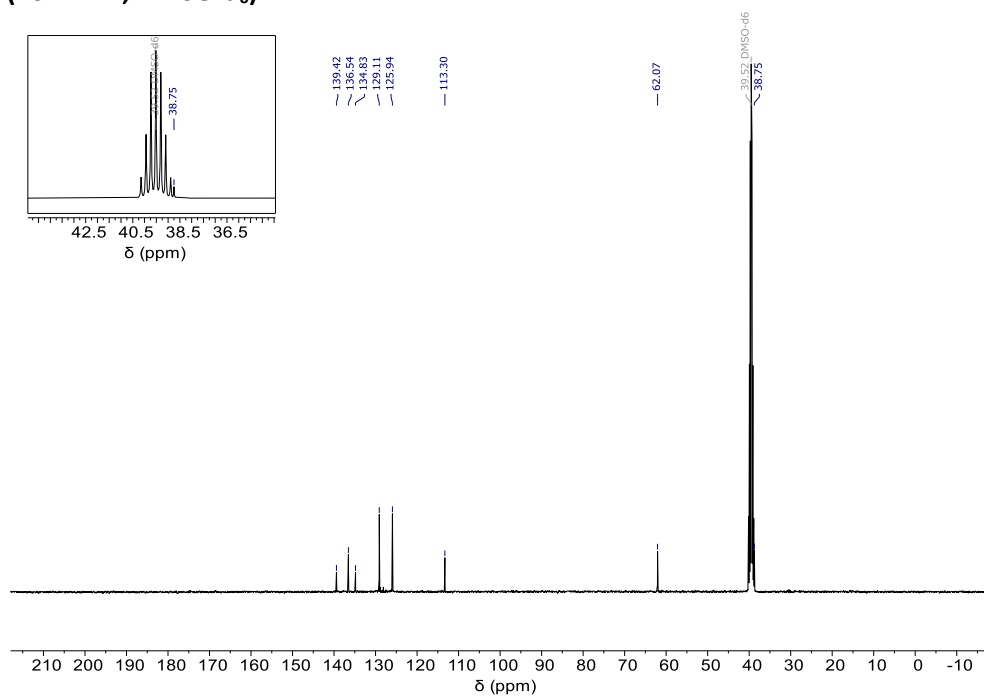


2-(4-Vinylphenyl)ethan-1-ol (3.4)

^1H NMR (400 MHz, $\text{DMSO}-d_6$):

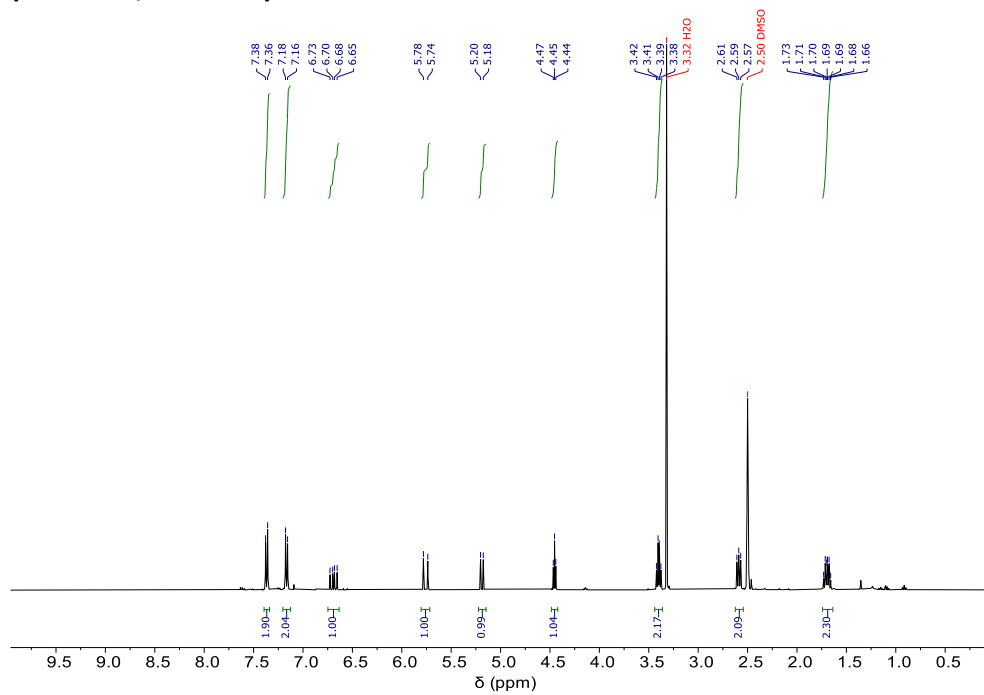


^{13}C NMR (101 MHz, DMSO- d_6):



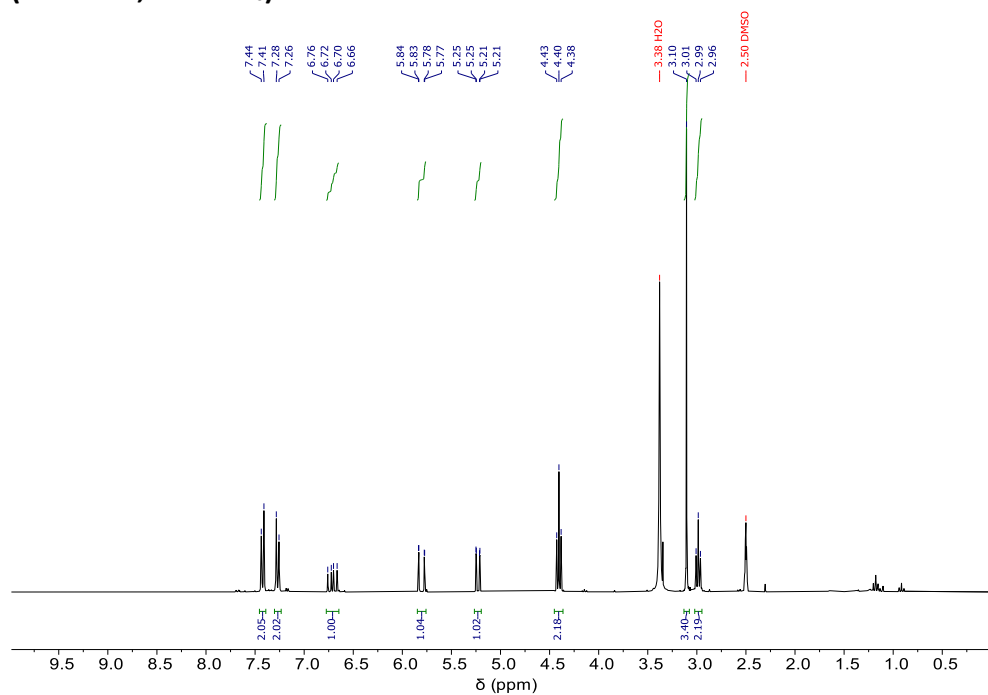
3-(4-Vinylphenyl)propan-1-ol (3.5)

^1H NMR (400 MHz, DMSO- d_6):

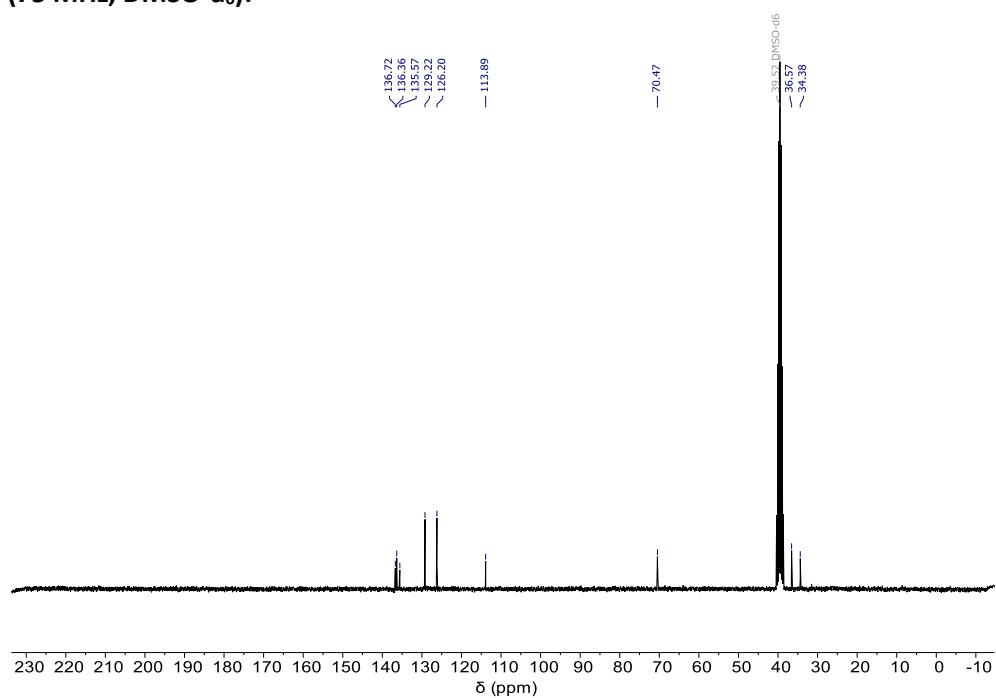


2-(4-Vinylphenyl)ethyl methanesulfonate (**3.6**)

^1H NMR (400 MHz, DMSO-d_6):

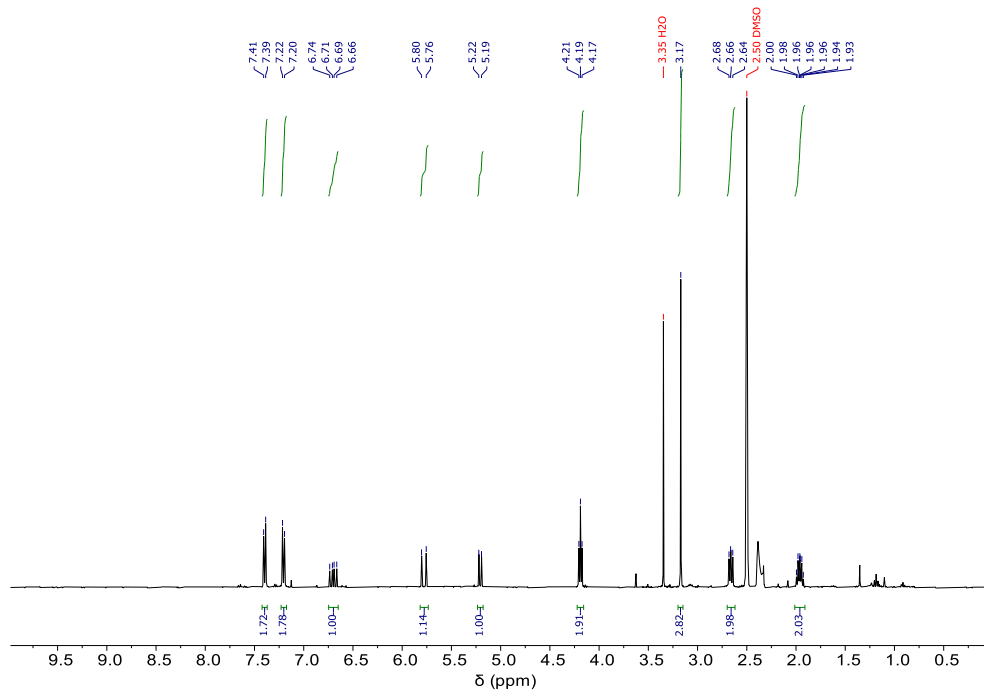


^{13}C NMR (75 MHz, DMSO-d_6):

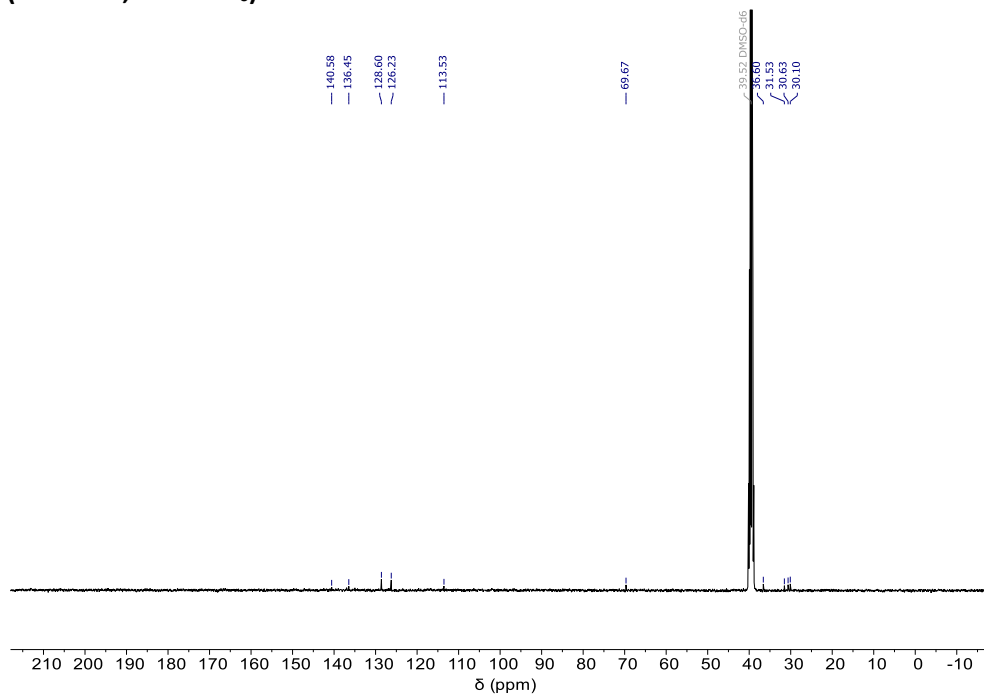


3-(4-Vinylphenyl)propyl methanesulfonate (**3.7**)

^1H NMR (400 MHz, DMSO- d_6):

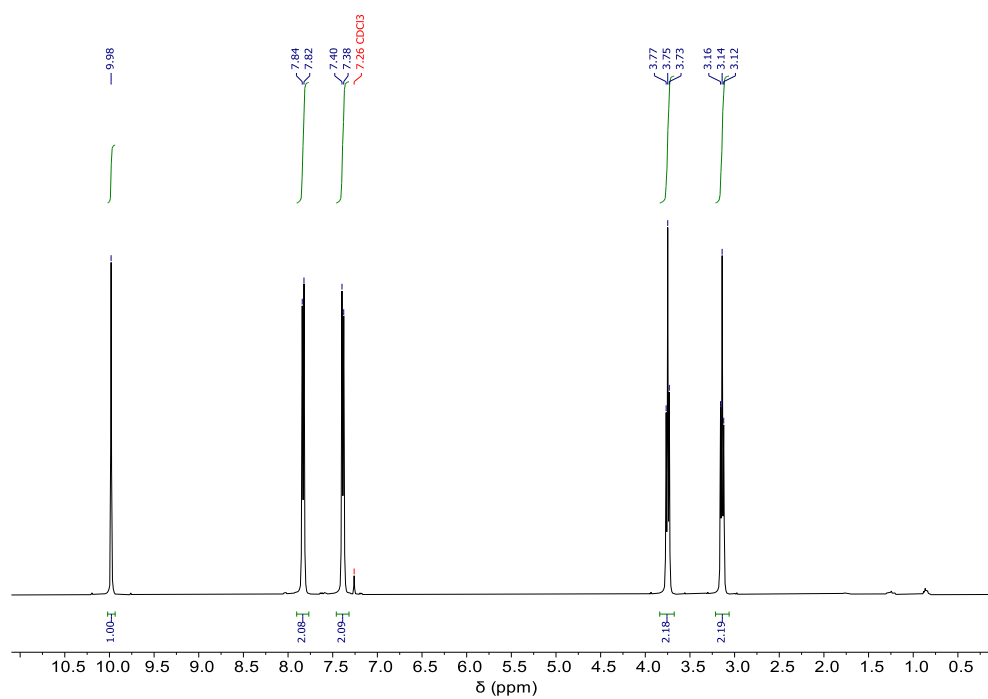


^{13}C NMR (101 MHz, DMSO- d_6):



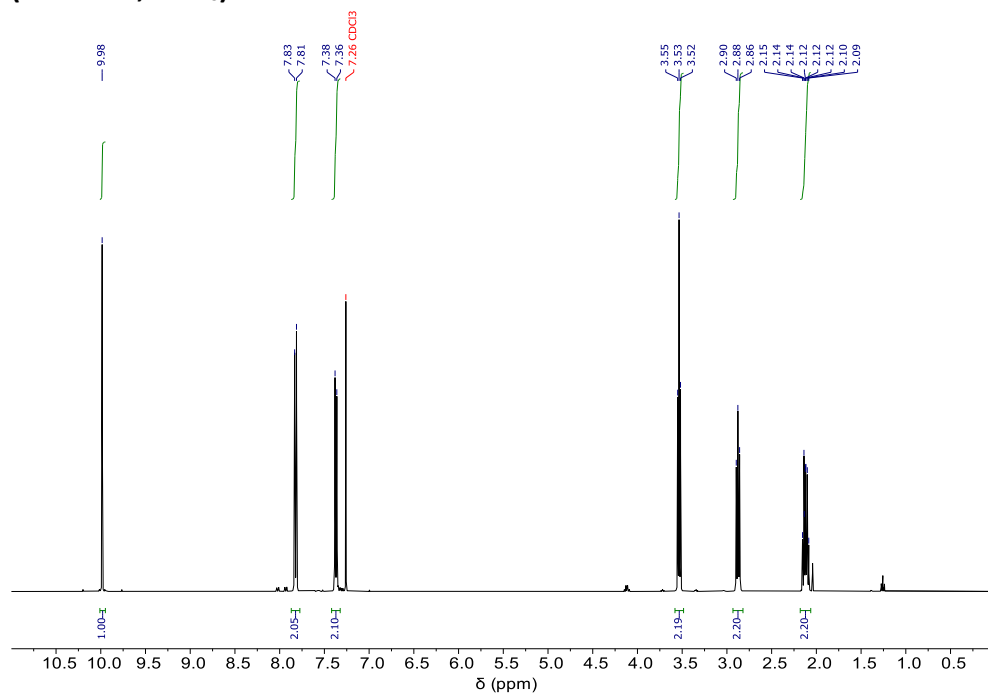
4-(2-chloroethyl)benzaldehyde (**3.8**)

^1H NMR (400 MHz, CDCl_3):

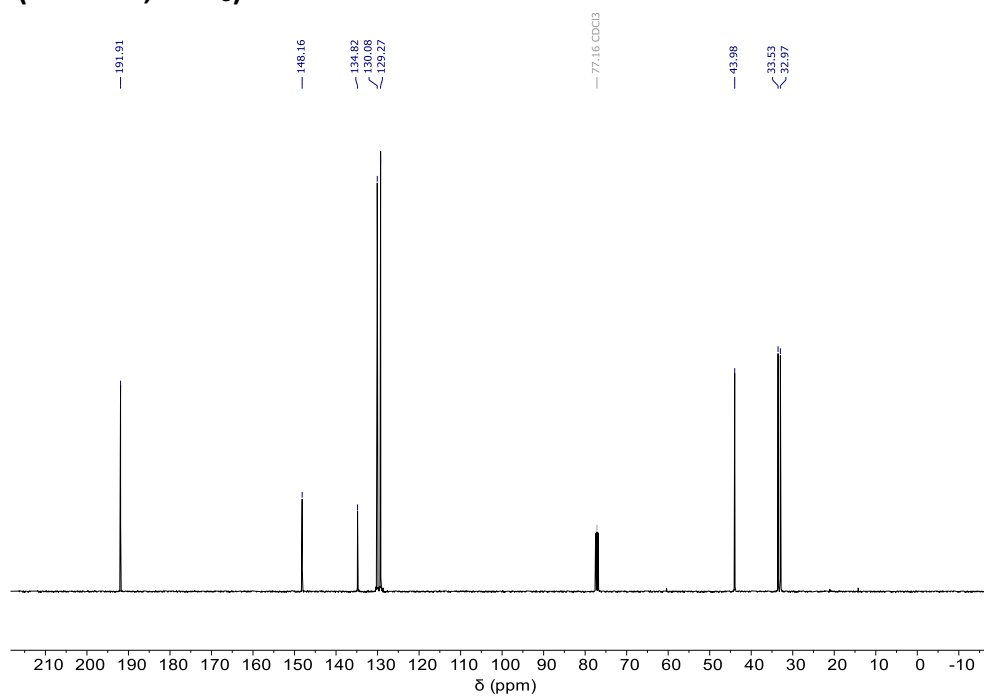


4-(3-chloropropyl)benzaldehyde (**3.9**)

^1H NMR (400 MHz, CDCl_3):

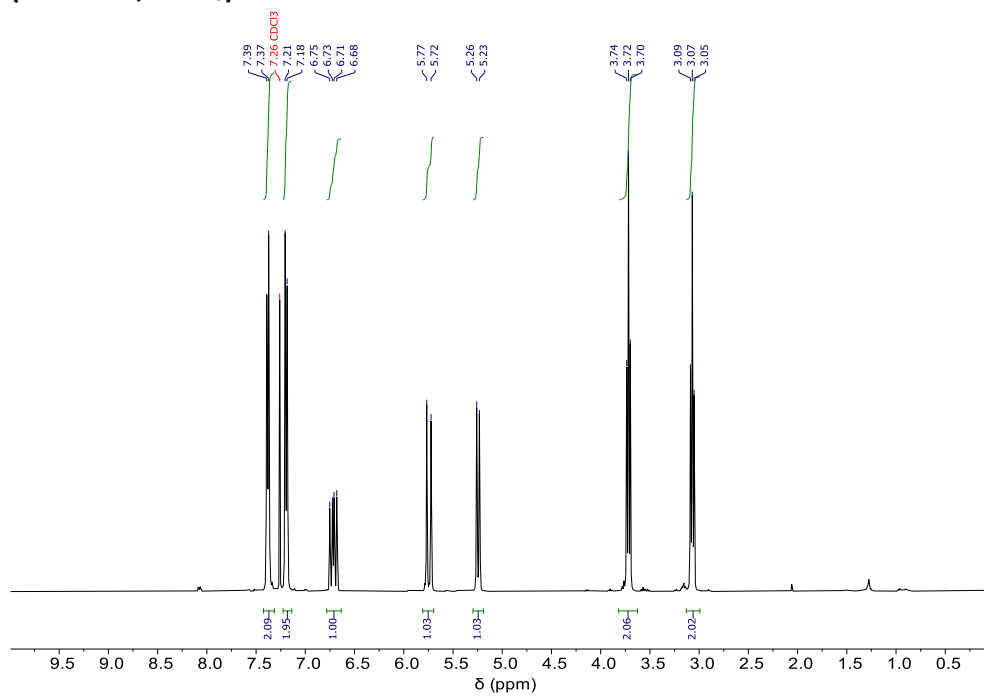


^{13}C NMR (101 MHz, CDCl_3):

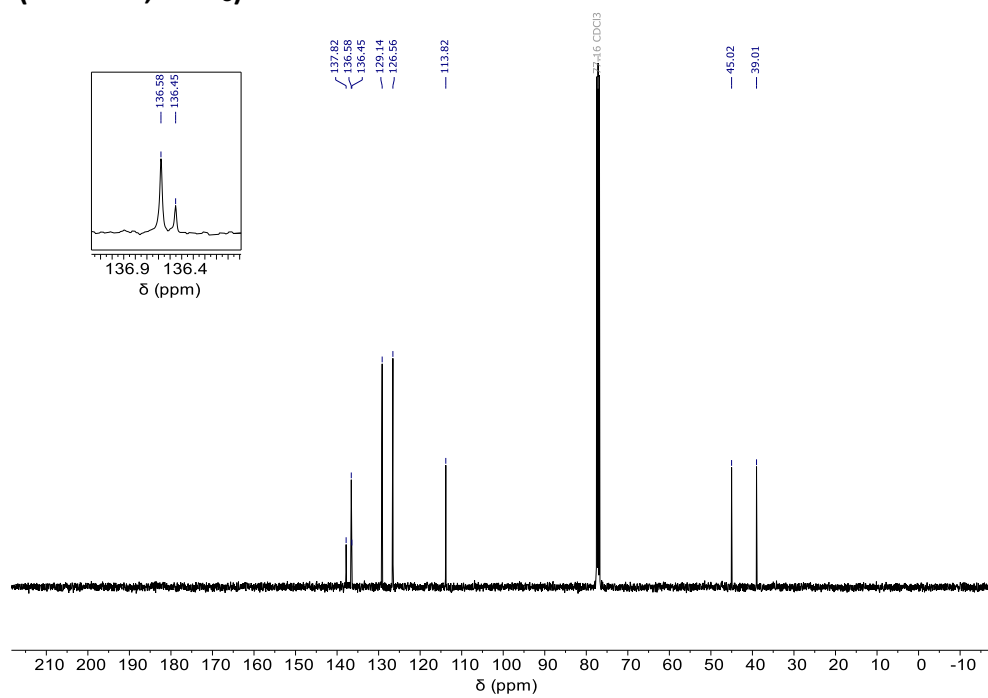


4-(2-chloroethyl)styrene (3.10)

^1H NMR (400 MHz, CDCl_3):

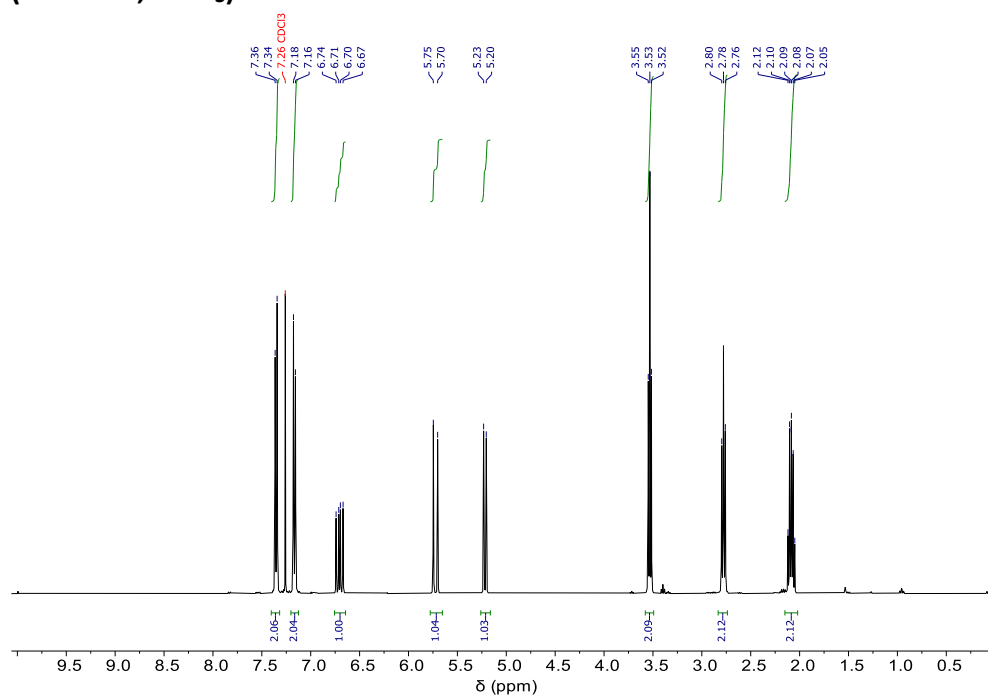


^{13}C NMR (101 MHz, CDCl_3):

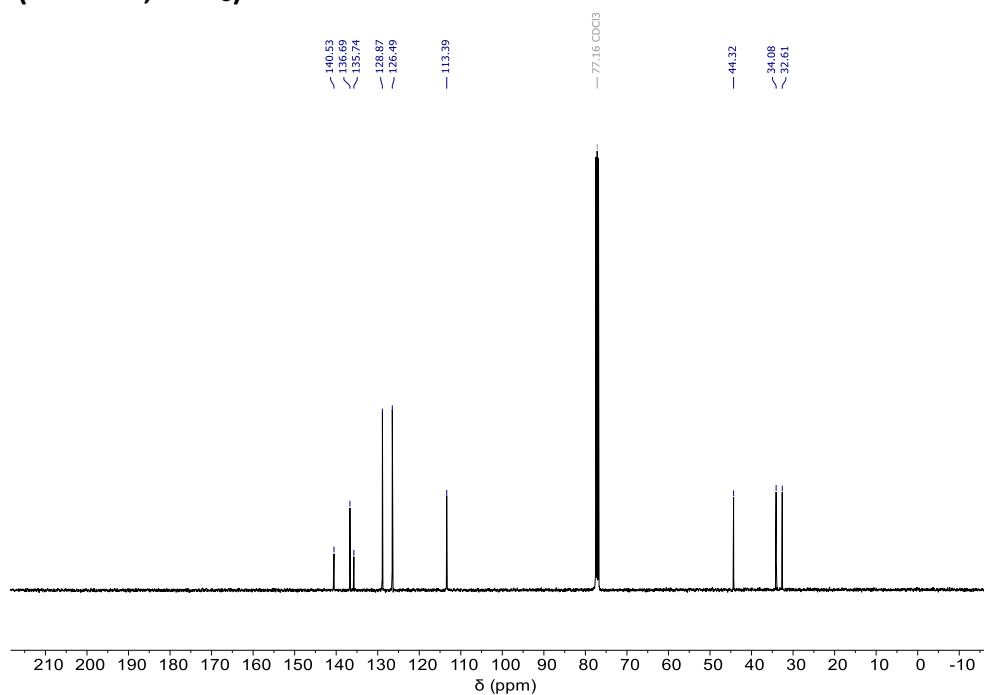


4-(3-chloropropyl)styrene (3.11)

^1H NMR (400 MHz, CDCl_3):

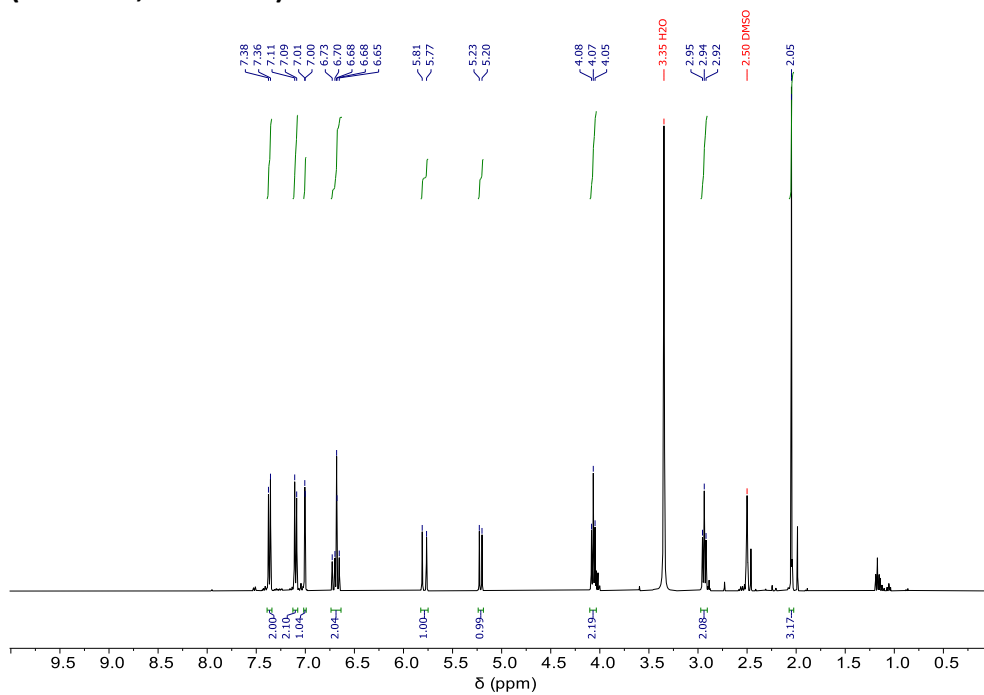


^{13}C NMR (101 MHz, CDCl_3):

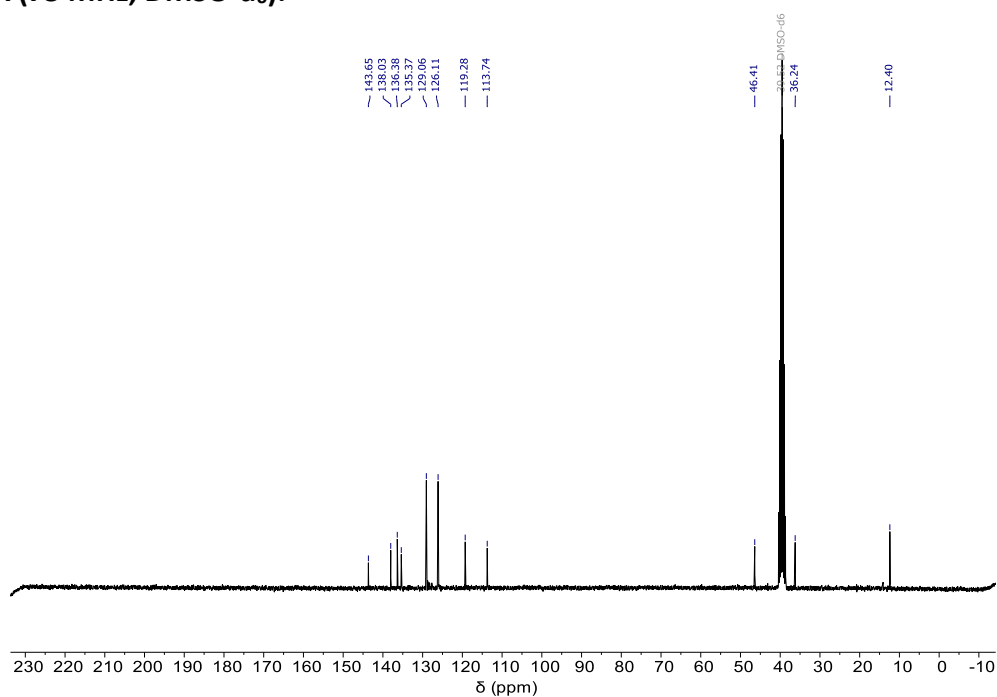


2-Methyl-(3-(4-vinylphenyl)ethyl)-imidazole (3.14)

^1H NMR (400 MHz, $\text{DMSO}-d_6$):

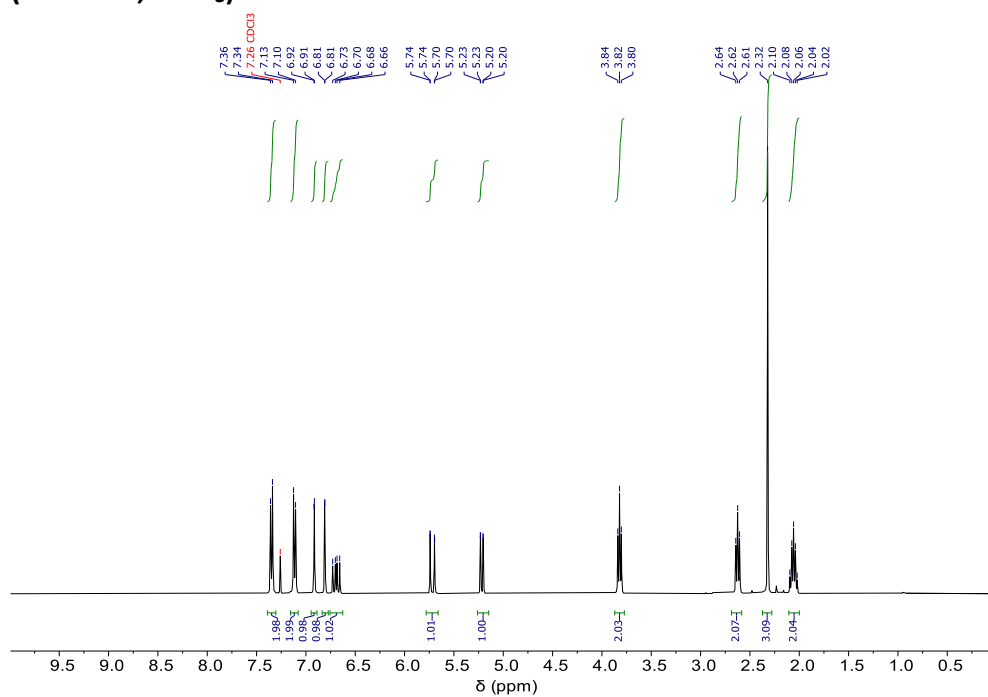


^{13}C NMR (75 MHz, DMSO- d_6):

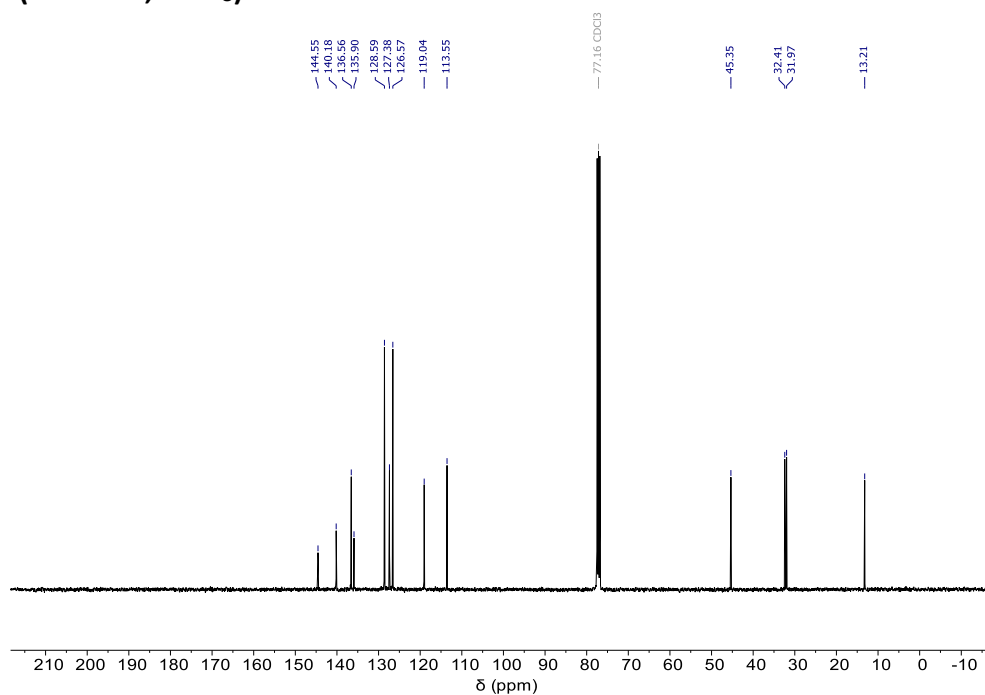


2-Methyl-(3-(4-vinylphenyl)propyl)-imidazole (3.15)

^1H NMR (400 MHz, CDCl_3):

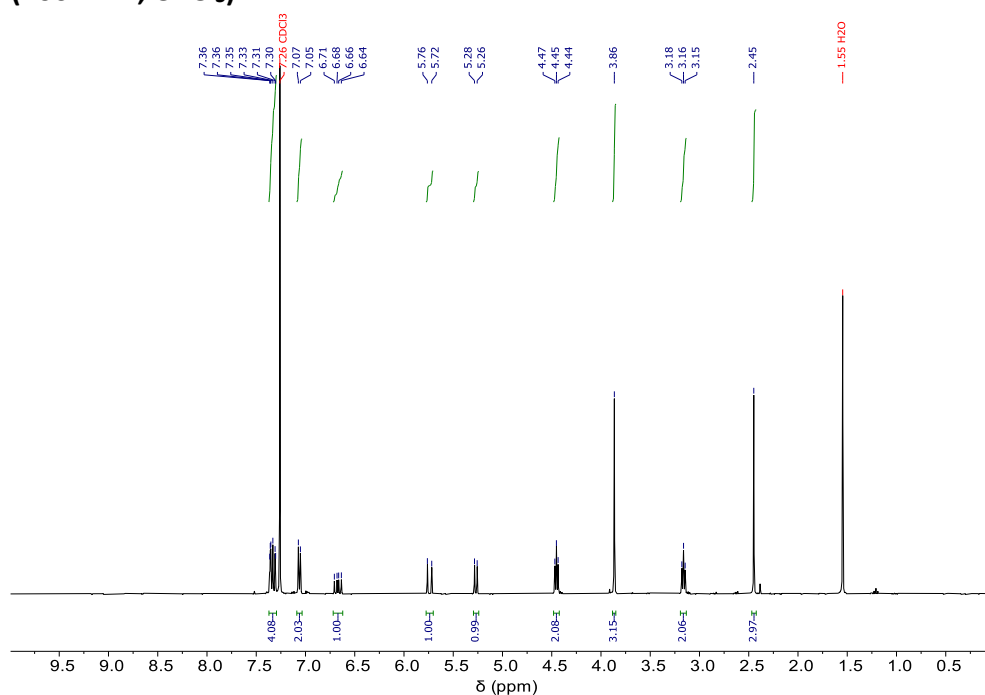


^{13}C NMR (101 MHz, CDCl_3):

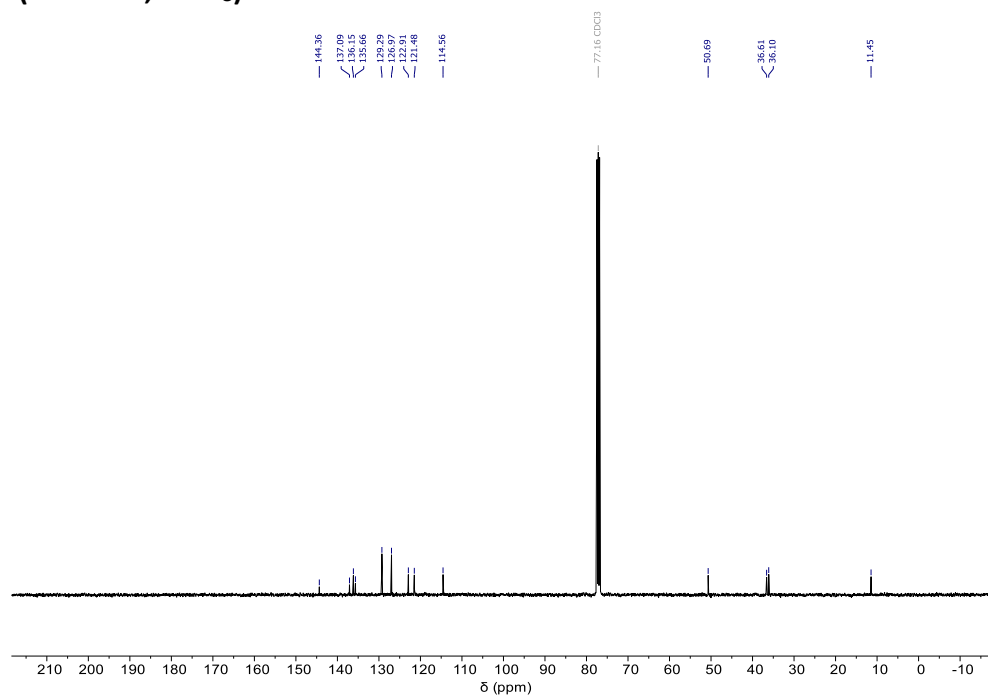


1,2-Dimethyl-(3-(4-vinylphenyl)ethyl)-imidazolium iodide (**3.16**)

^1H NMR (400 MHz, CDCl_3):

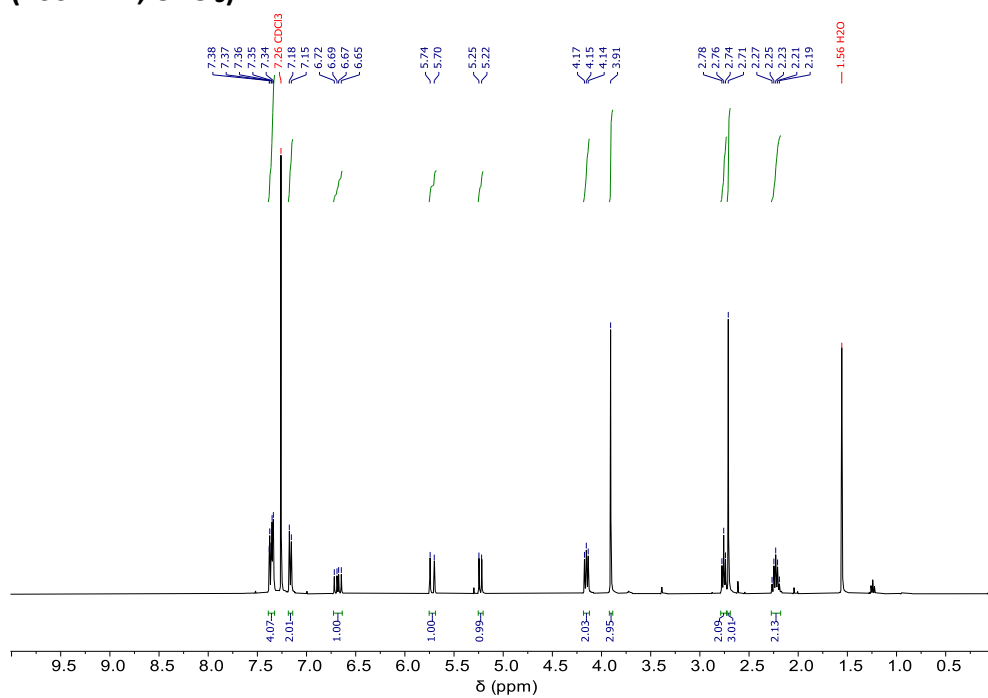


^{13}C NMR (101 MHz, CDCl_3):

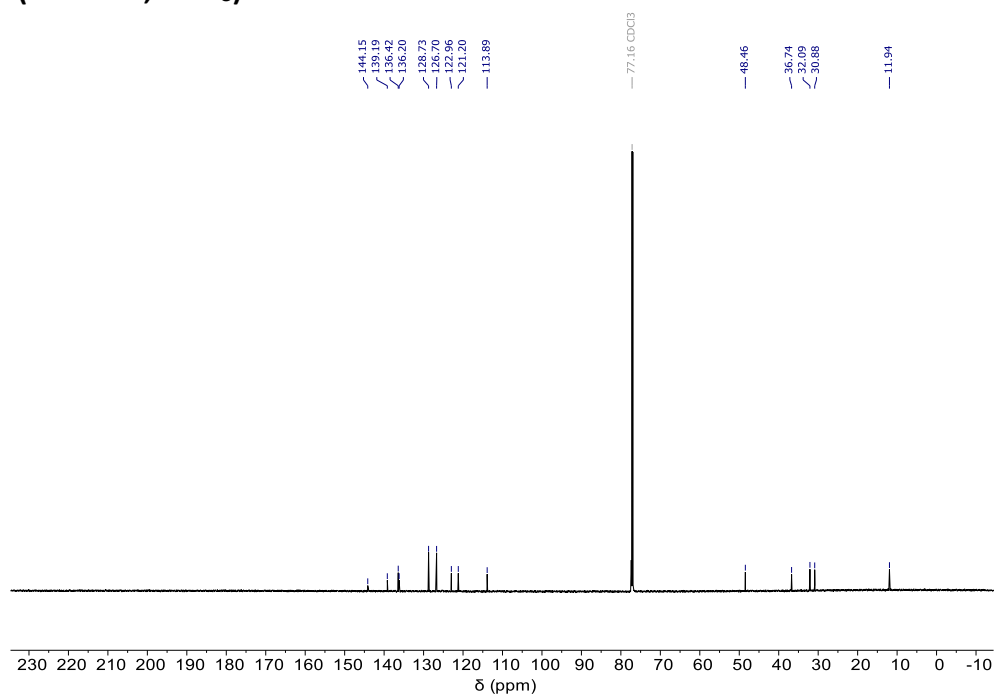


1,2-Dimethyl-(3-(4-vinylphenyl)propyl)-imidazolium iodide (3.17)

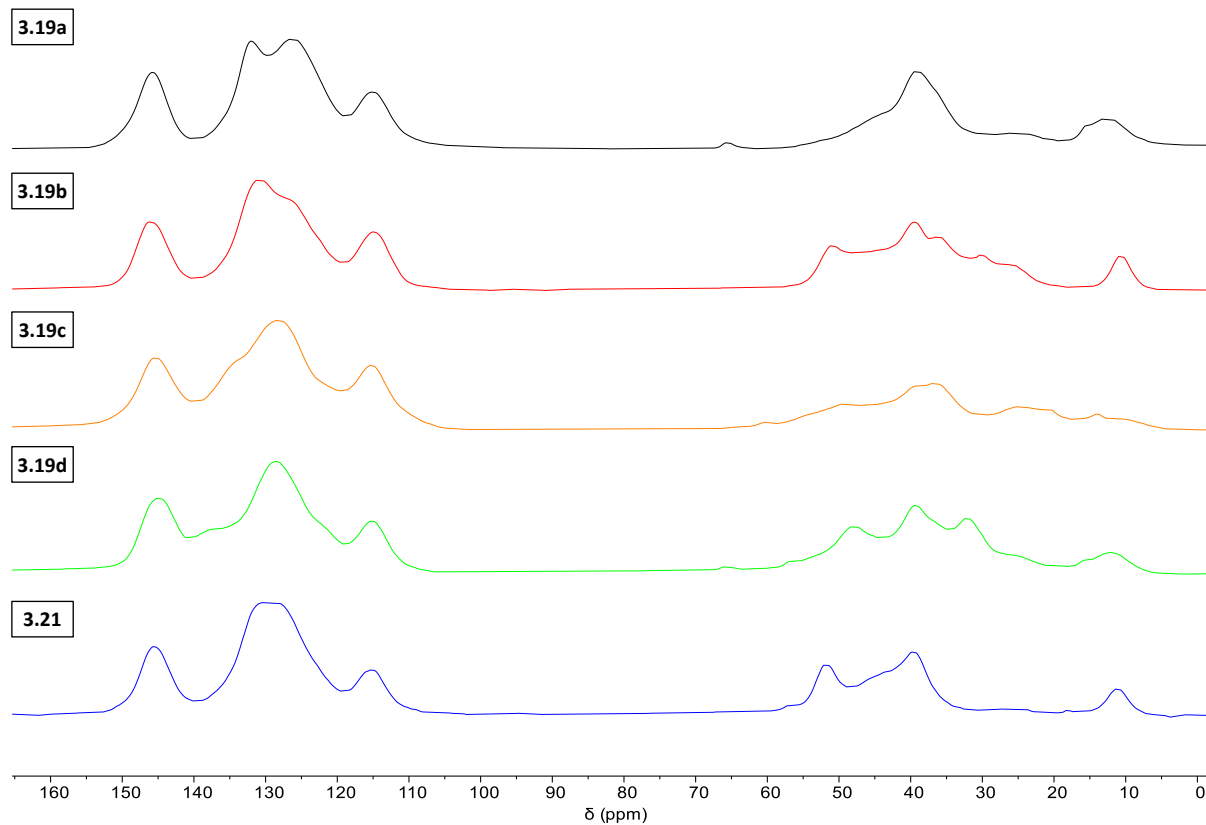
^1H NMR (400 MHz, CDCl_3):



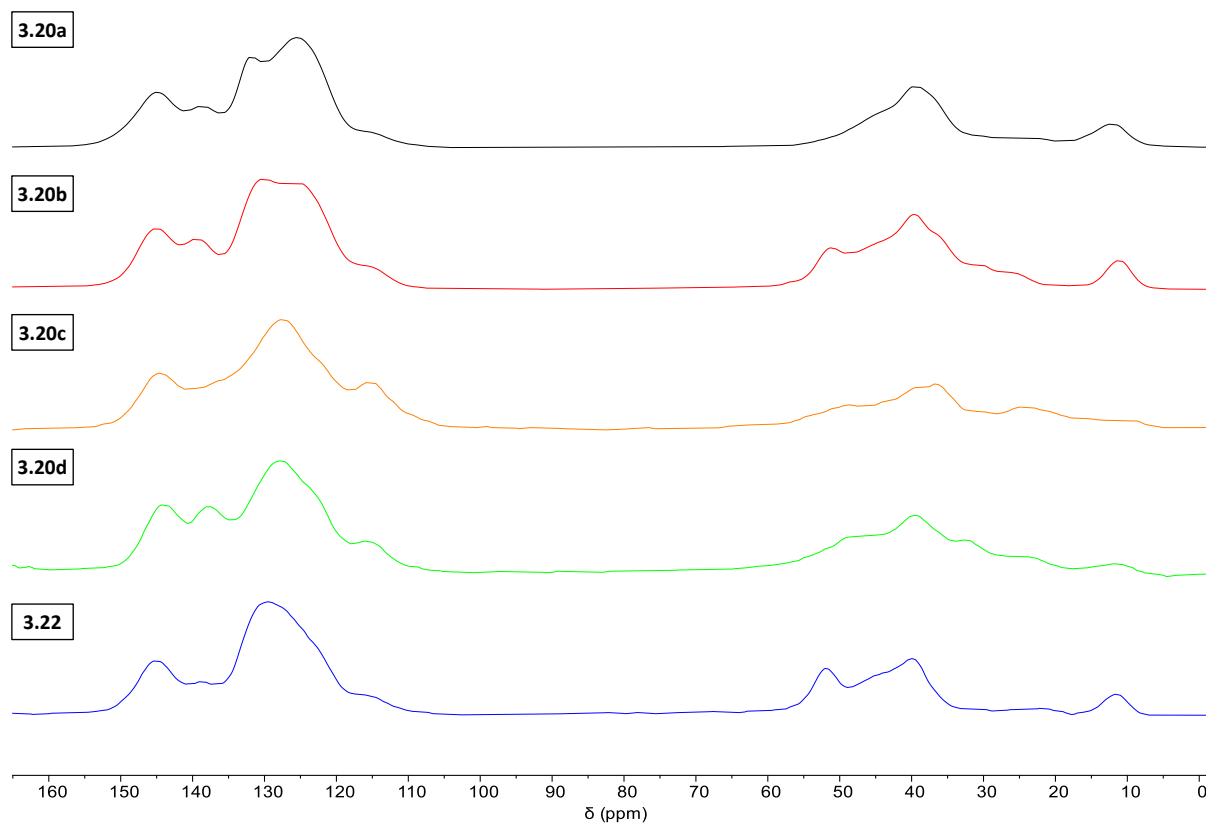
^{13}C NMR (176 MHz, CDCl_3):



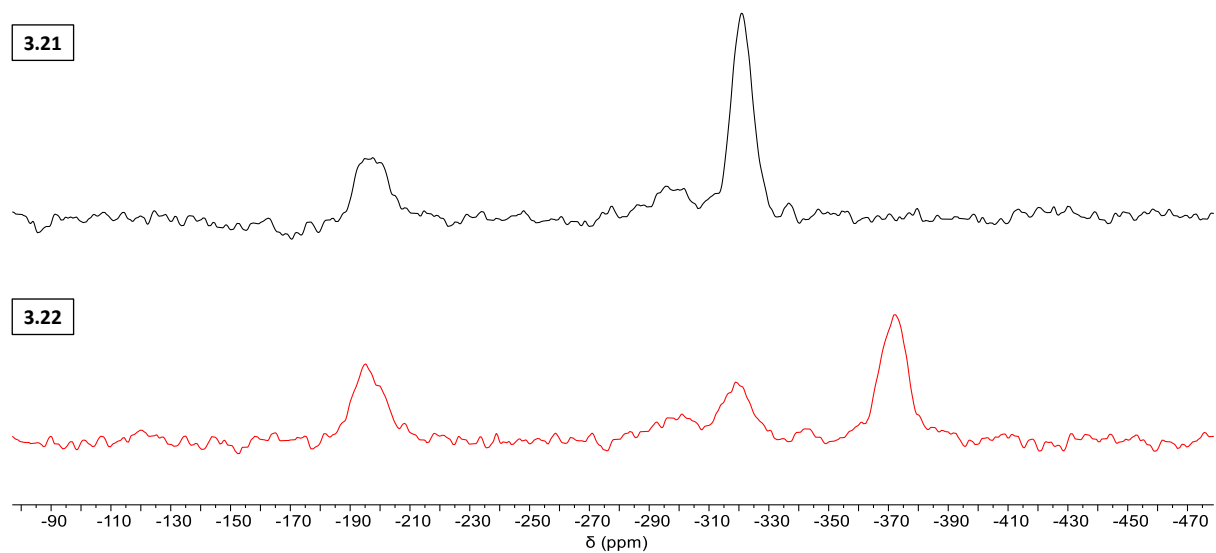
A.3.2 CP-MAS $^{13}\text{C}\{^1\text{H}\}$ NMR Spectra of Polymers 3.19a-d and 3.21



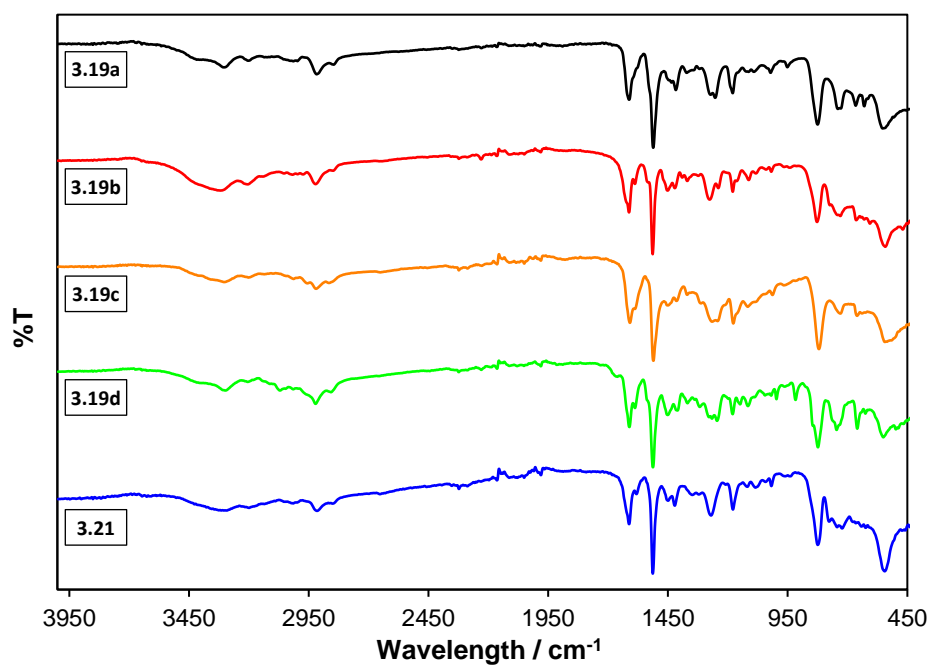
A.3.3 CP-MAS $^{13}\text{C}\{^1\text{H}\}$ NMR Spectra of Precatalysts 3.20a-d and 3.22



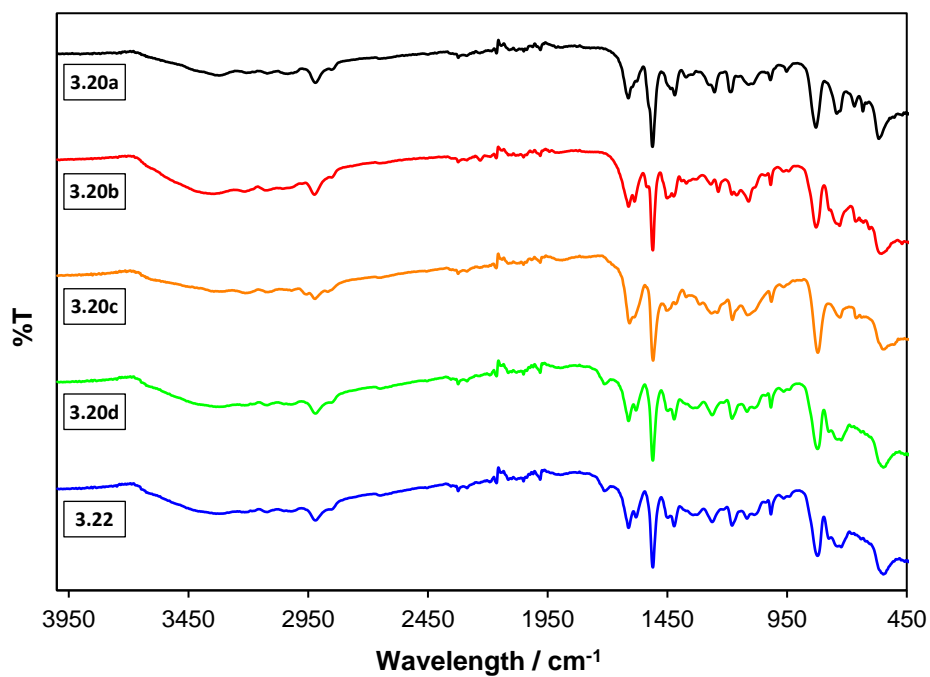
A.3.4 CP-MAS ^{15}N NMR Spectra of Polymer 3.21 and Precatalyst 3.22



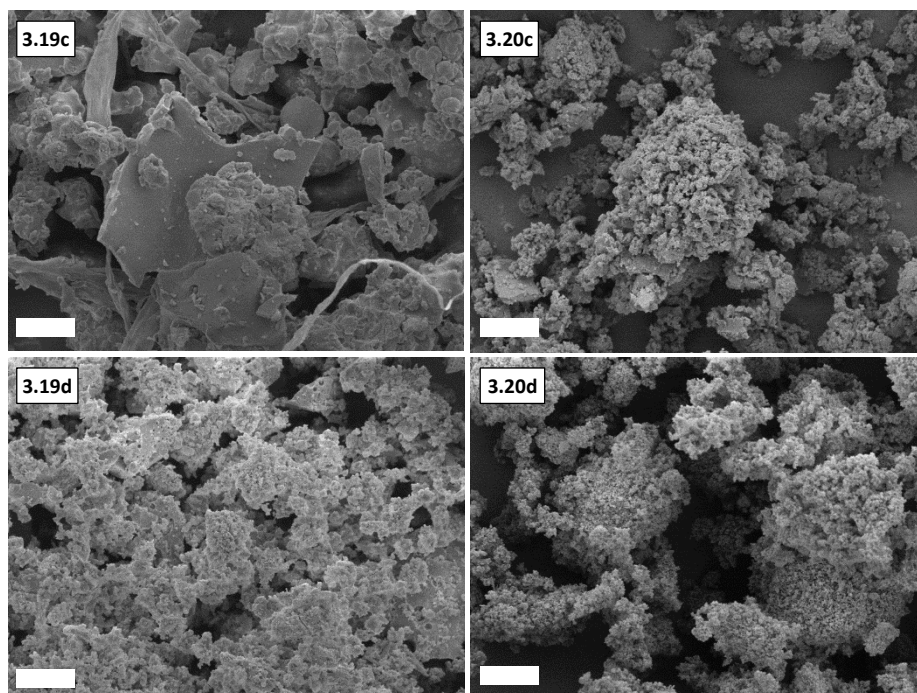
A.3.5 FT-IR Spectra of PIIL Supports 3.19a-d and 3.21



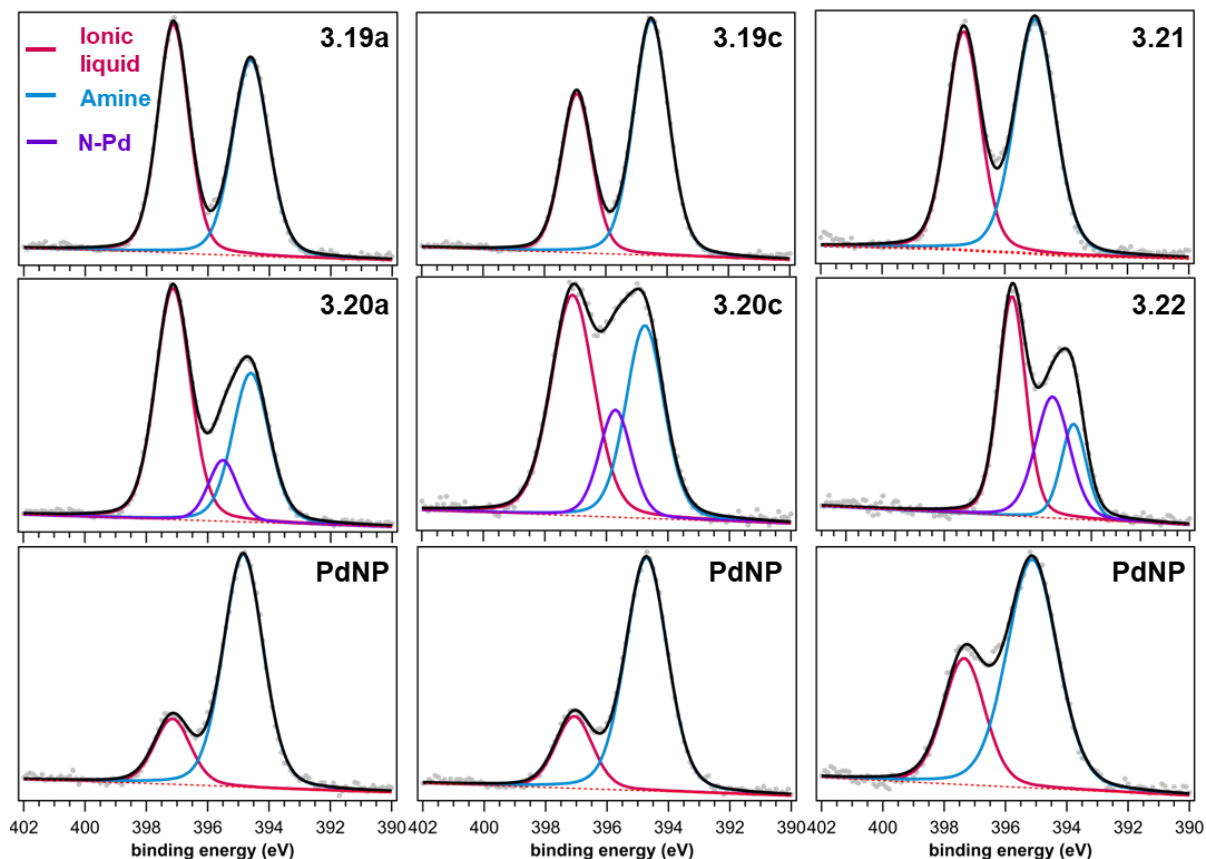
A.3.6 FT-IR Spectra of PdCl_4 Precatalysts 3.20a-d and 3.22



A.3.7 SEM Images of Polymers 3.19c-d and Precatalysts 3.20c-d



A.3.8 N 1s Core Level XPS Spectra of Polymers, Precatalysts, and NPs



A.3.9 Table of N 1s Core Level Binding Energies for Polymers 3.19a-d and 3.21

Sample	C1s	Imidazolium	Amine	N-Pd	Imidazolium	Amine	N-Pd
	Aliphatic				at.%	at.%	at.%
3.19a	280.0	397.1	394.6	-	50	50	-
3.19b	280.0	396.9	394.7	-	34	66	-
3.19c	279.8	397.0	394.5	-	37	63	-
3.19d	280.1	397.1	394.7	-	52	48	-
3.21	280.6	397.3	395.0	-	44	56	-

The aliphatic C 1s peak is given for reference.

A.3.10 Table of N 1s Core Level Binding Energies for Precatalysts 3.20a-d and 3.22

Sample	C1s	Imidazolium	Amine	N-Pd	Imidazolium	Amine	N-Pd
	Aliphatic				at.%	at.%	at.%
3.20a	280.1	397.1	394.6	395.5	53	36	12
3.20b	280.1	397.0	394.8	395.5	50	33	17
3.20c	280.1	397.1	394.8	395.7	47	36	17
3.20d	280.0	397.1	394.7	395.7	37	48	15
3.22	280.4	397.2	394.7	395.6	48	19	33

The aliphatic C 1s peak is given for reference.

A.3.11 Table of N 1s Core Level Binding Energies for Nanoparticles Generated from Precatalysts 3.20a-d and 3.22

Precatalyst	C1s	Imidazolium	Amine	N-Pd	Imidazolium	Amine	N-Pd
	Aliphatic				at.%	at.%	at.%
3.20a	279.9	397.2	394.8	-	20	80	0
3.20b	280.0	397.0	394.9	-	6	94	0
3.20c	279.9	397.1	394.7	-	21	79	0
3.20d	280.0	397.0	394.9	-	18	82	0
3.22	280.6	397.5	395.0	396.5	23	63	14

The aliphatic C 1s peak is given for reference.

A.3.12 Table of Pd 3d Core Level Binding Energies for Precatalysts 2.8a-e

Sample	C1s	Pd(II)-Cl	Pd(II)-I	Sat.	Pd(II)-N	Pd(II)-Cl	Pd(II)-I	Sat.	Pd(II)-N
	Aliphatic	3d _{5/2}	3d _{5/2}		3d _{5/2}	at.%	at.%	at.%	at.%
3.20a	280.1	332.9	331.2	340.3	-	87	11	3	-
3.20b	280.1	333.2	-	340.8	335.0	91	-	4	5
3.20c	280.1	333.2	331.3	340.6	-	87	12	2	-
3.20d	280.0	332.9	331.2	340.4	-	82	17	2	-
3.22	280.4	333.5	-	341.0	335.3	93	-	4	3

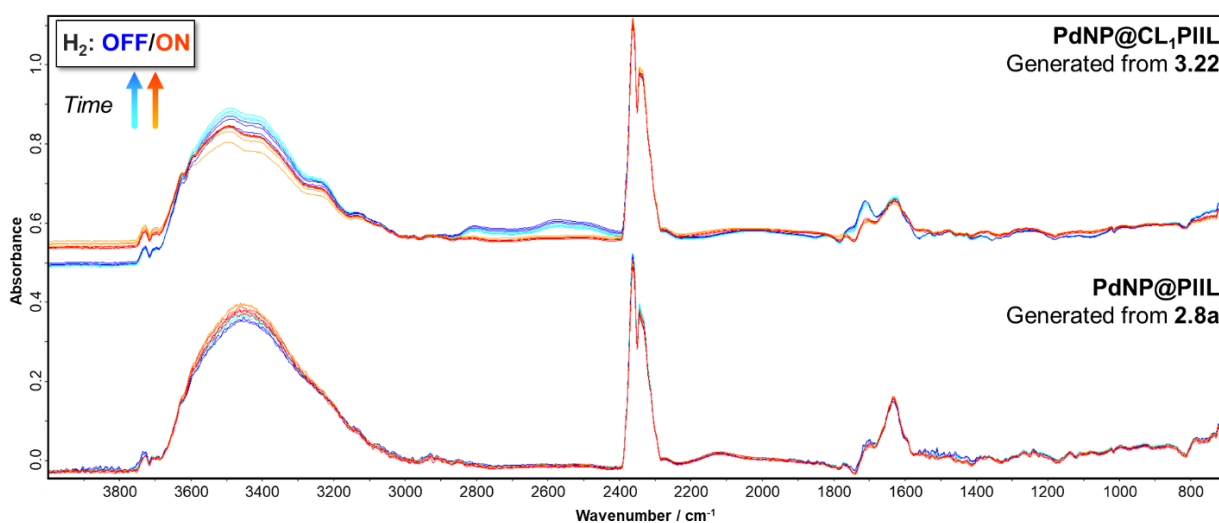
The aliphatic C 1s peak is given for reference.

A.3.13 Table of Pd 3d Core Level Binding Energies for Nanoparticles Generated from Precatalysts 2.8a-e

Precatalyst	C1s	Pd(II)	Pd(0)	Pd(II)	Pd(0)
	Aliphatic	3d _{5/2}	3d _{5/2}	at.%	at.%
3.20a	279.9	332.6	330.5	8	92
3.20b	280.0	333.0	331.2	25	75
3.20c	279.9	333.2	330.5	5	95
3.20d	280.0	333.4	330.6	7	93
3.22	280.6	333.2	331.3	41	59

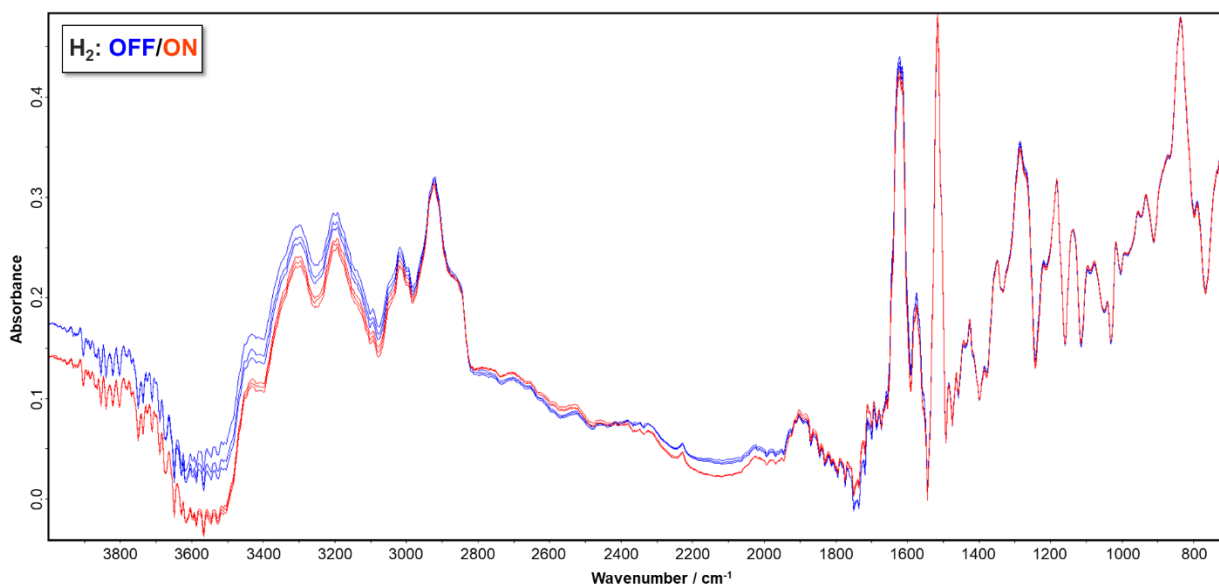
The aliphatic C1s peak is given as a reference point.

A.3.14 DRIFTS Spectra Showing the Hydrogenation of CO₂ Over PdNP@CL₁PIIL and PdNP@PIIL



Spectra were initially collected with a 10 vol% CO₂ and 4 vol% H₂O gas mixture diluted with Ar (blue). Spectra were collected every minute until saturation, at which point 10 vol% H₂ was introduced to the gas mixture (red).

A.3.15 DRIFTS Spectra Showing the Hydrogenation of Ammonium Carbamate Over PdNP@CL₁PIIL



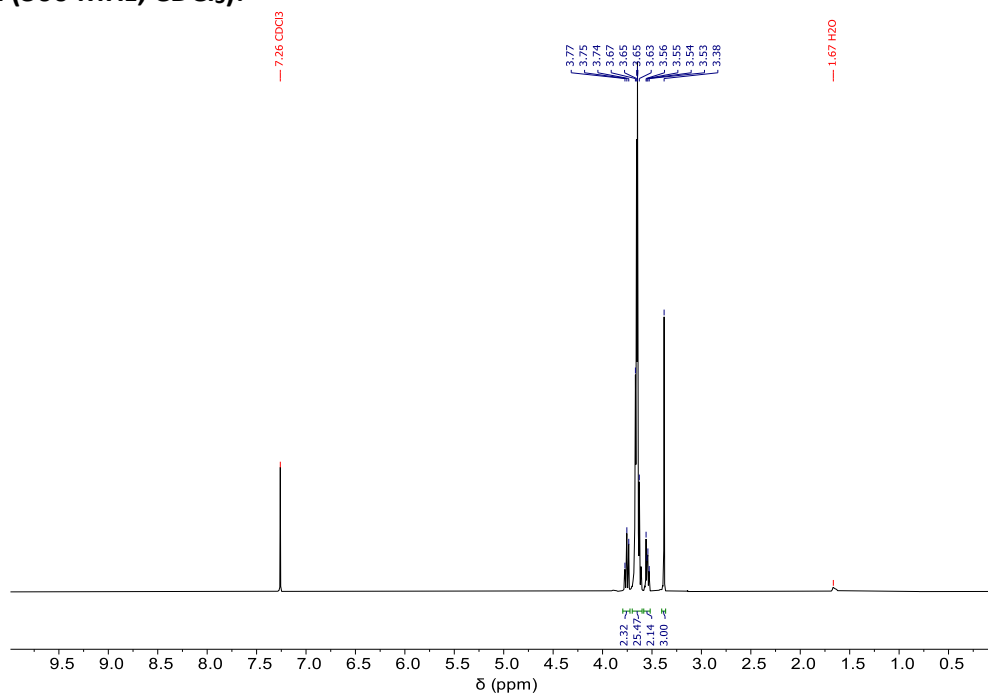
PdNP@CL₁PIIL (50 mg) was treated with an aqueous solution of ammonium carbamate (1 mL, 0.3 M). The resulting suspension was mixed mechanically and allowed to dry in air. The above DRIFTS spectra were acquired by first measuring a background using untreated PdNP@CL₁PIIL – spectra of the ammonium carbamate doped PdNP@CL₁PIIL were then measured under a flow of Ar before introducing 10 vol% H₂.

A.4 Chapter 4

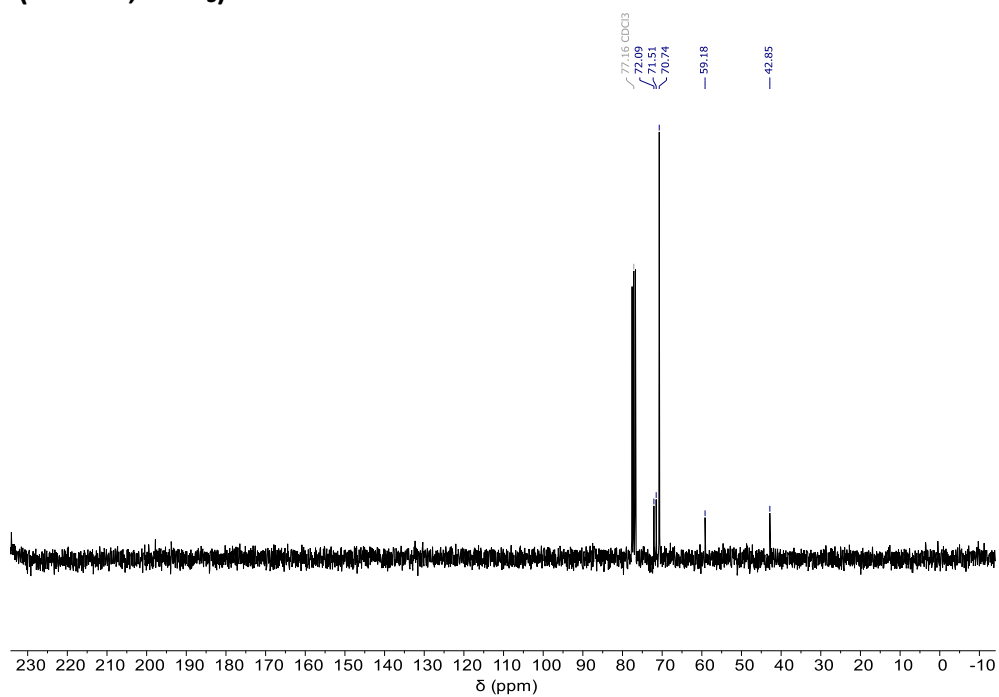
A.4.1 NMR Spectra of Monomers and Monomer Precursors

1-Chloro-3,6,9,12,15,18,21-heptaodocosane (4.1)

^1H NMR (300 MHz, CDCl_3):

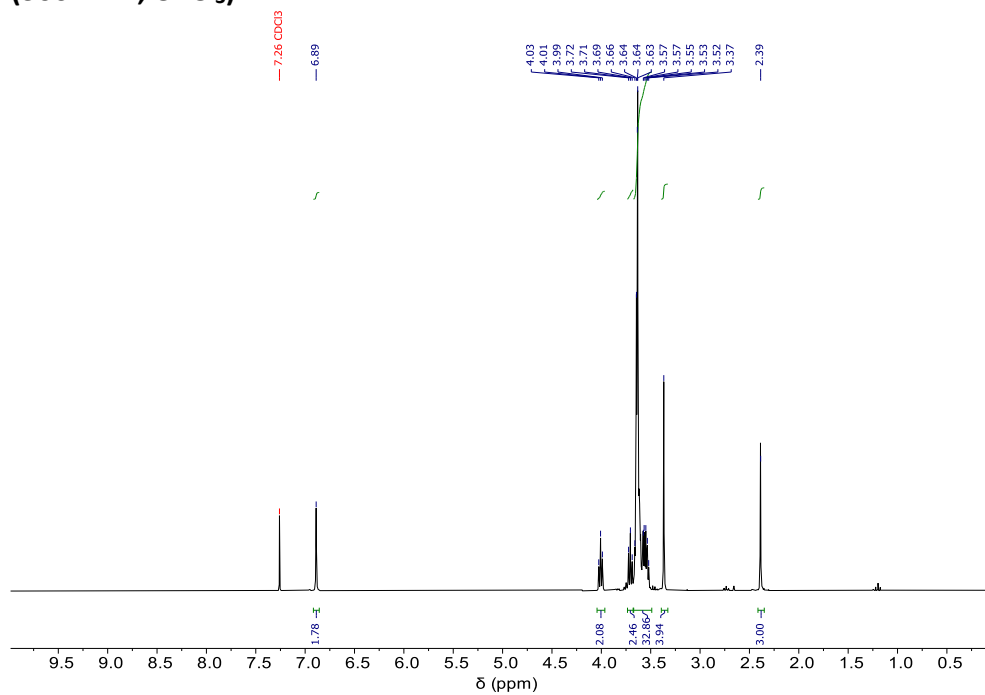


^{13}C NMR (75 MHz, CDCl_3):

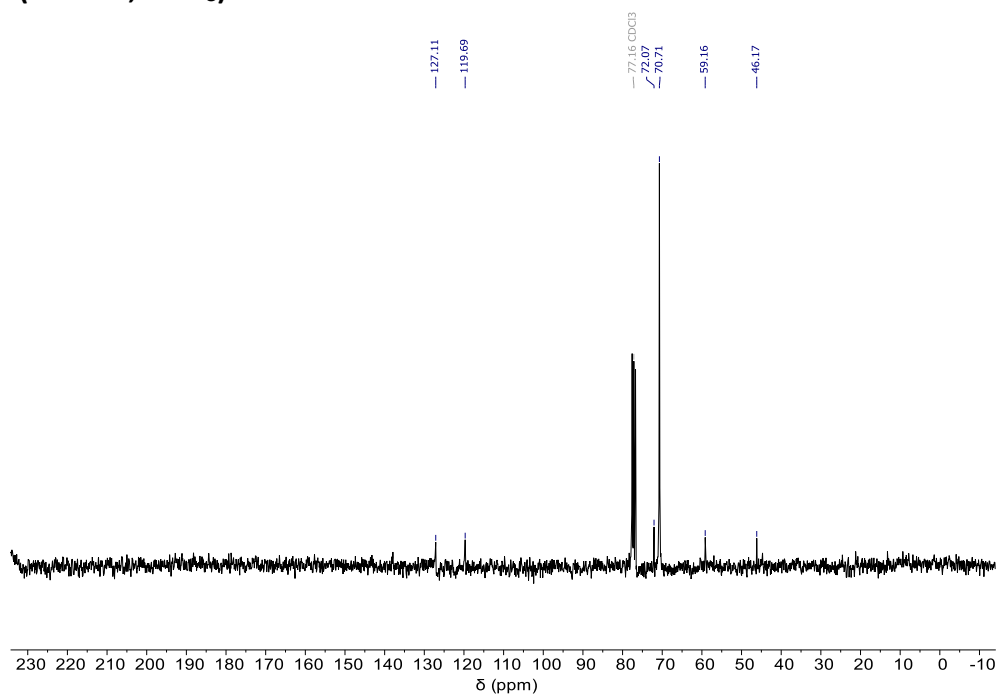


1-(3,6,9,12,15,18,21-Heptaodocosanyl)-2-methylimidazole (**4.2**)

^1H NMR (300 MHz, CDCl_3):

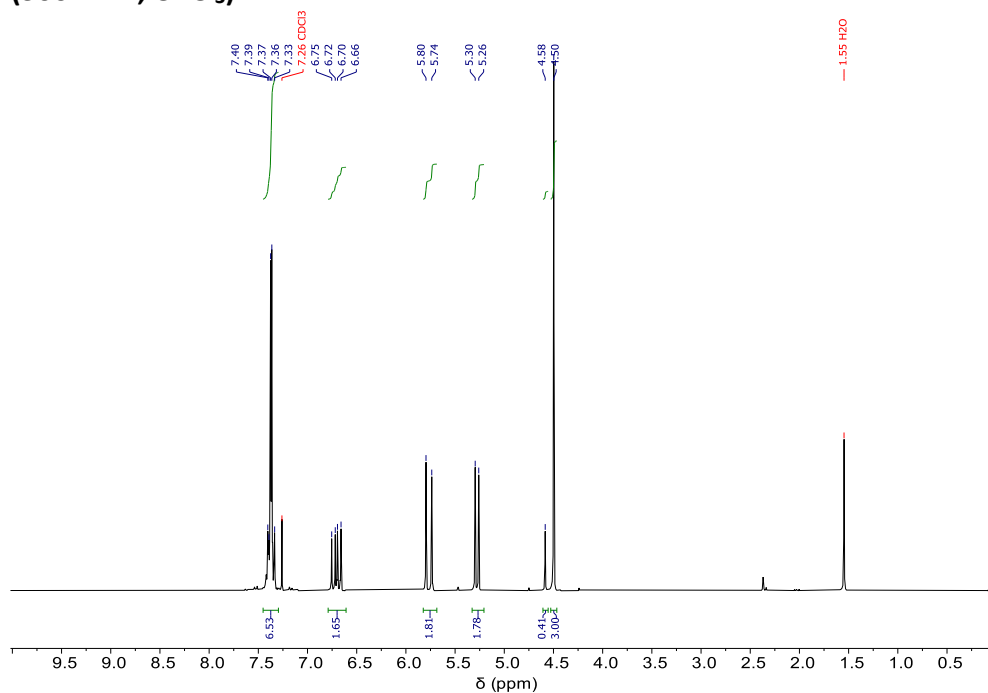


^{13}C NMR (75 MHz, CDCl_3):



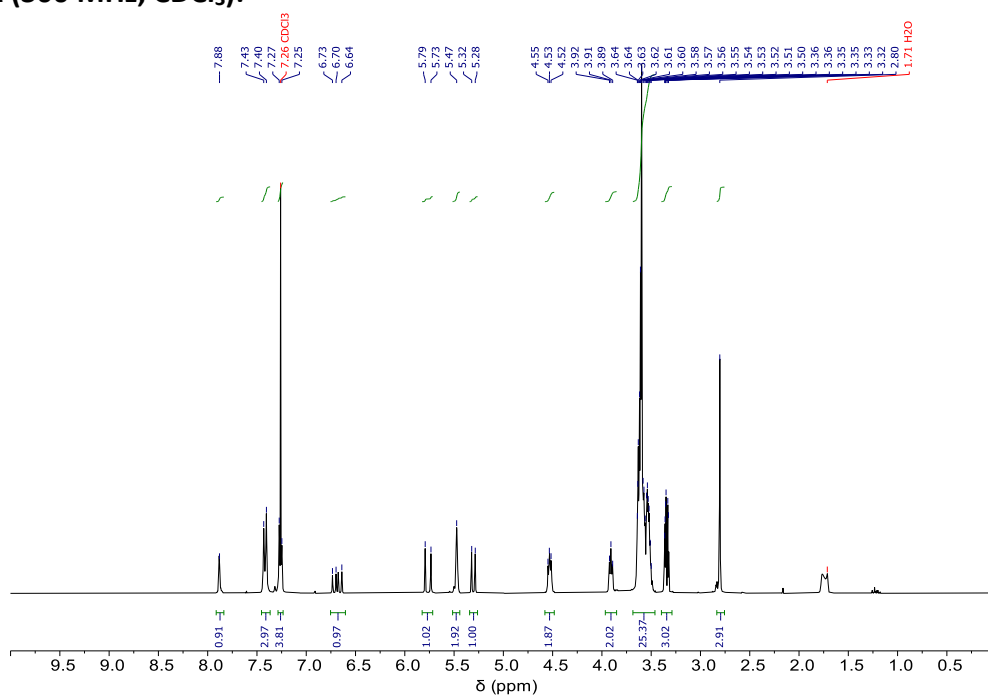
4-Bromomethylstyrene (**4.3**)

^1H NMR (300 MHz, CDCl_3):

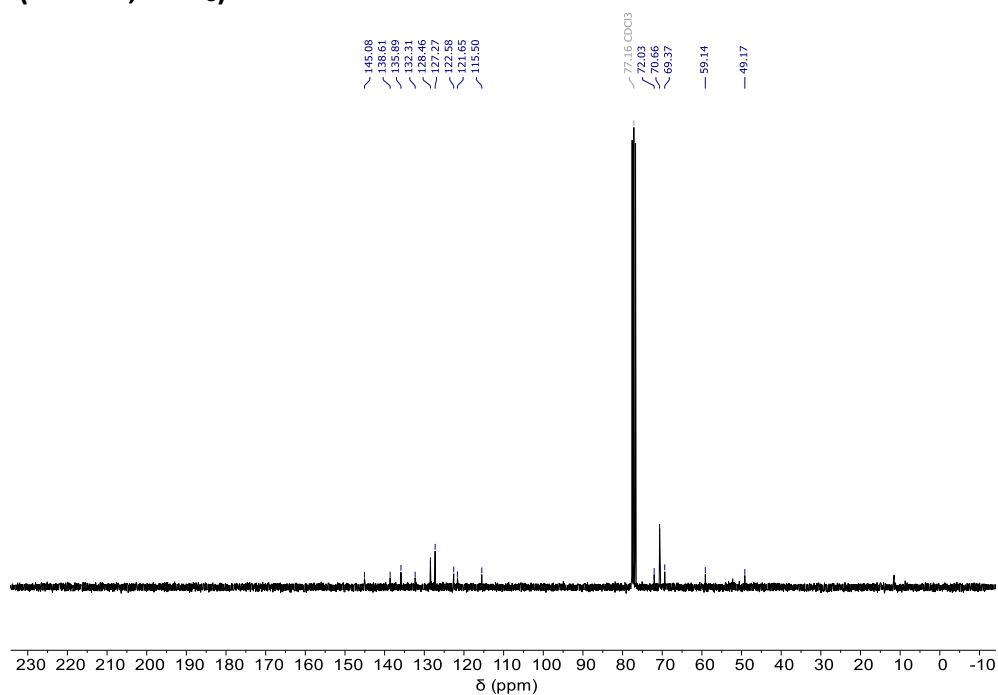


1-(3,6,9,12,15,18,21-Heptaaxadocosanyl)-2-methyl-3-(4-vinylphenyl)-imidazolium bromide (**4.4**)

^1H NMR (300 MHz, CDCl_3):

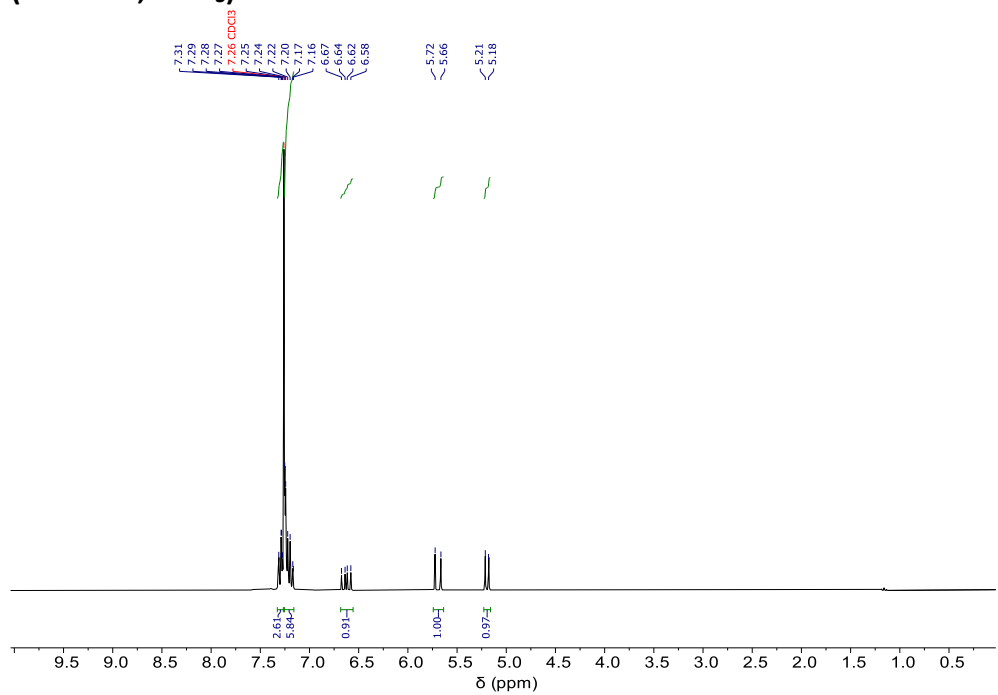


^{13}C NMR (75 MHz, CDCl_3):

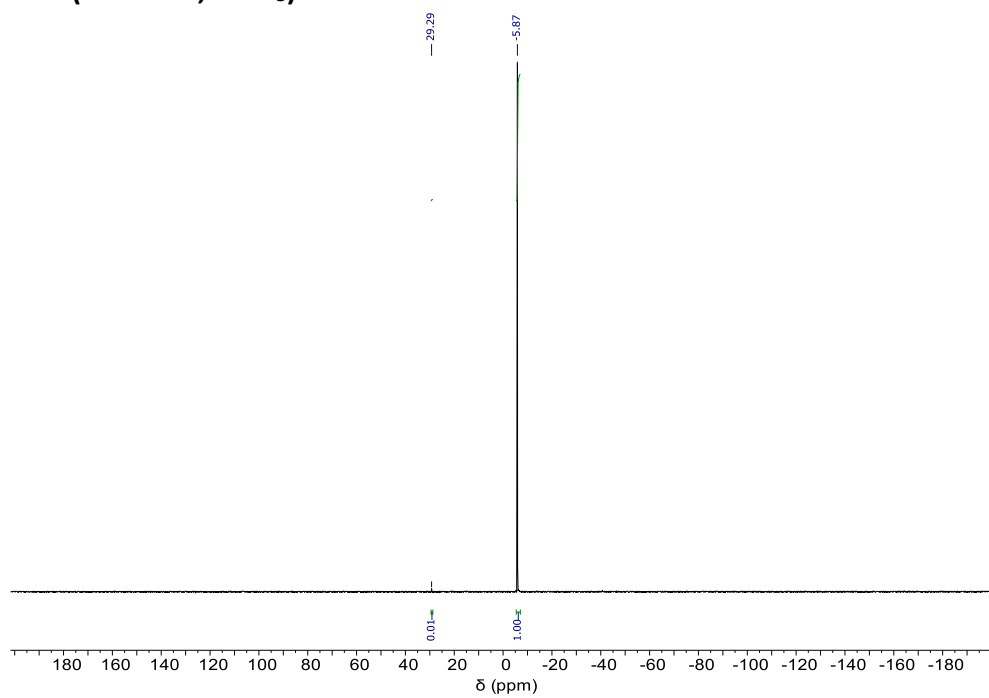


Diphenyl-(4-vinylphenyl)phosphine (4.5)

^1H NMR (300 MHz, CDCl_3):

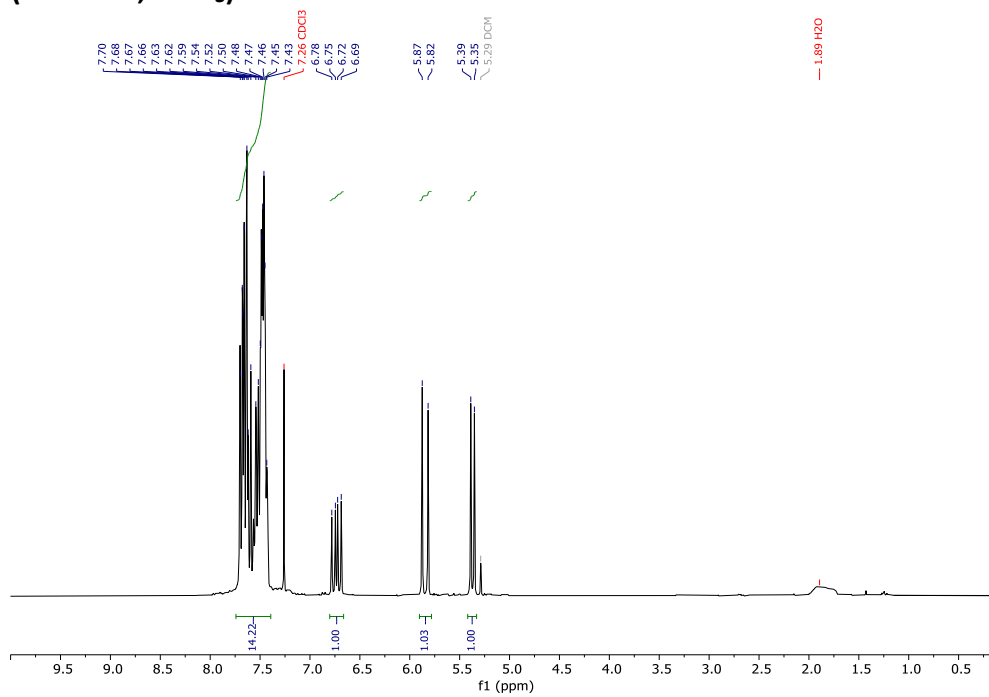


$^{31}\text{P}\{^1\text{H}\}$ NMR (121 MHz, CDCl_3)

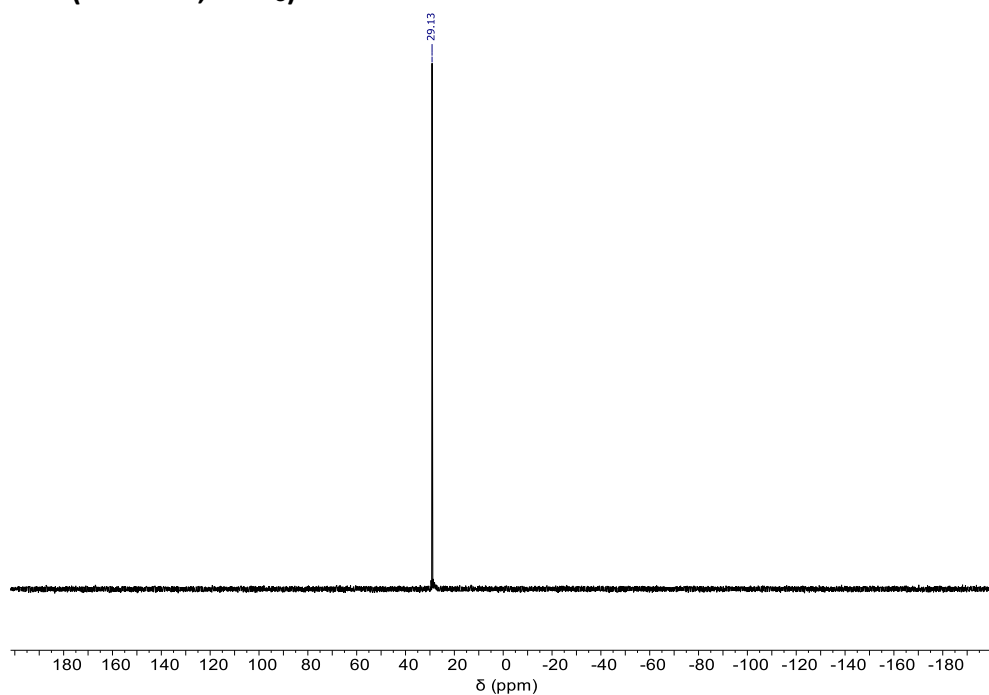


Diphenyl-(4-vinylphenyl)phosphine oxide (**4.6**)

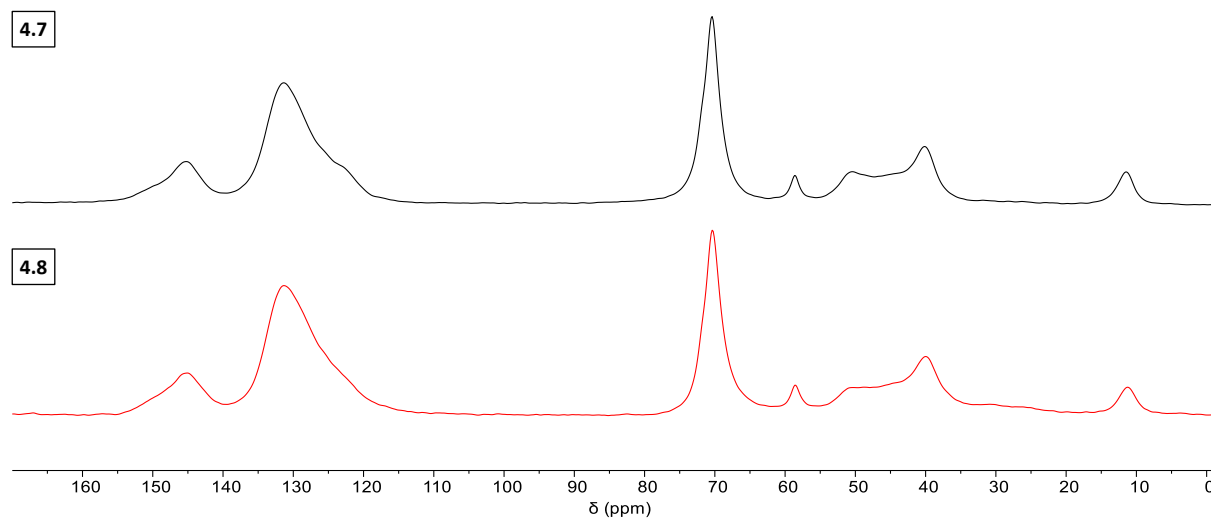
^1H NMR (300 MHz, CDCl_3):



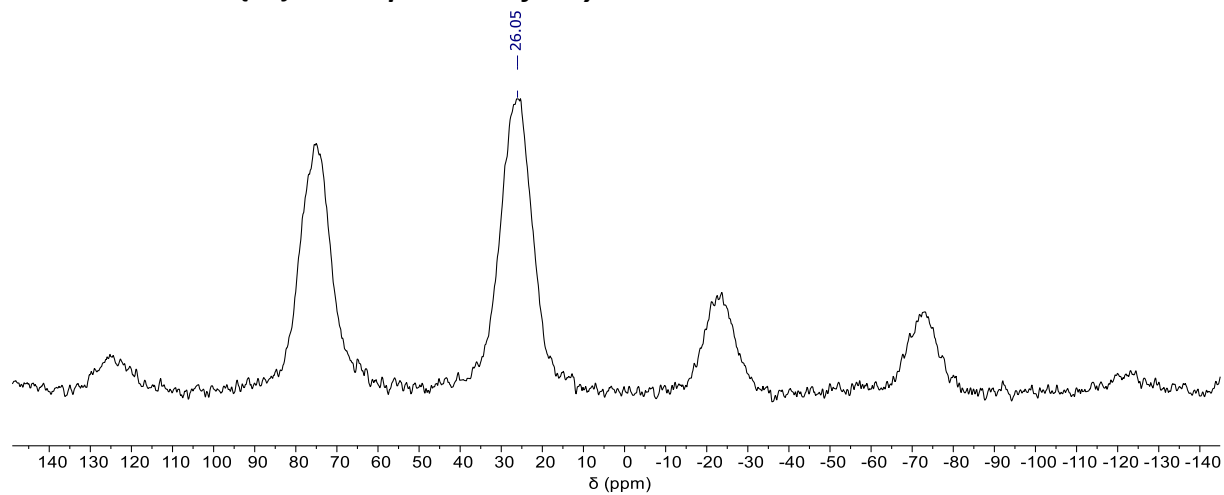
$^{31}\text{P}\{^1\text{H}\}$ NMR (121 MHz, CDCl_3)



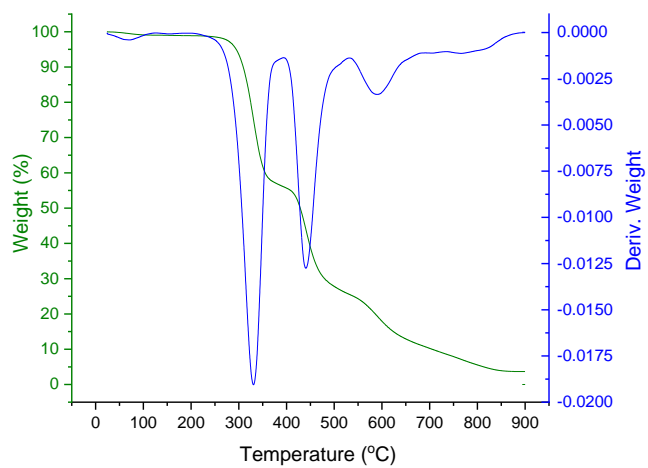
A.4.2 CP-MAS $^{13}\text{C}\{^1\text{H}\}$ NMR Spectrum of Polymer 4.7 and Catalyst 4.8



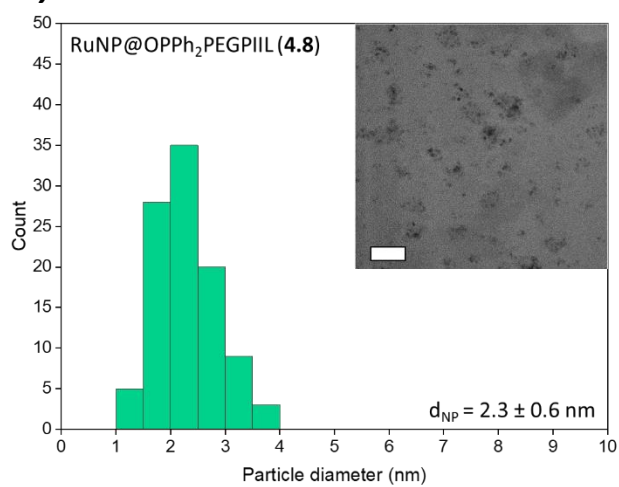
A.4.3 CP-MAS $^{31}\text{P}\{^1\text{H}\}$ NMR Spectrum of Polymer 4.7



A.4.4 Thermogravimetric Analysis of Polymer 4.7



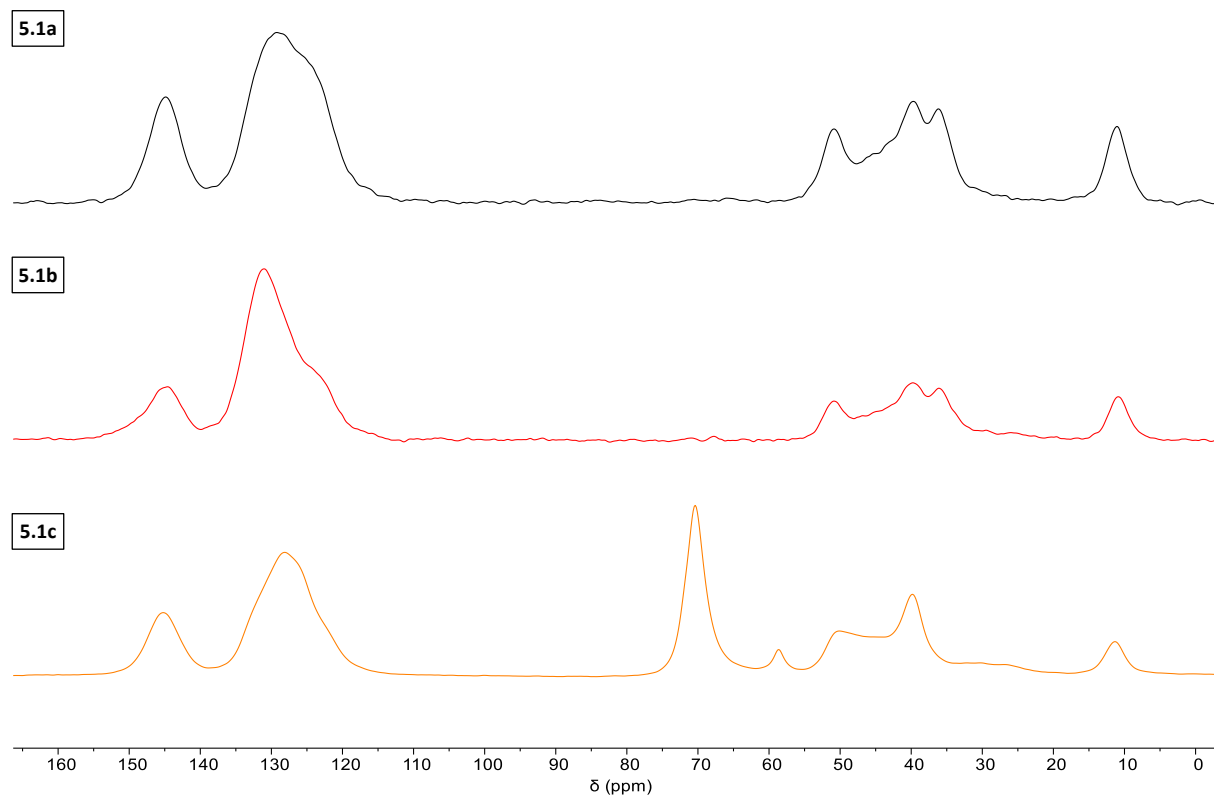
A.4.5 TEM of RuNP Catalyst 4.8



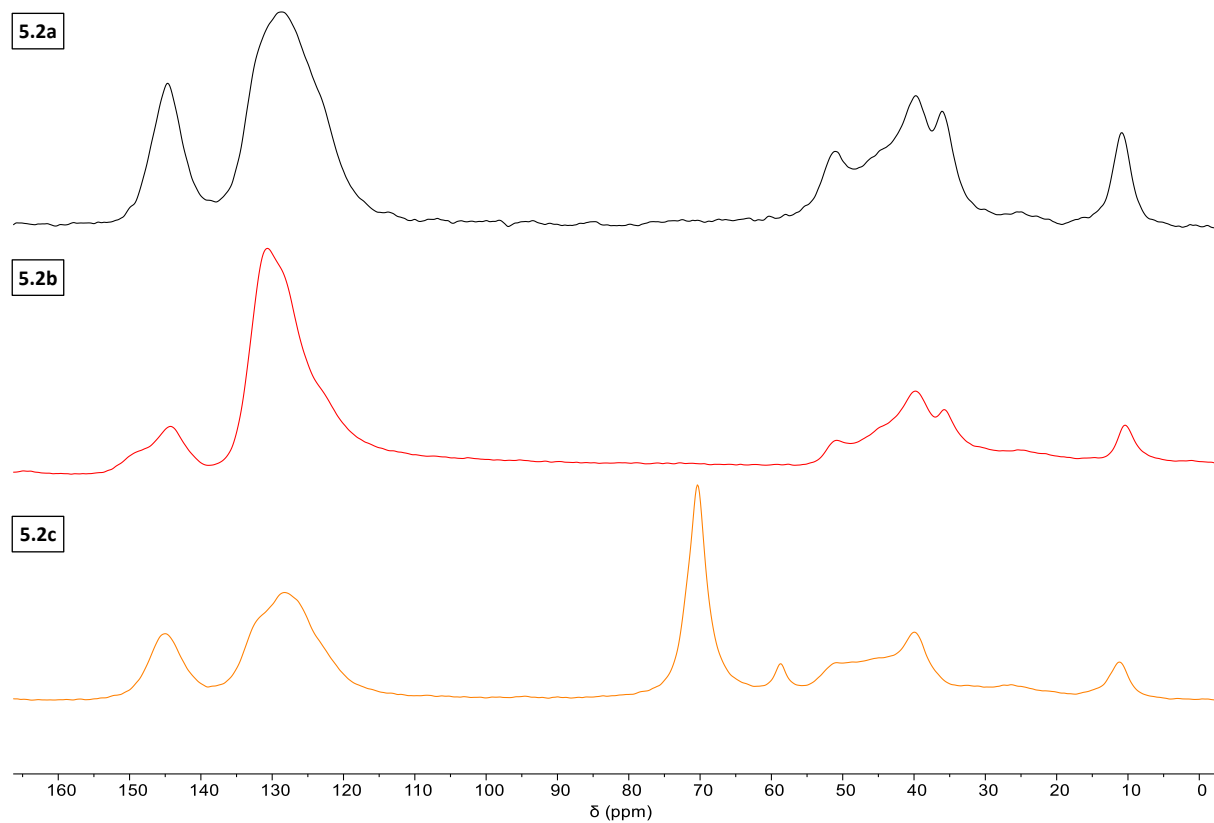
White scale bars = 20 nm

A.5 Chapter 5

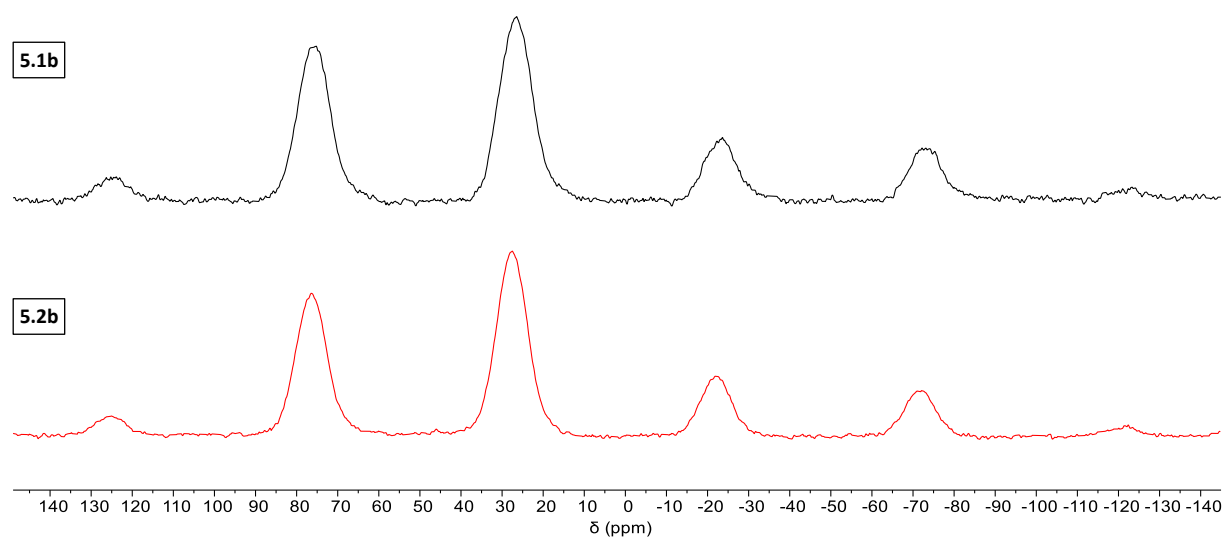
A.5.1 CP-MAS $^{13}\text{C}\{^1\text{H}\}$ NMR Spectrum of Polymer 5.1a-c



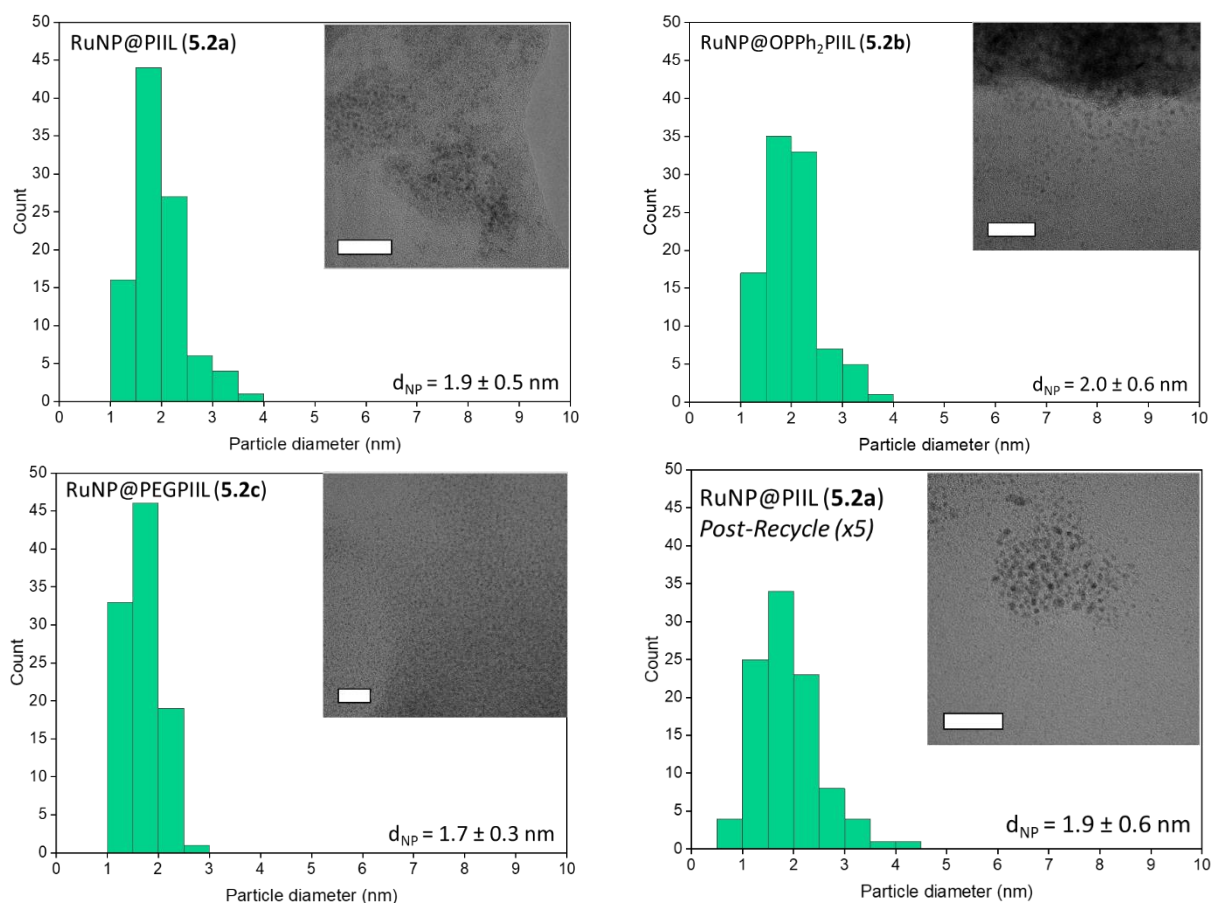
A.5.2 CP-MAS $^{13}\text{C}\{^1\text{H}\}$ NMR Spectrum of Polymer 5.2a-c



A.5.3 CP-MAS $^{31}\text{P}\{^1\text{H}\}$ NMR Spectrum of Polymer 5.1b and 5.2b

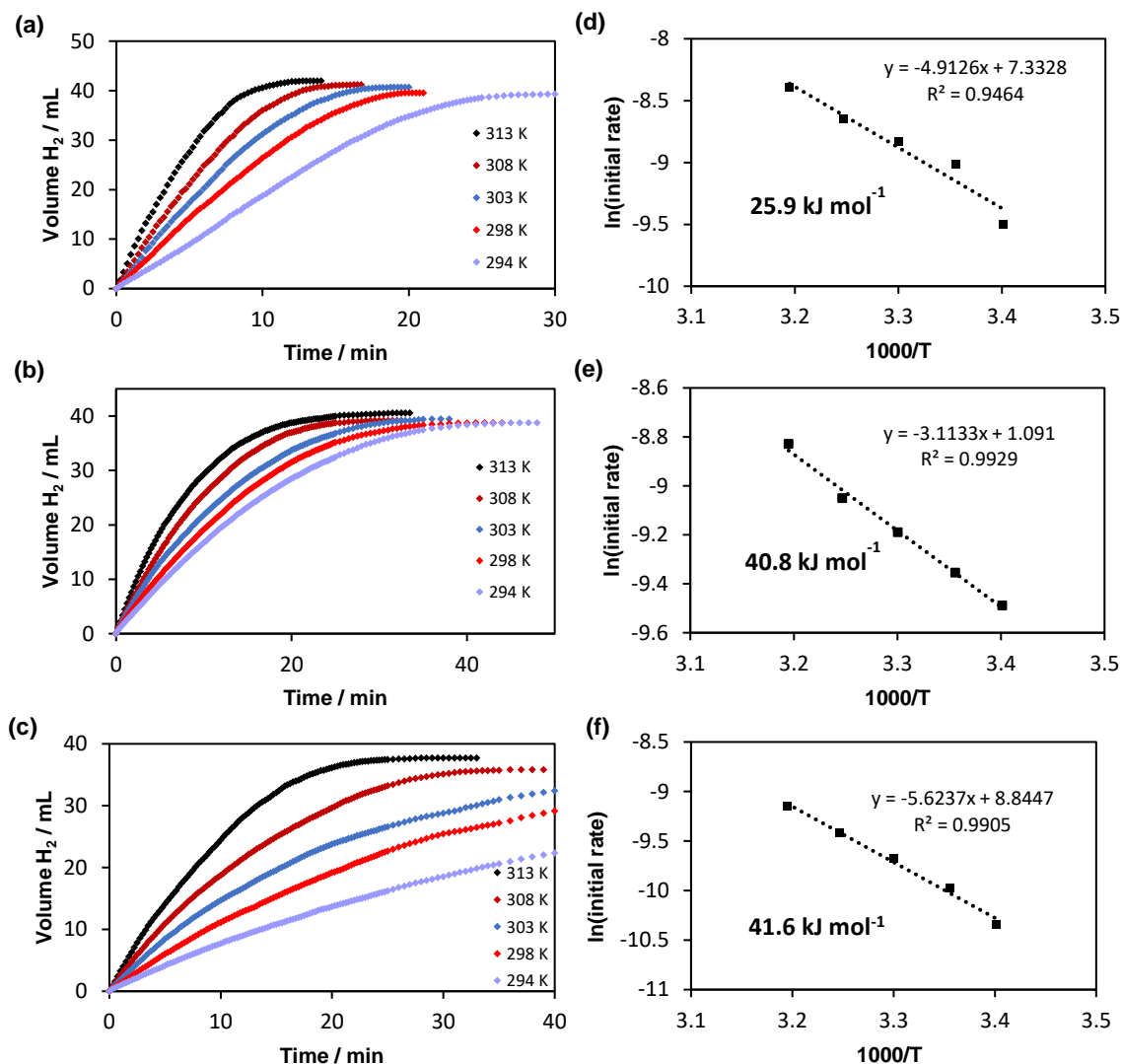


A.5.4 TEM of RuNP Samples



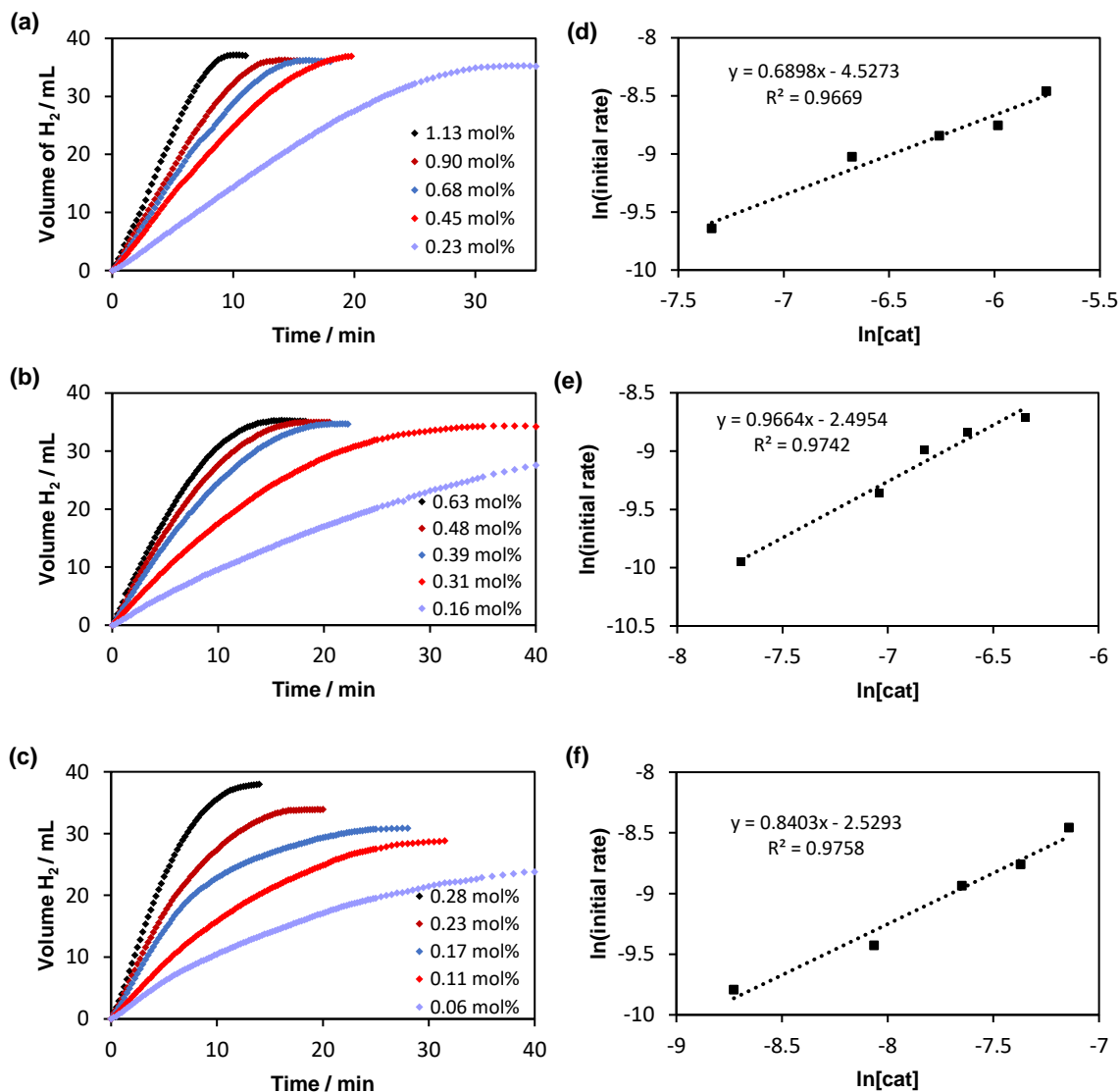
White scale bars = 20 nm

A.5.5 Determination of Activation Energies for Catalysts 5.2b-c and 4.8



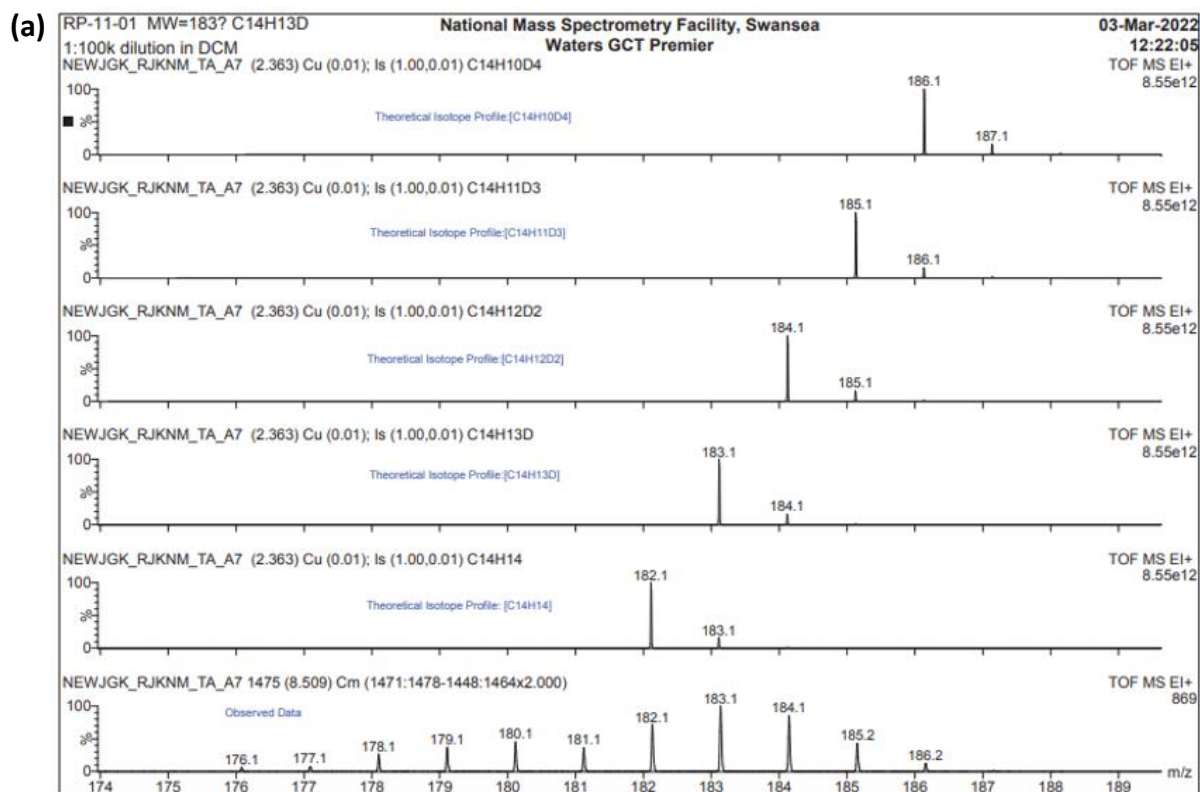
Plots of volume of hydrogen evolved against time at various temperatures catalysed by (a) 0.45 mol% **5.2b**, (b) 0.32 mol% **5.2c** and (d) 0.11 mol% **4.8**. Figures (d-f) show the corresponding Arrhenius plots, whereby the initial rates were determined from the linear portion of plots in Figures (a-c). Volumes measured are an average of three runs. Initial rate = $\text{mol}_{\text{H}_2} \cdot \text{min}^{-1}$

A.5.6 Determination of Reaction Order in Catalyst Concentration for 5.2b-c and 4.8



Plots of volume of hydrogen evolved against time for the hydrolysis of 2 mL of 0.28 M NaBH_4 at 294 K catalysed by various concentrations of (a) **5.2b**, (b) **5.2c**, (c) **4.8**. (d-f) Corresponding plots of the initial hydrogen generation rate against catalyst concentration in logarithmic scale, whereby the initial rates were determined from the linear portion of plots. Volumes measured are an average of three runs. Initial rate = $\text{mol}_{H_2} \cdot \text{min}^{-1}$

A.5.7 GC-TOF Mass Spectrum of Products Isolated from Tandem Hydrogenation Reaction



(b)

GC/MS NEWJGK_RJKNM			
m/z	Isotope	Intensity	% relative intensity
181	[¹² C ₁₄ ¹ H ₁₃]	314	10.4
182	[¹² C ₁₄ ¹ H ₁₄] and [¹³ C isotope of m/z 181]	618	20.5
183	Mix [¹² C ₁₄ ¹ H ₁₃ ² H ₁] and [¹³ C isotopes etc.]	869	28.8
184	Mix [¹² C ₁₄ ¹ H ₁₂ ² H ₂] and [¹³ C isotopes etc.]	741	24.5
185	Mix [¹² C ₁₄ ¹ H ₁₁ ² H ₃] and [¹³ C isotopes etc.]	374	12.4
186	Mix [¹² C ₁₄ ¹ H ₁₀ ² H ₄] and [¹³ C isotopes etc.]	105	3.5

(a) Theoretical and observed (bottom) GC-MS spectra for the products of the tandem hydrogenation reaction, conducted in D₂O, described in **Section 5.5**. Spectra were calibrated against an internal standard of perfluorotributylamine (FC43). (b) Relative intensities of the various isotopologues determined from the observed spectrum of the tandem hydrogenation reaction product(s).

